

BLDSC no:- DX 79985

LOUGHBOROUGH
UNIVERSITY OF TECHNOLOGY
LIBRARY

AUTHOR/FILING TITLE

WOOD, D J D

ACCESSION/COPY NO.

021008/02

VOL. NO.

CLASS MARK

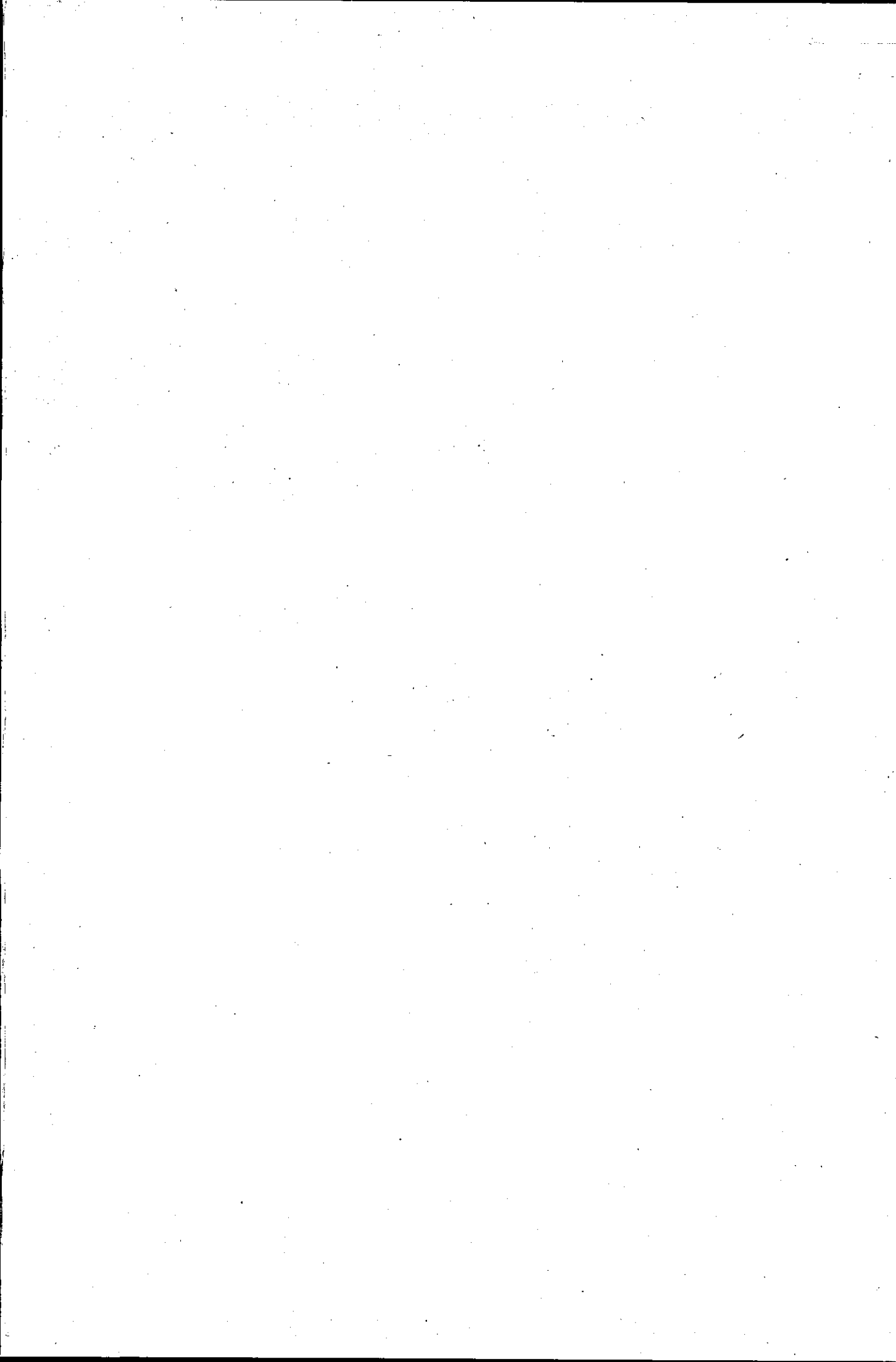
- 6 OCT 2000

LOAN COPY

LE 0021008027



THIS BOOK WAS BOUND BY
BADMINTON PRESS
18 THE HALF-CROFT
SYSTON
LEICESTER LE7 3LD
0533 60291



SOME ASPECTS OF THE HIGH-SPEED
ELECTRODEPOSITION OF METALS

by

David John Dudley Wood, BSc.

A Doctoral thesis submitted in partial
fulfilment of the requirements for the
award of Doctor of Philosophy of the
Loughborough University of Technology.

February 1988

Supervisor: Professor I.A.Menzies
Institute of Polymer Technology
and Materials Engineering

© by D.J.D.Wood, 1988

Loughborough University of Technology Library	
Date	AUG 88
Class	T
Acc. No.	021008/02

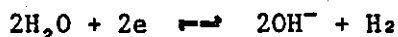
Abstract

The literature concerning the fast electrodeposition of metals has been reviewed with particular attention to the electrodeposition of nickel. A study of the electrodeposition of nickel has been carried out in concentrated Ni sulphamate solutions at 50-70°C in parallel plate cells at Reynolds numbers of up to 15,000. The cell design was substantiated by a preliminary study of the electrodeposition of copper. Additional studies have been made of current distribution in both the nickel and acid copper systems using segmented electrodes. Additional studies of mass transport have been made in the nickel system, as have polarisation studies.

It has been shown that in the case of acid copper the system performs under mass transport control and that the current distribution is as expected under these conditions. In the case of nickel it has not been possible to separate the nickel and hydrogen deposition processes electrochemically and an i_{\max} has been defined as the maximum current density attainable for the formation of foils 25 μm thick with sound fine grained structures and without addition agents. In Ni sulphamate solutions maximum current densities of 1.3 Acm^{-2} and $> 2.0 \text{Acm}^{-2}$, can be attained at 60°C and 70°C respectively. At 60°C, i_{\max} increases with increasing flow rate and in turbulent flow the following proportionalities are observed:

$L/d_e \leq 4.5$, i_{\max} is proportional to $\text{Re}^{0.66}$
and for $L/d_e \approx 11.7$, i_{\max} is proportional to $\text{Re}^{0.8}$

At 70°C, the relationship between these quantities is much less clear. Sound fine-grained electroforms are obtained under all flow and temperature conditions at current densities up to i_{\max} and current efficiencies are always $> 95\%$. The grain size of the foils decreases with increasing current density and the micro-hardness and brightness increases under conditions where the grain size is small. A uniform current distribution is achieved using a 10cm cathode and a 9cm anode and this is necessary to produce foils with uniform structure at high current densities and to avoid entry and exit effects. Detailed current distribution experiments indicated that the current distribution measured is typical of primary/secondary distribution and does not follow that expected for a true mass transport controlled process. Experimental evidence indicates that Ni is not deposited under simple mass transport control at current densities $\leq i_{\max}$, which is not a mass transport controlled limiting current density. Nickel hydroxide is precipitated at the cathode when the pH at the interface exceeds 6.6 and this results from the reduction of water by the reaction



It is the transport processes at the interface which control the interfacial pH, nickel hydroxide precipitation, and hence i_{\max} . The Ni deposition reaction is believed to be complex. There is experimental and modelling evidence that the effects of gas codeposition on mass transport can be explained if the gas bubbles are $< 0.1\mu\text{m}$ in diameter.

Dedicated to my parents
Albert and Kathleen Wood

ACKNOWLEDGEMENTS

The author would like to express his thanks and gratitude to the following:

Professor I.A.Menzies for his excellent guidance and support during the course of this project.

All the technical and support staff of the Department, in particular John Bates and Frank Page for their assistance with the electron microscopy, and Ken Ellison for his useful advice and careful construction of the flow cells.

My fellow students, Dr. David Ross and many others for stimulating discussions.

Ms.P.Denton for administrative assistance and numerous cups of coffee.

Mrs.Flitton for her patience and diligence in typing this thesis.

Drs.Kate Richmond, Dave Moore, Dave Eyre and Pat Lydon, Chris.G., Chris H., Ian, Naomi, Andy and many other good friends, regrettably too numerous to mention, for their continual support and encouragement.

Finally I would like to acknowledge the provision of financial support by the Ministry of Defence during the course of this project.

CONTENTS

Page No.

Chapter:

1. INTRODUCTION	1
2. REVIEW OF THE RELEVANT LITERATURE AND INTRODUCTION TO THE PRESENT WORK	4
2.1 Fundamental aspects of electrodeposition and factors which control deposition rates	5
2.2 Fast electrodeposition processes	19
2.3 Fundamental aspects of mass transfer and hydrodynamics in flowing electrolytes	39
2.4 Electrochemical and metallurgical aspects of the electrodeposition of nickel	71
Introduction to the present work	99
3. EXPERIMENTAL	101
3.1 Determination of the physical properties of the nickel based electrolytes and analytical methods for nickel based electrolytes	102
3.2 The design, construction and operation of the Mk 1 parallel plate cell and ancillary equipment	110
3.2.1 The design of the electrolytic cell and the flow system	110
3.2.2 Construction details of Cell 1 and the working electrode	118
3.3 The design, construction and operation of the Mk 2 parallel plate cell and ancillary equipment	125
3.3.1 The design of Cell 2 and the modified flow system	125
3.3.2 Construction details of Cell 2, the flow circuit and electrical circuit	129

<u>Chapter:</u>	<u>Page No.</u>
3.4 Mass transport and current distribution measurements in the acid copper sulphate electrolyte in the Mk2 parallel plate cell	133
3.4.1 Mass transport measurements	134
3.4.2 Current distribution measurements	139
3.5 Current distribution, electrode potential and mass transport measurements in the nickel sulphamate system	142
3.5.1 Current distribution measurements	142
3.5.2 The measurement of the electrode potential	144
3.5.3 Measurement of cathodic mass transfer coefficients - 'silver tracer' method	147
3.6 Post-deposition examination and measurements	151
4. RESULTS AND INTERPRETATION	154
4.1 Studies of the electroforming of nickel foils from concentrated Ni sulphamate solutions at 60°C in the Mk1 Parallel Plate Cell	155
4.1.1 Deposition under conditions of laminar flow (Re 400-650)	155
4.1.2 Deposition under conditions of turbulent flow (Re 2,300-13)	157
4.1.3 Summary of the results and discussion of the limitations of the cell design	170
4.2 Studies of the mass transport characteristics of the Mk2 Parallel Plate Cell and cathode current distribution distribution at segmented cathode using a $\text{CuSO}_4 - \text{H}_2\text{SO}_4$ electrolyte	172
4.2.1 Mass transport studies using the $\text{CuSO}_4 - \text{H}_2\text{SO}_4$ electrolyte	172
4.2.2 Cathode current distribution during the deposition of copper from the $\text{CuSO}_4 - \text{H}_2\text{SO}_4$ electrolyte	181

<u>Chapter:</u>	<u>Page No.</u>
4.3 Studies of the electroforming of nickel foils from concentrated Ni sulphamate solutions in the Mk 2 Parallel Plate Cell	185
4.3.1 The effect of cathode length during the electroforming of Ni foils at 60°C	185
4.3.2 The effects of temperature on the relationships between foil structures, flow rates and current densities using a long electrode system	204
4.4 Current distribution studies and polarisation measurements using the Mk 2 Parallel Plate Cell	220
4.4.1 Current distribution effects in the electroforming of nickel foils	220
4.4.2 Polarisation measurements in the electroforming of nickel foils	234
4.5 Mass transport studies in nickel sulphamate solutions at 60°C	245
4.5.1 Silver tracer studies of mass transport in nickel sulphamate solutions at 60°C	245
4.5.2 A model for predicting the mass transfer correlation for parallel plate cells with enhanced mass transfer due to concomitant gas evolution	251
Overview of the results	261
5. DISCUSSION	263
5.1 Mass transport studies	264
a) Copper sulphate system	
b) Nickel sulphamate system	
5.2 Current distribution studies	280
a) Copper sulphate system	
b) Nickel sulphamate system	
5.3 Polarisation studies in nickel sulphamate electrolytes	289
a) Anodic polarisation	
b) Cathodic polarisation	

Chapter:

Page No.

5.4	The nature of the nickel deposit	299
5.5	General and practical implications for the fast-rate electrodeposition from sulphamate solutions	304
6.	CONCLUSIONS AND SUGGESTIONS FOR FURTHER WORK	308
	References	313

Appendices:

1. Notation
2. Additional factors relating to cell and flow circuit design
3. Calculation of microhardness values and optimum indenter load
4. Additional measurements relating to the electroforming of nickel in Cell 2.

1. INTRODUCTION

From the earliest days of commercial electroplating, considerable effort has been applied to developing electrolytes which would allow faster deposition rates. However, acceptable deposit appearance and properties must be maintained at the higher current densities. This is of particular importance in electroforming, where the metal (commonly nickel or copper) is deposited on a conducting mandrel, which is later removed leaving the electrodeposited metal in the form of a foil or hollow article. The electroform may be several hundred microns thick. In this case, a rapid deposition rate is particularly advantageous in reducing processing time and costs. A very low-stressed deposit is essential to avoid distortion of the electroform.

The introduction of the 'low concentration' nickel sulphamate bath in the 1950's represented a significant advance in nickel electroforming solutions. This culminated in the development of the Ni-Speed or 'concentrated' nickel sulphamate bath(1) from which nickel may be electroformed at deposition rates of up to $\sim 0.3A\text{ cm}^{-2}$. The solution produces deposits of inherently low internal stress.

At high current densities the maximum current density for a good deposit may be dependent on the rate at which the reactant is supplied to the electrode (mass transfer control). For most commercial electrodeposition processes, agitation of the electrolyte (and/or movement of the electrode) is considered necessary to ensure a continued supply of metal ions to the workpiece.

In conventional nickel plating baths, agitation is often achieved by pumping air through the solution. However this type of agitation is inefficient and difficult to quantify and relate to the deposit morphology.

Several other agitation methods, which produce well-defined hydrodynamic conditions, are available e.g. flowing solutions, rotating systems etc. Metal deposition reactions have been investigated using several of these systems. However relatively few studies have used concentrated commercial-type electrolytes to assess the effect of solution

agitation on the deposition rate and the nature of the deposit. No detailed attempt has been made to relate the precise mass transfer conditions to the growth morphology of electroformed nickel foils. Similarly no attempt has been made to define the practical maximum current density.

In the present work a flowing electrolyte was chosen to provide a reproducible hydrodynamic environment, since this avoids the limited commercial applicability of rotating electrode systems.

The use of flow cells for high speed electrodeposition studies has been reported by industrial research organisations but few details have been given. There is a complete lack of precise experimental and design information. No detailed fundamental information is available and few, if any, such studies have been made. High speed deposition from a flowing concentrated nickel sulphamate bath has not been investigated previously.

The work to be described here involves detailed studies of nickel deposition from flowing concentrated nickel sulphamate solutions. Two parallel plate flow cells and the supporting systems were designed and constructed. The cell designs were based on sound hydrodynamic and mass transfer principles. Cell 1 was used for the initial investigation. As will be seen, from the experience gained using Cell 1, it was necessary to design and construct a second cell (Cell 2) for the main investigations. The mass transfer characteristics of Cell 2 were verified by the study of copper deposition, from dilute acid solution, where more background information is available.

Nickel was electroformed from the concentrated nickel sulphamate bath over the temperature range 50° - 70°C. The main objectives of this work were as follows:

- i) The maximum practical current density was to be defined and correlated with the solution hydrodynamics
- ii) A detailed study of the morphology of electroformed nickel foils as a function of flow rate and current density was to be carried out at 60 and 70°C.

As will be seen, a further series of diagnostic experiments was also necessary. This included studies of polarisation and current distribution and some additional mass transfer measurements. The relevant literature is reviewed in depth in Chapter 2 and this is followed by a detailed account of the design of the cells and other experimental details. For clarity the results are presented with full interpretation. Finally the results are discussed in relation to current knowledge in the field.

2. REVIEW OF THE RELEVANT LITERATURE AND INTRODUCTION TO THE PRESENT WORK

This review is divided into three main sections. The first of these deals with the fundamental aspects of the electrodeposition of metals and the factors which control the rates of the electrodeposition processes. As will be seen fast rates of deposition are favoured by high metal ion concentration in solution, high deposition temperatures and intense agitation. This leads to a review of the various cell and electrode geometries which have been used to establish well defined and reproducible hydrodynamic regimes for the investigation of electrode processes and fast electrodeposition. The review covers flow cell systems, rotating electrodes, particle bed, ultrasonics, and other techniques such as jet plating. From this it will become clear that flowing electrolytes in parallel plate cells have much to offer for conjoint studies of mass transport and electrodeposited foil morphology.

The second part of the review deals, in detail, with the fundamental aspects of mass transfer and hydrodynamics in flowing electrolytes and mass transfer in parallel plate cells. As will be seen later there is always some gas codeposition during the electrodeposition of nickel foils at high current densities, and, for completeness the formation of gas bubbles at electrodes and mass transport at gas evolving electrodes are discussed here.

The final section is concerned with the electrodeposition of nickel. This includes the chemistry and electrochemistry of nickel plating solutions, and the structure of nickel electrodeposits. From this it will become clear that concentrated nickel sulphamate solutions have considerable promise for the fast electrodeposition of nickel although there is no information concerning the use of flowing electrolytes or the nature of foils electroformed under these conditions.

Finally there is an introduction to the present experimental programme and its objectives.

2.1 Fundamental aspects of electrodeposition and factors which control deposition rates

The first part deals with electrochemical aspects and briefly with deposit growth. Because of the particular interest in fast electrodeposition the factors affecting deposition rates are discussed separately.

a) Electrodeposition processes

The fundamental aspects of electrodeposition have been covered in detail in many standard texts (e.g. 2-6). The following section summarises some of the basic background theory of electrodeposition.

Electrochemical aspects of electrodeposition

When a metal is immersed in an aqueous electrolyte, the metal M dissolves to form aquo ions $M^{z+} \cdot xH_2O$ in solution. At the electrode electrolyte interface there occurs an increasing separation of electric charge as shown schematically in Fig.2.1. Any such system is termed an 'electrode'. The charges tend to line up opposite one another, like a capacitor. However, the structure may be very complex. The system of charges is termed the Helmholtz double layer.

Metal dissolution continues until the adverse electric field strength results in the number of ions dissolving is exactly balanced by the number of metal atoms depositing and a dynamic equilibrium has been set up.

When a metal (M) is immersed in an aqueous solution of its own ions (M^{z+}) it attains a specific electrical potential which is characteristic of that particular metal and the concentration (or more specifically the activity, a^{z+}) of metal ions. If the system is at a dynamic equilibrium and reversible (e.g. Cu/Cu^{2+}), the potential (E) is given by the Nernst equation:

$$E = E^0_{M^{z+}/M} + \frac{RT}{zF} \ln a_{M^{z+}} \quad \dots \dots (2.1)$$

where $R =$ the gas constant = $8.315 \text{ J}^\circ\text{C}^{-1} \text{ mol}^{-1}$

$F =$ the Faraday constant = $96,486 \text{ C}$

and E^0 is the standard reversible electrode potential for the system

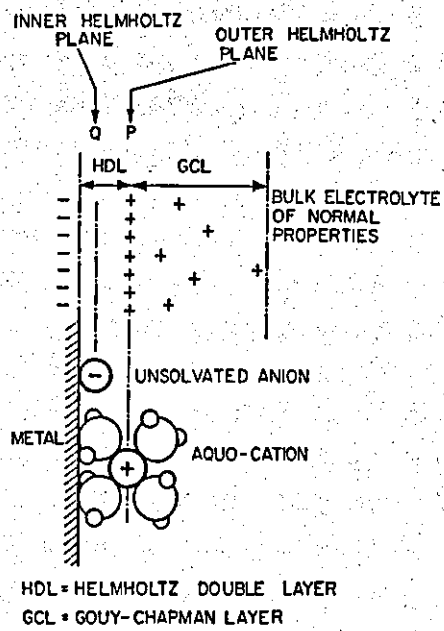


Fig.2.1 The structure of the electrical double layer

However, metals such as nickel, iron, chromium etc. when immersed in solutions of their ions do not give reversible systems. The potentials of these systems may be governed by other processes such as other electrode reactions, corrosion, etc.

It should be noted that the Nernst equation is only applicable to reactions at equilibrium, since it is based upon thermodynamic considerations (since $\Delta G = -EzF$). Catalytic effects, kinetic processes, overvoltages, reaction inhibitions etc. can greatly alter the behaviour of an electrode from that expected on the basis of the Nernst equation. The processes permitted by the Nernst equation may or may not take place, but processes forbidden by the Nernst equation certainly cannot occur.

When two electrodes are immersed in an electrolyte (a conducting solution of a salt, an acid or a base) and one connected to a d.c. source, a current flows through the solution, at a certain minimum voltage, and reactions occur at the electrodes.

In the case of metal deposition the electrodes are (usually) both metallic and the electrolyte is a solution containing metal ions. The solvent is usually water, although some conducting non-aqueous solvents or molten salts may be used. At the cathode (-tive pole), the metal ions are reduced and the metal is deposited. However, other reactions may also take place (e.g. the reduction of hydrogen ions to gaseous hydrogen) at the cathode. The anodes may be 'active' and of the same metal as that deposited, in which case metal dissolution is the principal reaction and the metal ion concentration of the electrolyte tends to be maintained. However other oxidation reactions may also occur, resulting in a decrease in the dissolution efficiency. When 'inert' anodes are used other oxidation processes occur e.g. oxygen or chlorine evolution.

The metal ions may be present either as cations, simple or complex, or as anionic complexes (e.g. $[\text{Cu}(\text{CN})_2]^{2-}$). Under the influence of the electric field, the ions in the electrolyte migrate towards the electrodes. However it should be noted that the ions responsible for electrolytic current conduction may not necessarily be those which take part in the electrode reactions.

The relationship between the current and the quantities of substances converted in electrolysis is given by the Faraday laws. These are of fundamental importance for electroplating technology.

Faradays first law: The quantity G of any substance converted when a current I passes in time t through an electrolyte is proportional to the quantity of electricity $It = Q$:

$$G = E_{el} Q \quad \dots \dots (2.2)$$

The constant E_{el} is termed the electrochemical equivalent and is the quantity of a substance converted by 1 As (= 1 coulomb).

Faradays second law: The electrochemical equivalents E_{el} are proportional to the chemical equivalent weights E_{chem} :

$$E_{el} F = E_{chem} \quad \dots \dots (2.3)$$

The constant F is termed the Faraday constant and $F = 96,494.5 \pm 1.5C$. One Faraday is the quantity of electricity required for the conversion of 1 gram-equivalent of any substance.

In electrodeposition, the Faraday laws are used to calculate the current efficiency, coating thickness, deposition time and current density as will be shown later (p.128).

In electrodeposition, the current efficiency is defined as the percentage of the total current usefully used for the cathodic deposition or anodic dissolution of the metal:

$$C.E. = \frac{G_{practical}}{G_{theoretical}} \times 100 \quad \dots \dots (2.4)$$

It is 100% when as much metal is deposited or dissolved, respectively as would be expected on the basis of Faraday's law. At a current efficiency under 100% the remainder of the current is used in secondary reactions e.g. the co-deposition of hydrogen at the cathode.

When a metal electrode is in dynamic equilibrium (at the reversible electrode potential), the partial currents \vec{i} (anodic dissolution) and

i (cathodic deposition) are precisely equal and opposite and no net reaction occurs. The currents produced are termed exchange currents (i_0). When an electrode process occurs at an electrode, its potential departs from its equilibrium value and the electrode is said to be polarised. The cathode becomes more negative and the anode becomes more positive. The potential difference between the equilibrium potential and the potential of a polarised electrode is termed the overpotential (η).

For electrodeposition to occur, the cathode potential must be negative to the reversible electrode potential of the depositing metal in the electrolyte as predicted by the Nernst equation.

In practice, the potential at which a metal ion discharges may vary greatly from the standard electrode potential, depending upon the concentration of metal ions, their degree of complexation and kinetic limitations. This potential difference is termed the overvoltage. For a reversible electrode system (e.g. Cu/Cu^{2+}), deposition occurs when the potential is made slightly less negative than the equilibrium value, while hydrogen is discharged irreversibly on copper at considerably more negative potentials. The existence of an appreciable overvoltage for the discharge of hydrogen on a nickel electrode enables nickel to be deposited from nickel sulphate solution at high efficiencies, even though the reduction of nickel ions to metal is also an irreversible process.

There are three components in the overall reaction polarisation. These are the activation overpotential, concentration overpotential and ohmic overpotential. The general form of the overpotential/current density relationship is shown in Fig.2.2.

Activation Overpotential The activation overpotential is the potential required for the reacting ion to overcome the energy barrier at the double layer, before that ion is discharged from solution. The activation overpotential associated with the deposition of transition metals such as iron and nickel, is large but is much smaller for other metals such as silver and copper.

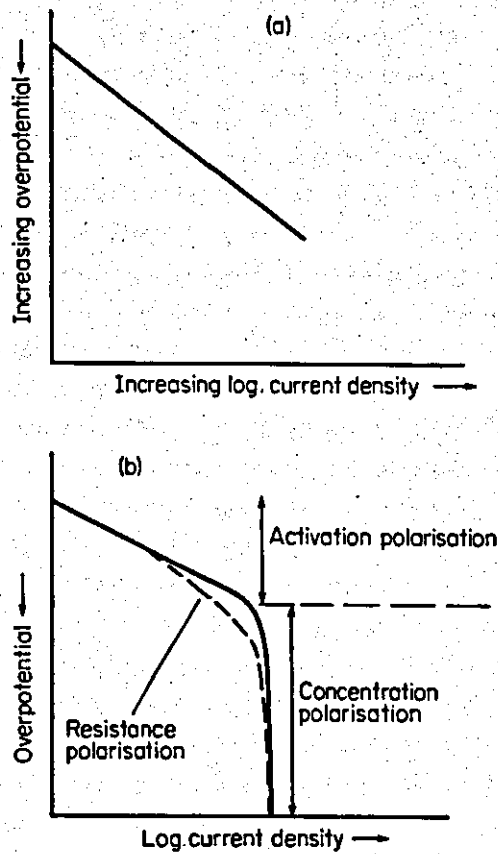


Fig.2.2 Current-potential relationships as the cathode is polarised to increasingly negative potentials. (a) At low overpotentials, electrode subject only to activation polarisation and Tafel behaviour is observed. (b) At high overpotentials, current reaches a limiting value due to concentration polarisation with current density for a given overpotential being reduced by resistance effects in solution, that is resistance polarisation is found in poorly conducting electrolytes.

The variation of current density with potential for cathodic activation polarisation, may be described by the Butler-Volmer equation:

$$i = i_0 \left\{ \exp \left(\frac{-\alpha z F \eta}{RT} \right) - \exp \left(\frac{(1-\alpha) z F \eta}{RT} \right) \right\} \dots \dots (2.5)$$

where α is a transfer coefficient.

The above equation can be simplified in two cases. For overpotentials much less than 0.03V, the current density is a linear function of current density and for a cathodic reaction

$$i = \frac{-i_0 z F \eta}{RT} \dots \dots (2.6)$$

For a given overpotential therefore a greater current flows when a reaction has a higher exchange current density. Hence a reversible electrode process can sustain a large current in either direction with little deviation of the potential from the equilibrium value.

For appreciable cathodic polarisation ($\eta > 0.03V$) the reverse reaction is almost entirely suppressed and the second exponential term is very nearly zero. Consequently equation (2.5) reduces to:

$$i = i_0 \exp \left(\frac{-\alpha z F \eta}{RT} \right) \dots \dots (2.7)$$

which may be expressed in the form

$$\eta^a = \frac{RT}{\alpha z F} \ln i_0 - \frac{RT}{\alpha z F} \ln i \dots \dots (2.8)$$

Similar equations were first obtained experimentally by Tafel and take the form:

$$\eta^a = a + b \log i \dots \dots (2.9)$$

where the 'Tafel constants' a and b are given by

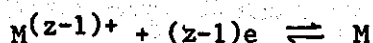
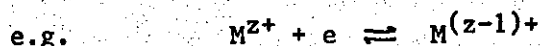
$$a = -\left(\frac{RT}{\alpha z F} \right) \ln i_0$$

$$b = -2.303 \frac{RT}{\alpha z F} \text{ for a cathodic reaction, and}$$

$$a = (RT/(1-\alpha)zF) \ln i_0$$

$$b = 2.303 RT/(1-\alpha) zF \text{ for an anodic reaction}$$

Metal deposition reactions rarely occur in a single step as may be indicated by the stoichiometric reaction scheme eg. $M^{z+} + Ze \rightleftharpoons M$ but electrons may be transferred in several steps:



In addition other processes, not involving electron (charge) transfers, e.g. hydration or dehydration of the ion, diffusion processes, crystal building processes etc. may be taking place. Therefore for a given overall reaction a sequence of mechanistic steps (a reaction path) are involved in the deposition process. At a given potential, one of these steps will be the slowest (the rate determining step) and will control the overall rate of the reaction. As a result, the number of unit charges transferred through the double layer each time the rate determining step occurs once may well be different from that (z) expected from the simple stoichiometric equation. Hence analysis of polarisation curves (overpotential/current density relationships) may be used to determine mechanistic information about an electrode process.

Concentration overpotential When the potential is made more negative, the potential/log current density relationship departs from the linear Tafel behaviour and the current density increases until it reaches a limiting value - the limiting current density (Fig.2.2). At the limiting current density (i_L) the rate of metal deposition is so rapid, that the metal ion concentration at the electrode/electrolyte interface is reduced to zero. A diffusion layer is built up where the concentration of metal ions varies from zero on the metal side of this layer to the bulk value on the solution side and the reaction is said to be diffusion or mass transport controlled.

The concentration differences across the diffusion layer give rise to the concentration overpotential (η^c) which is given by:

$$\eta^c = \frac{RT}{zF} \ln \frac{c_s}{c_b} = \frac{RT}{zF} \ln \left(1 - \frac{i}{i_L}\right)$$

where c_s and c_b are respectively the surface and bulk concentration of metal ions. This equation applies when the potential determining ions are the diffusing ions and the absence of significant migration of the reacting species in the electric field. The equation indicates that as i approaches i_L , theoretically the overpotential becomes infinite. However, in a real process i never equals the theoretical value of i_L and the potential reaches a value at which a secondary reaction occurs. In the case of metal deposition this is normally hydrogen evolution.

The rate at which ions are transported through a diffusion layer of thickness δ is given by

$$\frac{i}{zF} = \frac{D(c_b - c_s)}{\delta} \quad \dots \dots (2.10)$$

The value of δ is a function of the degree of 'stirring' of the solution. At the limiting current density when $c_s \rightarrow 0$

$$i_L = \frac{zF D c_b}{\delta} \quad \dots \dots (2.11)$$

The above equations and their derivation are dealt with more rigourously in Section 2.3. At this point it is important to note that this represents a simplified approach to mass transport.

Ohmic Overpotential Ohmic overpotential (η^o) arises mainly from two sources. In the first case, the presence of ionically-conducting films on the electrode levels to additional polarisation effects due to their higher electrical resistivity.

The second case arises from the comparatively low conductivity of the electrolyte affecting the measurement of the electrode potential. The potential of the electrode is normally measured versus a reversible half-cell (such as the Hg/Hg₂Cl₂/KCl or calomel electrode) using a

potential probe known as a Luggin-capillary positioned close to the electrode. However the probe must always measure the potential in the solution at a finite distance from the electrode surface. Therefore, particularly at high current densities and low conductivity electrolytes, some component of the measured potential will include a contribution from the iR drop in the main bulk of the solution due to the passage of the electrolysis current.

The total measured overpotential at a metal electrode is therefore the sum of all the components:

$$\text{Total } \eta = \eta^a + \eta^c + \eta^o$$

In electrodeposition reactions, the concentration overpotential is considered of some importance and as will be seen in the following sections, plating baths are usually agitated to reduce or eliminate the effects associated with it.

The electrodeposition process

As previously stated, an energy barrier exists at the electrode/electrolyte interface, which must be overcome prior to charge transfer. It can be shown (7) that there is a very small rate of classical emission over the energy barrier for electrons at an electrode. There must therefore, be tunnel transfers of the electrons from metal to solution. A fundamental condition for radiationless transfer of an electron through the energy barrier is that the energy of the electron in the metal is equal to the energy of the receptor state at the solution side of the barrier. Detailed calculation (7) has shown that it is the frequency of occurrence of the receptor states which determines the rate of transfer of the electron through the barrier to the solvated ion in solution.

In simple salt solutions, cations are present in the bulk solution as hydrated ions having the same oxidation state as the free ion. Consequently, before the cation is discharged there must be a preliminary dehydration. This process occurs in the double layer, where the high field strength results in alignment of the hydrating water molecules with the field and distortion of the electron orbitals.

The main energetic parameters which determine the probability of arrival of a solvated ion in the double layer to a configuration sufficiently stretched so that it has a suitable energy to act as a receptor state for electron tunnelling are:

- a) the ionisation energy of the atom concerned,
- b) the repulsion energy between the atom on the surface and the water molecules in the double layer,
- c) the heat of sublimation of the metal, and
- d) the solvation energy of the gaseous ion.

In the case of metal deposition, it is apparent that the center of the positive ion is several angstroms out into the solution when the interfacial charge transfer process occurs. However inside the metal (for metals such as silver, where an electron gas model is applicable for the bulk structure), it is still an ion and only an extra electron, not directly associated with it is 'inside the metal'. At this point the metal ion is only partially neutralised and still retains all or part of its hydration sheath which tends to stabilise the ion. The metal ion is adsorbed on the cathode surface (an ad-ion) at the original point of contact. (The ad-ion model is favoured over the ad-atom model, since less energy is required to form an ad-ion).

Initial transfer of the ion occurs at a planar site, where distortion of the hydration sheath is at a minimum (8). The ad-ion is incorporated into the crystal lattice before being finally neutralised. Incorporation occurs preferentially at edge sites and the ad-ions tend to diffuse across the metal surface to such sites.

The mechanism of electrocrystallisation may be influenced by the presence of impurities or specific additives to the solution. These may tend to adsorb or be preferentially incorporated at 'active' sites and hence sites of a lower co-ordination number may be energetically favoured.

Growth of electrodeposits

Crystal growth on a single crystal cathode surface occurs by way of growth layers (microsteps). As a result of impurity incorporation at active sites, microsteps tend to bunch together to form macrosteps. The other common growth forms are pyramids, which probably result from deposition on a complex aggregate of emergent screw dislocations.

Many other structures can be related to the basic pyramid and layer structures. Blocks can be regarded as truncated pyramids and ridges as a special kind of layer growth. Whiskers and dendrites arise under limiting current density conditions due to spherical diffusion.

Pyramid formation is favoured at low overpotentials while layer formation occurs at intermediate overpotentials (9). These growth forms apply to the growth of single crystals. At higher overpotentials many nucleation sites are equally favoured and the growth is polycrystalline. In commercial practice, the substrate metal is usually polycrystalline and hence the electrodeposited metal is polycrystalline. The growth type of a polycrystalline electrodeposit is determined by the metal, the electrolyte, the overpotential and various other deposition conditions. Five main types of electrodeposit have been categorised on the basis of microscopic examination (10):

- a) Field-oriented deposits when single crystals are formed,
- b) Basis-oriented type in which the deposit crystallites are parallel with those on the substrate surface,
- c) Field-oriented textured deposit, in which the electrodeposit exhibits preferential growth in the direction of the electric field. This results in growth of all the deposit crystallites in certain preferred directions and the deposit will have a fibrous texture,
- d) Twinning intermediate or transitional growth between basis-oriented and field-oriented growth types, and

- e) Unoriented or dispersed crystal growth type which is characterised by a random arrangement of the crystallites such that there is no preferred orientation within the electrodeposit. This type of crystal growth is very common and such deposits have a very fine crystal structure.

Bright deposits are often found to have a fine crystalline grain structure although bright deposits that have coarse structure or fibrous textures or a random orientation are known. Brightness is generally associated with surface roughness, i.e. smoother surfaces tend to be brighter. A surface will be effectively smooth from the point of view of reflectivity when the order of magnitude of the irregularities becomes less than the wavelength of the light being used. Bright deposits are, however, characterised by their large number of lattice defects due to the incorporation of impurities such as foreign metal ions or organic species, into the electrodeposit. The impurities or brighteners which are co-deposited with the metal cations are thought to function by inhibiting crystal growth parallel to the substrate surface. Very often bright deposits have a lamellar structure, the amount of this varying with the type of additive and its concentration in solution.

b) Factors affecting the deposition rate

The various factors affecting the electrodeposition rate from cationic species, may be illustrated with reference to the following equation referred to earlier in Section (2.1a):

$$i_L = \frac{DzFc_b}{\delta} \dots \dots (2.11)$$

The above equation represents an over-simplified approach to mass transfer in complex systems, but is adequate for a brief analysis of the subject.

The limiting current density is affected by four factors:

- i) The degree of agitation
- ii) The temperature of the electrolyte

- iii) The metal in concentration in solution.
- iv) Migration effects.

These factors will be examined in further detail.

i) Agitation effects

As a direct implication of equation (2.11) it is evident that i_L will be increased by decreasing the thickness of the diffusion layer δ .

The value of δ is related to the degree of agitation decreasing with faster stirring rates. The degree of agitation may be defined by the Reynolds number for the system:

$$Re = \frac{U_{cr} d_{cr}}{\nu} \dots \dots (2.12)$$

where U_{cr} and d_{cr} represent critical velocities and lengths respectively, for a given system. ν is the kinematic viscosity of the electrolyte. Hence highly agitated solutions favour increased current densities.

ii) Temperature effects

The deposition rate will increase with increasing diffusion coefficient (from equation (2.11)).

The diffusion coefficient and therefore the limiting current density will be increased by increasing the temperature. The diffusion coefficient (D) is related to temperature (T) and the dynamic viscosity of the electrolyte (η) by the equation (ref.350, see also Appendix 2f).

$$D = \text{CONSTANT} \times \frac{T}{\eta} \dots \dots (2.13)$$

The viscosity of the solution will also tend to decrease and hence contribute to a greater diffusion coefficient. In addition the lower viscosity would result in a lower energy requirement (i.e. a lower critical velocity) for the same degree of agitation (Reynolds number).

The solution temperature will be limited by the boiling point of the electrolyte and the need to minimise evaporation losses. In some cases the chemical stability of the electrolyte may be a critical factor.

iii) The metal ion concentration in solution

The limiting current density will be directly proportional to the bulk concentration (or more specifically the activity) of metal ions as a consequence of equation (2.11).

However the viscosity of the electrolyte will tend to increase with increasing metal ion concentration. Hence the diffusion coefficient may decrease with increasing concentration (equation 2.13), and the energy requirement (flow rate) for a given degree of agitation (Re) increase (equation 2.12). These effects tend to be less pronounced at higher metal ion concentrations and are compensated by the advantage of high metal ion activity. The concentration of metal ions will be limited by the solubility of the salt (this will increase with increasing temperature).

The metal ion concentration will also effect the conductivity of the solution, which in turn will decide the electrical power requirements. This may be of particular importance when using organic solvents. The conductivity will tend to increase with increasing metal ion concentration. In addition other conducting salts may be added to the solution to increase the conductivity.

It should also be noted that the current efficiency may also be a function of metal ion concentration, decreasing at very low and very high metal ion concentrations.

iv) Migration effects

In practice the limiting current may exceed that due to convective diffusion alone. The increased rate of mass transfer is caused by migration of the reacting ion in the electric field.

To estimate the contribution of migration to the limiting current, early investigators used the transport number (α) of the reacting ion to

modify equation (2.11) as follows:

$$i_L = \frac{DzFc_b}{\delta(1-\alpha)} \dots \dots (2.11a)$$

However, there is no theoretical basis for a simple manipulation of transport numbers to estimate migration currents in multi-component solutions and/or solutions with concentration gradients (11).

The migration current will be decreased by the presence of an excess inert electrolyte (supporting electrolyte). For many metal deposition reactions, with transport numbers of about 0.5, the migration current may increase the limiting current by a factor of 2 or 3 when a supporting electrolyte is absent (12,13). Therefore, a high concentration of the reacting metal ion and a low concentration of other ionic species (e.g. H^+) will favour high deposition rates.

However, in designing a high-speed plating process, other factors must be taken into account.

In particular these will include, the nature of the anode and the resistance of the electrolyte since these will affect the power requirements. At very high current densities, in order to limit the temperature rise due to ohmic heating, short experimental times would be necessary or the residence time must be reduced by high flow rates.

A faster rate of electrodeposition will be favoured by concentrated solutions, high temperatures and intense agitation. The necessity to maintain optimum plating conditions may finally decide the practical concentration and temperature ranges. As will be seen in this investigation, a high concentration, high temperature commercial type plating solution (the Ni-Speed bath (1)) has been used. Since all other variables have been optimised, the rate of deposition will be dependent on the method and degree of agitation.

2.2 Fast electrodeposition processes

The background to fast electrodeposition by controlled agitation

The subject of high-speed plating has been reviewed previously (14-19). Hart (20) has examined many of the problems involved in fast electrodeposition and some of the contemporary processes. Gabe (21) has also discussed the role of agitation in electro-chemical reactions.

Many electrochemical cell geometries have been devised to establish well-defined and reproducible hydrodynamic regimes for the investigation of electrode processes. Two common forms have been used in this context. The electrolyte may be pumped through pipes (22), rectangular channels (23-28) or annuli (29) of which the electrodes form part of the wall area. Alternatively the electrodes or the cell may be rotated (30-34). Some novel cells have been designed primarily for electrosynthesis or electrowinning applications (32,25,35-48).

A large number of these investigations are primarily concerned with establishing mass transfer correlations for electrochemical cells. Although metal deposition reactions, in particular copper deposition (25-28,48-50), have been studied for this purpose, the morphologies and properties of the deposits have been largely ignored. One exception is the production of metal powders obtained at the limiting current in electrowinning cells (35,51-53).

The flow of solutions in pipes etc. has also been used extensively in the study of high rate electromachining operations (54-59), anodic passivation phenomena (60-61), corrosion processes (62-64) and electrolytic purification of plating solutions (65).

The following review is primarily concerned with work involving the deposition of metals from commercial type plating solutions in conditions of controlled agitation. The object of these studies has been to investigate the effect of hydrodynamics on deposit morphology and properties and in some cases to achieve fast rate electro-deposition.

Controlled agitation methods previously used in studying metal deposition have included the following:

- a) Rotating systems
- b) Particulate bed systems
- c) Ultrasonics
- d) Other systems e.g. vibrating electrodes
jet plating
- e) Flowing systems

Rotating systems etc. will be dealt with briefly whilst flowing systems, which are of particular interest in the context of the present study, will be discussed in some detail. It should be noted that many of the previous investigations of high-speed plating were concerned with the development of suitable electrolytes for use with conventional agitation techniques e.g. the Ni-Speed process (1).

The deposition of metals in conditions of well-defined hydrodynamics has been studied for ~80 years. However most of the early investigations were at low current densities and empirical in nature. For example, in the case of deposition in flow cells (Table 2.1), the work of Dimon (66) on tin deposition over 40 years ago, used a maximum current density of only 0.1 Acm^{-2} , comparable with deposition rates using conventional agitation techniques.

The use of controlled agitation to significantly increase plating rates was initiated in 1948 by Wesley et al (67) (Table 2.1). These authors used a flowing system to give well defined hydrodynamics and deposit nickel (from sulphate and chloride solutions) at very high deposition rates. Few papers have since been published on high speed deposition in flow cells. As may be seen from Table 2.1, the high speed deposition of nickel from the sulphamate electrolyte in flowing systems has not been investigated. This is of particular interest, considering the value of the high concentration nickel sulphamate solutions, with inherently low internally stressed deposits, in electroforming, where an increased deposition rate would be of significance.

AUTHOR(S)	OBJECTIVES	CELL TYPE(S) /DIMENSIONS	MAX. FLOW RATE/Re No.	ELECTROLYTE(S)	MAX. CURRENT DENSITY
DIMON (66)	SIMULATE STRIP PLATING LINE EFFECT OF FLOW, TIN CONC. TEMPERATURE AND GLUE CONTENT ON REFLECTIVITY OF MELT BRIGHTENED PLATED STRIP.	PARALLEL PLATE ~1.9cm SQUARE SECTION ~24 cm LONG	~305 cms ⁻¹ Re 60,000	STANNOUS SULPHATE	~0.1 A cm ⁻²
MILLS and THWAITE (134)	SIMULATE STRIP PLATING LINE AS ABOVE	PARALLEL PLATE 11.4 x 1.9 cm RECTANGULAR SECTION 30.5 cm LONG	~305 cms ⁻¹ Re 100,000	STANNOUS SULPHATE	~0.3 A cm ⁻²
WESLEY, SELLERS and ROEHL (67)	HIGH SPEED DEPOSITION OF NICKEL. FIND MAXIMUM CURRENT DENSITY FOR A SOUND DEPOSIT	PARALLEL PLATE 5.1 x 0.63 cm RECTANGULAR SECTION CATHODE LENGTH 20.4 cm	~254 cms ⁻¹ Re 30,000	2.6M Ni Cl ₂ 2:6M Ni SO ₄ (70°C)	4.6 Acm ⁻² 0.86 A cm ⁻²
SAFRANEK and LAYER (71)	HIGH SPEED DEPOSITION OF METALS	PARALLEL PLATE CELL GAP: 0.16 to 0.32cm CELL WIDTH: 2.5cm(?)	240 cms ⁻¹ ~Re 13,000	3M Cr O ₃ 2.5MCo(BF ₄) ₂ 2M CuSO ₄ or Cu(BF ₄) ₂ 0.5M Au CN (citrate) 2.3MFe(NH ₂ SO ₃) ₂ 2.5MPb(BF ₄) ₂ 2MNiSO ₄ or NiCl ₂	6.2A cm ⁻² 6.2A cm ⁻² 3.1 A cm ⁻² 0.3 A cm ⁻² 6.9 A cm ⁻² 1.6 A cm ⁻² 3 A cm ⁻²

Table 2.1 Deposition of metals using flow systems

AUTHOR(S)	OBJECTIVES	CELL TYPE(S) /DIMENSIONS	MAX. FLOW RATE/Re No.	ELECTROLYTE(S)	MAX. CURRENT DENSITY
SAFRANEK and LAYER (72)	SYSTEM MODIFIED TO IN- CORPORATE A SLOWLY ROTATING DRUM, 2.5 cm WIDE IN THE FLOW CELL	MODIFIED PARALLEL PLATE CELL GAP: 0.25 to 0.62 cm CELL WIDTH: ~2.5 cm	360 cms ⁻¹ Re 36,000	Ni ₄ SO ₄ /NiCl ₂ (1.75M/1.0M) 1M Sn(BF ₄) ₂ 1M Cd(BF ₄) ₂ 2M Zn SO ₄	2.5 A cm ⁻² 3.0 A cm ⁻² 3.0 A cm ⁻² 3.0 A cm ⁻²
CHIN (142)	HIGH SPEED DEPOSITION OF CHROMIUM	PARALLEL PLATE 0.635 x 0.114 cm RECTANGULAR SECTION	460 cms ⁻¹ Re <9,000	CHROMIC ACID (40 - 70°C)	1 to 70 A cm ⁻²
LA BODA, HODEN and HOARE (59,70, 143) LA BODA(144,145)	HIGH SPEED DEPOSITION OF CHROMIUM	ANNULUS 0.38 cm GAP INNER TUBE CATHODE	615 cms ⁻¹ Re 47,000	CHROMIC ACID (41 - 91°C)	7.9 A cm ⁻²
POLL (146)	ELECTROPLATING AUTOMOBILE BUMPERS	CONFORMING ANODE 1.2 cm GAP	762 cms ⁻¹ Re >10 ⁵	COPPER STRIKE SEMI-BRIGHT NICKEL CHROMIUM	UP TO 1.4 A cm ⁻²
NAYBOUR (147)	EFFECT OF FLOW ON MORPHOLOGY OF ZINC DEPOSITS	PARALLEL PLATE 5 x 1 cm RECTANGULAR SECTION 60cm LONG	170 cms ⁻¹ Re 22,000	ALKALINE ZINCATE (20-25°C)	1.6 A cm ⁻² (?) (see p. 37)

Table 2.1 continued

AUTHOR(S)	OBJECTIVES	CELL TYPE(S) /DIMENSIONS	MAX. FLOW RATE/Re No.	ELECTROLYTE(S)	MAX. CURRENT DENSITY
IBL and ANGERER (68)	EFFECT OF FLOW ON MORPHOLOGY AND COMPOSITION OF GOLD - COBALT ALLOY DEPOSITION	PARALLEL PLATE 2 x 0.5 cm RECTANGULAR SECTION 40 cm ENTRANCE LENGTH	150 cm s^{-1} Re 13,400	15 g dm^{-3} K Au(CN) ₂ 0.07 g dm^{-3} Co (citrate) (27°C)	0.15 A cm^{-2}

Table 2.1 continued

Since the commencement of the present study, significant published work on flow cell deposition has been sparse although the detailed study by Ibl et al(68) of the effect of flow during gold alloy deposition and the investigations of La Boda et al (69,70) into high speed chromium deposition (see Table 2.1) are of interest.

However, most of the previous investigations of high-speed plating systems have been carried out by industrial research groups, notably International Nickel (67) and the Batelle Laboratories (71,72) and the information contained within published work is often incomplete and semi-empirical. Few workers have attempted to carry out a detailed study of deposit morphology as a function of the rate of mass transfer.

In the past 10-15 years electrochemical engineering has advanced considerably and mass transfer correlations are now available for most electrode geometries. It is hoped that these advances may be used to design flow cells more analytically and interpret the results of previous studies.

a) Rotating systems

Rotating cathodes have been used for electroplating studies for many years (73). A decrease in the current efficiency of nickel deposition on rotating the electrodes was noted 76 years ago (74-75). Narasimham and Udupa have reviewed the literature concerning the effects of cathode rotation in electrodeposition (76). The use of a rotating cathode has not found widespread application in commercial electroplating since odd-shaped articles are required to be handled for plating. Two main forms have been used for laboratory investigations, the rotating disc and the rotating cylinder systems.

The use of the rotating-disk electrode is widespread for the study of electrochemical kinetics (77). Analytical solutions have been formulated for the relevant transport equations (78). However for electroplating studies it has several limitations. The current distribution at sub-limiting current densities is uneven (79,80). This effect is accentuated with disks of large diameter and with concentrated

electrolytes. The occurrence of spiral patterns on electrodeposits is another feature of the rotating disk system (81,82).

The rotating disc has several disadvantages for metallurgical studies. It is difficult to measure metallurgical properties on a surface, of small area, over which the value of the current density may have varied considerably. However the distribution of metal over the disk surface has been measured and discussed for the copper-copper sulphate system (83,84). In addition, the hydrodynamics of the rotating disk system are very stable and as a consequence of this, turbulence is induced only at very high r.p.m. The disk is unsuitable for fast rate deposition which requires highly turbulent solutions.

The other common rotating electrode geometry is the rotating cylinder electrode (31,32). Turbulence is induced at low angular velocity and low Reynolds numbers (~200). At lower Reynolds numbers the flow is complex and may be laminar or exhibit Taylor vortices. The highly turbulent flow regimes that may be created can provide very high rates of mass transfer. The current distribution is relatively uniform at all current densities. The mass transfer correlation has been determined empirically (51,85). The cell is highly suitable for electrowinning applications (52) and has the advantage of requiring relatively small electrolyte volumes. However the electrode shape may be a disadvantage for metallurgical examinations and property evaluation. The geometry is not directly applicable to most commercial situations. The complex nature of the rotational equipment and the brush gear or mercury cup arrangement which carry the current may increase the energy consumption. For high current density operations IR drop and resistance heating may be critical factors.

However Swalheim (86) has used a 9.7 cm diameter cylindrical former around which a sheet substrate could be wrapped and fixed, providing a large surface area for subsequent examination. The rotating cathode was exposed to three shaped concentric anodes in half the cylindrical cell. The other half section was baffled to retard electrolyte rotation and shaped to expose equal areas of anode and cathode at an interelectrode distance of 2.5 cm. The apparatus (Fig.2.3) was

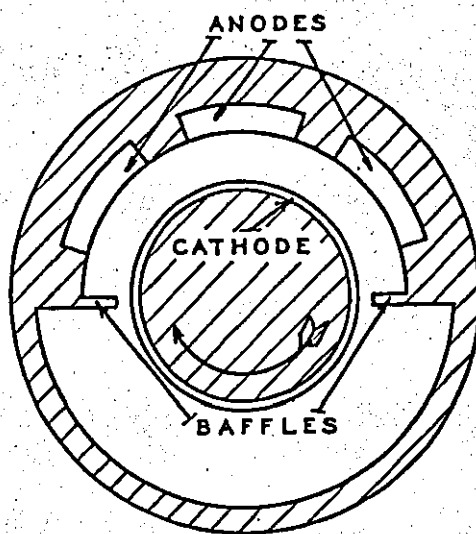


Fig.2.3. Swalheim rotating cylinder cell (86)

designed to simulate the conditions existing on an electrolytic tin strip line and operated at surface speeds of up to 305 cms^{-1} . ($Re \sim 3 \times 10^5$). Good quality tin was deposited from acid tin solutions at current densities of up to 1.1 A cm^{-2} at the highest cathode velocity. Similar work was also carried out by Beard et al (87).

Swalheim also deposited lead from sulphamate solutions at current densities up to 0.8 A cm^{-2} . The plating rate was correlated with surface velocity using the onset of deposit 'burning' as criterion for maximum current density. The maximum current density was proportional to [surface velocity]^{0.6} (82).

This relationship is in good agreement with semi-empirical analyses which predict a relationship of the form : $i \propto [\text{surface velocity}]^{0.67}$.

Graham and Pinkerton (88) used a conical anode to produce a range of current densities over a rotating cylinder cathode 0.635 cm or 3.81 cm in diameter. Surface velocities of up to 152 cms^{-1} ($Re \sim 5.8 \times 10^4$) were attainable. The cells were calibrated with a lead fluoroborate solution and used to evaluate addition agents for high-speed lead plating. Lead was deposited from the fluoroborate electrolyte without addition agents at current densities up to 1.9 A cm^{-2} . In the presence of selected addition agents a smooth sound deposit was produced at 3.2 A cm^{-2} .

The Xerox corporation (89) has used the rotating cylinder electrode to electroform continuous and seamless nickelfoil as a substrate for the photo-conductive materials used in electrophotographic applications. The solution was introduced into the $\sim 4.4 \text{ cm}$ gap between the rotating mandrel and the conforming anode basket containing sulphur depolarised nickel anode material. An annular manifold and vertical sponger risers distributed the solution uniformly over the cathode surface. The cathode of undisclosed dimensions, was rotated at 60 r.p.m. The nature of the hydrodynamics was not disclosed.

A series of nickel sulphamate based electrolytes were examined to assess the effect of solution chemistry on the electroform properties. A solution of the following composition was formulated: $101 \text{ g l}^{-1} \text{ Ni}^{2+}$,

13 g ℓ^{-1} $\text{Ni Cl}_2 \cdot 6 \text{H}_2\text{O}$, 37 g ℓ^{-1} $\text{H}_3 \text{BO}_3$ adjusted to pH 4.0 and operated at 66°C. Nickel electrodeposits of low internal stress and high tensile strength were deposited at current densities of 0.32 to 0.65 A cm^{-2} . Several unusual morphological features were found at these plating rates. The features included rounded mound structures, elongated ridge like structures and small pits extending through the deposit to the substrate. The author postulated that these effects were caused by small particles of nickel hydroxide adhering to the electrode surface. The property response to certain levelling agents was also investigated.

Safranek (71) has deposited chromium at high current densities on rotating rods 2.5 to 7.5 cm in diameter. The rod rotation rate was adjusted to provide a surface velocity of 125 cms^{-1} ($\text{Re } 3.1 \times 10^3$ to $\text{Re } 9.4 \times 10^3$). In another facility, 7 to 15 cm rings were stacked vertically and rotated at speeds corresponding to surface velocities of 200 cms^{-1} ($\text{Re } 3 \times 10^5$).

More recently nickel has been deposited at very high plating rates from sulphamate based solutions (350g ℓ^{-1} nickel sulphamate) on to a rotating cylinder electrode (Fig.2.4) (90). The cylinder was 5 cm in diameter and operated at surface speeds of 125 cms^{-1} ($\text{Re } 6.3 \times 10^4$) to 375 cms^{-1} ($\text{Re } 1.9 \times 10^5$). At an electrolyte temperature of 30°C, the current efficiency was found to decrease rapidly at current densities $>0.8 \text{ A cm}^{-2}$, from a maximum value of ~90%. At lower current efficiencies green nickel hydroxide was co-deposited. When the electrolyte temperature was increased to 55°C, high current efficiencies (~85%) were maintained up to ~2 A cm^{-2} , at which point the deposit cracked. The current efficiency was independent of the cathode surface velocity at 55°C (Fig.2.5). In some experiments the rotating cathode was simultaneously abraded with an Al_2O_3 'hone' at pressure of 5 kg cm^{-2} . Using this technique maximum current densities were greatly increased to 1.6 A cm^{-2} at 30°C and 3.2 A cm^{-2} at 55°C. However a marked decrease in current efficiency was found (50% at 30°C and ~65% at 55°C). The authors explained the decrease by the wear of the deposit. A similar industrial system for plating piston rings has been described (91,92).

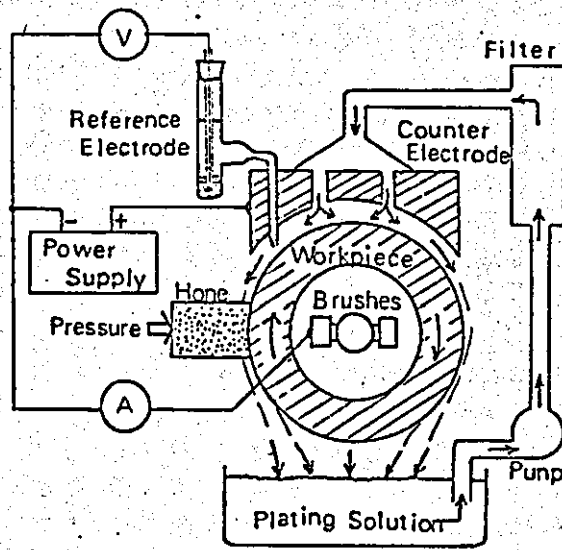


Fig.2.4 Abraded rotating cylinder cell of Suzuki et al (90)

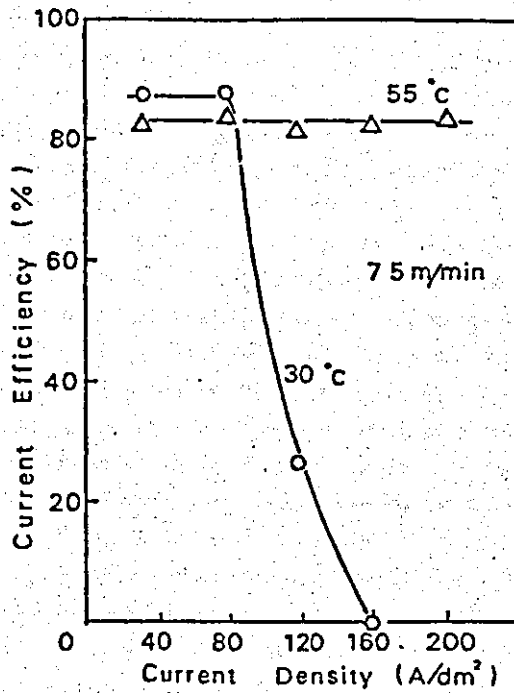


Fig.2.5 The relation between current efficiency and current density for the deposition of nickel from (350 gl⁻¹) sulphamate solutions at a rotating cylinder electrode (90)

b) Particulate bed systems

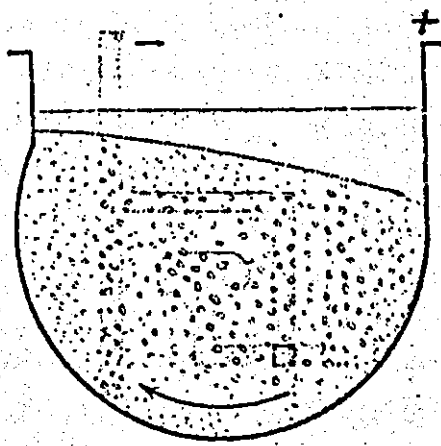
In particulate bed systems, the cell is filled with small particles which may be 'active' (conducting) or 'inert' (non-conducting) beads. In general two systems are commonly used: packed (or fixed) bed or fluidized bed systems. In the packed bed system, the beads are not free to move whereas in a fluidized bed the particles are in suspension. Fluidization is usually achieved by the flow of electrolyte. In both types of cell the beads act as turbulence promoters.

The mass transport characteristics of both types of cell have been extensively studied (96-98). The use of these cells has been confined to mainly electrosynthesis and electrowinning (96,98) applications, where the high electrode surface area of an 'active' bed is an added advantage. However the 'inert' fluidized bed principle in one form or another has been used for electroplating applications.

Eisener et al (101) have described a system (NET 11) consisting of a vibratory tub filled with an electrolyte containing suspended abrasive particles (Fig.2.6). The electrodes were fixtures within the tub. The tub was vibrated with a 0.315 to 0.4 cm amplitude and a 25 to 35 Hz frequency range. The method has the advantage of few restrictions on the shape and size of the article to be plated.

It has been claimed that these processes can be used to deposit a range of metals at rates which are a hundred to a thousand times faster than those which can be employed with conventional processes (Table 2.2). For example, nickel was electrodeposited from nickel sulphate, Watts type and proprietary nickel sulphamate based electrolytes operating at temperatures between 50 to 70°C at maximum current densities of 2.15 to 5.4 A cm⁻², depending upon the solution and temperature.

The abrasive action processes described by Eisner are thought to increase rates of mass transfer by the intimate contact between the abrasive particles and the working electrode. The resulting contact penetrates the mass transfer boundary layer and allows electrolyte of the bulk concentration to reach the electrode surface. The mechanism may be comparable to the penetration theories of mass transfer in turbulent flow (99) and at gas evolving electrodes (100). In addition the abrasive



Schematic diagram of N-E-TII. The anode and the cathode (a doorknob) are fixtured in the vibratory tub. The grain is depicted by the small particles. The grey area at the top of the tub is the supernatant electrolyte.

Fig.2.6 Vibratory tub electroplating cell of Eisener (101)

Metals	Bath	Temp. °C	Max CD used A/ft ² (A/dm ²)
Cadmium	Cadmium sulphate+H ₂ SO ₄	25	1000 (108)
Chromium	CrO ₃ +H ₂ SO ₄ 100:1	60	22000 (2370)
Copper	Copper sulphate+H ₂ SO ₄	25	4600 (495)
	Copper pyrophosphate	54	10800 (1165)
Iron	Iron chloride-iron sulphate	25	4600 (500)
Nickel	Watts (chloride free)	60	2150 (230)
	Watts	60	2000 (216)
	<u>Sulphamate</u>	60	5000 (540)
Silver	Used photographic fixer	25	200 (21.6)
Tin	Tin sulphate+sulphuric acid	25	56000 (6050)
Zinc	Various zinc sulphate systems	25	3200 (345)
	Zinc oxide+KOH	25	1000 (108)
	Zinc pyrophosphate	50	1000 (108)
<i>Alloys</i>			
Brass	Cyanide	50	600 (65)
	Pyrophosphate	25	500 (54)
	Mixture of acid zinc and acid copper sulphate	25	2300 (250)
Cu-Pb	Fluoroborate	25	1000 (108)
Cu-Ni	Ammoniacal nickel and copper sulphates	25	2000 (216)

Table 2.2 Maximum current densities claimed for the deposition of metals in the Eisener vibratory tub electroplating facility (101)

may also mechanically clean the electrode surface of other impurities and dendritic or nodular growth forms. However few experimental results were reported so it is difficult to assess the effectiveness of the process.

The suspended particle process has certain similarities with some types of fluidised bed electrochemical cells (93) and other systems containing suspended particles (102). A particularly suitable comparison is provided by the Chemelec cell (103-105). The process involves a vertical cell containing glass beads, fluidised by the electrolyte flow. The cathodes are of titanium mesh, suspended within the fluidised bed. Sound and coherent bright nickel has been deposited from sulphate based electrolytes of low nickel concentration at low current efficiency and high rates of mass transfer (38). The apparent absence of powdery and burnt deposits is unusual. In some cases bright nickel electrodeposits were produced without addition agents (96,105).

c) Ultrasonics

Ultrasonic vibrations are sound waves at a frequency generally greater than 16 Hz. The sound waves, when generated in a fluid media, produce rapidly alternating high and low pressure regions. Bubbles are formed inside the liquid which then grow with pressures of up to 1,000 atmospheres just before collapsing. The effect of cavitation is to cause intense agitation of the liquid which, in the case of electrodeposition, may result in increased rates of mass transfer. However, the input of energy may be so great that the deposition process is effected in more complex ways than simple agitation methods.

The power required to give such cavitation inside the liquid depends on the frequencies used. For example, it requires ten times as much power to make water cavitate at 400 Hz as at 20 Hz. Frequencies lower than 16 Hz generate audible noise. Therefore frequencies of the order 17 to 40 Hz are employed in the cleaning pickling and plating operations. The subject of ultrasonics in metal finishing processes has been comprehensively reviewed (106-108).

The literature contains conflicting reports on the influence of ultrasonics on electroplating and electrodeposits. In the case of nickel deposition from acid baths, increases in the deposition rate of between 3 and 25 fold have been reported (109-110). Significant changes in deposit properties have been claimed (111-113), including increased microhardness and brightness, decreased porosity and internal stress and grain refinement. These effects are thought to be due to cavitation shock waves resulting in work hardening and changes in the growth mechanism of the deposit (114-116). The effect of ultrasonics on nickel electrodeposited from sulphamate solution has not been reported.

In general, the production of fast rate nickel electrodeposits using ultrasonics has not been fully investigated. However, in the case of nickel, the high capital cost of the generating equipment would limit the use of the technique to special cases. The expenditure may be justified in the case of precious metal plating (e.g. gold (137)) where the high cost of the raw materials is offset by the higher deposition rates and improved physical properties of the deposit.

d) Other systems

The effect of abrasion on the rate of metal deposition was also studied by Eisner et al (cf p. 28). The authors developed a series of techniques for continuously abrading the cathode surface (118-120). Two processes involved abrasive pads (or activators) in the form of moving belts or discs impinging on the electrode (Fig.2.7). The abrasive pads were of synthetic non-woven fabric impregnated with resin containing silica, aluminium oxide or silicon carbide particles (500-600 mesh). The electrolyte was pumped onto the abraded surface by the action of the rotating disc or belt. The surface speeds of the activators were varied between 25 and 508 cm s^{-1} at pressures up to 253 g cm^{-2} . The maximum current density attainable was dependent upon the surface speed and pressure. At low speeds and/or low pressures the deposit was powdery and burnt at high current densities. The electrodeposits were found to be brittle with poor adhesion and increased wear at high speeds and pressures. With optimised deposition parameters, bright, ductile and

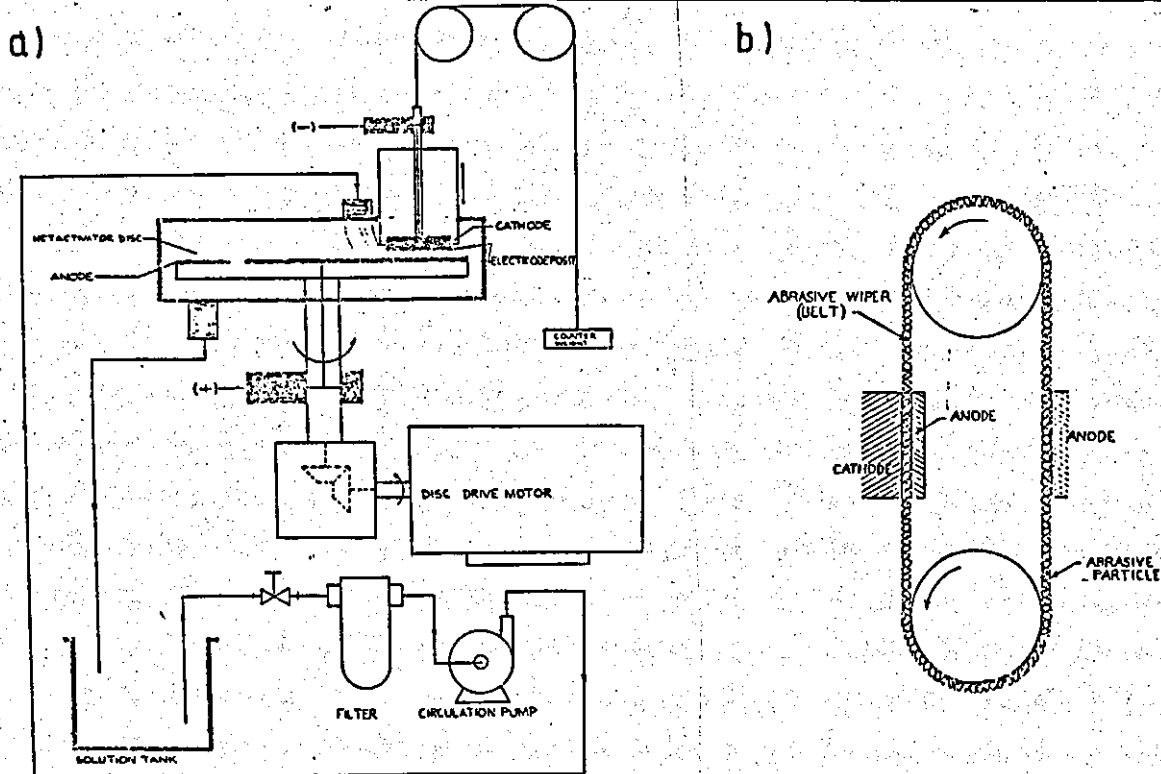


Fig. 2.7 Abrasive rotating disc (a) and abrasive belt (b) electroplating apparatus of Eisener et al (118,119,120).

Metal	Bath	CD A/dm ²	Approx. Max. Rate mil/min	Apparatus Used	Remarks
Cu	Pyrophosphate	1080	1	Disc	
Cu	Acid Sulfate	460	4	Disc	
Ni	Cl-Free	460	4	Belt	
Ni	Watts	215	1	Disc	
Ni	Proprietary Sulfamate	215	1	Disc	
Cr	Chromate 100:1 (SO ₄ Catalyst)	2350	3	Disc	
Sn	Sulfate	6000	94	Disc Belt	Plate was brittle, contained 8.7% SnO ₂
Sn	Sulfate	200	1	Disc	Plate ductile 99.4% tin
Zn	Zn, Na & Mg Sulfates	320	3	Disc Belt	Semibright deposit
Fe	Chloride-Sulfate	460	Estimated 4	Belt	Plating on a moving coil of brass shim stock
Ni-Cu	Ammonia-Sulfate	200	1.4	Disc	Plate composition 53% Ni, 47% Cu
Cu-Zn	Sulfate Cu:Zn = 3:1	230	2	Belt	25 mm diameter Plate composition 79% Cu & 21% Zn

Table 2.3 Maximum current densities claimed for the deposition of metals using the Eisener abrasive plating technique (118,119,120)

coherent plate was produced with high current efficiency at very fast deposition rates.

It was claimed that technique could be used to deposit a range of metals at very high current densities (Table 2.3). For example, a maximum current density of 2.16 A cm^{-2} was reported for nickel deposition from a proprietary sulphamate solution (118). However, once again (cf p.28) few experimental results were reported in the Eisener paper making assessment of the process difficult. For example, it would be of considerable interest to see how the current efficiency varied with the experimental conditions used.

Other high speed deposition processes of note, are the jet flow method (121-123). Copper and nickel have been electroplated by using a jet flow device in which the electrolyte is forced through a nozzle forming a high speed jet impinging upon the cathode specimen. Current densities of up to 1 A cm^{-2} were achieved with jet flow rates of 200 cms^{-1} . Mass transfer correlations have been determined in experimental studies of this type of system (124). More recently interest has been shown in the effect of laser beams on the rate of metal deposition (125). At the point at which the laser beams impinge, the equilibrium potential of the system M/M^{n+} was shifted, charge penetration was accelerated and material transport was increased up to 1000 X. This effect may be associated with the localised heating of the electrolyte close to the cathode surface.

e) Electrodeposition in flow cells

Advantages and construction

The flow cell geometry has several advantages for electroplating as compared to other cell designs. The laminar flow regime is maintained up to moderate Reynolds numbers ($< \text{Re } 2,200$) enabling correlations to be made in both laminar and turbulent flow. The system is relatively simple to construct and operate. This type of cell is more appropriate for application to practical plating problems. In addition, the temperature increase due to ohmic heating is more readily controlled using this type of cell.

Many designs have incorporated a rectangular cell within circular section ancillary pipework for ease of construction and operation purposes. In such cells, the anode and cathode are often parallel and opposite to each other. These designs (parallel plate cells) are particularly suitable for electrodeposition purposes when morphology and deposit properties are to be studied. The hydrodynamics and mass transfer characteristics of this type of cell are examined in section 2.3b. However pipe or annulus systems have also been used for electrodeposition studies.

A comparison between different designs of flow cells is often complicated by the authors of published work stating the linear flow velocity rather than the Reynolds number. The latter term is more significant since it defines the degree of agitation for the system. Where sufficient information may be obtained from published work the maximum Reynolds number (Re_{de}) for each system has been calculated (section 2.1b). It should be noted that the cathode length may also be a significant factor from a mass transport point of view. A summary of the cell dimensions, Reynolds numbers, electrolytes, objectives and current densities achieved for some of the more relevant work are shown in Table 2.1.

Initial developments

The initial use of parallel plate cells for evaluating electroplating processes was inspired by the assumed analogy with the electroplating of moving sheet and wire (126-133) with tin.

Dimon (66) pumped a stannous sulphate solution through a 1.9 cm^2 square circulation cell, $\sim 24 \text{ cm}$ in length (Fig.2.8). The maximum Reynolds number was $Re \ 6 \times 10^4$, giving a highly turbulent solution. Tin was deposited at a maximum current density of 0.1 A cm^{-2} . The effects of flow, temperature, tin concentration and glue content on the reflectivity of melt brightened plated strips was evaluated. A 'circulating Hull cell' was also constructed.

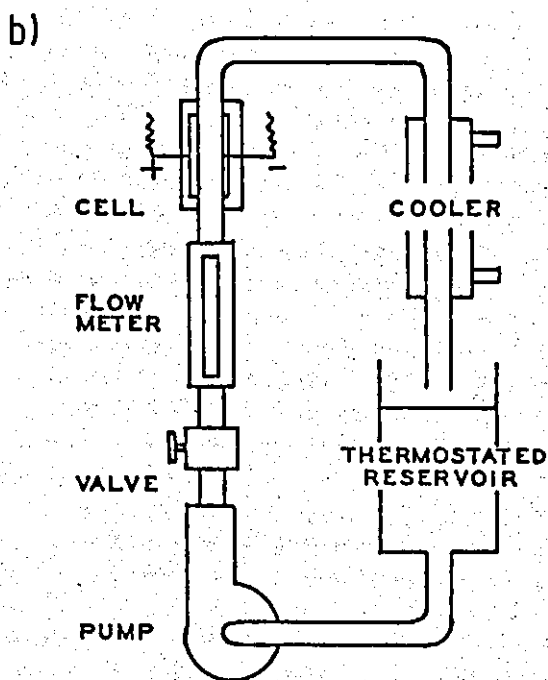
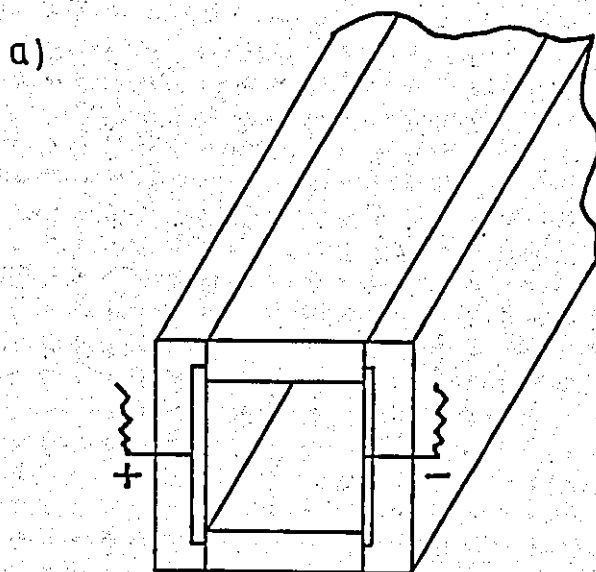


Fig.2.8 The square section parallel plate cell (a) and flow circuit (b) of Dimon (66) for the electroplating of tin.

Similar work was carried out by Mills and Thwaites (134). They used the same maximum flow velocity as Dimon ($\sim 305 \text{ cm s}^{-1}$). However since the cell dimensions were larger the Reynolds number was increased to $Re \ 1 \times 10^5$. Tin was deposited at current densities of up to 0.3 A cm^{-2} .

However, it should be noted that the hydrodynamics and therefore the mass transfer characteristics of rectangular flow cells are not directly comparable with a moving strip or wire plating process (135, 136).

High speed plating studies

The first published account of high-speed nickel electrodeposition in a parallel plate cell was a patent by Wesley, Sellers and Roehl (67). These investigators were specifically interested in achieving very high current densities in conditions of controlled agitation. They calculated a limiting current density for the deposition of nickel from chloride and sulphate electrolytes using a modified Nernst equation:

$$i_L = \frac{Dz F c_b}{\delta (1-\alpha)} \quad \dots (2.11a)$$

The calculations carried out are subject to several criticisms.

The values of the diffusion coefficients at 20°C were said to be taken from the work of Ohlm (137). The diffusion coefficients at 70°C were then calculated using literature values of temperature coefficients. However the values of the diffusion coefficients used were not those given by Ohlm and the authors did not use the temperature coefficients stated! The diffusion coefficients used in further calculations were:

$$D(\text{Ni SO}_4) = 1.04 \times 10^{-5} \text{ cm}^2 \text{ s}^{-1}$$

and

$$D(\text{Ni Cl}_2) = 2.18 \times 10^{-5} \text{ cm}^2 \text{ s}^{-1}$$

The transport no., α , was taken as 0.4. However, the use of transport numbers to calculate the contribution of migration current to the total limiting current has no theoretical justification (Section 2.1b).

The thickness of the diffusion layer was estimated to be:

$$\begin{aligned}\delta \text{ unagitated solution} &= 0.03 \text{ cm} \\ \delta \text{ violently agitated} &= 0.001 \text{ cm}\end{aligned}$$

Using the above data, and a metal ion concentration, c_b , of $1.3 \times 10^{-3} \text{ mol cm}^{-3}$ with $z = 2$, then i_L was calculated as follows:

For an unagitated solution:

$$\begin{aligned}i_L(\text{NiSO}_4) &= \frac{1.04 \times 10^{-3} \times 2 \times 96.500 \times 1.3 \times 10^{-3}}{0.03 (1-0.4)} \\ &\sim 0.14 \text{ A cm}^{-2}\end{aligned}$$

and with violent agitation $i_L(\text{NiSO}_4) \sim 4.3 \text{ A cm}^{-2}$. The corresponding figures for nickel chloride solution of similar concentration were much higher: in an unagitated solution, $i_L(\text{NiCl}_2) \sim 0.3 \text{ A cm}^{-2}$, and with violent agitation, $i_L(\text{NiCl}_2) \sim 9.0 \text{ A cm}^{-2}$.

It should be noted that the Nernst equation only applies to stagnant solutions and is not strictly applicable to agitated solutions. The simple calculations carried out by Wesley et al could only give values of i_L correct to within an order of magnitude and would appear to contain several arithmetical errors. A more accurate theoretical value of the limiting current may be derived from the application of mass transfer theory (Appendix 2).

The authors subsequently used a parallel plate cell to achieve highly turbulent flow conditions up to $Re \ 3 \times 10^4$. They concluded that the 'limiting' current density for sound nickel deposited from chloride solutions increased linearly with the flow rate (Fig.2.9). From mass transfer theory a relationship of the form $[\text{flow rate}]^{0.8}$ would be expected. The results were therefore in reasonable agreement with the theoretical predictions.

Burned, spongy or streaked areas were considered evidence of unsoundness. At the highest flow rate, sound deposits were obtained at $\sim 4.6 \text{ A cm}^{-2}$. The anode and cathode efficiencies were both 100%.

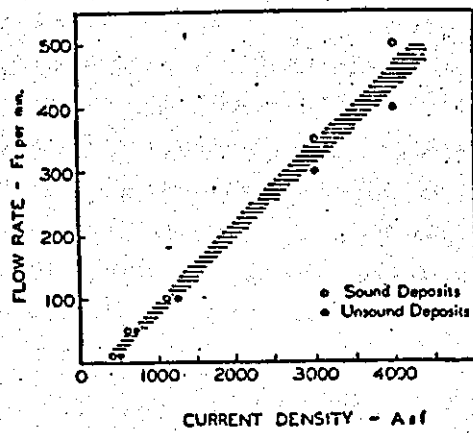


Fig.2.9 Relationship between the maximum current density for a sound deposit and flow rate, for the deposition of nickel from chloride solutions in a parallel plate cell (after Wesley et al (67.).

Using a nickel sulphate (Watts type) bath the current densities were lower ($<0.86 \text{ A cm}^{-2}$) and deposits exhibited roughness at high current densities. The roughness was believed to be caused, at least partly, by fines from the roughly corroding anodes being deposited on the cathode. However this was not confirmed by examination of deposit cross-sections.

Safranek and Layer (71, 53) (Battelle's Columbus Laboratories) later developed a similar system and extended its use to other metal plating systems (Table 2.1). Exact experimental details were not given, but the cell was of the parallel plate type with a very narrow cell gap of 0.16 to 0.32 cm. Flow velocities of up to 240 cm s^{-1} would correspond to a maximum Reynolds number of about $\text{Re } 1.3 \times 10^4$ for the largest interelectrode gap. The anode dimensions were adjusted to avoid excessively high current density areas on the cathode.

A later modification to the original cell design included a slowly rotating drum facility for production of continuously electroformed foil, 2.5 cm wide (72). Metals deposited included nickel foil electroformed from 2.5 M nickel chloride, 1.75 M nickel sulphate and 2.75 M nickel chloride/sulphate solutions operating at 60 to 70°C and current densities up to 2.5 A cm^{-2} with cell voltages of 6 to 10V. (It would appear that temperatures of 60 to 70°C are essential for a reasonably fast nickel deposition rate). Fast nickel deposits tended to have a higher tensile strength, a similar hardness and a lower density and resistivity than conventional deposits.

Brooman (138) of Battelle's Columbus Laboratory, has recently claimed stainless steel deposition rates of up to 50 times conventional plating rates, using these developments.

Other systems designed for the high speed electroplating of iron and nickel using forced circulation have also been described (139-141). The metals were deposited at current densities up to 5 A cm^{-2} at flow rates of up to 350 cm s^{-1} .

Several investigations into high-speed chromium plating in flowing systems have been undertaken recently. Chin (142) devised a very narrow (0.114 x 0.635 cm) parallel plate type flow cell. The maximum flow rate corresponded to $Re = 9,000$ although a very fast flow velocity (460 cm s^{-1}) was used. Chromium was deposited from chromic acid solutions, operating at 40 to 70°C , at current densities of 1 to 70 A cm^{-2} . At very high current densities the current efficiency decreased from a very high maximum of about 50% and the deposit structure deteriorated. This is not surprising, since at 70 A cm^{-2} , the limiting current density would be exceeded by about one order of magnitude.

The very high current efficiencies for chromium deposition are surprising, since, using conventional plating techniques, efficiencies of 15 to 20% would be the maximum values expected from this bath.

La Boda et al (69,70,143-145) have studied high-speed chromium plating at current densities up to 7.9 A cm^{-2} , using an annulus type flow cell. The cathode was the external surface of the inner tube. Chromic acid solutions (at temperatures up to 91°C) were pumped between the inner (cathode) and outer (anode) tube gap. The maximum flow rate corresponded to about $Re = 4.7 \times 10^4$. In some experiments a reciprocating anode or cathode was used to ensure even plating of the electrode.

An air pressure flow system was devised to overcome the problem of corrosion of conventional chemical pumps by the aggressive electrolyte (144,145).

An analogous industrial process, which utilised a conforming anode system, was the 'contour plating machine' for plating Pontiac car bumpers (146).

The interelectrode gap was $\sim 1.2 \text{ cm}$ and electrolyte was pumped through the gap at flow velocities of up to 762 cm s^{-1} (Under these conditions the Reynolds number may exceed 1×10^5 - a very turbulent solution). This enabled current densities of up to 1.4 A cm^{-2} to be reached and more uniform deposit distribution to be achieved than with conventional systems. The device was used to deposit copper strike, semi bright nickel, bright nickel and chromium.

However, the process was discontinued after about two years of operation for reasons that have never been fully reported, but there appear to have been a number of inherent problems with the process which could not be satisfactorily overcome (20). One of the most persistent of these was thought to have been the unreliability of the pump and flow system. It has also been suggested that the change in composition of the solution within the interelectrode gap, resulting from the combined effect of a high current density and an inert anode, gave rise to unacceptable variations in the deposit properties.

Morphology and deposit property studies

The majority of investigations of metal deposition from flowing electrolytes have emphasised the influence of high flow rates upon the rate of deposition. Other studies have been more concerned with the correlation between flow velocity and the morphology/physical properties of the deposit.

Naybour (147) used a rectangular flow channel cell to study the effect of electrolyte flow on the morphology of electrodeposited zinc at ambient temperature. Aqueous zincate solutions were forced through a cell 60 cm in length and of cross section 5 x 1 cm using a gravity-feed flow system.

The maximum flow velocity was 170 cm s^{-1} corresponding to $Re_{de} 2.2 \times 10^4$. A maximum current density of 1.6 A cm^{-2} was claimed. However a mass transport analysis would suggest a limiting current density of about 0.016 A cm^{-2} for the experimental conditions stated.

Three morphology types were identified dependent upon current density and flow rate. At a constant Reynolds number the deposit appearance was flat, bulbous and dendritic at increasing current densities. The deposit morphology was correlated with current density and Reynolds number. Based on a morphology criterion the relationship between current density and flow rate was almost linear under turbulent flow conditions. Once again this is in reasonable agreement with the theoretical value (p. 34)

The electrodeposition of gold-cobalt alloys in flowing electrolyte was studied by Ibl and Angerer (68). The electrolytic cell was of rectangular cross section with a 40 cm entrance length (Fig. 2.10). The dimension of the cross section was 2 x 0.5 cm. The electrolyte, operating at 27°C, was pumped through the cell at velocities from 30 - 150 cm s^{-1} , corresponding to Reynolds numbers of 2,900 - 13,400. The following features were examined quantitatively in the experiments: the current efficiency for gold deposition, the carbon and cobalt content, the porosity of the deposits and the deposit morphology. Gold was deposited at current densities up to 0.15 A cm^{-2} . At current densities $>0.05 \text{ A cm}^{-2}$ the deposition of gold and to a minor extent the incorporation of cobalt was mass transport limited, although this is complicated by the complex nature of the process. At current densities $<0.05 \text{ A cm}^{-2}$ the current efficiency may be affected by the reduction of dissolved oxygen. The deposit porosity was found to increase substantially with increasing current density and decreasing flow rate. It was noted that the morphology of the deposits produced at the highest current densities was rough and friable. It was also suggested that the concomitant hydrogen evolution accompanying the deposition of gold increased the overall rates of mass transfer and effected the current efficiency in a complex manner.

The applicability to fast electrodeposition of various designs of electrochemical cells has been discussed in the previous review. All may have advantages for certain applications. For example, rotating systems, such as the rotating cylinder electrode, are particularly suitable for the electrowinning of metals, where the quality of the deposit is of secondary importance. It would appear that the application of the rotating systems to practical electroplating problems is very limited.

However, the concept of electrolyte flow may be applied to many electrode geometries, and is of considerable interest with regard to the electroforming of foil. The flow cell geometry provides a well-defined hydrodynamic regime and mass transfer correlations are

available for design purposes. In the following section the fundamental aspects of mass transfer and the flow of fluids are discussed. This includes a detailed account of convective mass transfer in parallel plate cells. These ideas will be used later in design of the parallel plate cells and the flow system used in the current investigation.

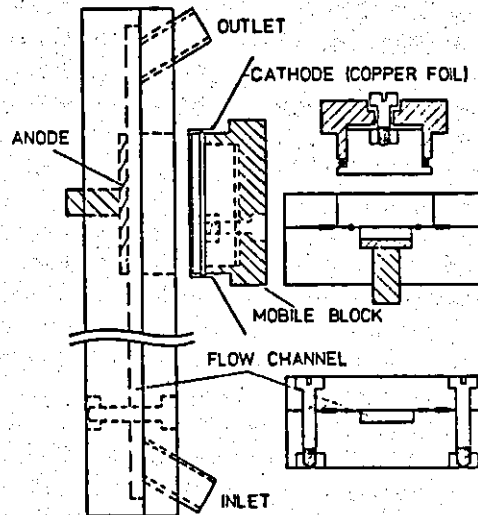


Fig.2.10 The parallel plate cell of Ibl and Angerer (68) used for the deposition of gold-cobalt alloys

2.3 Fundamental aspects of mass transfer and hydrodynamics in flowing electrolytes

In order to appreciate the complexity of electrodeposition in flowing electrolytes and the limitations imposed by the theoretical treatment, the background theory to mass transfer and hydrodynamics are presented in this section. It is from this that the basic design

parameters for the electrolytic deposition cells emerge. As will be seen, many of the concepts discussed will be used later in the design of the flow cells and the flow system.

The notation used by various authors in the literature shows some variance and the notation used throughout the present work is given for clarity in Appendix 1. For a more detailed treatment of this subject the reader is referred to several standard works (e.g. 99,148-153).

a) Diffusion and the flow of fluids

When electrode processes e.g. metal deposition, occur at a reasonably fast rate concentration overpotential becomes important, and in the classical treatment of Nernst (154), mass transfer was considered to occur by molecular diffusion through a thin layer of solution close to the electrode. This layer (Fig.2.11a) has a linear concentration gradient across it, and the concentration in the bulk (c_b) is assumed to be constant and maintained so by migration and convection. The molecular flux (N) across the Nernst diffusion layer can, using Ficks Law, be expressed as:

$$N = \frac{D}{\delta_N} (c_b - c_s) \quad \dots \dots (2.12)$$

where D is the diffusion coefficient, δ_N is the thickness of the diffusion layer and c_s is the concentration of the diffusing species at the electrode/electrolyte interface. Using Faraday's Laws (Section 2.1a), the flux can be expressed in terms of current density and hence:

$$i/zF = \frac{D}{\delta_N} (c_b - c_s) \quad \dots \dots (2.10)$$

which applies when the electrolyte is not in motion, i.e. stagnant and when the contribution of migration and convection to the flux are both very small.

The above view, however, is a simplified one since depletion of metal ions at the interface produces differences between the density of the solution at the interface and in the bulk of the solution and this

leads to natural convection and the concentration profile changes to that shown in Fig.2.11b. The concentration gradient is apparent over a narrower region at the electrode-electrolyte interface than for the case of diffusion alone, although the diffusion process still occurs at the electrode surface since any motion there is overcome by frictional forces. The most effective method of supplying fresh concentrated solution from the bulk is to increase bulk motion by stirring or flowing the electrolyte past the surface and this is known as forced convection. Forced convection is illustrated schematically in Fig.2.11c, where the region of the concentration gradient is again narrower, although the final process close to the electrode is a diffusion process.

Overall, in the presence of forced convection the process by which mass is transferred to the electrode is ultimately diffusion but the static layer thickness is considerably less than that indicated by the Nernst theory (δ_N). It is therefore more accurate to consider the concentration gradient at the electrode surface taken to be a vertical plane at $x=0$ i.e. $(\frac{dc}{dx})_{x=0}$. In this alternative form equation (2.10) then becomes,

$$\frac{i}{zF} = -D \left(\frac{dc}{dx} \right) \dots \dots (2.13)$$

The mass transfer coefficient (k) is defined as

$$k = \frac{-D}{c_b - c_s} \left(\frac{dc}{dx} \right)_{x=0} \quad \text{and hence}$$

$$\frac{i}{zF} = k(c_b - c_s) \dots \dots (2.14)$$

As the current density is increased the surface concentration of the particular component decreases until a constant or limiting current density is reached when the surface concentration of the species is close to zero. Hence it follows that:

$$\frac{i_L}{zF} = k c_b \dots \dots (2.15)$$

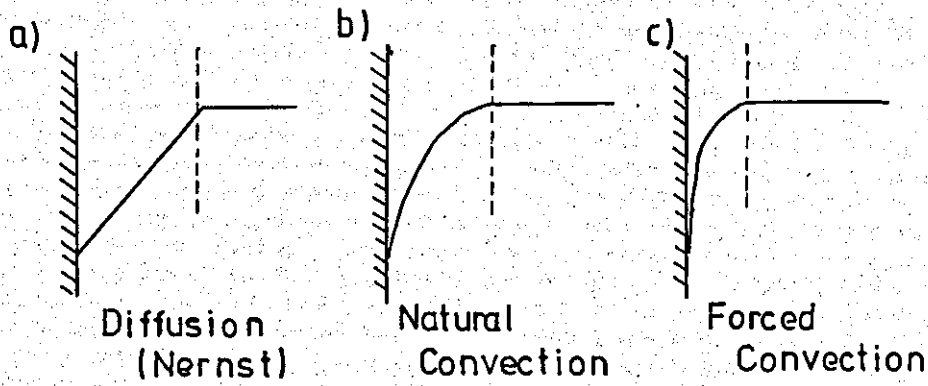


Fig.2.11 Concentration profiles adjacent to an electrode with a fast reaction

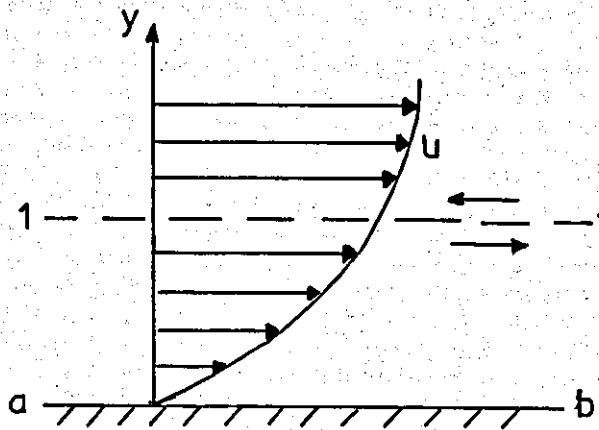


Fig.2.12 Shear stress in a viscous fluid

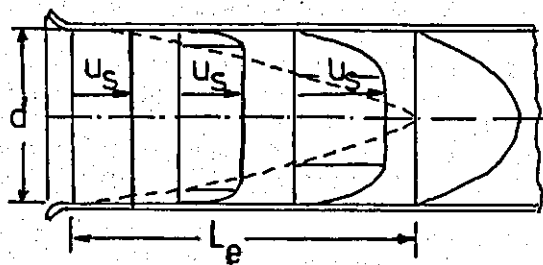


Fig.2.13 Development of a laminar velocity profile in the intake region of a tube

However, it should be noted that ionic migration to the electrode surface has not been taken to account. If the electro-active species is a major component of the electrolyte it will be a major current carrier in the solution and will tend to migrate in the electric field. Therefore, depending upon the ionic charge, it may well contribute to the overall current density. This subject is also dealt with elsewhere (Appendix 2).

In general it is assumed in this Section that the electro-active species is a minor component of the electrolyte (dilute solutions) and the current is carried by an inert supporting electrolyte. Hence the migration effects are minimised.

Flow in pipes and parallel to a flat surface - the hydrodynamic boundary layer

For a full account of these aspects of the subject the reader is referred to a number of standard texts (148,153). For the purposes of the present investigations it is necessary to introduce the concepts of hydrodynamic boundary layers, on flat plates and in pipes in order to appreciate the background problems to the study of convective mass transfer in parallel plate electroforming cells.

Basic concepts of fluid flow in pipes

Although liquids (and gases) have a measurable viscosity which results in frictional forces at solid surfaces when the fluid is in motion, real situations can be treated in some cases, by assuming a frictionless fluid. In such cases the relationship between the forces in a moving fluid, i.e. forces of inertia and pressure, can be related by the Bernoulli equation:

$$\frac{U^2}{2} + \frac{P}{\rho} + gz = \Psi \quad \dots \dots (2.16)$$

where P is the fluid pressure, ρ is the fluid density and g the acceleration due to gravity. When all the fluid is moving with a velocity U, Ψ represents the total energy per unit mass. In practice this condition may be approximated in turbulent liquids where frictional forces are dominant close to the solid wall of a pipe. Dividing Equation (2.16) by g:

$$\frac{U^2}{2g} + \frac{P}{\rho g} + z = C \quad \dots \dots (2.17)$$

Then each component has the dimensions of length and may be considered to contribute to the total fluid head. (C).

Thus: $\frac{U^2}{2g}$ is the velocity head due to the kinetic energy of the fluid

$\frac{P}{\rho g}$ is the pressure head due to the work done on the system

z is the potential head due to the potential energy of the system.

It can also be shown that:

$$\frac{\Delta U^2}{2} + \frac{1}{\rho} (P_2 - P_1) + g\Delta z + \frac{F}{\rho} = 0 \quad \dots \dots (2.18)$$

where F represents the contribution to the pressure loss due to frictional losses in the system, $P_2 - P_1$ is the pressure loss in the system and Δz is the change in potential head.

The most important physical property of a fluid which influences the pressure drop when it flows through a pipe is its viscosity which is a measure of the internal friction of a fluid. In laminar flow viscous forces result in shear stresses between streamlines. Streamline flow, close to a solid surface is depicted in Fig.2.12. The velocity u is directed parallel to the wall a-b and velocity differences occur in the y direction normal to the wall and shear stresses occur as a result of the viscosity in planes parallel to the wall. The value of the shear stress (R_y) at a point y is given by Newton's equation:

$$R_y = -\eta \frac{du_x}{dy} \quad \dots \dots (2.19)$$

and its direction is indicated by the arrows in Fig.2.12. It will be noted that the rate of shear is expressed as the velocity gradient du_x/dy in the fluid. High shear stresses only arise when the velocity

gradient is high since η (the dynamic viscosity) tends to have low values in aqueous solutions. This only arises near solid walls within a flow field. The maximum shear stress will be at the pipe wall, i.e.

$$R_0 = -\eta \left(\frac{du}{dy} \right)_{y=0} \dots \dots (2.20)$$

The stress R exerted by the fluid on the tube wall will be equal and opposite, i.e. $R = (-R_0)$. This term may be viewed as the resistance to flow per unit length. The distribution of shear stress in laminar pipe flow is given by:

$$\frac{Ry}{R_0} = 1 - \frac{y}{r} \dots \dots (2.21)$$

where r is the radius of the pipe. The corresponding velocity distribution is given by:

$$\frac{u_s}{u_{c.l.}} = 1 - \frac{s^2}{r^2} \dots \dots (2.22)$$

where u_s is the velocity at a distance s from the centre line and $u_{c.l.}$ is the centre line velocity (maximum velocity). The velocity profile is parabolic. The average velocity (U) is given by $\frac{u_{c.l.}}{2}$.

The development of laminar flow in a pipe is shown, for the inlet regions in Fig.2.13. The velocity in the core of the flow, outside the boundary layer increases with increasing distance from the entrance since the same amount of fluid flows through any cross-section as the boundary-layer thickness increases. After the entrance length (L_e) the velocity profile is a parabola.

The ratio of the entrance length (L_e) to the tube diameter (d) can be shown (148) to be given by:

$$\frac{L_e}{d} = 0.0288 \frac{Ud\rho}{\eta} \dots \dots (2.23)$$

Variations on this relationship have been suggested by Bird et al (152):

$$\frac{L_e}{d} = 0.035 \frac{Ud\rho}{\eta} \text{ and by Levich (155) } \frac{L_e}{d} = 0.05 \frac{Ud\rho}{\eta} \dots$$

In the study of fluid flow the dimensionless group $\frac{d_{cr} U_{cr}}{\nu}$ (cf. Equation 2.12) is of vital importance. This group is termed the Reynolds number (Re) and d_{cr} and U_{cr} are respectively a critical dimension and critical velocity of the system and $\nu (= \frac{\mu}{\rho})$ is the kinematic viscosity. The Reynolds number defines the degree of agitation of the system.

For pipe flow, the critical dimension is the pipe diameter (d) and the critical velocity is the average flow velocity (U). When the Reynolds number is plotted against the dimensionless group $R/\rho U^2 (= \varphi)$ a single curve results (for a given surface) for all fluids, pipe diameters and velocities (Fig. 2.14). The curve may be divided into three regions:

Region 1 ($Re < \sim 2,000$) corresponds to streamline motion and a single curve represents all the data, irrespective of the roughness of the pipe surface. The equation of the curve is $\varphi = R/\rho U^2 = 8Re^{-1}$.

Region 2 ($\sim 2,000 < Re < \sim 3,000$) is a transition region between streamline and turbulent flow conditions. Reproducible values of pressure drop cannot be obtained in this region, but the values of $R/\rho U^2$ is considerably higher than that in the streamline region.

Region 3 ($Re > \sim 3,000$) corresponds to turbulent motion of the fluid and $R/\rho U^2$ is a function of both Re and the roughness of the pipe. However, moderately rough pipes may behave as smooth pipes in this region. A number of expressions have been given for the calculation of $R/\rho U^2$ in terms of the Reynolds number of which the simplest is the Blasius equation (156) which is applicable for Reynolds numbers from 2,500 to 10^5 .

$$\varphi = R/\rho U^2 = 0.396 Re^{-\frac{1}{4}} \quad \dots \dots (2.24)$$

The frictional pressure drop (ΔP) over a pipe of length l is given by the Fanning-Darcy equation

$$-\Delta P = 4f \cdot \frac{\rho L U^2}{d} \quad \dots \dots (2.25)$$

where $f (= 2\varphi)$ is the Fanning friction factor and the corresponding head loss (h_f) due to friction is

$$h_f = \frac{4fL}{d} \cdot \frac{U^2}{2g} \quad \dots \dots (2.26)$$

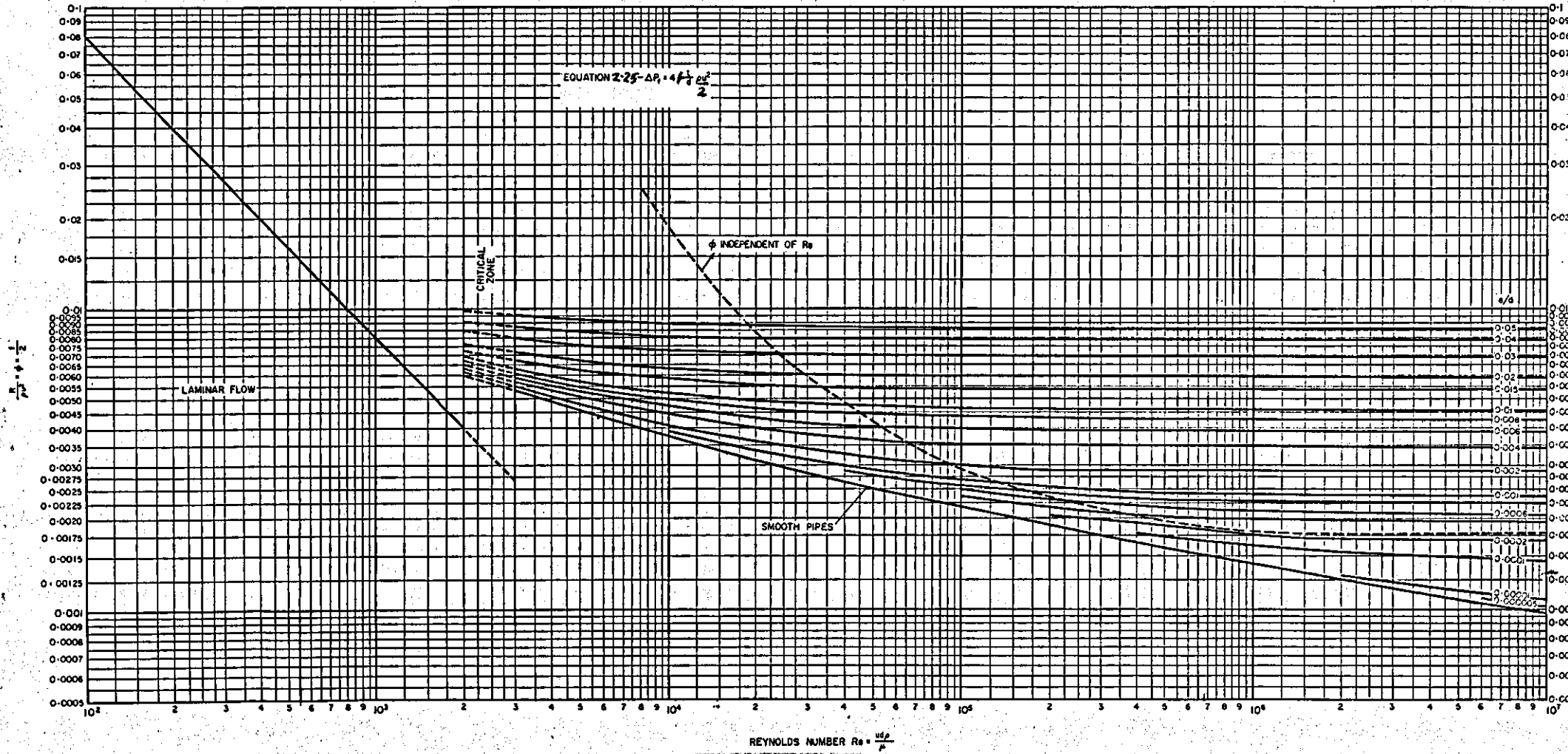


Fig.2.14 Pipe friction chart

Turbulent flow is characterised by random time - dependent velocity fluctuations superimposed on time-independent mean velocities. These are known as turbulent eddies.

For turbulent flow the velocity profile is much flatter than in laminar flow. In this case, turbulence dies down close to the wall and Prandtl (1956) introduced the concept that between a turbulent boundary layer (δ_T) and the wall, there is a laminar sub-layer (δ_b) within which the velocity increases linearly with distance y (Fig.2.15). Outside the narrow turbulent boundary layer the velocity (u_s) is assumed to be constant resulting in a more uniform velocity profile over the core of the fluid (Fig.2.16). Turbulent velocity profiles are developed more rapidly than laminar velocity profiles.

The velocity profile may be described by the Prandtl seventh power law

$$\frac{u_x}{u_{c.1.}} = \left(\frac{y}{r}\right)^{1/7} \dots \dots (2.27)$$

where y is the distance from the pipe wall. In this relationship the thickness of the laminar sub-layer is neglected and the Prandtl velocity distribution assumed to apply over the whole cross section. The result therefore is strictly applicable at high Reynolds numbers where the thickness of the laminar sub-layer is very small. The mean velocity (U) is given by $U = 0.82 u_{c.1.}$ At lower Reynolds numbers the mean velocity will be rather less than $0.82 u_{c.1.}$ (at very high Re , $U \approx u_{c.1.}$ i.e. the laminar sub-layer is negligible).

It can also be shown that:

$$\frac{R}{(u_{c.1.})^2} = 0.0228 \frac{\mu}{u_{c.1.} r}^{1/4} \dots \dots (2.28)$$

and for a pipe with $U = 0.82 u_{c.1.}$ and $d = 2r$

$$\frac{R}{\rho U^2} = 0.0384 Re^{-1/4} \dots \dots (2.29)$$

This equation may be compared with the semi-empirical Blasius equation (Equn. (2.24)).

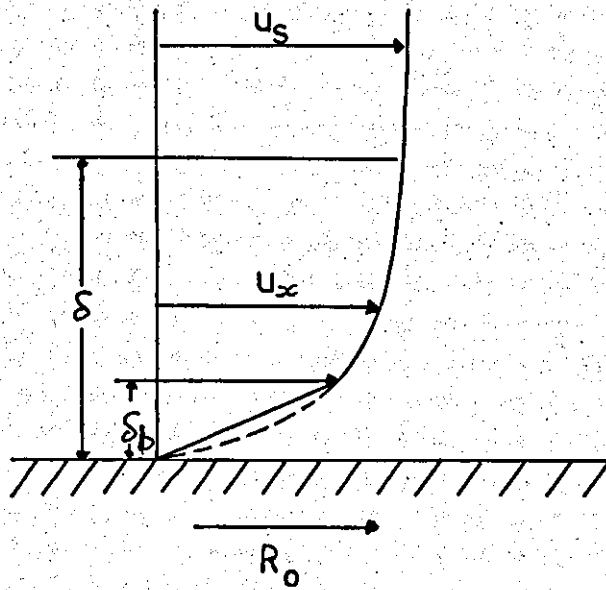


Fig.2.15 Laminar sublayer within a turbulent boundary layer

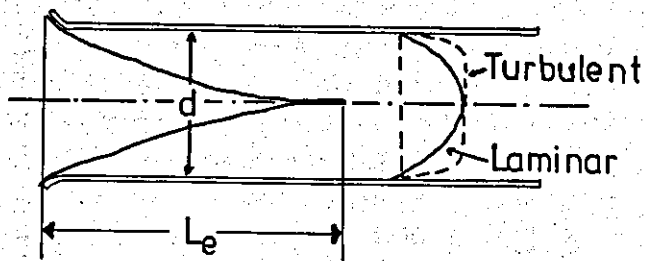


Fig.2.16 Flow development near the inlet of a pipe

The velocity at the edge of the laminar sub-layer u_b is given by:

$$\frac{u_b}{u_{c.1.}} = 2.0 \text{ Re}^{-1/8} \dots \dots (2.30)$$

and the thickness of the laminar sub-layer is :

$$\frac{\delta_b}{r} = 62 \text{ Re}^{-7/8} \dots \dots (2.31)$$

An alternative approach was used by Nikuradse (158) to produce a Universal Velocity Profile. The boundary layer was divided into three regions, a turbulent region, where turbulent eddies predominated, a buffer layer where eddy formation diminished and the laminar sub-layer.

Two dimensionless variables were derived, the dimensionless velocity u^+ ($= \frac{u_x}{U} \phi^{1/2}$) and the dimensionless distance from the wall,

$$y^+ (= \frac{y}{d} \phi^{1/2} \text{ Re})$$

In the laminar sub-layer $y^+ < 5$

$$u^+ = y^+ \dots \dots (2.32)$$

In the buffer layer $5 < y^+ < 30$

$$u^+ = -3.05 + 5.0 \ln y^+ \dots \dots (2.33)$$

and in the turbulent region $y^+ > 30$ (smooth pipes)

$$u^+ = 2.5 \ln y^+ + 5.5 \dots \dots (2.34)$$

the shear stress at the wall may be obtained from the expression:

$$\phi^{-1/2} = 2.5 \ln [(\text{Re}) \phi^{1/2}] + 0.3 \dots \dots (2.35)$$

The Universal Velocity Profile is only an approximation since it indicates discontinuities at $y^+ = 5$ and $y^+ = 30$ and also gives a finite velocity gradient at the axis of a pipe.

It would appear that both the Prandtl and the Nikuradse approach are over-simplifications of the real situation since both assume a

laminar sub-layer where the flow is streamline and viscous forces predominate. Observations of the sublayer using photographic techniques (159) have provided some evidence that this region is continuously disturbed by small-scale velocity fluctuations of low magnitude and periodically disturbed by fluid elements which penetrated into the region from positions further removed from the wall.

Flow over flat plates and boundary layer development

Flow over a flat plate in a free stream of velocity U_s can be considered as shown in Fig.2.17 and the hydrodynamic boundary layer builds up from zero at the leading edge and increases its thickness along the surface. At a critical distance x_{cr} from the leading edge, there is a change from laminar to turbulent flow. If the velocity u_s is increased the critical length x_{cr} becomes less in such a manner that the product $u_s x_{cr}$ is a constant. The laminar to turbulent transition occurs at a definite value of $\frac{u_s x_{cr}}{\nu}$. This dimensionless number is the Reynolds number for the system. The critical Reynolds number, thus defined constitutes an upper limit for laminar boundary layer flow on a flat plate. Estimates of boundary layer thicknesses are of interest in relation to understanding the effects of hydrodynamics on electrode and other mass transfer processes.

With laminar flow, the velocity profile has the shape shown in Fig.2.18 and it can be shown (148) that $\delta/x = 4.64/\sqrt{Re_x}$ where x is the distance from the leading edge of the plate. Thus defined δ is the distance from the wall at which the velocity reaches the value of the outside flow velocity. This is an arbitrary definition and various other definitions of δ and corresponding methods of calculation have been used. For example, Levich (155) has defined δ as the point at which the velocity reaches 90% of the free stream velocity and gives the expression $\delta/x = 5.2/\sqrt{Re_x}$.

In turbulent flow the expression for the boundary layer thickness $\delta/x = 0.376/Re_x^{1/5}$ has been derived. Here the thickness of the turbulent boundary layer is determined as if it began at the leading edge with zero thickness.

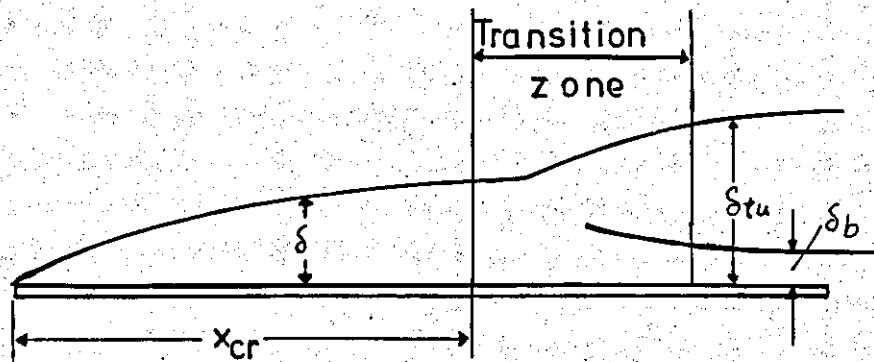


Fig.2.17 Laminar and turbulent boundary layers on a flat plate: δ laminar boundary layer, δ_{tu} turbulent boundary layer, δ_b laminar sublayer

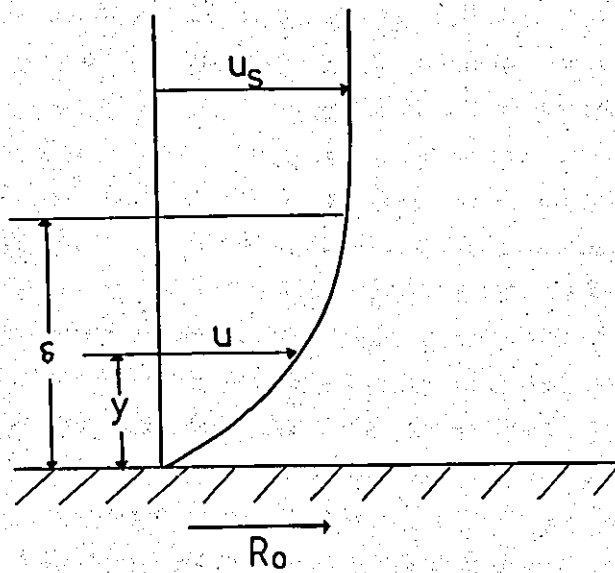


Fig.2.18 Laminar boundary layer on a flat plate

One of the difficulties in making satisfactory theoretical calculations is that there must be a transition zone from laminar to turbulent flow as seen in Fig.2.17. The treatment given here illustrates the problem of stabilising and characterising flow and boundary layer conditions on flat plates in a free stream, where there will be disturbances in flow at the leading edge of the plate.

Flow between parallel plates

In general (to a first approximation) flow in ducts may be treated in a similar manner as flow in pipes. However in this case the critical dimension is defined as the equivalent diameter d_e

$$d_e = \frac{4BS}{2(B + S)} \quad \dots \dots (2.36)$$

where B is the duct breadth and S the distance between the plates.

However, in the case of the entrance region of parallel plates in a free stream or infinitely wide plates, the flat plate approach may be applicable.

It should be clear from the above discussion that in considering cell design for experimental work due notice must be taken of entrance length requirements for the cell itself and the problems of establishing the flow pattern over individual electrodes.

Convective diffusion and mass transfer

The transport of solute in a moving liquid is controlled by two different mechanisms. The first of these is molecular diffusion which arises from concentration differences and in the second mechanism solute particles are entrained by the moving liquid and are transported with it. The combination of these two processes is known as convective diffusion. The diffusional component (j_D) can be shown to be

$$(j_D) = - D \nabla c \quad \dots \dots (2.37)$$

where the diffusion coefficient D is a function of solute concentration (c)

and temperature. When the solute concentration is low D can be considered constant and independent of composition. With solute entrainment there is also a convective flux $j_{\text{conv.}} = cU$ where c is the concentration and U is the flow velocity. With electrolytic processes there may also be the possibility of a migration component (j_m) which is given by:

$$j_m = z u_m F c \nabla \phi \quad \dots \dots (2.38)$$

The total mass flux (j) is the sum of the diffusional, migrational and convective components and

$$j = \underbrace{Z u_m F c \nabla \phi}_{\text{migration}} - \underbrace{D \nabla c}_{\text{diffusion}} + \underbrace{cu}_{\text{convection}} \quad \dots \dots (2.39)$$

In the presence of an excess supporting electrolyte, the migration component may be neglected and

$$j = -D \nabla c + cu \quad \dots \dots (2.39a)$$

The fluid velocity in a flowing electrolyte may be determined from the Navier-Stokes equation (160):

$$\frac{\partial u}{\partial t} + (u \cdot \nabla)u = -\frac{1}{\rho} \nabla p + \nu \nabla^2 u + g \quad \dots \dots (2.40)$$

Assuming that D is constant then a general equation can be developed for convective diffusion viz:

$$\frac{\partial c}{\partial t} + (u \cdot \nabla)c = D \nabla^2 c \quad \dots \dots (2.41)$$

In terms of Cartesian coordinates, equation (2.41) can be written as:

$$\frac{\partial c}{\partial t} + u_x \frac{\partial c}{\partial x} + u_y \frac{\partial c}{\partial y} + u_z \frac{\partial c}{\partial z} = D \left(\frac{\partial^2 c}{\partial x^2} + \frac{\partial^2 c}{\partial y^2} + \frac{\partial^2 c}{\partial z^2} \right) \dots (2.42)$$

and for a steady state process the convective mass transfer equation has the form:

$$u_x \frac{\partial c}{\partial x} + u_y \frac{\partial c}{\partial y} = D \left(\frac{\partial^2 c}{\partial x^2} + \frac{\partial^2 c}{\partial y^2} \right) \quad \dots \dots (2.43)$$

and use of this equation is made in the analysis of parallel plate cells in the following section.

b) Convective mass transfer in parallel plate cells

In this section the basic concepts related to the boundary conditions for convective mass transfer are discussed. Mathematical solutions are obtained in relation to whether (a) the surface concentration is constant or (b) the mass flux at the surface is constant. In general type (a) solutions correspond to an electrode which is operating at a limiting current density at all points on its surface, i.e. equation 2.15 applies. These solutions are, however, only adequate for smaller electrodes and the mass transfer coefficient varies from point to point along the electrode surface. In type (b) solutions "fully developed mass transfer" is associated with a linear variation of surface concentration along the electrode and applies to a very long electrode. In this case the mass transfer coefficient is independent of position on the electrode.

i) The parallel plate cell with short electrodes in laminar flow

Here there are three main cases.

Electrodes of infinite width with fully developed laminar flow
(Figure 2.19)

Here the convective mass transfer equation for a steady state process

$$u_x \frac{\partial c}{\partial x} + \frac{\partial c}{\partial y} = D \left(\frac{\partial^2 c}{\partial x^2} + \frac{\partial^2 c}{\partial y^2} \right) \quad \dots \dots (2.43)$$

can be modified if the electrodes are sufficiently far downstream from the cell entrance the flow will be fully developed and hence u_x is independent of x . For laminar flow $u_y = 0$ at all points in the flow and the Navier-Stokes equations 2.40 can be integrated to give:

$$u_x = 6U_{av} \left(\frac{y}{S} - \frac{y^2}{S^2} \right) \quad \dots \dots (2.44)$$

Hence we can rewrite equation (2.43) using equation (2.44) and since mass transfer in the x direction is mainly due to convection rather than diffusion we can approximate equation (2.43) to

$$6U_{av} \left(\frac{y}{S} - \frac{y^2}{S^2} \right) \frac{\partial c}{\partial x} = D \frac{\partial^2 c}{\partial y^2} \quad \dots \dots (2.45)$$

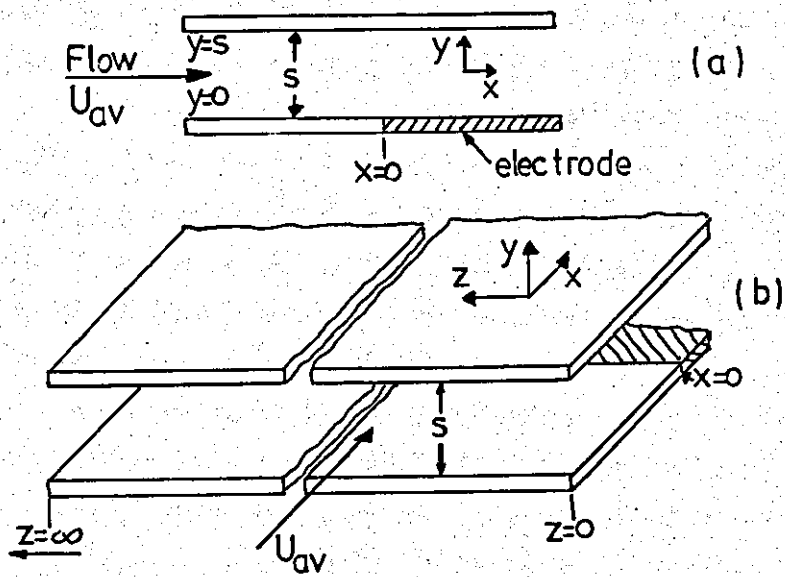


Fig.2.19 The parallel plate reactor with (a) hydrodynamic entrance length, (b) infinitely wide electrodes

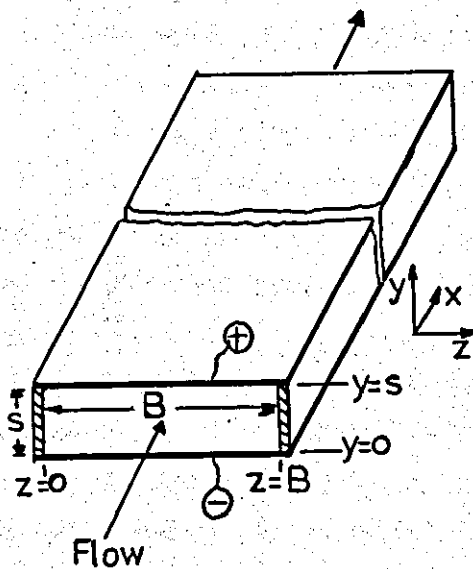


Fig.2.20 Parallel plate reactor with electrodes of finite width

According to Leveque (161) the local velocity close to the electrode is approximately linear i.e.

$$u_x = \frac{6U_{av}y}{S} \dots\dots(2.46)$$

which allows equation (2.45) to be simplified to

$$\frac{6U_{av}y}{S} \frac{\partial c}{\partial x} = D \frac{\partial^2 c}{\partial y^2} \dots\dots(2.47)$$

The boundary conditions related to equation (2.48) are that the reactant concentration at the cathode surface is constant (Type a), and that immediately upstream of the electrodes the concentration is uniform. There is also a condition that the local concentration becomes uniform away from the vicinity of the cathode.

In the simple case where the depletion of metal ions at the cathode is replaced and balanced by anodic dissolution it can be shown that the local mass transfer coefficient (k_x) is given by

$$k_x = \frac{D}{0.893} \left(\frac{2U_{av}}{3DxS} \right)^{\frac{1}{3}} \dots\dots(2.48)$$

which shows the variation of k_x with x along the electrode surface. Furthermore it can be shown that the average mass transfer coefficient k_{av} , and the corresponding average Sherwood No., Sh_{av} , over an electrode of length 'L' is given by

$$Sh_{av} = 1.85 \left\{ Re Sc \frac{d_e}{L} \right\}^{\frac{1}{3}} \dots\dots(2.49)$$

where d_e is the equivalent diameter of the cell. However it is virtually impossible, in practice, for cells to satisfy the electrode width and hydrodynamic entrance length requirements and hence a modified analysis can be made.

Electrodes of finite width with fully developed laminar flow (Fig.2.20)

In practice in a real electrolytic cell, the electrodes have a finite width B. In this case the velocity must be zero at the walls $z = 0$ and $z = B$ as well as at $y = 0$ and $y = S$. The velocity is still described by its x component and u_x is a function of both y and z . It

has been shown by Ong (162) that for a cell where $B > S$ the overall mass transfer coefficients are given approximately by

$$Sh_{av} = 0.807 [f(B,S)] \left\{ Re Sc \frac{d_e}{L} \right\}^{\frac{1}{3}} \dots (2.50)$$

where d_e is the equivalent diameter of the finite cell where $d_e = \frac{2BS}{B+S}$.

Rousar (163) has also derived the relationship

$$Sh_{av} = 1.85 \chi \left\{ Re Sc \frac{d_e}{L} \right\}^{\frac{1}{3}} \dots (2.51)$$

for a finite width reactor. Thus this relationship represents a modification of equation (2.49) for the situation where the electrodes have a finite width and the correction factors (χ) have been calculated (163) for aspect ratio values (ψ), where $\psi = \frac{S}{B}$, for values up to unity. When the aspect ratio is low (e.g. 0.05 to 0.10) the correction factor χ has values of $\sim 0.96 - 0.98$ and there is relatively little difference in the results using equations (2.49) and (2.51).

Other authors (164,165) have ignored the variation in velocity across the electrode and redefined the parameters in equations (2.49) and (2.51) in terms of equivalent diameter using $\frac{2BS}{B+S}$, rather than $2S$ for infinitely wide electrodes. This has given the relationship

$$Sh_{av} = 1.467 \left\{ Re Sc \frac{d_e}{L} \right\}^{\frac{1}{3}} \left\{ \frac{2}{1+\psi} \right\}^{\frac{1}{3}} \dots (2.52)$$

As $\psi \rightarrow 0$, $d_e \rightarrow 2S$, and this then reduces to equation (2.49). Experimental data give an empirical correlation with

$$Sh_{av} = 2.54 \left\{ Re Sc \frac{d_e}{L} \right\}^{0.3} \dots (2.53)$$

where Sh_{av} has been calculated for a measured limiting current i_L from the equation

$$Sh_{av} = \frac{i_L d_e}{zF D C_{av}} \dots (2.54)$$

where C_{av} is the average reactant concentration which is assumed to be equal to the bulk concentration and that the surface concentration is zero.

In general equations (2.49) and (2.53) can be used as cell design equations subject to the restrictions that the maximum electrode length is 35 equivalent diameters (165).

Long electrodes of infinite width in fully developed laminar flow

Only one relatively simple relationship, based on a uniform mass flux at the electrode has been derived. It can be shown that the mass transfer coefficient (k) is given by $k = \frac{2.692D}{S}$ (2.55)

and the Sherwood number defined in terms of the reactor equivalent diameter, $2S$ is given by $Sh = k \frac{2S}{D} = 5.384$ (2.56)

Equation (2.55) can be crudely modified to take into account other equivalent diameters viz:

$$Sh = \frac{2.692 d_e}{S} \quad (2.57)$$

but this has not been established experimentally.

ii) Parallel plate cells in turbulent flow

At Reynolds numbers >2000 the flow in a parallel plate cell becomes turbulent and random time-dependent velocity fluctuations are superimposed on time-independent mean velocities. The application of Navier-Stokes equations (2.40) in such circumstances results in additional terms which can only be accounted for on an empirical basis. Exact solutions of the basic convective mass transfer equation (2.43) on a similar basis as in laminar flow is not possible. The usual method of dealing with mass transfer in turbulent flow is to assume that mass and momentum are transferred by the same process, i.e. the motion of eddies. The rate of mass and momentum are characterised by empirical quantities called ϵ the eddy kinematic viscosity and ϵ_D the eddy diffusivity. Normally ϵ is determined from time-independent mean velocity, and assuming that ϵ_D is equal or proportional to ϵ the concentration distribution is obtained by integration of the mass transfer rate equation and the mass transfer coefficient determined from this. In the case of turbulent flow conditions fully developed concentration distributions or fully developed flow occurs over very short distances and the semi-empirical analyses obtained apply to these conditions.

The eddy kinematic viscosity ϵ , is used to define turbulent flow and is defined by the relation

$$R_y = \rho (v + \epsilon) \frac{du_x}{dy} \quad \dots \dots (2.58)$$

where R_y and $\frac{du_x}{dy}$ are the shear stress and mean time independent velocity gradient respectively at any chosen point. At a solid surface such as, for example, the cathode (where $y = 0$) the turbulent fluctuations die out (i.e. $\epsilon \rightarrow 0$) and the surface layers are in laminar motion. The shear stress at the surface R_0 is then given by:

$$R_0 = -\eta \left(\frac{du_x}{dy} \right)_{y=0} \quad \dots \dots (2.20)$$

By analogy the mass flux at any point (J) and at the cell wall (J_S) are given by:

$$J = - (D + \epsilon_D) \frac{dC}{dy} \quad \dots \dots (2.59)$$

and

$$J_S = -D \left(\frac{dC}{dy} \right)_{y=0} \quad \dots \dots (2.60)$$

where C is the time-independent concentration at a point. In order to solve equation (2.58) and hence equation (2.59) it is possible to adopt a universal velocity profile approach to describe the spacial dependence of u_x .

Following this type of approach Lin et alia (166) have developed a convective mass transfer equation of the form:

$$\frac{k_{de}}{D} = 0.057 (c_f/2)^{\frac{1}{2}} Re Sc^{\frac{1}{3}} \quad \dots \dots (2.61)$$

which applies at high Schmidt numbers, and where c_f is the skin friction factor. Also since the mass transfer coefficient is independent of electrode length (c.f. Equation (2.56) we can also write

$$Sh_{av} = 0.057 (c_f/2)^{\frac{1}{2}} Re Sc^{\frac{1}{3}} \quad \dots \dots (2.62)$$

It should be noted that in turbulent flow the mass transfer coefficient is velocity dependent (cf. equation 2.57).

Equation (2.61) can be extended for parallel plate cells using the Blasius relation for c_f i.e. $f = 0.074 Re^{-\frac{1}{2}}$ (c_f Equn.(2.24)) where

the Reynolds number is defined in terms of equivalent diameter, and this leads to the expression

$$\frac{kde}{D} = 0.0113 \text{ Re}^{0.875} \text{ Sc}^{\frac{1}{3}} \quad \dots \dots (2.63)$$

Other analyses (167,168) using variations in the method of ϵ/ν calculation lead to the relationship

$$\frac{kde}{D} = 0.0222 \text{ Re}^{0.875} \text{ Sc}^{\frac{1}{4}} \quad \dots \dots (2.64)$$

However, it should be noted that for values of Sc in the 2000 - 5000 range calculated values of the mass transfer coefficient are similar.

An even more empirical approach is to use the Chilton-Colburn analogy (169) which can be written as

$$\text{Sh}_{av} = 0.023 \text{ Re}^{0.8} \text{ Sc}^{\frac{1}{3}} \quad \dots \dots (2.65)$$

and where k_{av} is used instead of k in Sh_{av} to indicate that it is based on constant surface concentration data. The last equation gives both local and average mass transfer coefficients since the theoretical length dependency is only of a very low order and in practice is negligible.

There is also a parallel between equation (2.65) and the Dittus-Boelter equation (170)

$$\text{Nu} = 0.023 \text{ Re}^{0.8} \text{ Pr}^{0.3} \quad \dots \dots (2.66)$$

which applies to turbulent heat transfer in a pipe when cooling occurs. Experimental evidence (164,165) indicates that relations (2.61), (2.64) and (2.65) can be used for an electrode not less than 12.5 d_e in length. For much shorter electrodes fully developed concentration profiles do not arise and the mass transfer coefficient becomes length dependent. It has recently been indicated (149) that the best design relationship for a parallel plate electrode cell is

$$\text{Sh}_{av} = 0.145 \text{ Re}^{\frac{2}{3}} \text{ Sc}^{\frac{1}{3}} \left(\frac{d_e}{L}\right)^{\frac{1}{4}} \quad \dots \dots (2.67)$$

where L is the electrode length and $L/d_e < 7.5$.

Problems arising from cell entrance lengths and the development of flow in cells

In the preceding analyses fully developed flow has been assumed in relation to the calculations. However, there is a hydrodynamic entrance length over which the velocity distributions is not uniform and in carrying out experimental work, particularly under laminar flow conditions some account has to be taken of entrance length requirements. The development of flow and mass transfer in electrochemical cells with parallel plate electrodes is shown in Fig.2.21. At the entrance point in Fig.2.21a i.e. $x=0$, the velocity of flow will be uniform (U_{av}). There is however a frictional interaction with the walls until at $x=L_e$ fully developed flow is achieved, and L_e is defined as the hydrodynamic entrance length. There are two theoretical approaches to the problem of entrance length calculations. In one approach (Fig.2.21b) the electrode can be considered as an infinitely wide plate in a free stream of velocity U_{av} . In this situation the concentration distribution is altered due to the electrode process taking place. Alternatively the problem may be treated as a boundary layer situation where both the velocity and concentration distributions start to form at $x = 0$ and the region where velocity distributions exist is known as the hydrodynamic boundary layer (Fig.2.21c). Using the free streaming approximation an average Sherwood number relationship can be obtained, viz:

$$Sh_L = \frac{2}{\sqrt{\pi}} Re_L^{\frac{1}{2}} Sc^{\frac{1}{2}} \dots \dots (2.68)$$

Another approximation for laminar flow using the boundary layer approach yields the relationship

$$Sh_L = 0.646 Re_L^{\frac{1}{2}} Sc^{\frac{1}{3}} \dots \dots (2.69)$$

For practical systems where Schmidt numbers are of $\sim 2000 - 6000$ the first of these equations gives mass transfer coefficients of about one order of magnitude greater than in equation (2.69). The free streaming approximation is only valid when the velocity boundary layer is very much thinner than the concentration boundary layer, i.e. when $Sc \rightarrow \infty$.

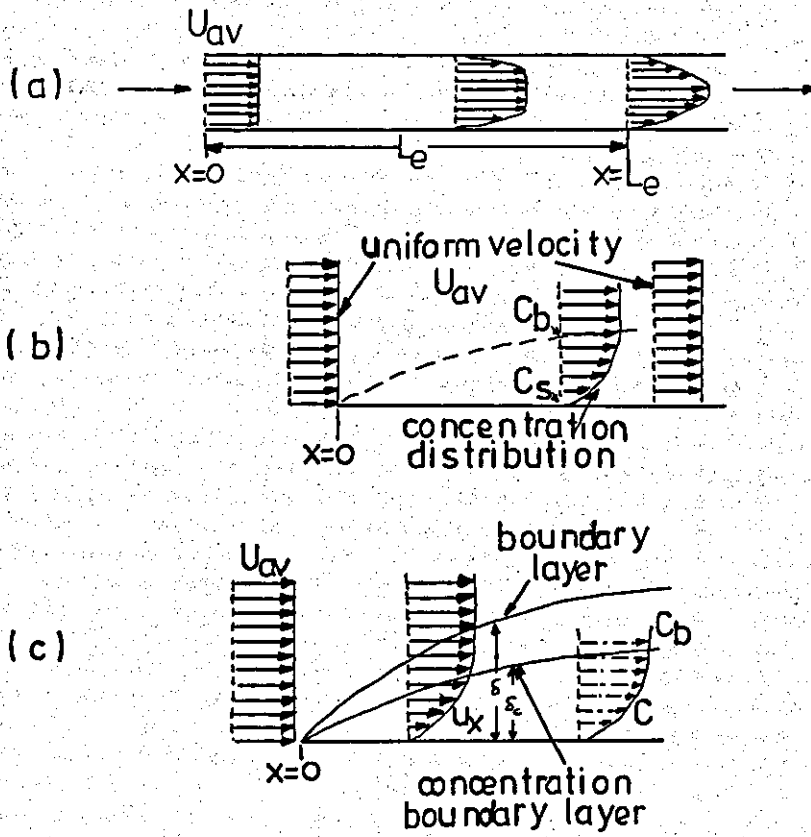


Fig.2.21 Flow and mass transfer in the hydrodynamic entrance region of a parallel plate electrochemical reactor
 a) hydrodynamic entrance length
 b) uniform velocity (free stream) assumption
 c) boundary layer assumption

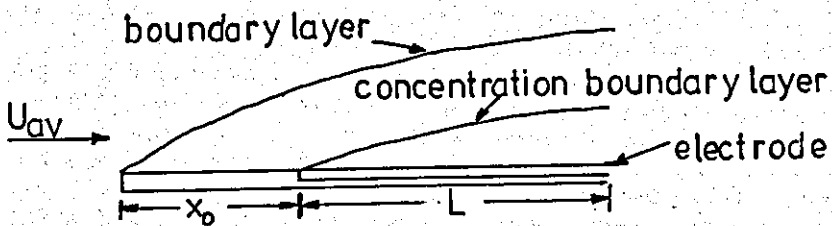


Fig.2.22 Mass transfer to an electrode with some previous flow development

Another important case arises where the electrode is some distance from the inlet and some flow development has already taken place (Fig.2.22). Here it can be shown (17) that the local mass transfer coefficient is given by

$$Sh_x = \frac{0.323 Re_x^{1/2} Sc^{1/3}}{\{1 - (x_0/x)^{3/4}\}^{1/3}} \dots \dots (2.70)$$

and coefficient is given by the average mass transfer

$$Sh_x = 0.646 Re_x^{1/2} Sc \frac{\{1 - (x_0/x)^{3/4}\}^{2/3}}{\{1 - x_0/x\}} \dots \dots (2.71)$$

Data concerning mass transfer in the entrance regions of parallel plate cells is sparse. The empirical relationship

$$Sh_x = 0.96 Re_x^{1/2} Sc \frac{\{1 - (x_0/x)^{3/4}\}^{2/3}}{\{1 - (x_0/x)\}} \left(\frac{de}{L}\right)^{-0.05} \dots \dots (2.72)$$

appear to fit experimental data for $Re < 2000$ and $Re_x < 5 \times 10^4$ (165), and for short electrodes $\frac{de}{L}^{-0.05} \sim 1$.

The shortage of supporting data and the theoretical limitations suggest that relationships (2.49) or (2.53) are used to obtain mass transfer coefficients and to assume that flow is fully developed.

For turbulent flow conditions entrance lengths of ~ 50 diameters are recommended. The application of turbulent boundary layer theory (162,165) leads to the relationship

$$Sh_x = 0.0366 Re_x^{0.8} Sc^{1/3} \frac{\{1 - (x_0/x)^{39/40}\}^{32/39}}{\{(1 - (x_0/x))\}} \dots \dots (2.73)$$

for $Re_x > 2 \times 10^5$, and this applies for an electrode length of 12.5 de with a hydrodynamic entrance length of ~ 8 de. The most useful estimates of mass transfer in developing turbulent flow can be obtained using the Chilton-Colburn equation (2.65) and by not taking into account the hydrodynamic entrance length. Equation (2.67) can be used for short electrodes in a developed turbulent flow and this has been confirmed experimentally (149).

c) Some aspects of electrolytic gas evolution

As will be seen (Section 4.0), the experimental results indicated that nickel deposition was often accompanied by considerable hydrogen evolution. The interpretation of the results required some understanding of the nature and possible consequences of electrolytic gas evolution. For completeness, this information is included in the following section. This includes firstly, a discussion of the formation of electrolytic gas bubbles and secondly, the implications for mass transport in gas evolving systems.

i) The formation of electrolytic bubbles

Electrolytic gas formation causes an effective mixing of the solution and in many respects is analogous to boiling of a liquid at a heated wall. The resulting effects of such phenomena include increased rates of mass transfer, a higher solution resistance and, in flowing solutions, a larger pressure drop. However, the phenomena are of great complexity and are influenced by many factors. The reproducibility of gas induced effects are insufficient to ensure accurate measurements. The quantitative treatments of electrolytic gas evolution are often similar to models developed for the analogous boiling of liquids and subsequent increase in heat transfer problems.

Electrolytic gas development takes place in three steps (172), the initial formation of nuclei, followed by growth of the bubble and finally separation of the bubbles.

The gas formed at the electrode is first dissolved in the electrolyte. However, for hydrogen, the solubility is low being typically about 2×10^{-4} mole dm^{-3} (173), and the solution rapidly becomes super-saturated (174). Then nuclei of bubbles can be formed through local fluctuations of density. Frequently new bubbles may be formed at preferred points of the electrode such as scratches. Some gas will remain in such surface irregularities and act as a bubble nucleus. Scratches of $\sim 5\mu\text{m}$ width have been found to be large active centres (175). As the defects become smaller the nucleation time of a new bubble at the same point increases. On highly polished surfaces this may take several minutes. Such behaviour is common at low current

densities. On increasing the current density the number of active sites will also increase. Fahidy and Abdo have found an empirical relationship of the form (176,177)

$$E_H = A_0 + A_1 / t_H \quad (2.74)$$

between the applied potential E_H and the induction time, t_H , for the first appearance of hydrogen bubbles on the cathode. The two constants A_0 and A_1 are affected by the cell geometry. The induction time probably depends on the nature of the electrolyte, its concentration and temperature and the rate of electronation of hydrogen ions, which is proportional to the voltage drop. The rate of mass transfer of super-saturated solution away from the cathode and the rate of super-saturation would also be important.

The nucleated bubbles then grow in two stages (175). In the first phase ($\sim 1m s$), the growth rate is dependent upon the quality of the electrode. The surface tension has a considerable influence on growth in this first phase. A second phase with slower growth then follows. The rate of growth will be controlled by the rate of mass transport from the super-saturated solution to the surface of the growing bubble. The relationship, $r \propto \sqrt{t}$, r = bubble radius at time t ., has been derived from integration of the relevant transport equations (178). This growth law has been found to be independent of the electrode material (175). In addition bubbles may grow by coalescence between two neighbouring bubbles.

The probability of separation and the size of the gas bubbles depends largely upon the magnitude of the wetting angle and hence upon the surface tension forces that result in bubble adhesion. However, electrostatic forces may also contribute to the adhesion (179).

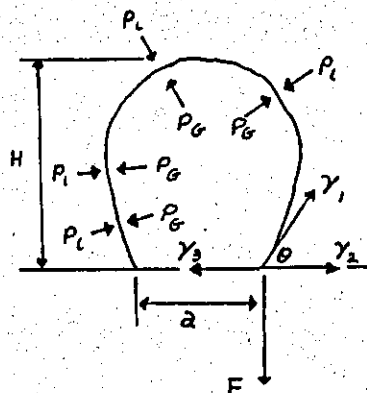


Fig. 2.23 Surface tension forces acting on an adherent bubble

From Fig.2.23 it may be seen that three surface tensions, solution/gas, γ_1 , solution/electrode, γ_2 and gas/electrode, γ_3 , act upon the three phase boundary gas/solution/electrode. The contact or wetting angle, θ , is obtained from the equilibrium of these forces. The vertical component of the surface tension gas/liquid, γ_1 , corresponds to the adhesion force F_Y . The adhesion force acting upon the whole three phase boundary is $\pi a \gamma_1 \sin \theta$, where a , is the diameter of the adhesion circle.

When the bubble adhering to the surface is at equilibrium, the forces must be equalised through the resulting forces of the hydrostatic pressure of the solution P_L and the gas pressure P_G on the boundary surface solution/gas. In this way Kabanov and Frumkin obtained the relationship (179):

$$\pi a \gamma_1 \sin \theta = V\rho g + \frac{1}{2}\pi a^2 \left(\frac{2\gamma_1}{R} \right) - H\rho g \quad \dots \quad (2.75)$$

where ρ - density of the solution, V - volume of the bubble, g the acceleration due to gravity, R - the radius of curvature and H , the height of the bubble.

For $\theta < 140^\circ$, this may be approximated, so the maximum bubble volume is given by (180)

$$V = \left(\frac{3}{\pi} \right)^3 \left(\frac{\gamma_1}{g} \right)^2 \theta^3 \quad \dots \quad (2.76)$$

Hence for a given surface tension gas/solution γ_1 , and solution density ρ the separation volume V is determined only by the contact angle θ .

It is evident that if the wetting angle is small, e.g. 18° and the surface is well wetted with water, the bubble adheres over a small area and the perimeter of the contact area is small. Such bubbles are easily detached from the surface and do not attain significant dimensions.

If the wetting angle is greater e.g. 75° , the perimeter of the contact area and consequently the force holding the bubble is greater, the bubbles can therefore become larger before they are detached.

The magnitude of the gas/electrode, γ_3 , and the solution/electrode, γ_2 , surface tensions are dependent upon the nature of the electrode material and upon the cathodic polarisation. Physically this means that the wettability of the metal by water increases with the charge density of the bubble layer. Water pushes the bubble away, hence wetting the electrode. Therefore, the wetting angle θ , is at a maximum when the surface charge is zero (at the potential of zero charge). If the gas is evolved at a potential close to the zero charge potential of the metal in a given solution, γ_2 is very high, so $\gamma_3 - \gamma_2$ and $\cos \theta$ are small and the wetting angle θ is large. Hence the bubbles grow to a large size before they are detached.

Conversely at very low cathodic potentials, the solution/electrode surface tension, γ_2 , is small and hence the detached bubbles are small. This relationship has been confirmed for slow rates of gas evolution, where conditions are close to equilibrium (100,181). However, at high rates of gas evolution, an increase in bubble size with increasing current density has been observed (182). This factor may be accounted for by coalescence of bubbles and the transport of gas from the super-saturated liquid, in conditions far removed from equilibrium.

In practice, the size of the generated gas bubbles has been found to be dependent upon the pH of the electrolyte (183,184) and whether the bubbles are generated anodically or cathodically (185,186). The measured bubble size may depend on whether the bubbles are observed on the electrode (100,183) or on rising bubbles (182, 185, 187). Momentum transfer from rising bubbles may result in early detachment of other bubbles leading to a wide distribution of bubble sizes. Janssen and Hoogland have measured the size distribution of bubbles under a series of experimental conditions (187). A large fraction of the bubbles were in the 40 to 60 μ m range, dependent upon exact experimental conditions. These roughly agree with the observation of Rousar et al (188). These workers used stagnant electrolytes and vertical electrodes. Horizontal electrodes often allow the formation of large bubbles which, under unfavourable conditions, may behave somewhat differently.

Landholt et al (182) have studied cathodic gas bubbles in a rectangular horizontal cell with an imposed flow velocity of 100 to 2,500 cm s^{-1} . A wide distribution of bubble sizes was observed. The median bubble diameters were 56, 78 and 99 μm for current densities of 5, 20 and 50 A cm^{-2} respectively (at $u = 400 \text{ cm s}^{-1}$). The median bubble diameters were 99, 69 and 35 μm for flow rates of 100, 200 and 400 cm s^{-1} respectively (at $i = 50 \text{ A cm}^{-2}$). However bubbles $< 20 \mu\text{m}$ in diameter were below optical resolution and bubbles close to the electrode were not discernible. They observed that the thickness of the gas layer increased along the electrode, reaching a maximum value about half way along. Loomba has referred to this effect as the 'gas wedge' (190). At low flow velocities bubbles may adhere to the electrode for prolonged periods.

The steady-state rise velocity due to buoyancy may be calculated from Stokes law for bubbles of less than 1 mm diameter (191) from the equation

$$v = \frac{g\rho d^2}{18\eta} \dots \dots (2.77)$$

g - acceleration due to gravity

ρ - density difference between gas and liquid

d - bubble diameter

η - dynamic viscosity of the liquid.

A bubble of diameter $\sim 50 \mu\text{m}$ will attain a rise velocity of only 2 mm s^{-1} . With rapid flow rates, the bubble will only rise a few microns over the electrode length. At downward facing electrodes, the buoyancy forces would tend to increase the adhesion to the metal. However, turbulent eddy formation and gas ejection (175) will act upon gas bubbles to move them away from the electrode.

A force balance may be applied to the case of a bubble developed in a flowing solution

$$F = F_i + F_b \dots \dots (2.78)$$

where F_b is the buoyancy force of the bubble and F_i is the inertia force

or shear force of the electrolyte. At high flow velocities, the contribution from F_b may be neglected. The magnitude of the two forces F_b and F_i are dependent upon the bubble volume and the bubble surface area respectively. Therefore the value of F must increase as the bubble grows and the forces F_b and F_i , acting upon it increase. This is achieved by increasing the value of the adhesion circumference, πa . Above a certain size, the bubble cannot compensate for the increased separating forces and the adhesion circumference is reduced. When $a = 0$, the bubble separates from the electrode.

Tong (192) developed a model, based on equation (2.78), which predicted that the bubble size varied with the square of the flow velocity. This result was confirmed qualitatively by Londhold et al (182).

In the case of simultaneous metal deposition a pit or pore will be left in the coating. When a pore is formed, it is likely that continuous, rapid nucleation of bubbles occur at the same site. In commercial plating, the production of pore free deposits are ensured by the lowering of the surface tension of the solution by the addition of surface active agents. A reduction of the surface tension from 60 - 70 dynes cm^{-1} to 20 - 30 dynes cm^{-1} is normally considered sufficient to achieve good wetting of the metal.

ii) Mass transfer at gas evolving electrodes

It is well established that gases evolving at an electrode do result in appreciable disturbance of the boundary layer. Many studies have been undertaken of mass transfer at gas evolving electrodes of various geometries, the most common of which are of the vertical gas evolving electrode/stagnant electrolyte type (100,193-198). Green and Robinson have studied mass transfer behaviour at gas evolving horizontal electrodes (199). The combined affect of gas evolution and surface roughness on the rate of mass transfer was investigated by Fouad and Sedahmed (200,201). The latter authors have also studied a gas evolving particulate-bed electrodes (202).

An alternative approach is to employ counter electrode gases to enhance cathodic mass transfer. A variety of cell geometries have been

used in conjunction with this technique (203-205).

Limiting current densities are not usually obtainable from polarisation data in the case of gas evolving electrodes. The normal method of obtaining mass transfer data for such systems is to employ an 'indicator reaction'. The concentration of an electroactive species in the solution is monitored with respect to time (e.g. (100, 195)). The mass transfer coefficient, k_L , is then given by:

$$k_L = \frac{C}{C_0 t A} \dots \dots (2.79)$$

where C is the concentration at time t, C_0 the original concentration of reactant and A, the surface area of the electrode.

Other workers have used the dissolution of a metal electrode to obtain mass transfer data (198,206).

An empirical correlation between the mass transfer coefficient, k_L and the rate of gas evolution, Q_g

$$k_L = C (Q_g / A)^{0.5} \dots \dots (2.80)$$

was first proposed by Roald and Beck (198) and later confirmed by Green and Robinson (199), Venczel (194) and Beck (207). However, the exact value of the exponent has been disputed by other workers (195,200,208,210).

The mechanism which explains the increase in the rate of mass transfer through bubble evolution is not completely established. Three models have been proposed to account for the experimental behaviour, namely the penetration, the hydrodynamic and the microconvective models.

The penetration or displacement model was developed by Ibl (100, 194,172,209) and considers that a bubble, on separating from the electrode, generates an empty space which is filled with fresh electrolyte flowing from the bulk of the solution to the electrode. Mass transfer is governed by transient diffusion in the quiescent liquid replacing the bubble. Afterwards the diffusional boundary layer is

reestablished and a new bubble begins to grow. The mass transfer coefficient, k_L , is then given by

$$k_L = \frac{6D Q_g (1-\theta)^{\frac{1}{2}}}{\pi r A} \dots (2.81)$$

where D - diffusion coefficient

Q_g - volumetric rate of gas development

A - electrode area

r - mean bubble radius

θ - fractional surface area

By introduction of dimensionless numbers (211) equation (2.81) may be transformed into

$$Sh = \frac{3.385}{C_1^{\frac{1}{3}}} [Re Sc (1-\theta)]^{0.5} \dots (2.82)$$

where $C_1^{\frac{1}{3}} = \frac{d}{R_b}$, d is the equivalent breakoff diameter, defined as the diameter of a sphere with the same volume as the real bubble and R_b is the radius of the departing bubble. $C_1 = 8$ for spherical (i.e. $d = 2R_b$) and $C_1 = 4$ for hemispherical bubbles. The following dimensionless numbers were defined:

$$Sh = \frac{k_L d}{D} \dots (2.83a)$$

$$Re = \frac{Q_g d}{A v} \dots (2.83b)$$

$$Sc = \frac{\nu}{D} \dots (2.83c)$$

The penetration theory represents a simple physical model.

The hydrodynamic model was suggested by Janssen and Hoogland (195). The rising gas bubbles carry along the liquid and a hydrodynamic flow develops along the electrode which accelerates the material transport. At steady state, the volume of the liquid transported upwards is equal to the volume of the liquid which flows downwards. The velocity distribution of the latter flow depends on many factors, such

as the dimensions of the electrolytic cell, the gas evolving electrode, the size of the ascending bubbles, the viscosity of the liquid and momentum transfer between liquid and gas bubbles. The problem is analogous to that of free convection, caused by electrolyte density differences.

Janssen has concluded that mass transfer can be explained on the basis of the hydrodynamic model (196) and described the model quantitatively (197). The mass transfer coefficient is given by the expression:

$$k_L = D^{2/3} \left[\frac{z g Q_g}{v U_g^t A} \right]^{1/3} \dots \dots (2.84)$$

where U_g^t is the terminal velocity of bubble rise, z the drag coefficient and g the acceleration due to gravity. The slope of the $\log k_L / \log Q_g$ relationship is 0.33. The bubble diameter is assumed to be roughly independent of the volumetric rate of gas evolution Q_g . However if the bubble diameter d_b is strongly dependent upon Q_g , the relationship will then be more complex.

Janssen has stated that, the hydrodynamic theory is applicable to cases where no coalescence of gas bubbles occurs (196). For this situation, at low current densities and for some gases, experimental evidence suggests a $\log k_L / \log Q_g$ slope of 0.33 (197). When coalescence occurs frequently, the slope will be higher, and the penetration model will be appropriate (196). Ibl (172) has correlated experimental data with the penetration theory (equation 2.82).

The microconvective model was introduced by Stephan and Vogt (211) and is based upon analogous boiling heat transfer models (212). It is assumed that rapidly increasing gas bubbles induce a convective flow within the surrounding liquid. After the bubble breaks off, the liquid flows back to the former bubble centre and a short time later the next bubble starts growing. It is assumed that the flow induced by the rapidly expanding gas bubble is decisive for the mass transfer process. The flow in the wake of the detached bubble is assumed to be unimportant and its influence on mass transfer negligible. A certain microarea was

attributed to each single bubble and the flow along the microarea is assumed to be laminar. The shape of the bubbles was regarded as either spherical or hemispherical. The induced convective flow was assumed to be plug-flow near the gas-liquid interface and boundary layer flow at some distance from the interface. From a theoretical analysis of the model they obtained the correlation (211)

$$\text{Sh} = 0.93 \text{Re}^{0.5} \text{Sc}^{0.487} \quad \dots \quad (2.85)$$

The dimensionless numbers were defined earlier (equations 2.83a,b,c). The authors correlated a great number of experimental results taken from other studies (e.g.(194,195,198,200,207,208, 2,4,9,7,17 etc.)), using equation (2.85). The experimental data were obtained from many gases and electrode materials over a wide range of temperatures, Schmidt numbers, Reynolds numbers, current densities and electrolytes. Most of the data lay within an error margin of +100% and -50%. The authors concluded that this level of accuracy was understandable considering the nature of the two-phase system and that equation (2.85) was an acceptable design equation.

Vogt has used equation (2.85) to give a relationship for the current efficiency of the hydrogen evolution reaction with a simultaneous, mass transport controlled metal deposition reaction (213). The current efficiency of hydrogen evolution, expressed as a function of the total current density is, in simplified form,

$$\text{C.E.}_{\text{H}_2} = 1 - \frac{[2X + 1]^{0.5} - 1}{X} \quad \dots \quad (2.86)$$

where

$$X = \frac{2.77 i p d z_2 / \nu D}{f_G R T F D_A (C_A^{z_1} / \nu_B)^2}$$

i = total current density

p = pressure

d = bubble departure diameter

z_2 = charge number for hydrogen evolution

z_1 = charge number for metal deposition

v_D = stoichiometric number for hydrogen

v_B = stoichiometric number for deposited metal

f_G = fraction of total amount of hydrogen evolved as gas

D_A = diffusion coefficient of dissolved metal

C_A = bulk concentration of metal

For a system of constant pressure and temperature, with $f_G = 1$, the current efficiency of the hydrogen evolution is a function of the total current density, bulk concentration of dissolved metal and bubble departure diameter. The validity of the equation (2.86) was confirmed by comparison with the experimental data of Sedahmed et al (214) and Venczel (194).

Combined effects in mass transfer

The case of mass transfer at gas evolving electrodes with superposition of hydrodynamic flow has been less fully investigated than the effect of gas evolution alone. The problem appears to have been studied first by Roald and Beck (198), who examined mass transfer rates on gas evolving rotating cylinders. Their results were re-drawn by Ibl (172), and are shown in Fig.2.24, as the mass transfer coefficient k versus the rotational speed for various rates of gas evolution

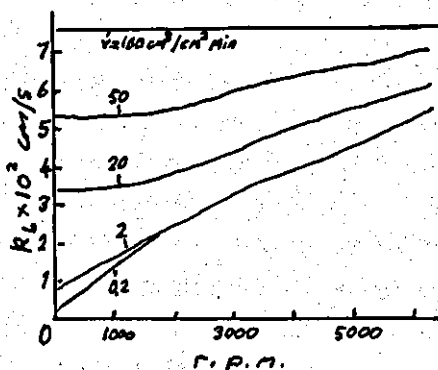


Fig.2.24 Mass transfer coefficient versus rotational speed for various rates of gas evolution (172)

evolution V . The rate of mass transport at a strongly gas-evolving electrode can be accelerated only by intense mechanical agitation.

At very high rates of gas evolution, the rate of mass transfer is independent of the forced convection.

Beck has proposed (207) that in such a situation where combined effects operate, the overall rate of mass transfer may be calculated by the summation of the independent mass transfer coefficients for each effect

$$k_L^{\text{TOTAL}} = k_L^1 + k_L^2 \quad \dots \dots (2.87)$$

where k_L^1 is the mass transfer coefficient for macroconvection (hydrodynamic flow) and k_L^2 is the mass transfer coefficient for microconvection (gas evolution).

Birkett and Kuhn (215) studied the combined effect of gas evolution with a flowing electrolyte in a rectangular channel. They obtained results which appeared to verify Beck's hypothesis at low flow rates. In a sufficiently turbulent flow the authors found that gas evolution had no further enhancement effects. Fahidy (216) has analysed the case of an annular flow cell with gas generation.

Vogt has stated (217) that if the gas generating current density is not extremely low, macroconvection will only exert an influence, on the overall rate of mass transfer, in turbulent flow. In laminar flow mass transfer will be dominated by gas evolution. By adoption of an equation developed for the case of heat transfer during nucleate boiling (218,219), Vogt proposed the following equation for the superposition of macro- and micro-convective mass transfer:

$$k_L^{\text{TOTAL}} = k_L^1 \left[1 + \left(\frac{k_L^2}{k_L^1} \right)^2 \right]^{0.5} \quad \dots \dots (2.88)$$

The agreement of equation (2.88) with the experimental results of Roald and Beck (198) was found to be satisfactory.

It is evident from the previous discussion that gas evolution is a complex process and hence accurate prediction of mass transport rates in gas evolving systems is difficult. However, it would appear

that for the purposes of interpretation of mass transport affects, the micro-convective approach of Vogt et al (e.g. equations (2.85) and (2.88) is suitable.

2.4 Electrochemical and metallurgical aspects of the electrodeposition of nickel

a) Review of systems for the electrodeposition of nickel

The commercial electrodeposition of nickel demands many requirements of the plating baths and the deposits produced from them. For economic reasons the bath should have a high conductivity and also be capable of depositing nickel at reasonably high current densities and current efficiencies to give a sufficiently rapid deposition rate. The deposit so produced must be uniform (i.e. a high throwing power electrolyte), coherent (i.e. not powdery) and adhere well to the substrate (i.e. of low internal stress). In electroforming operations, a deposit of low internal stress is important to avoid distortion of the electroform. In addition the mechanical properties of the electrodeposit such as the hardness, tensile strength, ductility and fatigue strength are of vital importance. For certain applications the electrical and magnetic properties, such as the resistivity and magnetic susceptibility may be of significance.

The choice of anion is of particular importance in determining the characteristics of the electrolyte and the deposits produced. The anion will affect the solubility of the nickel salt which in turn, will determine the deposition rate for a good deposit and the conductivity of the solution (and therefore the voltage requirements). The mechanical properties of the deposit, in particular the internal stress, are also related to the type of anion. Although nickel electrodeposits are generally fine grained, when compared to other deposits e.g. copper, the anion may have an effect on the deposit structure. Both the mechanical properties and the grain structure are often controlled by the addition of organic substances to the plating bath.

Certain anions, such as chloride, may be added to the bath to aid anodic corrosion. Chloride ions also have a marked effect on the properties of the deposit and tend to increase the internal stress.

The grain size is influenced by the pH of the bath, increasing with increasing pH. Since nickel deposition is accompanied by hydrogen evolution, the pH close to the cathode surface tends to increase during electrodeposition. The pH increase is commonly moderated by the addition of boric acid as a buffer to stabilise the pH close to the electrode. Boric acid usually buffers at about pH 4. If the catholyte becomes more alkaline, the deposits become brittle, cracked and highly stressed. At $\text{pH} > 6$, nickel hydroxide will be deposited. The addition of boric acid, whitens the nickel deposit and refines the grain structure. At low pH (< 3), the current efficiency for nickel deposition tends to decrease due to increased hydrogen evolution. The pH changes at the interface are discussed further in Section 2.4b(i).

Hydrogen evolution may result in hydrogen bubbles adhering to the electrode and forming pits or pores in the deposit. Therefore surface active agents (anti-pitting agents) may be added to the bath to lower the surface tension and facilitate bubble removal. Alternatively oxidising agents such as hydrogen peroxide or sodium perborate may be added to oxidise hydrogen. Solution agitation will also assist bubble removal.

In commercial nickel plating, the deposition reaction is generally considered to be diffusion controlled. As a result, solution agitation is generally used to ensure a low concentration overpotential and a good deposit. In conventional processes, the bath is agitated by blowing air through the solution, moving the workpiece (e.g. barrel plating) or some other simple technique.

Bath temperatures of 45 to 55°C are generally employed to ensure a reasonable deposition rate and a good deposit.

The theory and practice of nickel plating has been described in detail elsewhere (e.g. 220-226). In commercial practice several baths

are available for the electrodeposition of nickel. The composition of solutions and range of properties of deposits which may be obtained for nickel electrodeposits are summarised in Table 2.5. The main features of some of the more important baths are as follows:

Watts bath (227)

The most commonly used solution is the Watts bath or derivatives of it, such as the bright nickel solutions. The principal bath constituent is nickel sulphate which provides the major source of nickel ions. Nickel sulphate is used because it is readily soluble (570 gl^{-1} at 50°C), relatively cheap, commercially available and chemically stable. A typical Watts bath formulation is as follows:

$\text{Ni SO}_4 \cdot 6\text{H}_2\text{O}$	240 gl^{-1}
$\text{Ni Cl}_2 \cdot 6\text{H}_2\text{O}$	45 gl^{-1}
$\text{H}_3 \text{BO}_3$	30 gl^{-1}

anti-pitting agents

However, the range of concentration used may be relatively wide (e.g. $\text{Ni SO}_4 \cdot 6\text{H}_2\text{O}$ 150 to 400 gl^{-1}). Nickel chloride is added principally to assist anode corrosion. A typical operating current density would be about 0.05 A cm^{-2} (5 A dm^{-2}) at a current efficiency of $\sim 95\%$ (at $\text{pH} \sim 4$). The above bath produces standard dull deposits of nickel. Operating temperatures are normally in the range 45 to 55°C .

Bright nickel bath

Bright nickel is produced from Watts-type baths with the addition of organic substances. These components are incorporated in the deposit and produce a laminated structure characterised by very fine, often microscopically unresolvable grain size. The decomposition products of the brightness effect a decrease in ductility and an increase in internal stress and hardness. Sulphur-containing compounds are often used as brighteners. A typical bath formulation is shown overleaf:

Type of bath	Constituents of solution (typical concentrations in g/l)					
	Nickel sulphate (NiSO ₄ ·6H ₂ O)	Nickel chloride (NiCl ₂ ·6H ₂ O)	Nickel sulphamate (Ni(SO ₃ NH ₂) ₂ ·4H ₂ O)	Nickel fluoborate (Ni(BF ₄) ₂)	Boric acid (H ₃ BO ₃)	Other
Watts	240-330	37-52	-	-	30-45	-
Hard Watts (containing ammonia)	180-230	-	-	-	30	Ammonium chloride: 25
All chloride	-	250-300	-	-	25-30	-
Conventional sulphamate	-	0-15	300-450	-	30-45	-
Conventional sulphamate plus organic stress-reliever	-	30	300-450	-	30	Sodium naphthalene trisulphonate 7.5
Concentrated sulphamate Fluoborate	-	5-15	550-650	- 300-450	30-40 22-37	-

Type of bath	Ultimate tensile strength (N/mm ²)	Yield strength (N/mm ²)	Elongation (%)	Hardness (HV)	Internal stress (N/mm ²)	Limiting current density before burning (A/dm ²)
Watts	380-450	220-280	20-30	150-200	140-170	20
Hard Watts (containing ammonium ions)	1000*	750*	5-8	350-500	280-340	20
All chloride	750-900	650*	8-13	200-250	280-340	40
Conventional sulphamate	500-800	500*	10-20	160-240	7-70	20
Conventional sulphamate plus organic stress-relievers	1500*	800-1000	2-5	400-600	-40 to +14	20
Concentrated sulphamate Fluoborate	750-1000 380-550	-	10-15 17-30	200-300 170-220	-100 to +140 100-170	40 40

* Typical values

Table 2.5 Composition of some common electroplating solutions for nickel deposition and the range of physical properties of electrodeposited nickel from the baths listed (220).

Ni SO₄ · 6H₂O 210 gl⁻¹

Ni Cl₂ · 6H₂O 60 gl⁻¹

H₃ BO₃ 30 gl⁻¹

sodium benzene disulphonate 7.5 gl⁻¹

reduced fuchsin 0.01 gl⁻¹

Bright nickel coatings are generally used for decorative reasons (However see Duplex nickel).

Semi-bright nickel

These baths are of a similar composition to bright nickel baths but are only partially bright. The bath usually contains only one addition agent e.g. coumarin. The baths have good levelling properties and are primarily used to hide surface defects.

The deposits are harder than those plated from a Watts solution, the surface topography is smoother, and the grain size is smaller but not as small as that of bright deposits. The deposits are normally free of sulphur.

Duplex nickel

Bright nickel on semi-bright nickel (Duplex nickel) is now used extensively under chromium deposits. The sulphur content of the bright nickel results in the preferential corrosion of this layer and some protection for the metal substrate.

Hard nickel plating

The solution is basically a Watts bath operated at high pH (pH 5.6). This is mainly used for engineering purposes. The increase in hardness is achieved at the expense of other properties such as ductility and internal stress. The increase in pH is achieved by the addition of ammonium salts to the solution and the incorporation of ammonium ions results in modification of the structure and some deposit properties.

All-chloride solutions (228)

High concentration nickel chloride solutions (containing boric acid) have a higher conductivity than Watts bath formulations and may allow a faster deposition rate. The cathodic current efficiency tends to be higher than Watts solutions, particularly at low current density and low pH values, e.g. At pH2 and 0.012 A cm^{-2} , Watts 70%, All-chloride 95%. Nickel deposits from all chloride solutions are finer grained, smoother, harder and stronger but less ductile. These deposits are also less susceptible to pitting and nodular growths and have a wide range of plating conditions.

However, nickel chloride is a more expensive nickel salt and the deposits tend to be highly stressed. Although deposits are easily buffed to a bright finish, they are darker in appearance and more easily corroded.

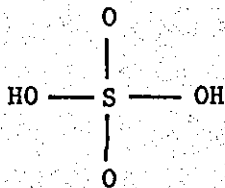
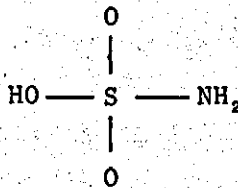
Fluoroborate solutions (229)

In addition to nickel fluoroborate this solution may also contain boric acid and chloride ions. The buffering capacity of the bath is intrinsically high and the solutions are easily controlled. The solutions have a high conductivity, good anode corrosion characteristics and excellent throwing power. However, nickel fluoroborate is an expensive nickel salt and the bath is usually reserved for specialist electroforming, heavy nickel plating and barrel plating operations.

Sulphamate solutions

The use of a sulphamate plating bath for the deposition of nickel was first suggested by Piontelli and Cambi (230) in 1938. Nickel plating from sulphamate solutions has been comprehensively reviewed by Hammond (231).

The basic constituent is nickel sulphamate, $\text{Ni}(\text{NH}_2\text{SO}_3)_2$, a salt of the strong monobasic sulphamic acid $\text{NH}_2\text{SO}_3\text{H}$ which is similar in structure to sulphuric acid with one hydroxyl group replaced by an amino group:

Sulphuric acid, H_2SO_4 Sulphamic acid, $\text{NH}_2\text{SO}_3\text{H}$

A characteristic of nickel sulphamate (and many other metal sulphamates) is the high solubility of the salt (in excess of 900 gl^{-1}).

Barrett (232) developed the first nickel sulphamate based plating solution of commercial importance. Subsequently Diggin (233,234) published the results of an extensive investigation in which he studied particularly the mechanical properties, internal stress and structure of deposits made from sulphamate solutions and the influence of electrolyte composition and operating conditions. These solutions and other baths containing 300 to 450 gl^{-1} nickel sulphamate are generally known as conventional sulphamate baths. A summary of the composition of nickel sulphamate based plating solutions is given in Table 2.6. All these baths contain boric acid to buffer the solution and many contain chloride ions to improve anode dissolution efficiency. The baths are generally operated at $\text{pH} \sim 4$ and about 50°C . Many investigations of deposition from conventional nickel sulphamate baths have been published (e.g. 235-239).

An important development was the introduction by Kendrick (1) of the 'Concentrated' nickel sulphamate bath (The Ni-Speed Process) in 1964. This bath, containing 600 gl^{-1} nickel sulphamate, permits deposits of good mechanical properties to be obtained at high deposition rates. Since this solution was used in the current investigations it will be reviewed in some detail in section (2.4b).

b) Electrochemical and morphological aspects of nickel deposition

As will be seen relatively little electrochemical research has been carried out in nickel sulphamate solutions. The general background is, however, of importance in the interpretation of the

Description	Nickel sulphamate g/litre	Boric acid g/litre	Nickel chloride g/litre	Other additions
Barrett-Type SN	450	30	—	Anti-pit agent 0.4 g/litre; SNSR stress reducer ¹
Ollard and Smith ²	320	27	—	
Diggin — Bath 1	300	30	30	NTS ³ — 7.5 g/litre
Bath 2	300	30	30	
Hanson-van-Winkle-Munning ⁴		— as Diggin Bath 2 —		
Albright and Wilson				Pb-N1 — 6.2 g/litre ⁵
Solution 1	350	35	5	
Solution 2	310	31	31	
Fanner and Hammond	340	30	3.3	Sodium lauryl sulphate 0.1 g/litre (as anti-pit, optional)
Kendrick ⁶	600	40	5	

Notes :

- (1) Proprietary solution.
- (2) *Handbook of Industrial Metal Finishing*, 1954, 2nd Edition, Iliffe & Sons, London.
- (3) Sodium naphthalene, 1, 3, 6 — trisulphonic acid.
- (4) H-vW-M process now marketed by M. & T. Chemicals, Rahway, New Jersey, U.S.A.
- (5) Proprietary hardening and stress-modifying agent.
- (6) Introduced to Industry as the Ni-Speed Process (U.K. Patents 999,117 and 1,101,093).

Table 2.6 Selected nickel sulphamate plating solutions (231)

experimental results as far as they relate to deposition mechanisms.

This part of the review is presented in two sections:

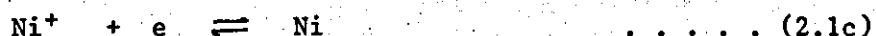
- i) Non-sulphamate systems
- ii) Nickel sulphamate systems

The latter section also includes a general review of electroplating from the concentrated nickel sulphamate ('Ni-Speed') system.

i) Electrodeposition of nickel from solutions other than sulphamate

The electrochemistry of nickel electrodeposition from solutions other than sulphamate

The electroplating of nickel from simple salt solutions is often thought to be a relatively simple process of the type



However a closer inspection of the literature suggests the process is more complex. The complexity is illustrated by some observations of the electrochemistry of nickel deposition.

Cathodic processes

Both cathodic deposition and the active anodic dissolution rates of nickel are dependent on the electrode potential, pH, concentration of metal ions, the nature of the anions present in the solution and the state of the electrode surface. The polarisation state often varies with time leading to hysteresis of polarisation curves (240). The deposition reaction is usually accompanied by the simultaneous formation of hydrogen.

The rest potential of nickel

The rest potential of nickel in oxygen free solutions has been found (241) to be independent of the activity of the Ni^{2+} ions and dependent upon the pH of the electrolyte. The rest potentials are

more positive than the hydrogen or nickel reversible potentials, except at very low pH when they are close to that of the H/H⁺ system. Increasing temperature (40 to 60°C) results in a negative shift in rest potential. As the pH of the solution increases, so the passivity of nickel increases. The rest potential of the electrode is highly dependent upon the activity of the anion. It is unlikely that in aqueous acid solution a 'clean' nickel metal/solution interface occurs.

Cathodic polarisation behaviour

In the presence of Ni²⁺ at pH ~ 4, a cathodic Tafel region exists at potentials lower than the reversible potential ($E < E_{Ni}^0$) corresponding to the simultaneous deposition of Ni and H. The experimental Tafel slopes for the reduction are normally about 60 mV/dec. After a suitable correction to account for the concomitant hydrogen evolution the Tafel slope is about 120 mV/dec. The Tafel lines are not so well defined in the presence of active anions such as chloride or at low pH ($\ll 4$) (241). The exchange current densities (i_0) for the reduction of nickel ions are strongly dependent on pH, the anion and the nickel ion activity (241). Values of the exchange current density, evaluated at the reversible potential, are in the range 10^{-6} , $\sim 10^{-8}$ A cm⁻². The experimental values of the exchange current density for the cathodic and anodic processes do not generally coincide (241). Therefore the reaction is highly irreversible.

Effect of temperature

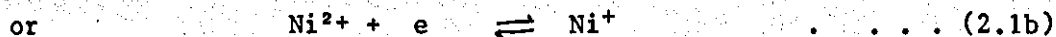
Appreciable decreases in polarisation are observed on increasing the temperature, in both cathodic and anodic regions. The cathodic (and anodic) Tafel slopes also tend to decrease with increased temperature. Vagramyam et al (242-246) have determined the following temperature coefficients ($\partial E/\partial T$) for 1m NiCl₂ and 1m NiSO₄ solutions at pH 1.5 (0.02 A cm⁻²)

	$\frac{\partial E_c}{\partial T} (\text{mV}_c^{\circ-1})$	
	25-75°C	175-200°C
1m NiCl ₂	2.4	0.2
1m NiSO ₄	3.3	0.4

Temperature coefficients ($\partial E_c/\partial T$) of $\sim 5 \text{ mV } ^\circ\text{C}^{-1}$ have been found in 2M NiCl_2 solution (247) over the temperature range 5 - 85°C. The low temperature behaviour is dominated by the adsorption of foreign species on the electrode. At very high temperatures this effect is absent. The temperature effects may be assigned to an increase of activity of the discharging ions and a decrease in inhibition by the foreign species.

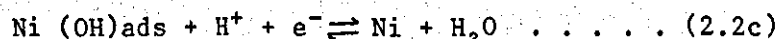
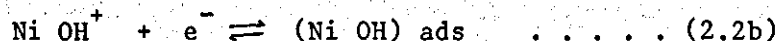
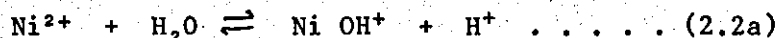
The mechanism of nickel deposition in the absence of chloride ions

In solutions containing sulphate or perchlorate ions (i.e. non-complexing anions) the Tafel slopes of $\sim 60\text{mV/dec}$ have provided evidence favouring a charge transfer step as rate determining (249). Early investigations (250) suggested that the deposition rate was independent of pH. However later studies have clearly shown that in the absence of chloride ions the rate of both deposition and dissolution of nickel is pH dependent (241,251). Consequently the simple mechanisms such as:



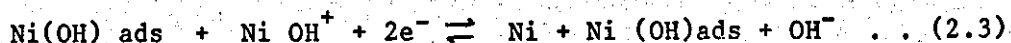
may be dismissed.

From the pH changes close to the cathode during electro-deposition and the existence of Ni OH^+ , (which is already present at appreciable quantities at pH4 (252)), the following mechanism has been deduced (241):



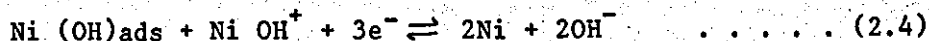
This mechanism is favoured by the experimental results which verify theoretical values of the electrochemical parameters (241). Different reactions leading to the electrocrystallisation of the metal have been considered; Heusler (251) has proposed a mechanism for the cathodic

deposition of the iron group metals involving Ni(OH) ads in a catalytic role, so:



In this reaction Ni^I ads also represents a self-perpetuating kink site where propagation occurs.

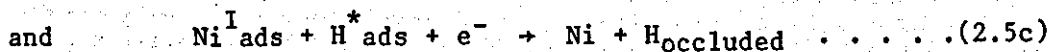
Epelboin and Wiart (253) have provided evidence to support the hypothesis that the cathodic reaction occurs in several steps probably involving an adion Ni (OH) ads. The adion acts as an intermediate and is consumed at the electrode by the reaction.



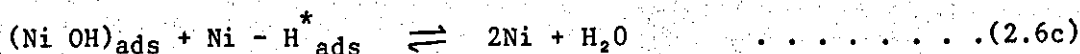
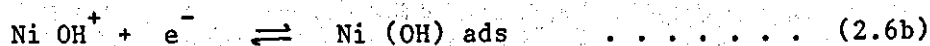
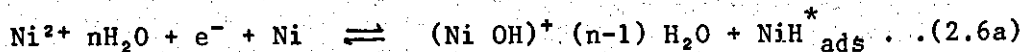
However, a more recent study (254) has supported the view that Ni(OH)ads acts as both an intermediate and as a catalyst for the production of an adsorbed hydrogen species



The H* ads may act as an inhibitor for the hydrogen evolution reaction and is slowly consumed by the reactions



Schaus et al (247) have criticised mechanisms involving the formation of Ni OH⁺ by the hydrolysis reaction proposing that the production of hydrogen ions should stimulate hydrogen ion discharge currents similar or greater than the nickel reduction current. An alternative mechanism involved a charge transfer reaction to a nickel aquo-ion complex

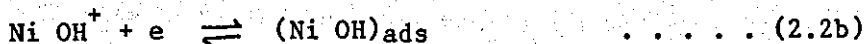


Hydrogen may also be evolved by the reaction



However, hydrogen ions are also consumed in other reaction schemes (2.2c), (2.5a) for the electrocrystallisation process. Hence the production of hydrogen ions by the hydrolysis mechanism (2.2a) may not stimulate hydrogen evolution.

Whilst the exact reaction mechanism for nickel deposition is still a matter of conjecture, the evidence indicates that the Ni OH^+ species is present at appreciable concentrations at $\text{pH} > 4$. It appears to be well established that in the absence of chloride ions the rate determining step is



However, some doubt exists about the mechanism of the electrocrystallisation reaction.

The effect of chloride ions on the electrochemical behaviour of nickel

The rate of cathodic processes are 1st order with respect to the nickel ion activity in chloride containing solutions. There is some evidence (255,256) to indicate that in chloride containing solutions, the reaction rate is independent of pH (pH 0.75 to 3.0). It has been suggested (256,257) that in chloride solutions metal-hydroxy species are not formed and aquo or chloro complexes participate in the cathodic process.

The electrochemical effects associated with the presence of chloride ions may be associated with the specific adsorption of the ion (5,246,257). This has the effect of decreasing the potential of the Helmholtz double layer and consequently the anodic overvoltage. In the region of the inner Helmholtz plane, the existing high field strength will result in the distortion of the atomic orbitals of the chloride ion. The distorted orbitals may then overlap with part of the nickel orbital system to form a distorted ligand.

The electronic structure of nickel (258,259) can be considered to be composed of three states, $(3d)^9 (4s)^0$, $(3d)^9 (4s)^1$, $(3d)^8 (4s)^2$ with a statistical average of $(3d)^{9.4} (4s)^{0.6}$. However, the electronic structure of the aqueous nickel ion is $(3d)^8 (4s)^0$. Hence electronic redistribution must take place during deposition and dissolution. It is thought that chloride ions may promote d- electrons by its adsorption. As a consequence of this the dissolution process is facilitated and the deposition process inhibited. However, the lower Tafel slopes and reaction rates observed in chloride ion containing solutions may be offset by the increased solubility and high activity coefficients of nickel chloride (260,261). In contrast to nickel sulphate solutions, the activity of nickel ions in chloride solutions increases with the concentration of the salt. The high activity may also be reflected in the high diffusion coefficients for nickel chloride solutions (137).

However, during the electrodeposition of nickel from electrolytes containing chloride, the ion may be included within the deposit (261). Nickel electrodeposits also exhibit an increased internal stress when plated from chloride containing solutions (Section 2.4a) and are not favoured for electroforming applications.

The pH of the electrode/electrolyte interface

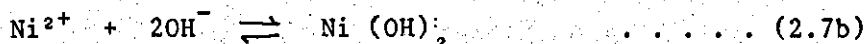
As will be seen (Chapter 4), the co-deposition of nickel hydroxide was observed to be a significant factor affecting the experimental nickel deposition studies. It is therefore of interest to examine some of the processes occurring at or very close to the electrode which may affect the pH of the electrolyte at the interface.

The co-deposition of an hydroxide film has been observed during previous studies of nickel deposition at high current densities or in the absence of boric acid. Early investigators (262,263) considered the formation of these films to be due to the removal of hydrogen ions from the cathode by the reaction

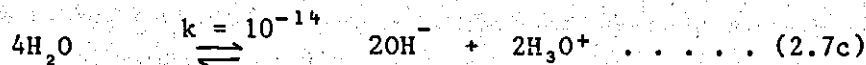


resulting in an increase in pH. Finally an hydroxide precipitate is

formed by



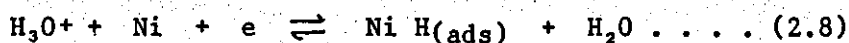
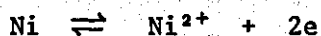
The hydroxyl ions arising from the dissociation of water



the hydrogen ions being consumed by reaction (2.7a). However, there is some evidence to suggest that at $\text{pH} \leq 4$, the nickel deposition reaction commences when the reduction of hydrogen ions becomes mass transport controlled (225,264) although this has recently been disputed (349).

Numerous experimental studies have confirmed that during the electrodeposition of nickel, the layer of electrolyte immediately adjacent to the cathode is more alkaline than the bulk of the electrolyte (e.g. 247,252,265,266).

Matulis and Slizys (252) have shown that the pH in the vicinity of the cathode surface increases rapidly after immersion of a nickel electrode in an acid electrolyte. The alkalisation was accounted for by the following overall processes



It was established that changes in the potential of both non-polarised and polarised electrodes was due to regular changes of the acidity of the solution in the layer near the cathode. The increase in pH was considered to result in the formation of the species Ni OH^+ at about pH 4 by the reaction

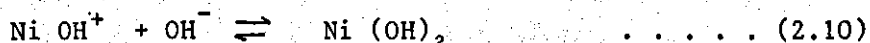


The concentration of Ni OH^+ depends on the ionization constant, K (267)

$$K = \frac{[\text{Ni}^{2+}] [\text{OH}^-]}{[\text{Ni OH}^+]} = 8.71 \times 10^{-6} \quad \dots \dots (2.9a)$$

When the initial pH exceeds pH 4, Ni OH^+ formation is thought to occur

throughout the bulk of the electrolyte. When the pH increases to about 6.6, $\text{Ni}(\text{OH})_2$ is formed,



The formation of Ni OH^+ results in an increased buffer capacity of the solution. Additional buffering of the solution with boric acid prevents the formation of $\text{Ni}(\text{OH})_2$ at the interface. The buffer capacity of the solution is then found to be highest at $\text{pH} < 4$ and therefore pH increases close to the cathode tend to be less significant. Evidence has been presented to support the view that a complex is formed between Ni^{2+} and H_3BO_3 (268).

Dorsch (264) has proposed that the hydroxyl ions arising as a consequence of reactions such as (2.7c) do not result in a precipitate of $\text{Ni}(\text{OH})_2$ from Ni OH^+ ions, providing the latter species has enough time to diffuse into the bulk of the solution.

Harris (269) has presented a theoretical analysis of the processes involved in the precipitation of nickel hydroxide at an electrode interface. Chemical equilibrium and transport processes in the cathodic diffusion layer were analysed by numerical integration of the transport equations. The analysis indicated that alkalisation was caused by the production of hydroxyl ions according to the reaction



Alkalisation will be prevented when the hydroxyl ions so produced react to form a soluble species such as metal hydroxy complexes, polynuclear complexes (270), metal anion complexes (268) or neutral ions pairs (271). When complexes are not formed, alkalisation occurs when the total hydrogen evolution current exceeds the mass transfer limited current for hydrogen ion reduction.

The situation that exists within the mass transfer boundary layer during nickel electrodeposition is obviously complex. The reactive species reduced at the electrode will be $\text{Ni}(\text{OH})^+$ rather than Ni^{2+} ions (in the absence of chloride ions).

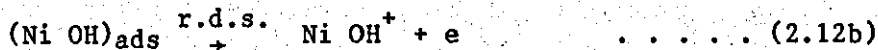
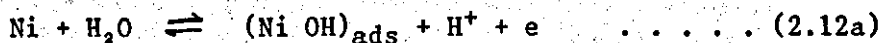
The concentration of NiOH^+ will be considerably less than that of Ni^{2+} in the bulk solution but will increase in proportion, near to the electrode, where the pH subsequently increases. Hydrogen ions are also transported towards the electrode, where they are discharged at the limiting current density. At a sufficiently negative cathode potential hydroxyl ions will also be produced by the reduction of water. The relative transport rates of hydrogen ions towards the electrode and hydroxyl ions away from the electrode will decide the pH profile across the boundary layer. In addition, the formation of metal ion complexes will influence the chemical equilibria and transport processes at the interface. The occurrence and extent of precipitation of hydroxide is dependent upon the extent to which alkalisation is moderated by the supply of hydrogen ions from the bulk and by buffering reactions in the diffusion layer. Therefore the electrodeposition of nickel represents a complex simultaneous multi-component transport process rather than the simplified situation of the transport of a single ion (Ni^{2+}) often assumed.

The anodic behaviour of nickel electrodes in non-sulphamate solutions

In practice nickel anodes are used as the counter-electrode during nickel electrodeposition. It is therefore of interest to examine the processes which may occur at the anode.

The active dissolution of nickel

The Tafel slope for nickel dissolution is normally about 60 mV dec^{-1} for electrolytes not containing chloride ions (241). At very low pH and/or in the presence of chloride ions considerable variation in this figure has been noted (249, 251, 272). The mechanism favoured by the experimental parameters is



The larger anodic Tafel slope ($\frac{RT}{F}$) than predicted theoretically ($\frac{2}{3} \frac{RT}{F}$) has been explained (241) by the supposition of an electron transfer

reaction taking place on a surface oxide film. The dissolution rate is independent of the nickel ion activity at high overpotentials (249) and in chloride solution (255).

The passivity of nickel

A nickel electrode will dissolve anodically to form the Ni OH^+ species. This ion will tend to accumulate near the interface as the current density is increased. The concentration of Ni OH^+ at the interface will be governed by the transport processes in the solution. When the solubility product $K = [\text{Ni(OH)}_2] / [\text{Ni OH}^+][\text{OH}^-]$ is exceeded, then a non-conducting film of Ni (OH)_2 will be deposited on the electrode (273). The film is not continuous and within cracks in the film the current density and hence the electrode potential will be very high. This results in the anodic oxidation of Ni (OH)_2 and hydrated Ni O (274,275). Passivity is associated with the formation of a semiconducting film of $\text{Ni O}_{1.5 - 1.7}$ and a conversion from ionic to electronic conduction (273).

The onset of passivity is marked by a current density maxima (i_c) on the anodic polarisation curve (Fig.2.25). The current density then decreases to a minimum value where passivation is complete (i_{pass}). The electrode potential at i_{pass} is known as the passivation or Flade potential (E_F). The passivation potentials may correspond to the thermodynamic formation potentials of the oxides and are therefore dependent upon pH and the nature of the anion. Some aggressive anions such as chloride may promote pitting corrosion of the passivated electrode (276). At a sufficiently high potential oxygen or chlorine is evolved on the semiconducting film. The Flade potential of nickel in acid solution has been found to be 0.3 to 0.4 V vs SHE (277).

The behaviour of nickel anodes in electroplating

In practice the anodic behaviour of nickel is very much dependent upon the composition of the electrolyte and the type of anode material (278). The adsorption of anions (277) and other bath constituents (280) may result in multiple peaks in anodic polarisation curves. When active anodes are employed the operating conditions are normally

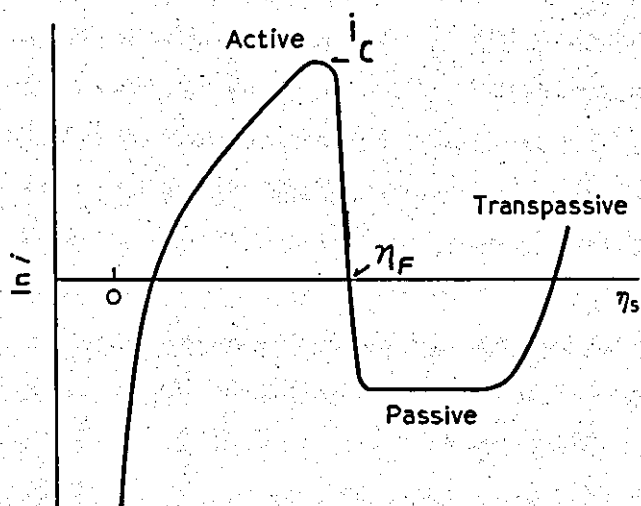


Fig.2.25 Illustration of current-potential relation for an electrode exhibiting passivation

chosen to facilitate active anode corrosion. For example, chloride ions are added to electroplating solutions to increase the anode dissolution rate.

Three types of active anode are commonly used for electroplating nickel, viz. electrolytic, cast and depolarised. Electrolytic nickel anodes are a very pure (99.98%) form of nickel which corrode unevenly in the absence of chloride ions (281). Cast nickel anodes are the cheapest to produce and prove satisfactory in solutions operating at low current densities. However they tend to disintegrate owing to the heterogenous nature of the crystal structure (282). Depolarised anodes corrode uniformly and with a high anodic current efficiency. The higher activity is achieved by the inclusion of other elements as trace constituents. Carbon (0.47%) and Silicon (0.25%) are often added to cast on cast and rolled nickel anodes (259,282,283). Oxygen is also commonly added to electrolytic nickel to improve activity. However, its effect may be due to promoting a more uniform distribution of the small amounts of sulphur in the metal (284). Sulphur has a very marked effect on the anodic behaviour of nickel. As little as 0.02% S in nickel may increase the critical current for passivity by a factor of 100. S nickel dissolves uniformly at more negative potentials and produces less metallic residue than other forms of nickel (282,285,287). It is the only form of anode material that does not readily passivate in chloride free nickel plating baths.

Electrocrystallisation of nickel and the morphology of nickel deposited from non-sulphamate solutions

The various species that are present close to the electrode may not only affect the mechanism of the reduction reaction, the pH at the electrode-electrolyte interface and the mass transport processes. There is some evidence to suggest that these species also influence the electrocrystallisation process and the morphology of the deposit.

Inhibition of nickel electrocrystallisation

In general nickel electrodeposits tend to be polycrystalline and in the absence of addition agents, exhibit a one-degree orientation or

texture. Inhibition of the growth rate of certain planes by absorbed species, may result in individual crystal planes growing at different rates and a preferred orientation may be developed (287-293).

Absorbed species are to be expected on a transition metal of high surface energy such as nickel.

As has been seen in previous sections, many chemical species e.g. H , H_2O , $.OH^-$, $Ni(OH)^+$ and $Ni(OH)_2$ also exist close to the cathode surface and may be capable of disturbing nickel electrocrystallisation. It has been suggested (294-296) that the active inhibiting species and hence the structure of the electrodeposit are a function of the nickel partial current density, the bulk solution pH and the electrolyte composition. Under certain conditions, the cathode surface may be relatively free of inhibiting species and nickel electrocrystallises in a free mode of growth. It has been proposed (297) that complexing anions may promote the free mode of growth. Nickel deposited in the free growth mode exhibits the highest ductility, the lowest internal stress and the lowest hardness (295).

Morphological features of nickel deposits

The morphology of nickel deposits from various electrolytes (but not sulphamate), were examined in a detailed study of electrodeposited nickel by the U.S. National Bureau of Standards in 1952 (298). Several minor studies have been undertaken since that date (e.g. 299,300).

Nickel electrodeposits are generally fine grained. In the absence of addition agents, the structure is columnar. At commercial current densities, once a coherent deposit has formed the surface structure tends to have the appearance of ill-defined hillocks and this does not change much with increasing thickness of deposit. However, a few investigators have detected other morphological features which may be associated with the presence of various species close to the electrode-electrolyte interface.

Ives and co-workers (301) have observed triangular growth forms, by electron transmission microscopy, in electrodeposits (0.01 A cm^{-2})

from Watts nickel solutions. The triangular growths were assigned to the inclusion of $\text{Ni}(\text{OH})_2$ in the plane of the deposit. The growths were always observed in deposits from unbuffered electrolytes, where the cathode layer pH was 6.4, after 120s plating. The hydroxide inclusions were never found in deposits from solutions containing 40g l^{-1} boric acid and were apparent only from stagnant solutions containing 30g l^{-1} boric acid. Baths of $\text{pH} > 4$ showed the formation of amorphous $\text{Ni}(\text{OH})_2$ on the surface of the electrodeposit under some conditions. However, nickel was not deposited at very high current densities during this investigation.

Other features within the electrodeposited nickel structure have been noted. Nakahara (302) has observed linear defects and spherical inclusions in thin films deposited from Watts nickel solutions. These effects were attributed to the adsorption and subsequent inclusion of hydrogen in the deposit. Banerjee and Walker (303) found microcavities and striations or steps in deposits formed at low current densities.

The incorporation of hydrogen and nickel hydroxide significantly alters the microstructure of electrodeposited nickel (304). It has been proposed that adsorption processes may affect the growth dislocation density (305) and therefore may also influence the internal stress of the deposit (306). Roshikov and Pangarov (307) have suggested that the rapid change in grain size with increase of current density may be evidence of adsorption phenomena.

Velinova et al (308) have identified two types of nickel surface morphology, pyramidal and lateral. The lateral form presents a series of planes or truncated pyramids at the surface. The reflectivity of deposits may be correlated with the occurrence of these two forms. Dull deposits are of the pyramidal form, while bright coatings have the lateral (or block) form. The formation of each type was associated with the preferential adsorption of addition agents upon selected growth planes thus allowing the development of cubic growth faces. The reflectivity was found to be largely independent of the preferred

orientation, the degree of perfection of the orientation or the number of twinning defects. However it should be noted that reflectivity has been found to be related to the roughness of electrodeposits and may be associated with inhibition (6).

Dendritic growth of nickel

The formation of rough or dendritic electrodeposits often represents evidence of a mass transfer controlled reaction. True dendritic growth has not been observed under conventional nickel plating operating conditions. However the formation of nickel dendrites in concentrated nickel chloride solutions at temperatures above 80°C have been reported (309-311). It was proposed that at high temperatures hydrogen evolution was inhibited. It is of interest to note that the decreased inhibition of the reaction has also been proposed (245) to account for the low temperature coefficient of the overpotential observed at high temperatures (p. 78).

ii) Electrodeposition of nickel from nickel sulphamate solutions

This section of the review is presented in two parts. In the first part, the electrochemical and morphological aspects of nickel deposition from both conventional and concentrated nickel sulphamate based electrolytes are presented. This includes a review of the studies of the anodic reactions, in particular the oxidation of the anion, which may take place in these solutions.

The second part of the review is concerned with a more detailed account of the 'Ni-Speed' system, since this is relevant to the present investigations.

Cathodic aspects

The cathodic behaviour of nickel in 1m nickel sulphamate solutions buffered with 0.5m boric acid was studied by Piontelli and Seraville (248). The polarisation curves were analysed by a semi-quantitative Tafel method (Table 2.7). For each curve, two linear Tafel regions were discernible. The Tafel slopes of $\sim 100 \text{ m V dec}^{-1}$

were not corrected for the effect of hydrogen evolution. Increases of temperatures greatly decrease the electrode potential. The temperature coefficient of electrode potential was found to be $-3.4 \text{ mV } ^\circ\text{C}^{-1}$ between 50 and 65°C ($< 0.03 \text{ A cm}^{-2}$). This semi-quantitative study would appear to be the only electrochemical investigation of the electrochemistry of nickel deposition from sulphamate electrolytes, although other work has been briefly referred to (343).

Anodic aspects

Dissolution behaviour of non-activated and sulphur activated nickel in sulphamate solutions

The passivation phenomena of non-activated and sulphur activated nickel have been studied in both conventional (312) and concentrated (312,313) nickel sulphamate solutions. These investigations have been concerned with the affect of chloride ions on the polarisation behaviour.

In concentrated solutions the critical current density for the active dissolution of electrolytic nickel was found to be $< 0.001 \text{ A cm}^{-2}$ for chloride concentrations over the range 0.1 to 25 g l^{-1} . The post-passivation breakdown potentials may be shifted up to 0.5 V in the less noble direction at higher chloride concentrations. Multiple peaks have been observed in the potential region -0.1 to $+0.3 \text{ V}$ (SHE).

In the case of sulphur activated nickel, no multiple peaks have been observed and it has been claimed that active dissolution may be maintained up to a maximum current density of 0.6 A cm^{-2} .

Anodic oxidation processes in nickel sulphamate electrolytes

The anodic behaviour of nickel in sulphamate-based solutions is more complex than in solutions based on nickel sulphate or chloride, due to the ability of the sulphamate ion to oxidise at the anode. The products of these oxidation reactions can affect the processes at the cathode and influence the properties of the deposit.

temperature		pH 2.5	pH 3.5	pH 4.8
25°C	c.d.range A cm ²	5x10 ⁻⁴ -3x10 ⁻²	5x10 ⁻⁴ -3x10 ⁻²	5x10 ⁻⁴ -3x10 ⁻²
	a V	0.705	0.740	0.748
	b V dec ⁻¹	0.095	0.080	0.080
50°C	c.d.range (A cm ⁻²)	-	5x10 ⁻⁴ -3x10 ⁻²	5x10 ⁻⁴ x3x10 ⁻⁴
	a V		0.558	0.618
	b V dec ⁻¹		0.140	0.097
	c.d.range (A cm ⁻²)	-	3x10 ⁻³ -3x10 ⁻²	-
	a V		0.642	
	b V dec ⁻¹		0.085	
65°C	c.d.range (A cm ⁻²)	5x10 ⁻⁴ -5x10 ⁻³	5x10 ⁻⁴ -5x10 ⁻³	5x10 ⁻⁴ -3x10 ⁻²
	a V	0.537	0.550	0.568
	b V dec ⁻¹	0.115	0.107	0.100
	c.d.range (A cm ⁻²)	5x10 ⁻³ -3x10 ⁻²	5x10 ⁻³ -3x10 ⁻²	-
	a V	0.590	0.570	
	b V dec ⁻¹	0.097	0.100	

Table 2.7 Coefficients of the Tafel equation, $E = a + b \log_{10} i$, for the cathodic deposition of nickel from 1M Ni(NH₂SO₃)₂ / 0.5M H₃BO₃ (after Piontelli and Seraville [ref. 248]).

The effect of the anodic reactions of the sulphamate ion on the properties of the nickel deposit has been studied by a number of workers notably Kendrick (314), Klingenmaier (315), Kendrick and Watson (316), Marti (317), Greene (318) and Hart, Wearmouth and Warner (313)

These studies demonstrate that the choice of anode material governs the type of oxidation product formed (313,317,318) and is critical in determining the stress (312,314,315) and sulphur content (312) of the deposits produced. For electroforming applications where the maintenance of low or zero stress conditions is essential, it is beneficial to be aware of and to understand, the factors which affect stress in sulphamate solutions. The control of sulphur content is also important as nickel deposits containing greater than approximately 0.01% sulphur become embrittled when exposed to temperatures in excess of 200°C.

It appears that the oxidation of the sulphamate ion only proceeds at potentials between 750 to 1250 mV (SHE) (313), since the reduction in stress levels of nickel electrodeposits associated with its production are absent at lower anode potentials (315-317). However Hart et al (313) detected no anodic current which could be associated with the oxidation of the anion. It is considered that the oxidation product is only produced very slowly due to kinetic limitations. Consequently the production of significant concentrations of the stress reducing species requires long periods of time and under normal operating conditions the sulphur content of deposits does not become excessive. The rate of reaction apparently does not increase with increasing anode potential or current density (316). The oxidation products of the sulphamate ion include nitrogen, water and sulphate ions, although the active agent has not been clearly identified. Marti (317) has suggested that the stress reducing species is sulphite ion. Greene (318) has oxidised sulphamate ions to azodisulphonate at a platinum anode and considered this to be the active species.

It is evident that stress reduction is not found when sulphur containing anodes are employed in plating baths (315-317). Since

sulphur activated nickel will sustain very high current densities at low potentials ($< +200$ mV vs SHE), the oxidation product is not formed. However, electrolytic anodes are found to passivate at low current densities. Under such conditions the oxidation product may accumulate and the stress levels of the electrodeposit decrease. Similar effects may be achieved using inert platinum or titanium anodes.

The stress conditions of the electrodeposit have been controlled by a continuous anodic oxidation of the anion on a passivated nickel or inert anode (316,319) in a separate conditioning tank. Sulphur activated nickel anodes are used in the main tank. When the operating parameters are optimised the sulphur content may be maintained at $< 0.01\%$ and the deposits are low or zero stressed. The oxidation product markedly reduces internal stress and may also result in increased brightness, reduced grain size and a decrease in the deposit hardness.

The growth and morphology of nickel electrodeposits from sulphamate solutions

In concentrated solutions the deposits tend to be lustrous in the lower part of the current density range (< 0.05 A cm⁻²) becoming less bright at higher current densities (1,231). Although previous investigators (e.g. 239,321) have in general found nickel deposits from sulphamate solutions to be very fine grained and columnar in structure, some authors (e.g. 320) have claimed that the deposit structure rapidly becomes coarser over the current density range 0.03 to 0.16 A cm⁻². This structural change corresponded to changes in microhardness and lustre. At a solution pH > 5.0 , the grain size progressively diminishes and the deposits become harder, stronger and less ductile (239,322). There appears to be little information regarding the effect of temperature on the grain size (320).

Verma and Wilman (323,324) and Rivolta et al (325) have examined the role of inhibition on the structure of nickel electrodeposits obtained from nickel sulphamate solutions. Both sets of authors agreed

that the adsorption of foreign species resulted in growth disturbance.

Rivolta et al (325) studied nickel deposited from a concentrated nickel sulphamate bath. They suggested that the orientation was determined by adsorption of OH^- ions at high current densities and adsorbed hydrogen at low current densities.

Verma and Wilman (323,324) deposited nickel from conventional nickel sulphamate solutions at current densities up to 0.6 A cm^{-2} . At the high current densities $\text{Ni}(\text{OH})_2$ was co-deposited. They suggested that $\text{Ni}(\text{OH})_2$ was responsible for determining the deposit orientation at high current densities. As the maximum current density was approached, an increased tendency for outward growth, twinning and polycrystallinity was observed. At the highest current densities, dependent on the temperature and degree of agitation, the current efficiency decreased and nickel hydroxide was deposited.

The morphology of nickel electrodeposits from a concentrated nickel sulphamate electrolyte was investigated by Saleem et al (326) At low current densities ($\sim 0.08 \text{ A cm}^{-2}$) the deposit showed isolated pyramidal growth centres at short times. After $\sim 30\text{s}$ the whole surface is covered with block growths, the final morphology being a smooth degenerate pyramid type structure. At 0.2 A cm^{-2} deposits were all of the block type and extensive twinning was observed at 0.4 A cm^{-2} . Nodular growths and generally rough deposits were found at 0.6 A cm^{-2} . Rough deposits were associated with extensive inhibition by foreign species.

Therefore there is some evidence to suggest that the structure and hence the properties of electrodeposited nickel are influenced by adsorption of foreign species. The role of $\text{Ni}(\text{OH})_2$ in this process has been, to some extent, confirmed by examination of the defects in such deposits.

Fast rate electrodeposition processes using nickel sulphamate electrolytes

Few reports of nickel deposition from sulphamate solutions in conditions of well-defined hydrodynamics, or using novel cell designs,

are available. The work of Eisner (101,119) using an abraded disc or belt method, Suzuki et al (90) using an abraded rotating cylinder and Bailey (89) using a rotating cylinder are of interest. Their studies have been reported in greater detail in Section 2.2.

Nickel plating from concentrated nickel sulphamate solutions
(the Ni - Speed process)

Preparation and properties of the solution

The Ni - Speed bath, as developed by Kendrick (1), has the following composition:

600 g ℓ^{-1} nickel sulphamate
40 g ℓ^{-1} boric acid
5 g ℓ^{-1} nickel chloride

The optimum specific gravity is 1.355 at 60°C (2.31). The chloride ions are added to assist anode dissolution. The bath has a higher conductivity (and throwing power) than the Watts or conventional sulphamate bath which may result in a reduction of electrical power requirements of up to 12% for a given plating rate (320).

Kendrick et al (1,320) has suggested that the bath should be filtered through activated charcoal and treated electrolytically to obtain optimum properties. The following treatment sequence was recommended:

low current density treatment - the passage of 10 Ah ℓ^{-1} of electricity with current densities of 0.0054 A cm^{-2} on both cathode and anode. The cathode was of corrugated nickel and the anode of a non-depolarised nickel. This process was carried out to purify the electrolyte and was followed by:

conditioning treatment - the passage of 30 Ah ℓ^{-1} of electricity with a current density of 0.043 A cm^{-2} on the corrugated cathode and 0.005 A cm^{-2} on the non-depolarised nickel anode (i.e. an anode of low activity). This process was considered necessary to obtain deposits

of low internal stress and is discussed further in Section 3. To maintain a low stress condition it was recommended that this process should be carried out continuously in a separate tank.

The bath is operated at pH 3.5 to 4.5 and temperatures of 60 to 70°C. A lower pH or a higher temperature results in an increased rate of hydrolysis of sulphamate ions to ammonium ions (1,330) and consequently increased deposit hardness. A higher pH or lower temperatures result in increased internal stress, poor deposits and a decreased maximum current density for a good deposit. The effect of temperature on the maximum current density for the zero stress condition and the internal stress are shown in Table 2.8. As may be seen, the internal stress tends to decrease with increasing temperature.

Kendrick (1) found that the internal stress was at a minimum and the current density before 'burning' was at a maximum at a nickel sulphamate concentration of 600 g l⁻¹ (Fig.2.26). For the specified plating conditions, using air agitation the maximum current density was ~0.4 A cm⁻² at 60°C and ~0.8 A cm⁻² at 70°C. However, it should be noted that in commercial practice the maximum current density rarely exceeds 0.2 A cm⁻². This represents a maximum current density of at least twice that obtained using Watts or conventional nickel sulphamate under similar conditions. It was claimed (1,320) that the bath may be operated without wetting agents given a sufficient degree of agitation.

The current efficiency for a good deposit was in the range 97 to 99% over the range of current densities studied (<0.4 A cm⁻² at 60°C) and was independent of temperature (320). The current efficiency was found to decrease with nickel sulphamate concentrations greater than 600 g l⁻¹ (1).

The internal stress of deposits obtained from the concentrated nickel sulphamate bath has been found (1,320) to be a function of the current density. At lower current densities the stress was compressive (Fig.2.27). The time to reach the zero stress condition was found to increase with increasing current density (Fig.2.28).

a)

Temperature (°C)	35	40	45	50	55	60	65	70
Current density (A/ft ²)	10	25	40	75	125	165	200	300
(A/dm ²)	1.1	2.7	4.3	8.1	13.5	17.8	21.6	32
Plating rate (approx.) (in x 10 ⁻³ /h)	0.5	1.2	2	3.7	6.2	8.2	10	15
micrometres/h	12	31	50	94	156	206	250	375

b)

	Temperature		Tensile stress	
	°F	°C	lbf/in ²	kgf/mm ²
93		34	+20 000	14.1
104		40	+ 7200	5
118		48	- 2500	1.76
140		60	-11 200	7.87

Table 2.8 a) Relationship between solution temperature, current density and plating rate for the zero deposit stress condition in the Ni-Speed process.

b) Effect of solution temperature on stress in deposits plated at 5.4 A cm⁻² from 600 gl⁻¹ nickel sulphamate solution (331,341)

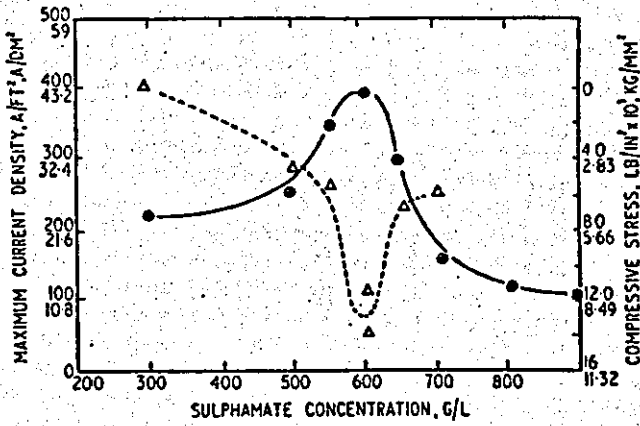


Fig.2.26 Effect of concentration of nickel sulphamate on maximum current density and stress in deposits 0.001 in (25 microns) thick obtained at 50 A/Ft² (5.4 A/dm²), 60°C (140°F). Δ --- Δ stress; \bullet --- \bullet maximum current density before burning (1)

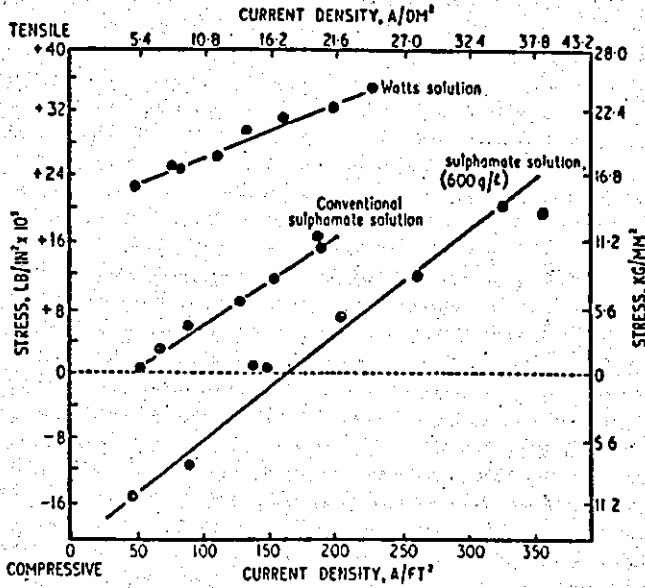


Fig.2.27 Variation of mean stress in 0.001 in (25 microns) thick deposits with current density at 60°C (140°F). (1)

The micro hardness of the deposits from concentrated solutions can be controlled over a limited range by varying the cathode current density (1,321,327). At current densities below 0.05 A cm^{-2} the deposits were moderately hard rising to 240 to $270 \mu\text{HV}$ at 0.02 A cm^{-2} . As the current density is raised above this value, the micro hardness decreased to between 210 and $230 \mu\text{HV}$ (Fig.2.29). The micro hardness/current density relationship appears to be substantially unaffected by the types of anode used (327). The micro hardness values of sulphamate deposits have been found (327) to be consistently lower than the corresponding macro hardness values.

For some electroforming applications, the high hardness and elasticity, or the degree of compressive stress required cannot be attained by the 'conditioning' treatment. In such cases conventional addition agents such as saccharin are sometimes employed or to obtain deposits of high hardness which will withstand heating without loss of mechanical properties, a modified Ni-Speed solution containing cobalt may be used, even though a certain degree of tensile stress must be tolerated (231,321,327,328,341).

Since the major review of the nickel sulphamate system by Hammond (231), little significant work has been published (e.g. 330-340).

It is therefore apparent that a suitably purified and conditioned nickel sulphamate solution allows the brightness and properties of the deposited nickel to be varied over a narrow range by suitable adjustment of the current density or temperature. The deposits so obtained have a low sulphur content (typically less than 0.006%) (320) and tend to be free of the embrittlement problems associated with sulphur incorporations, particularly in heat treated nickel deposits. However it should be noted that few investigations have been carried out of deposition at current densities $> \sim 0.4 \text{ A cm}^{-2}$.

Although the cost of nickel sulphamate based solutions is greater than Watts type baths, this may be offset by the very low internal stress of the deposits obtained without the use of addition agents, the improved throwing power and the higher deposition rates. These factors

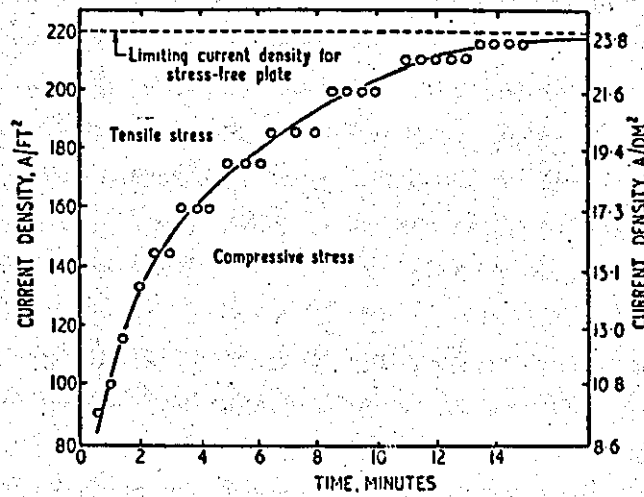


Fig.2.28 Change, with plating time, in the current density needed to give a stress-free deposit from the concentrated sulphamate solution (600 g/l) (1)

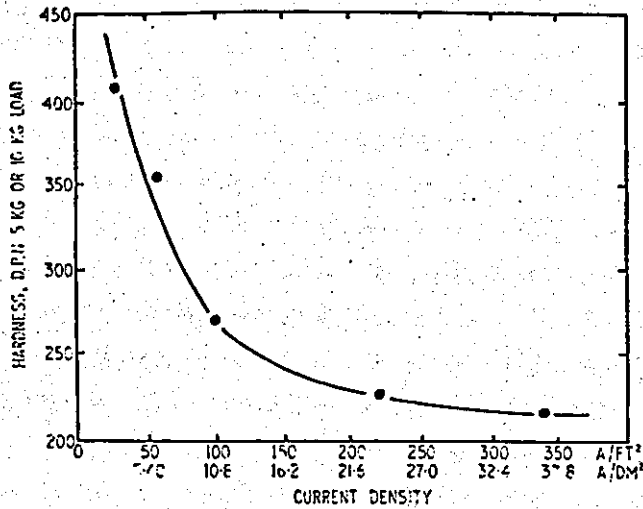


Fig.2.29 Effect of current density on hardness of nickel deposits obtained at 60°C (140°F) from concentrated sulphamate (600 g/l) solution: each value given is the average of four determinations (1)

have resulted in nickel sulphamate baths, in particular Ni-Speed, becoming one of the principal electrolytes for electroforming and heavy engineering purposes.

Introduction to the present work

It is clear from the literature review that the concentrated nickel sulphamate solution offers several advantages for high speed nickel electrodeposition studies. The system represents an established commercial process which produces electrodeposits with good physical properties. The inherently low internal stress and comparatively high deposition rates make it particularly suitable for electroforming. However few studies of electrodeposition at very high current densities have been undertaken in this system, although the high concentration of nickel salts make it particularly suitable for this purpose. Furthermore no quantitative studies of the electrodeposition of nickel from sulphamate solutions in flowing environments have been made.

It is also evident that studies of the electrodeposition of metals at very high current densities with the probability of reasonably full analytical interpretation of the results, requires a well-defined hydrodynamic regime. The flow system in the form of the parallel plate cell has not been fully exploited for this purpose.

The combination of studies in parallel plate cells using nickel sulphamate solutions opens up the possibility of combining electrochemical studies, transport studies and correlation with the structures and properties of the foils produced.

The design of the parallel plate cells for the deposition studies was assisted by the availability of many mass transfer correlations for various parallel plate cell geometries and hydrodynamic conditions. When designing the cells and the flow system, several interrelated factors must be taken into account. The design process is described in the following Chapter.

As will be seen, two parallel plate cells were designed and constructed. Cell 1 was used for preliminary deposition studies at 60°C.

to provide some initial information about the process. From the knowledge gained, a second cell (Cell 2) was designed and constructed and this cell was used for the major part of the current work.

The experimental programme in Cell 2 included the following work:

- (i) An experimental verification of the cell design using the mass transfer controlled deposition of copper.
- (ii) An extended study of the electroforming of nickel foils using various electrode lengths at both 60 and 70°C.
- (iii) Cathodic and anodic polarisation studies
- (iv) Current distribution studies
and
- (v) Mass transport studies of nickel deposition from sulphamate solutions.

As will be seen, it was found to be impossible to separate the nickel deposition and hydrogen evolution reaction and hence to measure directly limiting current densities for nickel deposition. Morphological features were used to correlate current density and flow rate. A maximum current density for a good deposit (i_{\max}) was defined for this purpose.

3. EXPERIMENTAL

The primary objectives of these investigations was the preparation and post-deposition examination of electroformed nickel foils. As a result, the cell design was of considerable importance to the programme. The use of a parallel plate cell was an appropriate choice for this type of study.

The following Chapter includes the detailed design procedures and the experimental methods used in these investigations. However, it was necessary to determine some of the relevant physical properties of the electrolyte before the cell and flow circuit could be designed. These methods, together with the analytical procedures used throughout this investigation along with the results are presented first in Section 3.1.

As will be seen, two parallel plate cells were found to be required and the nature of the system necessitated the use of a complex iterative design procedure, since many of the relevant factors are inter-dependent. Hence the design methods for the two cells are described in some detail. The cell construction and operation procedures are also described. This work is presented in Sections 3.2 and 3.3.

In the following sections (3.4 to 3.6), the experimental procedures used are described in detail. In Section 3.4, experimental methods used to characterise the Mk 2 cell are described. The cell was characterised using the mass transfer controlled deposition of copper from an acid copper sulphate electrolyte. This system was used to determine the mass transfer correlations and the current distribution curves for the unusual divided cell design.

Section 3.5 deals with the experimental methods used during nickel foil deposition from the sulphamate electrolyte in the Mk 2 cell. This Section includes current distribution measurements, the methods used for determining the electrode potential and the anodic and cathodic

polarisation curves. The mass transport measurements in the nickel sulphamate solution are also described.

The experimental procedures for the post-deposition examination of electroformed nickel foils, including optical and electron microscope examination and micro-hardness measurements are described in Section 3.6. These procedures were common to nickel foils prepared in both the Mk 1 and Mk 2 cells.

3.1 Determination of the physical properties of the nickel based electrolytes and analytical methods for nickel based electrolytes

Prior to beginning the major part of the investigation the physical properties of the nickel sulphamate based electrolytes were determined. This information was not readily available in the literature. The densities and viscosities of the solutions were required to permit the calculation of Reynolds numbers. A knowledge of the electrical conductivity was necessary to calculate solution resistance and cell voltages. The three properties were determined over the temperature range 50° to 70°C.

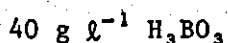
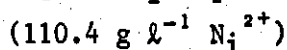
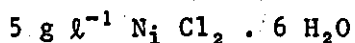
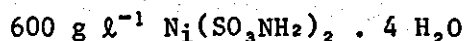
In order to maintain the solution composition, the electrolyte was analysed at regular intervals. The procedures for making suitable adjustments of the solution components are also described in this Section.

a) Physical properties of nickel based electrolytes

i) The densities of concentrated nickel sulphamate solutions

Experimental

The densities ($\rho_{Ni^{2+}}$) of a concentrated nickel sulphamate solution of the composition



$$\text{pH} \sim 4$$

were determined, using a 50 cm³ specific gravity bottle, at temperatures of 50, 60 and 70°C. Temperature control, to within $\pm 0.05^\circ\text{C}$, was achieved by a thermostatically controlled water bath. The specific gravity bottle was calibrated at the above temperatures using distilled water. The weight of the empty bottle and that of the bottle plus water at the equilibrium temperature, were accurately measured. The water was replaced by nickel sulphamate solution and the procedure repeated for each temperature. These results are given in Table 3.1.

Example calculation (data taken from Table 3.1)

The volume of the specific gravity bottle ($V_{T^\circ\text{C}}$) at the given temperature ($T^\circ\text{C}$) was determined using distilled water as the calibration fluid.

$$V_{T^\circ\text{C}} = \frac{(\text{Wt. of S.G. bottle} + \text{H}_2\text{O}) - (\text{Wt. of S.G. bottle})}{\rho_{\text{H}_2\text{O}} @ T^\circ\text{C}}$$

The dry weight of the S.G. bottle was 35.8442g. The values of the density of water ($\rho_{\text{H}_2\text{O}}$) at $T^\circ\text{C}$ were obtained from the literature (345).

$$\begin{aligned} T \sim 50^\circ\text{C}, \quad \rho_{\text{H}_2\text{O}} &\approx 0.9881 \text{ g cm}^{-3} \\ V_{50^\circ\text{C}} &= \frac{(85.0716 - 35.8442)}{0.9881} \\ V_{50^\circ\text{C}} &= \underline{49.820 \text{ cm}^3} \end{aligned}$$

The bottle was filled with the nickel sulphamate solution thermally equilibrated and reweighed. The density of the nickel sulphamate solution was calculated from the following equation:

$$\rho_{\text{(Ni)}}^{T^\circ\text{C}} = \frac{(\text{Wt. of S.G. bottle} + \text{Ni}(\text{SO}_3\text{NH}_2)_2 \text{ soln}) - (\text{Wt. of S.G. bottle})}{V_{T^\circ\text{C}}}$$

$$\begin{aligned} \text{Hence } \rho_{\text{(Ni)}}^{50^\circ\text{C}} &= \frac{(104.0480 - 35.8442)}{49.8203} \\ \rho_{\text{(Ni)}}^{50^\circ\text{C}} &= \underline{1.369 \text{ g cm}^{-3} @ 50^\circ\text{C}} \end{aligned}$$

Temperature T°C	Wt. of S.G. bottle + H ₂ O g	Wt. of H ₂ O g	Density of water @ T°C g cm ⁻³	Volume of S.G. bottle @ T°C V cm ³	Wt. of S.G. bottle + Ni(SO ₃ NH ₂) ₂ solution g	Density of Ni(SO ₃ NH ₂) ₂ solution @ T°C g cm ⁻³
50 C	85.0716	49.2274	0.9881	49.8203	104.0480	1.369
60 C	84.8426	48.9985	0.9832	49.8357	103.7990	1.364
70 C	84.5908	48.7466	0.9778	49.8533	103.4001	1.356

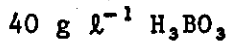
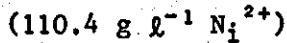
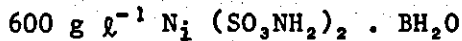
Weight of empty S.G. Bottle = 35.8442

Table 3.1 Density of nickel sulphamate solutions
as a function of temperature

Similar calculations were carried out for the other temperatures. The solution densities were used later, in conjunction with the dynamic viscosity to calculate the kinematic viscosity.

ii) The viscosities of concentrated nickel sulphamate solutions

The dynamic viscosities ($\eta_{\text{Ni}^{2+}}$) of a concentrated nickel sulphamate solution of the composition:



pH ~ 4

were determined using an Ostwald viscometer immersed in a glass fronted constant temperature water bath. Measurements were made at temperatures of 50, 60 and 70°C \pm 0.05°C. At each temperature, the viscometer was calibrated with distilled water (10 cm³). The discharge times ($t_{\text{H}_2\text{O}}$) through the viscometer capillary tube were measured using a stop watch.

10 cm³ of the nickel sulphamate solution, sampled at the experimental temperature was transferred to the dry viscometer. The discharge times ($t_{\text{Ni}^{2+}}$) of the electrolyte were measured at each temperature. The experimental data are summarised in Table 3.2.

Example Calculation (Data from Table 3.2)

The dynamic viscosity of the nickel sulphamate solution at each temperature was calculated from the equation

$$\eta_{\text{Ni}^{2+}} = \eta_{\text{H}_2\text{O}} \times \frac{t_{\text{Ni}^{2+}}}{t_{\text{H}_2\text{O}}} \times \frac{\rho_{\text{H}_2\text{O}}}{\rho_{\text{Ni}^{2+}}}$$

The density ($\rho_{\text{H}_2\text{O}}$) and dynamic viscosity ($\eta_{\text{H}_2\text{O}}$) of water are taken from the literature (345). The densities of the electrolyte were taken from Table 3.1.

Temp. T °C	$1/T \times 10^{-3}$ k ⁻¹	Dnsty. ρ_{H_2O} g cm ⁻³	Dnsty. $\rho_{Ni^{2+}}$ g cm ⁻³	Av. Time t_{H_2O} secs.	Av. Time $t_{Ni^{2+}}$ secs.	Dyna- mic Visco- sity η_{H_2O} centi poise	Dyna- mic Visco- sity $\eta_{Ni^{2+}}$ centi poise	Kinematic Viscosity $\nu_{Ni^{2+}}$ cm ² s ⁻¹ x 10 ⁻²
50	3.094	0.9881	1.369	43.4	117.0	0.5468	2.042	1.492
60	3.001	0.9832	1.364	38.2	97.5	0.4631	1.640	1.202
70	2.914	0.9778	1.356	34.1	85.2	0.4050	1.403	1.035

Solution composition

$Ni^{2+} = 110.4$ g/l

600 g/l Ni (SO₃NH₂) 4H₂O

40 g/l H₃BO₃

5 g/l Ni Cl₂ 6H₂O

Table 3.2 Viscosity and density of nickel sulphamate plating solution as a function of temperature

at 50°C

$$t_{\text{Ni}} \sim 1175, \quad t_{\text{H}_2\text{O}} \sim 43.45$$

$$\rho_{\text{Ni}^{2+}} \sim 1.369 \text{ g cm}^{-3}, \quad \rho_{\text{H}_2\text{O}} \sim 0.9881 \text{ g cm}^{-3}$$

$$\eta_{\text{H}_2\text{O}} \sim 0.5468 \times 10^{-2} \rho$$

$$\therefore \eta_{\text{Ni}^{2+}}^{50^\circ\text{C}} \approx 0.5468 \times 10^{-2} \times \frac{117.0}{43.4} \times \frac{1,369}{0.9881}$$

and

$$\eta_{\text{Ni}^{2+}}^{50^\circ\text{C}} = \underline{2.042 \times 10^{-2} \text{ poise}}$$

The kinematic viscosity of the electrolyte ($\nu_{\text{Ni}^{2+}}$) was calculated from:

$$\nu_{\text{Ni}^{2+}}^{50^\circ\text{C}} = \frac{\eta_{\text{Ni}^{2+}}^{50^\circ\text{C}}}{\rho_{\text{Ni}^{2+}}^{50^\circ\text{C}}}$$

$$\therefore \nu_{\text{Ni}^{2+}}^{50^\circ\text{C}} = \frac{2.042 \times 10^{-2}}{1.369}$$

and

$$\nu_{\text{Ni}^{2+}}^{50^\circ\text{C}} = \underline{1.492 \text{ cm}^2\text{s}^{-1}}$$

iii) The electrical conductivities of concentrated nickel sulphamate electrolytes

The specific conductivities of electrolytes of the following compositions were measured using a Phillips conductivity meter (Type PW 9501/01) and a conductivity cell (Type PR 9514/10) of cell constant 1 cm^{-1} . Measurements were made at a frequency of 2 kHz.

a) $600 \text{ g l}^{-1} \text{ Ni}(\text{SO}_3\text{NH}_2)_2 \cdot 4\text{H}_2\text{O}$

$40 \text{ g l}^{-1} \text{ H}_3\text{BO}_3$

$5 \text{ g l}^{-1} \text{ Ni Cl}_2 \cdot 6\text{H}_2\text{O}$

b) $600 \text{ g l}^{-1} \text{ Ni (SO}_3\text{NH}_2)_2 \cdot 4\text{H}_2\text{O}$

$40 \text{ g l}^{-1} \text{ H}_3\text{BO}_3$

$0 \text{ g l}^{-1} \text{ Ni Cl}_2 \cdot 6\text{H}_2\text{O}$

The solutions were placed in conductivity tubes and allowed to reach thermal equilibrium in a thermostated water bath. The specific conductivity (σ) was measured over the temperature range 50 to 70°C. Temperatures were controlled to within $\pm 0.05^\circ\text{C}$ in each case. The equivalent conductivity (Λ) was calculated from

$$\Lambda = \frac{\sigma}{c_{\text{Ni}^{2+}} z}$$

where $c_{\text{Ni}^{2+}}$ = concentration of nickel ions (moles dm^{-3}) and $z = 2$. The experimental data and calculated values of Λ , for each solution are given in Table 3.3.

The densities, viscosities and equivalent conductivities of the solutions, as a function of temperature are shown in Figs. 3.1 to 3.4.

b) Analysis of nickel based electrolytes

The composition of the nickel plating solutions was monitored by a series of titrametric procedures.

Total nickel concentration

The concentration of Ni^{2+} in a solution of composition 600 g l^{-1} , $\text{Ni (SO}_3\text{NH}_2)_2 \cdot 4\text{H}_2\text{O}$ and $5 \text{ g l}^{-1} \text{ Ni Cl}_2 \cdot 6\text{H}_2\text{O}$ was calculated as follows:

Molecular weight of $\text{Ni(SO}_3\text{NH}_2)_2 \cdot 4\text{H}_2\text{O}$ = 322.8

Wt. fraction Ni in $\text{Ni(SO}_3\text{NH}_2)_2 \cdot 4\text{H}_2\text{O}$ = 58.7

322.8

= 0.182

$\text{g l}^{-1} \text{ Ni}^{2+}$ in $600 \text{ g l}^{-1} \text{ Ni(SO}_3\text{NH}_2)_2 \cdot 4\text{H}_2\text{O}$ = 0.182×600

= 109.1 $\text{g l}^{-1} \text{ Ni}^{2+}$

Temperature T		Specific Conductivity σ	Equivalent Conductivity Λ
$^{\circ}\text{C}$	K	$\text{ohms}^{-1} \text{cm}^{-1}$	$\text{ohms}^{-1} \text{cm}^2 \text{equiv.}^{-1}$
60	333.2	0.112	29.6
65	338.2	0.119	31.5
70	343.2	0.126	33.3

Solution composition: $\text{Ni}^{2+} = 111.1 \text{ g/l} - 1.89 \text{ moles dm}^{-3}$

$\text{Ni}(\text{SO}_3\text{NH}_2)_2 \cdot 4\text{H}_2\text{O} = 600 \text{ g/l}$

$\text{H}_3\text{BO}_3 = 40 \text{ g/l}$

$\text{NiCl}_2 \cdot 6\text{H}_2\text{O} = 5 \text{ g/l}$

pH = 3.2

Temperature T		Specific Conductivity σ	Equivalent Conductivity Λ
$^{\circ}\text{C}$	K	$\text{ohms}^{-1} \text{cm}^{-1}$	$\text{ohms}^{-1} \text{cm}^2 \text{equiv.}^{-1}$
60	333.2	0.112	29.6
65	338.2	0.120	31.7
70	343.2	0.128	33.8

Solution composition: $\text{Ni}^{2+} = 111.1 \text{ g/l}$ (as $\text{Ni}(\text{SO}_3\text{NH}_2)_2 \cdot 4\text{H}_2\text{O} - 1.89 \text{ moles dm}^{-3}$)

$\text{H}_3\text{BO}_3 = 40 \text{ g/l}$

$\text{NiCl}_2 \cdot 6\text{H}_2\text{O} = 0.0 \text{ g/l}$

pH = 2.7

Table 3.3 Conductivity of nickel plating solutions as a function of temperature

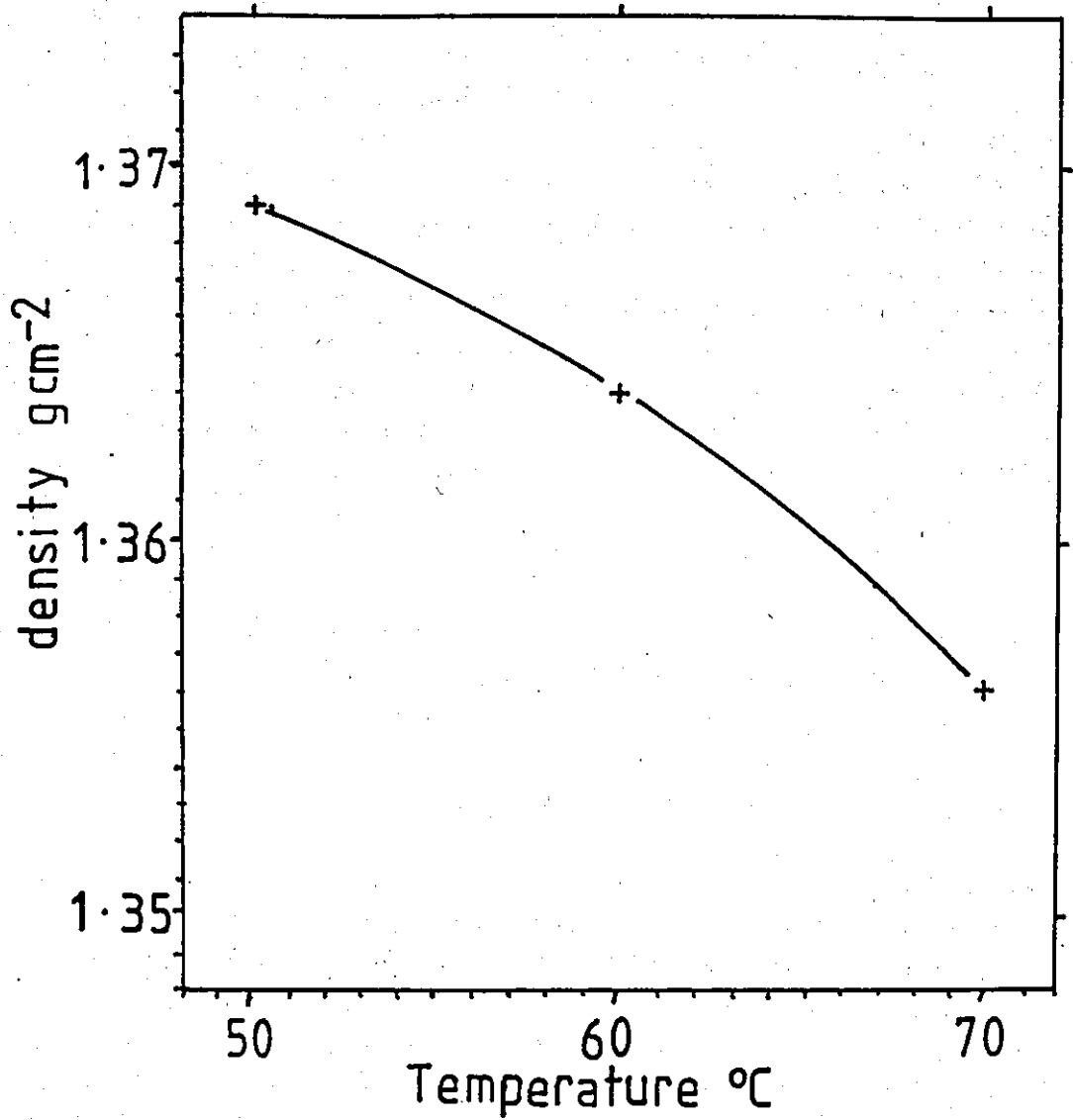


Fig.3.1 Density of 'Concentrated' nickel sulphamate electrolyte as a function of temperature

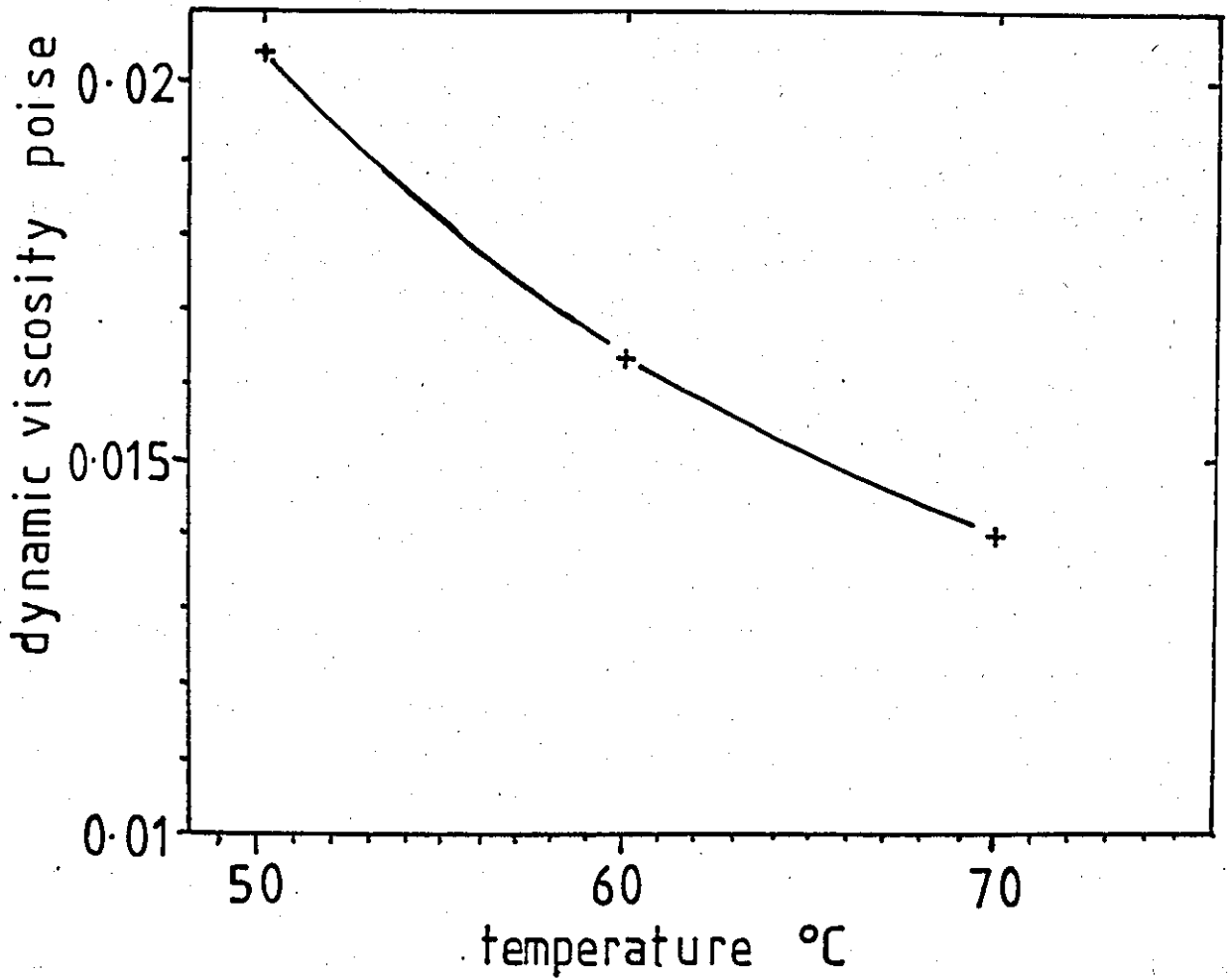


Fig.3.2 Dynamic viscosity of 'Concentrated' nickel sulphamate electrolyte, as a function of temperature

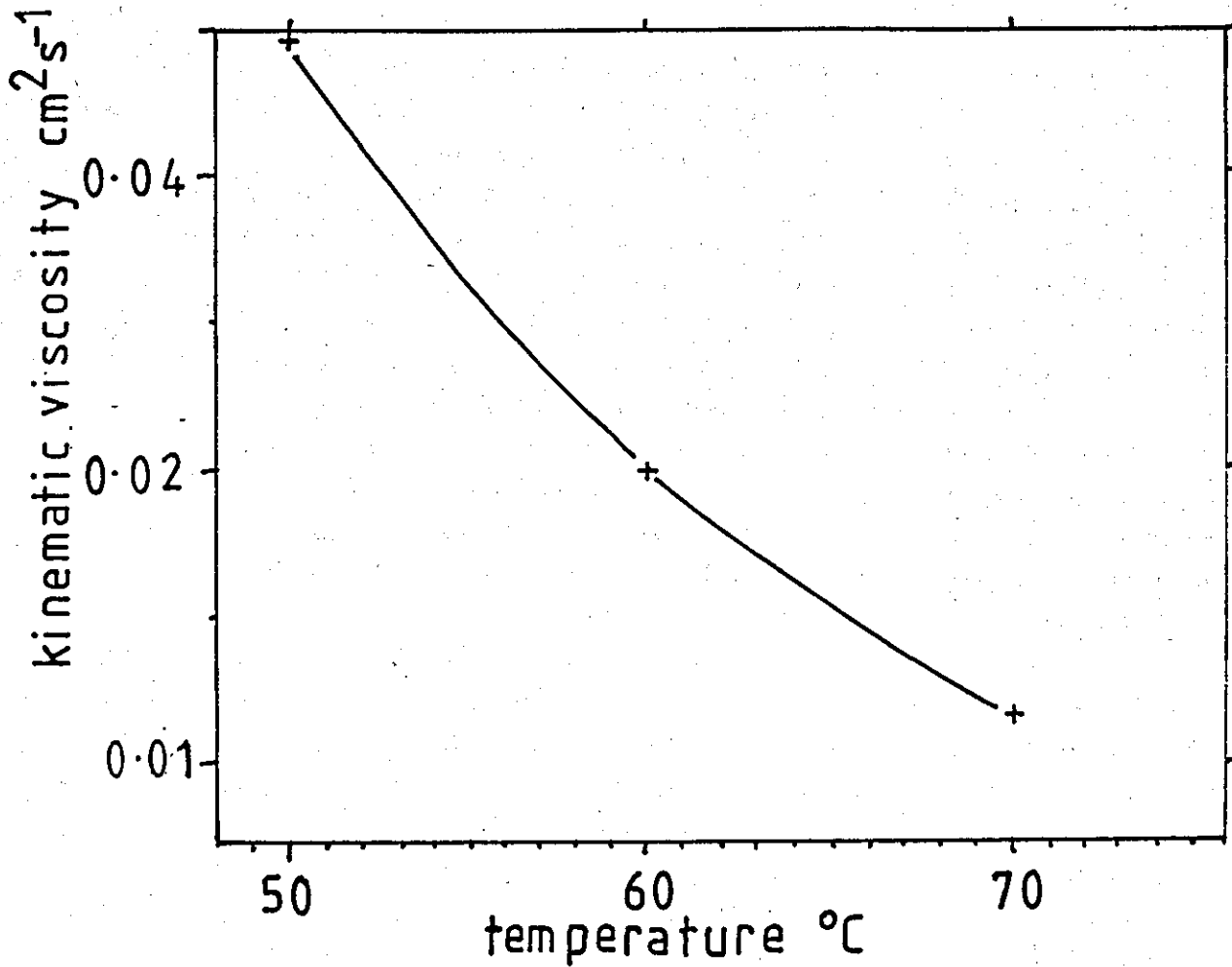


Fig.3.3

Kinematic viscosity of 'Concentrated' nickel sulphamate electrolyte as a function of temperature

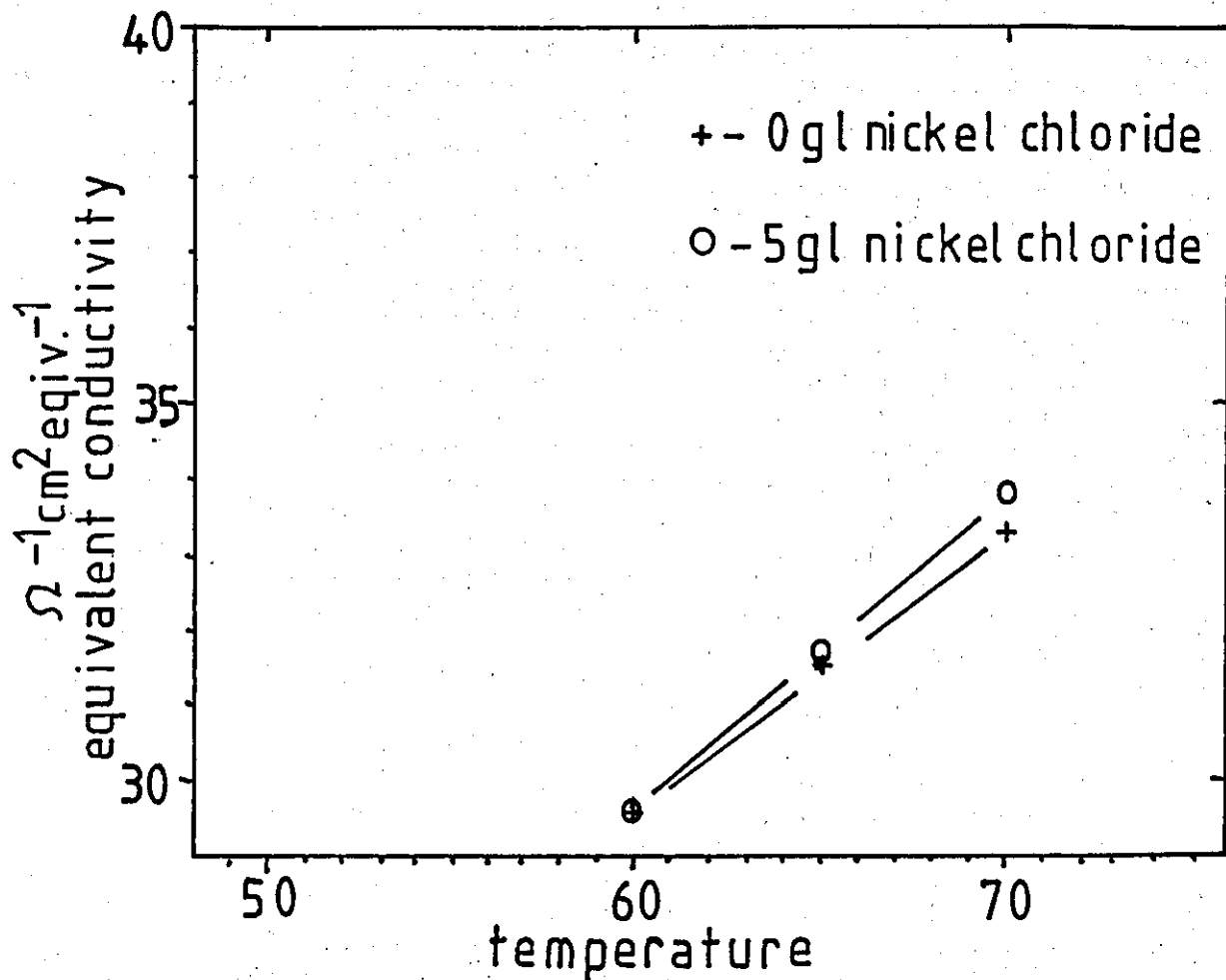


Fig.3.4

Equivalent conductivity of 'Concentrated' nickel sulphamate electrolyte as a function of temperature

$$\text{molecular weight of Ni Cl}_2 \cdot 6\text{H}_2\text{O} = 237.7$$

$$\text{Wt. fraction Ni in Ni Cl}_2 \cdot 6\text{H}_2\text{O} = \frac{58.7}{237.7}$$

$$= 0.247$$

$$\text{g } \ell^{-1} \text{ Ni}^{2+} \text{ in } 5 \text{ g } \ell^{-1} \text{ Ni Cl}_2 \cdot 6\text{H}_2\text{O} = 0.247 \times 5$$

$$= \underline{1.2 \text{ g } \ell^{-1} \text{ Ni}^{2+}}$$

$$\therefore \text{ Total concentration of Ni}^{2+} = 109.1 + 1.2$$

$$= 110.8 \text{ g } \ell^{-1}$$

$$= \underline{1.88 \text{ mole dm}^{-3}}$$

The nickel concentration of the electrolyte was maintained within $\pm 5\%$ of the above figure.

i) Determination of total nickel concentration (ref 220).

The total nickel concentration of the solution was determined by a complexometric titration with EDTA (ethylene diamine tetra-acetic acid, Fisons AR). A 5 cm³ aliquot of the electrolyte was diluted with distilled water, to 100 cm³ in a volumetric flask. A 20 cm³ aliquot of the diluted plating solution was transferred to an Erlenmeyer flask, diluted to ~50 cm³ with distilled water and 5 cm³ of ammonia solution (S.G. 0.88 g cm⁻³) added. Approximately 0.5 g of Murexide indicator (500:1, NaCl:Murexide) was added to the flask. The resulting brown solution was titrated versus a standard 0.1 mole dm⁻³ EDTA solution to a magenta end point.

Calculation

The total concentration of nickel in the solution was calculated (in g ℓ^{-1}) from:

$$\text{Ni}^{2+} \text{ concentration} = \frac{\text{Titre}}{1,000} \times 0.1 \times \frac{100}{20} \times \frac{1000}{5} \times 58.7$$

$$= \underline{\text{Titre} \times 5.87 \text{ g } \ell^{-1}}$$

ii) Determination of nickel chloride concentration (ref.220)

The nickel chloride concentration was determined by a Mohr type titration with a standard silver nitrate solution. A 5 cm³ aliquot of the plating electrolyte was transferred to an Erlenmeyer flask and diluted to ~150 cm³ with distilled water. To the solution was added ~2 cm³ of a 5% wt/vol aqueous solution of potassium chromate solution. The solution was titrated with a standard 0.1 moles dm⁻³ silver nitrate solution until the faint red tinge of silver chromate was detected.

Calculation

The concentration of nickel chloride was calculated from:

$$\begin{aligned} \text{Ni Cl}_2 \cdot 6\text{H}_2\text{O concentration} &= \frac{\text{Titre}}{10000} \times \frac{0.1}{2} \times \frac{1000}{5} \times 237.1 \\ &= \underline{\underline{\text{Titre} \times 2.38 \text{ g } \ell^{-1}}} \end{aligned}$$

and

$$\begin{aligned} \text{Ni}^{2+} \text{ concentration as NiCl}_2 \cdot 6\text{H}_2\text{O} &= \frac{\text{Titre}}{1000} \times \frac{0.1}{2} \times \frac{1000}{5} \times 58.7 \\ &= \underline{\underline{\text{Titre} \times 0.587 \text{ g } \ell^{-1}}} \end{aligned}$$

iii) Determination of the boric acid concentration (ref.346)

The boric acid concentration was determined by titration with sodium hydroxide following 'mannitol release'.

A 5 cm³ aliquot of plating solution was diluted with distilled water to 100 cm³ in a volumetric flask. A 20 cm³ aliquot of the dilute solution was transferred to an Erlenmeyer flask and further diluted to ~70 cm³ with distilled water. Four to five drops of a mixed indication consisting of 1g bromocresol purple and 0.2g bromothymol blue in ~100cm³ of alcohol, were added to the flask.

If the solution was yellow, it was titrated with 0.1 mol.dm⁻³ sodium hydroxide solution to the blue end point. If the solution was blue it was titrated with 0.1 mol.dm⁻³ hydrochloric acid to the yellow

end point. After the addition of ~1.5g of mannitol (Fisons AR), the solution turned yellow. A final titration with a standard 0.1 mol.dm^{-3} sodium hydroxide solution to the blue end point enabled the boric acid concentration to be calculated.

Calculation

The concentration of boric acid was calculated from:

$$\text{H}_3\text{BO}_3 \text{ concentration} = \frac{\text{Titre}}{1,000} \times 0.1 \times \frac{100}{20} \times \frac{1000}{5} \times 61.83$$

$$\underline{\text{Titre} \times 6.2 \text{ g l}^{-1}}$$

iv) Determination of hydrogen ion concentration

The pH of the nickel electrolytes was determined electrometrically using a Corning EEL pH meter (model 12) and a micro-analytical glass pH electrode. The instrument was calibrated using a phthalate buffer solution (pH 4.2 at 25°C), thermostated at the required temperature. Then

$$\text{pH} = -\log_{10} [\text{H}^+]$$

The pH was maintained between 3.5 and 4.0.

v) Maintenance of solution composition

Evaporation losses were compensated by suitable additions of distilled water. Deficiencies in the nickel content of the solutions, due to poor anode efficiency were corrected by additions of concentrated (900 g l^{-1}) nickel sulphamate solution. The pH of the electrolyte was adjusted, when necessary, by additions of sulphamic acid (HSO_3NH_2 , Fisons AR) at high pH ($\text{pH} \gg 4$) and basic nickel carbonate ($\text{Ni Co}_3 \cdot 2\text{Ni}(\text{OH})_2 \cdot 4\text{H}_2\text{O}$) at low pH ($\text{pH} \ll 4$). The nickel carbonate was added to the plating solution as a solid. The solution was maintained at 60°C, with continuous, vigorous stirring for 48h to effect dissolution of the solid carbonate. The solution was filtered and electrolytically purified prior to further deposition studies (p.122).

3.2 The design, construction and operation of the Mk 1 parallel plate cell and ancillary equipment

3.2.1 The design of the electrolytic cells and the flow system

The design of the rig may be broadly divided into two sections (a) Cell Design and (b) Flow Circuit Design. However, to some extent this division is artificial, as the design process was one of optimisation and compromise. This required an iterative technique, since many of the factors to be considered are interdependent. The parallel plate cell and the flow circuit were designed to meet the following specifications, which will be examined in detail later in this Section.

Overall cell design and flow circuit specifications

Design specification

- i) The cell was required to produce well defined mass transfer profiles and a sufficiently high mass transfer rate to achieve limiting current densities in excess of 1 A cm^{-2} .
- ii) A maximum flow velocity corresponding to Re 14,000 with a volumetric flow rate of up to 20 l mins^{-1} .
- iii) The critical dimensions of the cell and electrodes were to be as follows:
 - A demountable electrode system with an electrode length of about 5 cm.
 - An interelectrode gap of $< 1 \text{ cm}$ and duct breadth of $\sim 3 \text{ cm}$.
 - An hydrodynamic entrance length of $\sim 50 \text{ cm}$.
- iv) Means of measuring the inlet and outlet temperatures of the electrolyte were also required.

Flow circuit specifications

- (i) Approximately 30% electrolyte was to be used at operating temperatures of up to 70°C and maintained at constant temperature during electrolysis.

- (ii) The flow circuit was to be designed to pump a moderately hot and corrosive electrolyte from the reservoir, through the cell and return it to the reservoir.
- (iii) The pressure head across the circuit was to be optimised to allow the use of a small pump with an operating capacity of at least 20 l min^{-1} .
- iv) The rig was to be provided with a convenient means of measuring flow rates.

(a) Design of Cell I

Initial mass transfer considerations

In order to obtain an initial view of possible maximum current densities, the limiting current densities were estimated from the relevant transport equations. Previous investigators have claimed maximum current densities of $2 - 4 \text{ A cm}^{-2}$. The cell was to be designed to achieve maximum current densities of this order of magnitude.

Design calculations were based on a short electrode system in turbulent flow where the maximum mass transfer rate would be achieved at a relatively low flow rate. The appropriate design equation is:

$$\text{Sh}_{\text{Av}} = 0.145 \text{ Re}^{0.66} \text{ Sc}^{0.33} \text{ de}/L^{0.25} \quad \dots \dots (2.67)$$

The above equation was used for design calculations as described in Appendix 2b.

Flow rate considerations

It was evident that higher mass transfer rates would be achieved in turbulent flow. However, as the flow velocity increases, the pressure head increases and the size of the flow circuit and pump must increase to compensate. Hence, the volume of electrolyte required may also increase.

It was decided that an initial flow velocity corresponding to Re 14,000 with a volumetric flow rate of about 20 lmin⁻¹ would simplify the design requirements. Further consideration of frictional pressure loss and pumping capacity are described in Appendix 2c and d.

The critical dimensions of the cell and electrodes

Several factors had to be considered when specifying the dimensions of the cell and electrodes. Since many of these are inter-dependent, it is convenient to discuss these factors with reference to the expanded form of Equation 2.67 i.e

$$k_L = 0.145 \left(\frac{U \cdot de}{\nu} \right)^{\frac{2}{3}} \left(\frac{\nu}{D} \right)^{\frac{1}{3}} \left(\frac{de}{L} \right)^{\frac{1}{4}} \dots \dots (2.67a)$$

or

$$k_L = 0.145 U^{\frac{2}{3}} \nu^{-\frac{1}{3}} D^{\frac{2}{3}} de^{-0.083} L^{-0.25} \dots \dots (2.67b)$$

where k_L is the mass transfer coefficient at the limiting current density, $U = \frac{Q}{60 BS}$ (cm s⁻¹) where Q is the volumetric flow rate (cm³min⁻¹) through a cell of duct width B and interelectrode separation S. The equivalent diameter of the cell, de , is given by $\frac{2 BS}{B + S}$, (ν and D are the kinematic viscosity and diffusion coefficient of the electrolyte respectively and were regarded as constants for cell design purposes).

Electrode length

The use of demountable electrodes of moderate length (5 cm) would enable morphological work to be carried out conveniently and avoid the use of excessively large current generators. It should be noted that for Equation (2.67) to apply, $L/de < 8$ and hence for an electrode length (L) of 5 cm, de must be > 0.7 cm. However, the value of de (and B and S) must also be considered in relation to their effect on the Reynolds number (see Appendix 2a).

Duct breadth and inter-electrode separation

The selection of suitable values for B and S was dependent upon several other criteria. In order to minimise differences in mass transfer rates between the electrode edges and the centre, it has been found necessary (163) to have a small aspect ratio ψ defined by:

$$\psi = \frac{S}{B}$$

The aspect ratio should be < 0.33 to be reasonably effective

(k_L Laminar $>90\%$ of theory):

Stanmore (164) found that in using electrodes 3 cm in breadth, there was little difference (3%) in the mass transfer coefficient between the middle and edge and the system corresponded to a first approximation, to a system, of infinite parallel plates. It was also considered that better current distribution would be obtained if the parallel plate electrodes were the same breadth as the duct. Thus a provisional figure of 3 cm was selected for the duct and electrode breadth.

It was undesirable to make the interelectrode separation no larger than necessary since this would increase the power requirements, the volume of the duct and the aspect ratio. An inter-electrode separation of 1 cm was considered reasonable. It was hoped that this would be sufficient distance to overcome problems which might arise if there was any gas evolution, e.g. oxygen at the anode and hydrogen at the cathode.

Aspect ratio and equivalent diameter of the cell

The aspect ratio of the cell (S/B) was 0.33. The equivalent diameter of the cell was calculated from Equation 2.36:

$$d_e = \frac{2BS}{B+S} = \frac{2 \times 3 \times 1}{3+1} \sim 1.5 \text{ cm}$$

With an equivalent diameter of 1.5 cm, the electrode length (5 cm) corresponded to ~ 3.3 equivalent diameters in length.

Maximum flow velocity and Reynolds number

The maximum flow velocity through a cell of the stated dimensions was $\sim 111 \text{ cm s}^{-1}$ for a volumetric flow rate of 20 l min^{-1} . This corresponds to a maximum Reynolds number of $\text{Re } 13,866$ (see Appendix 2).

Hydrodynamic entrance length

In laminar flow long hydrodynamic entrance lengths (L_e) are required to eliminate the perturbations in streamline formation caused by bends etc. The maximum entrance length for fully developed laminar flow will be found at about $\text{Re } 2,500$ and may be calculated from (148)

$$L_e/d_e = 0.0288 \text{ Re} \quad \dots \dots (2.23)$$

At $\text{Re } 2,500$

$$L_e/d_e = 0.0288 \times 2,500 \sim 72$$

A minimum hydrodynamic entrance length of about 72 equivalent diameters may be necessary to ensure fully developed laminar flow.

However, the maximum rate of mass transfer will be found in turbulent flow. In turbulent flow, due to prior flow development in the connecting pipework, hydrodynamic entrance lengths tend to be shorter. In addition, the greater thickness of the hydrodynamic boundary layer, when compared to the mass transfer boundary layer, will ensure that the mass transfer profile will be fully developed at relatively short entrance lengths.

Therefore, with an entrance length (L_e) of 50 cm and $d_e = 1.5 \text{ cm}$ then,

$$L_e/d_e = 50/1.5$$

and $L_e \sim 33$ equivalent diameters.

This value was considered sufficient to allow reproducible and fully developed mass transfer profiles.

Approximate theoretical values of i_l

Having established suitable values of B, S and d_e , sample calculations were carried out to establish the likely mass transfer coefficients and limiting current densities which would be achieved using the specified design parameters at 60°C. Detailed calculations are shown in Appendix 2b and a summary of the results is presented below.

Limiting current densities in laminar flow were calculated from Equation 2.49.

$$Sh_{Av} = 1.85 \left\{ Re Sc \frac{d_e}{L} \right\}^{0.33} \dots (2.49)$$

At Re 2,000, the limiting current density was calculated to be 0.9 A cm².

In turbulent flow, limiting current densities were calculated from Equation 2.67.

$$Sh = 0.145 Re^{0.66} \frac{d_e}{L}^{0.25} Sc^{0.33} \dots (2.67)$$

At the maximum flow rate corresponding to Re 14,000, the limiting current density was calculated to be ~3.5 A cm⁻².

The selected design was therefore theoretically capable of electroforming nickel at rates in excess of 1 A cm⁻², as originally specified.

(b) Design considerations for the flow circuit and pump capacityi) Volume of electrolyte required and the method of temperature control

Several factors were decisive in selecting the appropriate electrolyte volume. With a small volume of plating solution, significant changes in the electrolyte composition may result from the electrode processes. A reasonable solution bulk would buffer this effect. In addition, the large pumping capacity required (20 l min⁻¹) and the

dimensions of the associated flow circuit also necessitate large volumes of solutions. A suitable glass reservoir capable of holding >30ℓ of electrolyte was therefore essential.

This volume of electrolyte required to be heated to and maintained at temperatures of up to 70°C under operating conditions. A sufficient thermal input would be provided by 3 x 0.5 kW immersion heaters, to reach thermal equilibrium in less than 1.5h. The heaters were silica sheathed to prevent contamination of the electrolyte by corrosion products. Additional heating of the pipework and suitable insulation would minimise heat loss.

The electrolyte temperature could be accurately controlled by a contact thermometer (immersed in the reservoir electrolyte) and a mercury switch.

The possibility of ohmic heating of the electrolyte was also considered. However this was only thought to be significant at current densities $\gg 2\text{A cm}^{-2}$. If necessary, a suitable heat exchanger would be inserted in the flow circuit.

ii) Materials of construction and pump selection

To withstand the relatively high temperatures and prevent contamination of the electrolyte most of the pipe work, valves, etc. was constructed from borosilicate glass. However, for convenience short sections of polythene tube were to be used for connecting to and from the pump.

It was also ascertained that there were several small chemical pumps available capable of handling nickel sulphamate solutions at temperatures of up to 70°C and which were able to give flow rates of up to 50 ℓ min⁻¹. However, the maximum delivery rate of the pump was dependent upon the pressure at the pump head. Further information concerning pump performance and selection is presented in Appendix 2c and d.

iii) Frictional head loss across the flow circuit

The frictional pressure head, h_f , is related to the flow velocity U , the tube dimensions and the physical properties of the solution. Under laminar flow conditions this relationship is determined by the Hagen-Poiseuille equation

$$h_f = \frac{U \ 8 \ \eta \ L}{r^2}$$

where r is the radius of a pipe of length L and η is the dynamic viscosity of the fluid. In turbulent flow the relationship is governed by the Fanning-Darcy equation

$$h_f = 4f \cdot \frac{L}{d} \cdot \frac{U^2}{2g} \quad \dots \dots (2.26)$$

where d is the diameter of the pipe, g the acceleration due to gravity and f a friction factor. f may be determined from the Blasius relationship

$$f/2 = 0.0396 \text{ Re}^{-0.25} \quad \dots \dots (2.24)$$

For square ducts the pipe radius and diameter may be approximated by the hydraulic radius r_h and the equivalent diameter d_e respectively, given by

$$r_h = \frac{BS}{2(B+S)}$$

and

$$d_e = 4 r_h \quad (\text{cf. Equation 2.36})$$

Hence it was evident that a large frictional pressure loss will develop using small bore tubes and ducts. Calculation has shown that the largest single frictional pressure loss would occur across the cell length. (Appendix 2c). However, small ducts were essential in relation to other restrictions inherent in the design of the cell.

Therefore a pump with sufficient power to produce a delivery rate of at least 20 l. min^{-1} against the total pressure head was chosen. (Appendix 2d).

iv) Measurement of the flow rate

The method of flow rate measurement must be convenient to use, cover a range of flow rates with reasonable accuracy. Borosilicate glass Rotameters with a ceramic float are available in various sizes and are suitable for this purpose. An example of the calculation of the maximum measurable flow rate through a Rotameter and the method of calibration and calibration curves are shown in Appendix 2e.

3.2.2 Construction details of Cell 1, the flow circuit and electrical circuits

i) The construction of Cell 1 and the working electrodes

The electrolytic cell is shown diagrammatically in cross section and in plan in Figs.3.5 and 3.6, a general view is presented in Fig.3.7(b). The cell body was constructed of Perspex due to its chemical resistance, electrical insulating properties and ease of machining. A duct 3 cm wide and 1 cm deep was milled into the upper section and the two sections were cemented together using Tensol.No.5 Perspex cement and ten, 1.75 in. long, 4 B.A. hexagon socket screws countersunk into the Perspex. The overall length of the channel was 75 cm and at each end a 25 cm i.d. x 3.75 cm o.d. Perspex pipe with a Perspex flange (a in Fig.3.5) was fitted. The flange matched the Q.V.F. backing flange (Type CF1). The seal was made using a rubber gasket with a PTFE gasket sheath. The point at which the pipes met the duct was profiled to provide a smooth hydrodynamic entrance to the duct. A stainless steel drain plug was provided at the downstream end of the cell. Two thermometers (10-80°C) were inserted into the channel, through PTFE glands screwed into the end pipes (A-A in Fig.3.5) to enable the inlet and outlet temperature of the electrolyte to be monitored.

The cathode, 5 cm in length, was machined from 18/8 stainless steel to assist removal of electroforms. The stainless steel cathode deck (f in Fig.3.8) was mounted on a nickel plated mild steel backplate (e in Fig.3.8). The anode (f in Fig.3.9) was machined from electrolytic nickel and provided with a similar backplate (e. in Fig.3.9). A stainless steel 'jacking' plate (a in Figs.3.8 and 3.9) was used to maintain the rubber

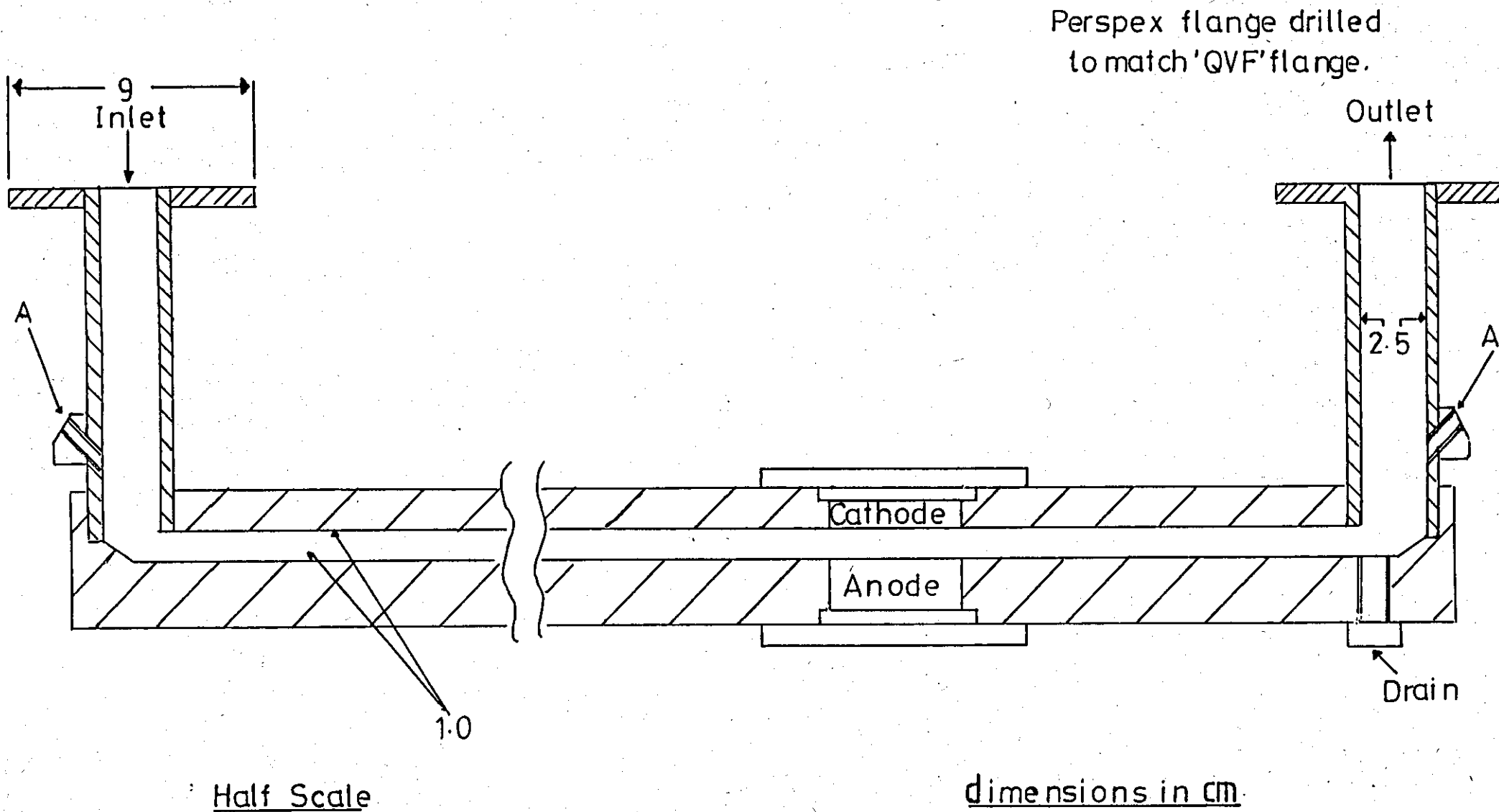
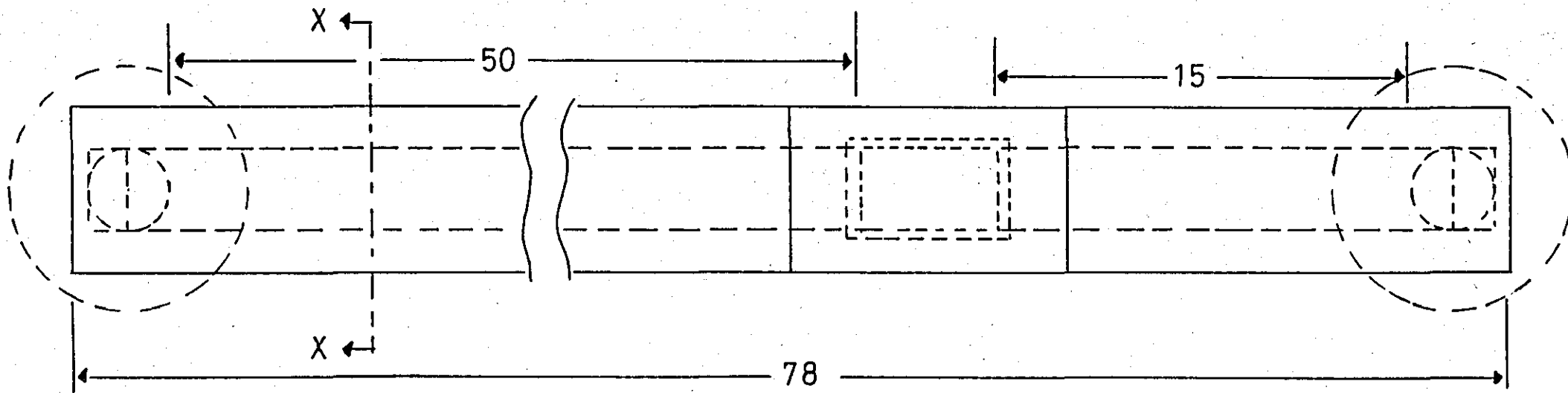
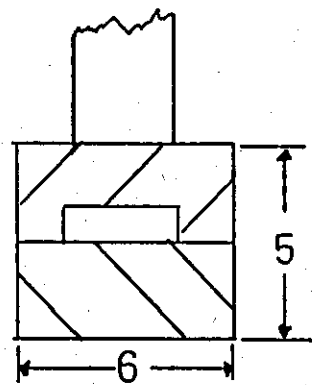


Fig.3.5 Cross-sectional side elevation of cell 1.



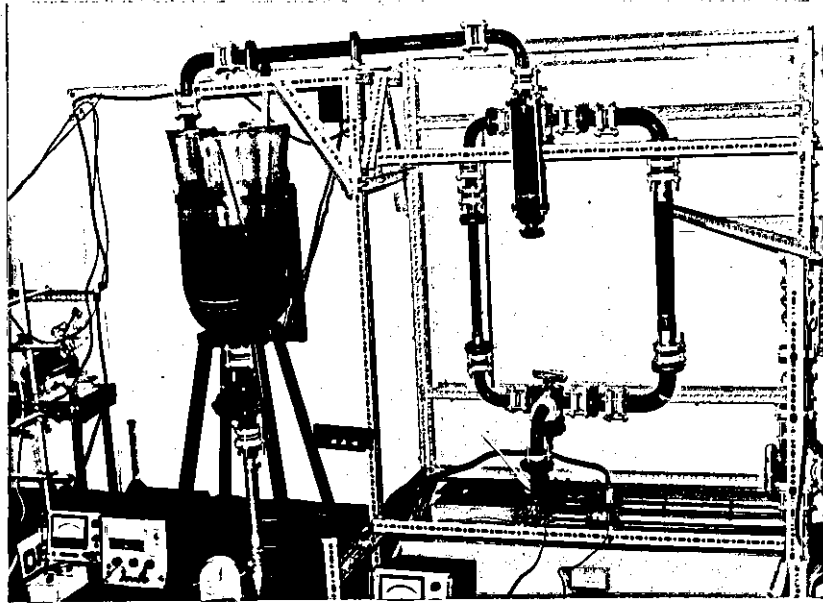
Half Scale



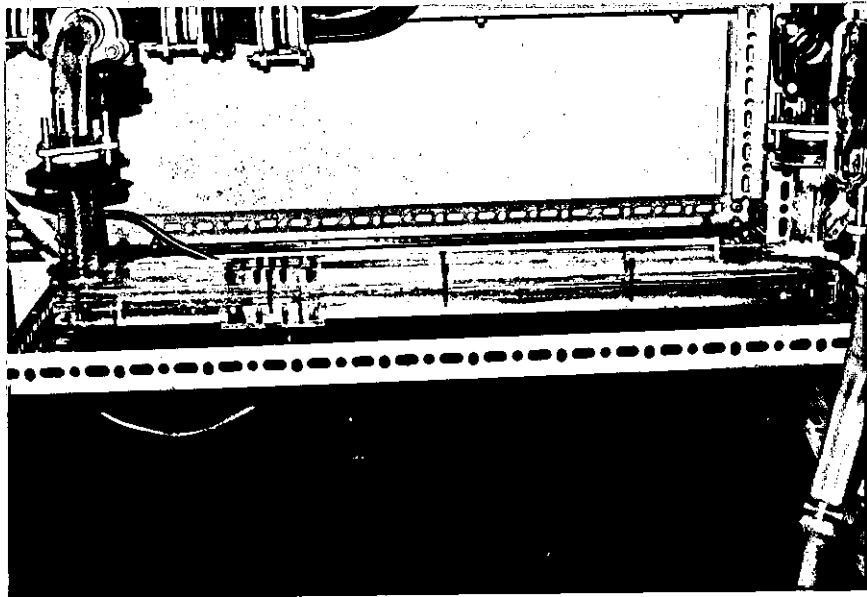
Cross Sectional End
Elevation Through XX

dimensions in cm

Fig.3.6 Plan view and cross-sectional side elevation (through XX) of Cell 1.



a)



b)

Fig.3.7 Cell 1 and ancillary apparatus
a) Overall view of flow system 1 reservoir,
filter and Rotameters.
b) Cell 1 in position in flow system

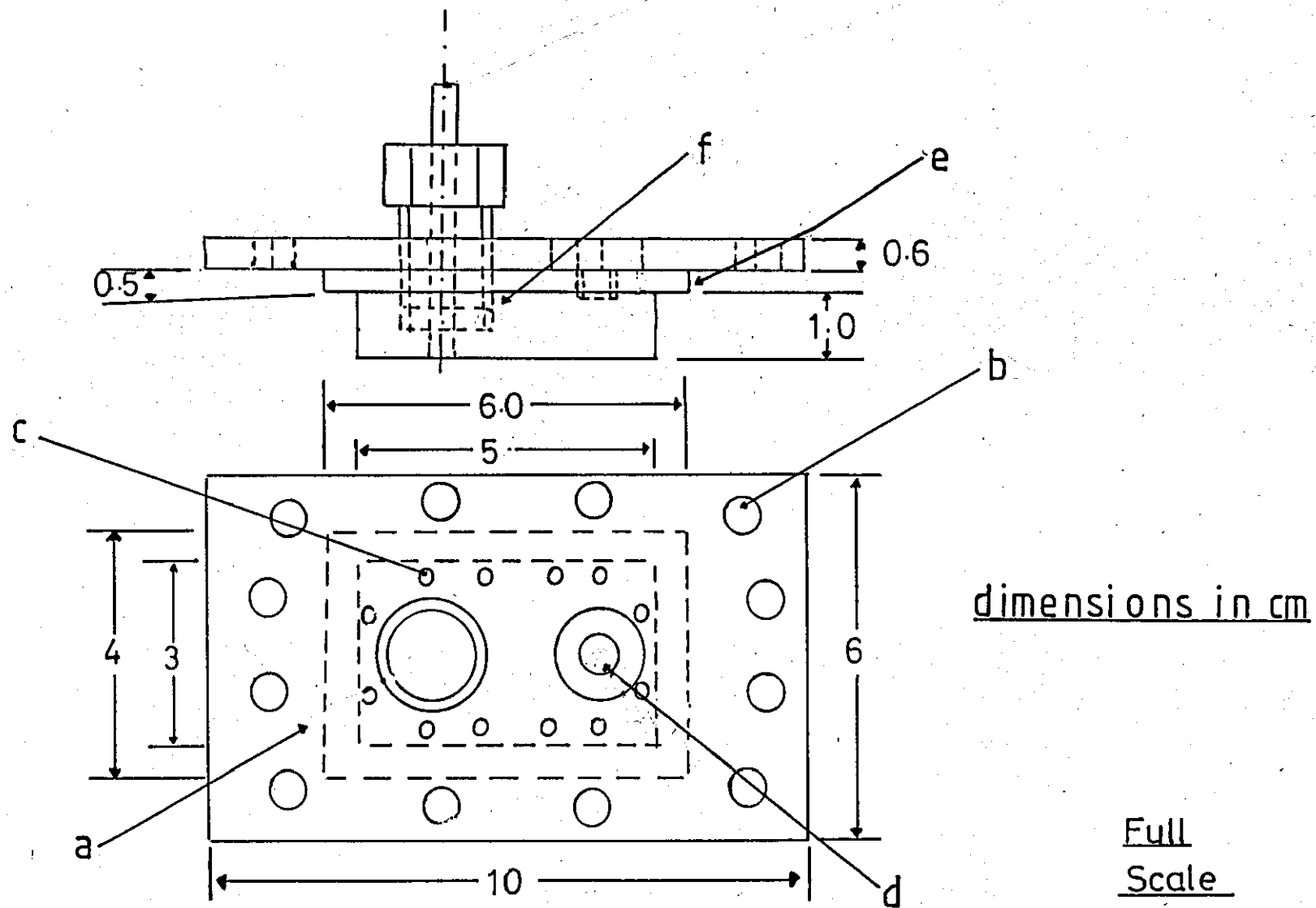
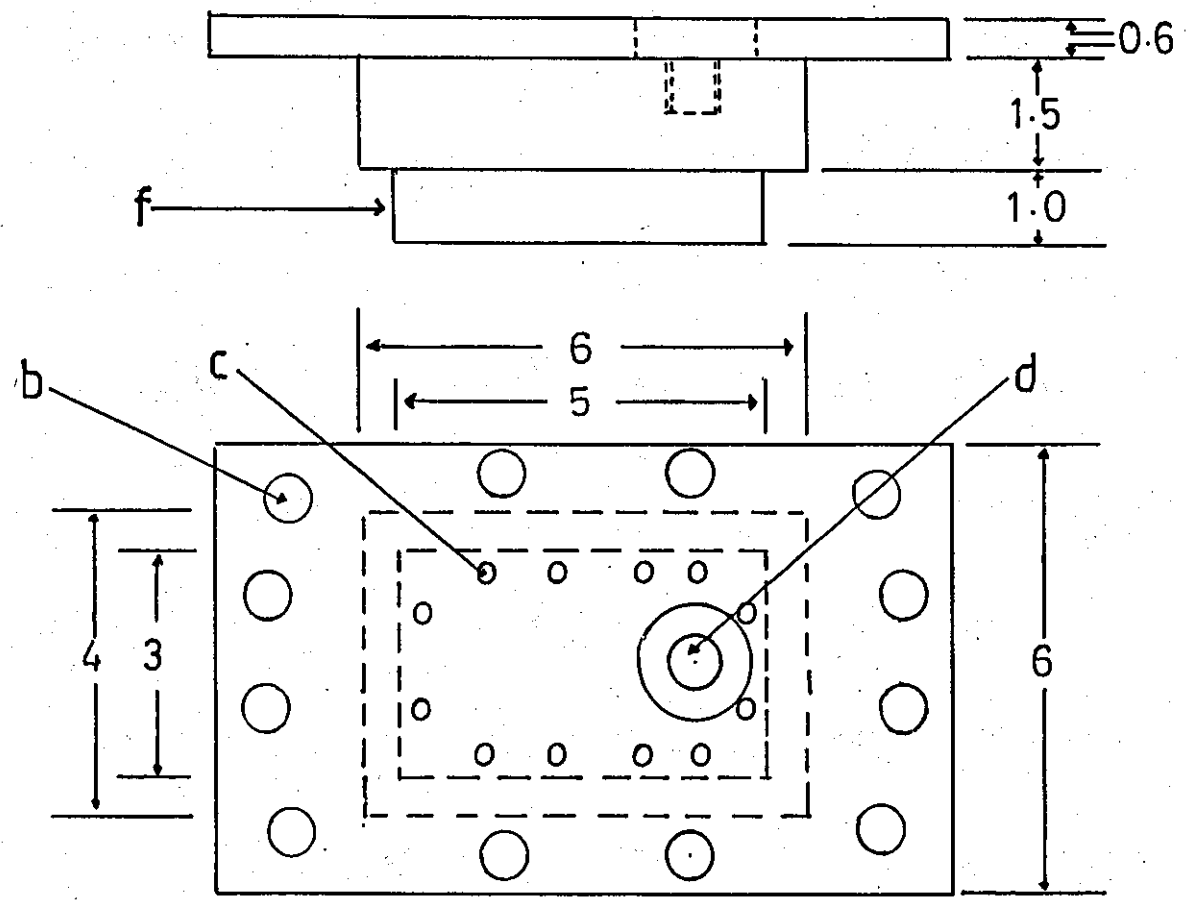


Fig.3.8 Cell 1. Cathode specifications



dimensions in cm

Full Scale

Fig.3.9 Cell 1. Anode specifications

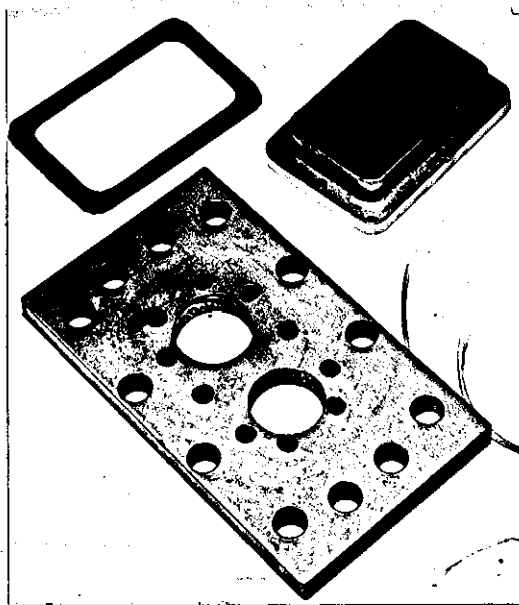
gasket seal between the electrode assembly and the cell. The electrode and backplate were mounted in the cell, flush with the exterior wall. The jacking plate was screwed into place over the electrode, by 12 x 2 BA hexagon head screws (b in Figs.3.8 and 3.9). The rubber gasket was then compressed by evenly tightening the 12 x 6 BA hexagon head grub screws (c in Figs.3.8 and 3.9). The electrode assembly is shown in Figs.3.10, a and b. The cathode deck, mounted in the cell is shown in Fig.3.10c. The electrical connection was made by screwing a brass adaptor into the electrode backplate (d in Figs.3.8 and 3.9).

ii) The construction of the flow circuit

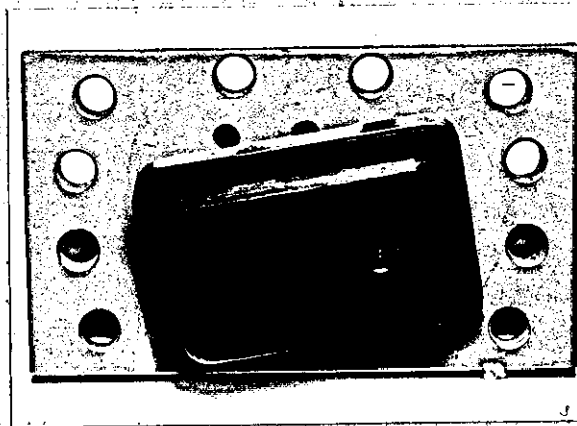
The circulation system (and the electrical circuit) used when operating Cell 1 is shown schematically in Fig.3.11. An overall view is shown in Figs. 3.7(b) and 3.12. The pipework was constructed from 1" tubing except for connecting pieces. Corning Q.V.F. glassware and associated joints, taps, etc. were used throughout (except where indicated) and the unit supported on a wall-fixed Dexion frame. The reservoir (i in Fig.3.11) was of 30 l capacity and the electrolytes were heated by three 500W silica-sheathed immersion heaters (f in Fig.3.11) mounted on Perspex brackets. The temperature was regulated using a contact thermometer (i in Fig.3.11) and mercury switch.

The pump (d in Fig.3.11) was a Beresford centrifugal pump (Type PV31). The shaft was of EN58J stainless steel. The motor was a fan-cooled series wound type operating at 4,000 to 4,300 r.p.m. and controlled by a Triac-type speed controller which allowed high-power operation with large reductions in r.p.m. Under normal operating conditions the pump was capable of delivering $\sim 20 \text{ l min}^{-1}$. Connections to and from the pump were made using internally threaded Portex polythene tubing (o in Fig.3.11).

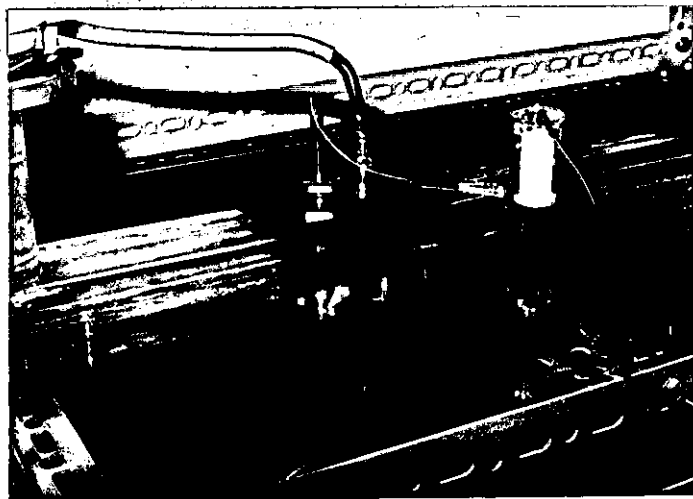
The rate of flow of the electrolyte was roughly controlled by means of the speed-controller and fine adjustments were made using the diaphragm valve (3 in Fig.3.11) and the flow was directed through the appropriate Rotameter (h in Fig.3.11) by means of directional valves (4) and (5) (Fig.3.11). The Rotameters were Rotameter Limited,



a)



b)



c)

Fig.3.10

Cell 1. Cathode assembly

- a) Cathode deck, rubber gasket and jacking plate.
- b) Cathode deck and jacking plate
- c) Cathode and jacking plate in position in cell with electrical connection (n.b. also reference electrode and Luggin capillary assembly used for development purposes).

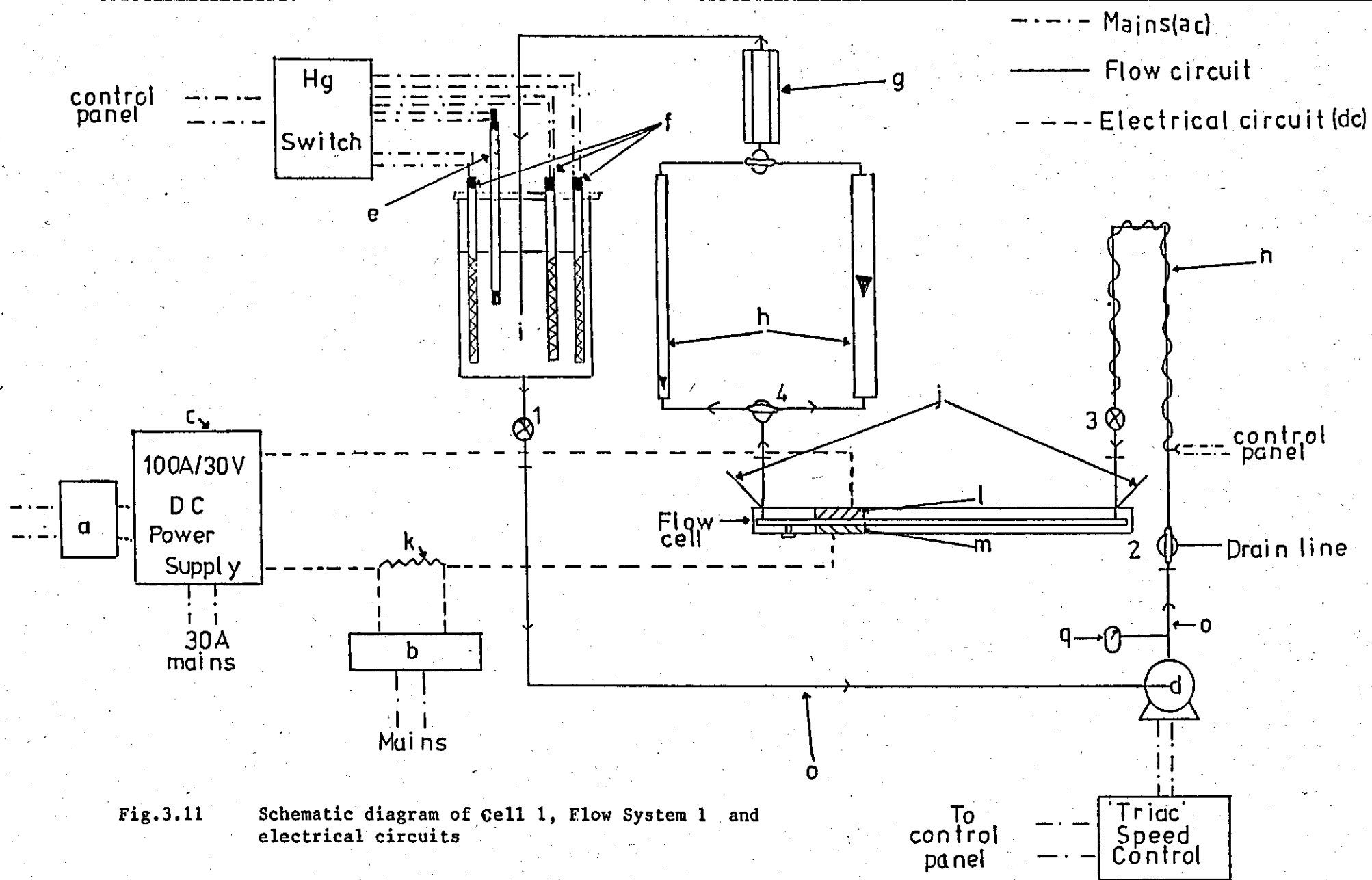


Fig.3.11 Schematic diagram of Cell 1, Flow System 1 and electrical circuits

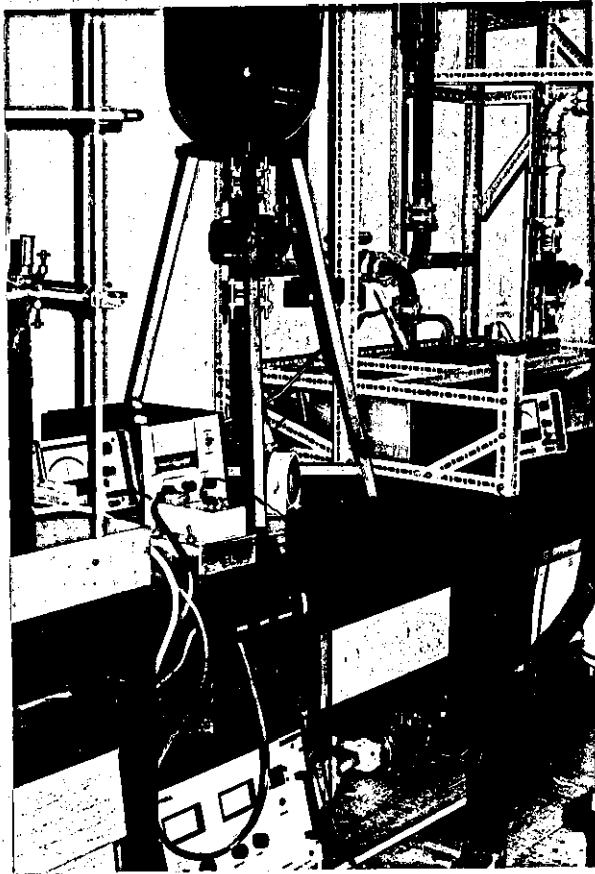


Fig.3.12 Flow system 1, pump, power supply and control panel.

Types 18X and 35X with K type floats. One type was designated for flow rates of up to $3\ell \text{ min}^{-1}$ and the other for rates up to $25\ell \text{ min}^{-1}$. The electrolyte solution was continuously filtered through a Q.V.F. (PCF1) ceramic filter ($30\mu\text{m}$) ((g) in Fig.3.11), to remove any anode or other sludge. The entrance pipe to the cell, which was of 1 in. bore was heated by means of a 'Hotfoil', 200 w. heating tape ((n) in Fig.3.11) and the pipework was lagged with glass wool as required.

iii) Power supply and Electrical circuits

The main power supply was through a Farnell H30/100 low ripple transformer rectifier unit ((c) in Fig.3.11). The power was fed to the electrodes via 70A copper cable. The supply was operated manually or remotely programmed by either a constant voltage input (5 A V^{-1}) or from the constant voltage across an external resistance (0.05 A ohm^{-1}) (a in Fig.3.11). The constant voltage was provided by a Farnell L 30 E, 0-30 V, 5A power supply and the standard resistance was obtained from a resistance box of tolerance 0.1% and range 0-10,000 ohm. This procedure enabled the desired constant current to be applied rapidly and accurately, which was essential for short electroforming operations at high current densities.

The current was measured indirectly by determining the voltage loss across a 0.005 ohm high current standard resistor ((k) in Fig.3.11) in series in the circuit. The voltage drop (in mV) was measured using a high impedance digital voltmeter (Sinclair, DV450 (b) in Fig.3.11).

Annotation for Fig.3.11

- a) Remote programming unit for main power supply (Farnell L 30E, 0-30V power supply or JJ resistance box 0-10,000 ohm)
- b) Digital voltmeter (Sinclair, DV450)
- c) Main power supply (Farnell, H 30/100)
- d) Centrifugal pump (Beresford, Type PV 31)
- e) Contact thermometer
- f) Silica sheathed immersion heaters (500 W)

- g) QVF filter (Part No.PCF 1, 30 μ ceramic filter)
- h) Rotameters (Types 18X and 35)
- i) Glass reservoir (30 l capacity)
- j) Thermometers (10-100°C)
- k) Standard resistor (0.005 ohm, 100A)
- l) Cathode deck
- m) Anode deck
- n) Heating tape ('Hotfoil' 200W)
- o) Polythene tube (1" i d Portex tube)
(All other tube was Corning QVF 1" bore (excluding the appropriate connecting pieces to the Rotameter))
- 1) Diaphragm valve (QVF No.SV1.5)
- 2) T-Port Stopcock (QVF No.TST1)
- 3) Diaphragm valve (QVF No.SV1)
- 4) L-Port Stopcock (QVF No.TSL1)
- 5) L-Port Stopcock (QVF No.TSL1)

3.2.3 Electroforming procedures using the Mk 1 parallel plate cell

i) Preparation of electrodes

The nickel anodes were polished to a 600 grit silicon carbide finish and degreased using Genklene (ICI), prior to insertion in the flow cell.

The stainless steel cathodes were polished to a series of finishes of which a 1200 silicon carbide or 6 μ m diamond provided the optimum surface conditions necessary to achieve adequate adhesion during deposition combined with good post formation foil stripping characteristics after removal of the electrode from the cell. The cathode was subsequently degreased using Genklene (ICI) either in an ultra-sonic bath or vapour degreased. This procedure was followed by an electrolytic alkali cleaning process of which the following method (347) was found to be satisfactory:

Electrolyte composition:

Sodium hydroxide	:	25 g l ⁻¹
Tri-sodium phosphate	:	75 g l ⁻¹
Sodium silicate	:	7.5 g l ⁻¹

Operating conditions:

Temperature	:	70 - 80°C
Anodic	:	1 min @ 5 A dm ⁻²
Cathodic	:	2 min @ 20 A dm ⁻²

The counter electrode was a lead sheet. The cathode deck was subsequently rinsed with water, and excess alkali and surface films removed with a 5% sulphuric acid solution, followed by a second rinsing with distilled water. The cathode was then screwed to the backing plate, and the complete electrode assembly bolted into the cell.

ii) Preparation of the electrolyte

The electrolyte was based upon the concentrated nickel sulphamate plating solution developed by Kendrick(1). The electrolyte had the basic composition 600 g l⁻¹ nickel sulphamate (BDH Ltd. 900 g l⁻¹ solution), 40 g l⁻¹ Boric acid (Fisons Ltd., A.R. Grade), pH ~4.0.

Certain solutions also contained 5 g l⁻¹ nickel chloride (Fisons Ltd., A.R. Grade) where required. The solutions were made up to the required volume using distilled water. When necessary the surface tension of the electrolyte was reduced by the addition of 52 mg l⁻¹ Fluowet S.P. (Hoechst UK Ltd.).

The nickel sulphamate solutions were conditioned as described in the literature (p.96) in batches of 25 to 50 l in a paddle stirred subsidiary tank. The electrolyte was heated by silica-sheathed immersion heaters and the temperature controlled by a contact thermometer or mercury phial thermostat. The three conditioning processes are summarised below:

- a) Activated charcoal treatment: Approximately 1.3 g l^{-1} of acid-washed activated charcoal was added to the electrolyte, which was then continuously stirred for 24 h at 60°C . The carbon was removed by pumping the solution through washed glass-fibre wool and filter-pulp until free of particles.
- b) Low current density treatment: The nickel sulphamate solutions were electrolysed for $\sim 10 \text{ A hr l}^{-1}$ between terylene-bagged electrolytic nickel anodes (Cannings Ltd.), and a corrugated nickel foil cathode. The current density at both the anode and cathode was 0.0054 A cm^{-2} .
- c) High current density treatment: This was similar to the low current density treatment except that the cathodic current density was 0.043 A cm^{-2} .

Hull cell tests

The nickel sulphamate electrolytes were all pre-conditioned to give semi-bright, low-stressed deposits in Hull cell tests (450 cm^3 in volume). The electrolyte was operated at 60°C and stirred by a magnetic stirring bar.

iii) Operation of the flow cell

The bulk of the electrolyte was pre-heated prior to fitting the electrodes in the cell. The reservoir heaters were switched on and the solutions agitated by pumping air, pre-saturated with water, through the electrolyte. After both electrodes had been fitted into the cell, the flow circuit was opened to the appropriate Rotameter and the cell flooded. The system took $\sim 1.5 \text{ h}$ to equilibrate at the required temperature. The operating temperature was measured at both ends of the cell. After equilibration, the flow rate was adjusted using the pump speed controller and the diaphragm valve ((3) in Fig.3.10). The deposition current was pre-programmed for the power supply, the electrical leads connected to anode and cathode and electroforming commenced. Deposition was continued for a predetermined time to give foils of known thickness. The deposition time was measured using a stop watch. After deposition

the current was switched off and the cell isolated. The cathode was then removed from the cell and the deposit washed in hot running water, distilled water and then acetone.

The foil was carefully removed from the substrate and weighed accurately.

The plating time to give foils of constant thickness and the current efficiency were calculated using the following equations:

Calculation of plating time and current efficiency

Since $96,495 \pm 5$ coulombs (1 Faraday) will deposit $\frac{58.7}{2}$ (= $\frac{\text{mol. Wt.}}{2}$)g of nickel, the electrochemical equivalent of nickel (E_{e1}) is given by the following expression (Equation 2.3):

$$E_{e1} = \frac{58.7}{2} \times \frac{1}{96,495} = 3.042 \times 10^{-4} \text{ g A}^{-1} \text{ s}^{-1}$$

The mass of nickel, deposited theoretically (G) is then given by:

$$G = I t E_{e1} \quad \dots \dots (2.2)$$

The current efficiency for nickel electrodeposition may be calculated from:

$$\text{Current efficiency Ni} = \frac{\text{Wt. of nickel deposited}}{I t E_{e1}} \times 100\%$$

The time (t) to electroform a foil of thickness (d) (at 100% current efficiency) is given by:

$$t = \frac{d \rho A}{E_{e1} I}$$

where

A = Area of the electrode

ρ = Density of nickel, 8.90 g cm^{-3}

As will be seen from the results of Section 4.1, several improvements to the design of the Mk 1 cell were considered necessary to improve the performance and flexibility of the cell. The following section details the design and construction of the Mk 2 cell. The general design procedure is similar to that described for Cell 1 (Section 3.2.1).

3.3 The design construction and operation of the Mk 2 parallel plate cell and ancillary equipment

3.3.1 Design of Cell 2 and the modified flow system

The electroforming studies undertaken using Cell 1 (Section 4.1) had identified certain unforeseen limitations of the original cell design. As a consequence, a modified cell design was necessary to eliminate undesirable effects and enable an expanded investigation to be carried out. The basic approach to the design of Cell 2 was similar to that envisaged for the design of Cell 1 (Section 3.2). However, the original cell specification was modified to include the following features:

- i) A method of dividing the cell and separating the anode and cathode. The specified mass transfer considerations were to be maintained as for Cell 1.
- ii) The critical dimensions of the cell were to be as follows:
 - An inter-electrode gap of <1 cm and a duct breadth of ~3 cm.
 - A demountable electrode system, with cathodes 2.5 cm and 10 cm in length.
 - A hydrodynamic entrance length of ~50cm.
- iii) The maximum Reynolds number to be maintained at ~Re 14,000 with a volumetric flow rate of up to 36 l min^{-1} .
- iv) An increased anode length of 25 cm.
 - So as to maintain the required rates of mass transfer, the flow system was also upgraded to enable larger volumetric flow rates.

Separation of anode and cathode

While carrying out electroforming operations in Cell 1, it was found that gases, evolving at the anode under some operating conditions were reaching the horizontal cathode (Section 4.1). Such phenomena may have an unpredictable effect on cathodic rates of mass transfer. The problem was most easily resolved by the provision of a porous polythene separator or diaphragm dividing the cell into two compartments of equal dimensions.

Hence the anode and cathode compartments were separated and anode gases were prevented from effecting mass transfer at the cathode.

The critical dimensions of the cell and electrodes

Duct breadth and inter-electrode separation

The considerations relating to these parameters were similar to those of Cell 1. Therefore, the inter-electrode gap (S) was maintained at 1 cm and the channel width (B) at 3 cm.

Aspect ratio and equivalent diameter of the cell

In calculating these quantities, the duct height (S') was taken as the distance between the electrode and the diaphragm (0.5 cm).

The aspect ratio of the cell ($\frac{S'}{B}$) was $\frac{0.5}{3} \sim 0.16$ (and $k_L^{\text{Laminar}} > 96\%$ of theory).

The equivalent diameter (de) of each cell compartment was calculated from (Equation (2.36)):

$$d_e = \frac{2 B S'}{B + S'} = \frac{2 \times 3 \times 0.5}{3 + 0.5} \sim 0.857 \text{ cm}$$

Hence the introduction of the diaphragm resulted in a decrease in the effective equivalent diameter, which would in turn influence the selection of cathode lengths and the overall rate of mass transfer. However, the hydrodynamic conditions in the cell will also be effected.

Cathode lengths

The cell was to be constructed to enable cathodes of various lengths to be used. The cell was to be operated using both 'short' and 'long' electrode systems.

For 'short' cathodes 2.5 cm in length, the dimensionless electrode length (L/d_e) was

$$L/d_e = \frac{2.5}{0.857} \sim 2.92$$

The maximum cathode length was 10 cm resulting in a dimensionless cathode length of

$$L/d_e = \frac{10}{0.857} \sim 11.7$$

Hydrodynamic entrance length

The entrance length of the cell (L_e) was kept at 50 cm to allow the new cell to be bolted into the existing rig. This value corresponds to an entrance length of about 58 equivalent diameters (cf. Cell 1, p.114).

Anode length

The anode area was increased to 25 x 3 \approx 75 cm in an attempt to increase the dissolution efficiency and modify the gas flow pattern in the anode compartment.

Flow rate considerations

An increase in the volumetric flow rate through the cell was necessary to maintain a Reynolds number of \sim Re 14,000. The reduction in equivalent diameter to 0.857 cm required an increase in flow velocity to \sim 200 cm s⁻¹ (since $Re = \frac{U d_e}{\nu}$). Hence the required volumetric flow rate (Q) was

$$\begin{aligned} Q &= 60 \text{ U S B} \\ &\approx 60 \times 200 \times 1 \times 3 \\ &\sim 36,000 \text{ cm}^3\text{min}^{-1} \sim 36 \text{ l mins}^{-1}. \end{aligned}$$

Mass transfer considerations

In turbulent flow, the rate of mass transfer to 'short' cathodes, less than 8 de in length, may be described by Equation (2.67)

$$Sh_{av} = 0.145 Re^{\frac{2}{3}} Sc^{\frac{1}{3}} \frac{de}{L}^{\frac{1}{4}} \dots (2.67)$$

The above equation was applied, for design purposes, to cathodes 2.92 de in length. At the maximum flow rate, corresponding to Re~14,000 the limiting current density at 60°C was calculated to be ~6.5 A cm⁻².

Similarly, for 'long' cathodes, the appropriate design equation was the Chilton-Colburn analogy,

$$Sh_{av} = 0.023 Re^{0.8} Sc^{0.33} \dots (2.66)$$

With cathodes 11.7 de in length, operating at Re 14,000, the limiting current density was calculated to be about 4.8 A cm⁻².

In laminar flow, the mass transport rate for both cathode systems may be described by a single equation

$$Sh_{AV} = 1.85 \left\{ Re Sc \frac{de}{L} \right\}^{0.33} \dots (2.49)$$

At Re 2,000 the limiting current densities were calculated as ~1.6 and ~1.0 A cm⁻² for cathodes 2.92 de and 11.7 de in length respectively.

Detailed sample calculations are shown in Appendix 2b. From this analysis it was evident that the mass transfer rates were maintained and, in some cases, significantly improved.

Modification to the flow system

The increased flow rates (~35 l min⁻¹) required with Cell 2 necessitated replacing the original pump, with one with a greater throughput. A third Rotameter was also required to measure the larger flow rate. The Rotameter calibration curves are given in Appendix 2e. The

factors effecting the choice of pump and Rotameter have been discussed earlier (Cell 1, p.116-118 and Appendices).

The flow circuit was modified to include a 'by-pass' system. The flow velocity through the cell was to be controlled by two valves. The excess electrolyte would be diverted through the by-pass and returned to the reservoir. This arrangement would allow more convenient flow control.

3.3.2 Construction details of Cell 2, the flow circuit and electrical circuit

The construction of Cell 2

The flow cell is shown diagrammatically in cross-section and in plan in Figs.3.13 and 3.14. The cell was again constructed from Perspex, in two sections. A duct 3 cm wide and 0.5 cm deep was milled into the upper and lower sections. A porous polythene (Vyon F, 1.5 mm thick, Porvair Ltd.) separator or diaphragm was inserted between the two sections. The cell was sealed by a nitrile rubber 'O' ring set into the lower section and bolted together using 38 (0.25in. Whitworth) stainless steel bolts 1.75 ins. long. The overall length of the channel was 75 cm with a 50 cm entrance length. At each end of the channel, a 2.5 cm i.d. x 4 cm o.d. Perspex pipe, 15 cm in length was screwed into the cell body (Fig.3.15). The Perspex flange matched the QVF backing flange (type CF1) used on the pipework. This joint was sealed with a rubber gasket with a P.T.F.E. gasket sheath. The point on which the pipes met the duct was profiled to provide a smooth hydrodynamic entrance to the duct. A stainless steel drain plug was provided at the downstream end of the cell.

The temperature at the inlet and outlet of the cell was monitored by two thermometers (20-100°C) screwed into the cell body via P.T.F.E. adapters. The assembled cell with the cathode (top) and anode (bottom) in place is shown in Fig.3.16.

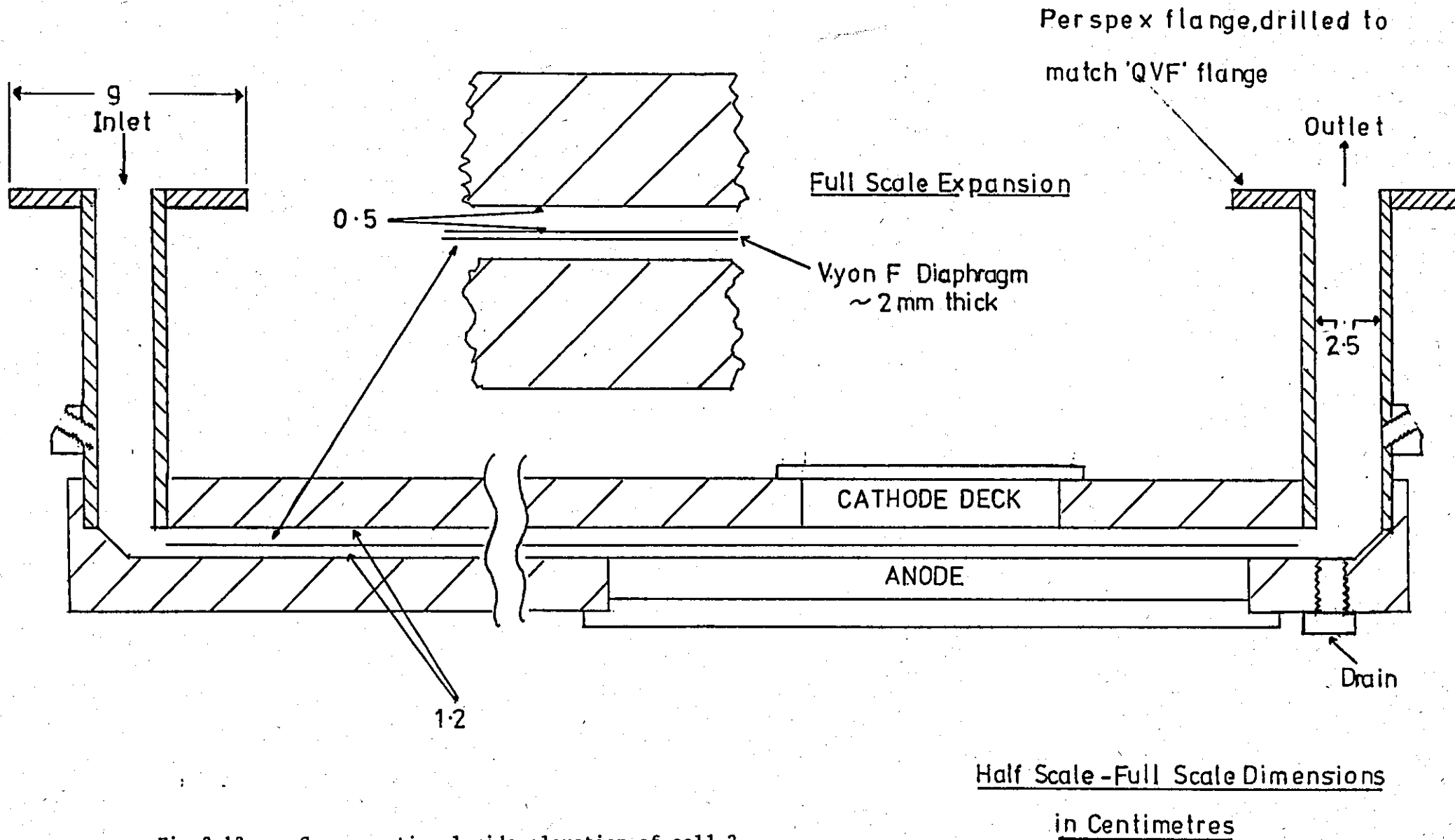
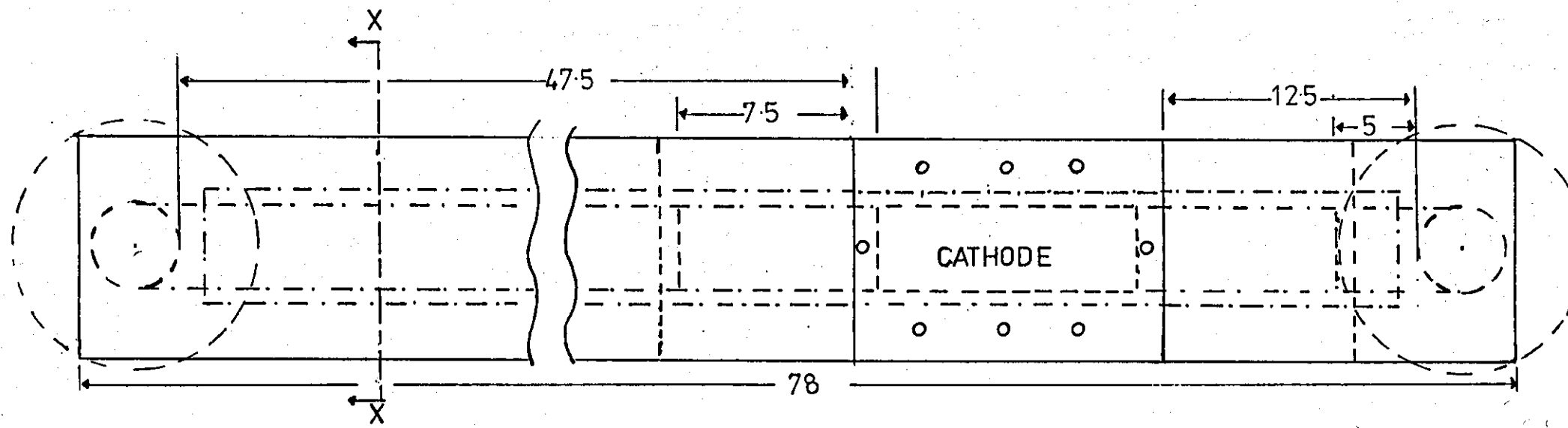
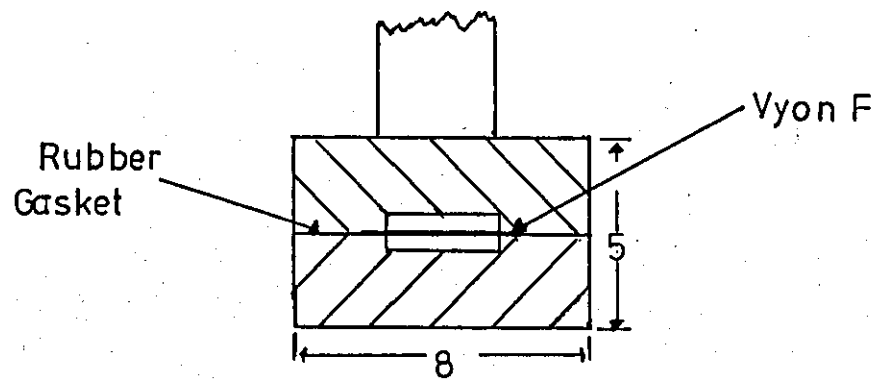


Fig.3.13 Cross-sectional side elevation of cell 2.



Half Scale



Cross Sectional End

Elevation Through XX

dimensions in cm

Fig.3.14 Plan view and cross-sectional side elevation (through XX) of cell 2.

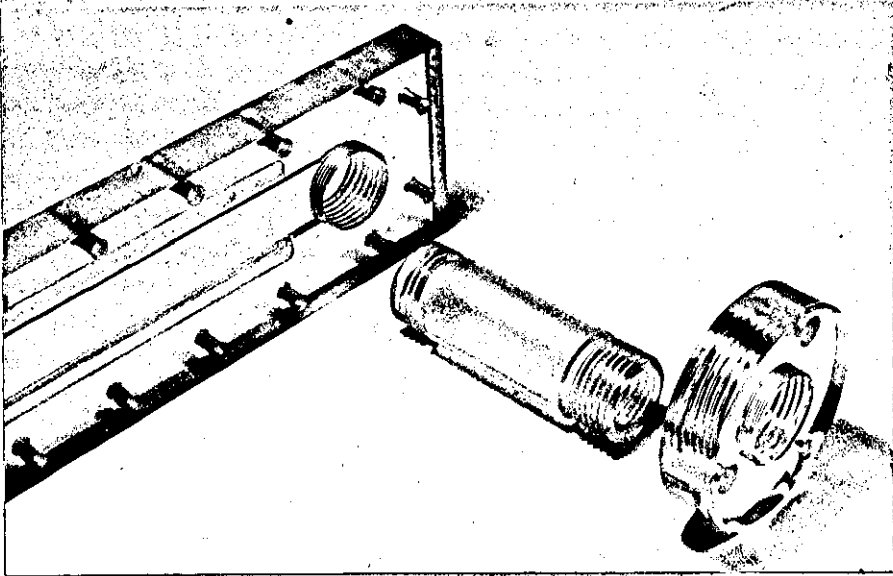
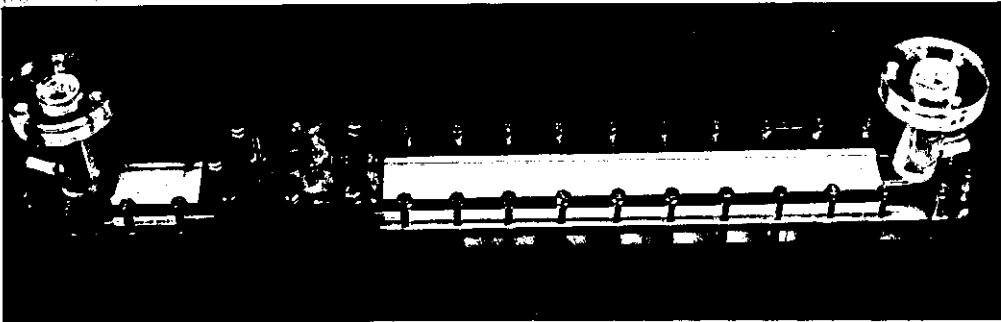
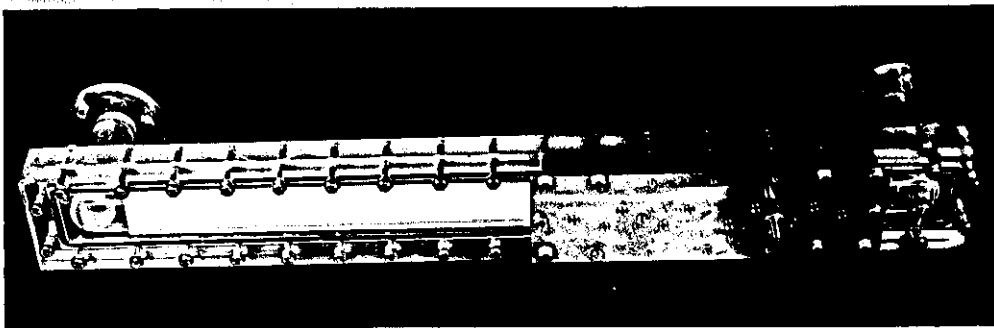


Fig.3.15 Cell 2. Construction details



a)



b)

Fig.3.16 Cell 2 with cathode and anode in position

a) top view

b) bottom view

Cathode construction

The electroforming cathodes (Fig.3.17) were machined from 18/8 stainless steel or Nickel 200, to assist removal of the electroforms. The maximum electrode length was 10 cm. When cathodes of reduced length (2.5 cm) were used, a Perspex block was screwed to the backing plate to provide a smooth hydrodynamic surface (Fig.3.18). The cathode deck was mounted on a stainless steel backplate with 6 hexagonal socket screws and sealed with 'O' rings (Fig.3.19).

The capillary tube for electrode potential measurements was positioned via a stainless steel adapter screwed into the backing plate and also 'O' ring sealed (Fig.3.19). The tube (Portex polythene, 1.27 mm o.d. x 0.86 mm i.d.) was an interference fit within the adaptor and a clearance fit through the cathode block. The Luggin probe was located 7 cm from the leading edge of a 10 cm cathode.

The electrode assembly was bolted into the cell by 6, 0.25 in. Whitworth bolts, 1.5 in. in length, projecting through the cell and insulated from the cathode deck by polythene washers. A seal was achieved using an 'O' ring set into the cell.

Anode construction

The anode was machined from electrolytic nickel anode material (Cannings and Co.Ltd.). The overall anode length was 25 cm. The anode block was mounted on a stainless steel backing plate by 10 hexagon head socket screws and sealed with 'O' rings (Fig.3.20).

A capillary tube adaptor identical to that used for the cathode was screwed into the backplate. The Luggin probe was located 17 cm from the leading edge of the anode. The complete electrode assembly is shown in Fig.3.19 .

The electrode assembly was bolted into position by fourteen 0.25 in. Whitworth bolts, 1.5 in. in length projecting through the cell. The anode was sealed by an 'O' ring, set into the cell.

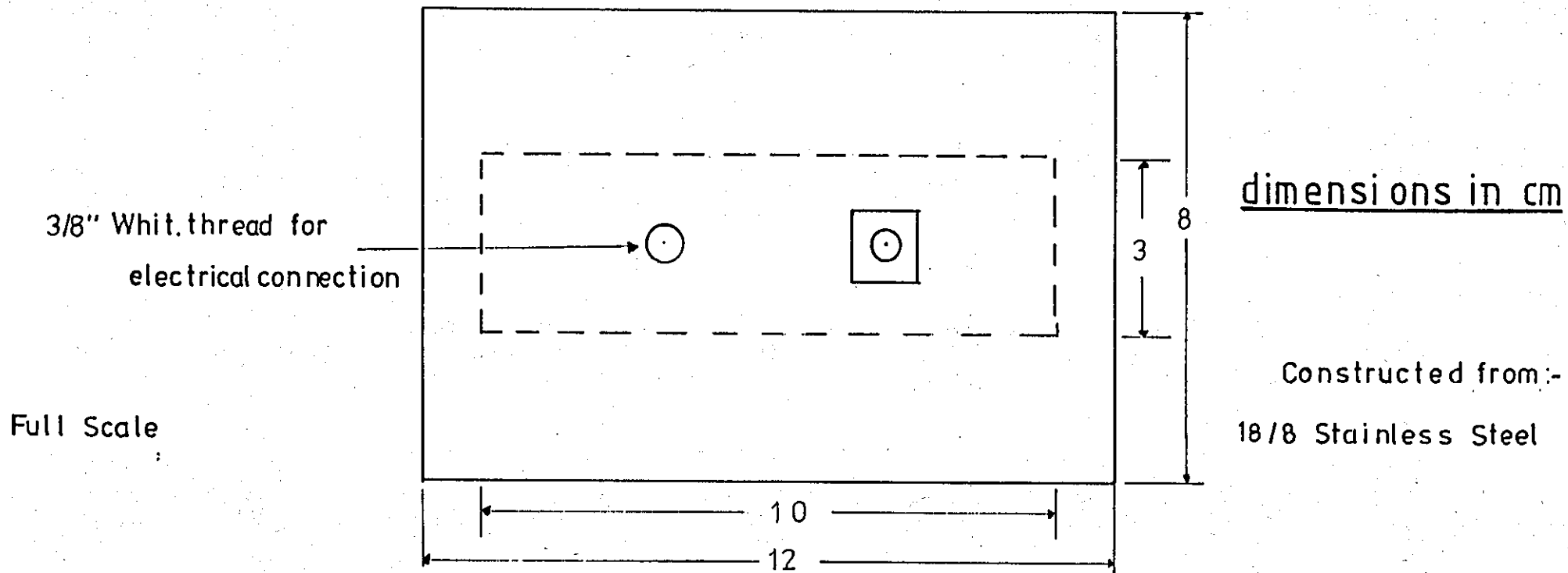
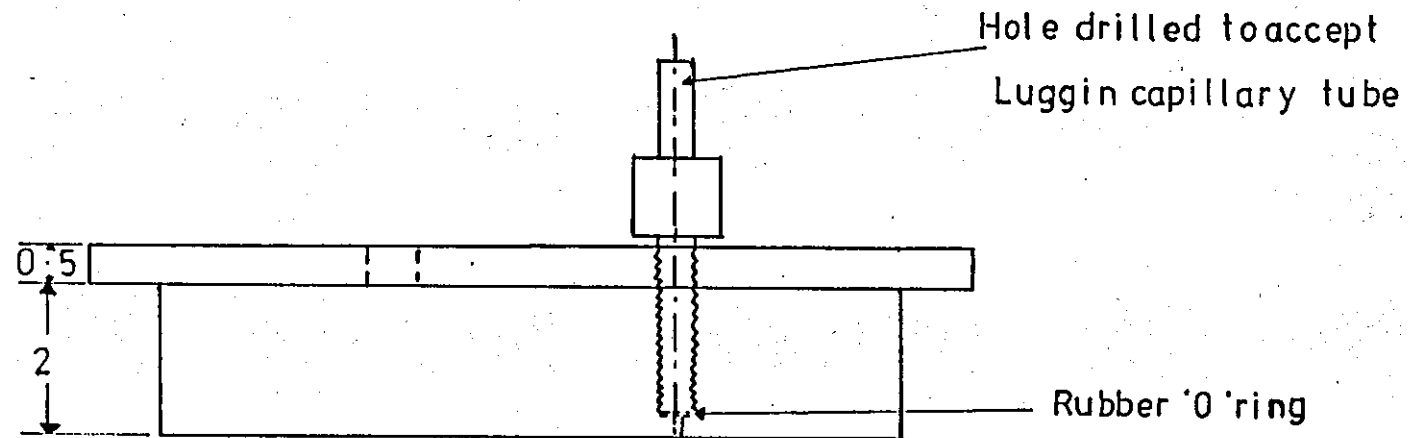


Fig.3.17 Cell 2. Cathode specifications

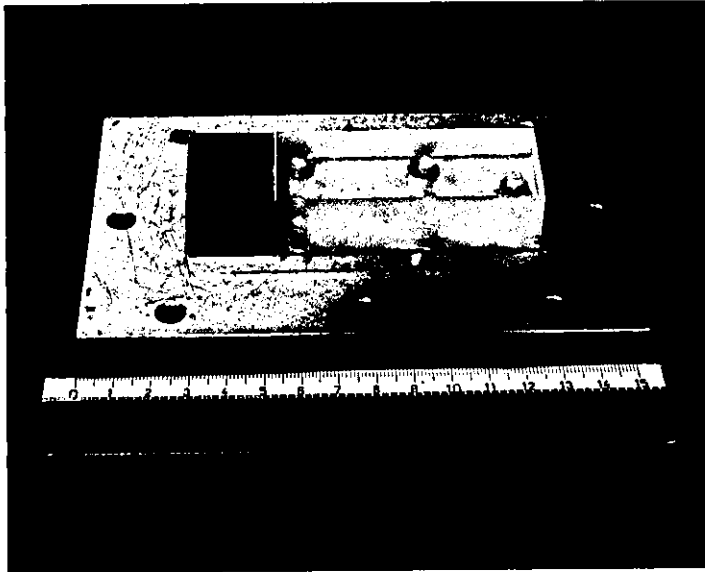
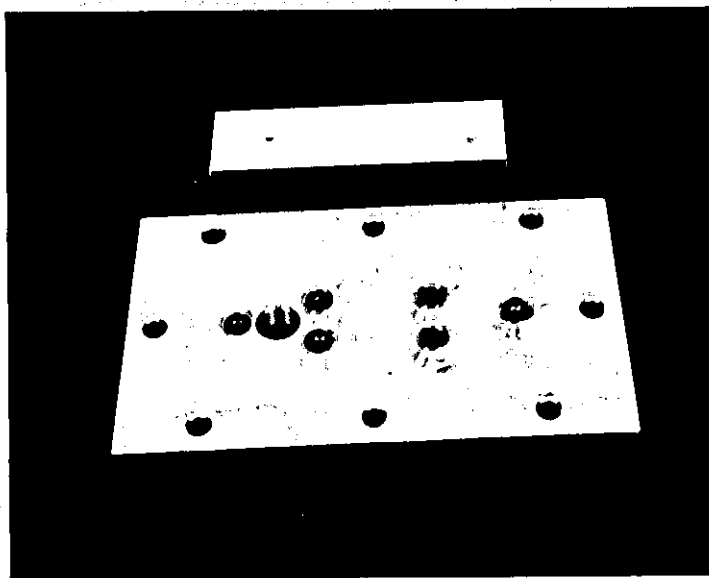
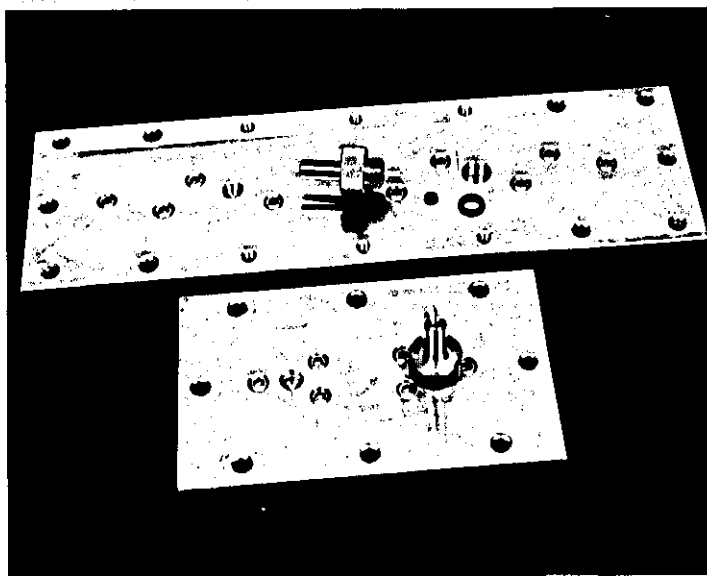


Fig.3.18 'Short' electrode system, $L/de \sim 2.92$ (nickel cathode, perspex blank).



a)



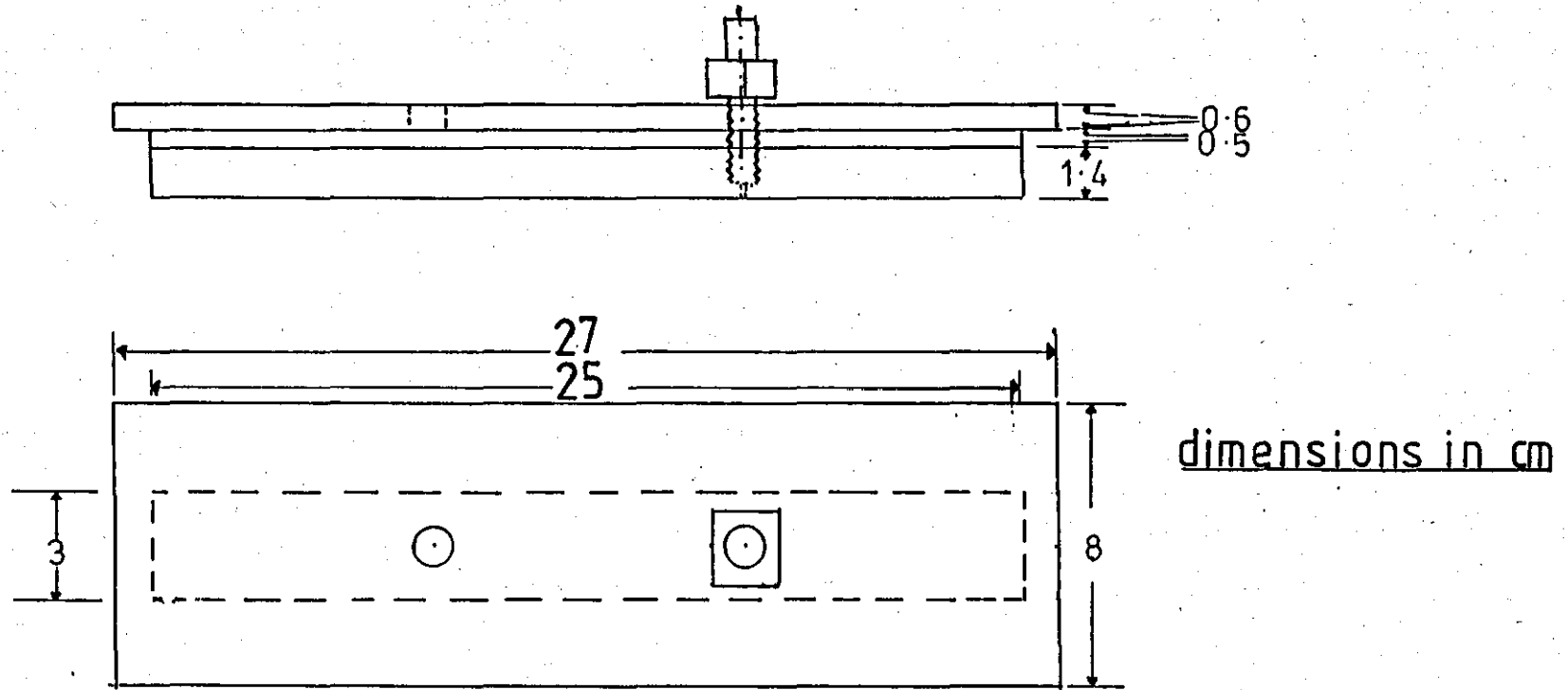
b)

Fig.3.19

Electrode construction details

a) Cathode deck and backing plate with 'O' rings.

b) Top view of anode and cathode assemblies with capillary tube holders



Half Scale

Constructed from :-

18/8 Stainless Steel &
Electrolytic Nickel

Fig.3.20 Cell 2 anode specifications

The construction of the modified flow circuit

A series of modifications was made to the flow circuit to allow for the higher flow rates required for Cell 2. The re-designed system is shown schematically in Fig.3.22 and an overall view in Fig. 3.21. A more flexible system was considered necessary for the incorporation of any future cell modifications.

A pump of increased flow capacity was necessary to enable higher Reynolds numbers to be obtained. The centrifugal pump (d) used was a Jabsco pump (ITT Ltd. Type 21510-200-01) with an epoxy plastic body and a neoprene rubber impeller. The shaft was of epoxy plastic with a mechanical seal with a carbon face and a ceramic seat seal. Operating at 1,500 r.p.m. the pump could deliver $\sim 35 \text{ l min}^{-1}$ under normal operating conditions. Connections to the pump were made via polypropylene adaptors to externally threaded 1 in. i.d. polypropylene tubing (O). The type 35X Rotameter could be replaced by a type 47 Rotameter allowing flow rates of up to 35 l min^{-1} of nickel sulphamate based electrolyte to be measured (h in Fig.3.22).

The flow rate through the cell was controlled accurately by means of a 'by-pass' arrangement. The 'by-pass' consisted of a T-piece and diaphragm valve (No.6 in Fig.3.22) by which the electrolyte could be directed through 1 in. i.d. Portex polythene tubing (P) and returned to the reservoir. The flow rate through the cell was regulated by adjustment of the flow cell control valve (No.3 in Fig.3.22) and the 'by-pass' control valve (No.6 in Fig.3.22). The basic layout of the remaining circulation system was as for Flow Circuit 1. The pressure at the pump head was monitored by a stainless steel tube Bourdon gauge (Q) (Budenberg, Type 316).

A subsidiary pump (Beresford, Type PVI) enabled the pre-conditioned electrolyte to be transferred from the conditioning tank via a holding vessel (25 l polythene aspirator) to the main reservoir (Fig.3.21c).

Power supply and electrical circuits

The power supply and electrical circuits were described previously in Section 3.2.1b.

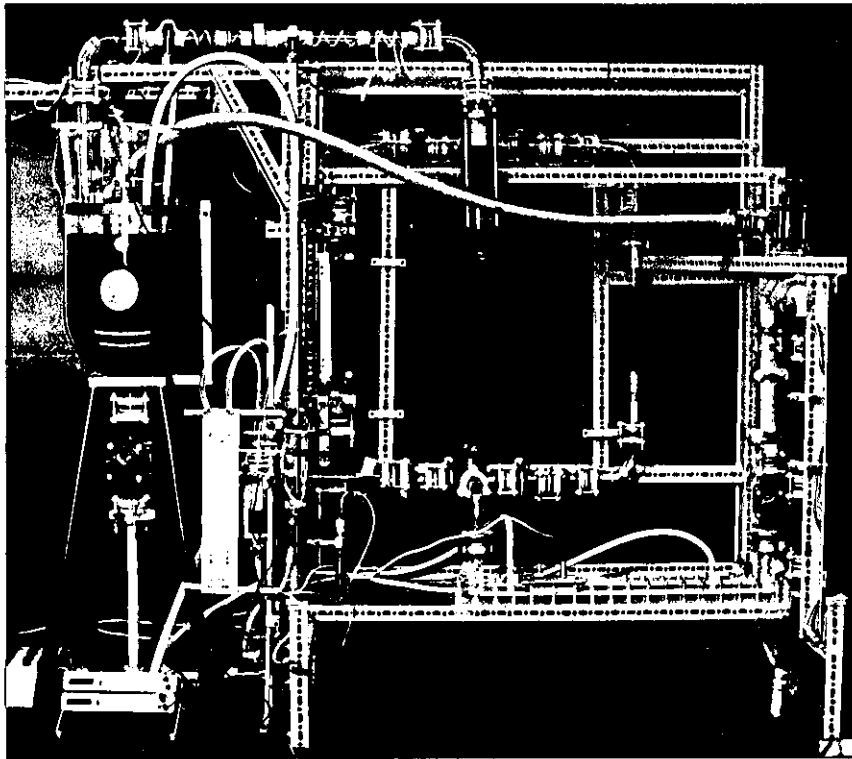


Fig.3.21

Cell 2 and ancillary apparatus

Overall view of flow system 2 reservoir,
Rotameters, filter and by-pass.

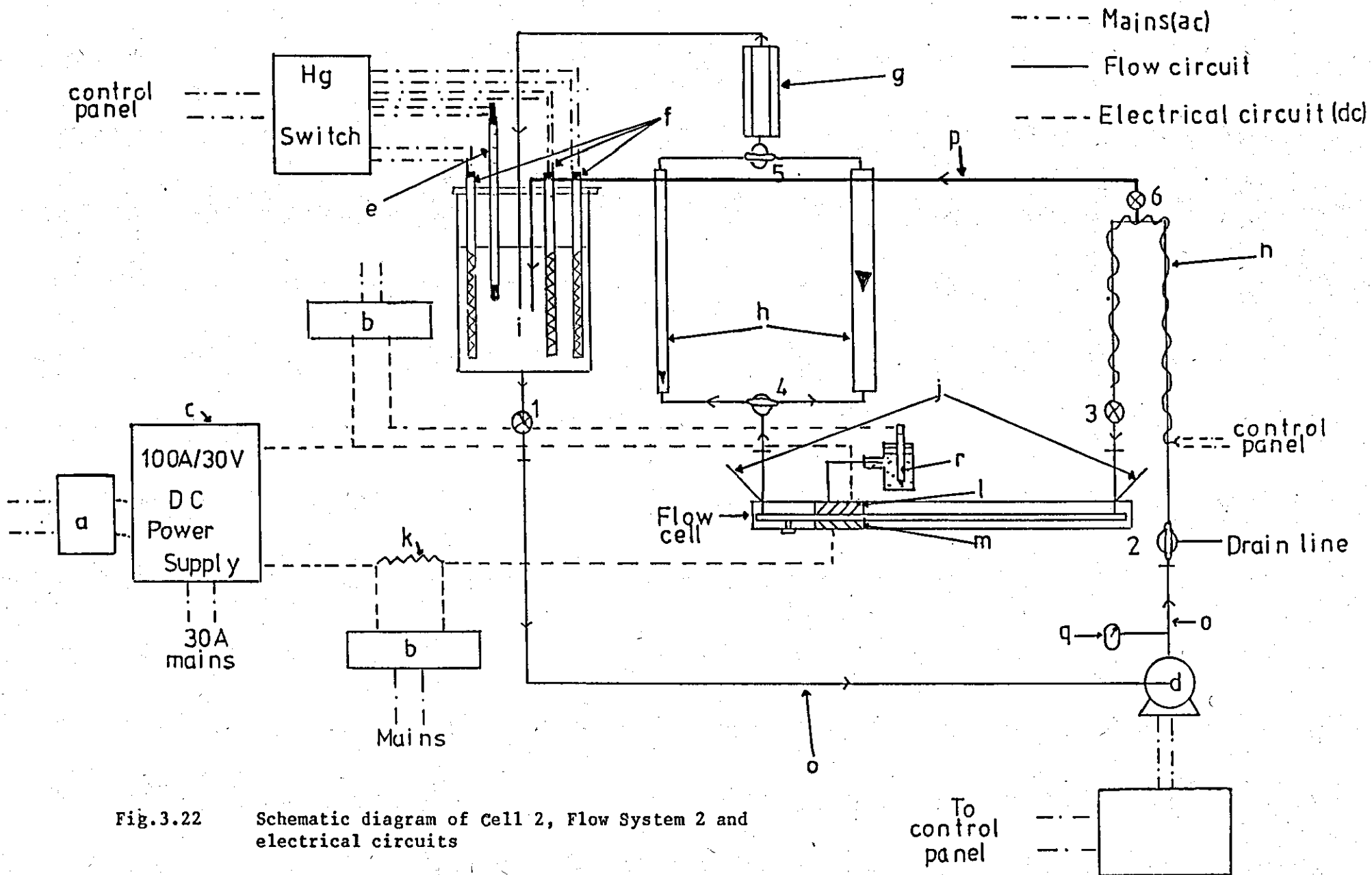


Fig.3.22 Schematic diagram of Cell 2, Flow System 2 and electrical circuits

3.3.3 Electroforming procedures using the Mk 2 parallel plate cell

i) Preparation of the electrodes

The electrodes were prepared as described previously in Section 3.2.3.i). When using nickel cathodes, the cleaning operation was similar, although a longer anodic electrocleaning cycle was found advantageous to assist with removal of the foil electroform.

ii) Preparation of the electrolyte

The electrolyte was prepared as described previously in Section 3.2.3.ii).

iii) Operation of the flow cell

The basic operating procedure was as described previously in Section 3.2.3, however, the flow rate through the cell was adjusted using diaphragm valve 6 in Fig.3.22, and hence altering the flow of electrolyte through the 'by-pass' circuit.

Annotation for Fig.3.22

- a) Remote programming unit for main power supply (Farnell L 30E, 0-30V power supply or JJ resistance box, 0-10,000 ohm).
- b) Digital voltmeter (Sinclair, DU 450).
- c) Main power supply (Farnell, H 30/100)
- d) Centrifugal pump (ITT Type 21510-200)
- e) Contact Thermometer
- f) Silica sheathed immersion heaters (500W)
- g) QVF filter (part No.PCFI, 30 μ m ceramic filter)
- h) Rotameters (Types 18X and 47, the 18X tube could be replaced by a Type 35 tube)
- i) Glass reservoir (30 l capacity)
- j) Thermometers (10 - 100°C)
- k) Standard resistor (0.005 ohm, 100A)

- l) Cathode deck
- m) Anode deck
- n) Heating tape ('Hotfoil', 200W)
- o) Polypropylene tube (2 cm i.d.)
- p) Polythene tube ('Portex' 2.5 cm i.d.)

All other tubing was Corning QVF 1" bore, (excluding the appropriate connecting pieces to the Rotameters etc.)

- q) Pressure gauge (Budenburg, stainless steel tube)
- r) Remote junction reference electrode assembly

- 1) Diaphragm valve (QVF No.SV 1.5)
- 2) Polypropylene tap
- 3) Diaphragm valve (QVF No.SV 1)
- 4) L-Port Stopcock (QVF No.TSL 1)
- 5) L-Port Stopcock (QVF No.TSL 1)
- 6) Diaphragm valve (QVF No.SV 1)

3.4 Mass transport and current current distribution measurements in the acid copper sulphate electrolyte in the Mk 2 parallel plate cell

The electrodeposition of copper was used to characterise the cell. This system allows limiting currents to be readily measured and the solution properties (viscosity, density and diffusion coefficients) are available in the literature (ref.342).

Copper was electroplated from an electrolyte of the following composition:

0.0014 moles dm^{-3} Copper sulphate ($\text{CuSO}_4 \cdot 6\text{H}_2\text{O}$)

and

1.5 moles dm^{-3} Sulphuric acid (H_2SO_4)

All reagents were Fisons AR grade dissolved in distilled water. The acid acted as an inert supporting electrolyte. The overall reduction reaction was:



The measurement of the limiting current density for the above reaction enabled mass transport and current distribution measurements for Cell 2 to be determined for a range of deposition conditions.

The results of these measurements were used for later comparison with the nickel sulphamate system.

3.4.1 Mass transport measurements

Construction of copper electrodes

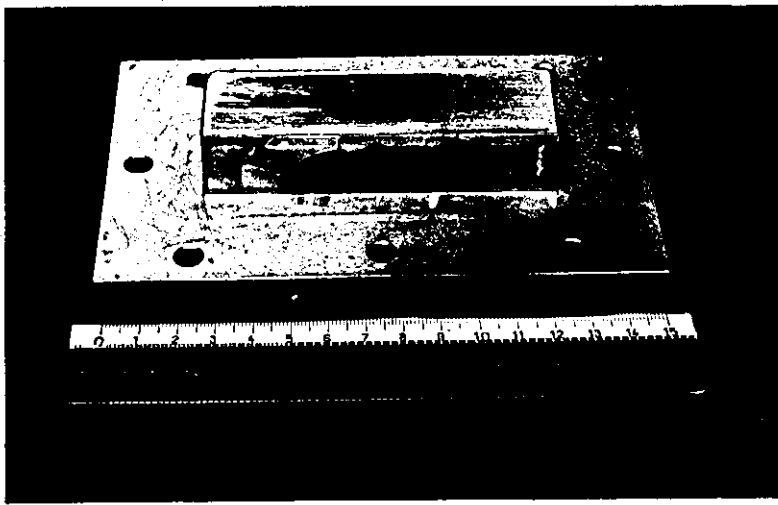
The stainless steel cathode and anode decks normally used for electroforming nickel were replaced by electrodes suitable for the deposition of copper. The cathode (Fig.3.23a) was constructed from annealed, rolled copper strip, 4mm. thick, screwed to a Perspex mounting block. Electrical contact to the electrode was achieved via two copper posts brazed to the copper strip and projecting through holes drilled through the Perspex block. The complete assembly was screwed to the conventional stainless steel backing plate, allowing the electrode surface to remain flush with the cell walls. The effective cathode dimensions were 9.74 x 2.75 cm.

Anode

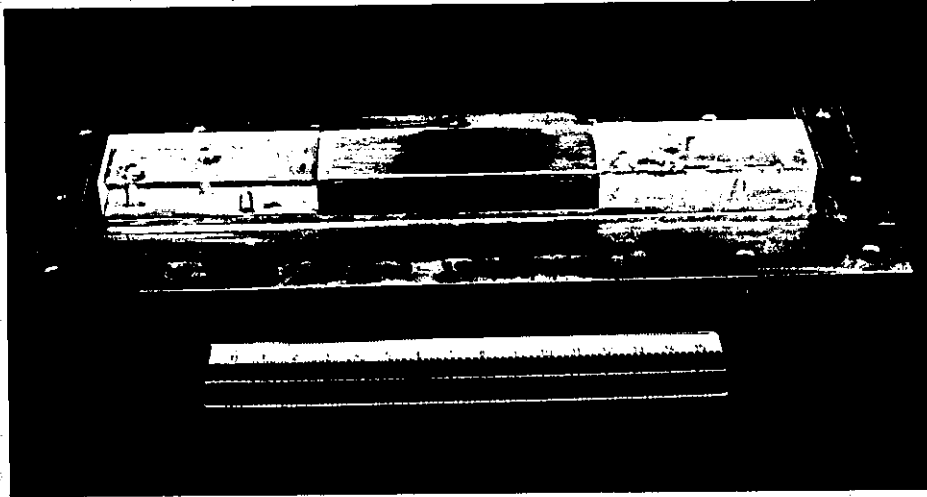
The anode was machined from the same material as the cathode and mounted in a similar manner. The counter electrode was of the same dimensions as the working electrode. The remaining electrode space within the cell was taken up by two Perspex blocks, allowing the anode to be positioned directly opposite the cathode (Fig.3.2 3b).

Measurement of the cathode potential

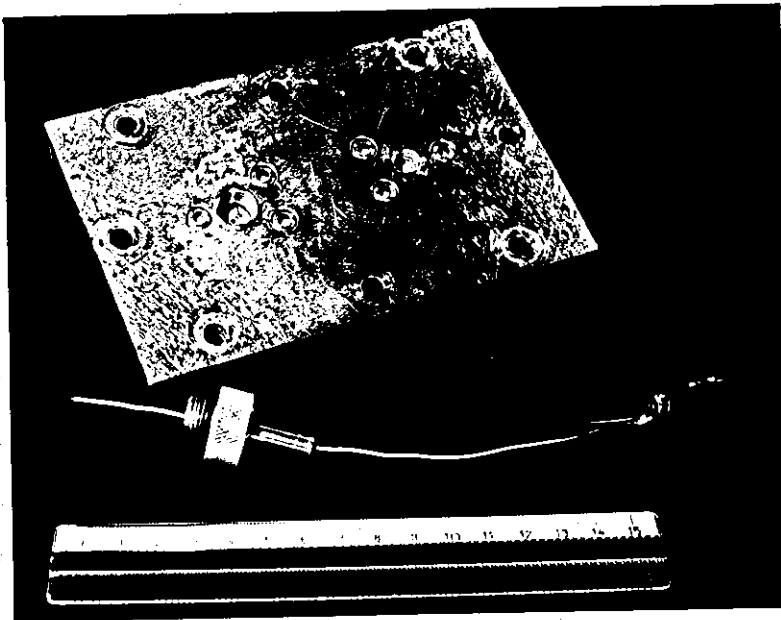
The electrode potential was measured with respect to a copper wire reference electrode. The copper wire, insulated along its length with polythene tubing, was inserted through the cathode via the capillary tube holder (Fig.3.23c). The reference wire projected through a 2mm hole drilled through the copper electrode block, 7 cm. from the leading edge of the working electrode, into the flowing electrolyte.



a)



b)



c)

Fig. 3.23 Electrodes used for copper electrodeposition

a) copper cathode

b) copper anode

c) cathode (top view) and copper reference electrode

Analysis of the bulk concentration of copper ions (ref.348)

A 4 cm³ aliquot of the electrolyte was withdrawn from the reservoir and diluted to 1000 cm³ with distilled water. The copper concentration of the diluted electrolyte was determined by atomic absorption spectroscopy using an Instrument Laboratory Ltd. Atomic Absorption/Emission Spectrophotometer Model IL151, equipped with a lamellar burner head. The sample was aspirated into an air acetylene flame and the absorption of radiation of wavelength 342.2 nm determined at a bandwidth of 0.5nm. The instrument was previously calibrated with suitable copper standard solutions (4µg cm⁻³ diluted from 1000 µg cm⁻³ stock standard solution (Fisons Ltd.)).

Calibration of Rotameters

The method of calibration and the calibration curves are given in Appendix 2e.

Preparation of copper electrodes

The electrodes were polished to a 1200 grit SiC. finish and degreased with acetone prior to use. The copper reference electrode was then screwed into position and the insulation between the cathode deck and the reference wire checked.

When cathodes of reduced length were required, the effective electrode length was defined by masking the remaining area with a proprietary 'stopping-off' lacquer ('Lacomit'). The lacquer was air dried before the electrode was bolted into the cell.

Deposition procedure

Both electrodes were bolted into the appropriate positions in the cell. The flow rate and temperature were determined in the usual manner (p.123). When the required equilibrium temperature had been attained, deposition was commenced.

Copper was deposited using a potentiodynamic technique (Fig.3.24). The potential of the cathode was controlled with respect to the copper wire reference electrode (Cu_{ref}) by a Thompson Associates potentiostat

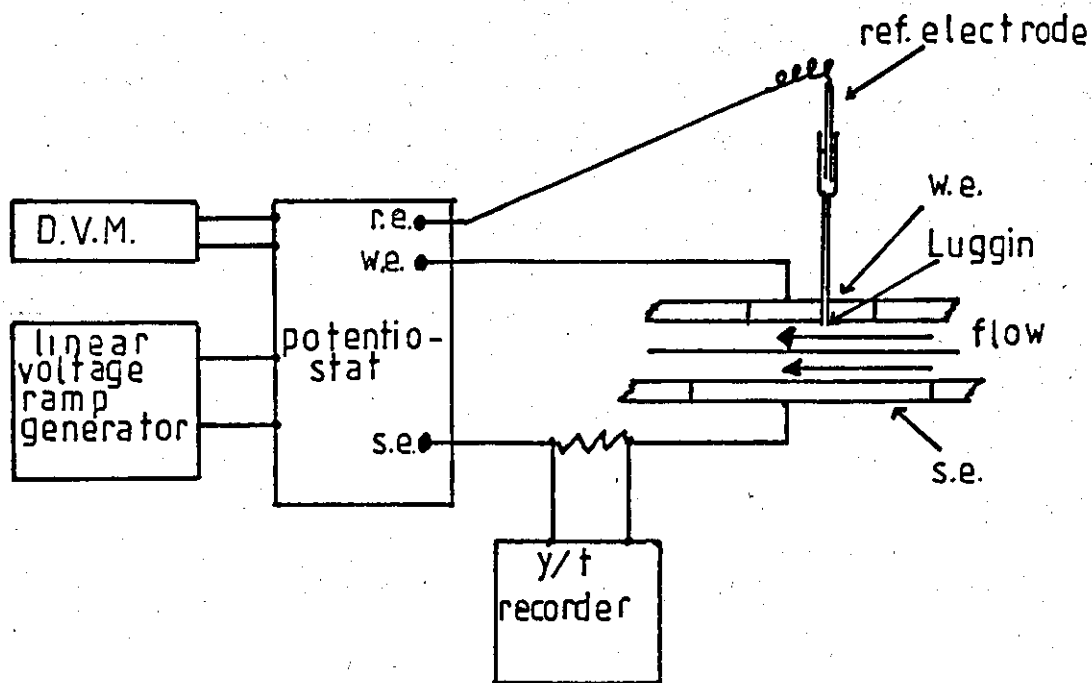


Fig.3.24 Schematic diagram of the potentiodynamic circuit for the measurement of polarisation curves

(Mini-stat ~1A/28V) driven by a linear voltage ramp generator (custom built, motor driven potentiometer). The rest and control potentials were measured using a digital voltmeter (Sinclair Electronics, DM350).

The current response was determined by measurement of the potential difference across a suitable measurement resistor in series with the secondary electrode. The current-potential data were recorded on a Servoscribe y/t chart recorder (type Re 511.20).

The cathode was pre-plated with copper at an overpotential of ~20mV for 15 mins. to provide a uniform surface. The electrode was allowed to come to equilibrium and the cathode potential was then decreased from the rest potential (0 mV vs Cu_{ref}) at a ramp rate of 60 mV s^{-1} . The corresponding current response was recorded on the chart recorder at a chart speed of 30 mm min^{-1} .

The deposition of copper was terminated when the limiting current was exceeded and the increased current due to hydrogen evolution was evident ($\eta < -700 \text{ mV vs Cu}_{\text{ref}}$).

Data were subsequently transferred from the chart (as an I/t curve) to overpotential/current density (η/i) co-ordinates and displayed graphically as η versus $\log i$. From these graphs the limiting current density was evaluated and the mass transfer data then calculated as follows:

Example calculation of mass transfer data for copper deposition

The following mass transfer data were derived for the polarisation curve 22L (Fig.4.40). The curve was obtained in the laminar flow regime at a measured flow velocity (U), of 10.72 cm s^{-1} and a temperature of 32.1°C . The cathode was of effective length (L) 8.01 cm and 22.0 cm^2 in area (A). The equivalent diameter, d_e , of the cell was 0.857 cm (p.126).

i) The dimensionless electrode length ($\frac{d_e}{L}$) was given by:

$$\begin{aligned} \frac{d_e}{L} &= \frac{0.857}{8.01} \\ &\approx \underline{0.107} \end{aligned}$$

ii) The Reynolds number (Re) describing the hydrodynamic conditions within the cell, was calculated from:

$$Re = \frac{U d_e}{\nu}$$

The kinematic viscosity (ν) of the electrolyte obtained from the data of Robinson (Fig.3.25) (342) was $0.92 \times 10^{-2} \text{ cm}^2 \text{ s}^{-1}$

$$\therefore Re \approx \frac{10.72 \times 0.857}{0.92 \times 10^{-2}}$$

$$\approx \underline{999}$$

iii) The limiting current density (i_L) was defined as the current density in the plateau region of the polarisation curve at $E \approx -0.45\text{V}$ vs Cu_{ref} . Limiting current densities were corrected (i_L^{corr}) where necessary, to account for 'leakage' current through the masking lacquer. The magnitude of the 'leakage' current is shown as a function of Reynolds number in Fig.3.28.

For example, from the polarisation curve 22L, the apparent limiting current density $i_L \approx 2.80 \times 10^{-3} \text{ A cm}^{-2}$ and therefore the total current was $I_L \approx 61.60 \times 10^{-3} \text{ A}$ at $E \approx -0.45\text{V}$ vs Cu_{ref} . The area (A_m) of the electrode that was lacquered was 4.79 cm^2 . From Fig.3.28 the current density (i_m) on masked area of the cathode at Re 999 was $0.28 \times 10^{-3} \text{ A cm}^{-2}$.

$$\therefore \text{Current on masked area } I_m = i_m A_m$$

$$= 0.28 \times 10^{-3} \times 4.79$$

$$\approx 1.34 \times 10^{-3} \text{ Amps.}$$

The corrected current I_L^{corr} on the electrode is given by:

$$I_L^{\text{corr}} = I_L - I_m$$

$$= (61.60 - 1.34) \times 10^{-3}$$

$$= 60.26 \times 10^{-3} \text{ Amps.}$$

$$\therefore \text{the corrected limiting current density } i_L^{\text{corr}} = \frac{60.26 \times 10^{-3}}{22.0}$$

$$i_L^{\text{corr}} \approx \underline{2.73 \times 10^{-3} \text{ A cm}^{-2}} \text{ at } E \approx -0.45 \text{ V vs } \text{Cu}_{\text{ref}}.$$

iv) The mass transfer coefficient, k_L , was calculated from (cf. Equation 2.15):

$$k_L = \frac{i_L^{\text{corr}}}{z F c_b} \dots \dots \dots (3.1)$$

The bulk concentration of copper ions c_b was found to be $\sim 1.29 \times 10^{-5} \text{ mol cm}^{-3}$, $z = 2$ and $F \approx 96,500 \text{ C}$.

$$\begin{aligned} \therefore k_L &= \frac{2.73 \times 10^{-3}}{2 \times 96,500 \times 1.29 \times 10^{-5}} \\ &= \underline{1.09 \times 10^{-3} \text{ cm s}^{-1}}. \end{aligned}$$

v) The dimensionless mass transfer coefficient, the Sherwood number Sh , is given by:

$$Sh = \frac{k_L d_e}{D}$$

The diffusion coefficient, D , at 32.1°C was $6.65 \times 10^{-6} \text{ cm}^2 \text{ s}^{-1}$ (from the data of Robinson (Fig.3.26)).

$$\therefore Sh \approx \frac{1.09 \times 10^{-3} \times 0.857}{6.65 \times 10^{-6}}$$

$$Sh \approx \underline{141}$$

vi) The physical properties of the solution are described by the Schmidt number, Sc

$$\begin{aligned} Sc &= \frac{\nu}{D} \\ &= \frac{0.92 \times 10^{-2}}{6.65 \times 10^{-6}} \end{aligned}$$

$$Sc \approx \underline{1384} \text{ at } 32.1^\circ\text{C}$$

(Calculated from the data of Robinson (Fig.3.27))

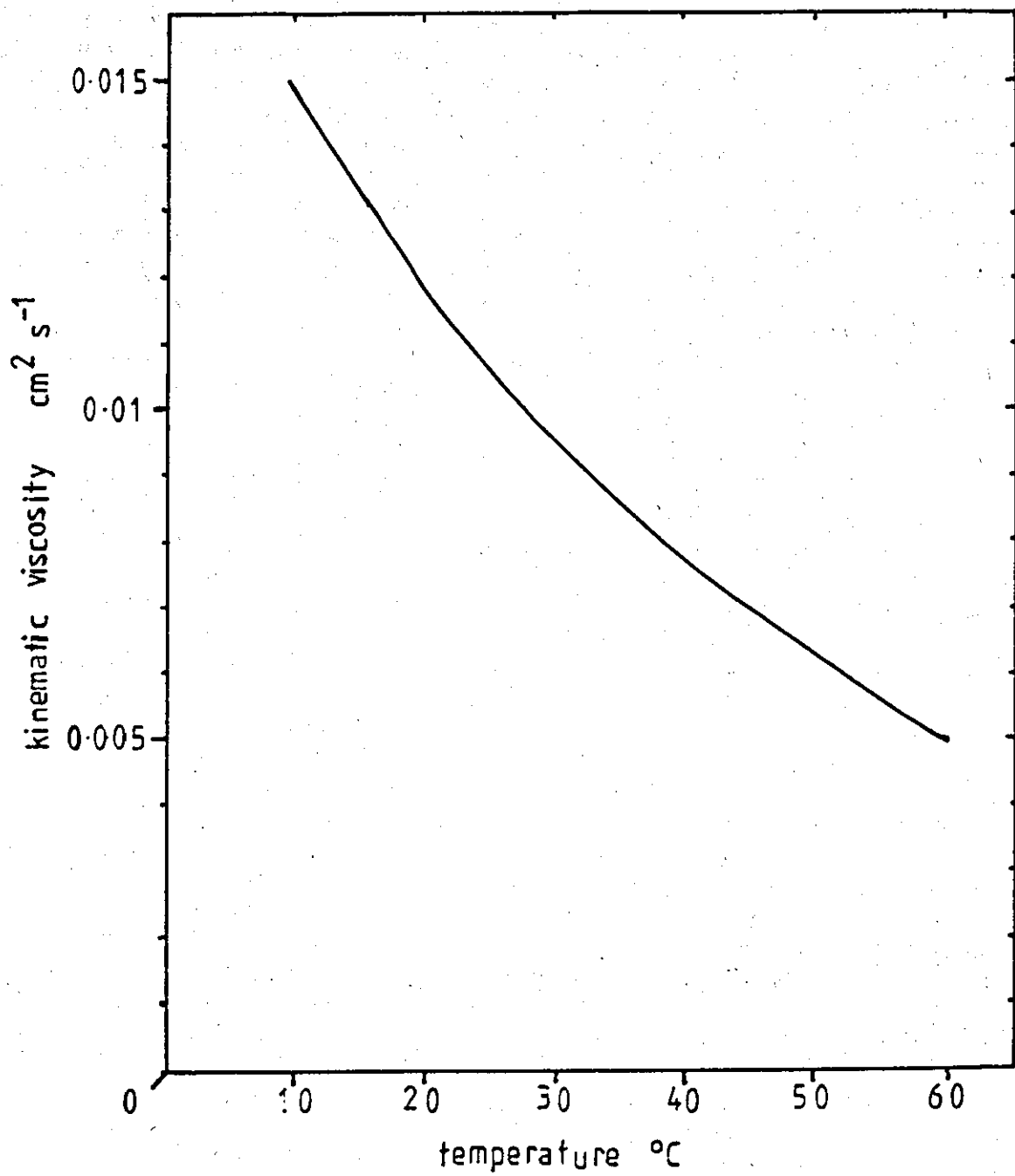


Fig.3.25

Kinematic viscosity of 0.014M copper sulphate soln. as a function of temperature (data of Robinson, ref.342)

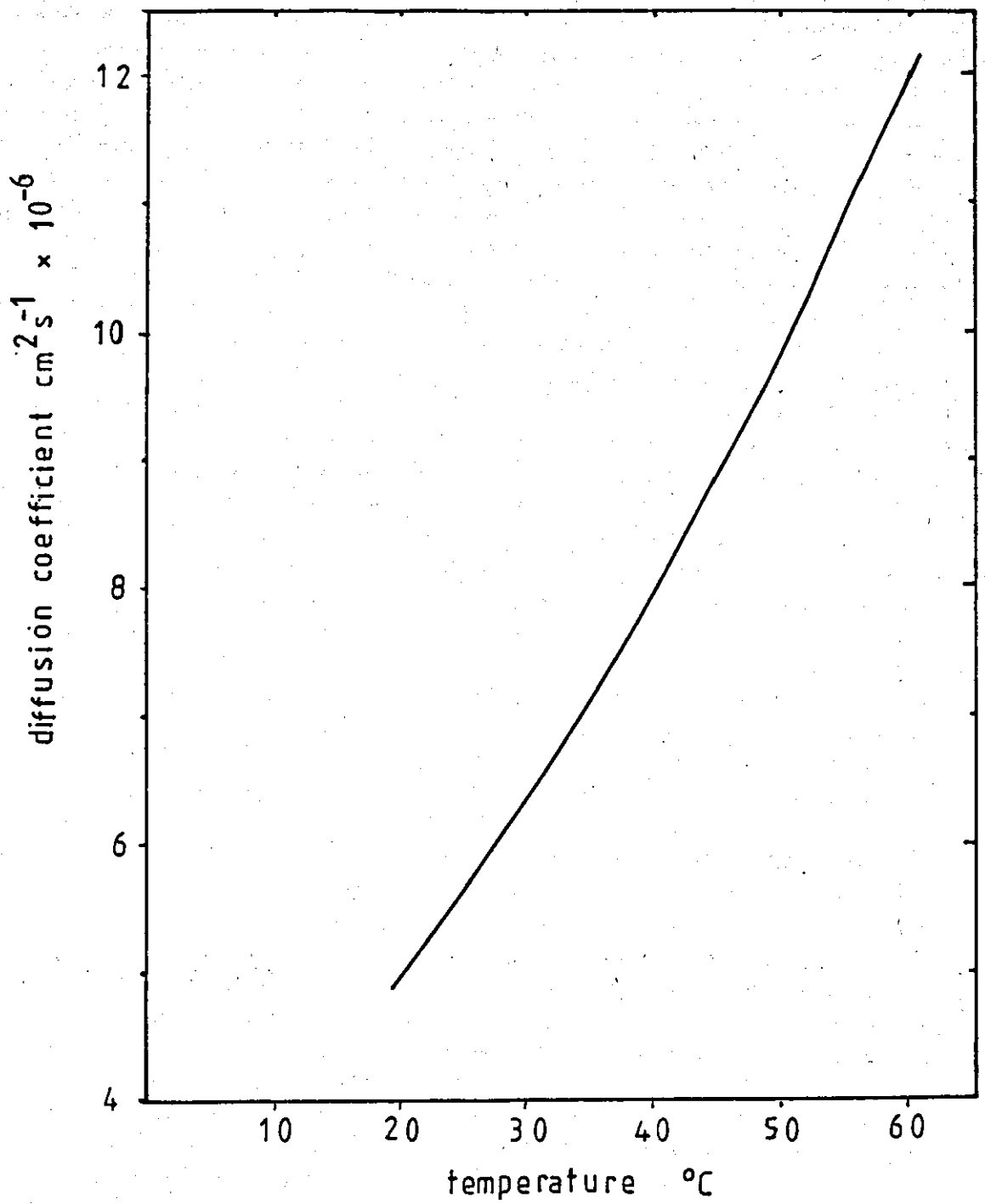


Fig.3.26

Diffusion coefficients of 0.014M copper sulphate soln. as a function of temperature (data of Robinson, ref.342).

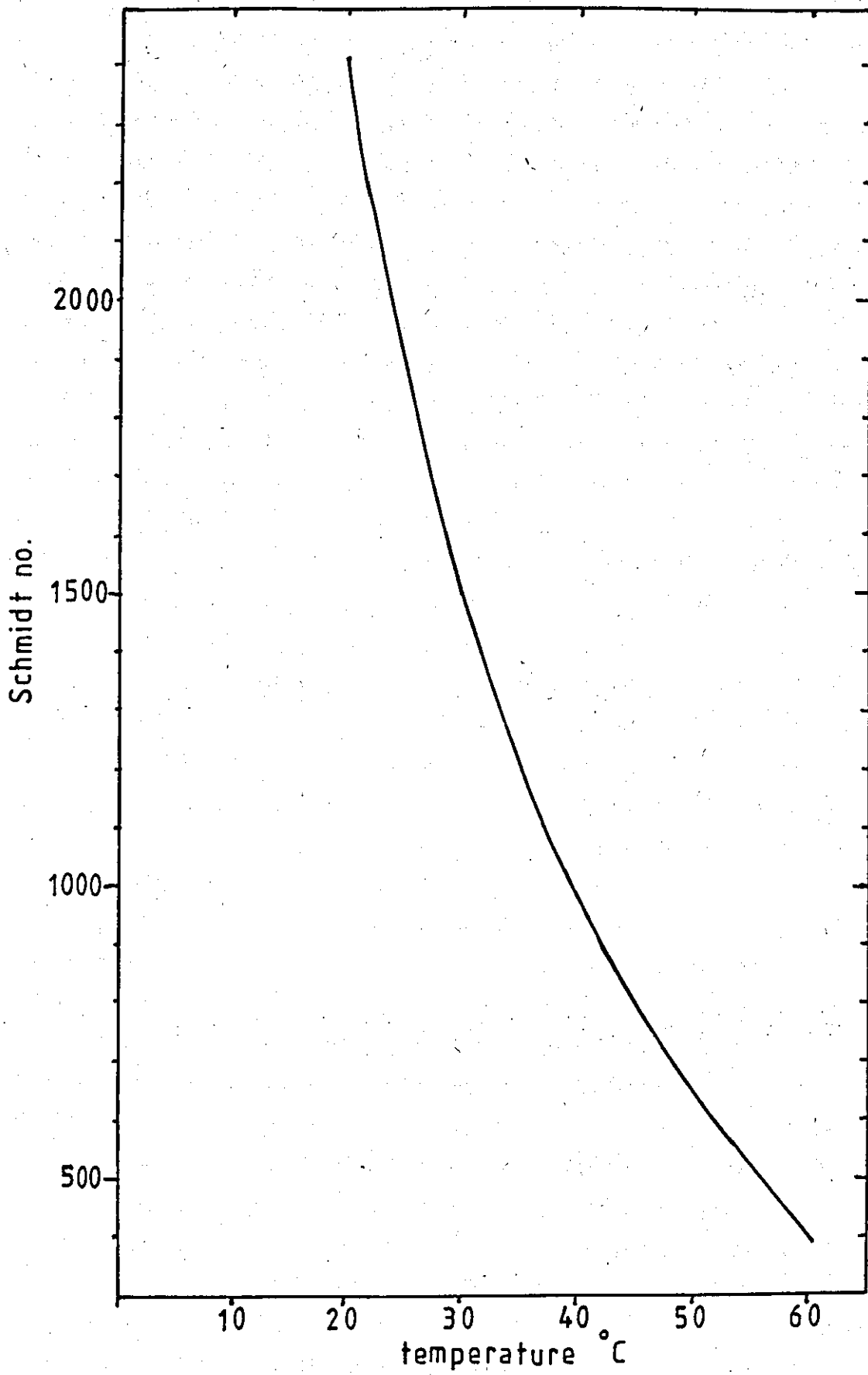


Fig.3.27

Schmidt numbers of 0.014M copper sulphate soln. as a function of temperature (derived from the data of Robinson, ref.342)

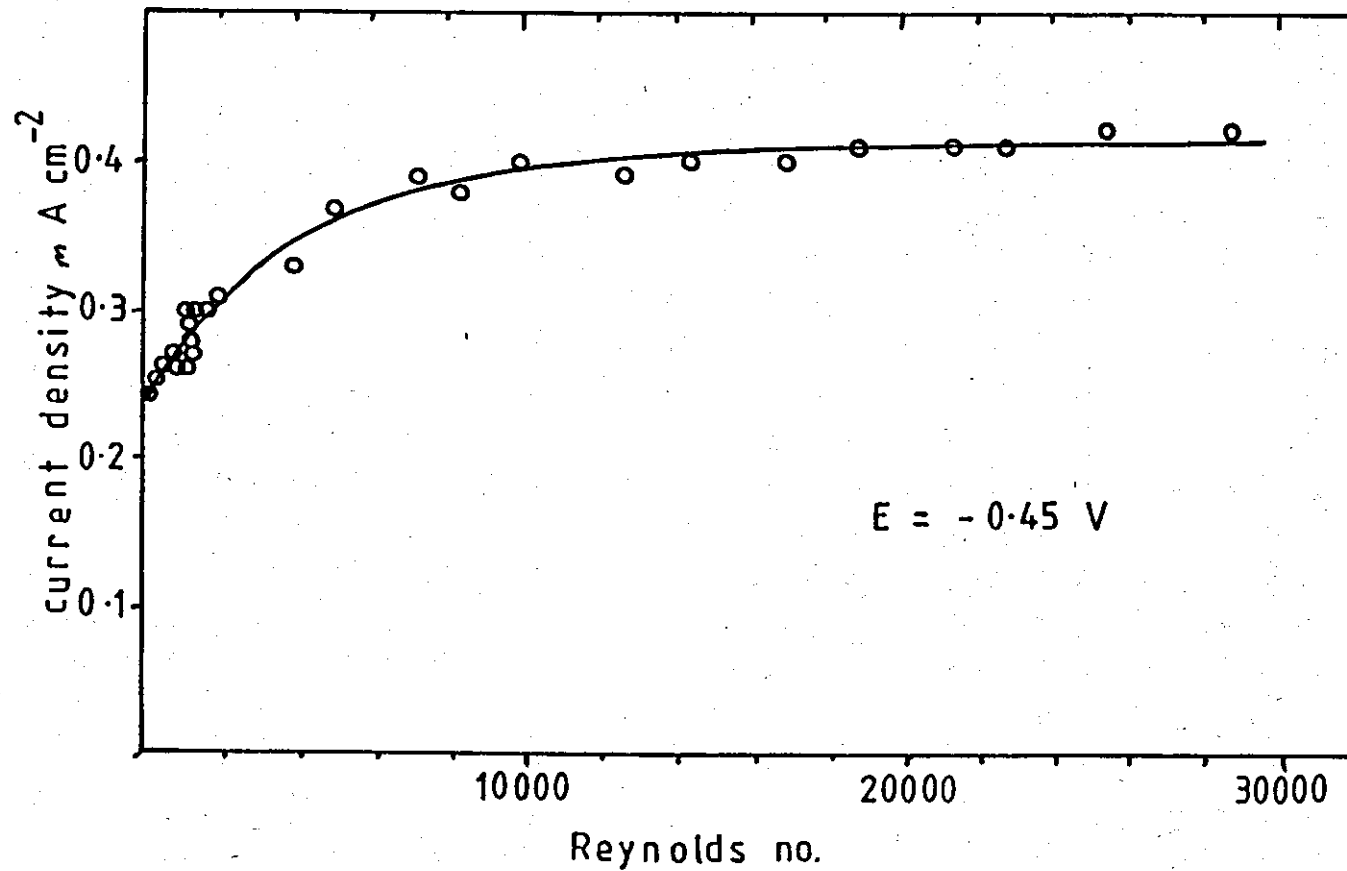


Fig.3.28

Effect of flow rate on the cathodic current density at a masked electrode using a 0.014M copper sulphate electrolyte at 37.5°C.

3.4.2 Current distribution measurements

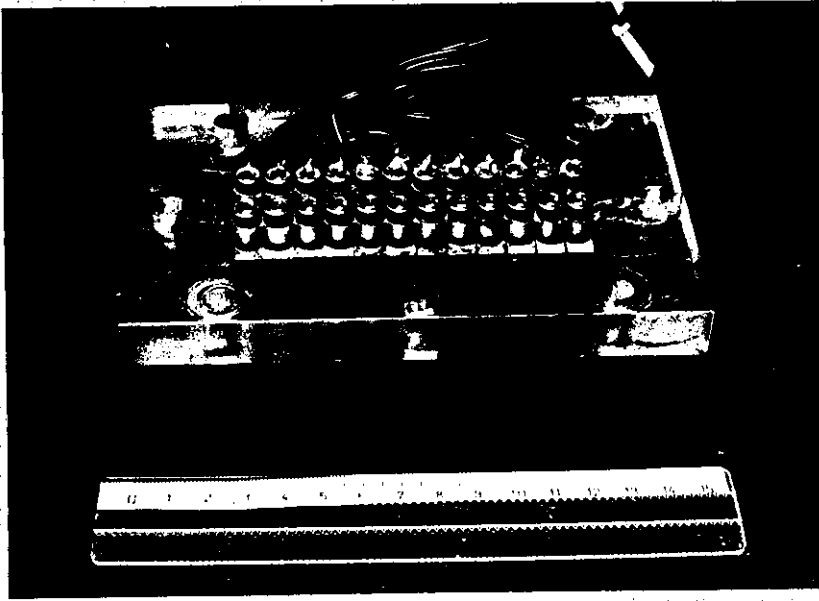
The segmented electrode

The measurement of the current density distribution along a cathode 10cm ($L/d_e \sim 11.7$) in length required the design and construction of a suitable electrode for the purpose. The electrode consisted of twelve individual segments machined from Nickel 200 bar. Each segment provided an effective electrode 3 cm in width and 0.8 cm long. The segments were each screwed by two stainless steel, hexagon head screws, to a 1 cm thick insulating Perspex backplate. The segments were insulated from each other by strips of polythene sheet, 0.036 cm thick inserted between adjacent segments. The overall length of the complete electrode was ~10cm and designed to replace the conventional electrode. To each of the fixing screws, 1m of 6A flexible cable was soldered using aluminium solder. The complete electrode is shown in Fig.3.29

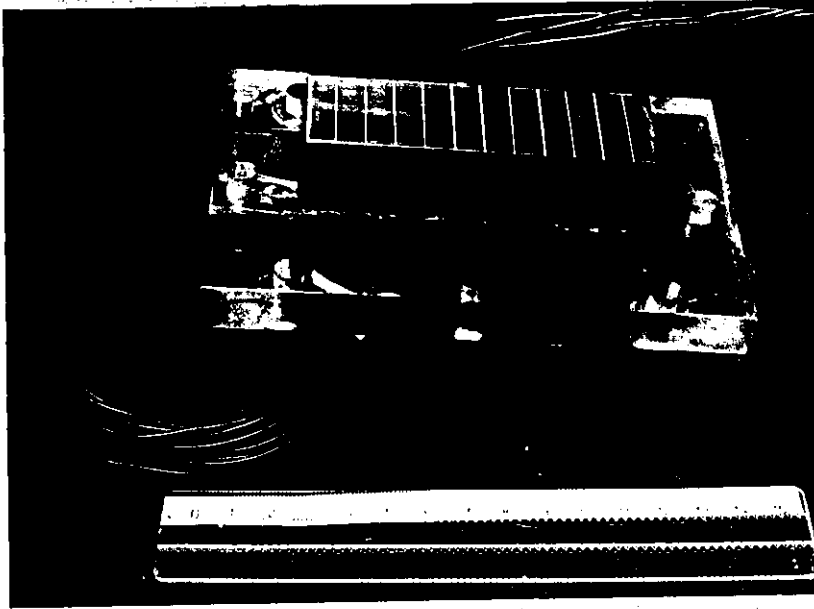
Current measurement instrumentation

The current to each electrode segment was determined by measurement of the voltage drop across a standard resistance in series with each segment. However, to ensure that the current distribution was defined by electrochemical parameters only, the resistance of each segment circuit must be the same. This was achieved by mounting a 10 ohm variable 'trimmer' potentiometer in parallel with the main 25w, $0.47 \pm 5\%$ ohm measurement resistor. Hence by a suitable adjustment of the 'trimmer', the resistance of the measurement resistor could be adjusted to maintain an equal resistance in each of the twelve independent circuits. The circuit diagram is shown diagrammatically in Fig.3.30. The measurement resistors were mounted upon three heat sinks. The twelve 'trimmers' were panel mounted for convenience and each channel was provided with a 7.5 A fuse. The unit could pass a total current of about 80 A.

The voltage drop across each measurement resistor was monitored using a twelve position, single pole switch which enabled each channel to be selected in turn.



a)



b)

Fig.3.29 Segmented cathode for current distribution measurements

a) top view

b) bottom view

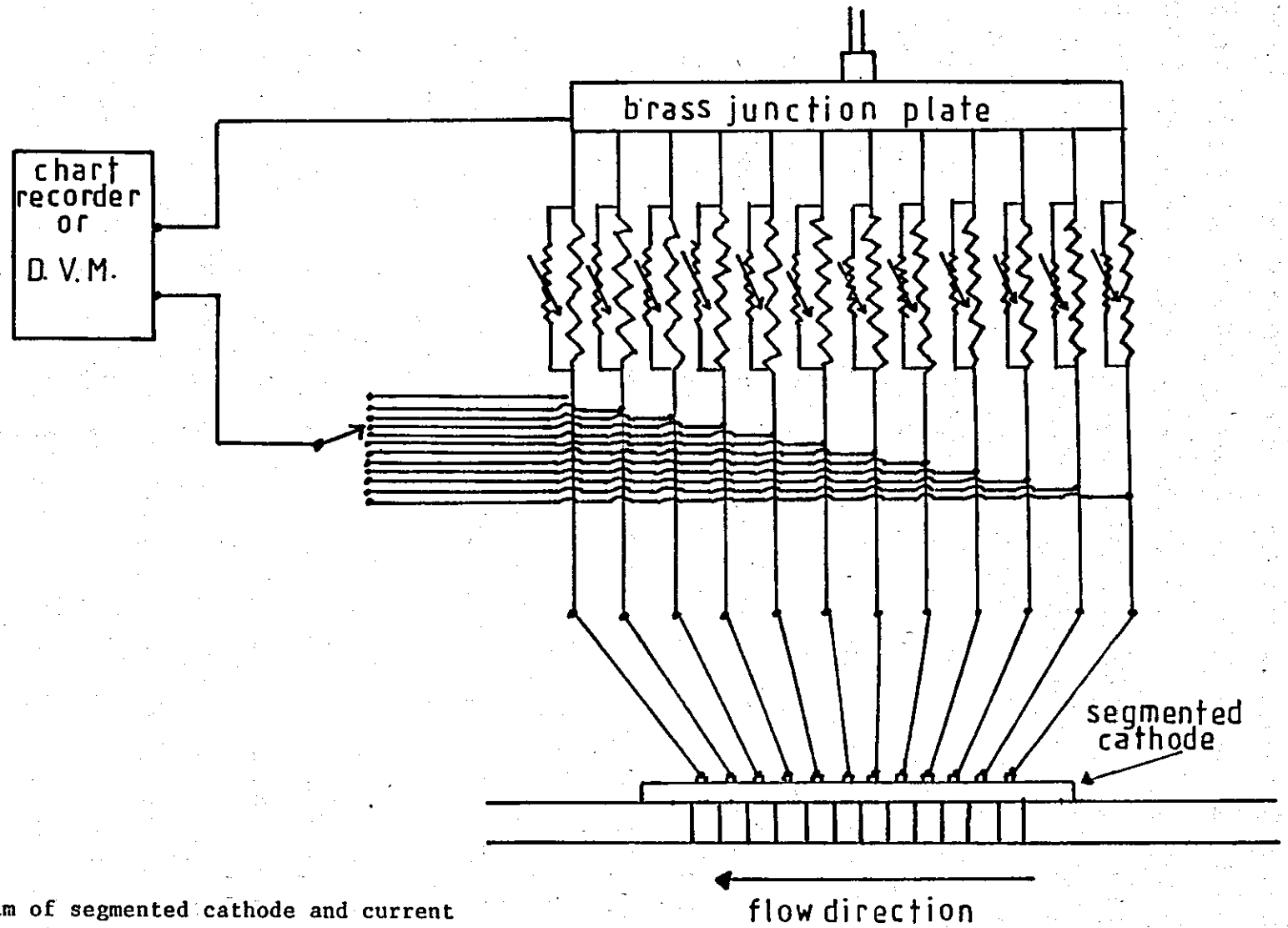


Fig.3.30 Schematic diagram of segmented cathode and current measurement apparatus.

Electrical contact to the measurement unit was provided by twelve connector posts. Spade connectors soldered to the electrode leads ensured a positive, minimum resistance contact.

Calibration of the measurement resistors

The resistance between the input and each output terminal was measured using a four terminal resistance bridge (Croydon Precision Instrument Co., Type KB1) with both current carrying and potential measurement leads joined. The trimmer potentiometer was then adjusted until the input-output resistance of each circuit was the same.

The potential measurement leads were then transferred to the potential measurement terminals of the current measurement unit. The resistance (~ 0.48 ohm) of each of the twelve measuring resistors was recorded.

Experimental Procedure

The segmented cathode was polished to a 1,200 grit SiC finish and degreased using 'Genklene' (I.C.I.). The electrode was subsequently fitted into the cell replacing the conventional cathode. The calibrated current measurement unit, was connected by the twelve segment leads and the attached spade connectors. The voltage loss across each measuring resistor was recorded on a y/t chart recorder (Servoscribe, RE 511.20) connected between the potential measurement terminals.

The current distributions for copper deposition were determined at limiting and sub-limiting ($0.5 i_L$) current densities. The value of the limiting current density was calculated from the results of the mass transfer measurements (Section 4.2). Copper was deposited using the potentiostat (Section 3.4.1) in the galvanostatic mode (Fig.3.24).

The cell was flooded, the required flow rate set and the electrolyte allowed to reach thermal equilibrium as described previously (p.123). On switching on the pre-programmed current, with the chart recorder operating at a suitable chart speed, the twelve position switch could be altered to determine the voltage across each measurement resistor. The current was calculated from the chart measurements as follows:

Example calculation (copper deposition)

The area of each segment (A_s) was 2.4 cm giving a total electrode area (A) of 28.8 cm. The average current density (i_{av}) for a total applied current I was given by:

$$i_{av} = \frac{I}{A}$$

Using data from Table 4.18

$$\begin{aligned} i_{av} &\approx \frac{0.060}{28.8} \\ &\approx \underline{2.08 \times 10^{-3} \text{ A cm}^{-2}} \end{aligned}$$

The partial current (I_x) passing through No.1 segment was calculated from the measured potential difference (V) across the measurement resistor of value R.

$$\begin{aligned} I_x &= \frac{V}{R} \\ I_x &\approx \frac{5.3 \times 10^{-3}}{0.498} \\ I_x &\approx \underline{10.6 \times 10^{-3} \text{ A}} \end{aligned}$$

and the partial current density (i_x) was calculated from

$$\begin{aligned} i_x &= \frac{I_x}{A_s} \\ i_x &\approx \frac{10.6 \times 10^{-3}}{2.4} \\ i_x &\approx \underline{4.42 \times 10^{-3} \text{ A cm}^{-2}} \end{aligned}$$

The dimensionless local current density was given by $\frac{i_x}{i_{av}}$

$$\begin{aligned} \therefore \frac{i_x}{i_{av}} &\approx \frac{4.42 \times 10^{-3}}{2.08 \times 10^{-3}} \\ \frac{i_x}{i_{av}} &\approx \underline{2.12} \end{aligned}$$

The local mass transfer coefficient (k_L^x) was calculated from

$$k_L^x = \frac{i_x}{zF C_b \text{Cu}^{2+}}$$

$$k_L^x = \frac{4.42 \times 10^{-3}}{2 \times 96,500 \times 1.29 \times 10^{-5}}$$

$$k_L^x = \underline{1.8 \times 10^{-3} \text{ cm s}^{-1}}$$

The fractional distance ($\frac{x}{L}$) along the electrode of total length L was:

$$\frac{x}{L} = \frac{0.4}{10}$$

$$\frac{x}{L} = \underline{0.04}$$

where x is the distance from the leading edge to the segment centre.

Similar calculations were carried out for the other segments and the current distribution constructed.

3.5 Current distribution, electrode potential and mass transport measurements in the nickel sulphamate system

3.5.1 Current distribution measurements

Current distributions were determined using the segmented cathode and instrumentation, described previously in Section 3.4b. Nickel foil was deposited on the segmented cathode using the basic electroforming procedure and the main power supply as described previously in Section 3.2.3 and 3.3.3. On switching on the pre-programmed current, with the chart recorder operating at a suitable chart speed, the twelve position switch, of the current measurement unit, could be altered to measure the voltage across each resistor. The current at each segment was calculated from the voltage measurements.

The cathodic current distributions for nickel were determined in laminar and turbulent flow at 60 and 70°C over a range of average current densities and anode lengths.

The current distribution was calculated from the current measurements as follows (cf.p.141):

Example Calculation (nickel electrodeposition)

The area of each segment (A_s) was 2.4 cm² giving a total electrode area (A) of 28.8 cm². The average current density (i_{av}) for a total applied current I was given by:

$$i_{av} = \frac{I}{A}$$

using data for Fig.4.121:

$$\begin{aligned} i_{av} &\approx \frac{93.9}{28.8} \\ &\approx \underline{0.33 \text{ A cm}^{-2}} \end{aligned}$$

The partial current (I_x) passing through No.1 segment was calculated from the measured potential difference (V) across the resistor of value R . Then I_x was found from

$$\begin{aligned} I_x &= \frac{V}{R} \\ I_x &\approx \frac{0.532}{0.498} \\ I_x &\approx \underline{1.07 \text{ Amps}} \end{aligned}$$

and the partial current density (i_x) was calculated from:

$$\begin{aligned} i_x &= \frac{I_x}{A_s} \\ i_x &\approx \frac{1.07}{2.4} \\ i_x &\approx \underline{0.45 \text{ A cm}^{-2}} \end{aligned}$$

The dimensionless local current density was given by $\frac{i_x}{i_{av}}$

$$\text{Hence } \frac{i_x}{i_{av}} = \frac{0.45}{0.33}$$

$$\frac{i_x}{i_{av}} = \underline{1.37}$$

The fractional distance ($\frac{x}{L}$) along the electrode of total length L

was

$$\frac{x}{L} = \frac{0.4}{10}$$

$$\frac{x}{L} = \underline{0.04}$$

where x is the distance from the leading edge to the segment centre.

Similar calculations were carried out for the other segments and the current distribution constructed.

Modification of the anode length and position with respect to the cathode in Cell 2

A technique for altering the length and position of the anode with respect to the cathode was introduced to modify the current distribution found under normal electroforming conditions.

Anode preparation

The anode, of overall length 25 cm, was abraded with 600 grade silicon carbide paper and vapour degreased in 'Genklene' (I.C.I.). The areas of the anode not required were masked using 'Lacomit' and p.t.f.e. tape to provide greater mechanical strength. The masked electrode was stoved at 120°C for 30 minutes to harden the masking lacquer. When cool, the anode deck was screwed to the backing plate and bolted into the cell.

3.5.2 The measurement of the electrode potential

The measurement of the electrode potential in a flowing system operated at high current densities presented some difficulty due to

the relatively high pressures developed and the possibility of gas bubbles blocking the Luggin probe.

A reproducible value of the electrode potential was achieved using a remote junction reference electrode (EIL, 3.8m calomel electrode). The method of measurement is shown in Fig.3.31. The polythene capillary tube, forming the Luggin probe at the tip, was pushed through a small hole bored through the rubber bung into a reservoir containing 600 g l^{-1} nickel sulphamate solution. (The boric acid was omitted from the reservoir solution to avoid precipitation of boric acid crystals within the capillary tube). The remote ceramic junction of the 3.8m calomel electrode was also positioned in the electrolyte reservoir via a second hole in the rubber bung. The capillary tube could be filled with nickel sulphamate solution by the application of slight pressure to the rubber bung.

Determination of cathodic polarisation data for nickel

The preparation of the electrodes and the operation of the flow system was similar to the procedure detailed in an earlier Section. The tip of the Luggin capillary tube was set at a distance of 0.5mm from the surface of the cathode for most of the investigation, although some experiments were undertaken with Luggin capillary distances of 0.2 and 0.4mm. The adjustment of the Luggin tip was undertaken with reference to a metal gauge of the required thickness. The working electrode was 10cm in length and 30 cm^2 in area. The method of data determination was dependent upon the current density range necessary, to comply with instrument output capability.

Low current densities

For measurement of cathodic polarisation data up to a current density of $\sim 0.37 \text{ A cm}^{-2}$, a potentiodynamic technique was used (Fig.3.24). The potential of the cathode was controlled with respect to the 3.8m calomel electrode by a Thompson Associates potentiostat (Ministat $\sim 1\text{A}/28\text{V}$) driven by a linear voltage ramp generator (custom built, motor driven potentiometer). The rest potential and control potential were measured

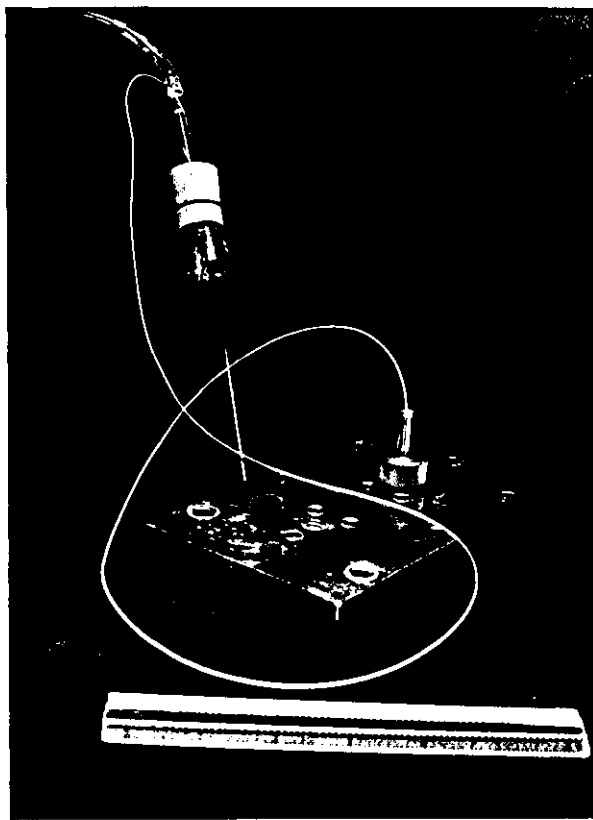
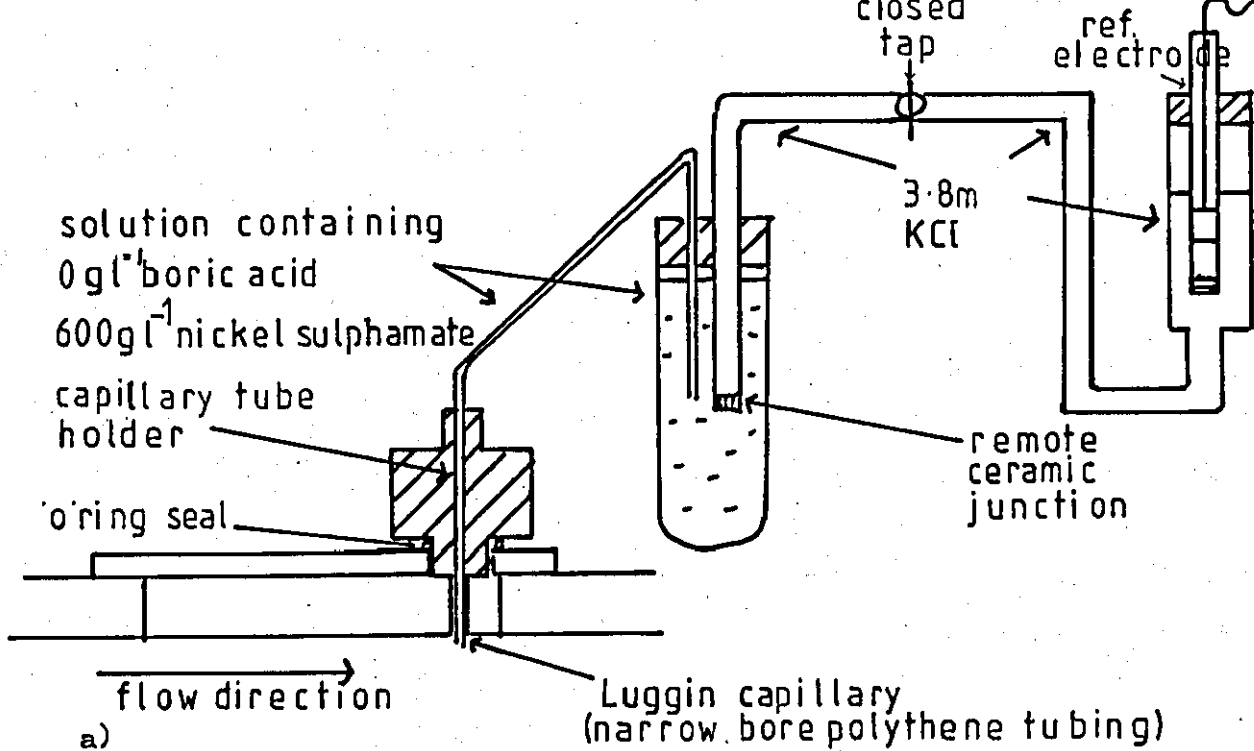


Fig.3.31

The Luggin capillary-reference electrode arrangement for the measurement of electrode potential

- a) Schematic diagrams of potential measurement apparatus
- b) Cathode assembly with Luggin capillary tube and the remote junction of the reference electrode

using a digital voltmeter (Sinclair Electronics, DM 350). The current was determined by measurement of the potential difference across a suitable resistor in series with the secondary electrode. The current - potential data were recorded on a Servoscribe y/t chart recorder (Type RE 511.20) running at a speed of 2mm s^{-1} .

The cathode was initially galvanostatically pre-plated with nickel, at a current density of 0.005 A cm^{-2} ($Re \sim 3,800$) for 30 mins. to give a more reproducible surface. The cathode was allowed to reach equilibrium again before the rest potential was measured. The potential was then decreased, from the rest potentials, at a rate of -1 mV s^{-1} . Data recorded on chart as current (as a function of voltage) versus time, was converted into current density (i) and cathode potential (E), and transferred to E versus $\log i$ co-ordinates.

Polarisation curves were determined, for the normal electroforming condition, in air saturated electrolytes. Additional data was obtained for electrolytes de-oxygenated by passing nitrogen through the solution in the reservoir.

High current densities

At current densities of up to 2 A cm^{-2} a galvanostatic technique was used to obtain cathodic polarisation data. The apparatus was set up as for the conventional electroforming procedure. The cathode potential was measured, versus the 3.8m calomel electrode by a high impedance (10^{10} ohm) digital voltmeter (Sinclair Electronics, D.M.350). The cathode was pre-plated in the same manner as for the low current density measurements. The electrode was allowed to return to equilibrium and the rest potential measured. The current density was increased by increasing the programming resistance of the power supply. The corresponding electrode potentials and the overall cell voltage were recorded for each current density.

The current was increased until excessive hydroxide formation resulted in a rapid increase in electrode potential to values of several volts or the output voltage of the power supply was exceeded.

Determination of anodic polarisation data

The electrolytic nickel anode was abraded with 600 grade S.C. and degreased with 'Genklene'. A proportion of the electrode was masked using Lacomit and P.T.F.E. tape, to leave exposed a centrally positioned effective electrode 9cm in length and 27cm² in area. The Luggin capillary system was fitted into position with the capillary tip protruding 0.5mm from the anode surface. The complete electrode assembly was then bolted into the cell.

The instrumentation used and the method of obtaining the anodic polarisation data were similar to that used for the cathodic polarisation data (p.145). The anode was pre-treated by a constant potential procedure at +1.0V (SHE) for 5 min.

3.5.3 Measurement of cathodic mass transfer coefficients - 'silver tracer' method (based on a method described in ref.344)

The conventional method for measurement of mass transfer coefficients in electrochemical cells, is to relate the limiting current density for the reduction reaction to the mass transfer coefficient. However, when operating with many concentrated electroplating solutions this technique is impractical. The problem was overcome by employing a 'silver tracer' method. A low concentration of a second ion, in this case silver, was added to the plating solution. The second ion was co-deposited with nickel, at the mass transfer controlled rate. Analysis of the deposit for silver enabled the apparent limiting current density for silver deposition to be calculated. This figure may then be related to the limiting current density for nickel reduction and a mass transfer correlation for the process, in the presence of concomitant gas evolution, derived.

The electrolyte composition

The solution had the following composition:

Ni ²⁺ (as Ni (SO ₃ NH ₂) ₂ . 4H ₂ O)	: 110.4 g l ⁻¹
H ₃ BO ₃	: 40 g l ⁻¹
pH	: 4.0

The chloride ion was omitted to prevent the precipitation of silver (as Ag Cl). The electrolyte was purified by pre-electrolysis, as described previously (Section 3.2.3). To this solution was then added 6 to 15 g cm⁻³ of silver ions (as Ag NO₃).

Electroforming procedure

The stainless steel and nickel cathodes were prepared as described in Section 3.3.3 and bolted into the cell. The cell was flooded and the heaters and pump switched on. When thermal equilibrium had been attained (60 ± 0.1°C), three 2cm³ aliquots of the electrolyte were withdrawn from the reservoir for later analysis.

The flow rate was adjusted, using the appropriate diaphragm valves to the required value. Nickel was then electroformed using the method described previously (Section 3.3.3). Two cathode lengths were studied. The 'short' electrode was 2.5cm ($L/d_e \sim 2.92$) in length and the 'long' electrode was 10cm ($L/d_e \sim 11.7$) in length. The foil was deposited at 0.4 A cm⁻² for ~165 s to electroform foil ~25µm thick. The anode in both cases was 25cm in length.

When deposition was complete, the cathode was removed from the cell, rinsed in hot water, then distilled water and dried. The foil was carefully stripped from the electrode using a scalpel and weighed prior to the analysis for silver.

Method of analysis for silver

Preparation of solutions

The deposit

(Dilutions quoted are typical for foils 2.5cm in length. The equivalent dilutions for foils 10cm in length are shown in parenthesis).

The nickel electroforms, containing trace amounts of silver, were dissolved in 5cm³ of concentrated nitric acid in 50cm³ Erlenmeyer flasks, warming gently over a hot plate to assist dissolution. When cool the acid solution was diluted by the addition of ~20cm³ of distilled

water. The solution was then quantitatively transferred to a 50cm³ (250cm³) volumetric flask and diluted to volume with distilled water.

To each of three 25cm³ volumetric flasks was added a 5cm³ aliquot of the above diluted solution and a known 'standard addition' of silver ions. The standard addition was added quantitatively from a 5cm³ burette containing a 100µg cm⁻³ standard solution of silver (as AgNO₃). (0.25cm³ of the standard, when diluted to 25cm³ represented a standard addition of 1µg cm⁻³). Solutions of the following compositions were prepared:

$$y + 0 \text{ } \mu\text{g cm}^{-3} \text{ Ag}$$

$$y + 1 \text{ } \mu\text{g cm}^{-3} \text{ Ag}$$

$$y + 2 \text{ } \mu\text{g cm}^{-3} \text{ Ag}$$

where y represents the unknown concentration of silver in the solution. The solutions were analysed for the silver concentration by atomic absorption spectrophotometry (A.A.S.).

The electrolyte

To the three 2cm³ aliquots of the nickel sulphamate based electrolyte, sampled immediately before the electroforming operation, were added 'standard additions' of silver using the same method as used for the deposit solutions. Typically the electrolyte samples were diluted to 25cm³ with distilled water, to produce solutions of the following compositions:

$$x + 0 \text{ } \mu\text{g cm}^{-3} \text{ Ag}$$

$$x + 1 \text{ } \mu\text{g cm}^{-3} \text{ Ag}$$

$$x + 2 \text{ } \mu\text{g cm}^{-3} \text{ Ag}$$

where x represents the unknown concentration of silver ions in the solution. The solutions were again analysed by A.A.S.

Analysis of prepared solutions for silver

(The background to this analysis may be found from ref.348)

The silver concentration of both electrolyte and the electro-

deposit were determined by the method of standard additions. This was necessitated by the difficulty of reproducing standard solutions of identical matrix composition to the sample. The silver concentrations of the solutions were maintained within the linear absorbance range for the wavelength used to ensure accurate analysis.

The absorbances of all solutions were measured using an Instrumentation Laboratories, IL151 Spectrophotometer with the following instrumental conditions (modified method of ref.348):

- a) Deuterium background correction (The intensity of the silver lamp was reduced by a polythene filter to give lamp compatibility).
- b) Photomultiplier Voltage HV : ~700 v
- c) Wavelength : 328.1 nm
(linear range 0+4 $\mu\text{g cm}^{-3}\text{Ag}$)
- d) Band pass : 1 nm
- e) Lamp current : 4 to 5 mA
- f) Flame-reducing : $\text{C}_2\text{H}_2/\text{air}$

The unknown concentration of silver in the deposit solution (y) and in the electrolyte solution (x) were determined by plotting the measured absorbance versus the standard addition. The (negative) intercept on the abscissa gave the value of the unknown concentration of silver (Fig. 3.32). In practice this quantity was calculated by means of a least squares linear regression procedure. The mass transfer coefficients were calculated as follows:

Calculation of G , $c_b^{\text{Ag}^+}$, $i_L^{\text{Ag}^+}$ and $k_L^{\text{Ag}^+}$

The bulk concentration of silver ions, $c_b^{\text{Ag}^+}$ was calculated from:

$$c_b^{\text{Ag}^+} = \frac{xa}{107.87} \times 10^{-6} \text{ moles cm}^{-3}$$

where a is the dilution factor for the electrolyte and 107.87 is the

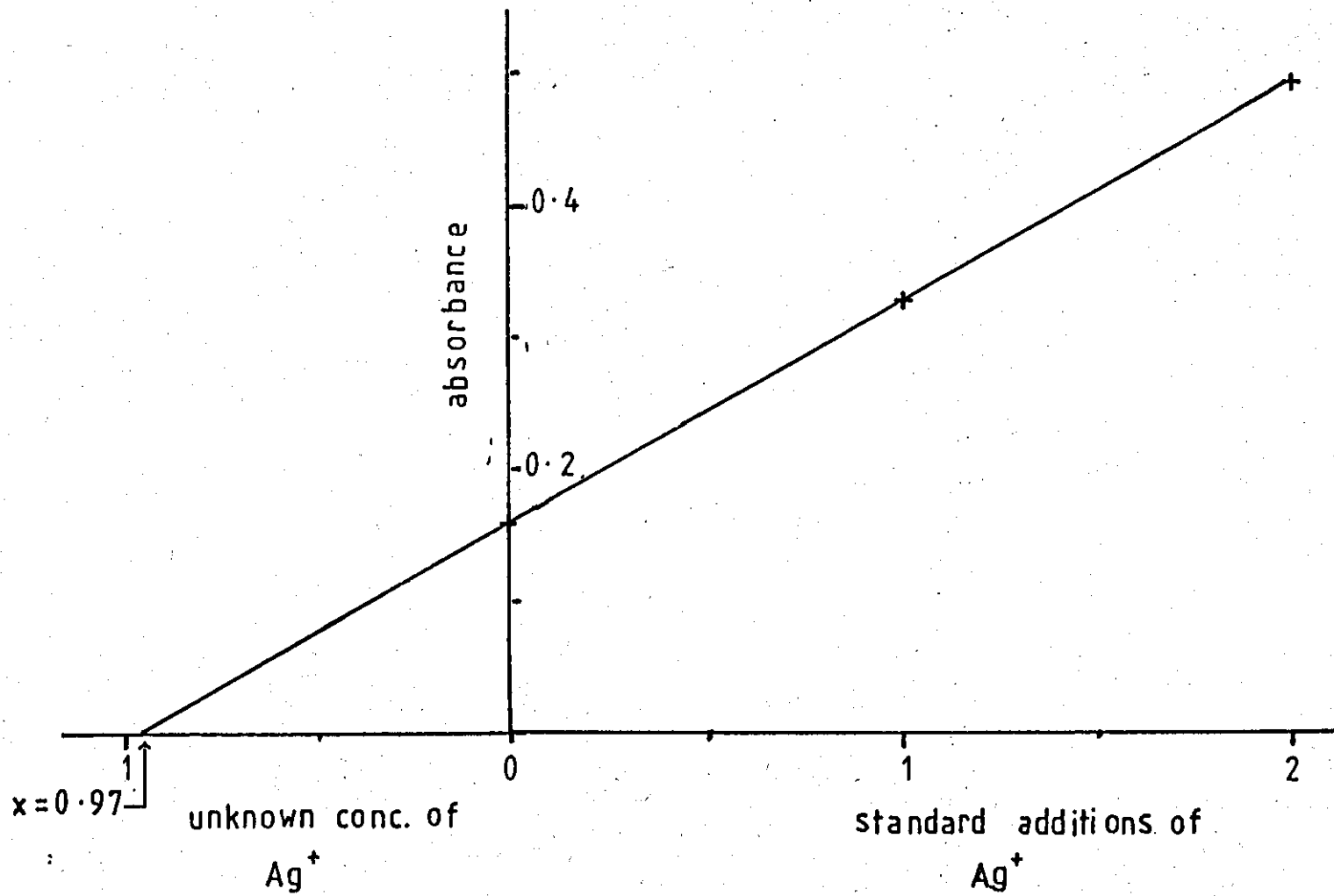


Fig.3.32

Graphical method for determination of silver content using the standard additions technique (data from Table 55, sample No.1).

molecular weight of silver. The weight of silver, G , deposited in time, t , was calculated from:

$$G = 10^{-6} y b \text{ g}$$

where b is the dilution factor for the deposit solutions.

The limiting current density for the reduction of silver ions, $i_L^{\text{Ag}^+}$ was calculated from:

$$i_L^{\text{Ag}^+} = \frac{Z F G}{t A 107.87} \text{ A cm}^{-2}$$

where t was the deposition time in seconds and A the area of the electrode.

The mass transfer coefficient for the process $k_L^{\text{Ag}^+}$, was given by (cf. Equation 2.15):

$$k_L^{\text{Ag}^+} = \frac{i_L^{\text{Ag}^+}}{F c_b^{\text{Ag}^+}} \text{ cm s}^{-1} \quad \dots \dots (3.2)$$

or

$$k_L^{\text{Ag}^+} = \frac{G}{107.87 A t c_b^{\text{Ag}^+}} \text{ cm s}^{-1}$$

The calculation of mass transfer coefficients will be discussed further in Section 4.5.

3.6 Post-deposition examination and measurements

Optical microscopy

The deposits were examined, using the optical microscope, prior to removal of the foil from the substrate. The cathode deck, complete with the electrodeposited nickel was removed from the backplate, and clamped, foil surface downwards, on the stage of a Reichart MF2 incident light projection microscope with a tungsten lamp (12V, 100W). The majority of the examinations were made using bright field illumination (although filters and polarised light facilities were used occasionally).

The foil surface was examined for pitting, streaking and large growth formations. Areas of interest on the foil surface were later examined in the electron microscope.

Microhardness measurements

Hardness measurements were made using a microhardness attachment on the Reichart microscope. The cathode deck and the deposit was set up as described above. The stage and electrode could be moved linearly by means of a rack and pinion device and the movement measured on a vernier scale.

Using this device longitudinal microhardness traverses could be made along the cathode. Microhardness values were determined at locations free of surface defects, using a load of 40g applied for ~15 s (Appendix 3). About five measurements were made in each region and an average microhardness value calculated.

On specimens where microhardness profiles were not determined, the average microhardness value was calculated from indentations distributed over the central area of the foil (L/d_e 0.1 to 0.9).

Visual examination and calculation of current efficiency

Following microhardness measurements (where applicable) the foils were carefully removed from the substrate, using a scalpel and examined visually. Perforations in the deposit were observed by holding the foil up to a strong light. The qualitative distribution of perforations over the foil surface was subsequently recorded.

Scanning electron microscopy (SEM)

Samples of the foil (~0.2 x 0.5 cm) were cut from the foils for further examination in the electron microscope. Selected areas of interest were the main deposit region (L/d_e 0.1 to 0.9) and the leading and trailing edges. Foil sections were cleaned by immersion in acetone, agitated using ultra-sonics and subsequently dried. Specimens were attached to Al or Cu specimen holders (up to 3 per holder) by means of silver 'Dag', which provided the electrical contact. Some specimens were sputtered with gold to limit surface charging effects.

Examination was carried out using one of two electron microscopes. The Cambridge Stereoscan type 2A microscope gave a good depth of focus but the picture quality was inferior at magnifications greater than 5,000X. The S.E.M. column received the Al specimen holders, the chamber was automatically vacuum cycled and the microscope set in operation. The tilt angle was adjusted to 45°. Selected areas of interest were recorded by means of a 35mm camera using a semi-automatic exposure system attached to the secondary oscilloscope.

The Jeol JEM 100 CX microscope is a scanning transmission electron microscope (S.T.E.M.) used in S.E.M. mode. Very good resolution may be obtained at magnifications >100,000X. The column received the Cu specimen holders and was rapidly pumped down. The tilt angle was adjusted to achieve maximum contrast. Selected areas of interest were recorded by means of a 120mm camera.

4. RESULTS AND INTERPRETATION

The results of the experimental investigations are presented in five main Sections. The first of these describes studies of the electroforming of nickel foils at 60°C in the Mark 1 Parallel Plate Cell. As will be seen all of these studies were carried out with short electrodes and there were problems with gas evolution from the anodes. The experience gained highlighted the need for an improved design of cell to allow separation of the anolyte compartment and the use of electrodes of varying lengths. Facilities were also incorporated to permit an examination of current distribution at the cathode, and polarisation measurements to be made. It also seemed desirable to test experimentally both the mass transport characteristics of the Mark 2 Cell and the cathode current distribution characteristics of a segmented cathode using a simple metal ion electrolyte. A $\text{CuSO}_4 - \text{H}_2\text{SO}_4$ system was chosen for these studies which are described in Section 2.

Section 3 is concerned with detailed studies of the electroforming of nickel foils from the concentrated Ni sulphamate system at temperatures in the range 50 - 70°C, as a function of flow rate (Re), and current density, using a range of electrode geometries. Additional studies of electrode polarisation measurements and current distributions under various cathode geometries are described in Section 4.

The final section is concerned with Ni transport studies using a silver tracer method and with the development of a model for predicting mass transport correlations in parallel plate cells with enhanced mass transport due to gas codeposition.

4.1 Studies of the electroforming of nickel foils from concentrated Ni sulphamate solutions at 60°C in the Mark I Parallel Plate Cell

A limited programme of investigations was carried out in the cell to establish the broad characteristics of the electroforming of nickel foils. This included studies of deposition under conditions of laminar flow (Re 400-650) and turbulent flow (Re 2,300-13,328).

Nickel was electroformed from the concentrated nickel sulphamate plating solution on to prepared stainless steel substrates 3.3 equivalent diameters (5cm) in length. The working electrode occupied the full width of a square channel, 3cm in width and 1cm in depth, of corresponding equivalent diameter 1.5cm. The nickel counter electrode was of identical dimensions and positioned directly opposite the cathode. Details of the cell and electrodes are given in Section 3.2.

A series of electrolyses was carried out at linear flow rates of 3.5 to 106.8 cms^{-1} with corresponding Reynolds numbers of Re 437 to Re 13,328. In each experiment, electrolysis was carried out for a specified period of time to give deposits 7 - 32 μm thick for subsequent visual and microscope examinations after removal from the electrode surfaces.

The results may be conveniently divided into two flow types corresponding to laminar and turbulent flow. The transition between the two occurs at about Re 2,100. For each foil the principal region of interest was the main deposit representing >>90% of the foil surface for sound compact nickel electroforms.

Additional features at the leading and trailing edges were also of interest due to possible variations in mass transfer rate or flow conditions in these regions.

4.1.1 Deposition under conditions of laminar flow (Re 400-650)

Two nickel foils were electroformed in laminar flow at 60°C at current densities of 0.28 A cm^{-2} and 0.52 A cm^{-2} . At such low

electrolyte flow velocities ($\sim 4 \text{ cm s}^{-1}$) a large volume of gas was evolved from the anode and there also appeared to be gas evolution from the cathode during the deposition process. The inter-electrode gap rapidly filled with gas bubbles and large bubbles accumulated downstream within the cell. Small hydrogen bubbles, originating at the cathode leading edge, were swept slowly along the electrode surface. The formation of large gas bubbles affected flow conditions and made close flow control difficult.

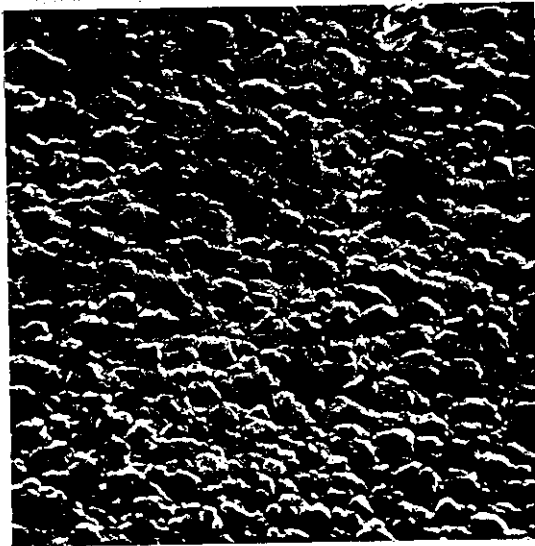
The electroformed foils were both of relatively uniform appearance over the main deposit region. At both leading and trailing edges, narrow bands ($\sim 0.2 \text{ mm}$ wide) of brighter material were apparent. However, the effect of the observed gas evolution was reflected in the final pitted appearance of the deposit. Pitting and surface 'streaks' were distributed in a linear fashion, parallel with the flow direction over the entire surface area. Close to the leading edge large holes through the foil were observed, particularly at the higher current density. Both foils were subsequently examined using the S.E.M.

Main deposit region

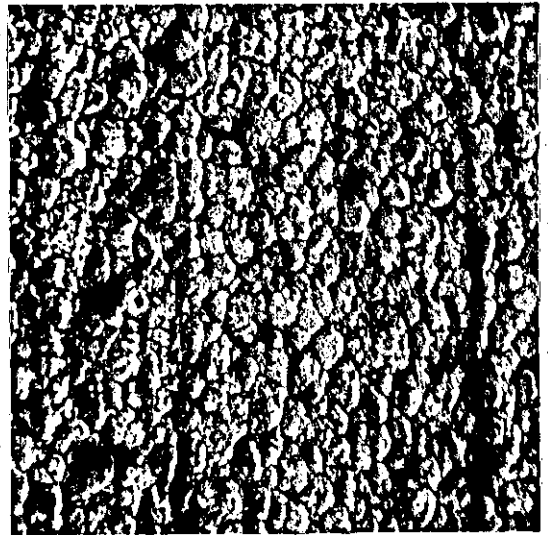
The morphology characteristic of a sound, coherent nickel foil i.e. a fine grained deposit, was maintained over 95% of the surface area, reflecting the relatively high current efficiencies (88% at 0.28 A cm^{-2} and 94% at 0.52 A cm^{-2}). At 0.28 A cm^{-2} the grains were uniform size, $\sim 2 \mu\text{m}$ in diameter (Fig.4.1a). An undulating character was evident in areas where 'streaking' had been observed visually (Fig.4.1b). This feature may be associated with gas streaming along the electrode surface. At 0.52 A cm^{-2} the grain size was less uniform and in regions varied between 2 and $6 \mu\text{m}$ (Fig.4.1c,d). This is perhaps due to local variations in current distribution.

Edge effects

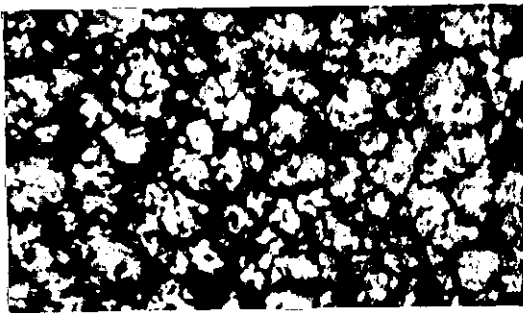
At a current density of 0.28 A cm^{-2} , both the leading edge (Fig.4.2a) and the trailing edge (Fig.4.2b) were relatively smooth and featureless. In the region of the leading edge extensive pitting, with pits between 2 and $5 \mu\text{m}$ in diameter, was evident (Fig.4.2c).



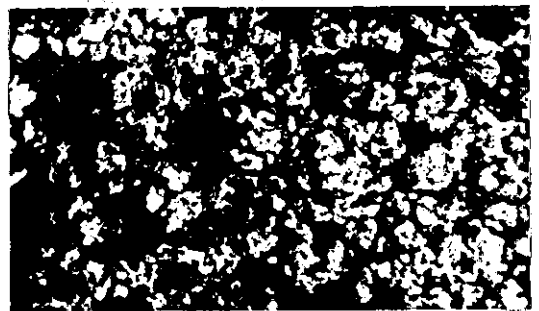
a) 45° tilt



b) 45° tilt



c) 0° tilt



d) 0° tilt

Fig.4.1 S.E.M. micrographs of surfaces of nickel foils deposited in laminar flow. (x 2,000)

a) Re 636, 0.28 A cm^{-2}
main deposit.

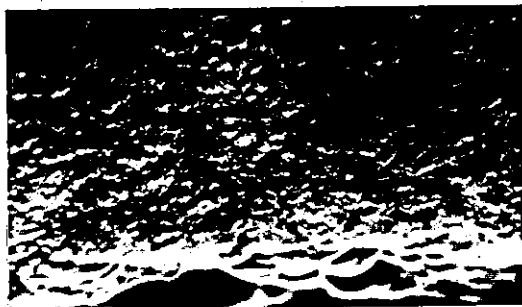
b) Re 636, 0.28 A cm^{-2}
'streaked' area.

c) Re 437, 0.52 A cm^{-2}
main deposit.

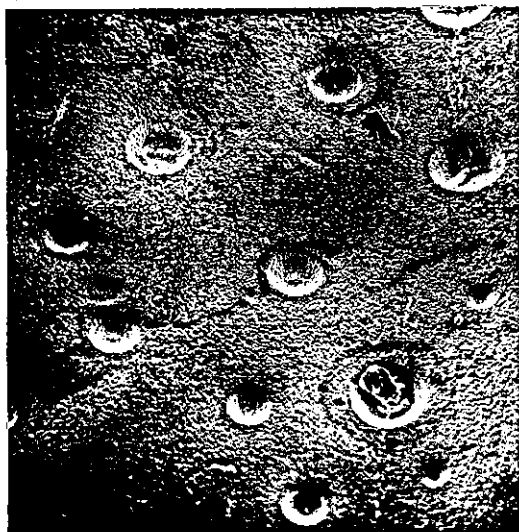
d) Re 437, 0.52 A cm^{-2}
near trailing edge.



a) 0° tilt



b) 0° tilt



c) 45° tilt

Fig.4.2 S.E.M. micrographs of surfaces of nickel foils deposited at the leading and trailing edges of the electrode, Re 636, 0.28 A cm^{-2} .
a) Leading edge section (x 2,000)
b) Trailing edge section (x 2,000)
c) Pitted area (x 200)

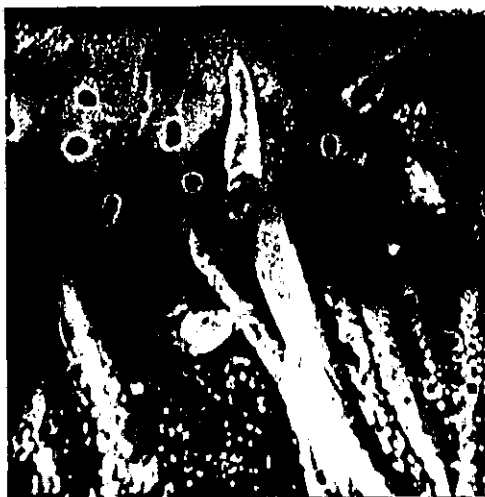
In contrast, at the higher current density of 0.52 A cm^{-2} , the leading edge area showed a ridge type structure (Fig.4.3a) and these ridge growths originated from an area $\sim 10\mu\text{m}$ downstream from a smooth leading edge. Many pits were also evident. The ridge region extended for $\sim 2000\mu\text{m}$ from the leading edge. The trailing edge was also pitted with some surface reliefs indicating a tendency towards powder type growth forms (Fig.4.3b). When the foil was peeled off and held up to the light, holes were evident in the leading edge and in lines along the entire length of the foil.

The slow removal of evolved gases from the inter-electrode gap under laminar flow conditions may result in these highly porous structures. At the higher current density the gas 'build up' resulted in gas bubbles blocking the cathode surface. Under these conditions large areas of the electrode remained unplated and the deposition process irreproducible due to fluctuating local current densities.

Nickel foils were prepared in flow regimes corresponding to Reynolds numbers of 2,300-2,500, 3,500-10,700, $11,350 \pm 350$, and $13,000 \pm 300$. The first of these regimes allowed direct comparison with the laminar flow region, whilst the studies at $\text{Re } 3,500-10,700$ were directed towards gaining information concerning the effects of flow on foil morphology and structure, and the maximum current densities for the preparation of foils with fine grain structures and without formation of powders. Detailed studies of the effects of current density upon grain structure and microhardness, and deposit brightness were made at $\text{Re } 11,350 \pm 350$. The effects of current density on deposit structure and morphology were also studied at $\text{Re } 13,000 \pm 300$ since this represented the maximum flow rates possible in the cell.

4.1.2 Deposition under conditions of turbulent flow (Re 2,300-13,350)

In the turbulent flow regime deposition was carried out over a wide range of Reynolds numbers ($\text{Re } 2,300-13,328$). The high flow rates ensured rapid removal of evolved gases from the cell and hence minimised the large-scale gas effects found in laminar flow. The upper limit of the Reynolds number was determined by the design of the cell and flow circuit.



a) 0° tilt



b) 0° tilt

Fig.4.3 S.E.M. micrographs of surfaces of nickel foils near the leading and trailing edges. Re 437, 0.52 A cm^{-2} .

a) Leading edge section (2,000 x)

b) Trailing edge section (200 x).

(a) Nickel electroforms deposited in the flow range $Re\ 2,400 \pm 150$

A series of nickel foils $26 \pm 6 \mu m$ in thickness were electroformed over the current density range $0.05\ A\ cm^{-2}$ to $0.78\ A\ cm^{-2}$ as shown in Table 4.1. The deposits electroformed at current densities $< 0.55\ A\ cm^{-2}$ appeared to be sound over the entire electrode length and were deposited at current efficiencies close to 100%. The overall appearance of the foils was lustrous. The brightness tended to increase with increasing current density, particularly in the leading and trailing edge regions.

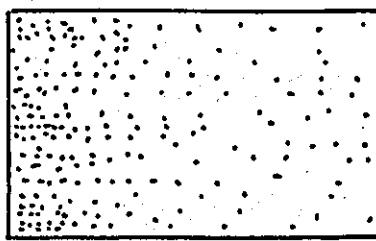
At the highest current densities (0.63 and $0.78\ A\ cm^{-2}$) in addition to the sound, semi-bright nickel deposited over about 70% of the electrode surface, a brown powder type formation was observed (Fig. 4.4f,g) although the current efficiency remained at $\sim 100\%$. This type of deposit was evident at the leading and trailing edges and at the sides of the electroforms. At $0.78\ A\ cm^{-2}$, a green band of hydroxide and cracking of the underlying nickel were observed at the leading edge. The distribution of powder may be accounted for by the large scale 'blanketing' of the electrode surface by evolved gases and the subsequent distortion of the current distribution.

During the electroforming operation, codeposited hydrogen was observed to be streaming along the cathode surface. At the anode, evolved oxygen took the form of a gas 'wedge'. The codeposited gases occupied a greater volume of the cell gap as the gas was swept downstream by the flowing electrolyte and gas bubbles appeared to break away at the trailing edge of the electrode. The anode gas tended to predominate due to the higher rate of gas evolution and the upward facing geometry. This effect is shown schematically in Fig. 4.5(a) for a deposition current density of $0.05\ A\ cm^{-2}$. The evolved gas occupied about one third of the inter-electrode gap. Small hydrogen bubbles, originating near the leading edge were observed moving along the cathode surface and coalescing further downstream. At a current density of $0.38\ A\ cm^{-2}$ the evolved gases occupied more than three-quarters of the cell gap (Fig. 4.5b) and at faster deposition rates ($> 0.55\ A\ cm^{-2}$) anode gases may have been in contact with the cathode.

Flow rate U cm s ⁻¹	Reynolds number Re	Average current density i/A cm ⁻²	Deposition time t s	Average deposit thick- ness d/ μ m	Weight deposited g	Current effici- ency %
19.5	2.433	0.05	1,620	28	0.3285	102
19.5	2.433	0.11	690	26	0.3363	101
19.0	2.371	0.23	305	24	-	-
19.5	2.433	0.38	150	20	0.2480	99
19.5	2.433	0.55	150	28	-	-
20.3	2.533	0.63	118	25	-	-
19.5	2.433	0.78	120	32	0.4195	102

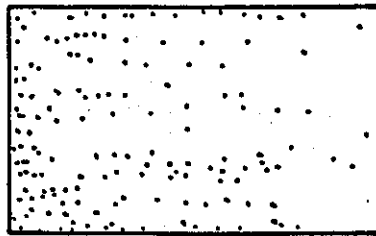
Table 4.1 Nickel foils deposited under conditions of turbulent flow, Re 2,400 \pm 150, at 60°C, (Cell 1, L/de 3.3)

a) 0.05 A cm^{-2}



flow direction

b) 0.11 A cm^{-2}



flow direction

c) 0.23 A cm^{-2}



flow direction

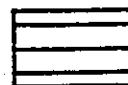
key to diagrams



sound deposit



bright deposit

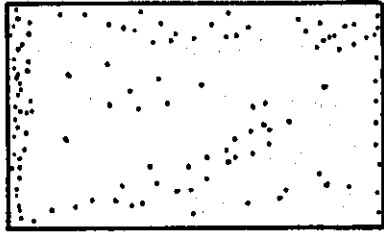


powder deposit

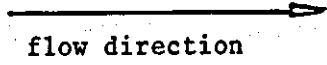


hydroxide deposit

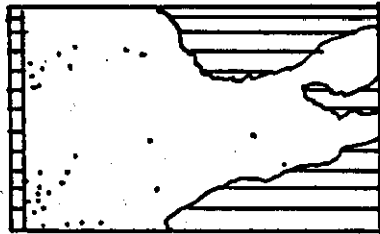
Fig. 4.4 Schematic representation of the visual appearance of nickel foils deposited at $Re\ 2,400 \pm 150$



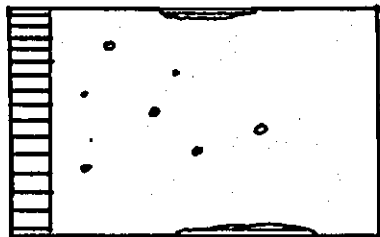
d) 0.38 A cm^{-2}



e) 0.55 A cm^{-2}



f) 0.63 A cm^{-2}



g) 0.78 A cm^{-2}

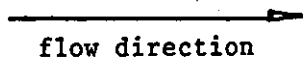


Fig. 4.4 continued

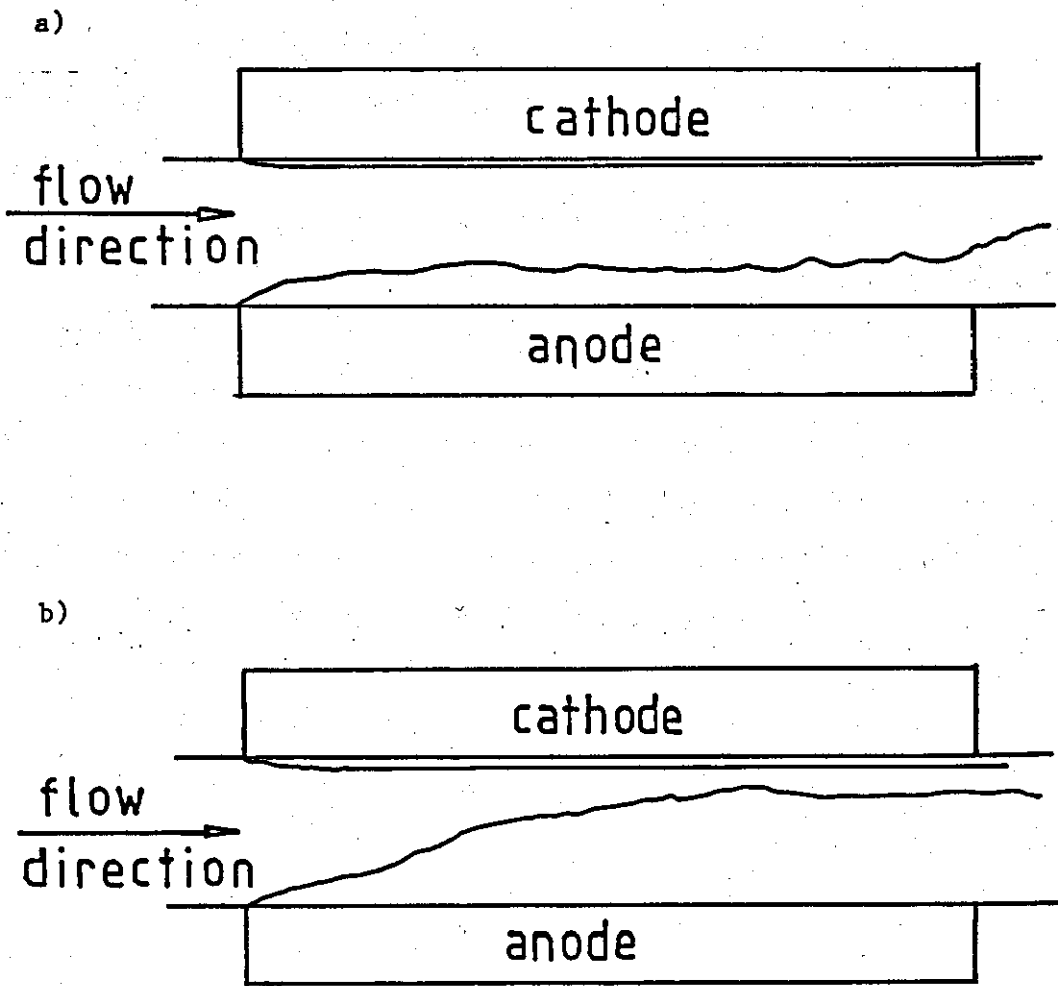


Fig. 4.5 Visual observation of gas flow pattern during electroforming at $Re\ 2,400 \pm 150$

a) $0.05\ A\ cm^{-2}$

b) $0.38\ A\ cm^{-2}$

Pitting was present in all foil samples. The pits were particularly numerous close to the leading edge of the foil, but were not confined to this area. At the lowest current densities (0.05 and 0.11 A cm⁻²) the pitting was distributed in lines parallel with the flow direction (Fig.4.4a,b). Individual pits showed the 'tailing' characteristic of gas bubble adhesion. A significant decrease in the number of pits was apparent at higher current densities. However some large (up to 2mm) holes were observed in stripped foils deposited at current densities >0.55 A cm⁻² (Fig.4.4e-g).

The nickel foils electroformed at 0.11 and 0.55 A cm⁻² were examined using the S.E.M.

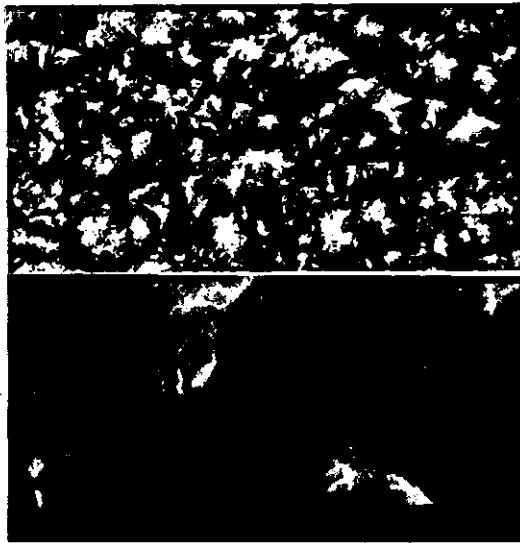
Main deposit region

A sound deposit of relatively uniform fine grain structure was found over >95% of the surface area for both foils. At 0.11 A cm⁻², (Fig.4.6a) the 'grain' size was variable between 1 and 6µm. At high magnification there was evidence of the formation of crystalline faces and layer growth. This current density was similar to the corresponding deposition rates in conventional nickel plating.

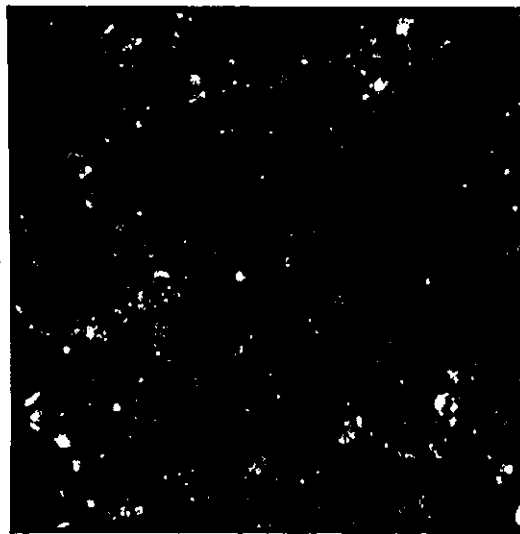
At the higher current density, the grain boundaries were more clearly apparent and better defined (Fig.4.6b). A sub-grain structure was evident with an array of irregular grains <5µm in diameter. This effect may be associated with the initial stages of the formation of a powdery deposit. Gas bubble induced mass transfer phenomena may contribute to small variations in the morphology at low flow rates.

Edge effects

At low current density, marked changes in morphology at the electrode edges were absent. The main deposit structure was maintained up to the leading and trailing edges of the foil (cf Fig.4.7a,b with 4.6c). The leading edge section was smooth and fine grained but heavily pitted (Fig.4.8a). The trailing edge was similar although less pitted (Fig.4.8b).



a) 0° tilt

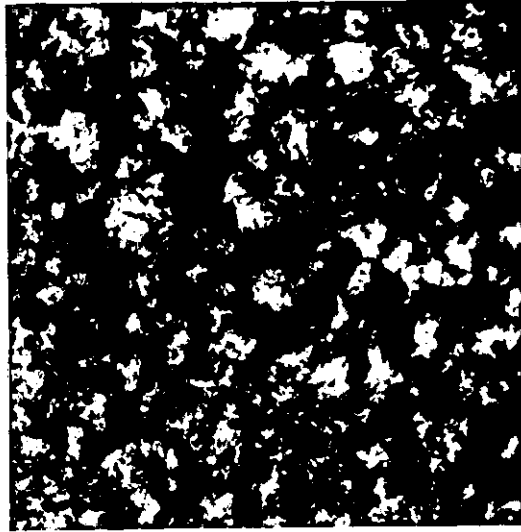


b) 0° tilt

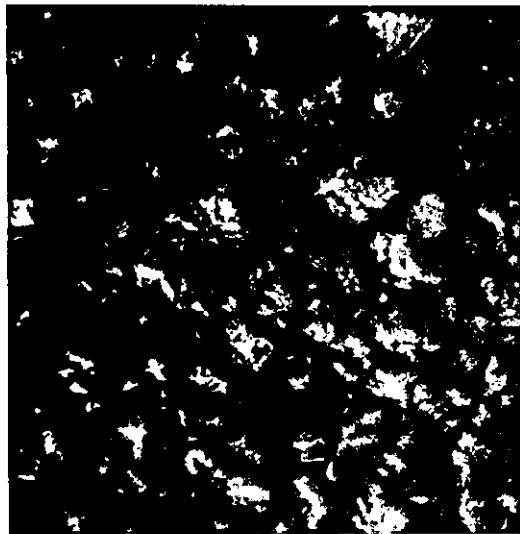
Fig.4.6 S.E.M. micrographs of surfaces of nickel foils deposited at $Re\ 2,400 \pm 150$

a) $0.11\ A\ cm^{-2}$ (top : 2,000 x)
(bottom : 10,000 x)

b) $0.56\ A\ cm^{-2}$ (2,000 x)



a) 0° tilt



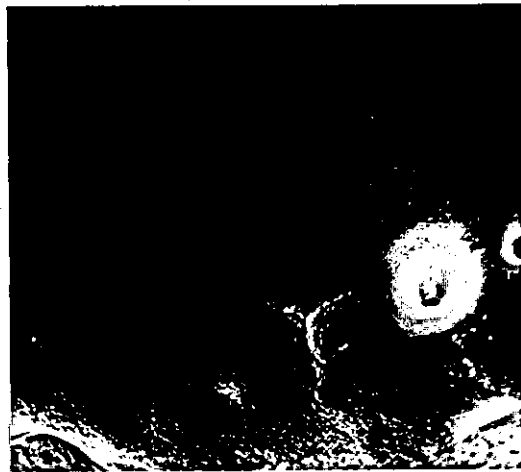
b) 0° tilt

Fig.4.7 S.E.M. micrographs of surfaces of nickel foils deposited at $Re\ 2,400 \pm 150$, $0.11\ A\ cm^{-2}$ (x 2,000)

- a) $\sim 600\ \mu m$ from the leading edge
- b) $\sim 100\ \mu m$ from the leading edge



a) 0° tilt



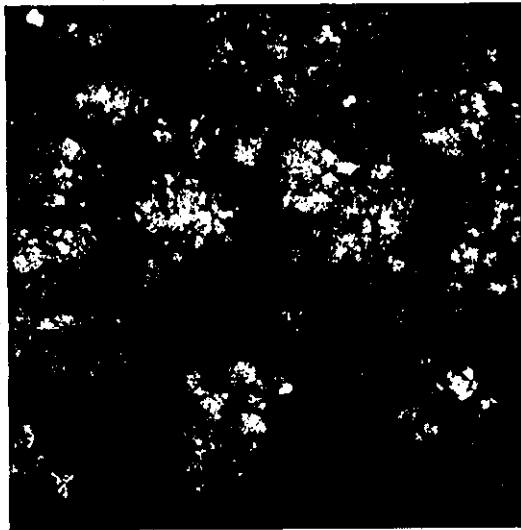
b) 0° tilt

Fig.4.8 S.E.M. micrographs of surfaces of nickel foils deposited at $Re\ 2,400 \pm 150$, $0.11\ A\ cm^{-2}$

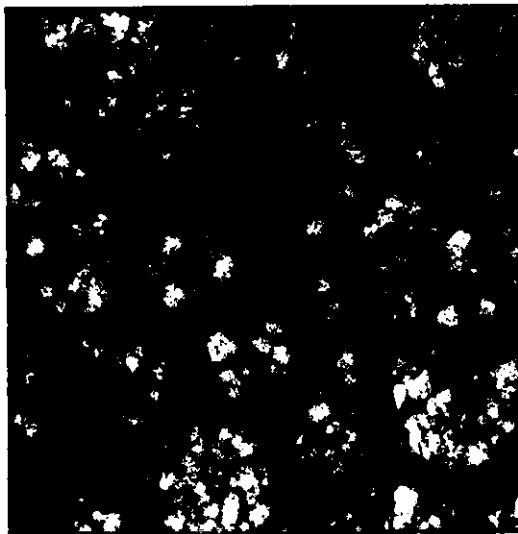
a) Leading edge Section (x 50)

b) Trailing edge Section (x 200)

At 0.56 A cm^{-2} a narrow band of a brown, powdery deposit was formed at the leading edge. In the regions adjacent to the leading and trailing edges, the deposit exhibited a structure similar to that of the main deposit but with a larger 'grain' size of $5 - 10 \mu\text{m}$ (Fig. 4.9a,b). At the leading edge, the morphology was nodular in character with some pitting (Fig.4.10a). Cracked and exfoliated foils, with corresponding nodular growths, were typical of the region at the trailing edge (Fig.4.10b). The increased grain size at the higher current density, particularly in the edge regions, may represent the precursors of the more prominent nodular features. It was apparent that for these flow conditions the maximum current density for a sound deposit over the entire electrode length was about 0.5 A cm^{-2} .



a) 0° tilt



b) 0° tilt

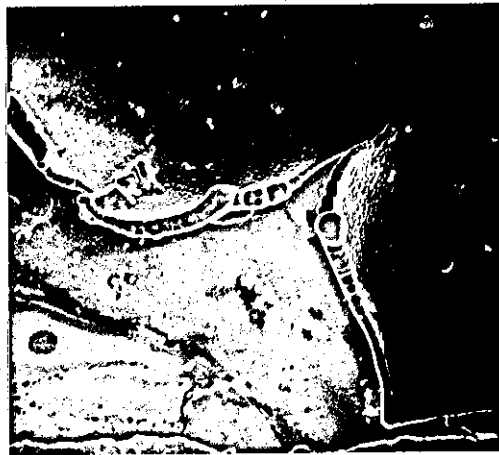
Fig.4.9 S.E.M. micrographs of surfaces of nickel foils deposited at $Re\ 2,400 \pm 150$, $0.56\ A\ cm^{-2}$ (x 2,000)

a) $\sim 1,000\ \mu m$ from the leading edge

b) $\sim 1,000\ \mu m$ from the trailing edge



a) 0° tilt



b) 0° tilt

Fig.4.10 S.E.M. micrographs of surfaces of nickel₂ foils deposited at $Re\ 2,400 \pm 150$, $0.56\ A\ cm^{-2}$ (x 50).

a) Leading edge section

b) Trailing edge section

(b) Nickel electroforms deposited in the flow range Re 3,518 to Re 10,745

A series of nickel foils 7-21 μ m thick was electroformed over the range of Reynolds numbers Re 3,518 to 10,745. A range of current densities was chosen in order to define approximately the maximum current density for good deposits. A good deposit was defined as one that had not become powdery even although pores or holes might be evident. The deposit quality was assessed by visual inspection of the electroforms but on the substrate and after foil stripping. Sound deposits were electroformed at current efficiencies close to 100% and were all lustrous, although of variable visible porosity. The deposition conditions are given in Table 4.2 and the appearances of the deposited foils are shown schematically in Fig.4.11 a-i.

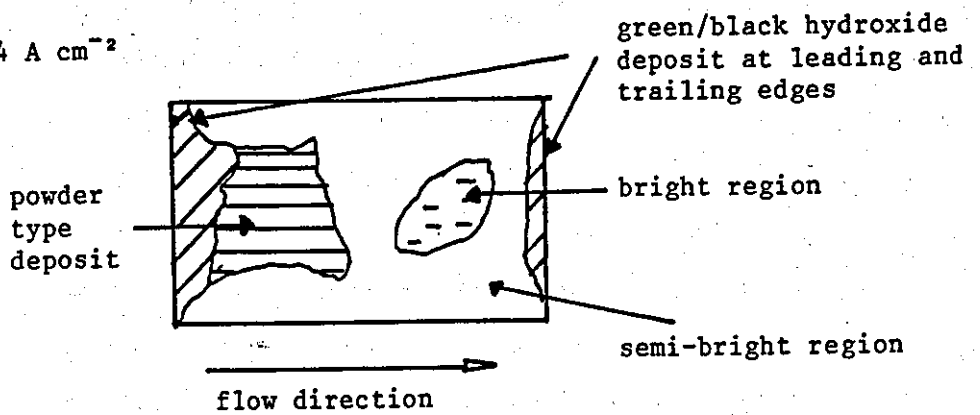
Previous results at Re 2,433 suggested a maximum current density of $<0.55 \text{ A cm}^{-2}$ for the preparation of good foils. At a current density of 1.04 A cm^{-2} at Re 3,518 (Fig.4.11a), the maximum current density was exceeded and powder was deposited, together with a green-black hydroxide at the leading and trailing edges. An area of brighter nickel was found in the main deposit region. This feature may be associated with changes in current distribution due to the formation of a more resistive hydroxide layer and a corresponding increase in the current density in other areas.

At Re $\sim 4,700$ and 0.58 A cm^{-2} (Fig.4.11b) the deposit was sound, but with many small perforations through the foil. Bands of brighter nickel were formed at the leading and trailing edges. The gas evolved at the anode did not appear to contact the cathode (Fig.4.11.1). An increase in current density to 0.76 A cm^{-2} (Fig.4.11c) resulted in the formation of a brown powder deposit at the leading edge and over about one third of the foil area towards the trailing edge of the electrode. The remaining area of sound nickel was bright with few holes. At 0.95 A cm^{-2} (Fig.4.11d) powder was again deposited at the leading and trailing edges. However, the area of coverage was considerably less than observed at the lower current density. Although, clearly, the results were some-

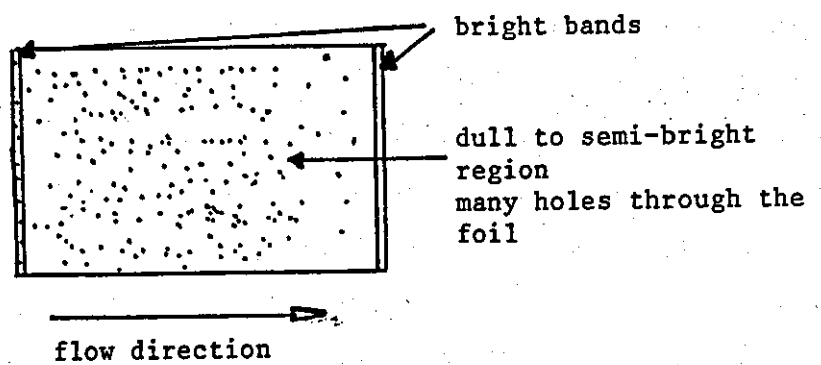
Flow rate U cm s ⁻¹	Reynolds number Re	Average current density i/A cm ⁻²	Deposition time t	Average deposit thick- ness μm	Weight deposited g	Current effici- ency %
28.2	3,519	1.04	60	21	-	-
37.3	4,655	0.58	60	12	0.1495	97
37.3	4,655	0.76	28	7	-	-
37.7	4,705	0.90	33	10	-	-
41.4	5,166	0.76	30	8	0.1038	103
58.4	7,288	0.69	47	11	-	-
62.9	7,849	0.95	30	-	-	-
83.6	10,433	0.52	60	11	-	-
86.1	10,745	0.52	56	10	-	-
86.1	10,745	1.21	25	10	-	-

Table 4.2 Nickel foils deposited under conditions of turbulent flow Re 3,519 to Re 10,745 at 60°C (Cell I, $L/d_e \sim 3.3$)

a) Re 3,519 1.04 A cm^{-2}



b) Re 4,655 0.58 A cm^{-2}



c) Re 4,655, c.d. 0.76 A cm^{-2}

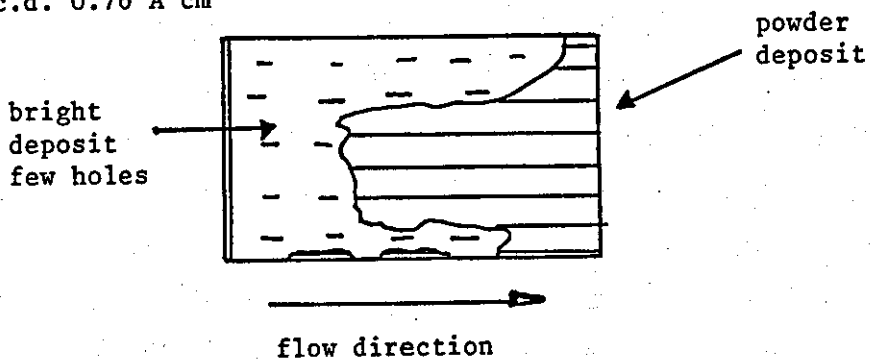
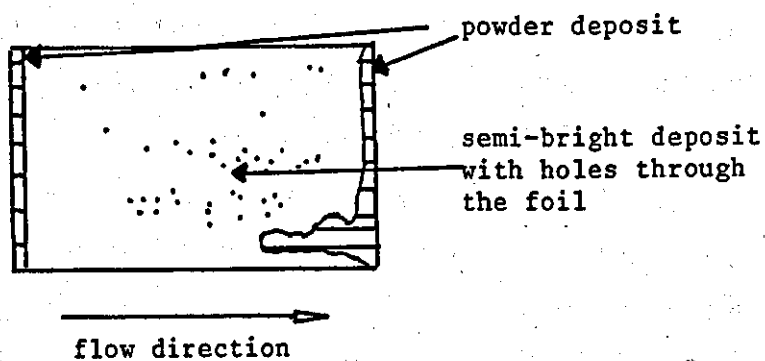
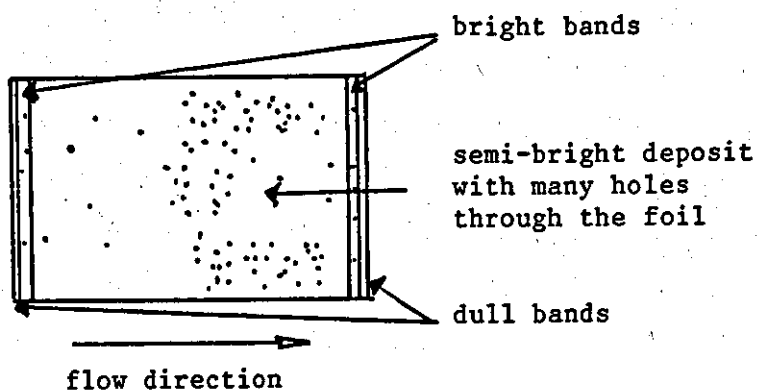


Fig.4.11 Schematic representation of the visual appearance of nickel foils deposited over the Reynolds number range Re 3,500 - 10,700.

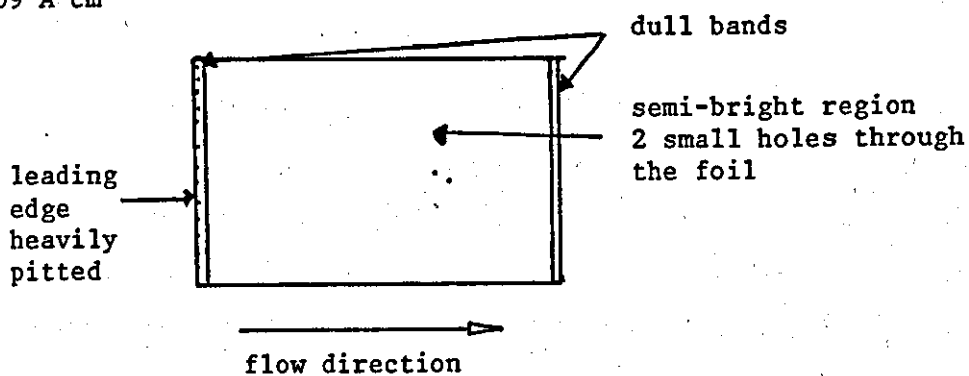
d) Re 4,705, 0.90 A cm⁻²



e) Re 5,166, 0.76 A cm⁻²



f) Re 7,288, 0.69 A cm⁻²



g) Re 7,849 0.95 A cm⁻²

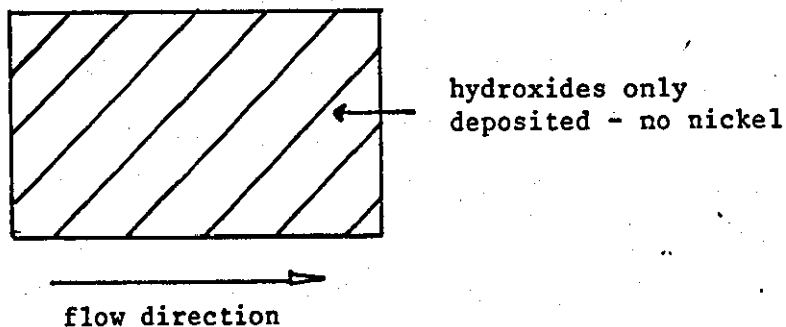
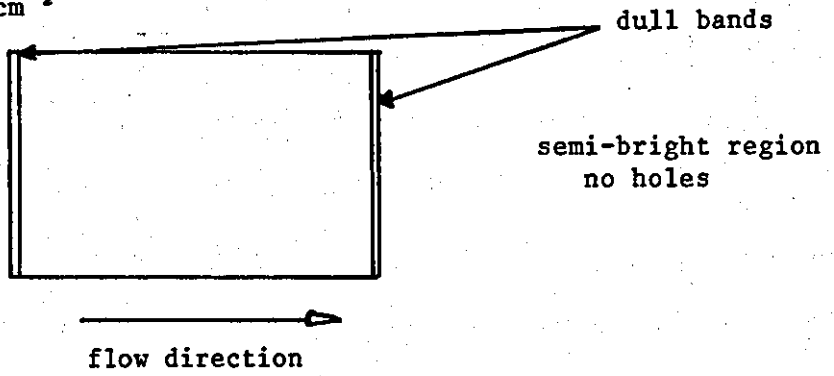
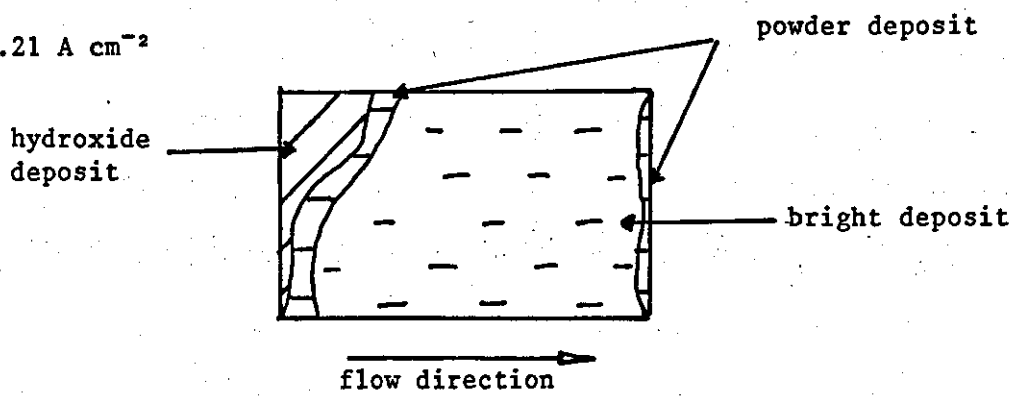


Fig.4.11 continued

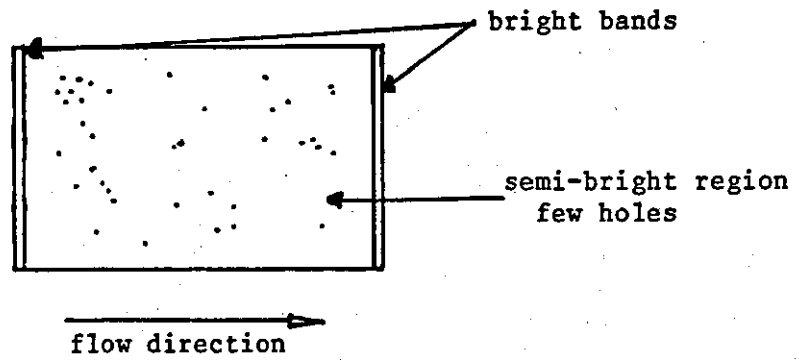
h) Re 10,433, Re 10,745, 0.52 A cm^{-2}



i) Re 10,745, 1.21 A cm^{-2}



j) Re 8,835, 0.52 A cm^{-2}



k) Re 9,509, Re 9,921, 0.52 A cm^{-2}

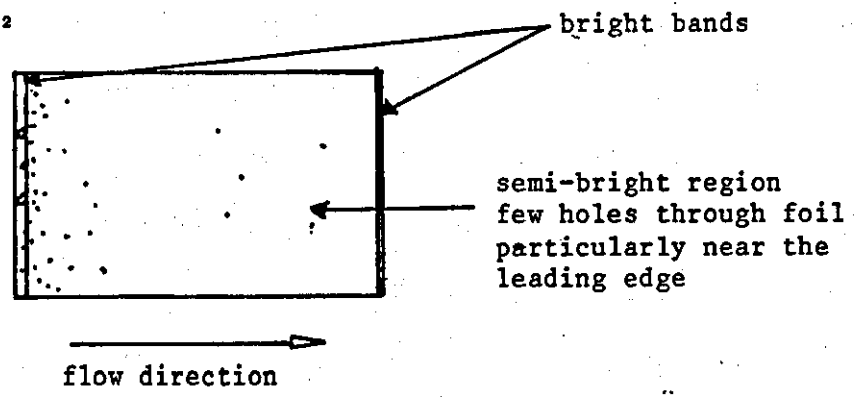


Fig.4.11 continued

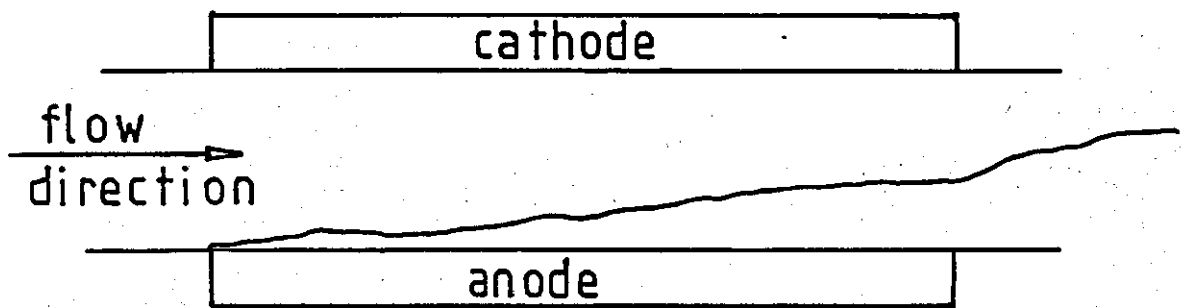


Fig.4.11.1 Visual observation of gas flow pattern during electroforming at $Re\ 4,655$, $0.58\ A\ cm^{-2}$.

what variable they suggest that the maximum current density for good deposits is $\sim 0.6 - 0.7 \text{ A cm}^{-2}$.

At Re 5,166, the deposit was sound at 0.76 A cm^{-2} (Fig.4.11e c.f. Fig.4.11c) with many small perforations through the foil, particularly towards the trailing edge. Narrow bands of bright and dull material were observed near the leading and trailing edges at Re 7,849 and a current density of 0.69 A cm^{-2} , (Fig.4.11f). The deposit was sound over the entire length. The foil was almost completely free of visible porosity although the leading edge was heavily pitted. However, on increasing the current density to 0.95 A cm^{-2} (Fig.4.11g) the deposition of sound nickel was suppressed and only hydroxides were formed. The maximum current density for good deposits was between 0.7 and 0.9 A cm^{-2} .

At Re $\sim 10,500$ and a current density of 0.52 A cm^{-2} , (Fig.4.11h) the foil was sound and semi-bright, with dull bands at the leading and trailing edges. Holes through the foil were not observed. At 1.21 A cm^{-2} (Fig.4.11i), a hydroxide deposit was formed at the leading edge. Further downstream a powder type deposit was formed. Powder deposit was also observed at the trailing edges. The region of sound nickel was bright and free of holes through the foil. Clearly the maximum current density for good deposits was $< 1.0 \text{ A cm}^{-2}$.

It appeared that the current density for sound deposits tended to increase with increasing Reynolds number in this range.

A further series of good deposits $\sim 10\mu\text{m}$ thick was electroformed in the flow range Re 8,835 to Re 9,921 (Table 4.3). The current density, (0.52 A cm^{-2}), was well below the expected maximum current densities for these Reynolds numbers. The current efficiencies were about 93%. The appearance of the deposited foils is shown schematically in Fig.4.11j,k. The deposits were sound over their entire length with bands of brighter nickel at the leading and trailing edges. A few holes through the foil were observed. At the highest Reynolds number the leading edge of the foil was heavily pitted.

Flow rate U cm s ⁻¹	Reynolds number Re	Average current density i/A cm ⁻²	Deposition time t	Average deposit thick- ness μm	Weight deposited g	Current effici- ency %
70.8	8,835	0.52	60	10	0.1348	97
76.2	9,509	0.52	60	11	0.1291	94
79.5	9,921	0.52	60	11	0.1230	89

Table 4.3 Nickel foils deposited under conditions of turbulent flow, Re 8,835 to Re 9,921 at 60°C (Cell 1, L/d_e ~3.3)

A sound nickel foil and a powder type deposit were examined using the S.E.M.

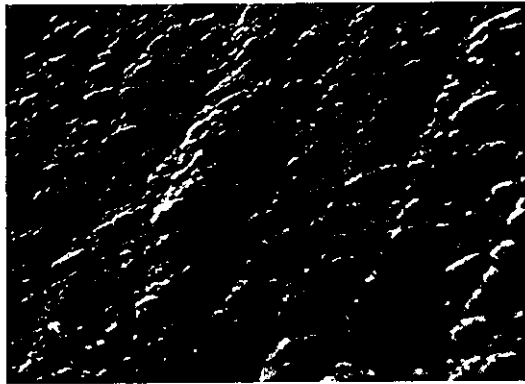
Main deposit region

At 0.52 A cm^{-2} (Re 9,509), the deposit appeared to be sound over the entire electrode length. Downstream of the leading edge ($100\mu\text{m}$), the fine grain structure, typical of this type of deposit, was co-incident with a series of ridge formations (Fig.4.12a). Also present in this region were some bubble induced defects through the foil. Within 0.3 cm of the leading edge, the ridge formations were absent (Fig.4.12b). This area of the deposit was fine structured with grains about $2\mu\text{m}$ in diameter. A similar morphology was maintained up to the trailing edge of the deposit (Figs. 4.12b and 4.13b). Sub-microcavities were distributed over the foil and can be seen as black spots. Centres of increased roughness (Fig.4.12c) in the main deposit region, were an additional feature.

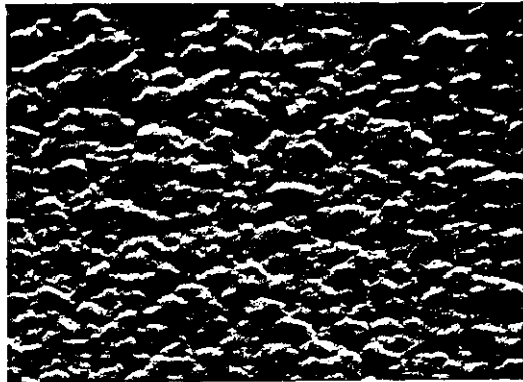
Edge effects

The leading edge of the sound deposit (0.52 A cm^{-2} , Re 9,509) was a bulbous ridge, $\sim 50\mu\text{m}$ wide (Fig.4.14b). In some areas the ridge had a rough granular appearance (Fig.4.14a). Adjacent to the leading edge section, the structure was ridged, with many centres of roughness (Fig.4.14c). Some micro-cracking was evident in between the ridges. Many holes through the foil were observed in this area. The trailing edge of the deposit was comparatively smooth and featureless.

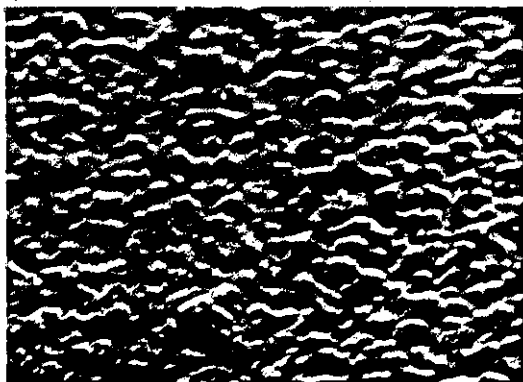
At 0.76 A cm^{-2} (Re 4,655), the current density for a sound deposit was exceeded. Under these conditions a brown powder type material was deposited over about two thirds of the electrode surface. The powder type growth near the centre of the foil, was nodular and rough (Fig.4.15b) when compared to the good deposit (Fig.4.13). This deposit had a coarse grained leading edge section. The irregular grains were $>10\mu\text{m}$ in diameter with well defined grain boundaries (Fig.4.15a). This type of deposit appeared almost 'spongy'.



a) 45° tilt



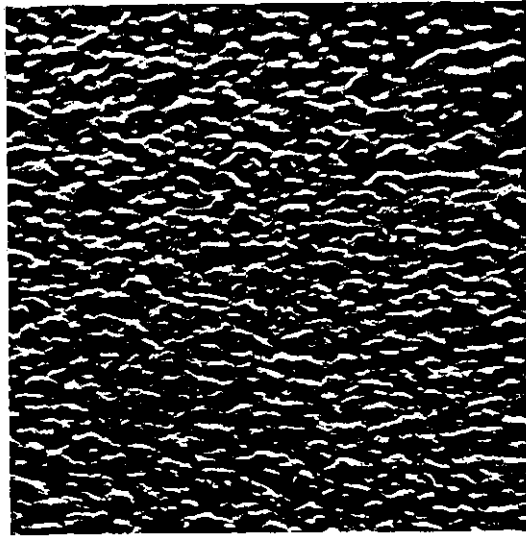
b) 45° tilt



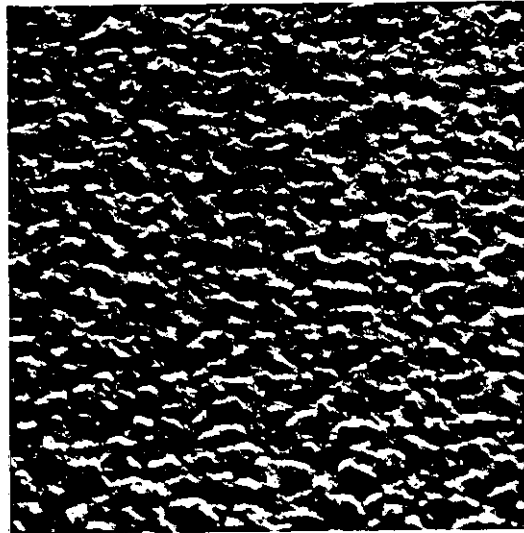
c) 45° tilt

Fig. 4.12 S.E.M. micrographs of surfaces of nickel foils deposited at $Re\ 9,509$, $0.52\ A\ cm^{-2}$ ($\times\ 2,000$)

- a) 0.01 cm from the leading edge
- b) 0.3 cm from the leading edge
- c) 1.8 cm from the leading edge



a) 45° tilt

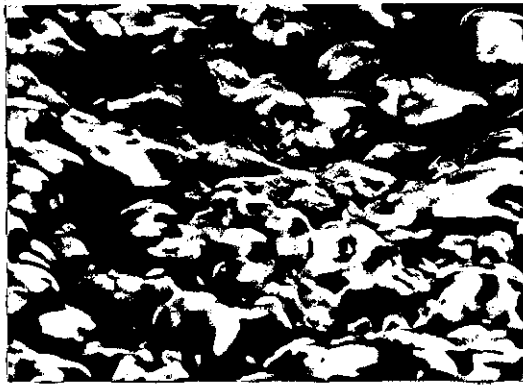


b) 45° tilt

Fig. 4.13 S.E.M. micrographs of surfaces of nickel foils deposited at $Re\ 9,509$, $0.52\ A\ cm^{-2}$ (x 2,000)

a) ~3 cm from leading edge

b) ~4.8 cm from the leading edge



a) 45° tilt



b) 0° tilt



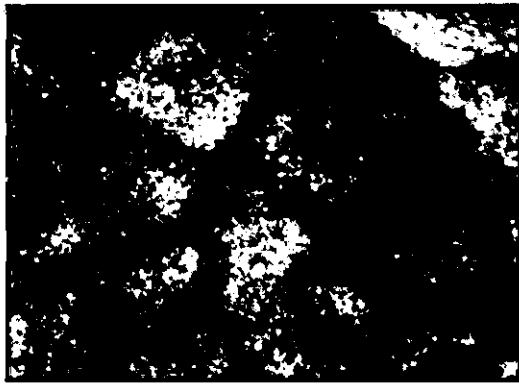
c) 45° tilt

Fig. 4.14 S.E.M. micrographs of surfaces of nickel foils deposited at $Re\ 9,509$, $0.52\ A\ cm^{-2}$.

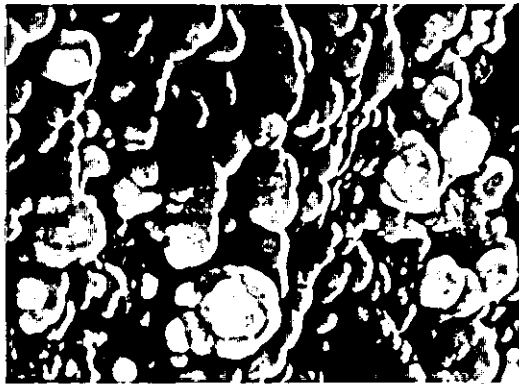
a) Magnified view of leading edge (x 2,000)

b) Leading edge section (x 200)

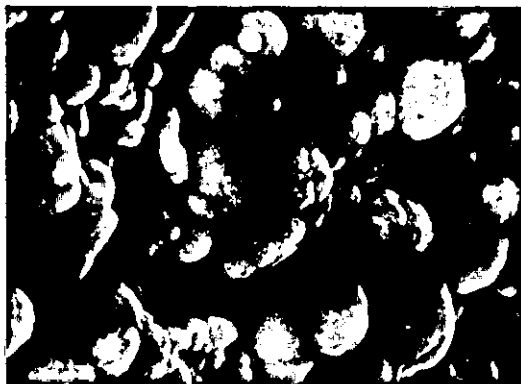
c) Ridged area $\sim 50\ \mu m$ from the leading edge (x 2,000)



a) 30° tilt



b) 30° tilt



c) 30° tilt

Fig. 4.15 S.E.M. micrographs of surface of nickel foils deposited at
Re 4,655, 0.76 A cm^{-2} (x 2,000)

a) ~0.03 cm from leading edge

b) ~3.4 cm from leading edge

c) ~4.99 cm from leading edge

In contrast, the trailing edge of the powder deposit had a more nodular structure. Near the trailing edge, the deposit remained nodular (Fig.4.15c) although the size of the nodules and the degree of coverage of the electrode surface appeared to be greater.

(c) Nickel foils electroformed in the flow range, $Re\ 11,350 \pm 350$

A series of nickel foils, 11-27 μ m in thickness was electroformed over the current density range 0.17 - 1.24 A cm⁻² and details are shown in Table 4.4. The deposits electroformed at current densities <0.81 A cm⁻² appeared to be sound over the entire electrode length and were deposited at current efficiencies close to 100%. The deposits were all semi-bright, increasing in brightness with increasing current density. Narrow bands of brighter material were deposited near the leading and trailing edges of the foils (Fig.4.16).

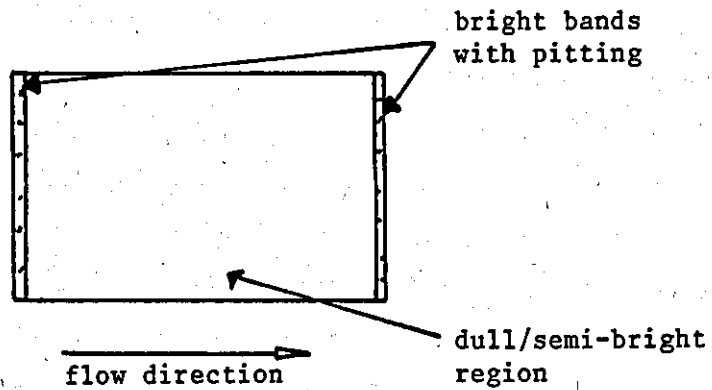
The leading and trailing edges in these deposits were relatively smooth and featureless in the S.E.M., although a few macro-features in the form of mounds ~100 μ m dia. were observed (Fig.4.17). Narrow bands of brighter material were deposited near the leading and trailing edges of the foils. At current densities of 0.17, 0.29 and 0.4 A cm⁻² there was pitting in these bright areas, whereas at 0.6 and 0.76 A cm⁻² there was little evidence of pitting in these areas (Fig.4.16d,e). Micro-hardness profiles measured longitudinally along deposits gave some interesting results for these areas (Fig.4.18). Where the bright bands were pitted e.g. 0.29 A cm⁻² the bright regions appeared to be softer whereas at 0.60 and 0.76 A cm⁻² there was a substantial increase in the microhardness in the bright regions. S.E.M. observations (Fig.4.19a, b) of the bright areas of the leading and trailing edges of deposits at the lower current density showed the presence of a relatively large grain size in the deposits. Comparison of the electron micrograph of the leading edge of the deposit obtained at 0.6 A cm⁻² (Fig.4.19c) showed the grain refinement associated with this deposit. The trailing edge was similar. It thus appears that at lower current densities pitting and relatively large grains give low microhardness values in the bright region whereas the presence of small grains and no pitting at 0.6 - 0.76 A cm⁻² corresponds with the relatively high hardness values observed in these areas.

At the higher current densities (1.04 to 1.24 A cm⁻²), ~90% of the foil surface was of sound appearance and the current efficiency

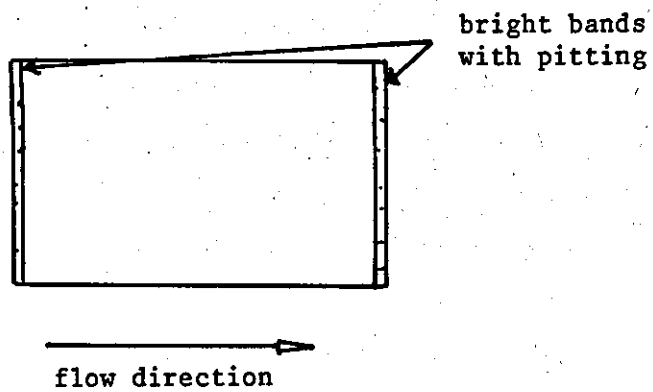
Flow rate U cms ⁻¹	Reynolds number Re	Average current density i/A cm ⁻²	Time t s	Average deposit thick- ness μm	Weight deposited g	Current efficiency %
88.6	11,057	0.17	424	25	0.3272	103
88.6	11,057	0.29	191	19	0.2473	101
89.0	11,106	0.40	193	22	0.3432	101
88.6	11,057	0.60	130	27	-	-
88.6	11,057	0.76	90	23	-	-
88.2	11,007	0.81	91	25	0.3246	100
89.0	11,106	1.04	63	22	-	-
91.7	11,443	1.08	30	11	-	-
92.3	11,518	1.10	31	12	0.1528	102
90.3	11,127	1.24	31	13	-	-
93.6	11,681	1.24	30	13	0.1659	101

Table 4.4 Nickel foils electroformed in turbulent flow, Re 11,007 to Re 11,681. (Cell 1, L/de ~3.3).

a) 0.17 A cm^{-2}



b) 0.29 A cm^{-2}



c) 0.40 A cm^{-2}

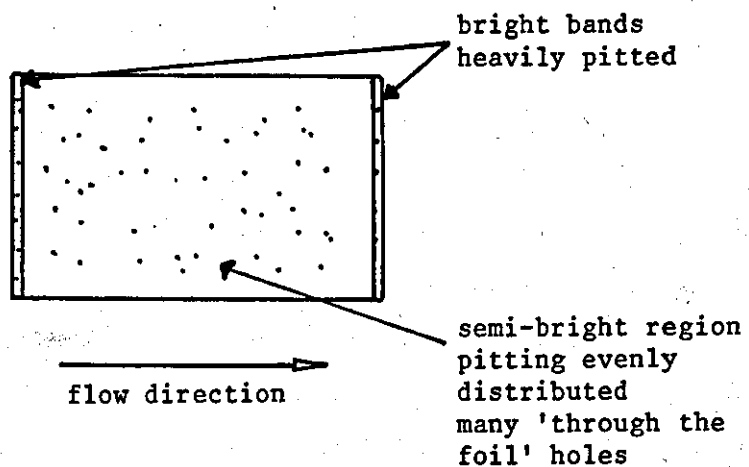
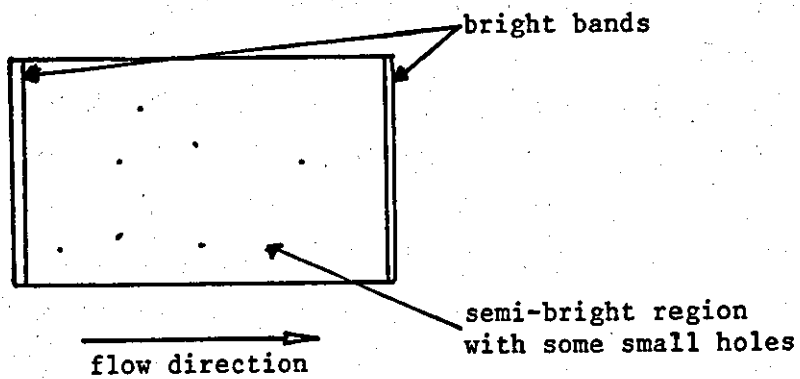
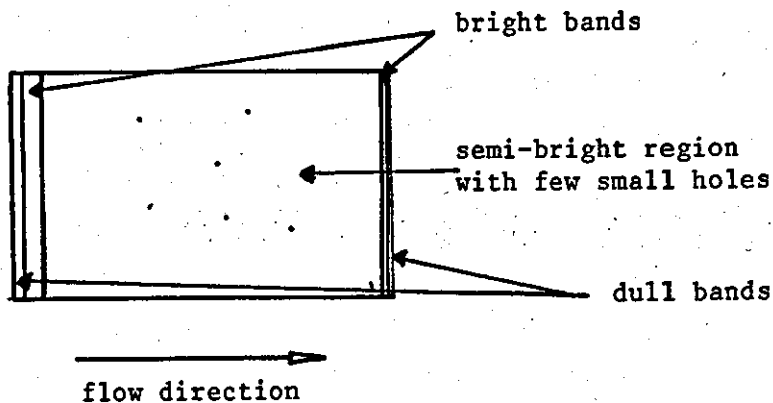


Fig. 4.16 Schematic representation of the visual appearance of nickel foils deposited at $\text{Re } 11,350 \pm 350$

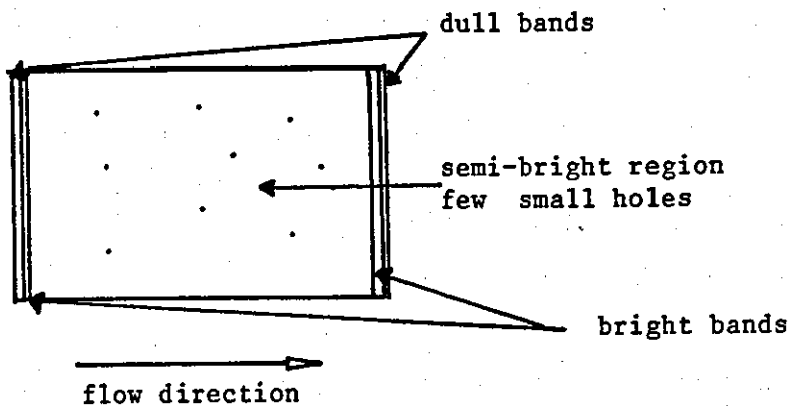
d) 0.60 A cm^{-2}



e) 0.76 A cm^{-2}



f) 0.81 A cm^{-2}



g) 1.04 A cm^{-2}

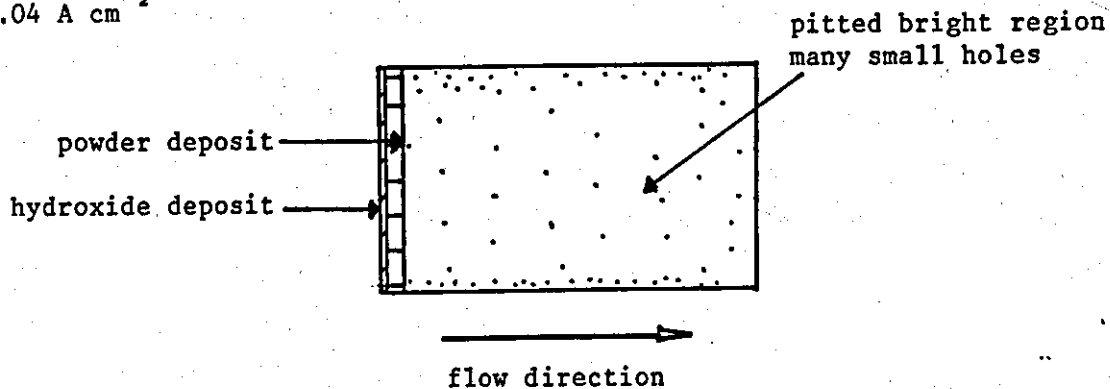
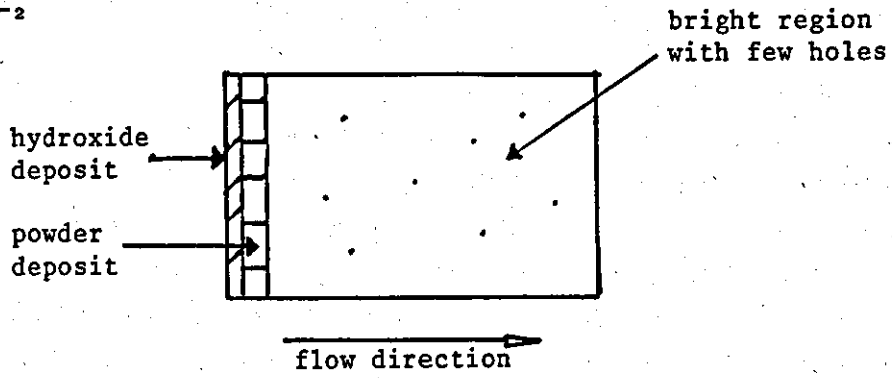
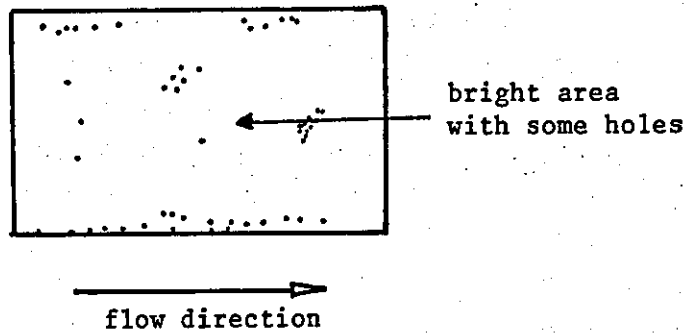


Fig.4.16 continued

h) 1.08 A cm^{-2}

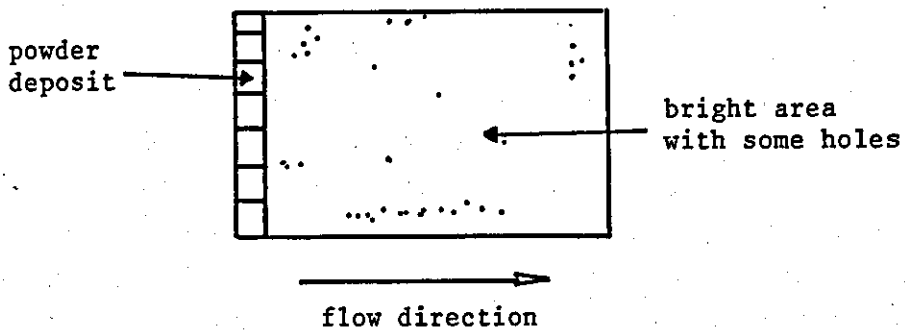


i) 1.10 A cm^{-2}



j) 1.24 A cm^{-2}

i)



ii)

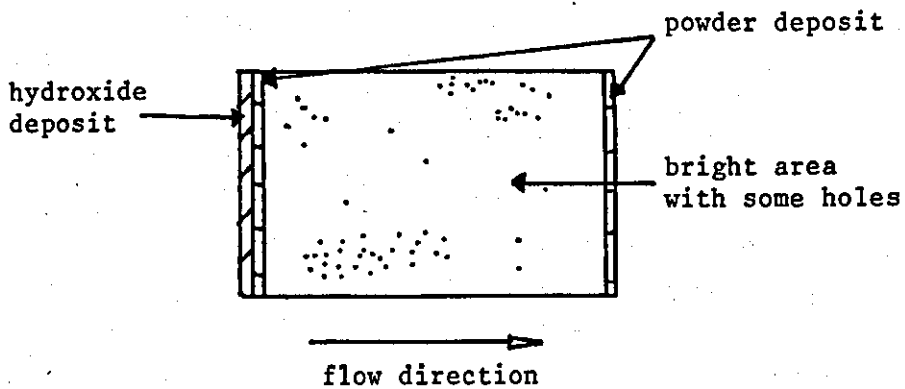


Fig.4.16 continued

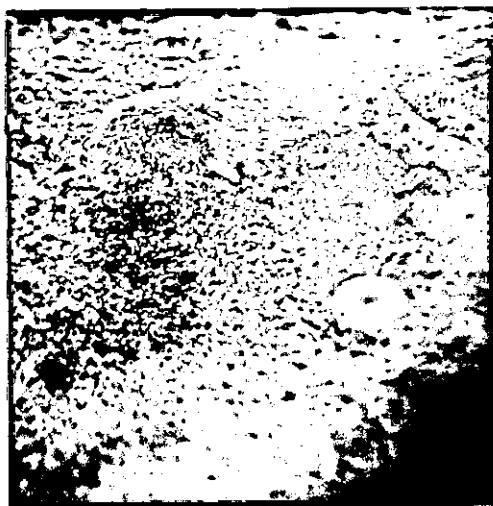


Fig.4.17 S.E.M. micrograph of the surface of the leading edge section of nickel foil deposited at $Re\ 11,350 \pm 350$, $0.17\ A\ cm^{-2}$ (30° tilt, $\times 200$).

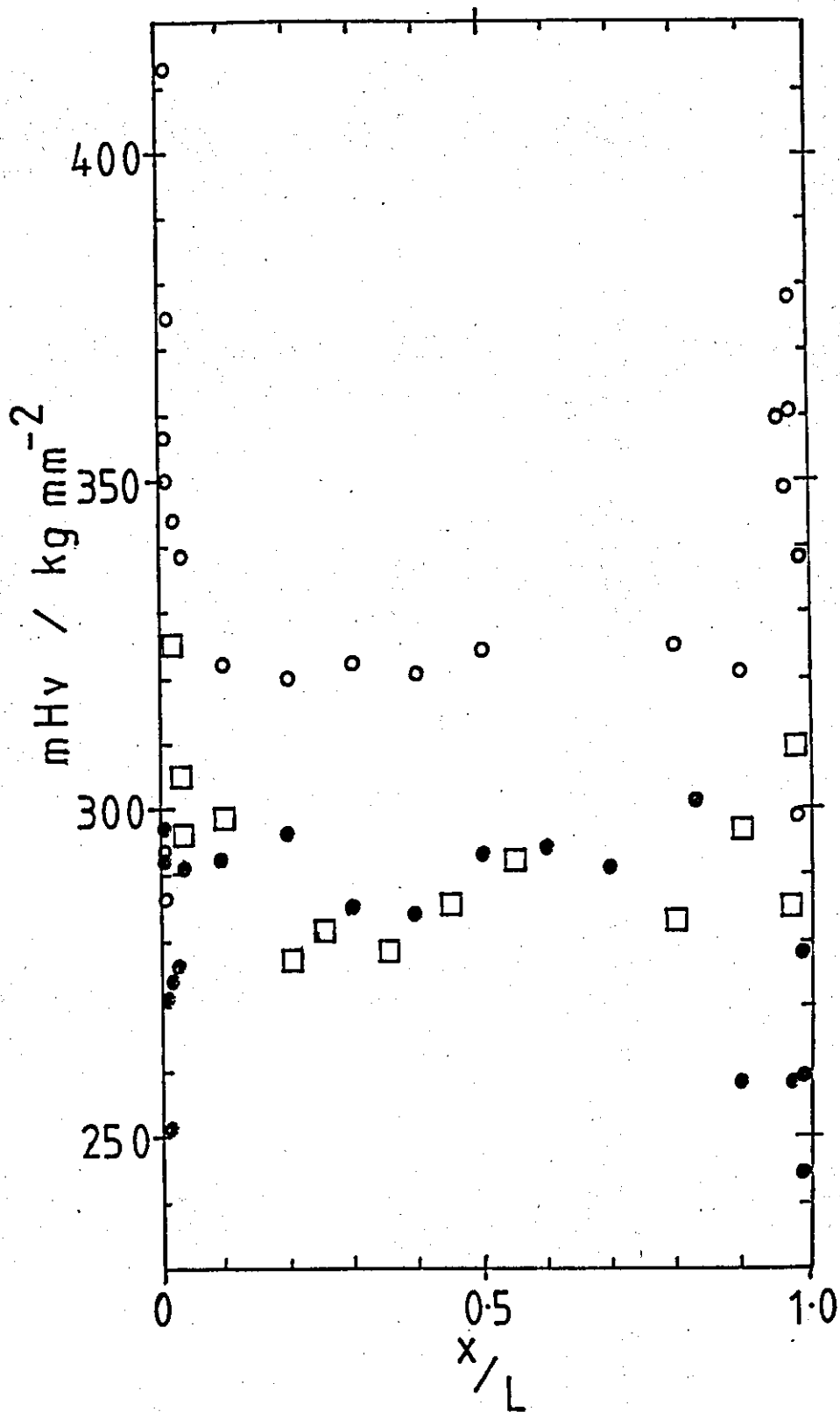


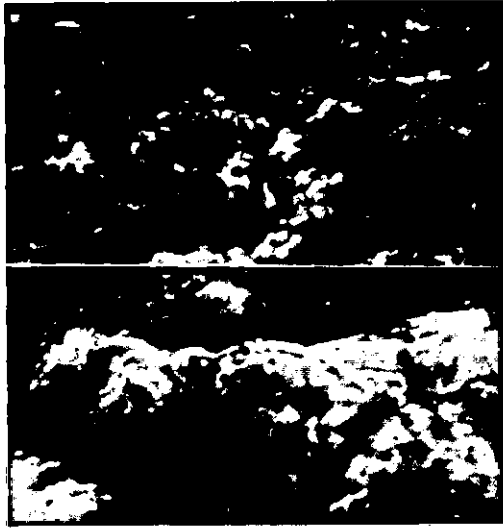
Fig.4.18 Microhardness profiles (mHv) along the length of nickel foils deposited at various current densities. (60°C , $L/d_e 3.3$).

Re $11,350 \pm 350$

● - 0.29 Acm^{-2}

□ - 0.60 Acm^{-2}

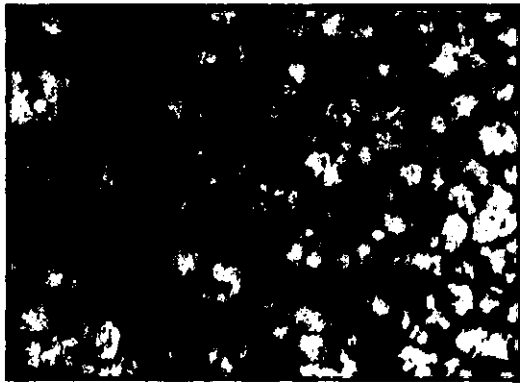
○ - 0.76 Acm^{-2}



a) 30° tilt



b) 30° tilt



c) 0° tilt

Fig.4.19 S.E.M. micrographs of the surfaces of nickel foils deposited at $Re\ 11,350 \pm 350$.

- a) $0.17\ A\ cm^{-2}$, 0.02 cm from the leading edge
(Top: x 2,000; bottom: x 10,000)
- b) $0.17\ A\ cm^{-2}$, 0.02 cm from the trailing edge
(Top: x 2,000; bottom: x 10,000)
- c) $0.60\ A\ cm^{-2}$, 0.05 cm from the leading edge
(x 2,000)

remained close to 100%. The areas of main deposit were brighter than those produced at lower deposition rates. Powder type deposits were formed at the leading edge of most foils (Fig.4.16g,h,j). At 1.04 A cm^{-2} , a narrow band ($200\mu\text{m}$) of green hydroxide was found at the leading edge (Fig.4.19a). Adjacent to this area, powder structures were observed. Along the trailing edge a ridge of bulbous material was observed (Fig.4.20b). Close to both the edges, the structure was very fine grained with a few microcavities (Fig.4.20c). At the high current density of 1.24 A cm^{-2} powdery deposits were also observed at the trailing edge (Fig.4.16i).

Main deposit region

In all deposits over the current density range ($0.17 - 1.04 \text{ A cm}^{-2}$), the main deposit structures formed over $>90\%$ of the surface area of the foil were of relatively uniform grain size. Surface S.E.M. examinations were made and typical grain structures are shown in Fig. 4.21. At 0.17 A cm^{-2} the grains were reasonably well defined and were up to $10\mu\text{m}$ in diameter. There was also evidence of sub-grain structures (Fig.4.21a). As the current density was increased to 0.6 A cm^{-2} the grains were a little irregular but the average grain size had decreased to $\sim 5\mu\text{m}$ in diameter (Fig.4.20b). Although sub-structures were less evident, examination of the surfaces at higher magnifications suggested the presence of some grain boundary defects or cavities. At 1.04 A cm^{-2} (Fig.4.21c) there was considerable grain refinement and the structure was regular with a grain size of $\sim 3\mu\text{m}$ diameter.

The micro-hardnesses of foils were measured along the length of the foils for foils deposited at 0.29 , 0.60 and 0.76 A cm^{-2} and the results are shown in Fig.4.18 and it is clear that there was relatively little variation in hardness along the length of the foils and average values of 288 ± 13 , 281 ± 3 , and $322 \pm 2 \text{ Kg mm}^{-2}$ were obtained at the above current densities respectively. An average value of $261 \pm 11 \text{ Kg mm}^{-2}$ was obtained at 0.17 A cm^{-2} . These results suggest that there is a considerable increase in hardness of the deposits at high current density corresponding to a decrease in the grain size from $\sim 5\mu\text{m}$ to $3\mu\text{m}$. There was also evidence to suggest that there was an increase in grain



a) 0° tilt



b) 0° tilt



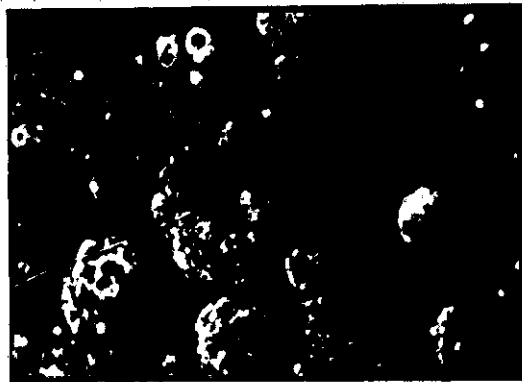
c) 0° tilt

Fig.4.20 S.E.M. micrographs of the surface of nickel foil deposited at $Re\ 11,350 \pm 350$, $1.04\ A\ cm^{-2}$.

a) Hydroxide deposit at leading edge of foil
(x 1,000)

b) Trailing edge section (x 200)

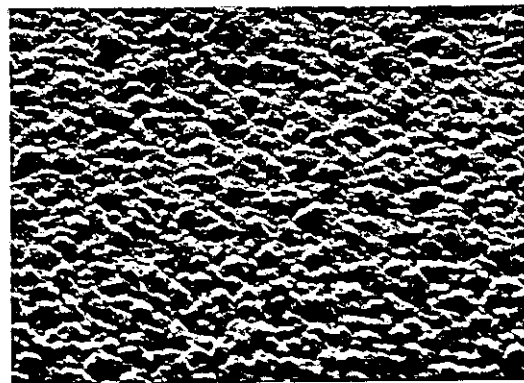
c) 0.01 cm from trailing edge (x 10,000)



a) 30° tilt



b) 0° tilt



c) 45° tilt

Fig.4.21 S.E.M. micrographs of the surfaces of nickel foils deposited at $Re\ 11,350 \pm 350$ ($\times 2,000$), Main deposit sections.

a) $0.17\ A\ cm^{-2}$

b) $0.60\ A\ cm^{-2}$

c) $1.04\ A\ cm^{-2}$

boundary cavitation at current densities $> 1.04 \text{ A cm}^{-2}$, and (Fig.4.22) that there may have been some interference in the deposition process by anodically evolved gas which came into contact with the downstream half of the electrode.

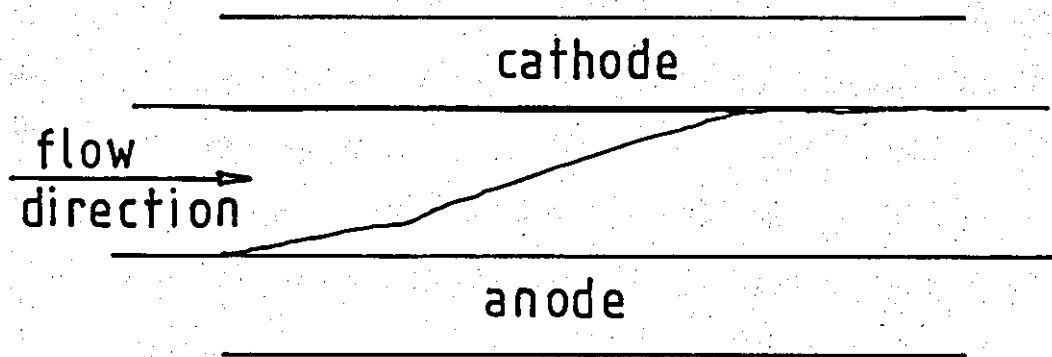


Fig.4.22 Visual observations of gas flow pattern during electroforming at $Re\ 11,350 \pm 350$, $1.04\ A\ cm^{-2}$.

(d) Nickel electroforms deposited in the flow range $Re\ 13,000 \pm 300$

A series of nickel foils $11 \pm 5\ \mu\text{m}$ in thickness was electroformed over the current density range 0.14 to $1.38\ \text{A cm}^{-2}$ as shown in Table 4.5. The main characteristics of these deposits are summarised in Fig.4.23. Electroforms were deposited at current efficiencies of $96 \pm 3\%$. The brightness of the foils increased with increasing current density. At $1.04\ \text{A cm}^{-2}$ the deposit was bright over the main deposit region with narrow bands of semi-bright material at the leading and trailing edges of the foil (Fig.4.23d). At $1.38\ \text{A cm}^{-2}$, the deposit was sound over 95% of the surface, but with bands of a grey-brown powder deposit at the leading and trailing edges (Fig.4.23e).

Large volumes of gas were evolved at the high current densities. The rapid flow rate resulted in the removal of the anode gas away from both electrodes into the inter-electrode gap further downstream before the anodically evolved gas bubbles could reach the working electrode. Cathode hydrogen gas streamed along the cathode, close to the electrode surface, but adhesion of large gas bubbles was not observed. Pitting of the foil was particularly prevalent at low current density ($0.14\ \text{A cm}^{-2}$). Many lines of holes through the foil could be seen (Fig.4.23a). At current densities $>0.36\ \text{A cm}^{-2}$ the number of holes was considerably reduced (in some cases <10 holes per foil) (Fig.4.23b-c). The leading edge of the foil deposited at $0.52\ \text{A cm}^{-2}$ was heavily pitted (Fig.4.23c). However, this effect was not observed at higher current densities (Fig. 4.23d,e). The foils deposited at 0.52 and $1.04\ \text{A cm}^{-2}$ were examined using the S.E.M. in order to obtain more detailed information.

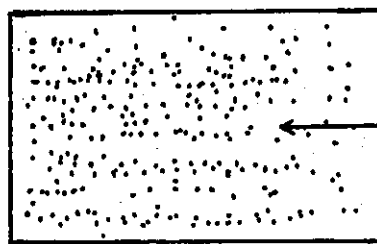
Main deposit region

A sound deposit of relatively fine grain structure was found over $>95\%$ of the surface area for both foils (Figs.4.24 and 4.25). At $0.52\ \text{A cm}^{-2}$ the structure was of uniform grain size 2 to $5\ \mu\text{m}$ in dia. In some areas of the foil ($\sim 0.5\ \text{cm}$ from leading edge) the grain boundaries appeared to be wide and this suggested that there may be some grooving or possibly porosity. These features were much less evident further downstream (Fig.4.24a,b). An increase in current density to $1.04\ \text{A cm}^{-2}$

Flow rate U cms ⁻¹	Reynolds number Re	Average current density i/A cm ⁻²	Deposition time t s	Average deposit thick- ness d/μm	Weight deposited g	Current effici- ency %
102.3	12,766	0.14	120	6	0.0730	99
106.0	13,228	0.36	120	15	0.1846	97
106.8	13,328	0.52	60	11	0.1187	87
106.8	13,328	0.52	90	16	-	-
106.8	13,328	0.52	60	11	0.1302	95
104.7	13,066	1.04	30	11	0.1276	93
104.7	13,066	1.04	30	11	0.1317	96
104.7	13,066	1.38	17	8	-	-

Table 4.5 Nickel foils deposited under conditions of turbulent flow, Re 12,766 to Re 13,328 (Cell 1, $L/d_e \sim 3.3$)

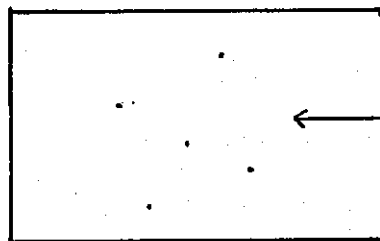
a) 0.14 A cm^{-2}



bright - many holes

flow direction

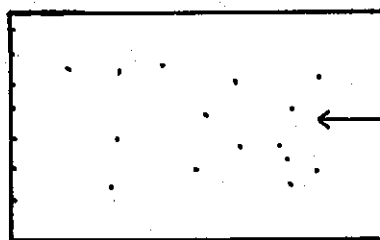
b) 0.36 A cm^{-2}



semi-bright region

flow direction

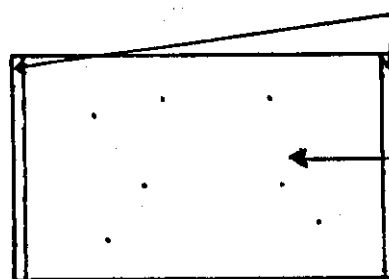
c) 0.52 A cm^{-2}



semi-bright region

flow direction

d) 1.04 A cm^{-2}

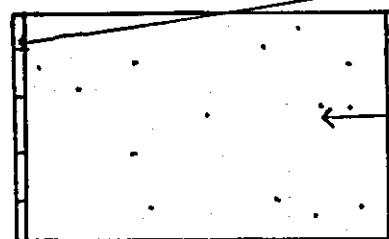


semi bright bands

bright region

flow direction

e) 1.38 A cm^{-2}

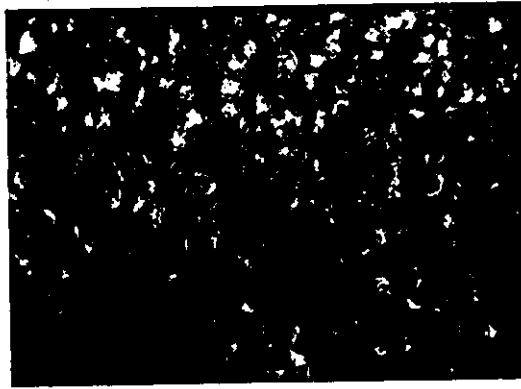


powder deposit

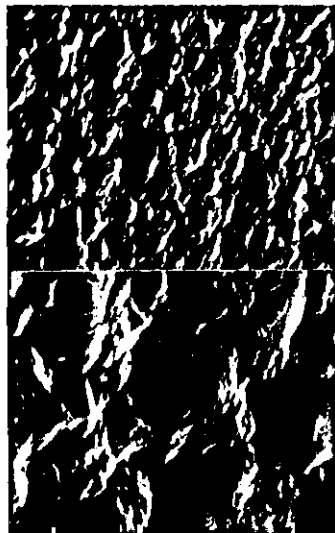
bright region

flow direction

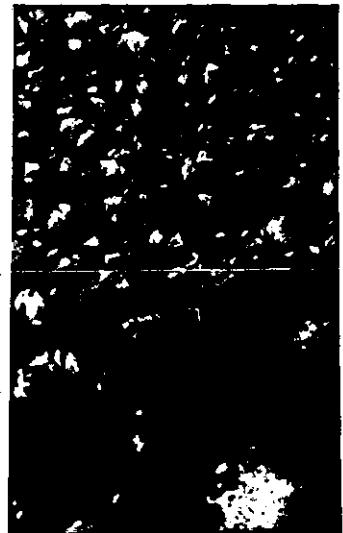
Fig.4.23 Schematic representation of the visual appearance of nickel foils deposited at $Re\ 13,000 \pm 300$



a) 0° tilt

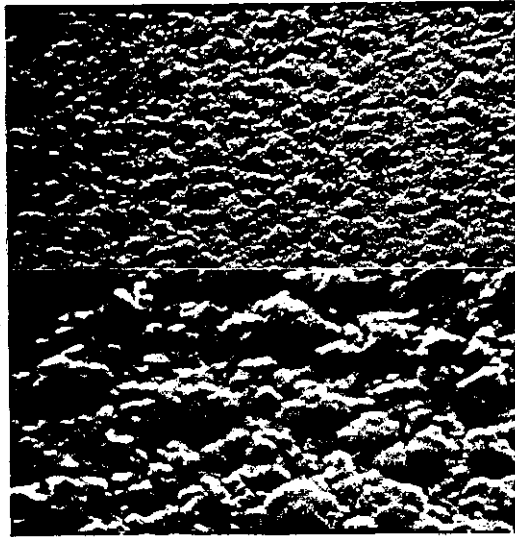


b) 35° tilt



0° tilt

Fig. 4.24 S.E.M. micrographs of surfaces of nickel foils deposited at the $13,000 \pm 300$, 0.052 A cm^{-2} .
a) 0.5 cm from the leading edge ($\times 2,000$)
b) Main deposit (Top: $\times 2,000$; bottom: $\times 10,000$)



a) 45° tilt



b) 45° tilt

Fig.4.25 S.E.M. micrographs of surfaces of nickel foil deposited at $Re\ 13,000 \pm 300$, $1.04\ A\ cm^{-2}$

a) 1.5 cm from the leading edge
(Top: x 2,000; bottom: x 5,000)

b) 3.1 cm from the leading edge (x 2,000)

resulted in a decrease in grain size to 1-2 μm in dia. Some larger grains were evenly distributed within a matrix of smaller grains (Fig.4.25a). Within the main deposit region a few micro-cavities were observed (Fig.4.25b). A few centres of roughness were also evident in this area, a common feature of some of the high current density deposits.

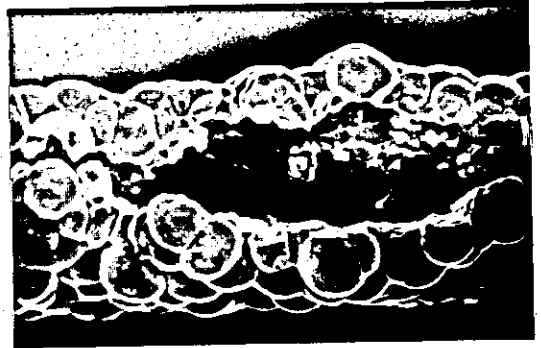
Edge effects

At both current densities, the leading edge effects were more prominent. At 0.52 A cm^{-2} the foil edge was relatively smooth, although many ridge-like features parallel to the flow direction and surface reliefs, were formed adjacent to the edge. This area was also heavily pitted. The ridging, parallel to the flow direction, extended up to 500 μm downstream. The ridge areas were composed of larger grains and mounds 10-30 μm in diameter (Fig.4.26a) with some sub-grain structure. Corresponding features were absent at 1.04 A cm^{-2} , where the leading edge section exhibited a bulbous type structure (as viewed in plan) about 150 μm in width (Fig.4.26b). Where the bulbous edge had cracked, there was evidence of nickel salt (possibly hydroxide) deposition within the fissure. Pitting or holes through the foil were not found in this area. At higher magnification (Fig.4.26c) deposit close to the leading edge was found to consist of very fine uniform grains of sub-micron dimensions. A few micro-cavities were observed. At a distance of 1000 μm from the leading edge, the structure showed a slight increase in grain size to about 1 μm (Fig.4.25d).

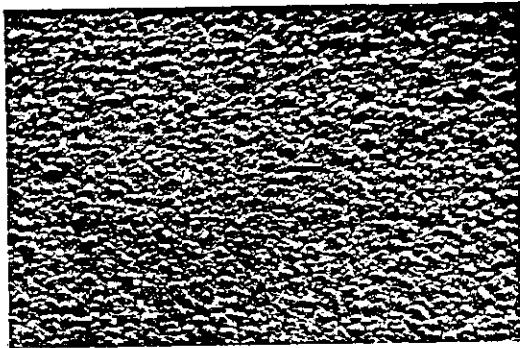
The trailing edge sections of both foils were fine grained and relatively featureless. At 0.52 A cm^{-2} , the trailing edge showed a slight ridge-type character (Fig.4.27). At higher magnification a few micro-cavities were observed (Fig.4.27d).



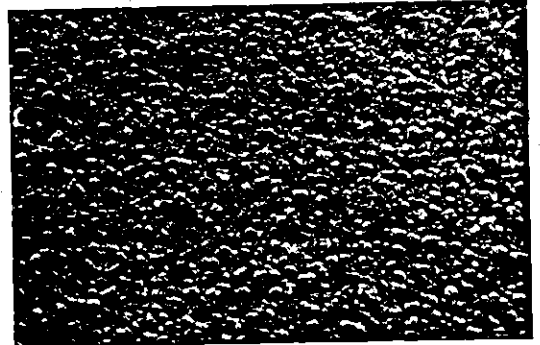
a) 0° tilt



b) 0° tilt



c) 45° tilt



d) 45° tilt

Fig.4.26 S.E.M. micrographs of surfaces of nickel foils deposited at $Re 13,000 \pm 300$

a) 0.52 A cm^{-2} , 0.015cm from the leading edge
(x 2,000)

b) 1.04 A cm^{-2} , leading edge (x 200)

c) 1.04 A cm^{-2} , 0.03 cm from the leading edge
(x 2,000)

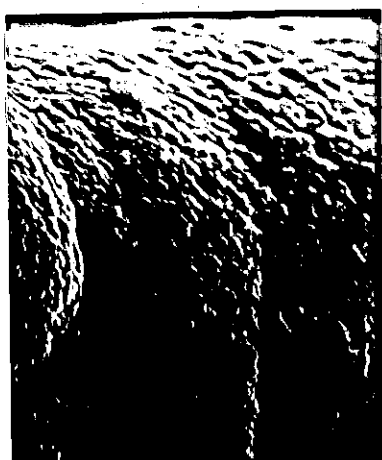
d) 1.04 A cm^{-2} , 0.1 cm from the leading edge
(x 2,000)



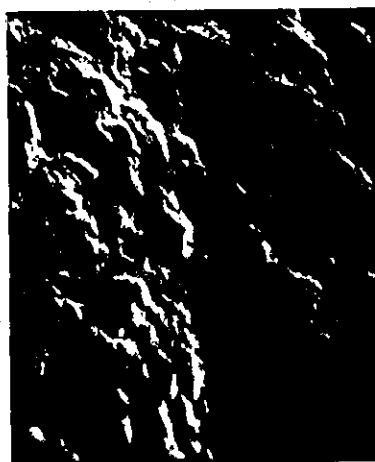
a) 45° tilt, x 2,000



b) 45° tilt, x 10,000



c) 35° tilt, x 2,000



d) 35° tilt, x 10,000

Fig.4.27. S.E.M. micrographs of the surface of the trailing edge sections of nickel foils deposited at $Re\ 13,000 \pm 300$, $0.52\ A\ cm^{-2}$.

4.1.3 Summary of the results and discussion of the limitation of the cell design

This section of the research programme allowed experience to be gained in relation to cell operation and control and the techniques associated with the evaluation of deposits. There were a number of major features which emerged from the programme and these can be summarised as follows:

- (a) The cathode current efficiency for nickel deposition was ~95% under all deposition conditions.
- (b) Gas evolution at the anode was troublesome under conditions of laminar flow and at higher current densities in turbulent flow and under some conditions anodically evolved gas reached the downstream end of the cathode.
- (c) Under all flow conditions relatively fine-grained deposits were obtained in the main central length of the cathode.
- (d) Bright deposits were obtained at high Re and current density in turbulent flow.
- (e) The microhardness and brightness of deposits increased with decreasing grain size.
- (f) There were perturbations in foil structure in the entry (leading) and exit regions (trailing) of the cathode where mass transfer conditions were non-uniform.
- (g) In the leading edge regions there was pitting and formation of large pores in the foils.

Overall the studies at this stage indicated that deposits of fine grain structure could be obtained at high Re at current densities up to $\sim 1 \text{ A cm}^{-2}$ without the presence of addition agents. The small pores observed in the main areas of the foils were not considered serious as there was no addition of anti-pitting agents to the electrolyte.

It was of considerable interest to gain some impression of the relationship between the maximum current density for sound deposits (i_{\max}) and Reynolds number to see if there was any correlation of the type which might be expected between i_L and Re . This of course assumes that the controlling variable for sound deposits is mass transport. In Fig.4.28 the nature of the deposit i.e. sound (uniform fine grained) or unsound (powdery) is plotted from the data obtained in the experimental studies. The solid line A-A in Fig.4.28 of slope 0.67 is in approximate agreement with the division between sound and unsound deposits obtained under turbulent flow conditions. An approximate theoretical mass transfer limited current density was calculated from the design equations for the cell (page 115) and the limiting current densities are shown in B-B in Fig.4.28. As can be seen the experimentally determined relationship indicates that the maximum current densities for sound deposits are less than those predicted by theoretical analysis.

In laminar flow the theoretical line C-C in Fig.4.28 has a slope of 0.33 and the experimental points indicate that sound nickel deposits were obtained at higher current densities than might have been expected. These effects may be associated with the influence of gas evolution on the mass transport processes.

Overall these results indicated the need for modifications to the cell. These included:

- (a) the need to separate anodically evolved gas from the region of the cathode;
- (b) the need to provide facilities for the use of longer electrodes which would allow both long and short electrode studies to be made.

These features with other improvements were incorporated into the design of the Mark 2, cell details of which follow.

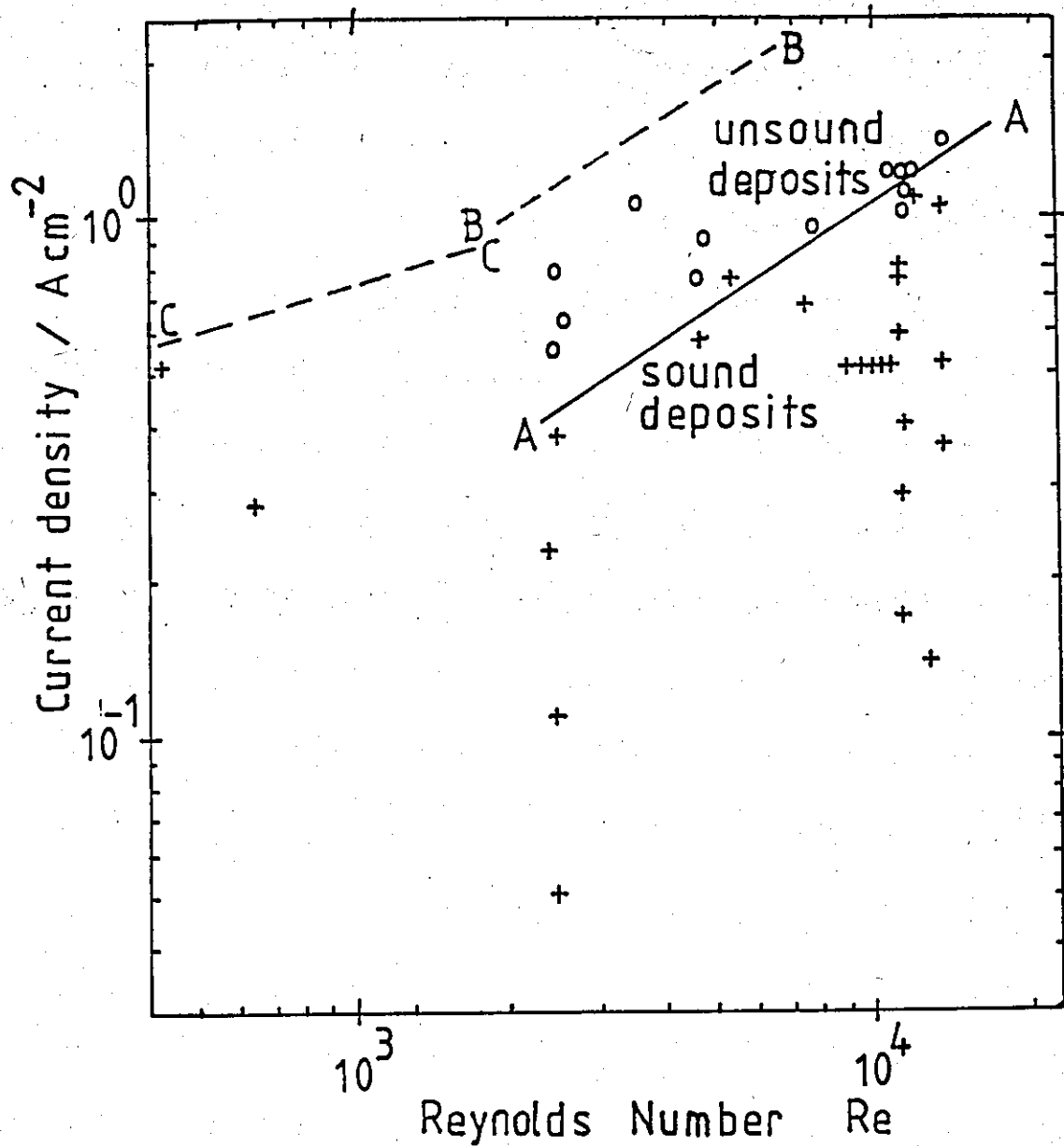


Fig. 4.28 The relationship between the flow rate (Reynolds Number) and the maximum current density (i_{\max}) for a sound deposit

$$T \sim 60^\circ\text{C}, \quad L/d_e \sim 3.3$$

- o - powdery and/or hydroxide deposit
- + - coherent nickel electroform

4.2 Studies of the mass transport characteristics of the Mark 2 Parallel Plate Cell and cathode current distribution at segmented cathodes using a $\text{CuSO}_4 - \text{H}_2\text{SO}_4$ electrolyte

The results of the nickel foil preparation studies in Section 4.1 indicated some differences between the experimental results and those predicted by the design equations. In particular it was clear that: (i) the experimental values of i_{max} for a good deposit were lower than expected; and (ii) the slope of the log-log relationship between i_{max} and R_e was lower than the theoretical value. From these observations it seemed essential to establish the mass transport characteristics of Cell 2 independently from the nickel system. It was decided to use an acid copper sulphate electrolyte (0.014 CuSO_4 in 1.5M H_2SO_4) since a wide range of physical property data is available and it is well known that limiting current densities are clearly defined. The first sub-section describes the mass transport studies.

It will be seen later that studies of the current distribution at cathodes during nickel deposition gave interesting results and it became clear that data for the more simple copper system would provide a valuable comparison. Details of the results of these studies in the second sub-section.

4.2.1 Mass transport studies using the $\text{CuSO}_4 - \text{H}_2\text{SO}_4$ electrolyte

For convenience the work was divided into two flow regimes as follows:

- a) laminar flow (Re 243 - 2,400); and
- b) turbulent flow (Re 2,872 to Re 30,837).

For each set of experimental conditions, the cathodic polarisation curve was determined and the limiting current density measured.

(a) Mass transport under conditions of laminar flow

The investigation is in two parts. Limiting current densities were measured at the maximum electrode length using a soluble copper anode and a copper cathode of the same length (9.74 cm, $L/d_e \sim 11.4$).

The limiting current densities were measured as a function of flow rate (and hence Re) at constant temperature for temperatures of 28°, 32°, 40°, 50° and 60°C. The object of this is to demonstrate that normal mass transfer characteristics applied in the cell. Some additional experiments using cathodes 2.4 cm long ($L/d_e = 2.8$) in length at $36 \pm 1^\circ C$ were carried out for comparison with the results of the long electrode studies.

The relationship between the limiting current density and the electrode length (L/d_e 0.6 to 11.4) was measured at a constant flow rate (Re 1,018 \pm 96) and temperature ($33 \pm 1^\circ C$).

The results of all the experimental results from the studies carried out in laminar flow were then correlated by a single equation using dimensionless numbers.

The relationship between the limiting current density and the flow rate

The cathodic polarisation behaviour is shown in Figs.4.29 - 4.34 for the maximum electrode length ($L/d_e \sim 11.4$) and a series of electrolyte temperatures and flow rates. For each set of measurements, the current density rapidly increased over the initial 50 mV of overpotential (A-A in Fig.4.29). The current density then increased less rapidly to a long plateau of approximately constant current density at $E < -0.2V$ (versus Cu reference electrode). At $E < -0.55V$ (B-C in Fig.4.29) the current density again increased as the secondary reaction of hydrogen evolution predominated (C-D in Fig.4.29). At a constant temperature the limiting current density tended to increase with increasing flow velocity (e.g. Fig.4.29). The copper deposits formed were smooth and featureless.

Similar polarisation curves for a cathode length of 2.8 d_e at 37°C are shown in Figs.4.35 to 4.38.

From the polarisation curves, the limiting current densities were measured at $E = -0.45V$. The values of i_L are summarised in Table 4.6 for $L/d_e = 11.4$ and Table 4.7 for $L/d_e = 2.8$.

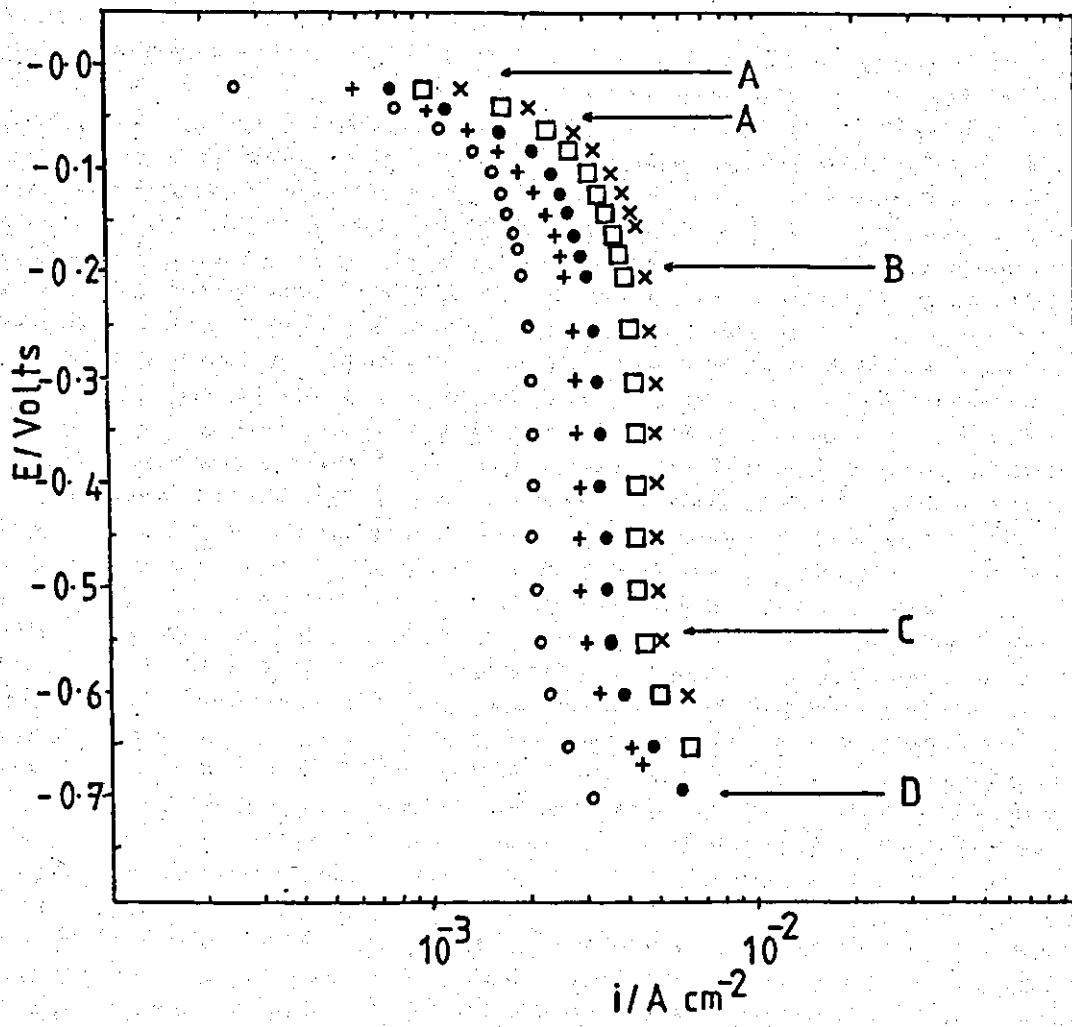


Fig.4.29 Cathodic polarisation during the electrolysis of 0.014 M copper sulphate electrolyte in laminar flow. Effect of electrolyte flow rate

$T = 60.0 \pm 0.1^\circ\text{C}$, $L/d_e \sim 11.4$

1L	○	-	1.39 cm s^{-1}	(Re 243)
2L	+	-	4.44 cm s^{-1}	(Re 777)
3L	●	-	7.67 cm s^{-1}	(Re 1,341)
4L	□	-	10.9 cm s^{-1}	(Re 1,904)
5L	X	-	14.4 cm s^{-1}	(Re 2,517)

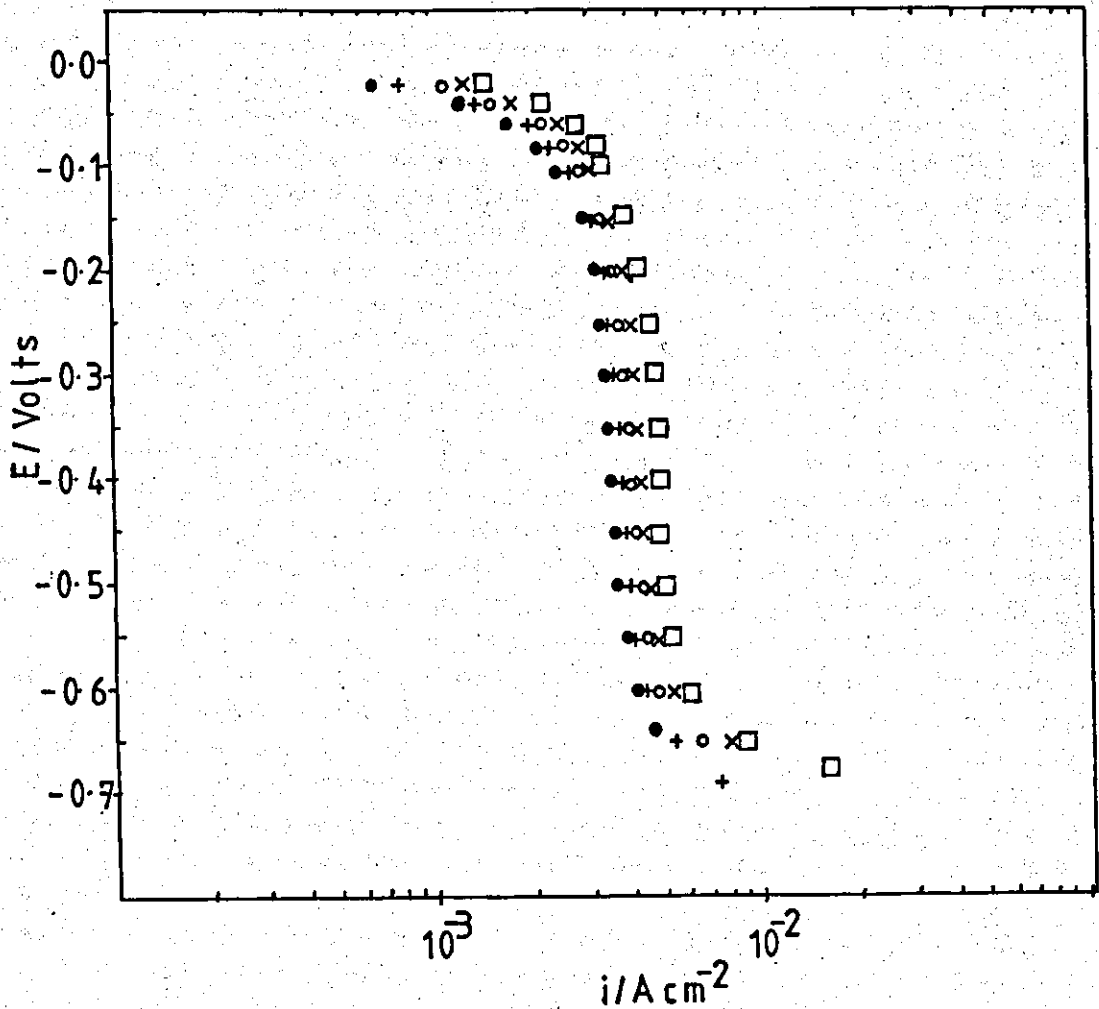


Fig.4.30 Cathodic polarisation during the electrolysis of ~ 0.014 M copper sulphate electrolyte in laminar flow. Effect of electrolyte flow rate

$$T = 50.2 \pm 0.9^\circ\text{C}, L/d_e \sim 11.4$$

6L	●	-	11.7 cm s ⁻¹ (Re 1,587)
7L	+	-	12.8 cm s ⁻¹ (Re 1,738)
8L	○	-	15.0 cm s ⁻¹ (Re 2,040)
9L	X	-	16.7 cm s ⁻¹ (Re 2,267)
10L	□	-	18.9 cm s ⁻¹ (Re 2,569)

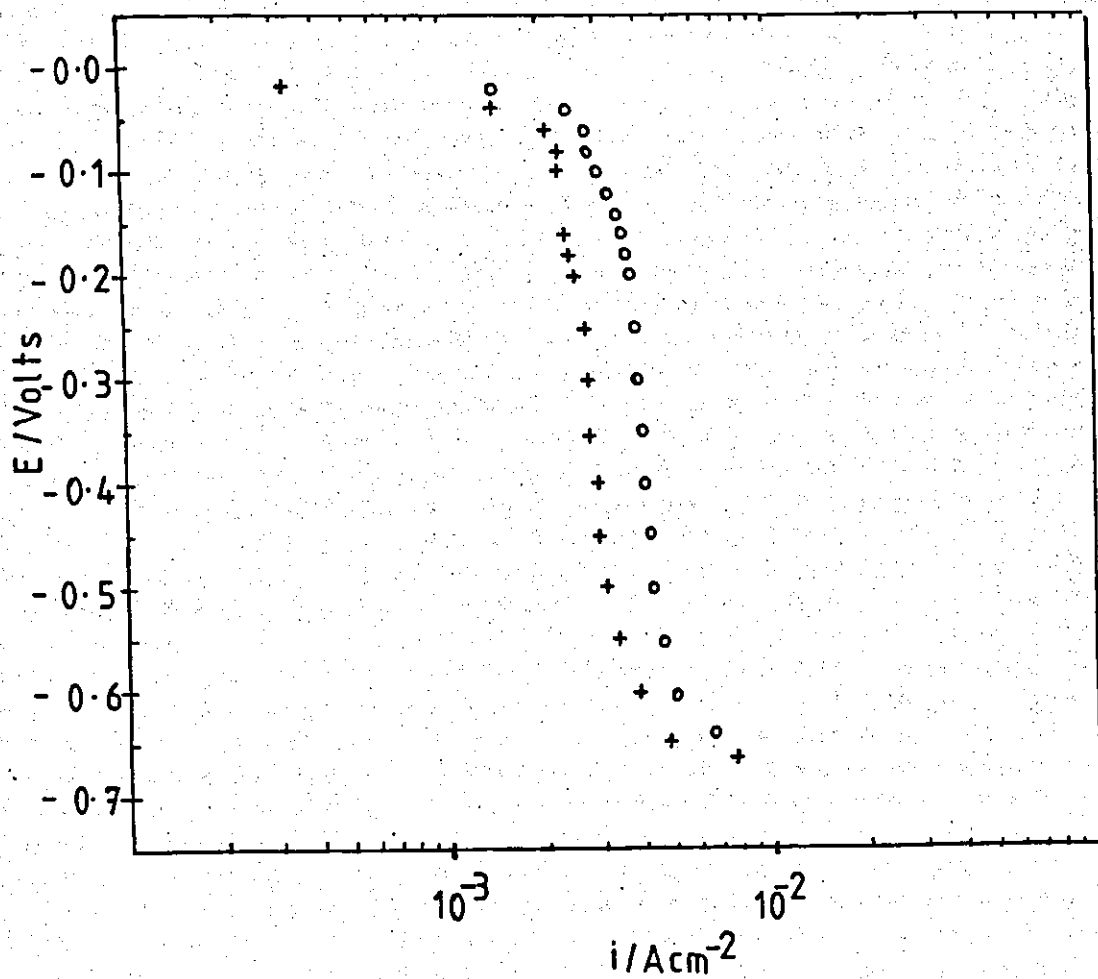


Fig.4.31 Cathodic polarisation during the electrolysis of ~ 0.014 M copper sulphate electrolyte in laminar flow.

$$T = 40^\circ\text{C}, \quad L/d_e \sim 11.4$$

11L - + - 11.1 cm s^{-1} (Re 1,221)

12L - o - 22.2 cm s^{-1} (Re 2,442)

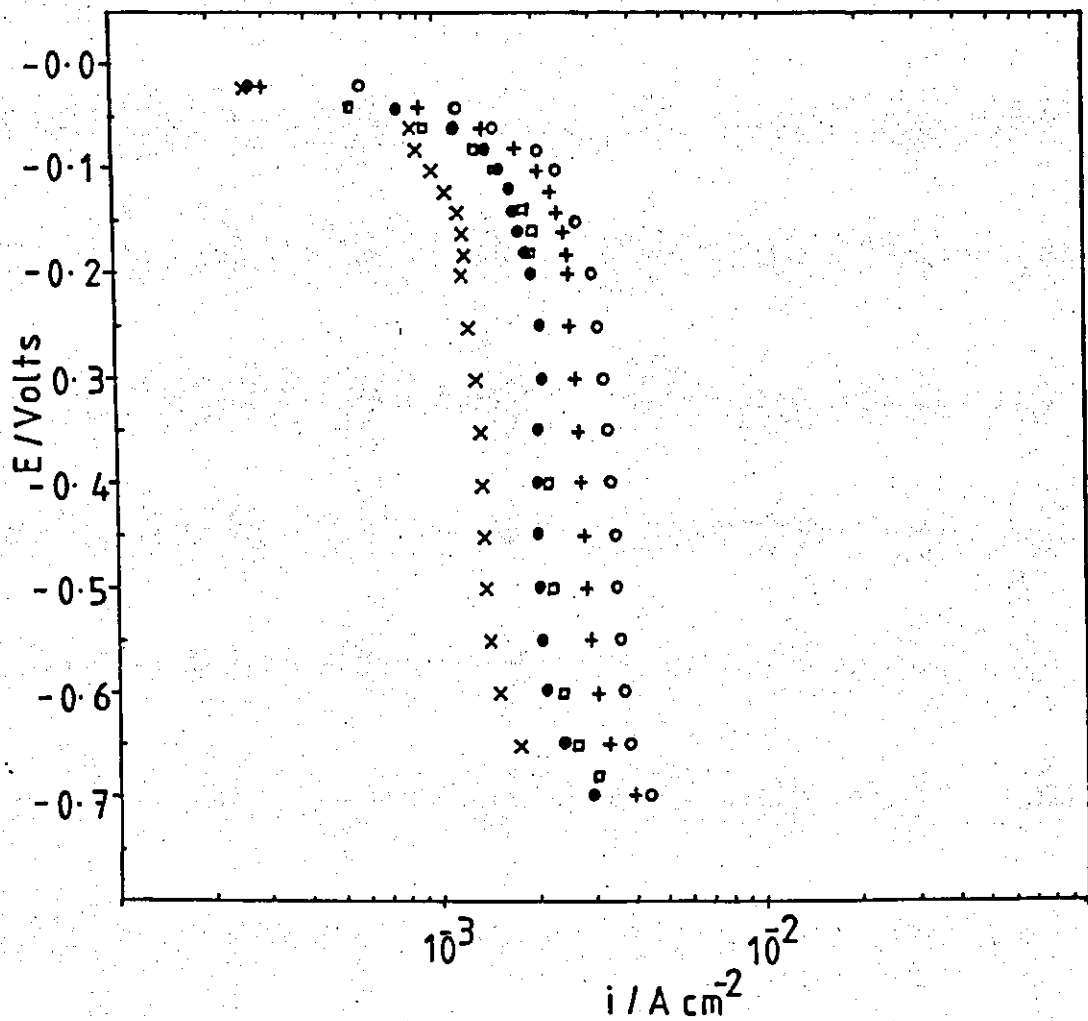


Fig.4.32 Cathodic polarisation during the electrolysis of 0.014M copper sulphate electrolyte in laminar flow.

Effect of electrolyte flow rate

$$T = 32 \pm 1^\circ\text{C}, L/d_e \sim 11.4$$

15L	X	-	2.33	cm s ⁻¹	(Re 220)
17L	●	-	4.67	cm s ⁻¹	(Re 426)
16L	□	-	7.11	cm s ⁻¹	(Re 662)
13L	+	-	10.7	cm s ⁻¹	(Re 1,033)
14L	o	-	16.1	cm s ⁻¹	(Re 1,546)

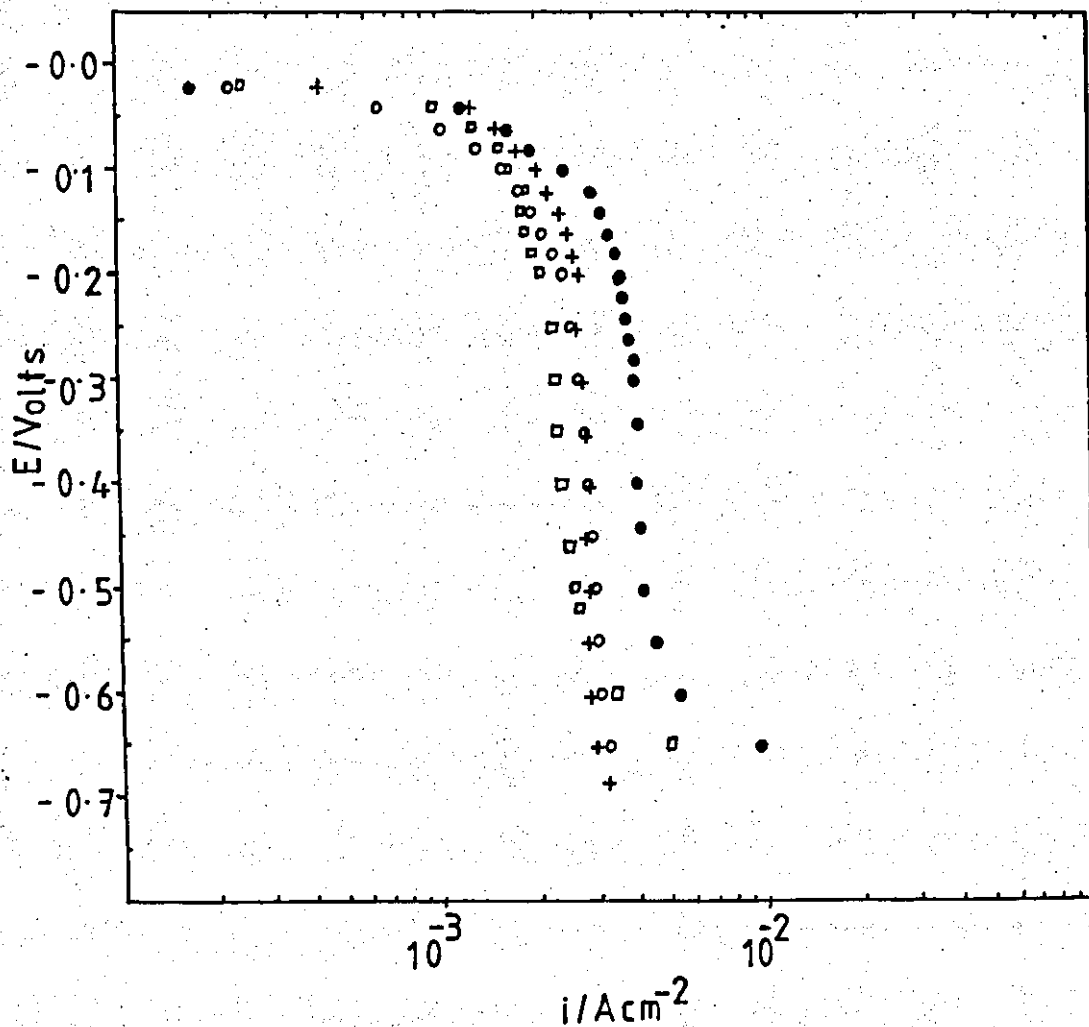


Fig.4.33 Cathodic polarisation during the electrolysis of 0.014M copper sulphate electrolyte in laminar flow.

Effect of electrolyte flow rate

$$T = 27.8 \pm 0.2^\circ\text{C}, L/de \sim 11.4$$

19L	+	-	15.0 cm s ⁻¹ (Re 1,299)
18L	o	-	13.2 cm s ⁻¹ (Re 1,206)
21L	□	-	11.1 cm s ⁻¹ (Re 952)
20L	●	-	25.6 cm s ⁻¹ (Re 2,190)

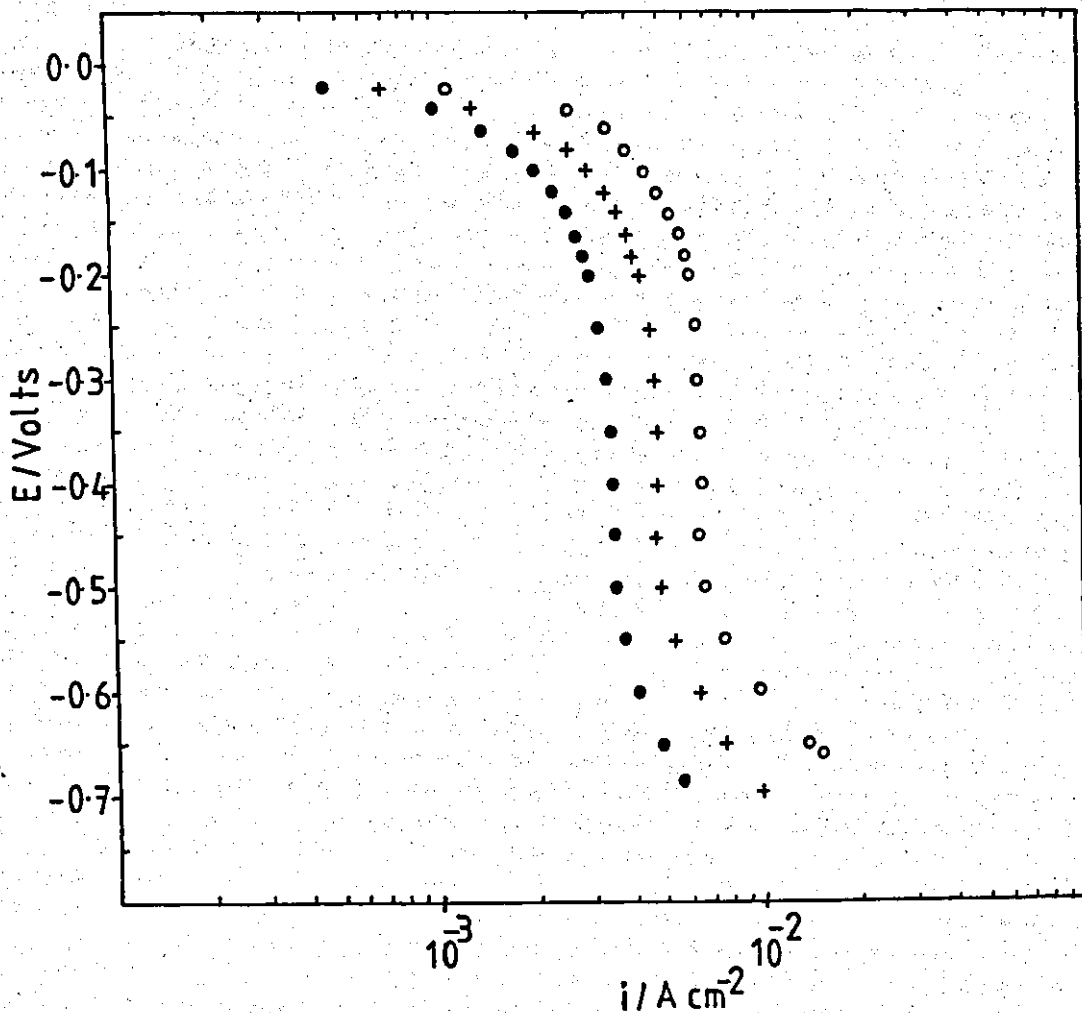


Fig.4.34 Cathodic polarisation during the electrolysis of 0.014M copper sulphate electrolyte in laminar flow.

$$T = 37 \pm 1^\circ\text{C}, \quad L/d_e \sim 2.8$$

25L	●	-	4.11 cm s ⁻¹ (Re 430)
26L	+	-	7.11 cm s ⁻¹ (Re 743)
27L	○	-	13.4 cm s ⁻¹ (Re 1,399)

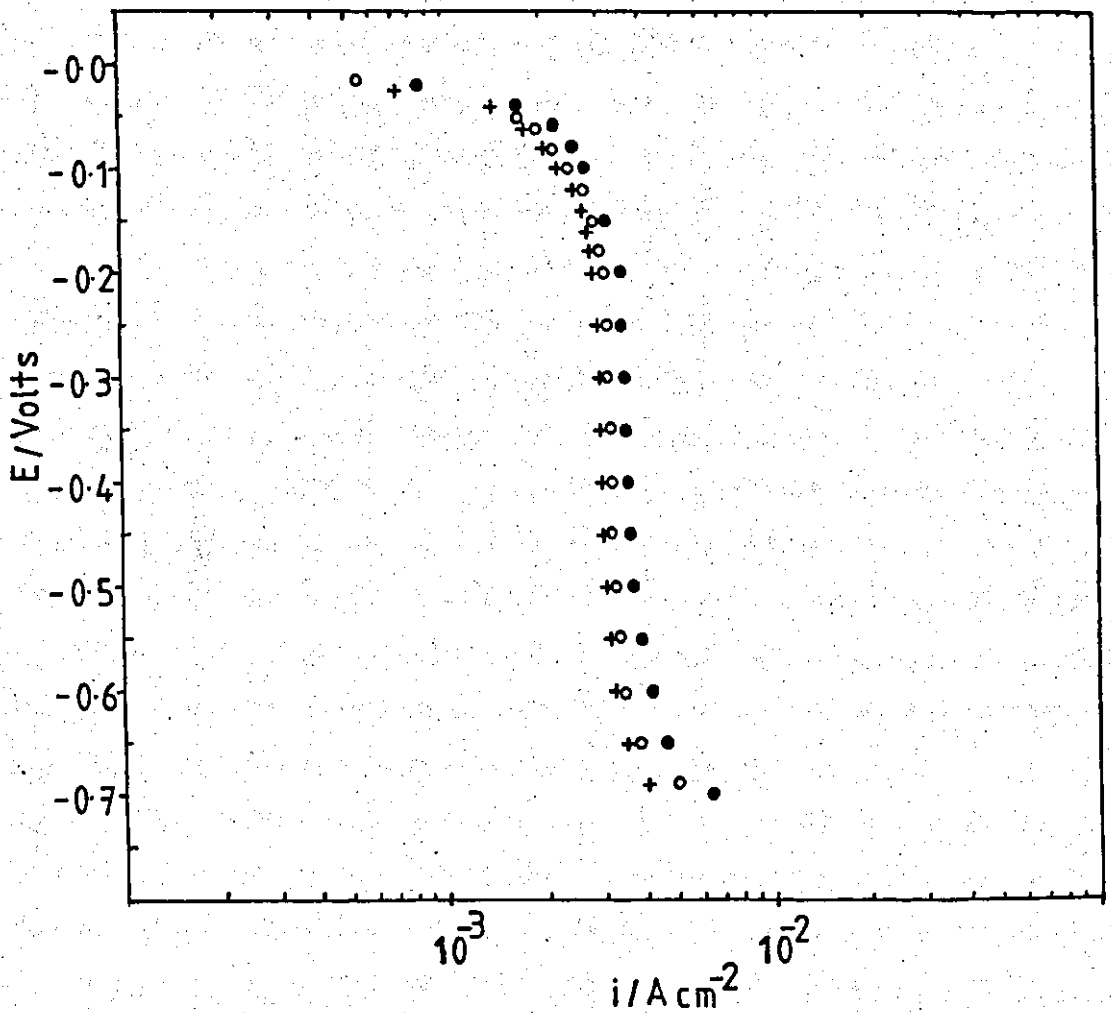


Fig.4.35 Cathodic polarisation during the electrolysis of 0.014M copper sulphate electrolyte in laminar flow.

$$T = 37 \pm 1^\circ\text{C}, \quad L/de \sim 2.8$$

28L	+	-	1.33 cm s^{-1}	(Re 141)
29L	o	-	1.78 cm s^{-1}	(Re 188)
30L	•	-	2.28 cm s^{-1}	(Re 241)

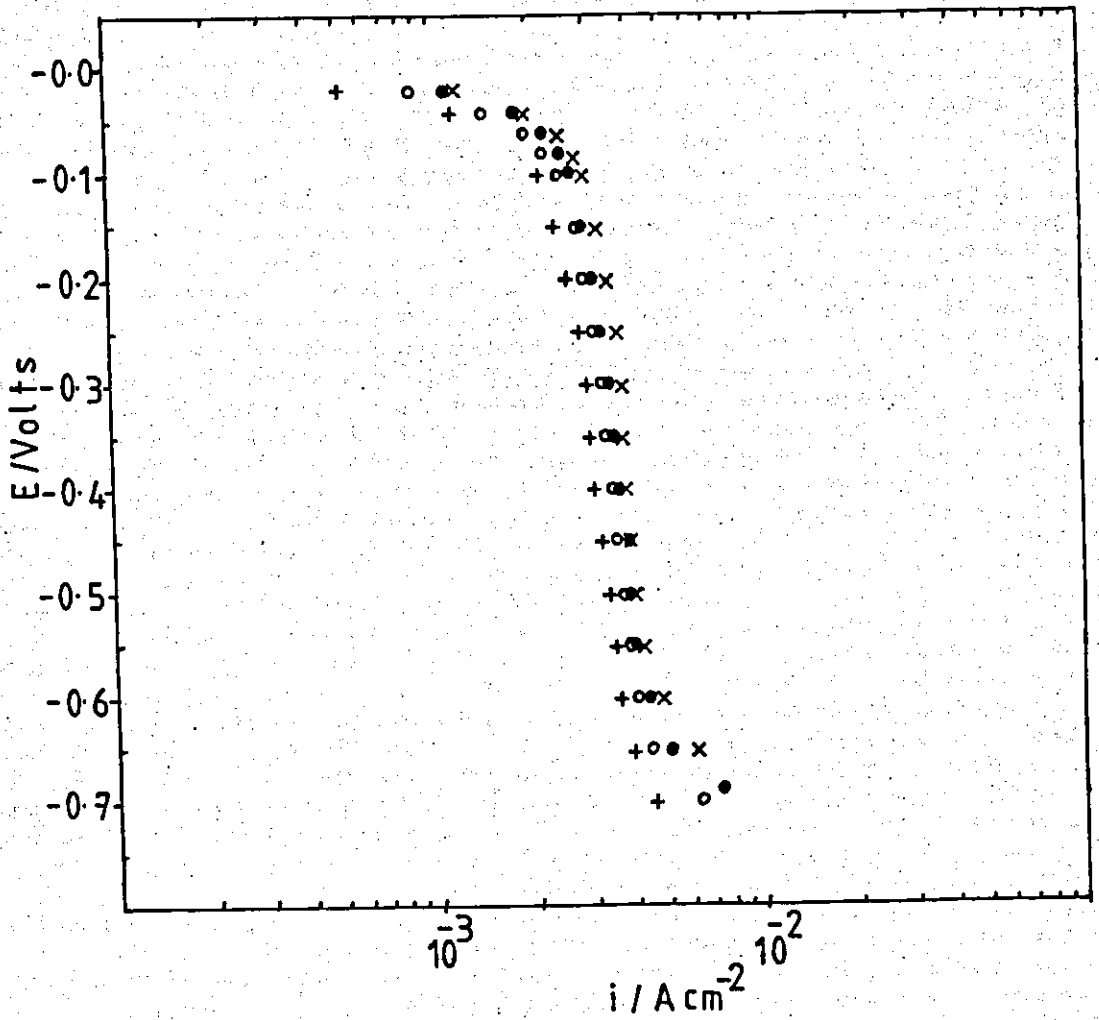


Fig.4.36 Cathodic polarisation during the electrolysis of 0.014M copper sulphate electrolyte in laminar flow.

$$T = 37 \pm 1^\circ\text{C}, L/de \sim 2.8$$

31L	+	-	2.89 cm s ⁻¹	(Re 306)
32L	o	-	3.28 cm s ⁻¹	(Re 347)
33L	x	-	4.11 cm s ⁻¹	(Re 430)
34L	●	-	4.56 cm s ⁻¹	(Re 482)

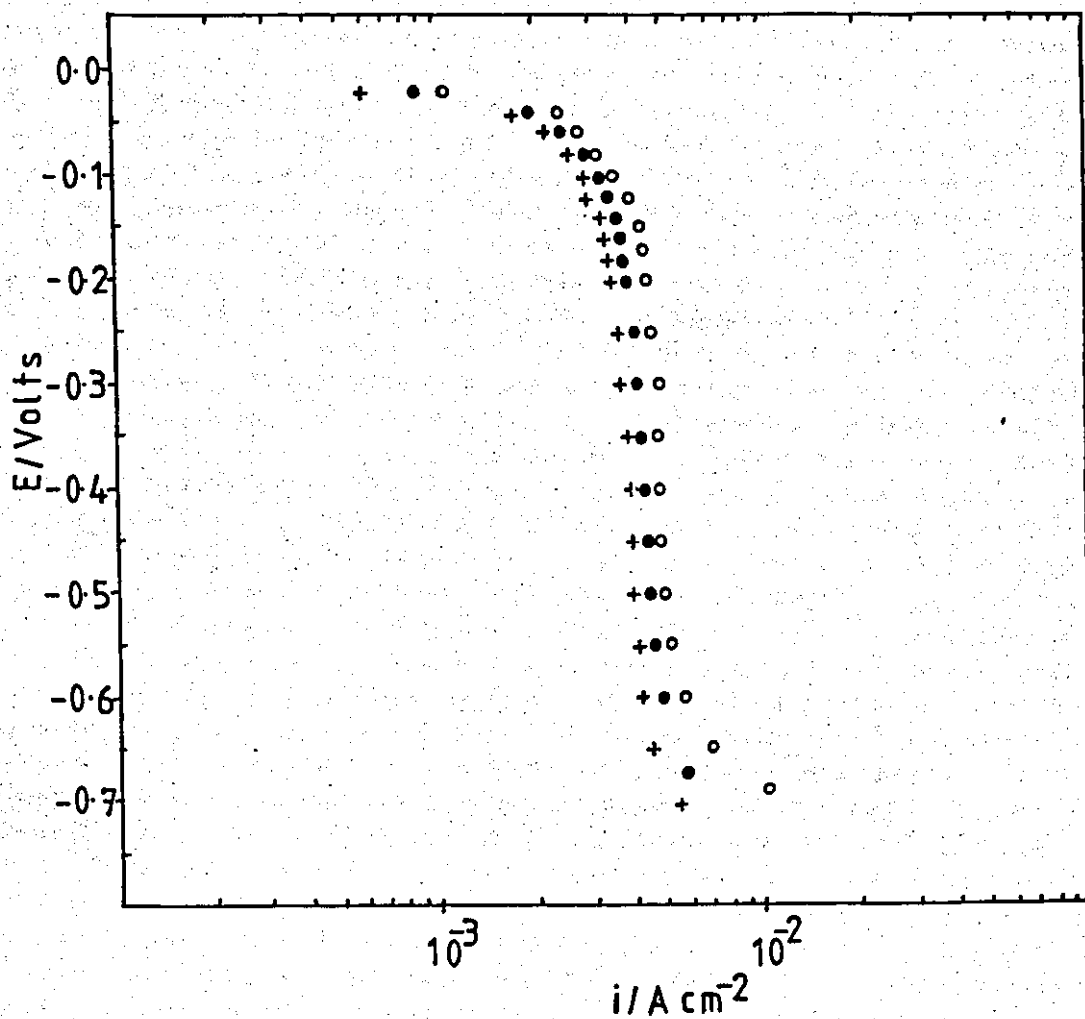


Fig.4.37 Cathodic polarisation during the electrolysis of 0.014M copper sulphate electrolyte in laminar flow.

$$T = 37 \pm 1^\circ\text{C}, L/d_e \sim 2.8$$

35L + - 5.61 cm s^{-1} (Re 594)

36L • - 7.11 cm s^{-1} (Re 752)

37L ○ - 9.06 cm s^{-1} (Re 958)

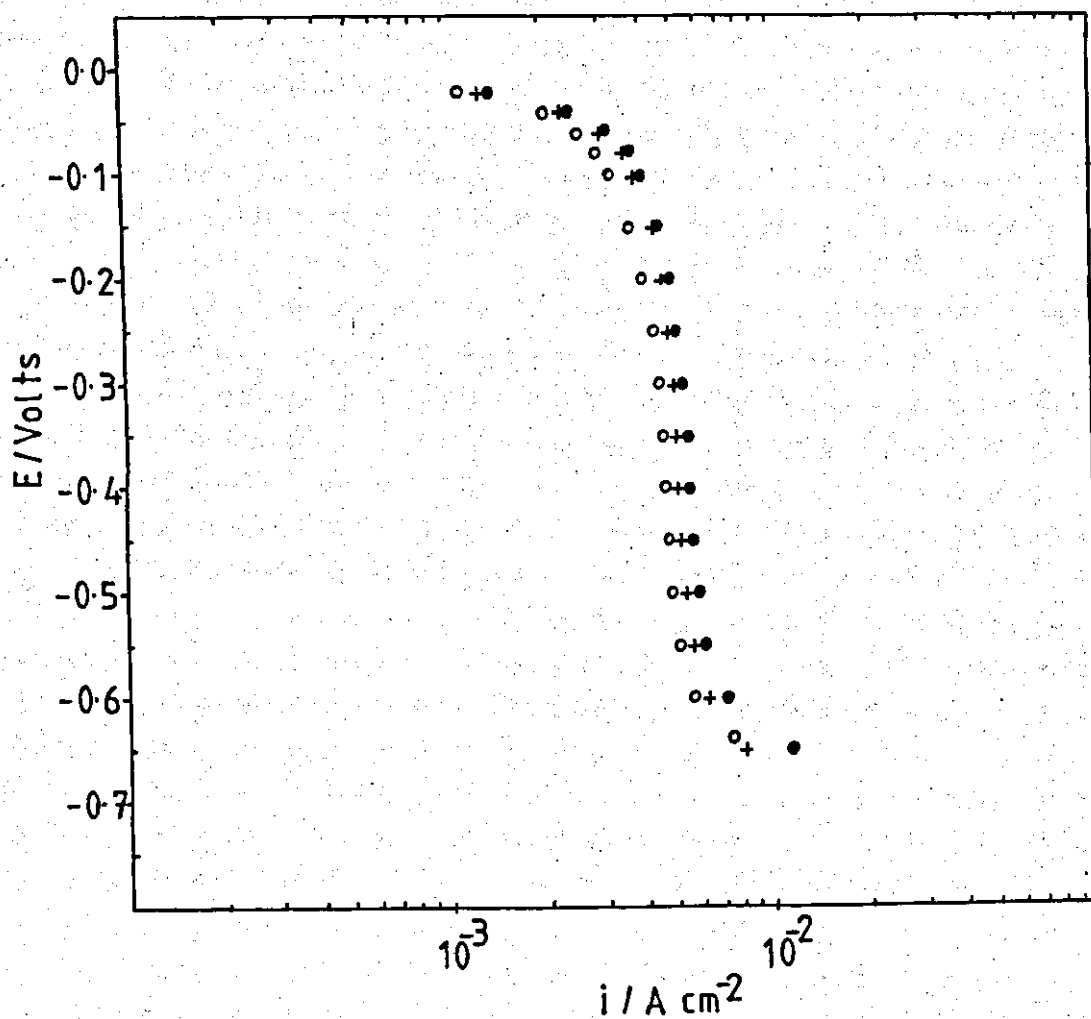


Fig.4.38 Cathodic polarisation during the electrolysis of 0.014M copper sulphate electrolyte in laminar flow.

$$T = 37 \pm 1^\circ\text{C}, \quad L/d_e \sim 2.8$$

38L	+	-	12.7 cm s ⁻¹	(Re 1,346)
39L	o	-	13.3 cm s ⁻¹	(Re 1,394)
40L	•	-	15.1 cm s ⁻¹	(Re 1,593)

Temperature T °C	Flow Rate U cms ⁻¹	Re	Limiting Current Density i_L A cm ⁻² x 10 ⁻³
27.8 ± 0.2	11.1	952	2.27
	15.0	1,298	2.77
	25.6	2,190	2.99
	13.22	1,200	2.95
	2.33	220	1.46
32 ± 1	4.67	426	2.04
	7.11	662	2.33
	10.72	1,033	2.85
	16.06	1,546	3.52
40.0 ± 0.0	11.1	1,221	3.01
	22.2	2,442	4.11
50.2 ± 0.1	11.7	1,587	3.58
	12.8	1,738	3.85
	15.0	2,040	4.07
	16.7	2,267	4.33
60.1 ± 0.1	1.39	243	2.09
	4.44	777	2.91
	7.67	1,341	3.53
	10.8	1,904	4.22

Table 4.6 Limiting current densities for the deposition of copper on cathodes 11.4 de in length at 28, 32, 40, 50 and 60°C in laminar flow.

Flow Rate U cms ⁻¹	Reynolds Number Re	Limiting Current Density i _L A cm ⁻² x 10 ⁻³
1.33	141	2.22
1.78	188	2.31
2.28	241	2.84
2.89	306	2.45
3.28	347	2.87
4.11	430	2.80
4.11	435	3.08
4.56	482	3.01
5.61	594	3.21
7.11	743	3.95
7.11	752	3.66
9.06	958	4.03
12.72	1,346	4.35
13.33	1,394	3.97
13.39	1,399	5.57
15.06	1,593	4.82

Table 4.7 Limiting current densities for the deposition of copper on cathodes 2.8 de in length at 37 ± 1°C in laminar flow.

In Fig.4.39, the values of i_L are plotted as a function of flow velocity (U) on logarithmic coordinates. As may be seen from Fig.4.39 the deposition rate was greatest at a given flow velocity, on the shorter cathodes ($L/d_e = 2.8$).

Using long electrodes ($L/d_e = 11.4$), an approximately linear relationship between i_L and U was observed, at each temperature. Each set of data were correlated by a line (A-A) with a slope of about 0.3. As has been seen elsewhere (p.128), similar slopes may be predicted from the design equation. With cathodes 11.4 d_e in length an increase in temperature resulted in significant increases in the limiting current density at a constant flow rate.

The relationship between i_L and the electrode length, L/d_e

Cathodic polarisation measurements were made at a flow rate corresponding to $Re = 1,015 \pm 96$ using a range of cathode lengths (L) from 0.5 to 9.8 cm ($L/d_e = 0.6$ to 11.4) (Fig.4.40). The electrolyte temperature was $32 \pm 1^\circ C$.

The general features of the curves were similar to those observed previously (p.173). The very short cathodes ($L/d_e < 2.3$) had a less well defined limiting current density plateau. The limiting current densities were determined at a potential (E) of $-0.45V$ versus the Cu reference electrode. The results are summarized in Table 4.8.

In Fig.4.41 the limiting current density is plotted versus the cathode length in equivalent diameters (L/d_e). As the effective cathode length was progressively increased, at a constant flow rate, the average limiting current decreased. The mass transfer rate was greatest at very short electrode lengths when mass transfer entrance effects are greatest.

Dimensionless number correlations of mass transfer data and interpretation

The rate of mass transfer in laminar flow may be correlated by a single equation in terms of the properties of the electrolyte at each

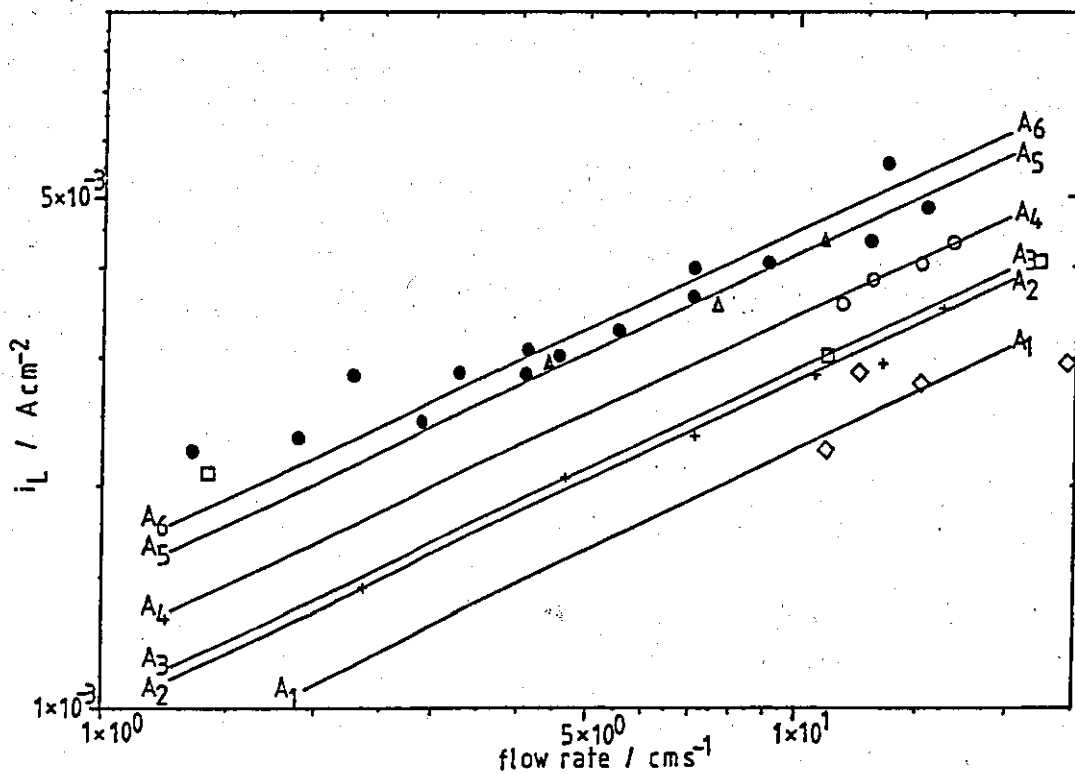


Fig.4.39 Effect of flow rate (laminar flow) on the limiting current density for the cathodic deposition of copper from 0.014M copper sulphate electrolyte.

- ◇ - 28°C
- + - 32°C
- - 40°C $L/d_e \sim 11.4$
- - 50°C
- △ - 60°C
- - 37°C $L/d_e \sim 2.8$

T = 32 ± 1°C

Re 1,019 ± 96

Electrode Length L/de	Average Limiting Current Density i_L A cm ⁻² x 10 ⁻³
0.6	13.2
2.4	5.10
4.7	3.50
6.9	3.10
9.3	2.70
11.4	2.85

Table 4.8 Corrected limiting current densities for copper deposition on cathodes 11.4 de in length.

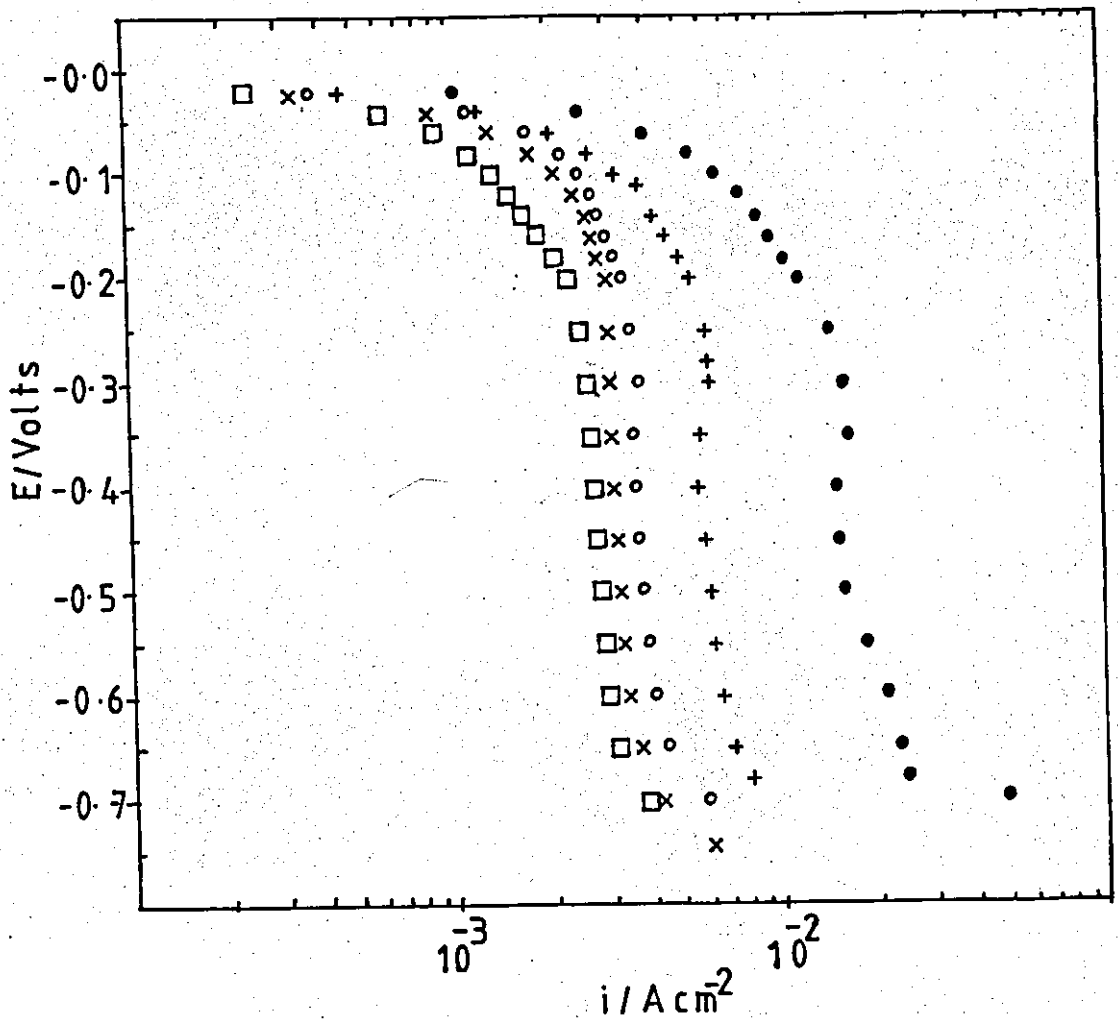


Fig.4.40 Cathodic polarisation during the electrolysis of 0.014M copper sulphate electrolyte at $32 \pm 1^\circ\text{C}$ and $\text{Re } 1,1015 \pm 96$.
Effect of electrode length

22L	□	-	$L/de \sim 9.3$
23L	X	-	$L/de \sim 6.9$
24L	○	-	$L/de \sim 4.7$
41L	+	-	$L/de \sim 2.4$
42L	●	-	$L/de \sim 0.6$

↓
decreasing
cathode
length

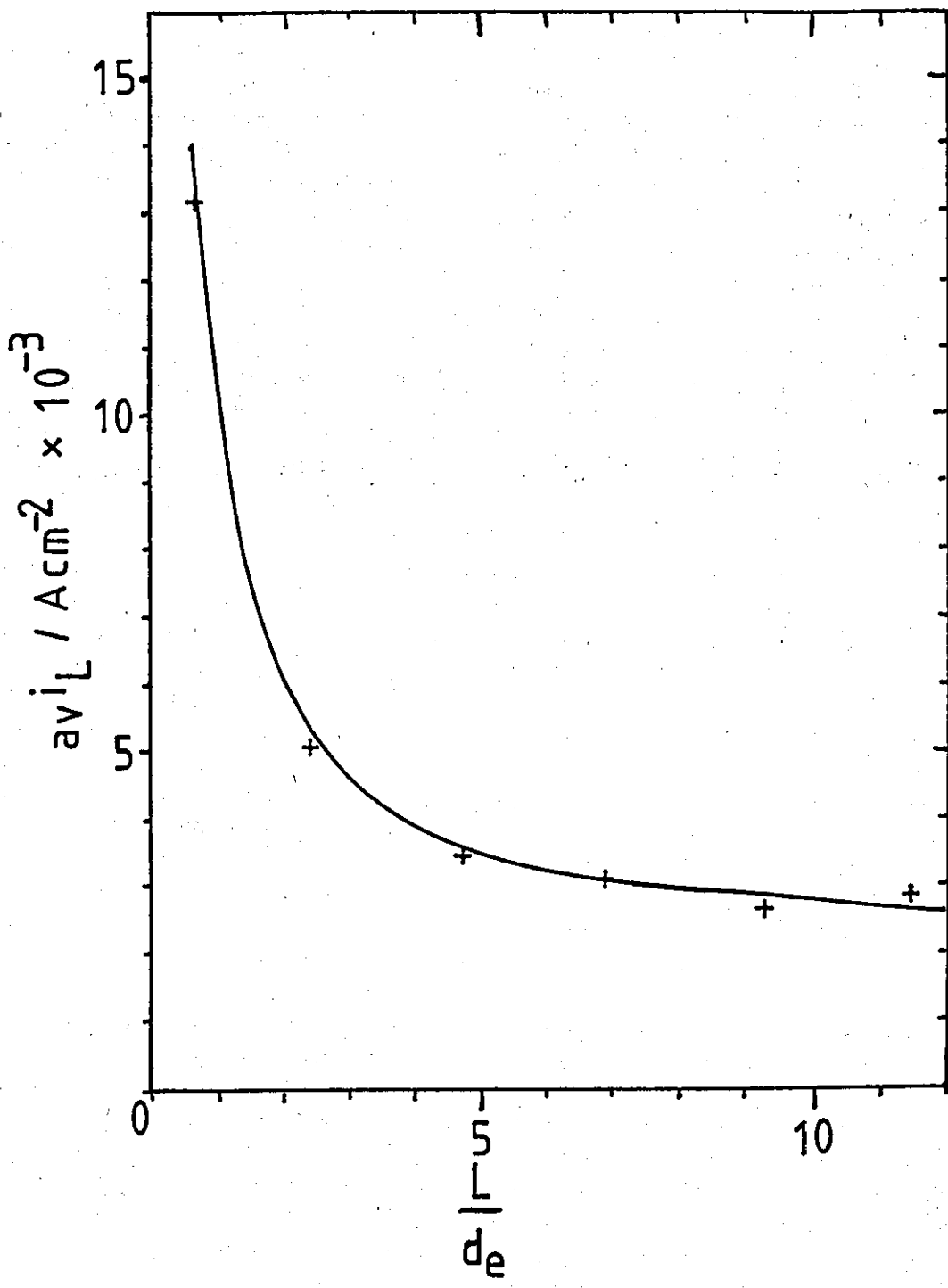


Fig.4.41 Effect of the cathode length on the limiting current density for the cathodic deposition of copper from 0.014M copper sulphate electrolyte at $32 \pm 1^\circ C$ and $Re 1,019 \pm 96$.

temperature, the geometry of the cell, the flow rate and the mass transfer coefficients calculated using the measured values of i_L obtained from the polarisation curves. The results are summarised in Table 4.9.

The system was described by the four dimensionless numbers Re , Sc , $\frac{de}{L}$ and Sh (Table 4.10 derived from the primary data of Table 4.9) (Detailed calculations are shown in Section 3.4.1). In Fig.4.42 the term $[Re Sc \frac{de}{L}]$ known as the Graetz No. is plotted versus the dimensionless mass transfer coefficient (Sh) on logarithmic coordinates. The data were correlated, using linear regression analyses by the following equation:

$$Sh = 2.8 [Re Sc \frac{de}{L}]^{0.33} \quad \dots \dots (4.1)$$

The correlation coefficient (r^2) was 0.951. The solution of Eqn.(4.1) is shown by the line A-A, of slope 0.3 in Fig.4.42 .

The theoretical design equation for Cell 2 with laminar flow was

$$Sh = 1.85 [Re Sc \frac{de}{L}]^{0.33} \quad \dots \dots (2.49)$$

The solution of the above equation is shown by the line B-B in Fig.4.42.

It would appear that the unusual divided cell configuration used in the present study results in higher mass transfer rates than would be expected from the simple analysis. The good agreement in the value of the exponent of the Graetz number may also indicate that cell geometry is the decisive factor. From a practical fast deposition viewpoint the high-mass transport rates are an advantage.

(b) Mass transport under conditions of turbulent flow

In turbulent flow fully developed mass transfer profiles were obtained over much shorter electrode lengths. The rate of mass transfer

Dimensionless Electrode Length de/L	Temperature T °C	Kinematic Viscosity ν cm^2s^{-1} $\times 10^{-2}$	Diffusion Coefficient $D_{\text{Cu}^{2+}}$ cm^2s^{-1} $\times 10^{-6}$	Flow Rate U cm s^{-1}	Corrected Limiting Current Density $i_{L, \text{corr.}}$ A cm^{-2} $\times 10^{-3}$	Bulk Concentration c_b mol cm^{-3} $\times 10^{-5}$	Mass Transfer Coefficient k_L cm s^{-1} $\times 10^{-3}$
0.088	60.1	0.49	12.04	1.39	2.09	1.32	0.82
0.088	60.1	0.49	12.04	4.44	2.91	1.32	1.14
0.088	60.1	0.49	12.04	7.67	3.53	1.32	1.39
0.088	60.1	0.49	12.04	10.89	4.22	1.32	1.66
0.088	60.1	0.49	12.04	14.38	4.80	1.32	1.88
0.088	50.2	0.63	9.85	11.67	3.58	1.36	1.36
0.088	50.2	0.63	9.85	12.78	3.85	1.36	1.47
0.088	50.2	0.63	9.85	15.00	4.07	1.36	1.55
0.088	50.2	0.63	9.85	16.67	4.33	1.36	1.65
0.088	50.2	0.63	9.85	18.89	4.67	1.36	1.78
0.088	40.0	0.78	7.92	11.11	3.01	1.41	1.11
0.088	40.0	0.78	7.92	22.22	4.11	1.41	1.51
0.088	33.0	0.89	6.80	10.72	2.85	1.28	1.15
0.088	33.0	0.89	6.80	16.06	3.52	1.28	1.43
0.088	32.5	0.91	6.72	2.33	1.46	1.28	0.59
0.088	32	0.92	6.64	7.11	2.33	1.28	0.94
0.088	31.0	0.94	6.48	4.67	2.04	1.28	0.83
0.088	31.0	0.94	6.48	13.22	2.95	1.28	1.19
0.088	27.7	0.99	6.00	15.00	2.77	1.28	1.11
0.088	28.0	1.00	6.04	25.56	3.99	1.28	1.62
0.088	27.9	1.00	6.02	11.11	2.27	1.28	0.92

/continued

Table 4.9 Summary of electrolysis conditions for the deposition of copper in laminar flow.

($de \sim 0.857 \text{ cm.}$)

Table 4.9 continued

d_e/L	T °C	v cm^2s^{-1} $\times 10^{-2}$	$D_{\text{Cu}^{2+}}$ cm^2s^{-1} $\times 10^{-6}$	U cm s^{-1}	i_L^{corr} A cm^{-2} $\times 10^{-3}$	$c_b^{\text{Cu}^{2+}}$ mol cm^{-3} $\times 10^{-5}$	k_L cm s^{-1} $\times 10^{-3}$
0.107	32.1	0.92	6.65	10.72	2.70	1.29	1.09
0.145	32.3	0.91	6.68	10.72	3.10	1.30	1.24
0.214	32.7	0.90	6.76	10.72	3.50	1.30	1.40
0.357	36.0	0.82	7.24	4.11	2.80	1.33	1.09
0.357	36.0	0.82	7.24	7.11	3.95	1.33	1.54
0.357	36.0	0.82	7.24	13.39	5.57	1.33	2.17
0.365	37.9	0.81	7.60	1.33	2.22	1.29	0.89
0.365	37.9	0.81	7.60	1.78	2.31	1.29	0.93
0.365	37.9	0.81	7.60	2.28	2.84	1.29	1.14
0.365	37.9	0.81	7.60	2.89	2.45	1.29	0.98
0.365	37.9	0.81	7.60	3.28	2.87	1.29	1.15
0.365	37.9	0.81	7.60	4.11	3.08	1.29	1.24
0.365	37.8	0.81	7.60	4.56	3.01	1.29	1.21
0.365	37.9	0.81	7.60	5.61	3.21	1.29	1.29
0.365	37.9	0.81	7.60	7.11	3.66	1.29	1.47
0.365	37.9	0.81	7.60	9.06	4.03	1.29	1.62
0.365	37.9	0.81	7.60	12.72	4.35	1.29	1.75
0.365	37.7	0.82	7.55	13.33	3.97	1.29	1.60
0.365	37.9	0.81	7.60	15.06	4.82	1.29	1.94
0.429	28.0	1.00	6.04	10.72	5.10	1.28	2.07
1.71	30.9	0.94	6.48	10.72	10.00	1.29	4.02

Dimensionless Electrode Length d_e/L	Schmidt No. $[\frac{v}{D}]$ Sc	Reynolds No. $[\frac{u d_e}{v}]$ Re	Sherwood No. $[\frac{k_L d_e}{D}]$ Sh	Graetz No. $[Re Sc^{d_e/L}]$ Gz_4 $\times 10^4$
0.088	407	243	58.4	0.87
0.088	407	777	81.1	2.78
0.088	407	1,341	98.9	4.80
0.088	407	1,904	118	6.82
0.088	407	2,517	134	9.02
0.088	640	1,587	118	8.94
0.088	640	1,738	128	9.79
0.088	640	2,040	135	11.5
0.088	640	2,267	144	12.8
0.088	985	1,221	120	10.6
0.088	985	2,442	163	21.2
0.088	1,309	1,033	145	11.9
0.088	1,309	1,546	180	17.8
0.088	1,354	220	75.4	2.62
0.088	1,386	662	122	8.07
0.088	1,451	426	109	5.44
0.088	1,451	1,206	157	15.4
0.088	1,650	1,299	159	18.9
0.088	1,656	2,190	230	31.9
0.088	1,661	952	131	13.9
0.107	1,384	999	141	14.8
0.145	1,362	1,110	159	21.9

/continued

Table 4.10 Dimensionless variables and experimental mass transfer coefficients for the deposition of copper in laminar flow. ($d_e \sim 0.857$ cm).

Table 4.10 continued

d_e/L	Sc	Re	Sh	Gz $\times 10^4$
0.214	1,331	1,021	178	29.1
0.357	1,133	430	129	17.4
0.357	1,133	743	182	30.1
0.357	1,133	1,399	257	56.6
0.365	1,066	141	101	5.49
0.365	1,066	188	105	7.32
0.365	1,066	241	129	9.38
0.365	1,066	306	111	11.9
0.365	1,066	347	130	13.5
0.365	1,066	435	140	16.9
0.365	1,066	482	136	18.8
0.365	1,066	594	146	23.1
0.365	1,066	752	166	29.3
0.365	1,066	958	183	37.3
0.365	1,066	1,346	197	52.4
0.365	1,086	1,394	182	55.3
0.365	1,066	1,593	219	62.0
0.429	1,656	919	294	65.3
1.71	1,451	978	531	243

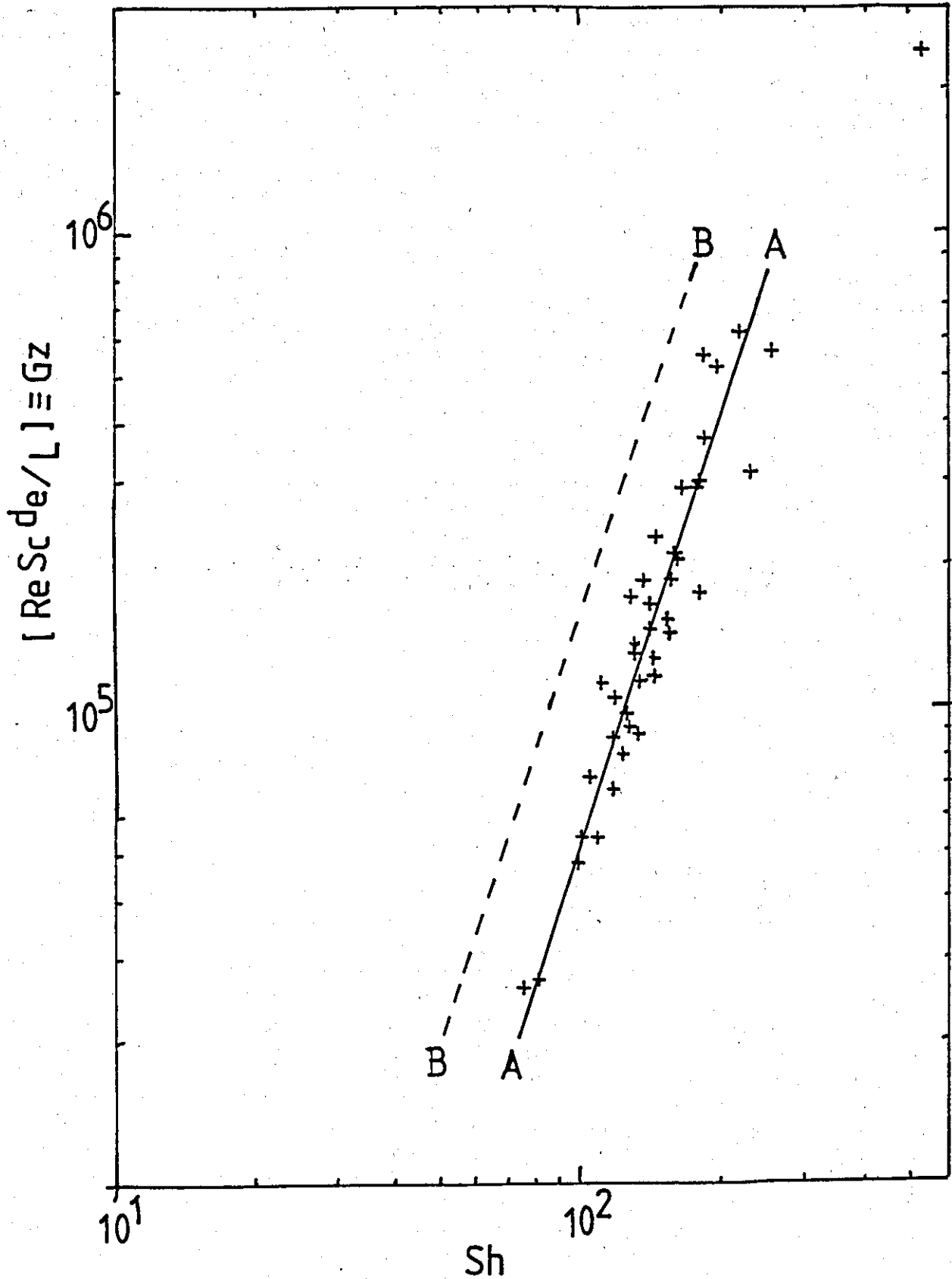


Fig.4.42 Mass transfer correlation for the cathodic deposition of copper from 0.014M copper sulphate electrolyte in laminar flow.

A - A line of best fit of data
(Equation 5.1)

B --- B theoretical correlation
(Equation 2.46)

may be described by two equations. Consequently, the turbulent flow data were more conveniently examined by dividing them into two electrode types.

Long electrodes. The maximum cathode length of 9.74 cm ($L/d_e \sim 11.4$) was used for polarisation measurements.

Short electrodes. A range of cathode lengths ($L/d_e = 0.53$ to 9.4) was used for these experiments.

For each set of experimental conditions, the cathodic polarisation curve was determined and the limiting current density (i_L) measured at -450 mV versus the Cu reference electrode.

(i) Long electrodes

Cathodic polarisation measurements were made over a range of flow rates 14 to 276 cm s^{-1} (Re 2,872 to 30,337). The relationship between i_L and flow rate was measured at temperatures of 28°, 40°, 50° and 60°. Some additional experiments were made at intermediate temperatures (37°, 45° and 55°C).

The cathodic polarisation behaviour is shown in Figs. 4.43 to 4.48. The general characteristics of each curve were similar to those observed in laminar flow (p.173). However, the limiting current density was less well defined in turbulent flow, particularly at high flow rates (e.g. Fig.4.47, 276 cm s^{-1}). At each temperature the limiting current density increased with increasing flow velocity.

The copper deposited in turbulent flow was rougher in appearance than laminar flow deposits. The distribution of the powdery deposit was non-uniform and predominated near the leading edge of the cathode.

The measured values of i_L are recorded in Table 4.11. In Fig.4.49 the values of i_L are plotted versus flow velocity (U) on logarithmic coordinates. At each temperature an approximately linear relationship between i_L and U was observed. Each set of data were correlated by a line (A-A) of slope ~ 0.8 . Similar slopes were predicted

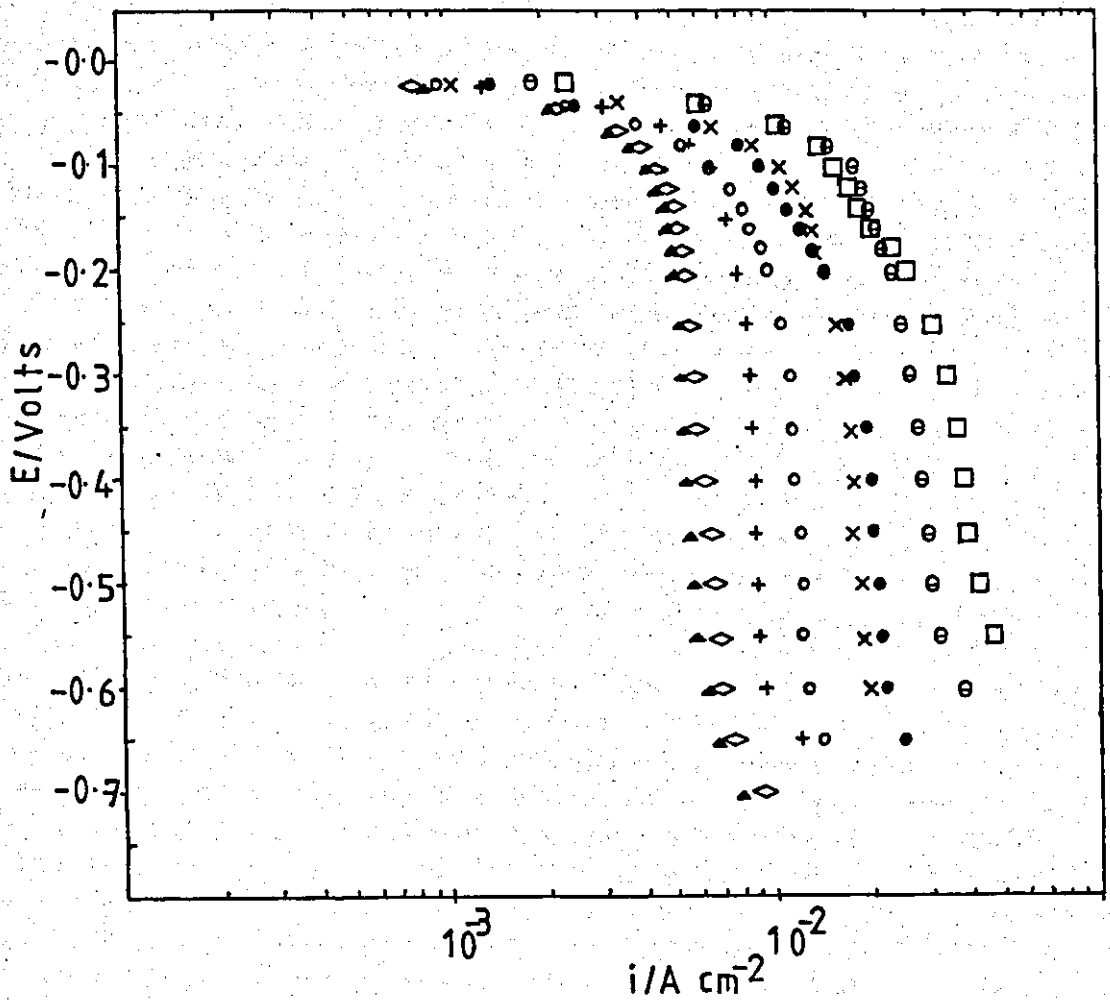


Fig.4.43 Cathodic polarisation during the electrolysis of 0.014M copper sulphate solution in turbulent flow. Effect of flow rate.

$$T = 60.1 \pm 0.1^\circ\text{C}, \quad L/d_e \sim 11.4$$

1T	▲	-	18.0 cm s ⁻¹	(Re 3,148)
2T	◇	-	19.9 cm s ⁻¹	(Re 3,479)
3T	+	-	27.8 cm s ⁻¹	(Re 4,858)
4T	o	-	40.0 cm s ⁻¹	(Re 6,996)
5T	x	-	59.4 cm s ⁻¹	(Re 10,397)
6T	●	-	73.3 cm s ⁻¹	(Re 12,826)
7T	□	-	148 cm s ⁻¹	(Re 25,846)
8T	⊖	-	101 cm s ⁻¹	(Re 17,684)

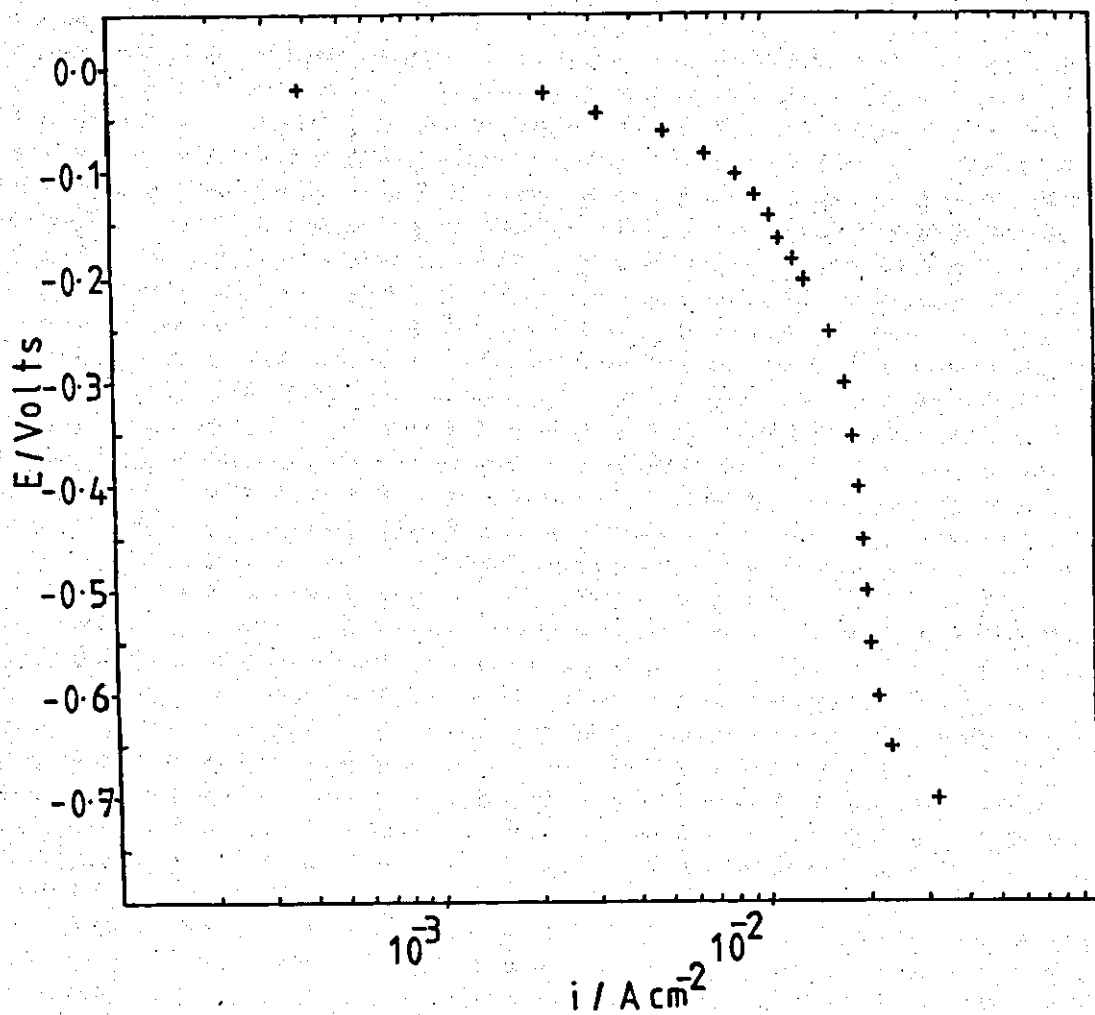


Fig.4.44 Cathodic polarisation during the electrolysis of 0.014M copper sulphate solution in turbulent flow at 55°C (9T, 76.7 cm s^{-1} , Re 11,733, $L/d_e \sim 11.4$).

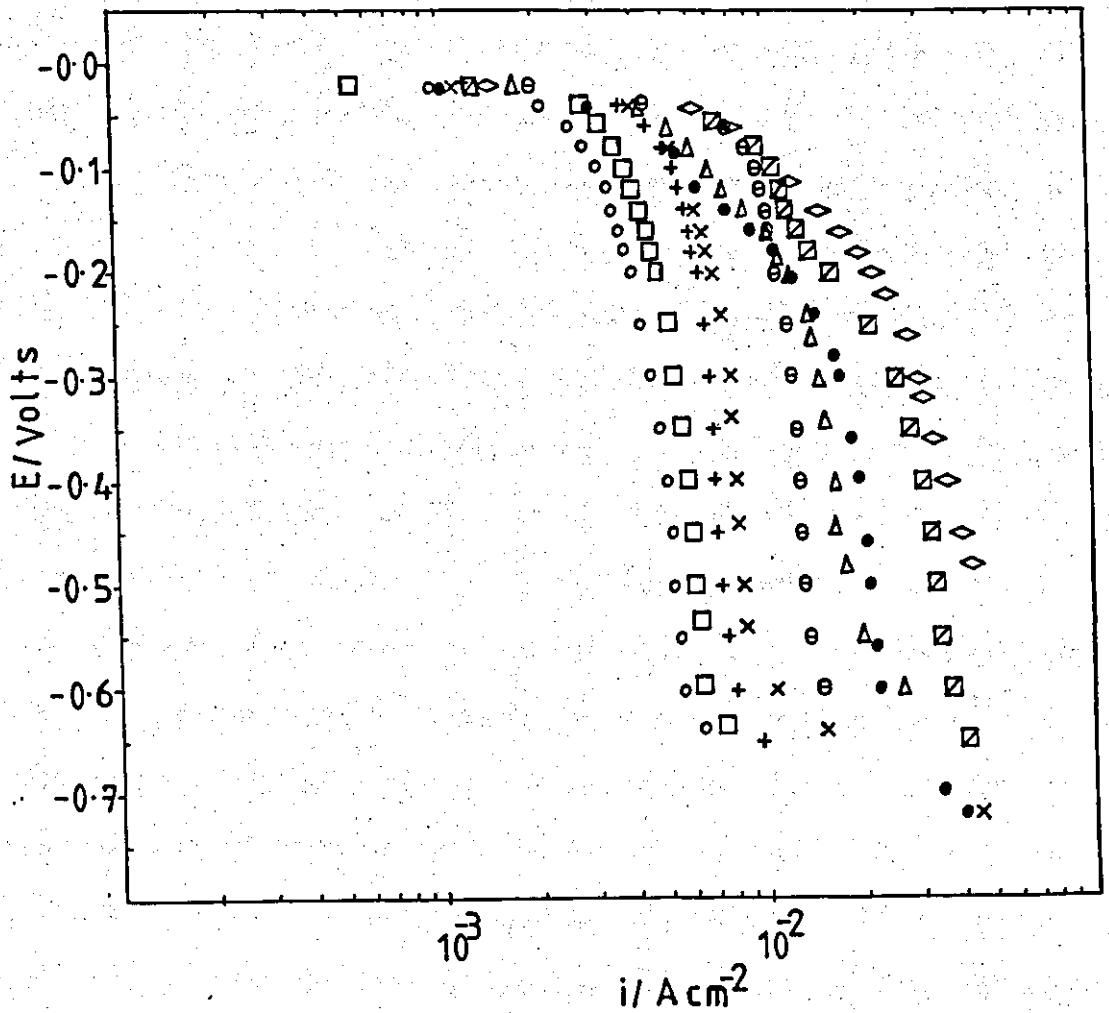


Fig.4.45 Cathodic polarisation during the electrolysis of 0.014M copper sulphate electrolyte in turbulent flow. Effect of flow rate

$$T = 50.2 \pm 0.1^\circ\text{C}, \quad L/de \sim 11.4$$

10T	○	- 45.6 cm s ⁻¹ (Re 13,208)
11T	○	- 21.1 cm s ⁻¹ (Re 2,872)
12T	□	- 23.3 cm s ⁻¹ (Re 3,174)
13T	+	- 29.4 cm s ⁻¹ (Re 4,008)
14T	x	- 34.4 cm s ⁻¹ (Re 4,686)
15T	●	- 58.9 cm s ⁻¹ (Re 8,011)
16T	△	- 71.1 cm s ⁻¹ (Re 9,673)
17T	◻	- 158 cm s ⁻¹ (Re 21,463)
18T	◇	- 164 cm s ⁻¹ (Re 22,370)

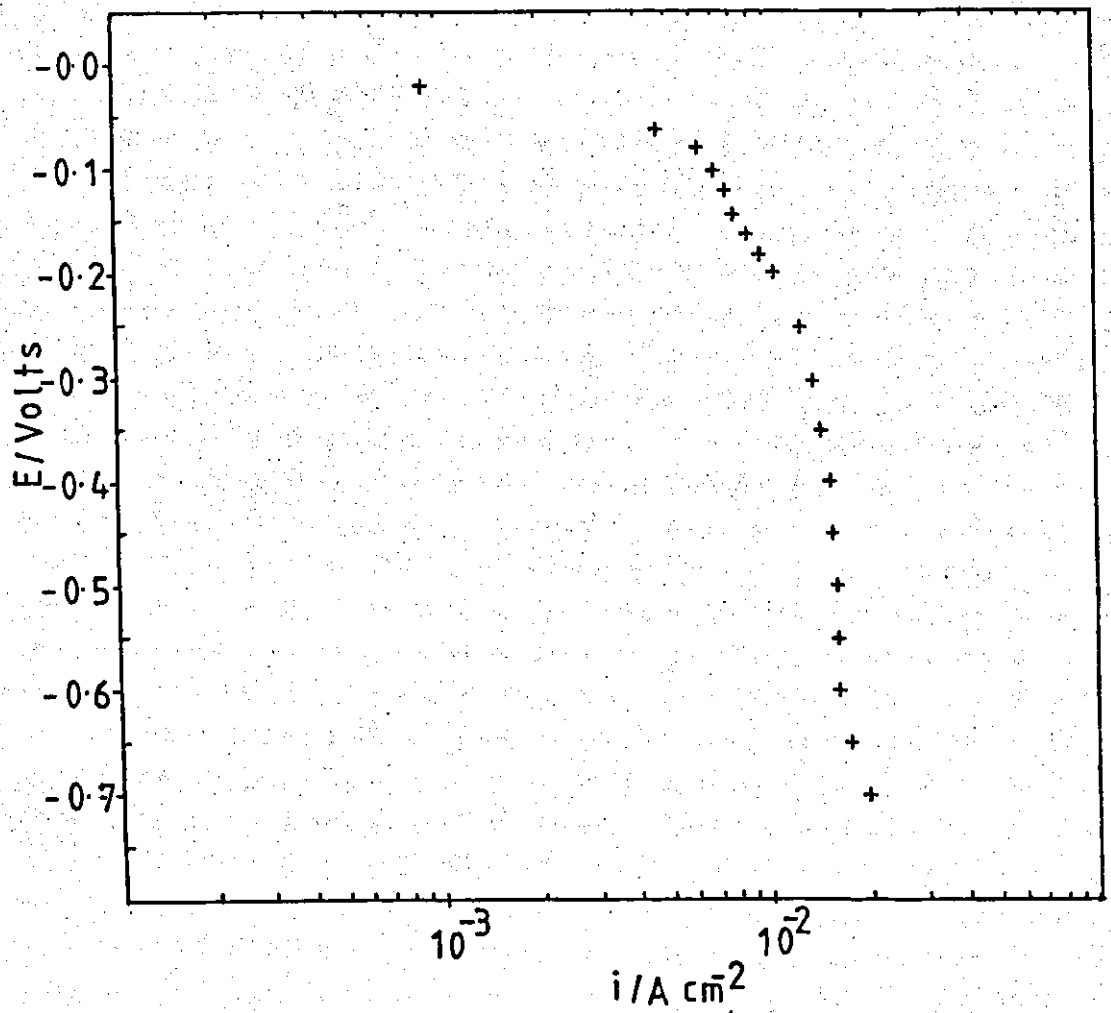


Fig.4.46 Cathodic polarisation during the electrolysis of 0.014M copper sulphate electrolyte in turbulent flow at 45°C (9T, 76.7, Re 9,386, $L/d_e \sim 11.4$)

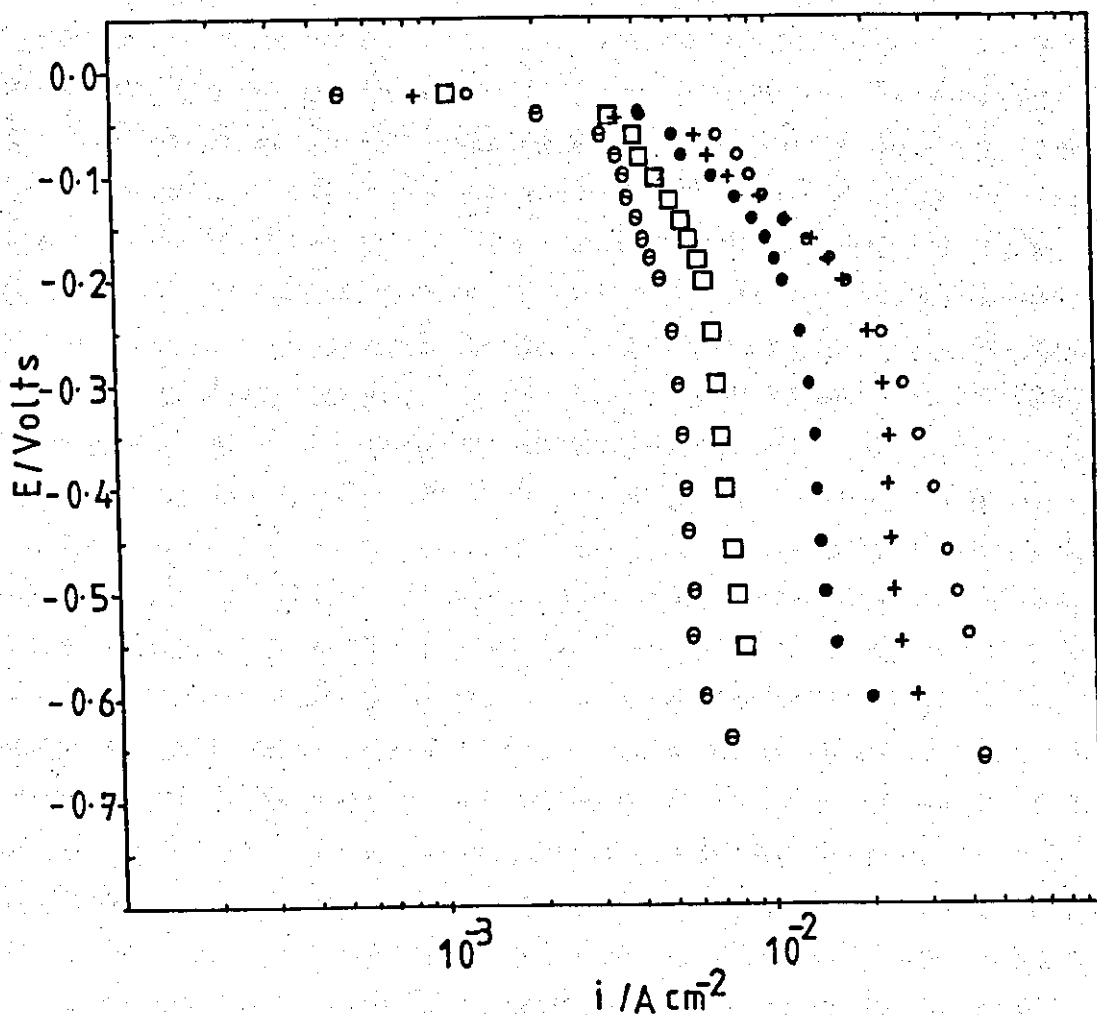


Fig.4.47 Cathodic polarisation during the electrolysis of 0.014M copper sulphate electrolyte in turbulent flow. Effect of flow rate.

$$T = 40^{\circ}\text{C}, L/d_e \sim 11.4$$

20T - ○ - 28.9 cm s^{-1} (Re 3,174)

21T - □ - 38.9 cm s^{-1} (Re 4,273)

22T - ● - 73.3 cm s^{-1} (Re 8,057)

23T - + - 144 cm s^{-1} (Re 15,870)

24T - ○ - 276 cm s^{-1} (Re 30,337)

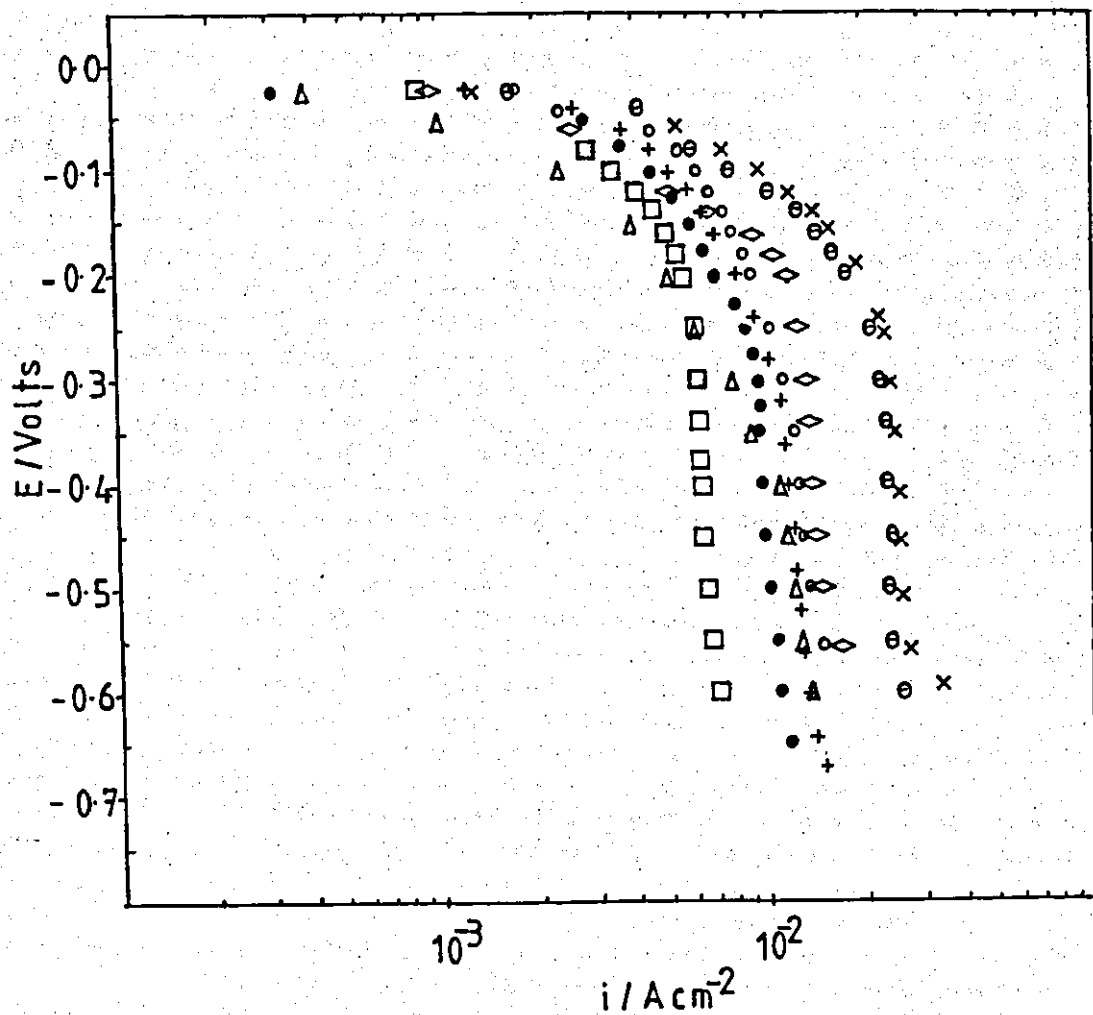


Fig.4.48 Cathodic polarisation during the electrolysis of 0.014M copper sulphate electrolyte in turbulent flow. Effect of flow rate.

$$T = 36.6 \pm 0.2^\circ\text{C}, \quad L/de \sim 11.4$$

25T + - 73.3 cm s⁻¹ (Re 7,664)

26T 0 - 73.3 cm s⁻¹ (Re 7,664)

27T Δ - 73.9 cm s⁻¹ (Re 7,629)

$$T = 28.0 \pm 0.4^\circ\text{C}, \quad L/de \sim 11.4$$

29T □ - 50.0 cm s⁻¹ (Re 4,328)

30T ● - 86.7 cm s⁻¹ (Re 7,502)

31T ◇ - 130 cm s⁻¹ (Re 11,254)

32T θ - 218 cm s⁻¹ (Re 18,852)

28T X - 277 cm s⁻¹ (Re 24,194)

Temperature °C	Flow Rate cm s ⁻¹	Limiting current density A cm ⁻² x 10 ⁻³	Re
27.8 ± 0.1	50.0	6.23	4,328
	86.7	9.89	7,502
	130	13.9	11,254
	218	22.3	18,852
40.0 ± 0.0	28.9	5.67	3,174
	38.9	6.94	4,273
	73.7	13.3	8,057
	144	22.4	15,870
50.2 ± 0.1	276	34.7	30,337
	18.9	4.67	2,569
	21.1	5.19	2,872
	23.3	5.67	3,174
	29.4	7.06	4,006
	34.4	8.18	4,686
	58.9	12.7	8,011
	71.1	16.2	9,673
60.1 ± 0.1	95.6	20.3	13,208
	158	35.3	21,463
	164	31.5	22,370
	14.4	4.80	2,517
60.1 ± 0.1	18.0	5.94	3,148
	19.9	6.50	3,478
	27.8	9.05	4,858
60.1 ± 0.1	40.0	12.3	6,996
	59.4	17.9	10,397
	73.3	20.8	12,826
	101	28.9	17,684
	147.8	39.1	25,846

Table 4.11 Experimentally determined limiting current densities for the deposition of copper from 0.014M copper sulphate solution at 28, 40, 50 and 60°C in turbulent flow.

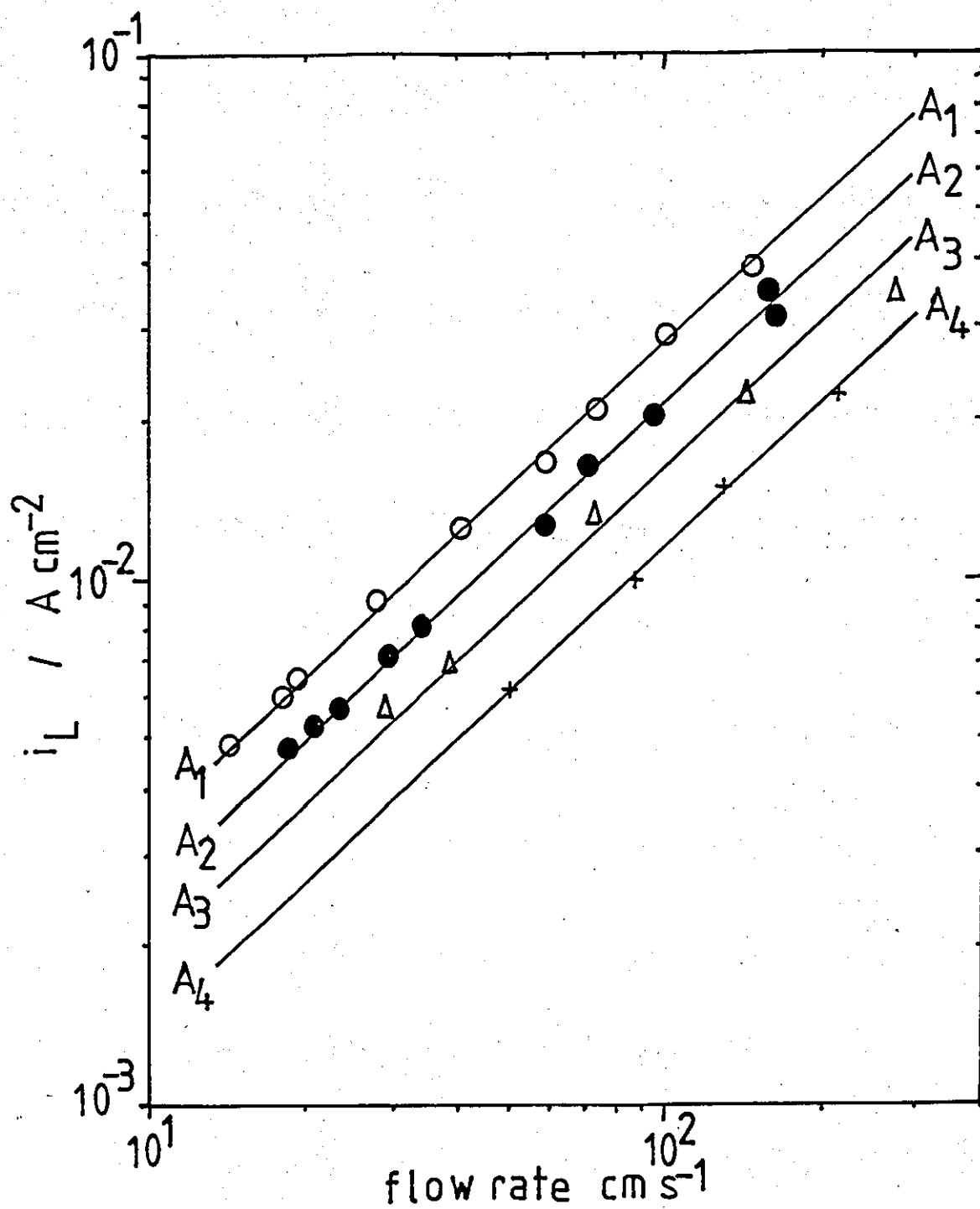


Fig.4.49 Effect of flow rate (turbulent flow) on the limiting current density for the cathodic deposition of copper from 0.014M copper sulphate electrolyte.

- + - 28°C
- Δ - 40°C
- - 50°C
- - 60°C

$L/d_e \sim 11.4$

from the design equation for the cell (p.128):

$$Sh = 0.023 Re^{0.8} Sc^{0.33} \dots (2.66)$$

As may be seen elsewhere (p.174) an increase in temperature resulted in significant increases in the limiting current density, at a constant flow velocity.

Dimensionless number correlation of mass transfer data and interpretation

The rate of mass transfer to long electrodes in turbulent flow was correlated by a single equation in terms of the properties of the electrolyte at each temperature, the equivalent diameter (d_e) of the cell, the flow rate, and the mass transfer coefficients calculated using the measured values of i_L obtained from the polarisation curves. The results are summarised in Table 4.12.

The system was described by the three dimensionless numbers Re , Sc and Sh (Table 4.13) derived from the data of Table 4.12, and correlated, using three dimensional linear regression analyses, by the following equations:

$$Sh = 0.023 Re^{0.87} Sc^{0.32} \dots (4.2)$$

The correlation coefficient (r^2) was 0.990. In Fig.4.51 the term $Sh Sc^{-x}$ where $x = 0.32$, (Table 4.12) was plotted versus the Reynolds number. The solution of Equation 4.2 is shown by the solid line A-A, of slope 0.87, in Fig.4.50.

The empirical design equation for Cell 2 for turbulent flow with long electrodes was (p.128):

$$Sh = 0.023 Re^{0.8} Sc^{0.33} \dots (2.66)$$

The solution of Equation (2.66) is shown by the broken line B-B in Fig.4.50.

Temperature T °C	Kinematic Viscosity ν cm^2s^{-1} $\times 10^{-2}$	Diffusion Coefficient $D_{\text{Cu}^{2+}}$ cm^2s^{-1} $\times 10^{-6}$	Flow Rate U cm s^{-1}	Limiting Current Density i_L A cm^{-2} $\times 10^{-3}$	Bulk Concentration $c_b^{\text{Cu}^{2+}}$ mol cm^{-3} $\times 10^{-5}$	Mass Transfer Coefficient k_L $\text{cm s}^{-1} \times 10^{-3}$
60.1	0.49	12.04	18.0	5.94	1.32	2.33
60.1	0.49	12.04	19.9	6.50	1.32	2.55
60.1	0.49	12.04	27.8	9.05	1.30	3.61
60.1	0.49	12.04	40.0	12.3	1.30	4.90
60.1	0.49	12.04	59.4	17.9	1.30	7.14
60.1	0.49	12.04	73.3	20.8	1.31	8.23
60.1	0.49	12.04	147.8	39.1	1.30	15.6
60.0	0.49	12.00	101.1	28.9	1.36	11.0
55.0	0.56	10.90	76.7	20.1	1.35	7.72
50.3	0.62	9.88	95.6	20.3	1.36	7.73
50.2	0.63	9.85	21.1	5.19	1.36	1.98
50.2	0.63	9.85	23.3	5.67	1.36	2.16
50.2	0.63	9.85	29.4	7.06	1.36	2.69
50.2	0.63	9.85	34.4	8.18	1.37	3.09
50.2	0.63	9.85	58.9	12.7	1.36	4.84
50.2	0.63	9.85	71.1	16.2	1.35	6.22
50.2	0.63	9.85	157.8	35.3	1.37	13.4
50.2	0.63	9.85	164.4	31.5	1.36	12.0
45.2	0.70	8.92	76.7	15.9	1.35	6.10
40.0	0.78	7.92	28.9	5.67	1.36	2.16
40.0	0.78	7.92	38.9	6.94	1.29	2.79

/continued

Table 4.12 Summary of electrolysis conditions for the deposition of copper on 'long' electrodes in turbulent flow (de/L 0.088)

Table 4.12 continued

T °C	ν cm^2s^{-1} $\times 10^{-2}$	D cm^2s^{-1} $\times 10^{-6}$	U cm s^{-1}	$i_{L \text{ corr}}$ A cm^{-2} $\times 10^{-3}$	$c_b^{\text{Cu}^{2+}}$ mol cm^{-3} $\times 10^{-5}$	k_L cm s^{-1} $\times 10^{-3}$
40.0	0.78	7.92	73.3	13.3	1.31	5.26
40.0	0.78	7.92	144.4	22.4	1.28	9.07
40.0	0.78	7.92	276.1	34.7	1.33	13.5
36.8	0.82	7.39	73.3	12.6	1.35	4.82
36.8	0.82	7.39	73.3	13.4	1.35	5.16
36.5	0.83	7.36	73.9	12.2	1.34	4.72
28.4	0.98	6.10	276.7	23.5	1.28	9.51
27.7	0.99	6.00	50.0	6.23	1.28	2.52
27.7	0.99	6.00	86.7	9.89	1.28	4.00
27.7	0.99	6.00	130.0	13.9	1.28	5.63
27.7	0.99	6.00	217.8	22.3	1.28	9.03

Schmidt No. $[\frac{\nu}{D}]$ Sc	Reynolds No. $[\frac{u_{de}}{\nu}]$ Re	Sherwood No. $[\frac{K_L de}{D}]$ Sh	$\frac{Sh}{Sc^{0.33}}$	j-Factor $[Sh Sc^{-\frac{1}{3}} Re^{-1}]$ $\equiv f/2$ j $\times 10^{-3}$
407	3,148	166	22.5	7.15
407	3,479	182	24.6	7.07
407	4,858	257	34.8	7.16
407	6,996	349	47.2	6.75
407	10,397	508	68.7	6.61
407	12,826	586	79.2	6.18
407	25,846	1,110	150	5.80
408	17,684	786	106	5.99
514	11,733	607	75.9	6.47
628	13,208	671	78.5	5.94
640	2,872	172	20.0	6.96
640	3,174	188	21.9	6.90
640	4,006	234	27.2	6.79
640	4,686	269	31.3	6.68
640	8,011	421	49.0	6.12
640	9,673	541	62.9	6.50
640	21,463	1,166	136	6.34
640	22,370	1,044	121	5.41
785	9,386	586	63.7	6.79
985	3,174	234	23.6	7.37
985	4,273	302	30.4	7.11
985	8,057	569	57.3	7.11

/continued

Table 4.13 Dimensionless variables and experimental mass transfer coefficients for the deposition of copper on 'long' electrodes in turbulent flow.

(See also Appendix 4 for explanation of 'j-factor').

Table 4.13 continued

Sc	Re	Sh	$\frac{Sh}{Sc^{0.33}}$	$j \times 10^{-3}$
985	15,870	981	98.8	6.23
985	30,337	1,461	147	4.85
1,110	7,664	559	54.1	7.06
1,110	7,664	598	57.9	7.56
1,128	7,629	550	53.0	6.95
1,607	24,194	1,336	114	4.03
1,650	4,328	360	30.5	7.05
1,650	7,502	571	48.4	6.45
1,650	11,254	804	68.2	6.06
1,650	18,852	1,290	109	5.78

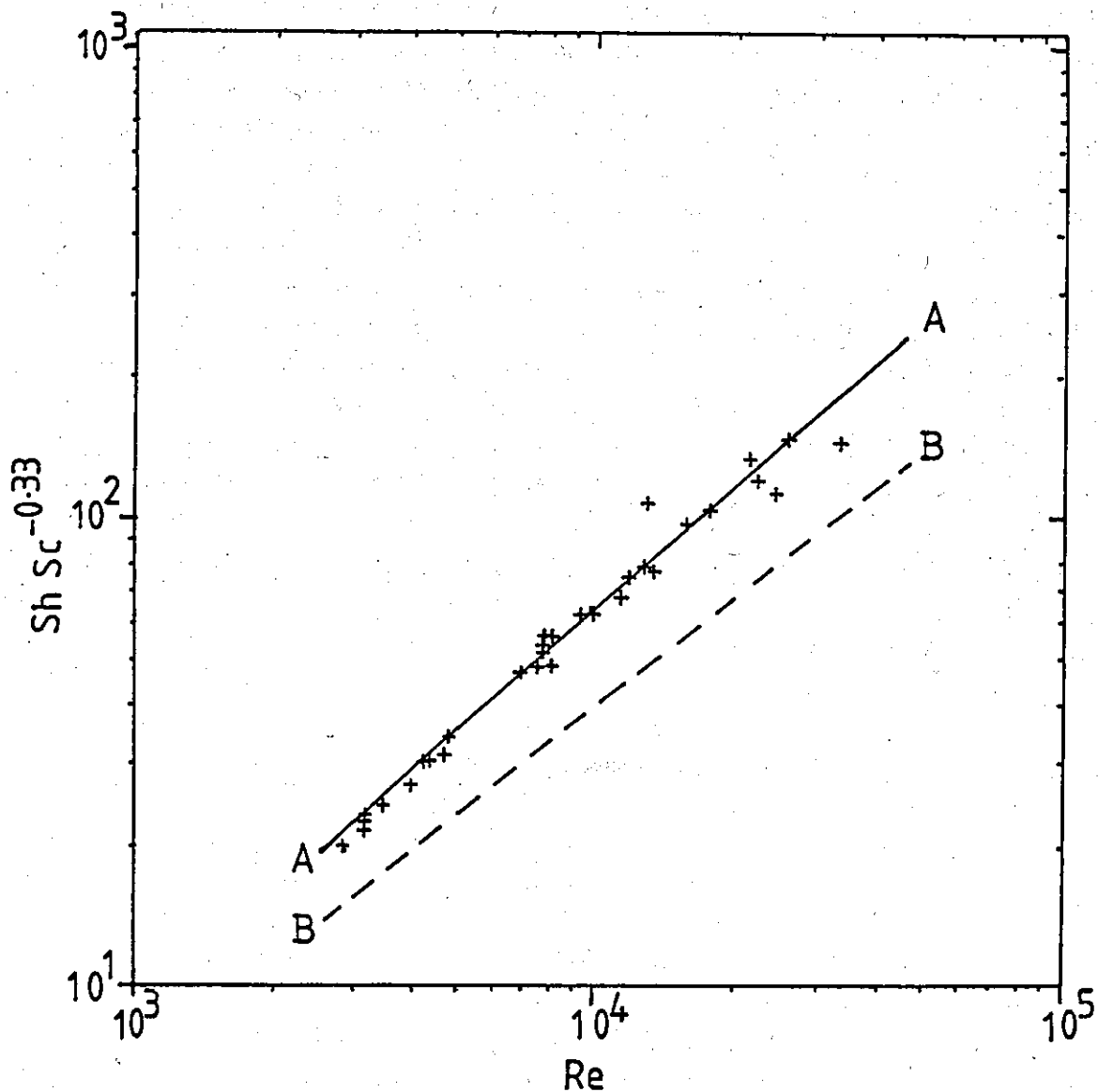


Fig.4.50 Mass transfer correlation for the cathodic deposition of copper from 0.014M copper sulphate electrolyte in turbulent flow ('long' electrodes, $L/d_e \sim 11.4$).

- A - A line of best fit of data (Equation 5.2)
- B---B Theoretical correlation (Equation 2.66)

The experimental mass transfer correlation (Eqn.4.2) would appear to be in good agreement with the design equation (Eqn.2.66) for the value of the constant and the exponent of the Schmidt number (Sc). However, the mass transfer coefficient (Sh) has a greater dependence upon the flow rate (Re) than would be predicted. It is evident from Fig.4.50 that the rate of mass transfer is again greater than expected (cf. p.175). (See also Appendix 4).

(ii) Short electrodes

Using short cathodes ($L/d_e < 10$), the mass transfer profile is developed over a significant proportion of the overall electrode length. Hence the overall mass transfer rate exhibits length dependence. The investigation is in two parts:

- (a) The relationship between i_L and flow rate (U) was studied at $34 \pm 2^\circ\text{C}$ using cathodes 2.4 cm ($2.8 d_e$) in length for a range of flow rates 44.4 to 191 cm s^{-1} (Re 4,645 to 19,973). (cf Long electrodes (p.176)).
- (b) The relationship between i_L and electrode length (L/d_e) was studied at 32°C using cathodes 0.45 to 8 cm (L/d_e 0.53 to 9.4) length and two flow rates corresponding to:
 - i) Low turbulent flow, Re $6,500 \pm 600$
 - ii) High turbulent flow, Re $23,600 \pm 2,300$

Polarisation measurements were determined for each set of experimental conditions. The polarisation behaviour (Figs.4.51 - 4.53) was similar to that described earlier (p.173). The limiting current densities were measured at a potential of -0.45 versus the Cu reference electrode.

(a) The relationship between i_L and U

The polarisation curves show an increase in the limiting current density with flow rate (Fig.4.51). The limiting current densities are summarised in Table 4.14. In Fig.4.54, i_L is plotted versus U on

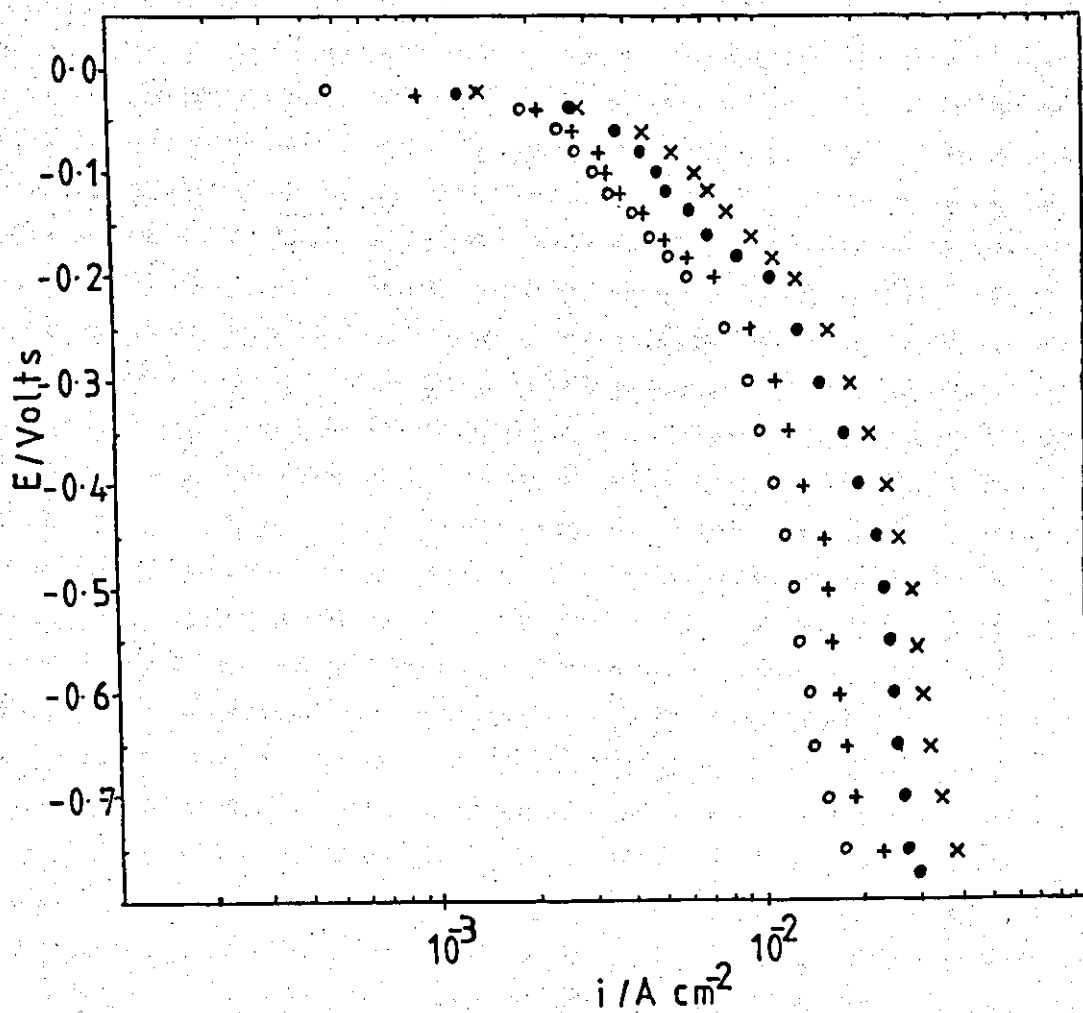


Fig.4.51 Cathodic polarisation during the electrolysis of 0.014M copper sulphate electrolyte in turbulent flow. Effect of flow rate

$T = 36^{\circ}\text{C}, L/de \sim 2.8$

7T	○	-	44.4 cm s^{-1} (Re 4,645)
8T	+	-	102 cm s^{-1} (Re 10,683)
9T	●	-	143 cm s^{-1} (Re 14,980)
10T	X	-	191 cm s^{-1} (Re 19,973)

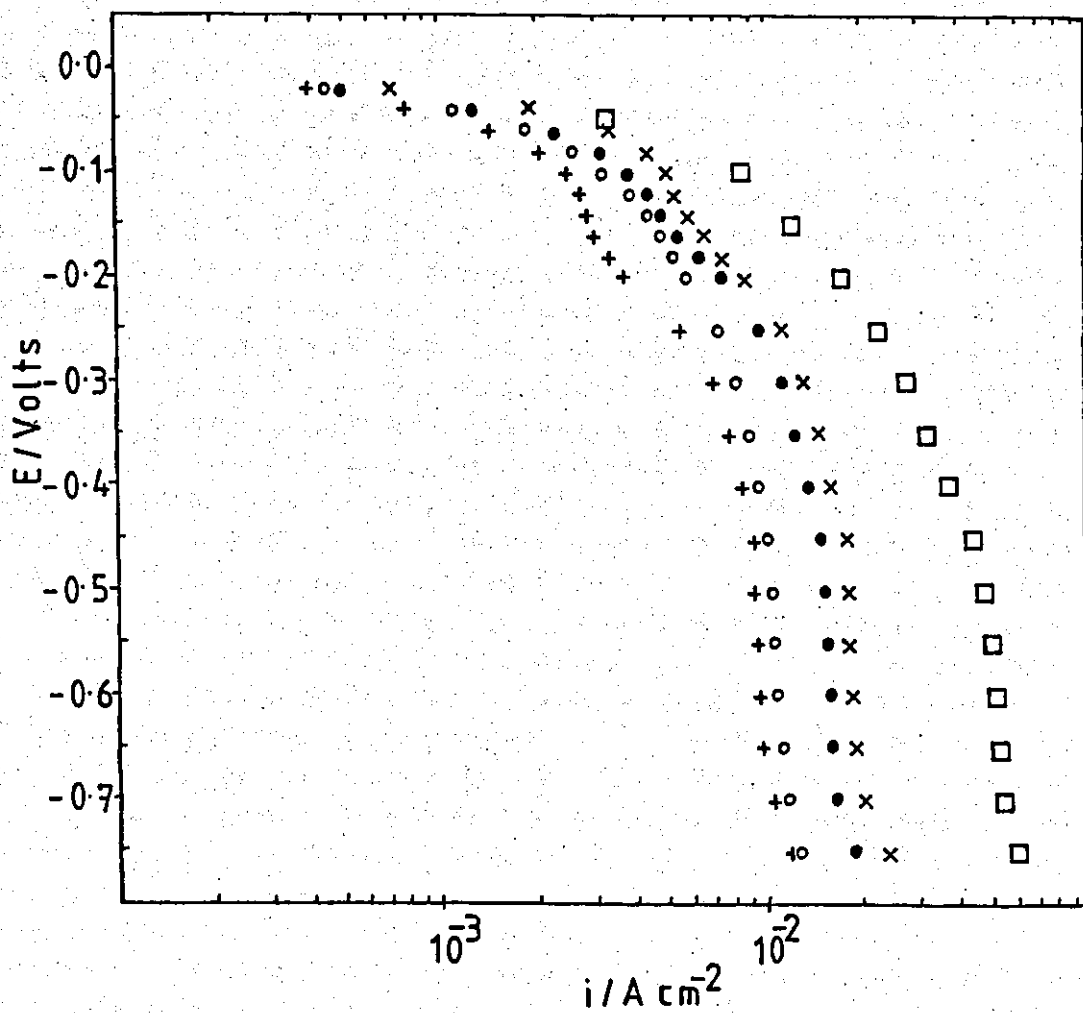


Fig.4.52 Cathodic polarisation during the electrolysis of 0.014M copper sulphate electrolyte at 32°C and $Re\ 6,500 \pm 600$.

- 1T + $L/de \sim 9.3$
- 3T o $L/de \sim 7.1$
- 6T ● $L/de \sim 3.0$
- 11T x $L/de \sim 2.4$
- 14T □ $L/de \sim 0.5$

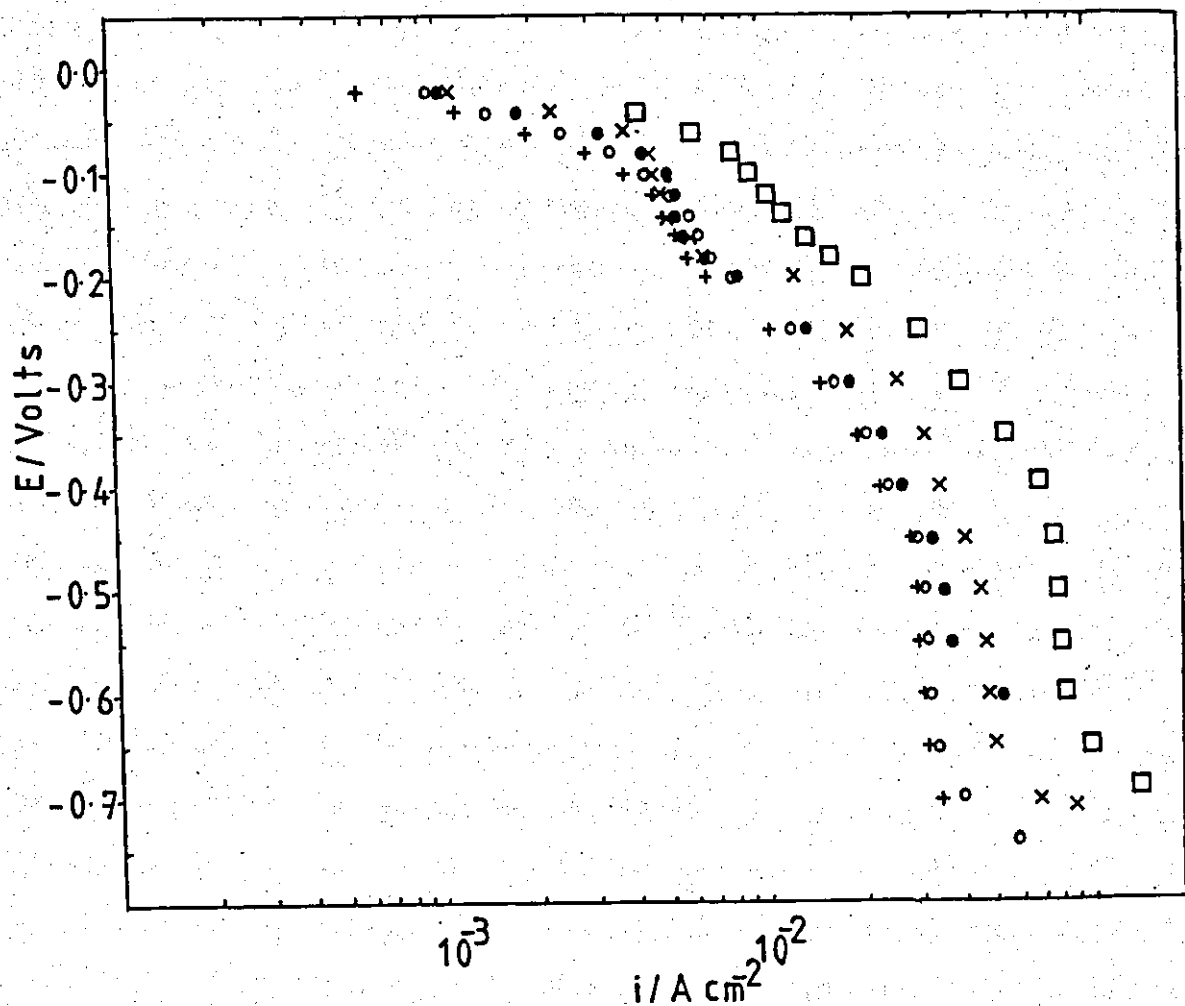


Fig.4.53 Cathodic polarisation during the electrolysis of 0.014M copper sulphate at 32°C and $Re\ 23,600 \pm 2,300$

- 2T + $L/de \sim 9.3$
- 4T ○ $L/de \sim 6.9$
- 5T ● $L/de \sim 4.7$
- 12T × $L/de \sim 2.3$
- 13T □ $L/de \sim 0.6$

Flow Rate U cm s ⁻¹	Reynolds Number Re	Corrected limiting current densities i _L /A cm ⁻² x 10 ⁻³
44.4	4,645	10.7
102	10,683	15.3
143	14,980	21.3
191	19,973	24.4

Table 4.14 Limiting current densities for copper deposition on cathodes 2.8 de (2.4 cm) in length at 36°C.

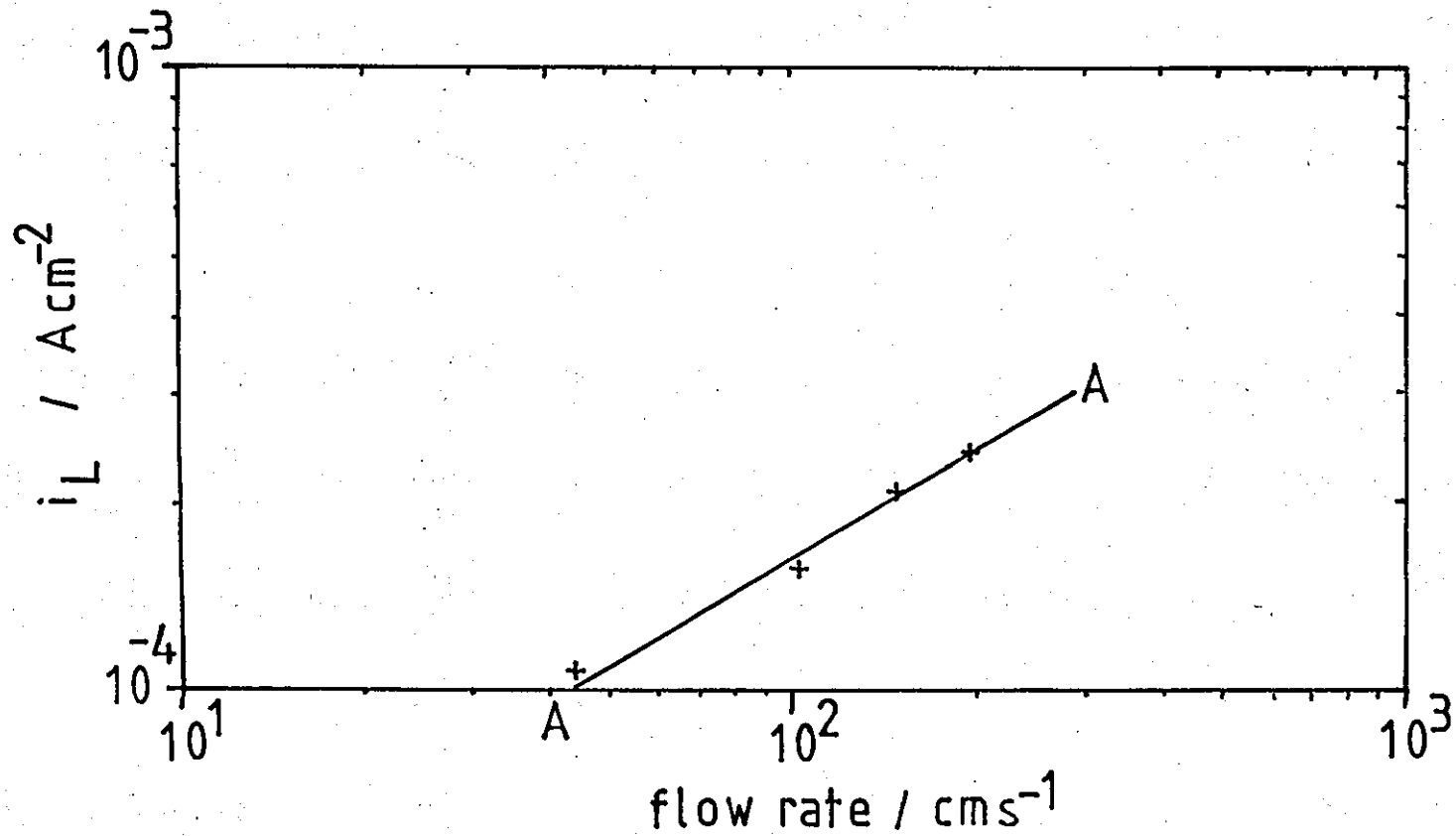


Fig.4.54 Effect of flow rate (turbulent flow) on the limiting current density for the cathodic deposition of copper, from 0.014M copper sulphate electrolyte, on cathodes 2.8 de in length at 36°C.

logarithmic coordinates. The data may be correlated by a line (A-A) of slope ~ 0.6 . This is in reasonable agreement with the slope of 0.67 predicted from the empirical design equations

$$\text{Sh} = 0.145 \text{ Re}^{0.67} \frac{d_e}{L}^{0.25} \text{Sc}^{0.33} \dots (2.67)$$

(b) The relationship between i_L and L/d_e

i) Re 6,500 \pm 600. The polarisation measurements (Fig.4.52) indicated that the limiting current densities increased as the cathode length decreased. The average limiting current densities are summarised in Table 4.15.

In Fig.4.55 i_L is plotted versus the cathode length (L/d_e). With very short electrodes ($L/d_e < 4.7$), the high mass transfer rates at the leading edge resulted in high average current densities. As the cathode length increased, the effect of the mass transfer entrance length became less significant and the average current density becomes more constant.

ii) Re 23,600 \pm 2,300. The polarisation curves are shown in Fig.4.53 and the corrected values of i_L are summarised in Table 4.16. In Fig.4.55, i_L is plotted versus L/d_e . The deposition rate was again greater on the shorter cathodes. The value of i_L was greater than observed at Re 6,500 \pm 600 for all cathode lengths. The data obtained in laminar flow are also shown for comparison.

Dimensionless number correlation of mass transfer data and interpretation

The rate of mass transfer to short electrodes in turbulent flow was correlated by a single equation in terms of the properties of the electrolyte, the geometry of the cell, the flow rate and the mass transfer coefficients calculated using the corrected values of i_L obtained from the polarisation measurements. The results are summarised in Table 4.16.

Electrode Length L/de	Average Limiting Current Density i_L $A\ cm^{-2}$ $\times 10^{-3}$
0.5	37.0
2.4	16.7
3.0	14.1
7.1	10.6
9.3	9.3

Table 4.15 Corrected limiting current densities for copper deposition on cathodes $< 9.3\ de$ in length at $Re\ 6,500 \pm 60$ and $32^\circ C$.

Electrode Length L/de	Average Limiting Current Density i_L $A\ cm^{-2}$ $\times 10^{-3}$
0.6	66.0
2.3	41.8
4.7	32.9
6.9	29.3
9.3	28.6

Table 4.16 Corrected limiting current densities for copper deposition on cathode $< 9.3\ de$ in length at $Re\ 23,600 \pm 2,300$ and $32^\circ C$.

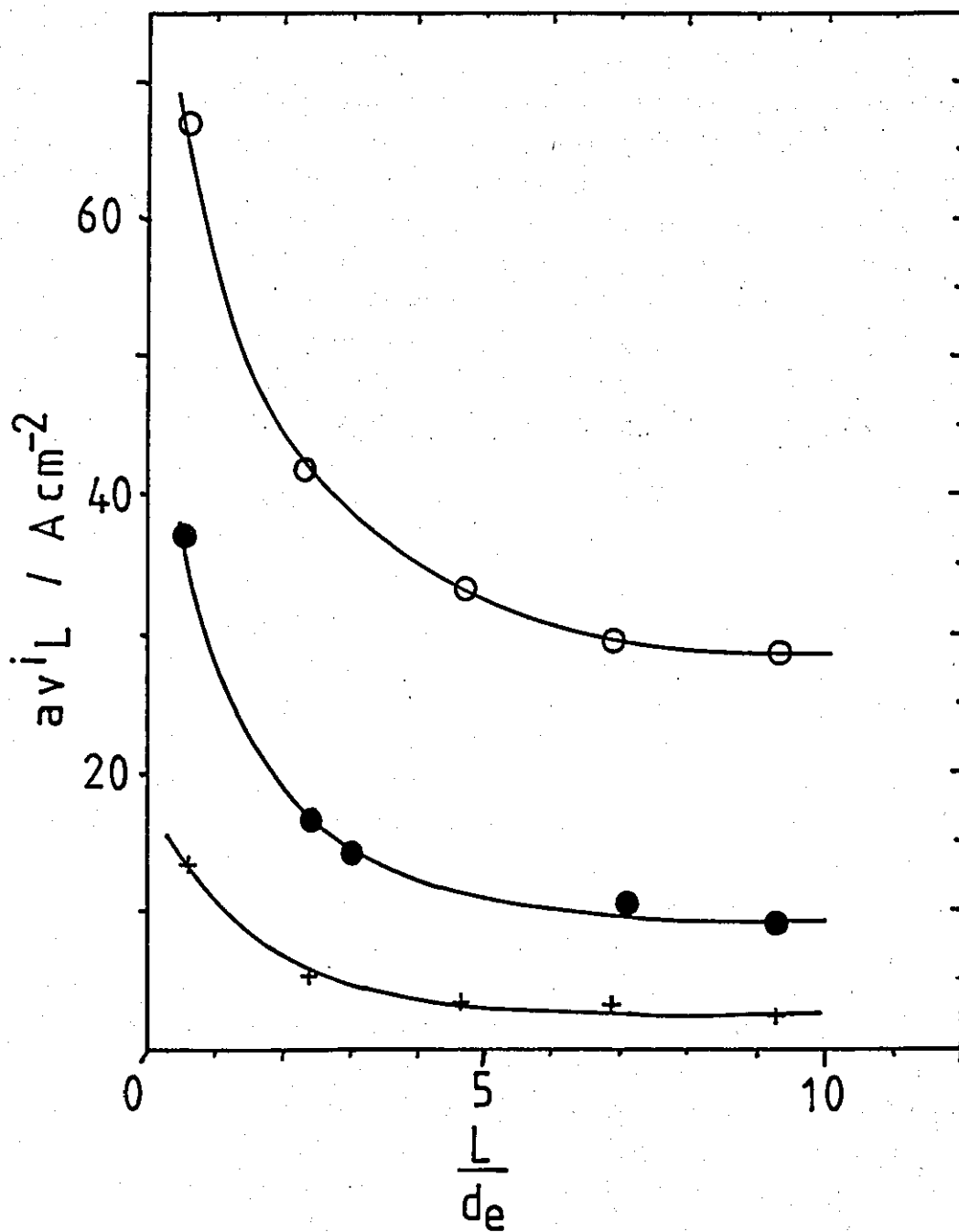


Fig.4.55 Effect of the cathode length on the limiting current density for the deposition of copper from 0.014M copper sulphate electrolyte at $32 \pm 1^\circ C$

- - $Re\ 23,600 \pm 2,300$
- - $Re\ 6,500 \pm 600$
- + - $Re\ 1,019 \pm 96$

The system was described by the four dimensionless numbers Re , Sc , d_e/L and Sh (Table 4.18) derived from the data of Table 4.17 and correlated using linear regression analysis by the following equation:

$$Sh = 0.181 Re^{0.72} d_e/L^{0.42} Sc^{0.33} \dots \dots (4.3)$$

The correlation coefficient (r^2) was 0.91. In Fig.4.56 the experimental values of Sh are plotted versus the solution of Equation (4.3). The calculated solution of Equation (4.3) is shown by the line A-A.

The empirical design equation for short electrodes in turbulent flow was (p.128):

$$Sh = 0.145 Re^{0.67} d_e/L^{0.25} Sc^{0.33} \dots \dots (2.67)$$

It may be seen by inspection of the two equations (2.67) and (4.3) that the rate of mass transfer in the cell is slightly greater than would be expected from Equation (2.67) (cf. Long electrodes p.177). (see Table 4.18).

Overall summary of Section 4.2.1

Copper was deposited potentiodynamically from an electrolyte of nominal composition, 0.014M $Cu SO_4$ and 1.5M H_2SO_4 on copper cathodes at Reynolds number up to Re 19,973. Polarisation measurements were determined as a function of flow rate, electrolyte temperature and cathode length. From limiting current density measurements (at $E = -450mV$) the mass transfer coefficients were calculated. The data were correlated using dimensionless numbers.

The following trends were observed:

- (i) The limiting current density increased with increasing flow rate (U) at a constant cathode length and temperature.

Dimensionless Electrode Length d_e/L	Temperature T °C	Kinematic Viscosity ν cm^2s^{-1} $\times 10^{-2}$	Diffusion Coefficient $D_{\text{Cu}^{2+}}$ cm^2s^{-1} $\times 10^{-6}$	Flow Rate U cm s^{-1}	Corrected Limiting Current Density i_L corr. A cm^{-2} $\times 10^{-3}$	Bulk Concentration c_b mol cm^{-3} $\times 10^{-5}$	Mass Transfer Coefficient k_L cm s^{-1} $\times 10^{-3}$
0.107	32.5	0.91	6.72	73.9	9.3	1.30	3.71
0.107	32.3	0.91	6.68	271.1	28.6	1.30	11.4
0.143	31.9	0.92	6.64	73.9	10.6	1.30	4.11
0.145	32.3	0.91	6.68	271.1	29.3	1.30	11.7
0.214	32.9	0.90	6.78	271.1	32.9	1.30	13.1
0.343	24.5	1.07	5.54	73.9	14.1	1.30	5.62
0.357	36.0	0.82	7.24	44.4	10.7	1.32	4.20
0.357	36.0	0.82	7.24	102.2	15.3	1.32	6.01
0.357	36.0	0.82	7.24	143.3	21.3	1.32	8.36
0.357	36.0	0.82	7.24	191.1	24.4	1.32	9.58
0.429	30.2	0.95	6.36	73.9	16.7	1.29	6.71
0.440	31.5	0.92	6.56	271.1	41.8	1.29	16.8
1.71	31.9	0.92	6.64	271.1	66.0	1.29	26.5
1.90	32.8	0.90	6.76	73.9	37.0	1.29	14.9

Table 4.17 Summary of electrolysis conditions for the deposition of copper on 'short' electrodes in turbulent flow ($d_e = 0.857$ cm).

Dimensionless Electrode length d_e/L	Schmidt No.. $[\frac{v}{D}]$ Sc	Reynolds No. $[\frac{u d_e}{v}]$ Re	Sherwood No. $[\frac{k_L d_e}{D}]$ Sh	$Re^{0.72} Sc^{0.33}$ $d_e/L^{0.42}$	$Re^{2/3} Sc^{1/3}$ $d_e/L^{1/4}$
0.107	1,354	6,959	473	2,522	2,308
0.107	1,362	25,532	1,463	6,444	5,502
0.143	1,386	6,883	531	2,849	2,482
0.145	1,362	25,532	1,501	7,321	5,937
0.214	1,327	25,816	1,656	8,615	6,535
0.343	1,931	5,918	869	4,121	3,119
0.357	1,133	4,645	497	2,947	2,244
0.357	1,133	10,683	711	5,368	3,912
0.357	1,133	14,980	990	6,848	4,901
0.357	1,133	19,973	1,134	5,938	8,424
0.429	1,494	6,666	904	4,528	3,279
0.440	1,402	21,376	2,195	10,367	7,027
1.71	1,386	21,376	3,420	18,265	9,829
1.90	1,331	7,036	1,888	8,463	4,745

Table 4.18 Dimensionless variables and experimental mass transfer coefficients for the deposition of copper on 'short' electrodes ($d_e = 0.857$ cm).

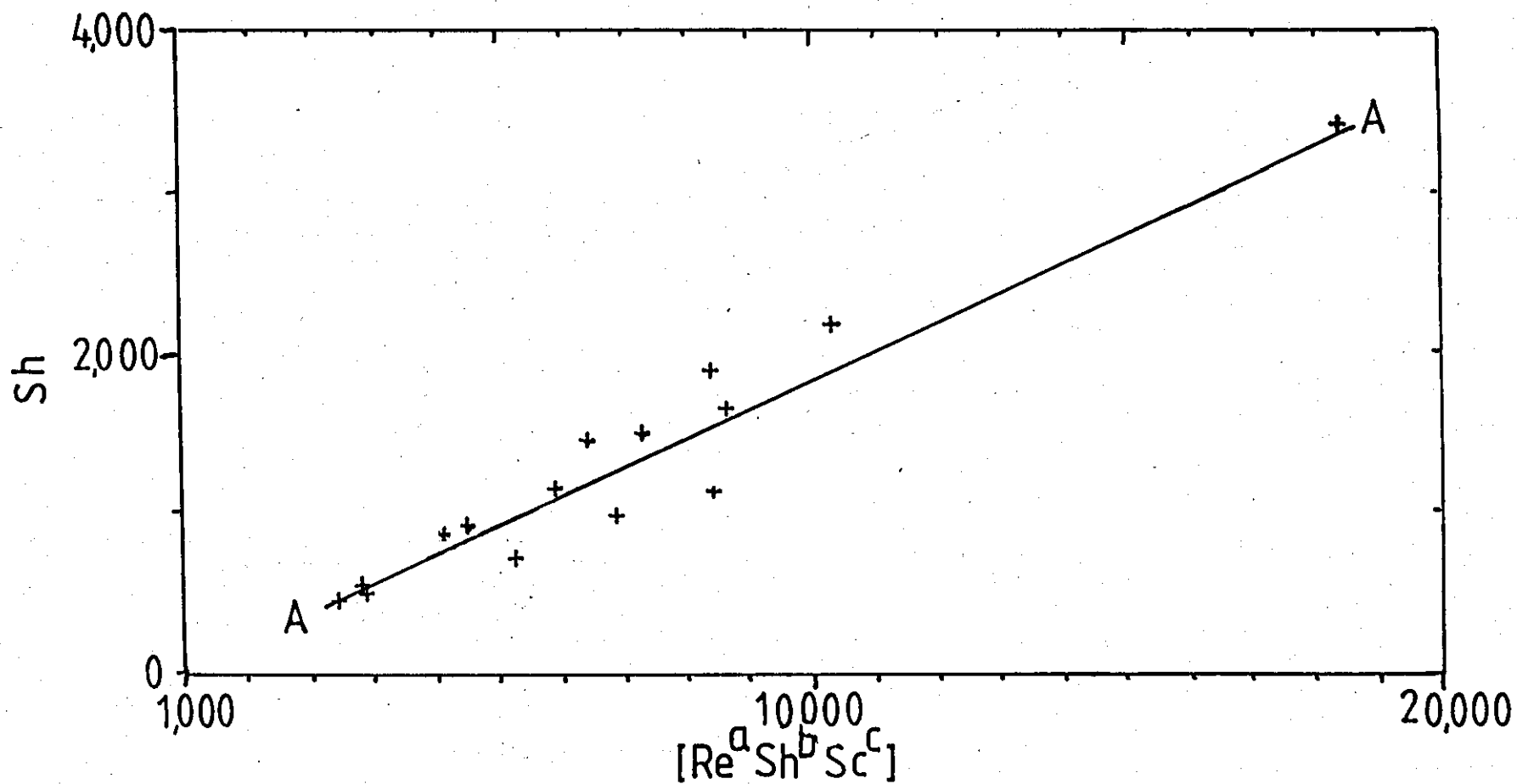


Fig.4.56 Mass transfer correlation for the cathodic deposition of copper from 0.014M copper sulphate electrolyte in turbulent flow ('short' electrodes, $L/de < 9.4$).

A — A line of best fit of data
(Equation 5.3)

- (ii) The average limiting current density increased with decreasing cathode length at a constant flow rate and temperature, particularly with cathodes < 5 cm in length.
- (iii) The limiting current density increased with increasing temperature.

The following dimensionless mass transfer correlations were calculated from limiting current density measurements:

- (i) In Laminar flow ($Re < 2,500$) the rate of mass transfer in Cell 2 may be described by the equation:

$$Sh = 2.8 \left\{ Re \frac{de}{L} Sc \right\}^{0.33} \dots \dots (4.1)$$

- (ii) In Turbulent flow ($Re 2,500$ to $31,000$), the rate of mass transfer to Long electrodes ($L/de \geq 11.4$) may be described by the equation:

$$Sh = 0.023 Re^{0.87} Sc^{0.33} \dots \dots (4.2)$$

- (iii) In Turbulent flow, the rate of mass transfer to Short electrodes ($L/de < 11.4$) may be described by the equation:

$$Sh = 0.181 Re^{0.72} \frac{de}{L}^{0.42} Sc^{0.33} \dots \dots (4.3)$$

For all conditions the experimental results suggest that the mass transport rate in Cell 2 is slightly greater than would be expected from the design equations. The differences may be due to the unusual split cell design and error in the calculation of the equivalent diameter of the cell.

4.2.2 Cathode current distribution during the deposition of copper from the $CuSO_4 - H_2SO_4$ electrolyte

The appearance and structures of the nickel foils produced in the Mark 1 cell showed similarities when the leading and trailing edges were examined. This suggested that deposition conditions might be similar. Information from the copper system was desirable for comparison purposes.

Copper was deposited from an electrolyte of nominal composition, 0.014M $\text{CuSO}_4 \cdot 6\text{H}_2\text{O}$ in 1.5M H_2SO_4 supporting electrolyte at 36°C on to a preplated segmented nickel cathode 10 cm ($L/d_e = 11.7$) in length. Electrolysis was carried out at a constant average current density (i_{av}) in Laminar flow (Re 743) and Turbulent flow (Re 14,864 and Re 18,580).

Details of the segmented cathode, current measuring instrumentation and calibration, and the experimental procedures with a sample calculation are given in Section 3.4.2.

For each experiment, the voltage drop (V) across each resistor (R) was measured, the partial (local) current density (i_x), the local mass transfer coefficient (k_L^x) and the dimensionless current density ($\frac{i_x}{i_{av}}$) calculated.

a) Laminar Flow

Copper was deposited on the segmented cathode under limiting current conditions at Re 743. The average limiting current density ($2.08 \times 10^{-3} \text{A cm}^{-2}$) for the system was determined from Fig.4.42 and the current adjusted accordingly. The results are summarised in Table 4.19.

In Fig.4.57, the ratio $\frac{i_L^x}{i_L^{av}}$ was plotted versus the fractional distance along the cathode, $\frac{x}{L}$. The resulting current distribution showed a high current density ($>2 i_L^{av}$) at the leading edge segment of the cathode. The deposition rate then progressively decreased further downstream reaching a value of $\sim 0.7 i_L^{av}$ at the trailing edge segment.

b) Turbulent Flow

The current distributions for copper deposition were measured for limiting current conditions at two flow rates, corresponding to Re 14,864 and Re 18,580. An additional experiment was carried out at Re 18,580 at $0.5 i_L$ to determine the current distributions at sub-limiting current densities. The average limiting current densities

Segment No.	Resistance Ohms R	p.d. Volts, V $\times 10^{-3}$	Partial Current $\frac{V}{R}$ amps $\times 10^{-3}$	Partial Current Density i_x A $\text{cm}^{-2} \times 10^{-3}$	$\frac{x}{L} \times 10^{-2}$
Leading edge					
1	0.498	5.3	10.6	4.42	4
2	0.468	2.9	6.2	2.58	12.36
3	0.480	2.6	5.4	2.25	20.73
4	0.484	2.3	4.8	2.0	20.09
5	0.485	2.4	5.0	2.08	37.46
6	0.477	2.1	4.4	1.83	45.82
7	0.486	2.0	4.1	1.71	54.18
8	0.485	1.9	3.9	1.63	62.55
9	0.484	1.9	3.9	1.63	70.91
10	0.485	1.8	3.7	1.54	79.28
11	0.486	1.7	3.5	1.46	87.64
12	0.485	1.8	3.7	1.54	96.00

Table 4.19 Deposition of copper on to a segmented cathode in laminar flow.

Flow Rate $\sim 7.11 \text{ cm s}^{-1} \equiv \text{Re} \sim 743$

Segment Area $\sim 2.4 \text{ cm}^2$

Total Electrode Area $\sim 28.8 \text{ cm}^2$

Total Current $\sim 0.060 \text{ A}$

Average Current Density, $i_L^{\text{av}} \sim 0.00208 \text{ A cm}^{-2}$

Bulk Concentration, $c_B^{\text{Cu}^{2+}} \sim 1.29 \times 10^{-5} \text{ mol cm}^{-3}$

Average Mass Transfer Coefficient $k_{LAV}^{\text{Cu}^{2+}} \sim 0.84 \times 10^{-3} \text{ cm s}^{-1}$

Temperature, T 36.3°C

Total Electrode Length, L $\sim 10.0 \text{ cm}$, Segment Length $\sim 0.8 \text{ cm}$

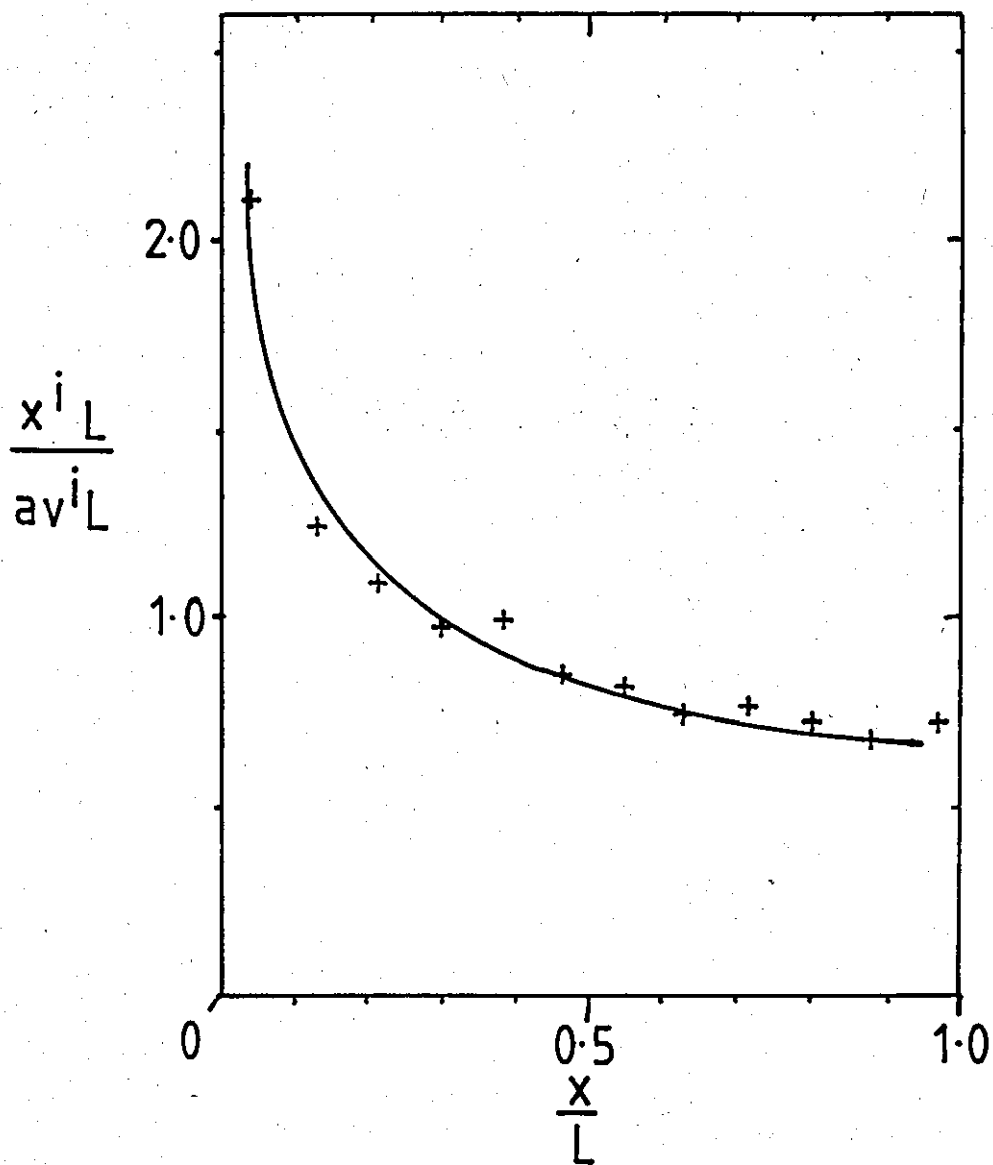


Fig.4.57 Longitudinal current distribution (copper deposition) along a segmented electrode 11.7 equivalent diameters in length at $\sim 36^\circ\text{C}$ and $\text{Re } 743$.

were determined from Fig.4.50. At Re 14,864, copper was deposited at an average limiting current density of $14.3 \times 10^{-3} \text{ A cm}^{-2}$ (Table 4.20). The current distribution (Fig.4.58) again showed the high current density region ($>1.3 i_L^{av}$) at the leading edge segment. The deposition rate remained constant ($0.98 \pm 0.02 i_L^{av}$) when $\frac{x}{L} > 0.3$.

At Re 18,580, copper was deposited at an average limiting current density of $16.1 \times 10^{-3} \text{ A cm}^{-2}$ (Table 4.21). The current distribution is shown in Fig.4.58. There was a high deposition rate ($>1.54 i_L^{av}$) at the leading edge and a more constant current density ($1.0 \pm 0.05 i_L^{av}$) further downstream ($\frac{x}{L} > 0.3$). In turbulent flow the mass transfer boundary layer develops more rapidly and the entry length is shorter. The current distribution for laminar flow is also shown in Fig.4.58 for comparison.

At a sub-limiting current density ($0.5 i_L^{av}$) of $8.4 \times 10^{-3} \text{ A cm}^{-2}$ (Table 4.22), a different type of current distribution was observed (Fig.4.59). The current distribution was much more symmetrical, with relatively small increases at both leading and trailing edges. This type of profile is similar to the primary current distribution.

The current distribution for limiting current operation is also shown in Fig.4.59, where the high value of current density at the leading edge may be noted.

Summary of Section 4.2.2

A segmented electrode was used to determine the cathodic current distribution for copper deposition at $34 \pm 2^\circ\text{C}$. Current distributions were obtained in both laminar and turbulent flow.

- a) In laminar flow (Re 733) with limiting current operation, the current density decreased from a maximum at the leading edge to a minimum at the trailing edge.

Segment No.	Resistance Ohms, R	p.d. Volts, V $\times 10^{-3}$	Partial Current $\frac{V}{R}$ amps $\times 10^{-3}$	Partial Current Density i_x A cm^{-2} $\times 10^{-3}$	$\frac{x}{L}$ $\times 10^{-2}$
Leading edge					
1	0.498	22.7	45.6	19.0	4
2	0.468	16.6	35.5	14.8	12.36
3	0.480	19.0	39.6	16.5	20.73
4	0.484	16.3	33.7	14.0	29.09
5	0.485	16.9	34.9	14.5	37.46
6	0.477	15.6	32.7	13.6	45.82
7	0.486	16.3	33.5	13.9	54.18
8	0.485	16.7	34.4	14.3	62.55
9	0.484	16.4	33.9	14.1	70.91
10	0.485	16.2	33.4	13.9	79.28
11	0.486	16.7	34.4	14.3	87.64
12	0.485	17.4	35.9	14.9	96.00

Table 4.20 Deposition of copper on to a segmented cathode in turbulent flow, Re 14,864.

Flow Rate $\sim 142.2 \text{ cm s}^{-1} \equiv Re \sim 14,864$

Segment Area $\sim 2.4 \text{ cm}^2$

Total Electrode Area $\sim 28.8 \text{ cm}^2$

Total Current $\sim 0.428 \text{ A}$

Average Current Density, $i_L^{av} \sim 0.0148 \text{ A cm}^{-2}$

Bulk Concentration, $c_b^{Cu^{2+}} \sim 1.29 \times 10^{-5} \text{ mol cm}^{-3}$

Average Mass Transfer Coefficient $\sim 5.96 \times 10^{-3} \text{ cm s}^{-1}$

Temperature, $T \sim 36.3^\circ\text{C}$

Total Electrode Length, $L \sim 10.0 \text{ cm}$, Segment Length $\sim 0.8 \text{ cm}$

Segment No.	Resistance Ohms, R	p.d. Volts, V $\times 10^{-3}$	Partial Current $\frac{V}{R}$, amps $\times 10^{-3}$	Partial Current Density i A cm^{-2} $\times 10^{-3}$	$\frac{x}{L}$ $\times 10^{-1}$
Leading edge					
1	0.429	23.9	55.7	23.2	4
2	0.429	18.3	42.7	17.8	12.36
3	0.430	20.1	46.7	19.5	20.73
4	0.430	17.3	40.2	16.8	29.09
5	0.428	16.7	39.0	16.3	37.46
6	0.428	16.6	38.8	16.2	45.82
7	0.428	17.1	39.9	16.7	54.18
8	0.431	17.6	38.2	15.9	62.55
9	0.430	17.1	39.8	16.6	70.91
10	0.427	17.1	40.1	16.7	79.28
11	0.428	17.7	41.4	17.2	87.64
12	0.428	18.0	42.1	17.5	96.00

Table 4.21 Deposition of copper on to a segmented cathode in turbulent flow, Re 18,580.

Flow Rate $177.8 \text{ cm s}^{-1} \equiv \text{Re } \sim 18,580$

Segment Area $\sim 2.4 \text{ cm}^2$

Total Electrode Area $\sim 28.8 \text{ cm}^2$

Total Current $\sim 0.463 \text{ A}$

Average Current Density, i_L^{av} $\sim 0.0161 \text{ A cm}^{-2}$

Bulk Concentration, $c_b^{\text{Cu}^{2+}}$ $\sim 1.29 \times 10^{-5} \text{ mol cm}^{-3}$

Average Mass Transfer Coefficient $\sim 6.45 \times 10^{-3} \text{ cm s}^{-1}$

Temperature, T $\sim 36.3^\circ\text{C}$

Total Electrode Length, L $\sim 10.0 \text{ cm}$, Segment Length $\sim 0.8 \text{ cm}$

Segment No.	Resistance Ohms, R	p.d. Volts, V $\times 10^{-3}$	Partial Current $\frac{V}{R}$, Amps $\times 10^{-3}$	Partial Current Density i A cm^{-2} $\times 10^{-3}$	$\frac{x}{L}$
Leading Edge					
1	0.428	8.9	20.8	8.66	4
2	0.428	8.5	19.9	8.28	12.36
3	0.427	8.3	19.4	8.10	20.73
4	0.430	8.4	19.5	8.14	29.09
5	0.431	8.5	19.7	8.22	37.46
6	0.428	8.2	19.6	7.98	45.82
7	0.428	8.1	18.9	7.89	54.18
8	0.428	8.2	19.2	7.98	62.55
9	0.430	8.4	19.5	8.14	70.91
10	0.430	9.2	21.4	8.92	79.28
11	0.429	8.8	20.5	8.54	87.64
12	0.429	10.1	23.5	9.79	96.00

Table 4.22. Deposition of copper, at sub-limiting current density, on to a segmented cathode in turbulent flow, Re 18,580.

Flow Rate $177.8 \text{ cm s}^{-1} \equiv \text{Re} \sim 18,580$

Segment Area $\sim 2.4 \text{ cm}^2$

Total Electrode Area $\sim 28.8 \text{ cm}^2$

Total Current $\sim 0.242 \text{ A}$

Average Current Density $0.5 i_L^{\text{av}} \sim 0.0084 \text{ A cm}^{-2}$

Bulk Concentration $c_b^{\text{Cu}^{2+}} \sim 1.29 \times 10^{-5} \text{ mol cm}^{-3}$

Average Mass Transfer Coefficient $k_L^{\text{Cu}^{2+}} \sim 3.37 \times 10^{-3} \text{ cm s}^{-1}$

Temperature, T $\sim 36.3^\circ\text{C}$

Total Electrode Length, L $\sim 10.0 \text{ cm}$, Segment Length $\sim 0.8 \text{ cm}$

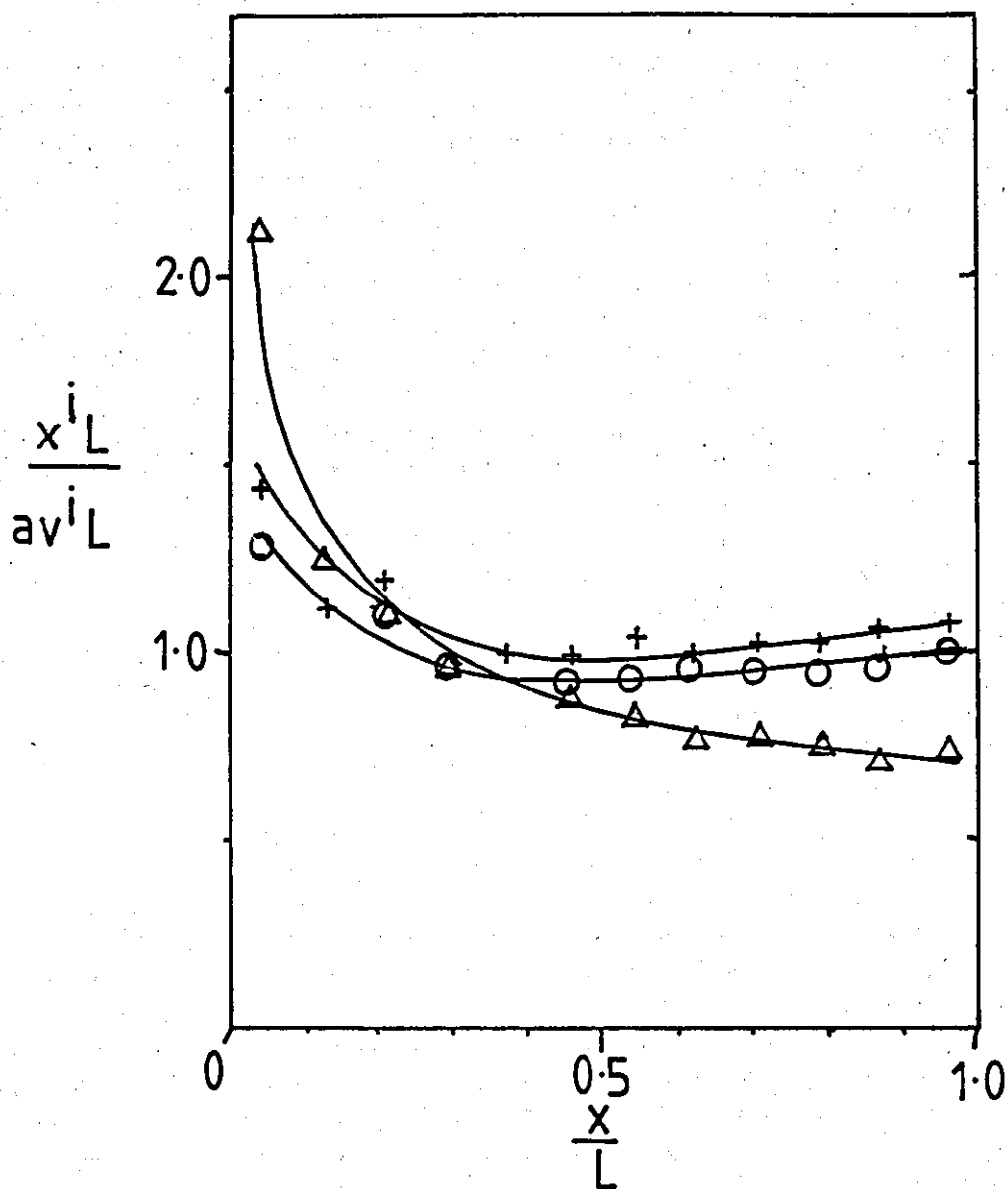


Fig.4.58 Longitudinal current distribution (copper deposition) along a segmented electrode 11.7 equivalent diameters in length at $\sim 36^\circ\text{C}$.

- Δ - Re 743
- \circ - Re 14,864
- $+$ - Re 18,580

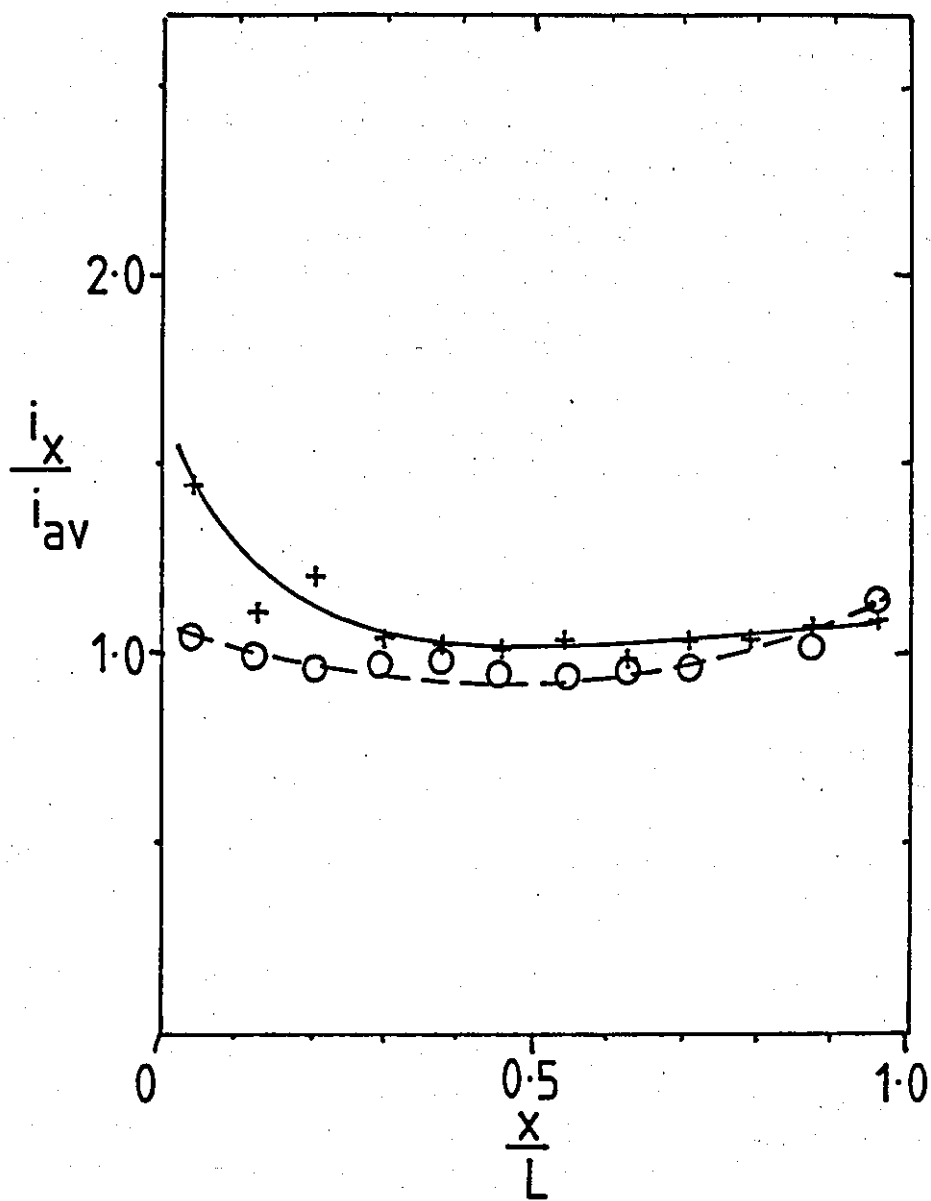


Fig.4.59 Longitudinal current distribution (copper deposition) along a segmented electrode 11.7 equivalent diameters in length at $\sim 36^\circ\text{C}$ and $\text{Re } 18,580$.

——— $av^iL \quad \equiv 0.0161 \text{ A cm}^{-2}$
 - - - $av^iL/2 \quad \equiv 0.0084 \text{ A cm}^{-2}$

- b) In turbulent flow (Re 14,864 and 18,580) with limiting current operation, the deposition rate was greatest at the leading edge segment. However, due to rapid development of the mass transfer profile, the deposition rate was similar for $\frac{x}{L} > 0.3$.
- c) At sub-limiting current densities ($0.5 i_L^{av}$) the current distribution was more symmetrical and only relatively small increases in current densities were observed at both the leading and trailing edges.

4.3 Studies of the electroforming of nickel foils from concentrated Ni sulphamate solutions in the Mark 2 Parallel Plate Cell

The experimental results are presented in two main sections. The first of these deals with all of the work carried out at 60°C and this is primarily concerned with the effects of electrode length upon the nature of the appearance and characteristics of the foils produced under a range of deposition conditions in which the flow rate and current density were the main variables. The second main section deals with the effects of temperature on the relationships between foil structures, flow rates and current densities, using long electrode systems only.

4.3.1 The effects of cathode length during the electroforming of Ni foils at 60°C

The mass transfer entrance length of an electrode in pipe-flow is characterised by faster transport rates. In the turbulent flow regime, the entrance region develops rapidly and electrode systems have to be comparatively short to exhibit length dependent mass transfer rates. In parallel plate cells, the electrode length may be defined in terms of the ratio L/d_e (Section 3.3).

In Cell 2, the maximum cathode length was 10cm ($L/d_e \sim 11.7$) and several stainless steel or nickel cathodes of this length were constructed. In addition a nickel electrode, 2.5cm ($L/d_e \sim 2.92$) in length was also available. The remaining electrode length was replaced by a suitable 'Perspex' block (Fig.3.18).

For cathodes of other lengths, the effective electrode length was altered by masking with P.T.F.E. tape and 'Lacomit' to leave exposed the necessary electrode area.

(a) Electroforming studies at 60°C, on cathodes 2.92 equivalent diameters in length in the Mark 2 cell

The cathode was of the 'short electrode' type and was therefore broadly similar to the Cell 1 electrode systems (L/d_e 3.3). The objective

of this work was to provide some confirmation of the previous (Cell 1) observations and to assess the effectiveness of the diaphragm. The programme of investigation included studies of the following:

i) Deposition at constant current density (0.4 A cm^{-2}) over the flow range Re 1,343 to Re 7,414

The constant current density investigation was designed to study the effect of flow rate on the current efficiency and assess the performance of the diaphragm with respect to deposit perforations.

ii) Deposition under conditions of turbulent flow (Re 3,050 - 13,864)

Nickel foils were prepared over a range of current densities at three Reynolds numbers, $\text{Re} \sim 3,075$, $\text{Re} \sim 7,650$ and $\text{Re} \sim 13,864$. The deposit structures were examined as a function of current density at each flow rate to determine the maximum current density for sound deposits.

i) Deposition at constant current density (0.4 A cm^{-2})

A series of nickel foils $23 \mu\text{m}$ thick was electroformed over the flow range Re 1,343 to Re 7,414 as shown in Table 4.23. Under these conditions all the deposits were sound (fine grained), coherent and lustrous. The current efficiency was $96 \pm 6\%$ and there was no evidence of flow rate effects. On visual examination, the foils were found to have significantly less macro-porosity than similar Cell 1 deposits. At the highest flow-rates, the number of perforations was small with only 2-3 random holes being observed.

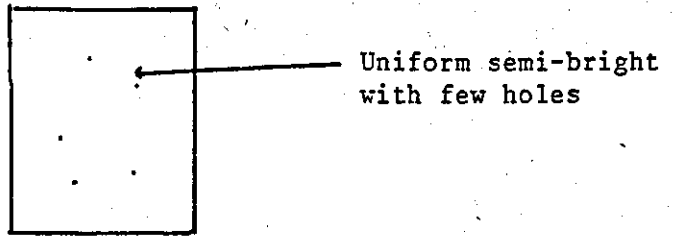
ii) Deposition under conditions of turbulent flow
Nickel electroforms deposited at a flow rate of $\text{Re } 3,075 \pm 25$

Nickel foils, $22 \pm 2 \mu\text{m}$ thick, were electroformed at current densities of 0.4, 0.7 and 0.8 A cm^{-2} , as shown in Table 4.24. No foils showed significant visible porosity. At current densities $< 0.7 \text{ A cm}^{-2}$, the deposits were sound, lustrous and fine grained over the entire electrode length. Narrow bands of brighter material were deposited at the leading and trailing edges at 0.7 A cm^{-2} (Fig.4.60 (a) and (b)). The current efficiency was 97% for both foils.

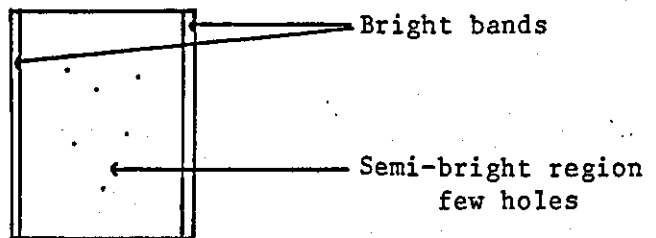
Reynolds Number	Weight Deposited g	Current Efficiency %
1,343	0.1432	95
1,576	0.1424	95
1,808	0.1346	89
2,376	0.1459	97
2,377	0.1464	97
2,377	0.1441	96
2,428	0.1415	94
2,971	0.1464	97
3,100	0.1465	97
4,417	0.1494	99
4,443	0.1461	97
4,443	0.1409	94
5,244	0.1455	97
5,502	0.1391	92
5,502	0.1452	96
6,587	0.1521	101
6,897	0.1480	98
7,233	0.1444	96
7,388	0.1406	93
7,414	0.1402	93
7,414	0.1437	95
7,414	0.1468	98

Table 4.23 Nickel foils deposited on electrodes 2.92 equivalent diameters in length at a current density of 0.04 A cm^{-2} for 165s at 60°C .

a) 0.4 A cm^{-2}



b) 0.7 A cm^{-2}



c) 0.8 A cm^{-2}

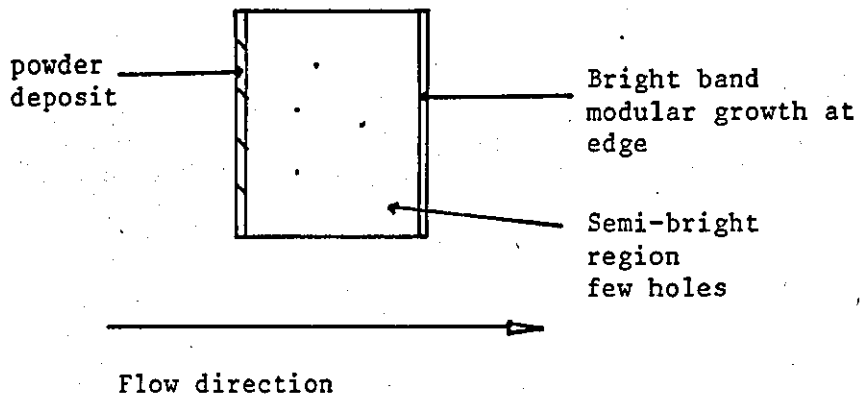
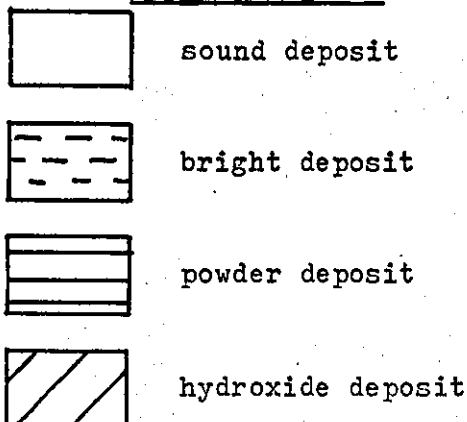


Fig.4.60

Schematic diagrams of nickel foils deposited on electrodes 2.92 equivalent diameters in length at $Re \ 3,075 \pm 25$ and 60°C .

key to diagrams



Current Density i $A\ cm^{-2}$	Deposition Time s	Weight Deposited g	Current Efficiency $\%$	Deposit Thickness μm
0.40	165	0.1465	97	22
0.70	104	0.1615	97	24
0.80	91	0.1535	92	23

Table 4.24 Nickel foils deposited on electrodes 2.92 equivalent diameters in length at 60°C and $Re\ 3,075 \pm 25$

Current Density i $A\ cm^{-2}$	Deposition Time s	Weight Deposited g	Current Efficiency $\%$	Deposit Thickness μm
0.40	165	0.1445	96	22
0.68	97	0.1416	94	22
0.70	97	0.1478	95	22
1.05	70	0.1605	96	24
1.21	60	0.1512	91	-
1.36	53	0.1358	83	-

Table 4.25 Nickel foils deposited on electrodes 2.92 equivalent diameters in length at 60°C and $Re\ 7,650 \pm 250$.

At the highest current density (0.8 A cm^{-2}) >90% of the foil surface was sound and semi-bright. However at the leading edge of the deposit a narrow band of the powder type material was formed. At the trailing edge a band of bright nickel was deposited (Fig.4.60(c)). The formation of powder may be reflected in the slightly low current efficiency (90%). At Re 3,075 the maximum current density for sound foil was about 0.75 A cm^{-2} .

Nickel electroforms deposited at a flow rate of Re $7,650 \pm 250$

A series of nickel foils $22 \pm 2 \mu\text{m}$ thick was electroformed over the current density range 0.40 to 1.36 A cm^{-2} (Table 4.25). The main characteristics of these deposits are summarised in Fig.4.61. Sound foils were electroformed at current efficiencies of about 95%. All of these foils were lustrous, showing a tendency to increased brightness with increasing current density. Pitting and foil perforation were not widespread. At current densities $>0.68 \text{ A cm}^{-2}$, bright bands were observed near the leading and trailing edges. At 1.05 A cm^{-2} , alternating bands of dull and bright nickel were deposited in these areas (Fig.4.61d). The inlet and outlet edges of the foil were coarse, nodular and pitted.

Foils deposited at current densities $>1.21 \text{ A cm}^{-2}$ were sound and fine grained over the central region of the electrode. However, at the leading and trailing edges of the foil bands of powder type material and hydroxide formations were evident. The main deposit was more pitted and porous at these high current densities. At the highest current density, the current efficiency showed a marked decrease to 83%. A lower current efficiency may be associated with the production of poor deposits in some regions of the electroform.

It was evident that an increase in flow rate had resulted in an increase in the maximum current density for sound deposits to about 1 A cm^{-2} .

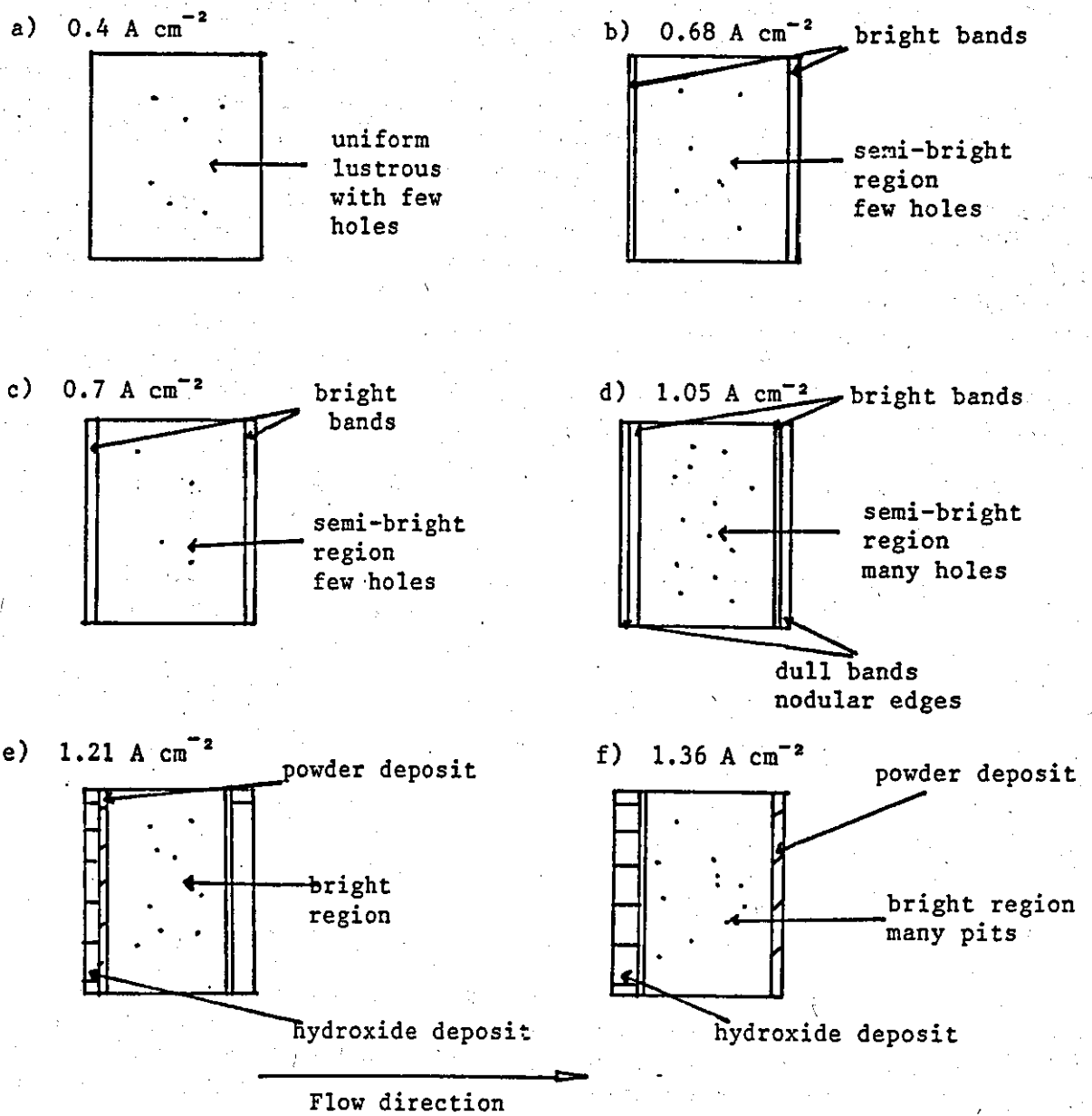


Figure 4.61 Schematic diagrams of nickel foils deposited on electrodes 2.92 equivalent diameters in length at $\text{Re } 7,650 \pm 250$ at 60°C .

Nickel electroforms deposited at a flow rate of Re 13,864

Deposition was carried out over the current density range 1.32 to 2.00 A cm⁻² (Table 4.26). The deposits were 22 ± 2 μm thick. The main characteristics of these deposits are shown in Fig.4.62. At 1.32 A cm⁻², the main deposit was bright, fine grained and deposited with high current efficiency (94%). Visual inspection indicated few holes through the foils. In the leading and trailing edge regions, alternate dull and bright bands were evident (Fig.4.62a). The inlet and outlet edges were coarse and nodular with some pitting.

At very high current densities (1.61 A cm⁻²), coherent, fine-grained nickel foil was not deposited. The deposit had an unusual spongy structure of coarse metallic looking grains 10 to 50 μm in diameter (Fig.4.63b). The structure was highly porous, with patches of green hydroxide on the surface (Fig.4.63a). The current efficiency was very low (62%).

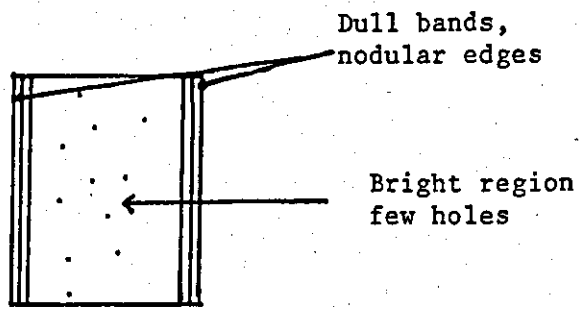
An excessively high current density (2 A cm⁻²), resulted in the deposition of a thin and patchy green nickel hydroxide deposit. Nickel metal was not deposited. During the electroforming operation large volumes of gas were evolved.

At the highest flow rate, the maximum current density for the deposition of sound nickel foil was about 1.3 A cm⁻². Further increases would result in rapid deterioration in the deposit structure.

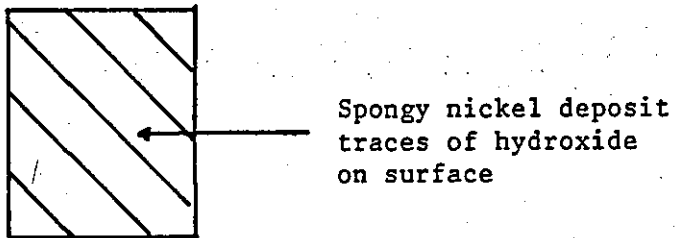
Current Density i A cm ⁻²	Deposition Time s	Weight Deposited g	Current Efficiency %	Deposit Thickness μm
1.32	55	0.1550	94	23
1.61	45	0.1025	62	-
2.00	36	-	-	-

Table 4.26 Nickel foils deposited on electrodes 2.92 equivalent diameters in length at 60°C and Re 13,864.

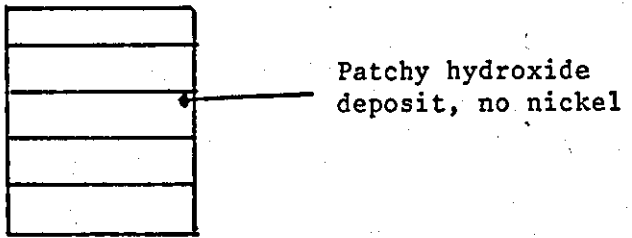
a) 1.32 A cm^{-2}



b) 1.61 A cm^{-2}



c) 2.00 A cm^{-2}



Flow direction

Fig.4.62 Schematic diagram of nickel foils deposited on electrodes 2.92 equivalent diameters in length at Re 13,864 and 60°C .

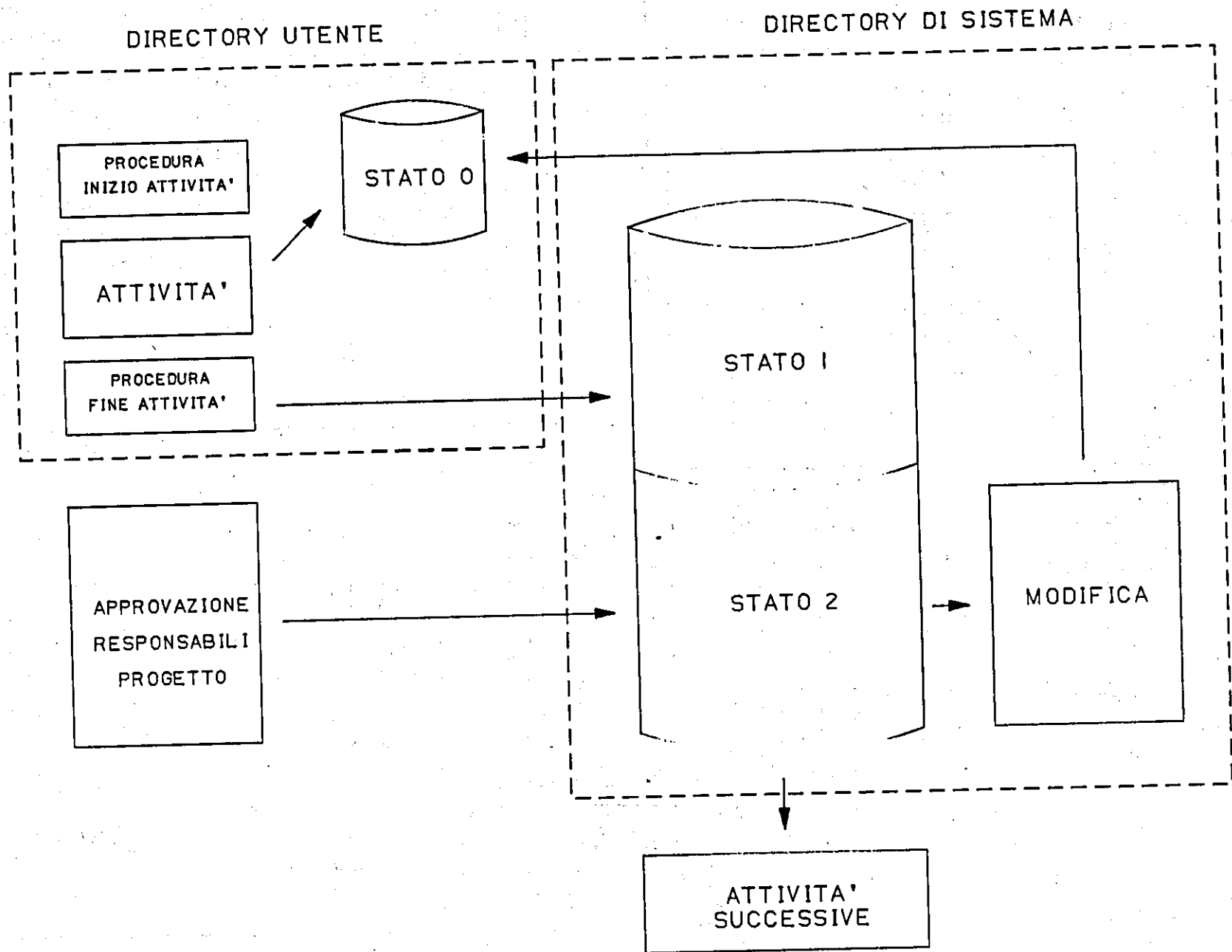
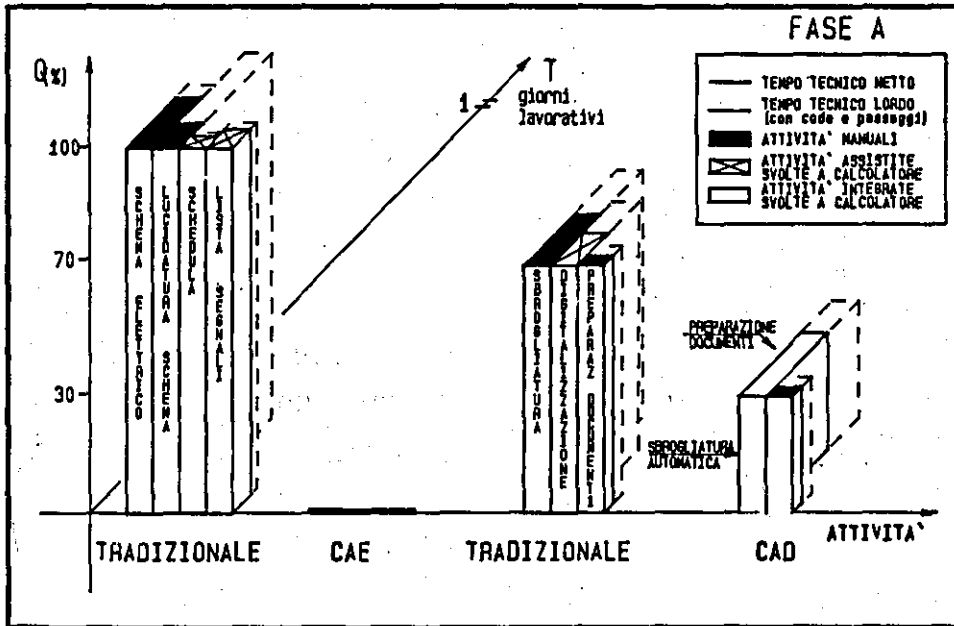
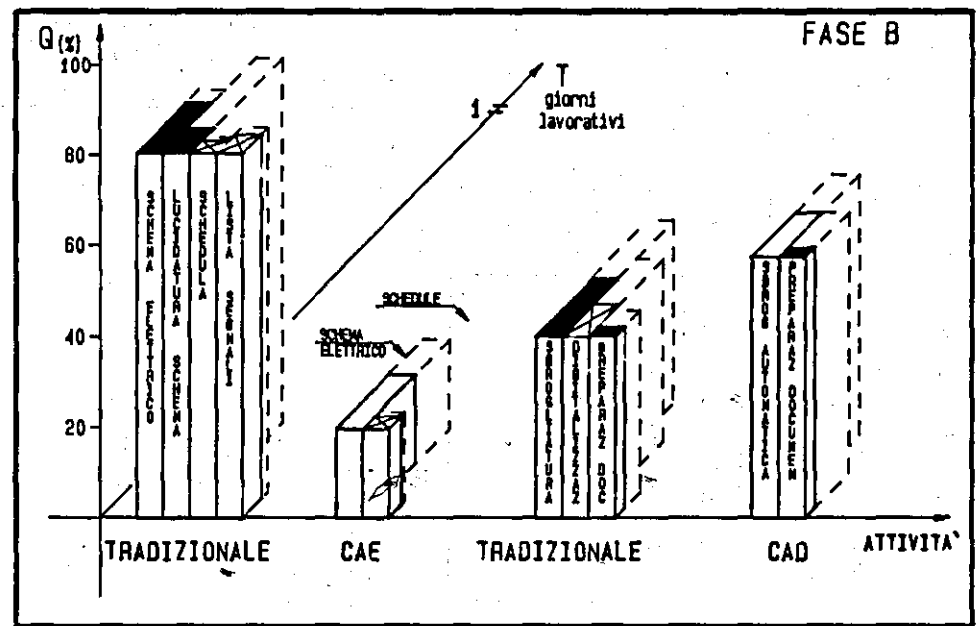


FIG. 6



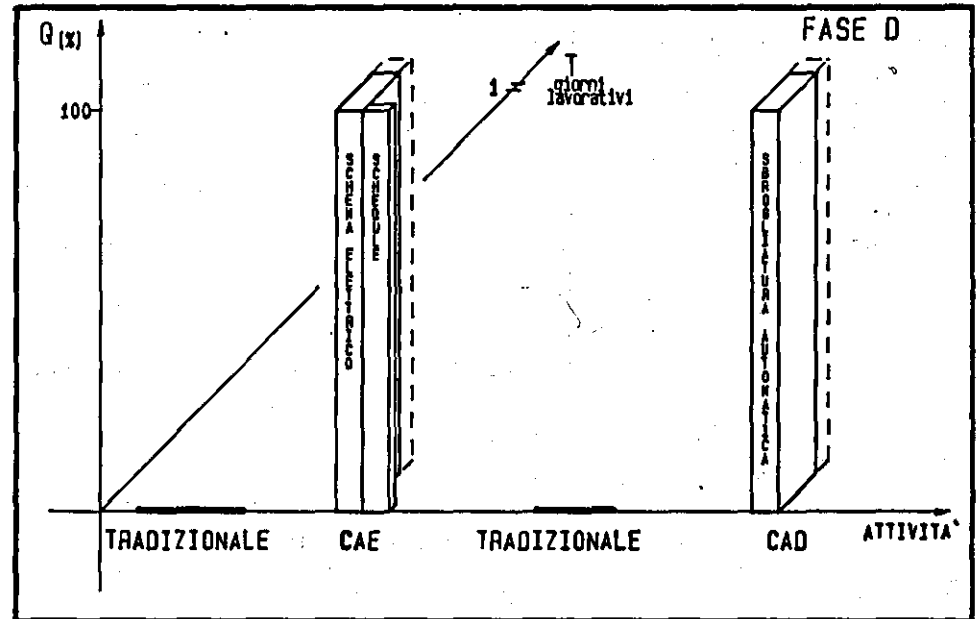
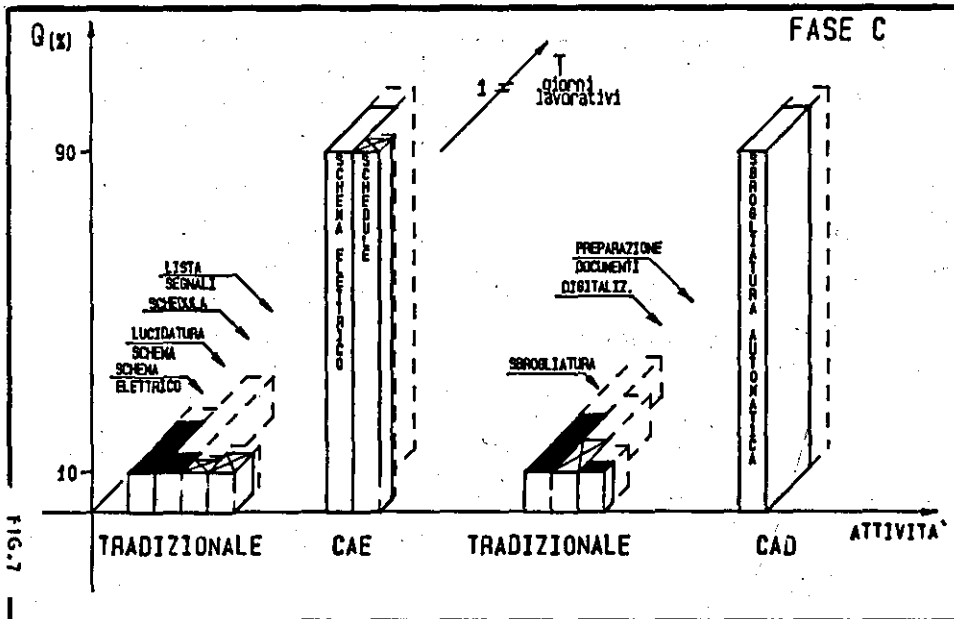
PROGETTO ELETTRICO C.S.

PROGETTO LAYOUT C.S.



PROGETTO ELETTRICO C.S.

PROGETTO LAYOUT C.S.



TEMPI MEDI (PESATI) DI PROGETTO UNITA' C.S. (ATTIVITA' CAE/CAD)

N° giorni

80

70

50

30

10

Attività di:

- Schematica
- Lista Segnali
- Scheda
- Sbrogliatura
- Digitalizzazione

Tempo fisico
in
(GIORNI SOLARI)

Complessità C.S. costante

COSTO (IN GIORNI SOLARI)

COSTO (IN GIORNI LAVOR.)

68

38

27

35

25

18

24

18

13

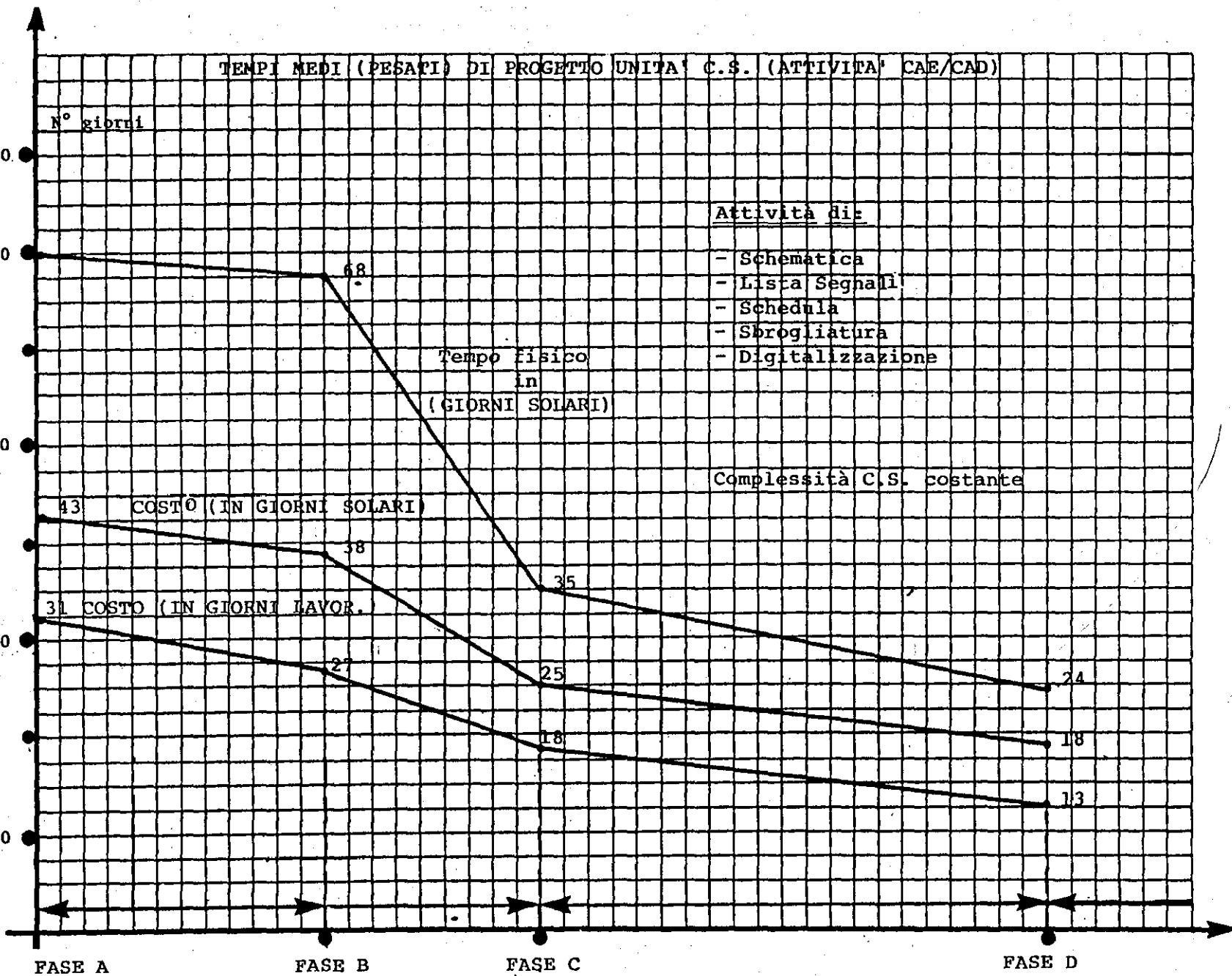
FASE A

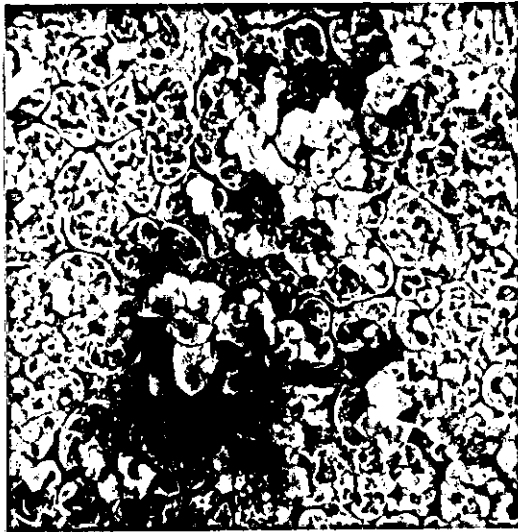
FASE B

FASE C

FASE D

FIG. 8





a) 0° tilt, 200x



b) 0° tilt, 2,000x

Fig.4.63 SEM micrographs of main deposit sections of nickel foil deposited at 1.61 A cm^{-2} and $\text{Re } 13,864$ ($L/d_e \sim 11.7$, 60°C)

a) Green hydroxide on surface of 'spongy' nickel

b) Individual 'grain'.

Summary of major features

- a) The dividing diaphragm was effective in preventing gas evolved at the anode contacting the cathode. The numbers of perforations in the foil were considerably reduced. However, at very low flow rates, cathodically evolved hydrogen may coalesce to form large gas bubbles.
- b) Foils were deposited at high current efficiency, approaching 100%, for all sound electroforms. Depositions of large areas of powder or hydroxide may result in significant decreases in current efficiency.
- c) The structural features of the electroforms were similar to those found in Cell 1. Fine grained sound deposits were produced in the main central region of the cathode, under most conditions.

Significant changes in morphology were initially observed at the entry and exit regions. At very high current densities powder type or green hydroxide deposits were obtained over the entire electrode length.

Good deposits could be obtained at high Reynolds numbers at current densities of $>1 \text{ A cm}^{-2}$. The approximate relationship between the maximum current density for sound deposits and Reynolds number is illustrated in Fig.4.64. The deposit quality was defined as previously described for Cell 1 (page 171).

The approximate theoretical mass transfer limited current densities were calculated from the design equations for the cell (p.128). These are shown in Fig.4.64 by the broken lines B-B (of slope 0.67) and C-C (of slope 0.33) for turbulent and laminar flow respectively. The solid line A-A in Fig.4.64, of slope 0.67 is in approximate agreement with the division between sound and unsound deposits obtained under turbulent flow conditions. As found for Cell 1 deposits, the experimentally determined relationship indicates that the maximum current densities for sound deposits were less than the mass transfer limited current densities. Maximum current densities are slightly higher than comparable Cell 1 results due to the unavoidable changes in the critical dimensions of Cell 2.

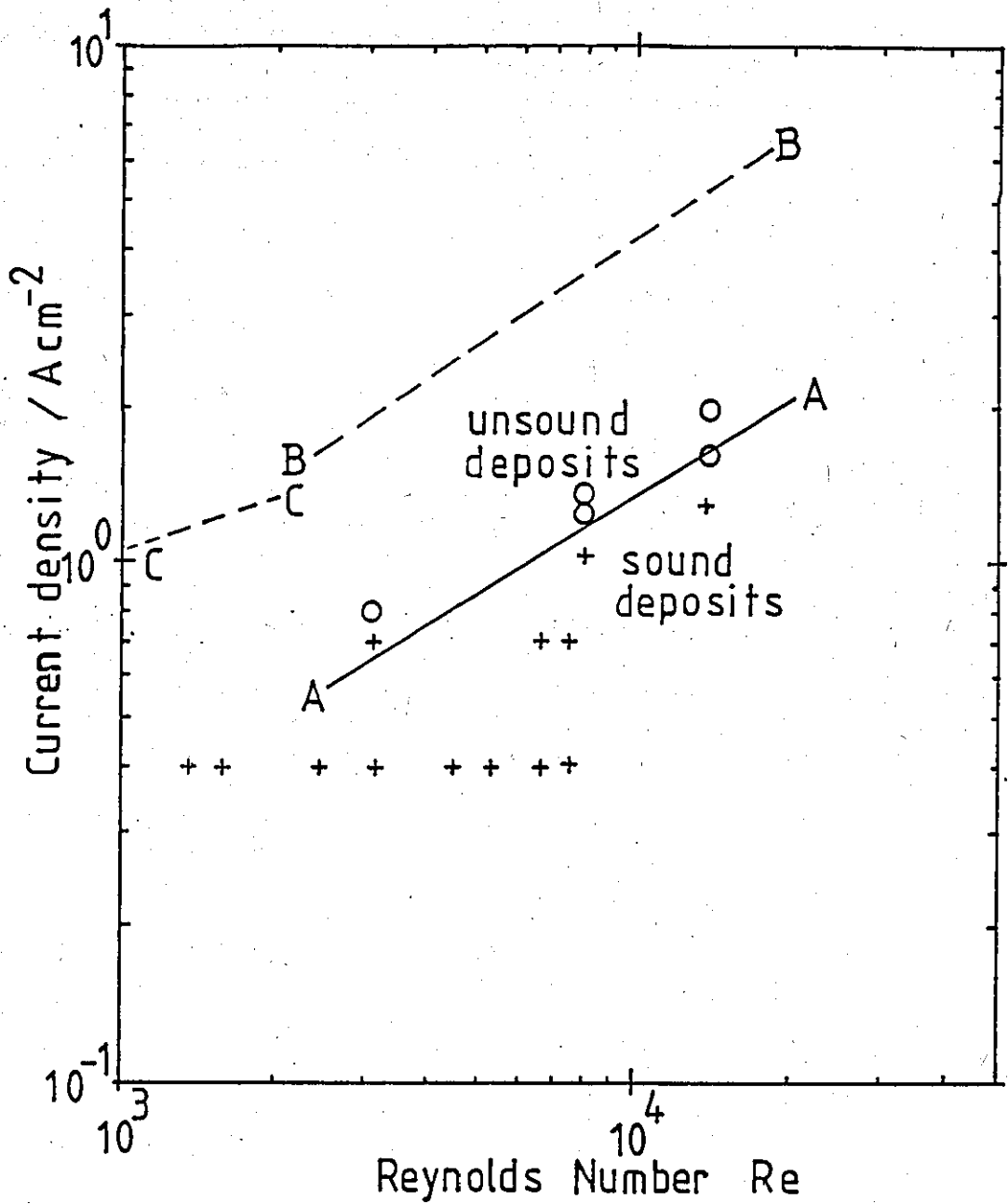


Fig.4.64 The relationship between the flow rate (Reynolds Number) and the maximum current density (i_{max}) for a sound deposit

$T \sim 60^{\circ}\text{C}$, $L/d_e \sim 2.92$

- o - powdery and/or hydroxide deposit
- + - coherent nickel electroform

(b) Electroforming studies at 60°C on cathodes 11.7 equivalent diameters in length in the Mark 2 Cell

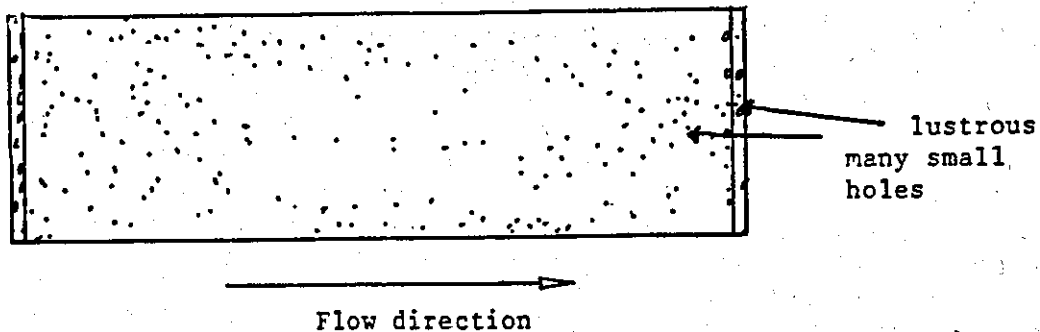
(i) Nickel foils deposited at low flow rates (Re 3,358 - 4,107)

Two foils were electroformed under these flow conditions at current densities of 0.4 and 0.58 A cm⁻². Current efficiencies of close to 100% were obtained. The visual appearances of the foils are summarised schematically in Fig.4.65. The main deposit region of both foils was lustrous and uniform. The electroforms exhibited large numbers of small perforations through the foil, in lines parallel with the flow direction. With longer electrodes accumulation of hydrogen bubbles may occur, particularly at low flow velocities.

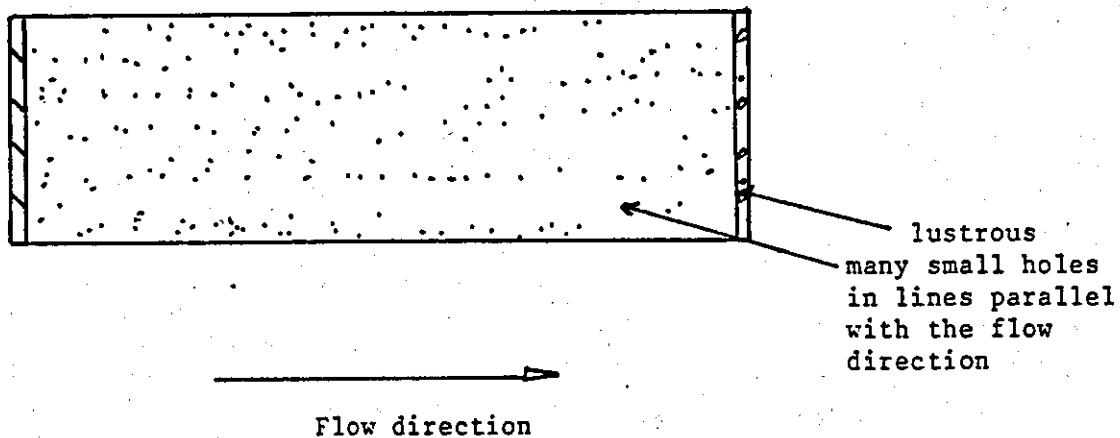
Microhardness profiles were determined longitudinally along the deposit (Fig.4.66a and b). The main deposit region (x/L0.1 to x/L0.9) was of relatively uniform hardness. Increased microhardness values were found at the leading and trailing edges, coinciding with the narrow bright bands observed in these areas.

Main deposit

SEM examinations of the main deposit regions showed that the fine grained morphology characteristic of a good deposit was maintained over 95% of the foil surface at both current densities. At 0.4 A cm⁻², the grain size was 2-6µm with some sub-grain structure (Fig.4.67a). At 0.58 A cm⁻², the range of grain sizes was similar, although the number of smaller grains was proportionately greater (Fig.4.67b). The surface was smoother and the grain boundaries less well defined. Microporosity was observed at or near the grain boundaries. The main deposit microhardness values were 276 ± 2 kg mm⁻² and 288 ± 17 kg mm⁻² at current densities of 0.4 and 0.58 A cm⁻² respectively. The larger variability in microhardness value at 0.58 A cm⁻² may reflect the changes in grain size at this current density.



a) 0.40 A cm^{-2}



b) 0.58 A cm^{-2}

Fig.4.65 Schematic representations of the visual appearance of nickel foils deposited at $\text{Re } 3,700 \pm 400$. (60°C , $L/d_e \sim 11.7$)

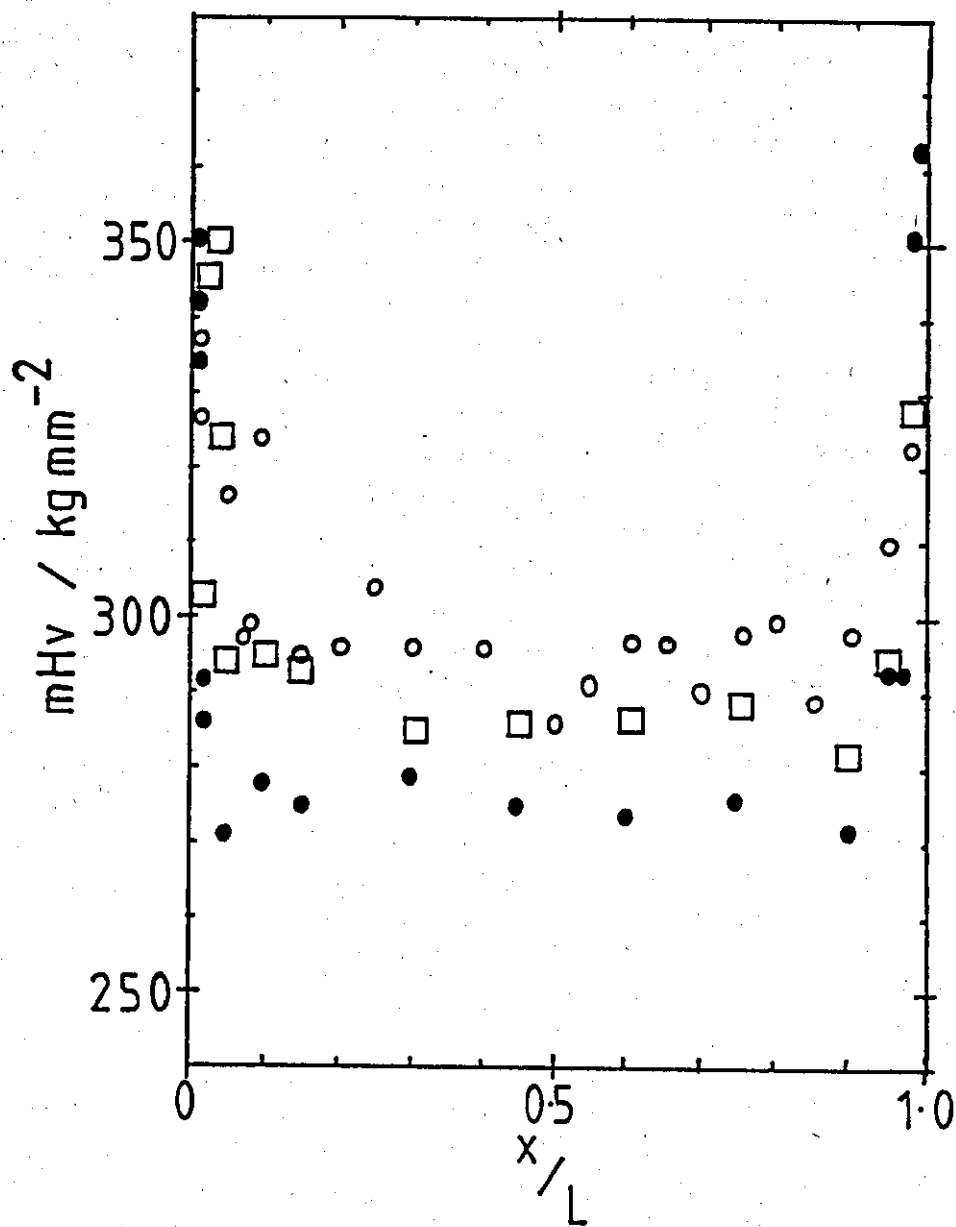


Fig.4.66 Microhardness profiles (mHv) along the length of nickel foils deposited at various current densities. (60°C, $L/d_e \sim 11.7$).

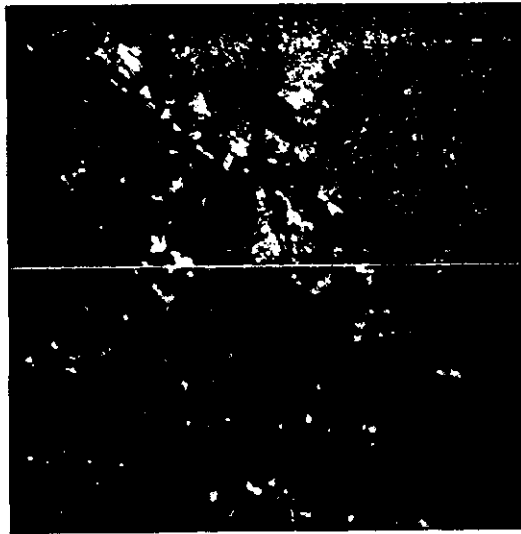
a) ● - 0.40 Acm⁻²

Re 3,358 - 4,107

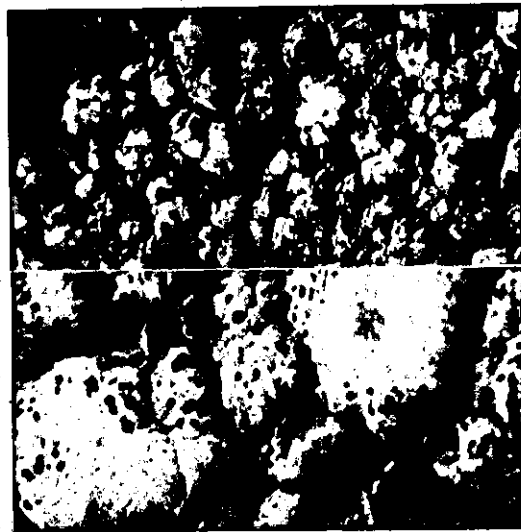
b) □ - 0.58 Acm⁻²

c) ○ - 0.65 Acm⁻²

Re 6,750 ± 200



a) Top: 2,000x; bottom 10,000x
0° tilt



b) Top: 2,000x; bottom 10,000x
0° tilt

Fig.4.67 SEM micrographs of surfaces of foils of nickel deposited at $Re\ 3,700 \pm 400$ ($60^{\circ}C$, $L/de \sim 11.7$) main deposit sections

- a) $0.40\ A\ cm^{-2}$
- b) $0.58\ A\ cm^{-2}$

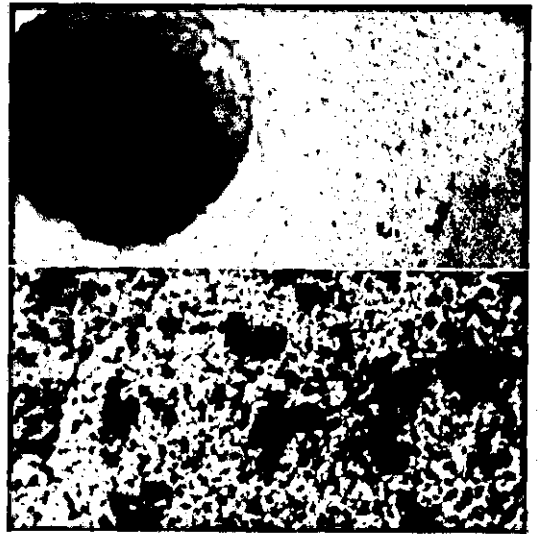
Edge effects

SEM examination of the leading and trailing edge areas of the foils has shown the hard, bright bands (Fig.4.66) to be associated with very fine grained deposits (Fig.4.68b,d and Fig. 4.69b,d). Some larger features were also present (Figs.4.68d and 4.69b). At 0.4 A cm^{-2} , the leading edge was of the bulbous ridge form with extensive pitting in this area (Fig.4.68a). At 0.58 A cm^{-2} , a coarse nodular powder deposit, $\sim 1\text{-}2\text{mm}$ in width, was present at the leading edge (Fig.4.68c). Similar structures were found at the trailing edges of both foils (Fig.4.69a and c). The pitted, bright bands were generally fine grained with some larger features (cf.Fig.4.69b and d).

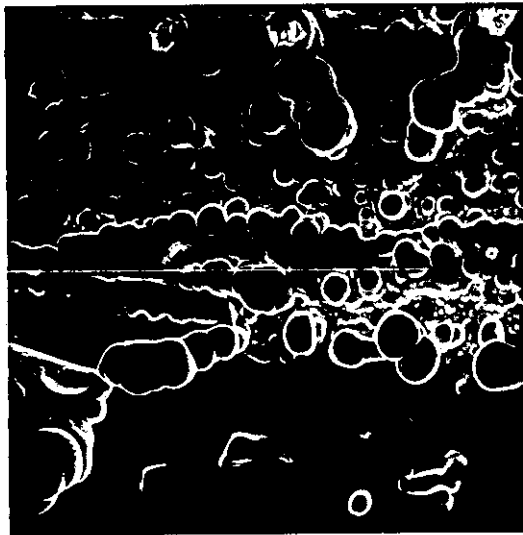
In the flow range $\text{Re } 3,358 - 4,107$, the maximum current density for a good deposit was 0.5 A cm^{-2} .



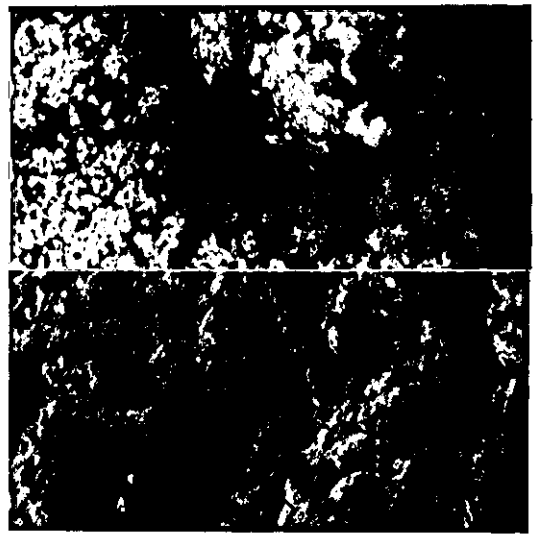
a) x200, 0° tilt



b) Top: 2,000x; bottom: 10,000x
0° tilt



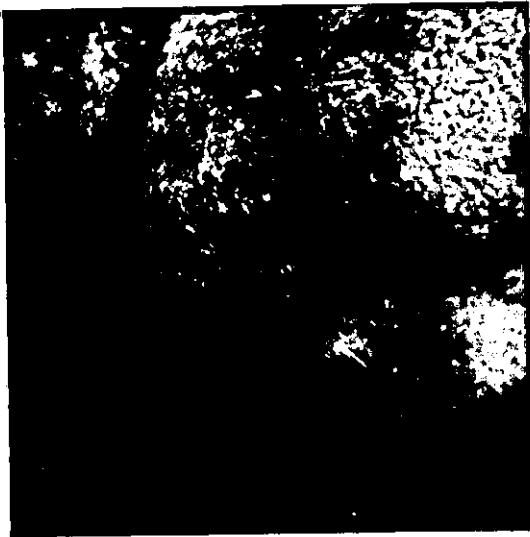
c) x50, 20° tilt



d) Top: 2,000x; bottom: 10,000x
35° tilt

Fig.4.68 SEM micrographs of surfaces of foils of nickel deposited at $Re\ 3,700 \pm 400$ ($60^\circ C$, $L/d_e \sim 11.7$)

- a) $0.40\ A\ cm^{-2}$, leading edge sections
- b) $0.40\ A\ cm^{-2}$, $\sim 0.03\ cm$ from leading edge
- c) $0.58\ A\ cm^{-2}$, leading edge section
- d) $0.58\ A\ cm^{-2}$, $\sim 0.1\ cm$ from leading edge



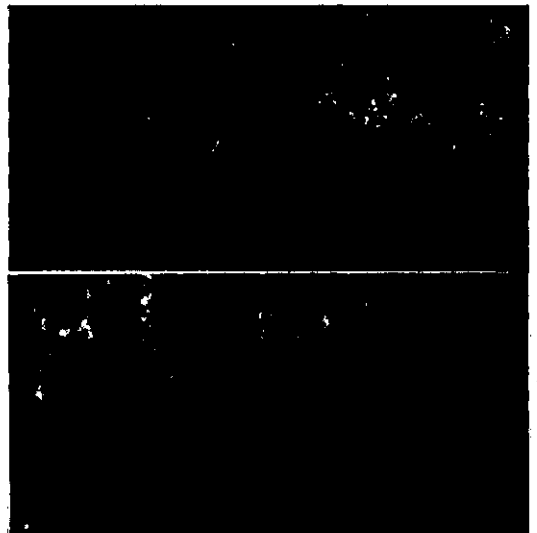
a) x500, 0° tilt



b) x2,000, 0° tilt



c) x100, 35° tilt



d) Top: 2,000x; bottom: 10,000x
35° tilt

Fig.4.69 SEM micrographs of surfaces of foils of nickel deposited at $Re\ 3,700 \pm 400$ ($60^\circ C$, $L/de \sim 11.7$)

- a) $0.40\ A\ cm^{-2}$, trailing edge sections
- b) $0.40\ A\ cm^{-2}$, $\sim 0.01\ cm$ from trailing edge
- c) $0.58\ A\ cm^{-2}$, trailing edge section
- d) $0.58\ A\ cm^{-2}$, $\sim 0.06\ cm$ from trailing edge

(ii) Nickel foils deposited at intermediate Reynolds numbers, Re $5,700 \pm 200$ and deposition rates near the maximum current density for good deposits

A series of nickel foils 21 to $26\mu\text{m}$ thick was electroformed over the current density range 0.4 to 0.65 A cm^{-2} . Experimental details are given in Table 4.27. Current efficiencies close to 100% were obtained for the deposition of most foils. Some variability in current efficiency was noted when powder-type deposits were formed at the leading edge (Fig.4.70c and d). A good coherent deposit was found over $>90\%$ of the foil surface for all deposits. The brightness and visible porosity of the foils tended to increase with increasing current density (Fig.4.70). Some electroforms showed a 'streaked' effect on the foil surface (e.g. Fig.4.70b).

Microhardness profiles determined longitudinally along deposits indicated that the main deposit regions (x/L 0.1 to x/L 0.9) was of relatively uniform microhardness. The bright and pitted regions, close to the leading and trailing edges were substantially harder than the main deposit.

Detailed examination of deposits was carried out in the SEM.

Main deposit

At 0.45 A cm^{-2} , the structure was of irregular grains $1-5\mu\text{m}$ in diameter (Fig.4.71a). At 0.59 A cm^{-2} , the grains were $1-4\mu\text{m}$ in diameter with a greater proportion of smaller grains (Fig.4.71b). The grain boundaries were less well defined at 0.65 A cm^{-2} (Fig.4.71c), although the grains were of a similar size.

The main deposit area of all foils was sound and coherent. However, the number of pits and small holes increased at the higher current densities (Fig.4.71d), when hydrogen evolution was the predominant reaction at the leading edge. The hydrogen bubbles adhered to the electrode surface, grew and coalesced until they were of sufficient size to be detached by the flowing electrolyte.

Flow Rate U cms^{-1}	Reynolds Number Re	Average Current Density i A cm^{-2}	Time t s	Average Deposit Thickness μm	Weight Deposited g	Current Efficiency $\%$
77.2	5,502	0.40	165	22	0.5950	99
82.2	5,864	0.45	163	25	0.8594	99
79.0	5,631	0.59	120	24	0.6478	100
79.0	5,631	0.64	110	24	0.6464	101
79.0	5,631	0.65	110	24	0.6036	93

Table 4.27 Nickel foils deposited at $Re\ 5,700 \pm 200$
 $(60^\circ\text{C}, \frac{L}{de} \sim 11.7)$

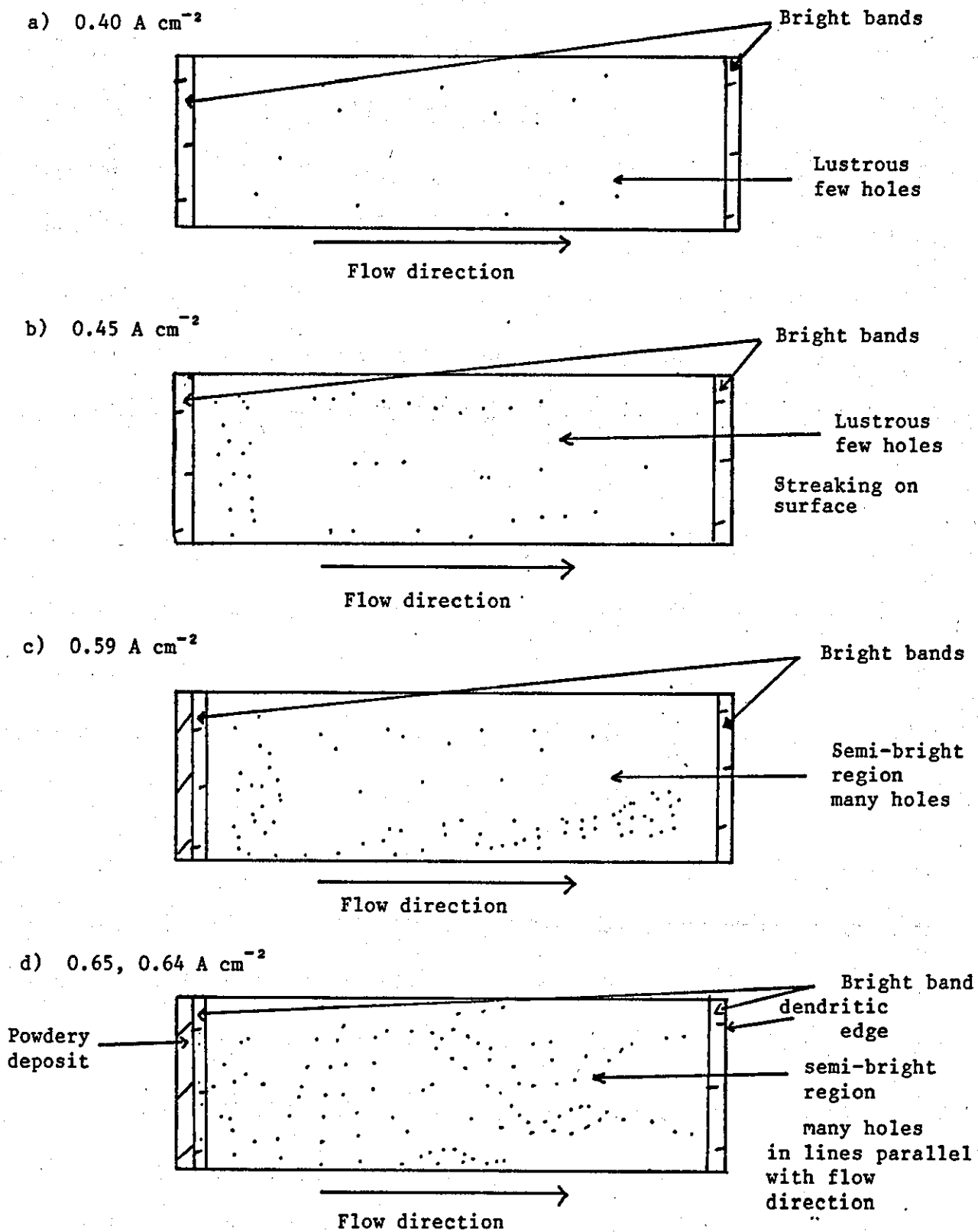
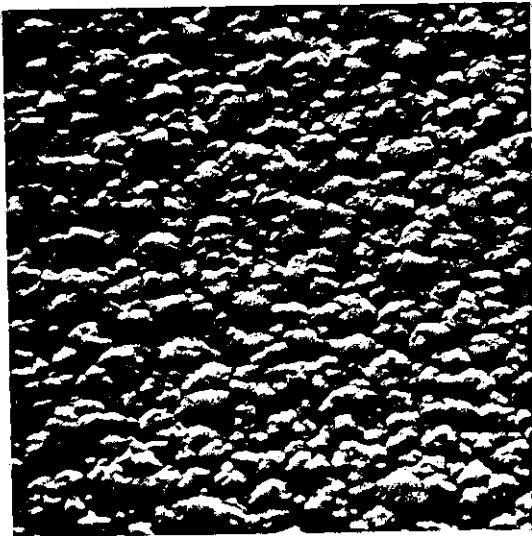
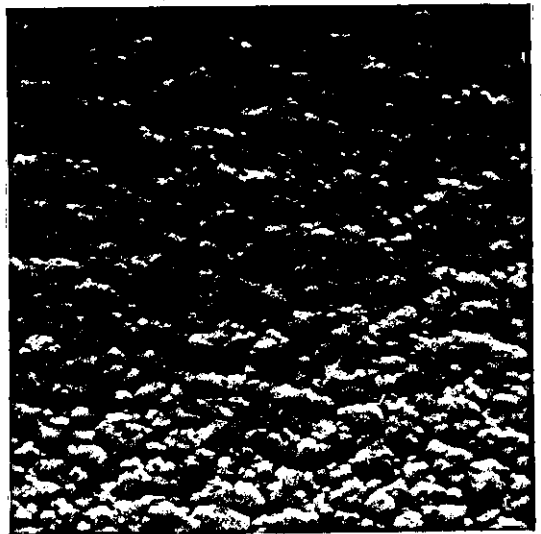


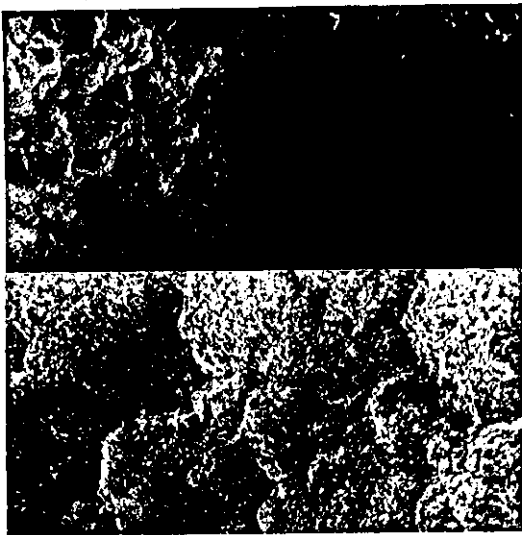
Fig.4.70 Schematic representation of the visual appearance of nickel foils deposited at $Re\ 5,700 \pm 200$. (60°C , $L/d_e \sim 11.7$)



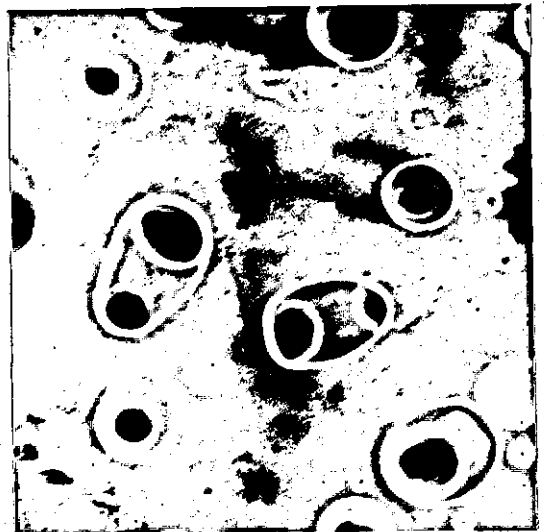
a) x2,000, 45° tilt



b) x2,000, 45° tilt



c) Top: x2,000;
bottom: x10,000
20° tilt



d) x100, 20° tilt

Fig. 4.71 SEM micrographs of the surfaces of foils of nickel deposited at $Re\ 5,700 \pm 200$ ($60^\circ C$, $L/de \sim 11.7$)
main deposit sections

- a) $0.45\ A\ cm^{-2}$
- b) $0.59\ A\ cm^{-2}$
- c) $0.65\ A\ cm^{-2}$
- d) $0.65\ A\ cm^{-2}$, pitted and perforated area.

The microhardness values obtained for the main regions of the foils were similar in the narrow range of current densities used. The values were 307 ± 6 , 294 ± 4 and 296 ± 7 kg mm⁻² at 0.45, 0.59 and 0.65 A cm⁻².

Edge effects

The leading edge of foils electroformed at 0.4 and 0.45 A cm⁻² were visually smooth and brighter than the main deposit areas. SEM examination showed a relatively featureless appearance (Fig.4.72b) and unresolvable grain structure (Fig.4.72b). The edge section was highly micro-porous.

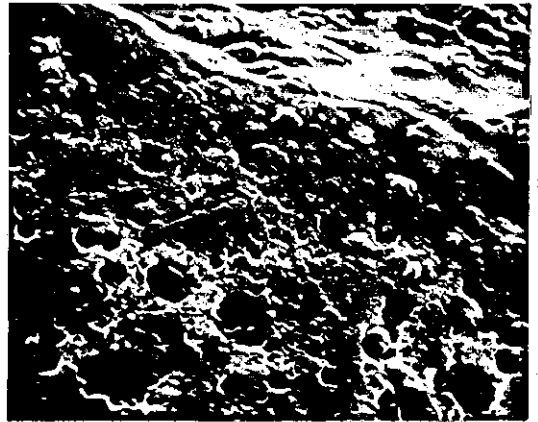
At the higher current densities (0.59 - 0.65 A cm⁻²), grey-brown powder deposits were observed at the entry regions of the foils. The powder deposit had a coarse nodular structure (Fig.4.72c). Exfoliation of the foil had occurred with globular growth. The hard bright band, near the edge, was fine grained and heavily pitted. Similar features were observed at 0.65 A cm⁻² (Fig.4.72d). Larger features were observed in areas adjacent to the powder region (Fig. 4.72e). The presence of surface cracks may indicate high internal stress in this area.

The trailing edges of the deposits appeared to increase in roughness with increasing current density. On all deposits, a narrow band of brighter material was found near the edge. SEM examination showed the trailing edge ridge becoming more nodular and pitted with increasing current density in the range 0.45 to 0.65 A cm⁻² (cf. Fig. 4.73 a,c and e). The hard bright bands were very fine grained (Fig.4.73 b, d and f) although with larger surface reliefs in some areas (Fig.4.73b).

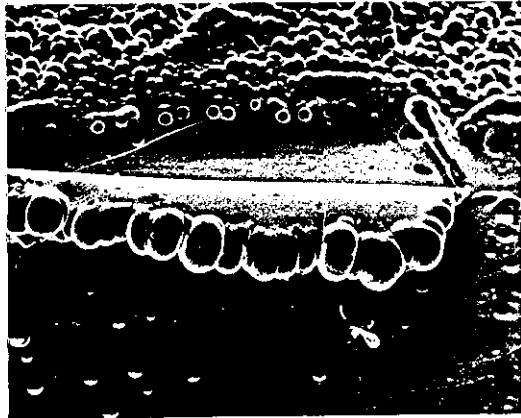
At Re $5,700 \pm 200$ the maximum current density for a good deposit was about 0.59 A cm⁻².



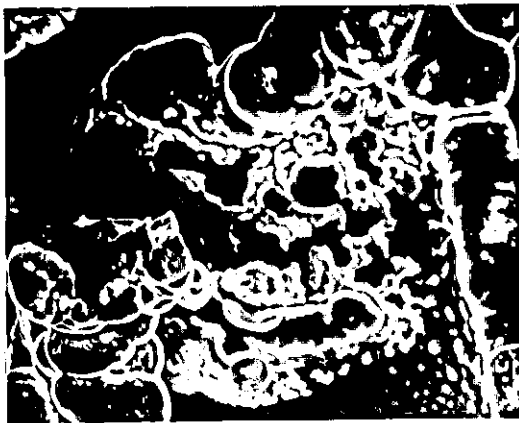
a) x200, 0° tilt



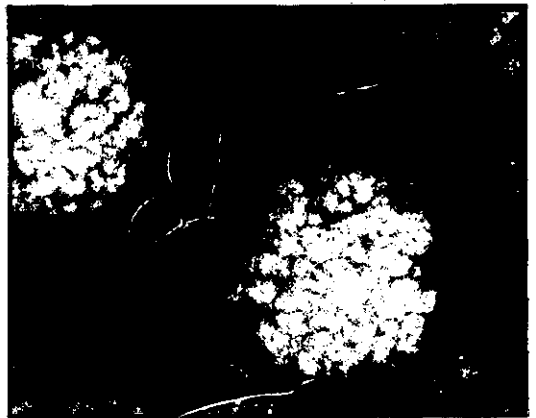
b) x2,000, 0° tilt



c) x50, 45° tilt



d) x100, 0° tilt



e) x2,000, 20° tilt

Fig.4.72 SEM micrographs of surfaces of foils of nickel deposited at $Re\ 5,700 \pm 200$, ($60^\circ C$, $L/de \sim 11.7$) leading edge sections.

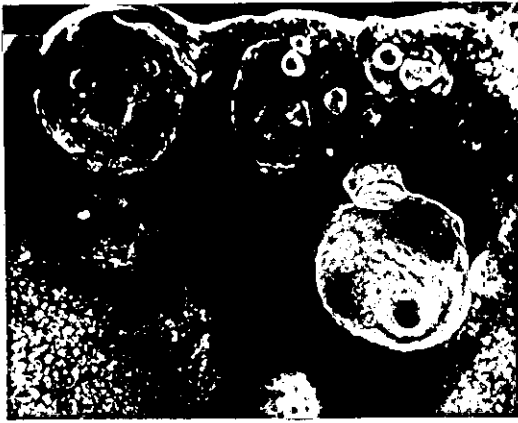
- a) $0.45\ A\ cm^{-2}$
- b) $0.45\ A\ cm^{-2}$, leading edge
- c) $0.59\ A\ cm^{-2}$
- d) $0.65\ A\ cm^{-2}$
- e) $0.65\ A\ cm^{-2}$, surface cracks and mounds $\sim 0.05\ cm$ from leading edge.



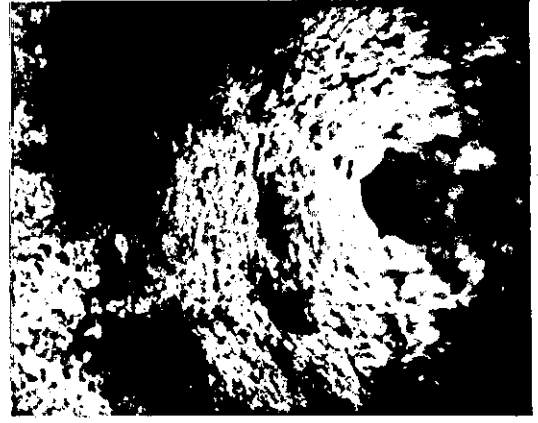
a) x200, 0° tilt



b) x1,000, 0° tilt



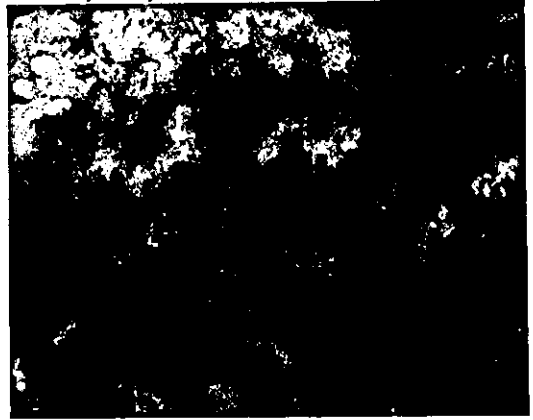
c) x200, 0° tilt



d) x2,000, 0° tilt



e) x200, 0° tilt



f) x2,000, 20° tilt

Fig. 4.73 SEM micrographs of surfaces of nickel deposited at $Re\ 5,700 \pm 200$, ($60^\circ C$, $L/de \sim 11.7$), trailing edge sections.

- a) $0.45\ A\ cm^{-2}$
- b) $0.45\ A\ cm^{-2}$, $\sim 0.01\ cm$ from trailing edge
- c) $0.59\ A\ cm^{-2}$
- d) $0.59\ A\ cm^{-2}$, $\sim 0.02\ cm$ from trailing edge
- e) $0.65\ A\ cm^{-2}$
- f) $0.65\ A\ cm^{-2}$, $\sim 0.02\ cm$ from trailing edge

(iii) Nickel foils deposited at intermediate Reynolds numbers:
Re $6,750 \pm 200$ and deposition rates greater than the
maximum current density for good deposits

A series of nickel electroforms 21 to $26\mu\text{m}$ thick was deposited over the current density range 0.4 to 1.0 A cm^{-2} . The details of the deposition conditions are given in Table (4.28). Schematic representations of the visual appearance of the electroforms are shown in Fig. 4.74. The brightness, the number of small perforations through the foil and the leading edge roughness increased with increasing current density.

At current densities $<0.65 \text{ A cm}^{-2}$, the foils were sound and coherent over the entire electrode length. The current efficiencies were close to 100%. At current densities $>0.65 \text{ A cm}^{-2}$, powder type deposits were formed at both leading and trailing edges of the foils and visible porosity was significantly greater, (Fig.4.74 f and h). Green-brown hydroxide deposits were formed at higher current densities and there was a corresponding reduction in current efficiency.

Microhardness profiles were determined longitudinally along the foil deposited near the maximum current density (0.65 A cm^{-2}) (Fig.4.66c). Variations in microhardness values were insignificant over the main deposit region (x/L 0.1 to x/L 0.9). The deposit was harder near the leading and trailing edges of the foil. The harder areas corresponded to the bright bands.

The deposits were examined in detail in the SEM after removal from the substrate.

Main deposit

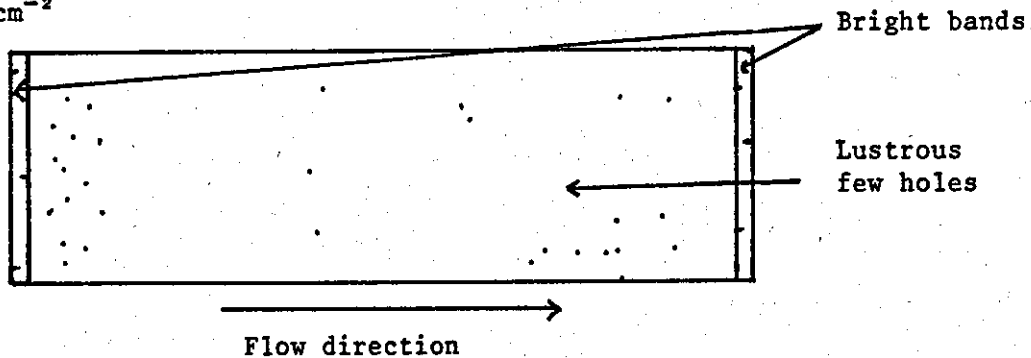
The electroforms deposited over the current density range 0.4 to 1.0 A cm^{-2} had relatively uniform grain sizes over the main deposit area. The grain structures of the deposits are shown in Fig. 4.75 .

At current densities $<0.64 \text{ A cm}^{-2}$, irregular well defined grains, $< 7\mu\text{m}$ in diameter were deposited (Fig.4.75a and b). The proportion of

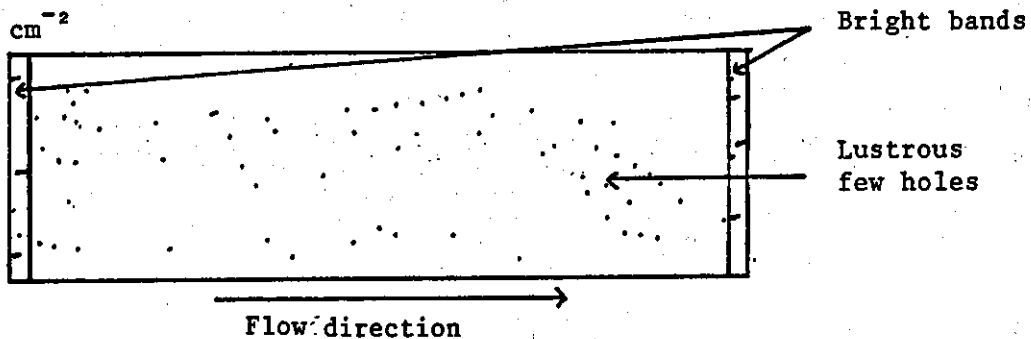
Flow Rate U cm s ⁻¹	Reynolds Number Re	Average Current Density i A cm ⁻²	Time t s	Average Deposit Thickness μm	Weight Deposited g	Current Efficiency %
94.2	6,716	0.4	165	22	0.5943	99
91.3	6,510	0.49	150	25	-	-
93.0	6,629	0.53	140	25	0.6769	99
97.1	6,923	0.60	122	24	-	-
90.4	6,448	0.64	118	26	0.6891	100
97.1	6,923	0.65	116	25	0.6897	99
97.1	6,923	0.78	78	21	0.5219	94
97.1	6,923	0.89	82	25	-	-
97.1	6,923	1.00	67	23	-	-

Table 4.28 Nickel foils deposited at Re 6,750 ± 100
(60°C, L/d_e ~11.7)

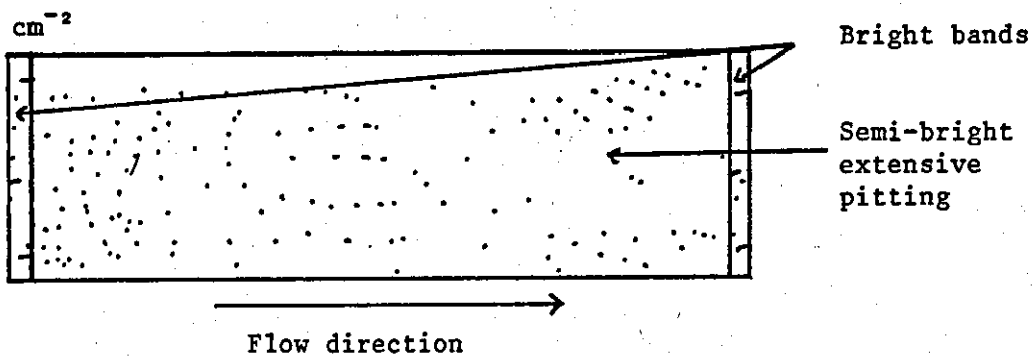
a) 0.4 A cm^{-2}



b) 0.49 A cm^{-2}



c) 0.53 A cm^{-2}



d) 0.60 A cm^{-2}

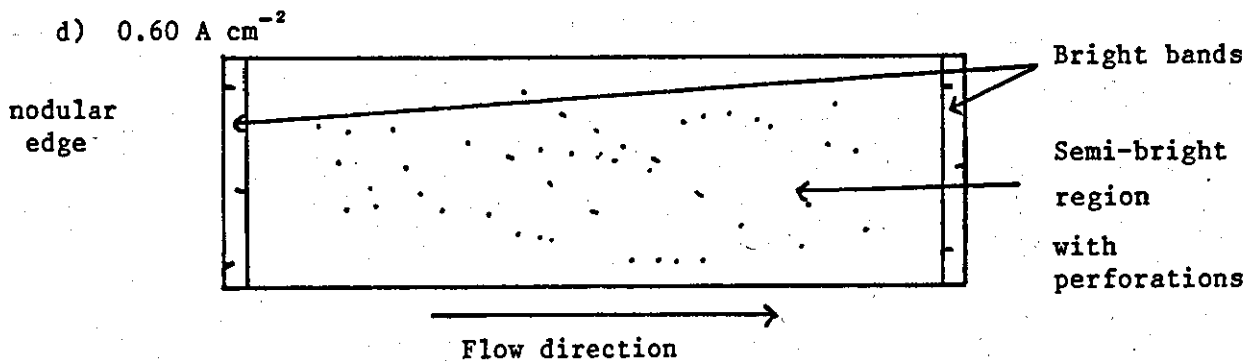


Fig.4.74 Schematic representations of the visual appearance of nickel foils deposited at $Re\ 6,600 \pm 400$. (60°C . $L/d_e \sim 11.7$)

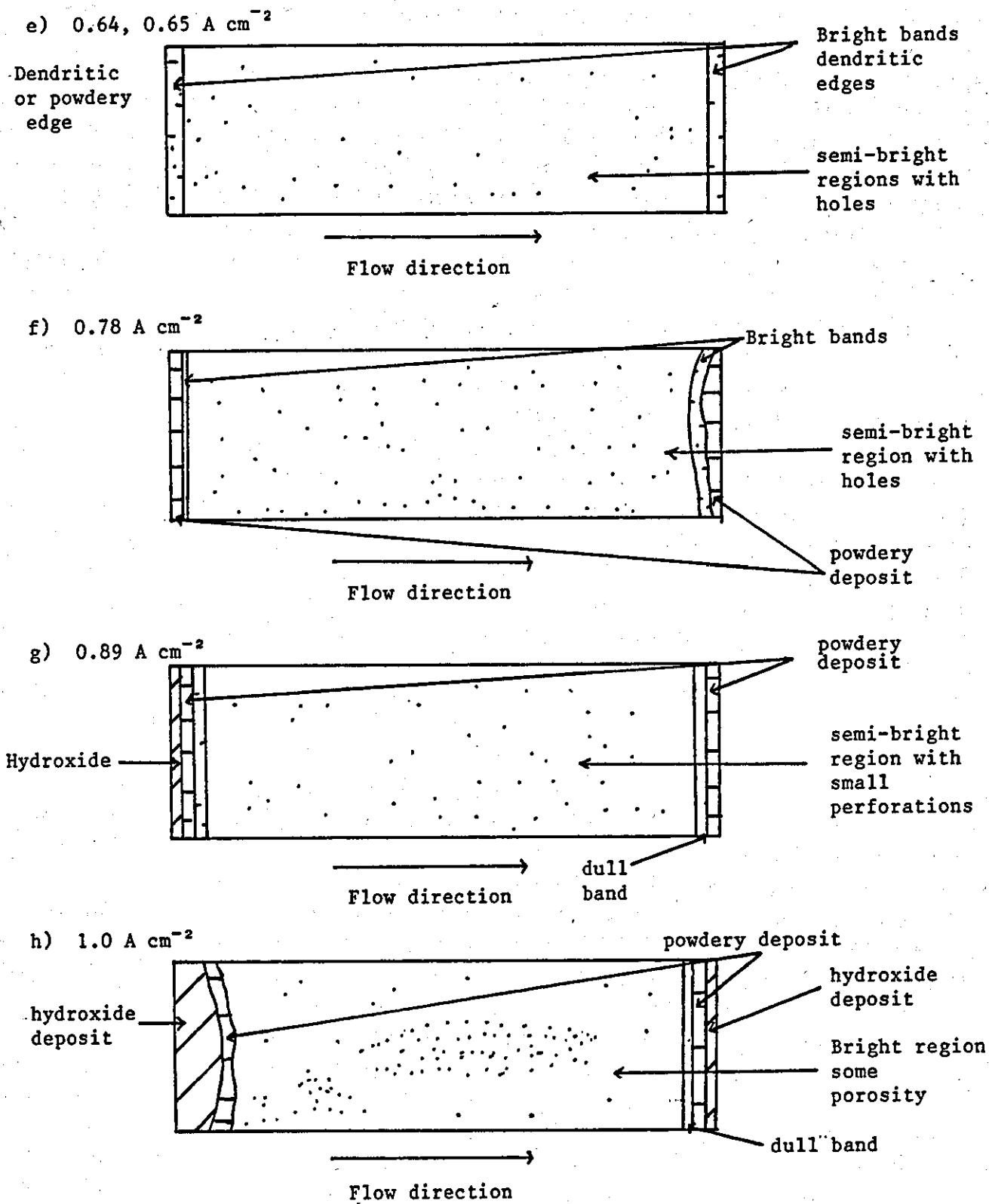
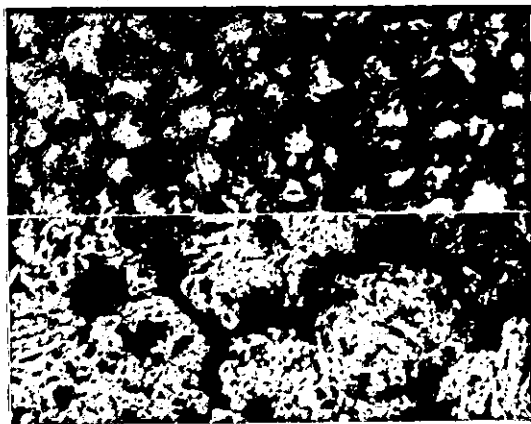
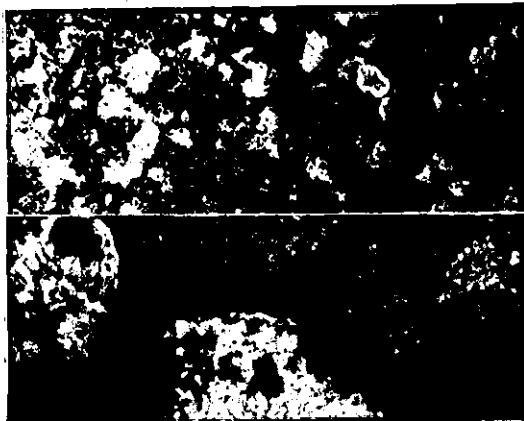


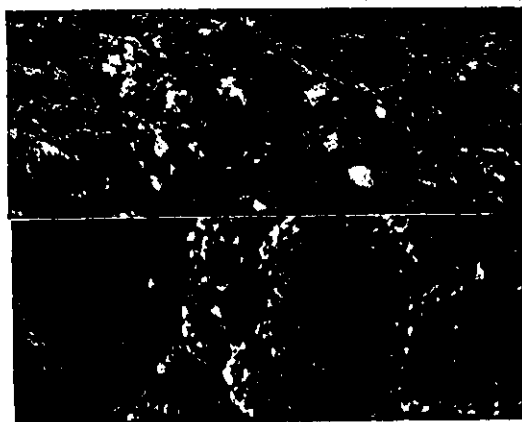
Fig.4.74 continued



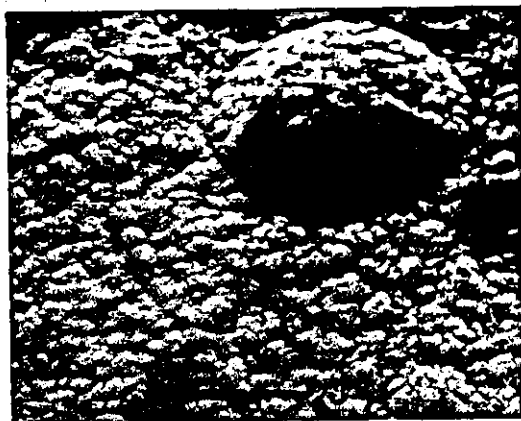
a) Top: x2,000;
bottom: x10,000
0° tilt



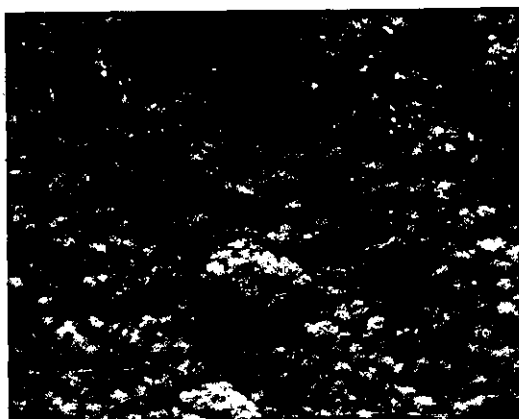
b) Top: x2,000;
bottom: x10,000
0° tilt



c) Top: x2,000
bottom: x10,000
30° tilt



d) x2,000, 45° tilt



e) x2,000, 45° tilt

Fig.4.75 SEM micrographs of surfaces of foils of nickel deposited at $Re\ 6,600 \pm 400$ ($60^\circ C$, $L/de \sim 11.7$), main deposit sections.

- a) $0.53\ A\ cm^{-2}$
- b) $0.64\ A\ cm^{-2}$
- c) $0.78\ A\ cm^{-2}$
- d) $0.89\ A\ cm^{-2}$
- e) $1.00\ A\ cm^{-2}$

smaller grains increased with increasing current density. At 0.78 A cm^{-2} , the grains were of similar dimensions but were less well defined.

The high current density deposits (0.89 to 1.00 A cm^{-2}) were of small grain size ($<3\mu\text{m}$) and were bright in appearance (Fig.4.75 d and e). Some larger features $5\text{--}17\mu\text{m}$ in diameter were also found. Streaked areas, resulting from gas streaming along the electrode surface, were evident at 1.00 A cm^{-2} (Fig.4.75e).

At current densities of 0.53 , 0.64 and 0.65 A cm^{-2} , the average values of microhardness were 283 ± 4 , 291 ± 6 and $297 \pm 9 \text{ kg. mm}^{-2}$. When the maximum current density was exceeded, the variability of the microhardness in the main deposit region increased. At current densities of 0.78 and 0.89 A cm^{-2} , the microhardness values were 311 ± 27 and $329 \pm 13 \text{ kg mm}^{-2}$ respectively.

Edge effects

The leading edges of foils deposited at $<0.53 \text{ A cm}^{-2}$ were relatively featureless. A coarser structure developed at 0.53 A cm^{-2} , where the growth of small globules was apparent at the leading edge (Fig.4.76a). At $\sim 0.64 \text{ A cm}^{-2}$, the edge section was more bulbous (Fig.4.76b). A nodular powder morphology with some micro porosity was evident at 0.78 A cm^{-2} (Fig.4.76c). Within individual nodules a sub-grain structure was observed at high magnification (Fig.4.76d).

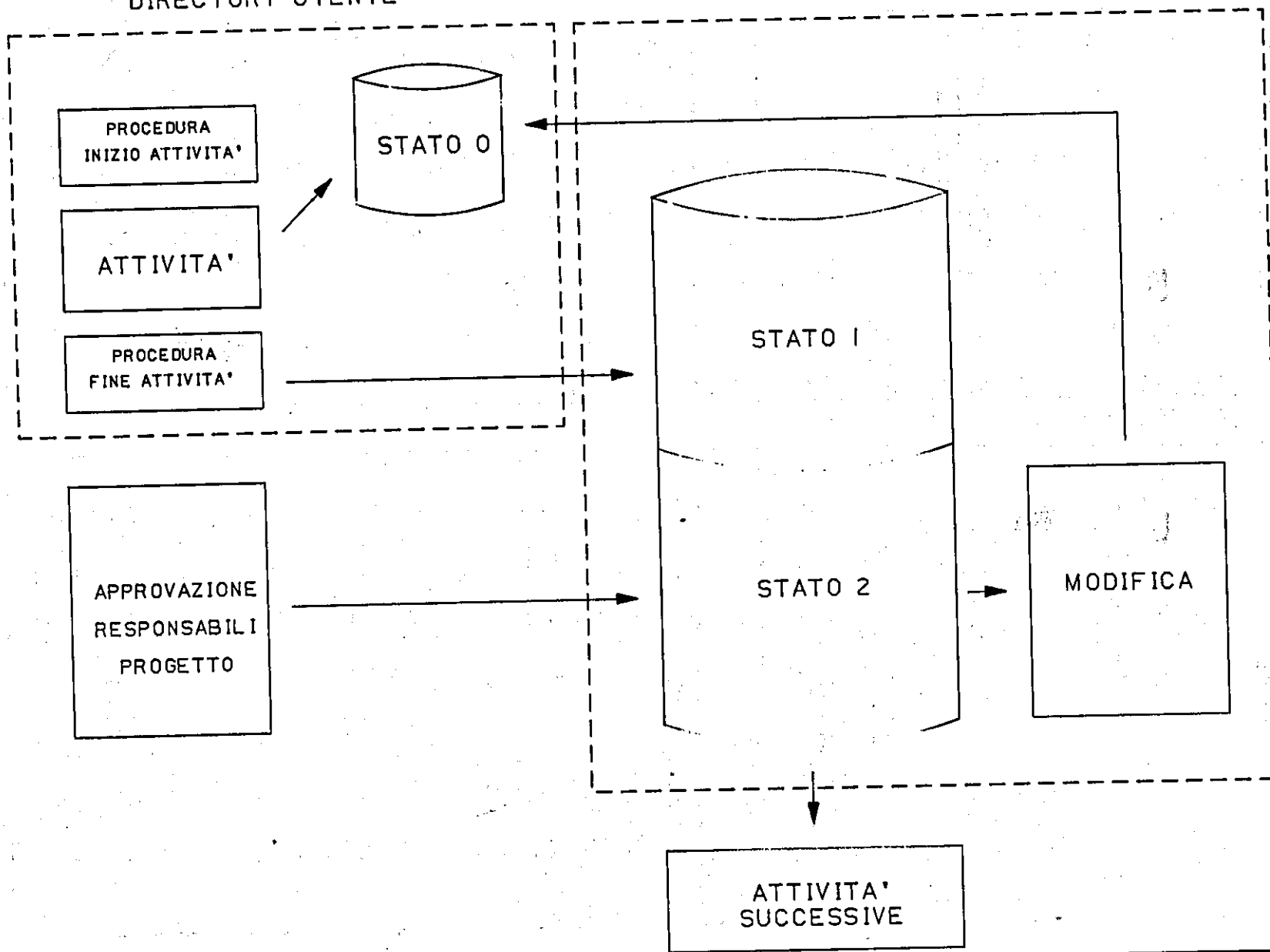
At current densities $>0.89 \text{ A cm}^{-2}$, a friable green hydroxide deposit was formed at the leading edge of the foil (Fig.4.76 d and e). At high current densities, partial exfoliation and pitting occurred at the foil edges.

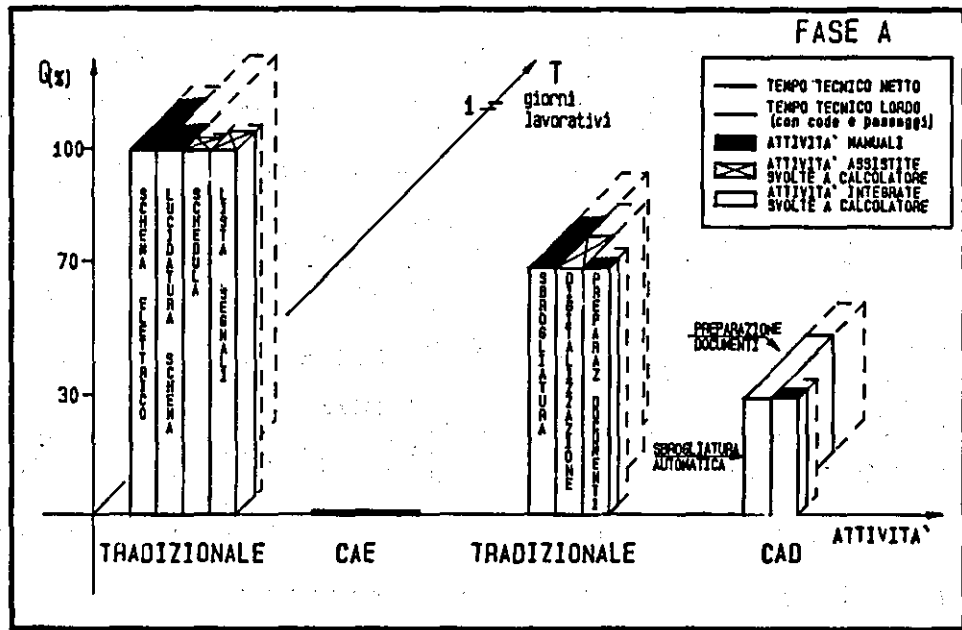
Adjacent to the leading edge bands of visibly brighter nickel of very fine grain structures were deposited (Fig.4.77). Over the current density range 0.53 to 0.78 A cm^{-2} , the grains tended to become smaller and less well defined.

Surface SEM examination of trailing edge sections are shown in Fig.4.78. Morphological changes were similar to those at the leading

DIRECTORY UTENTE

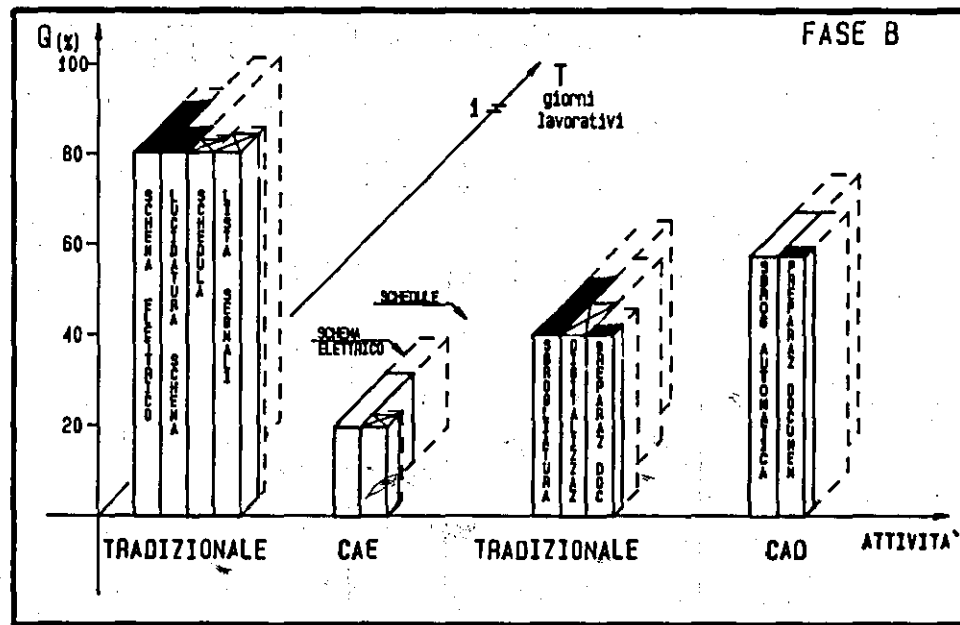
DIRECTORY DI SISTEMA





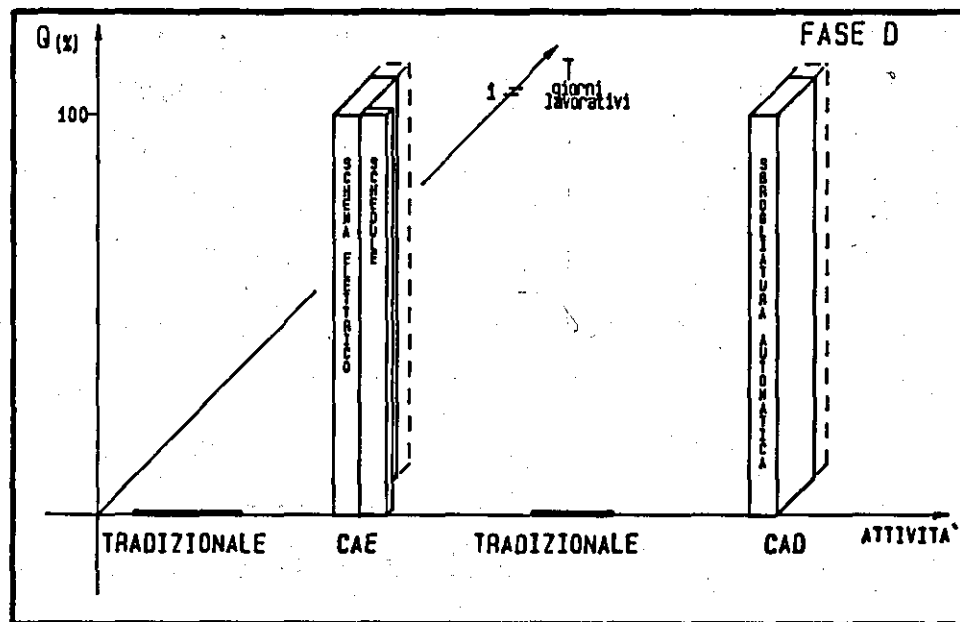
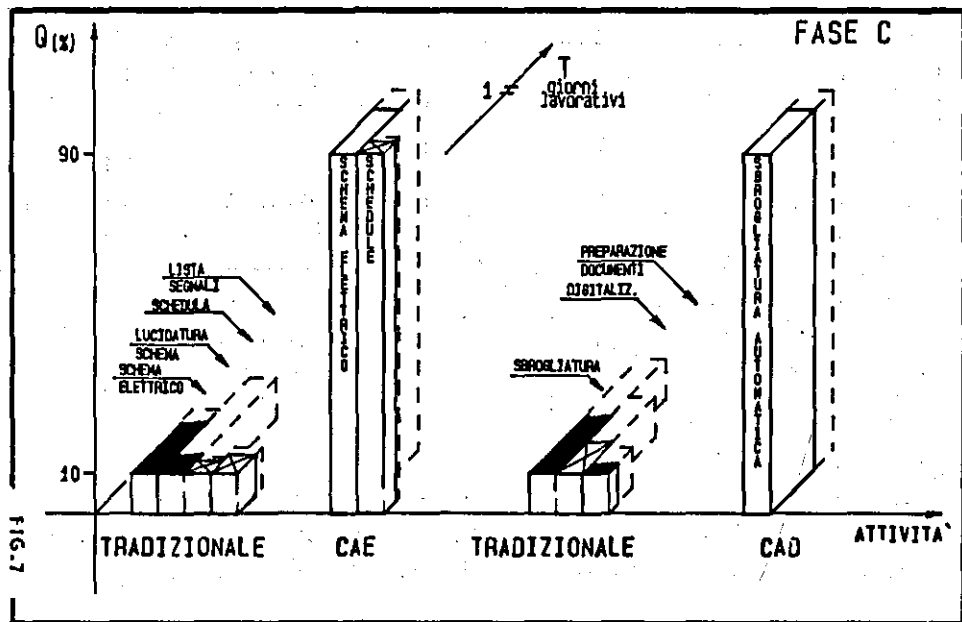
PROGETTO ELETTRICO C.S.

PROGETTO LAYOUT C.S.



PROGETTO ELETTRICO C.S.

PROGETTO LAYOUT C.S.



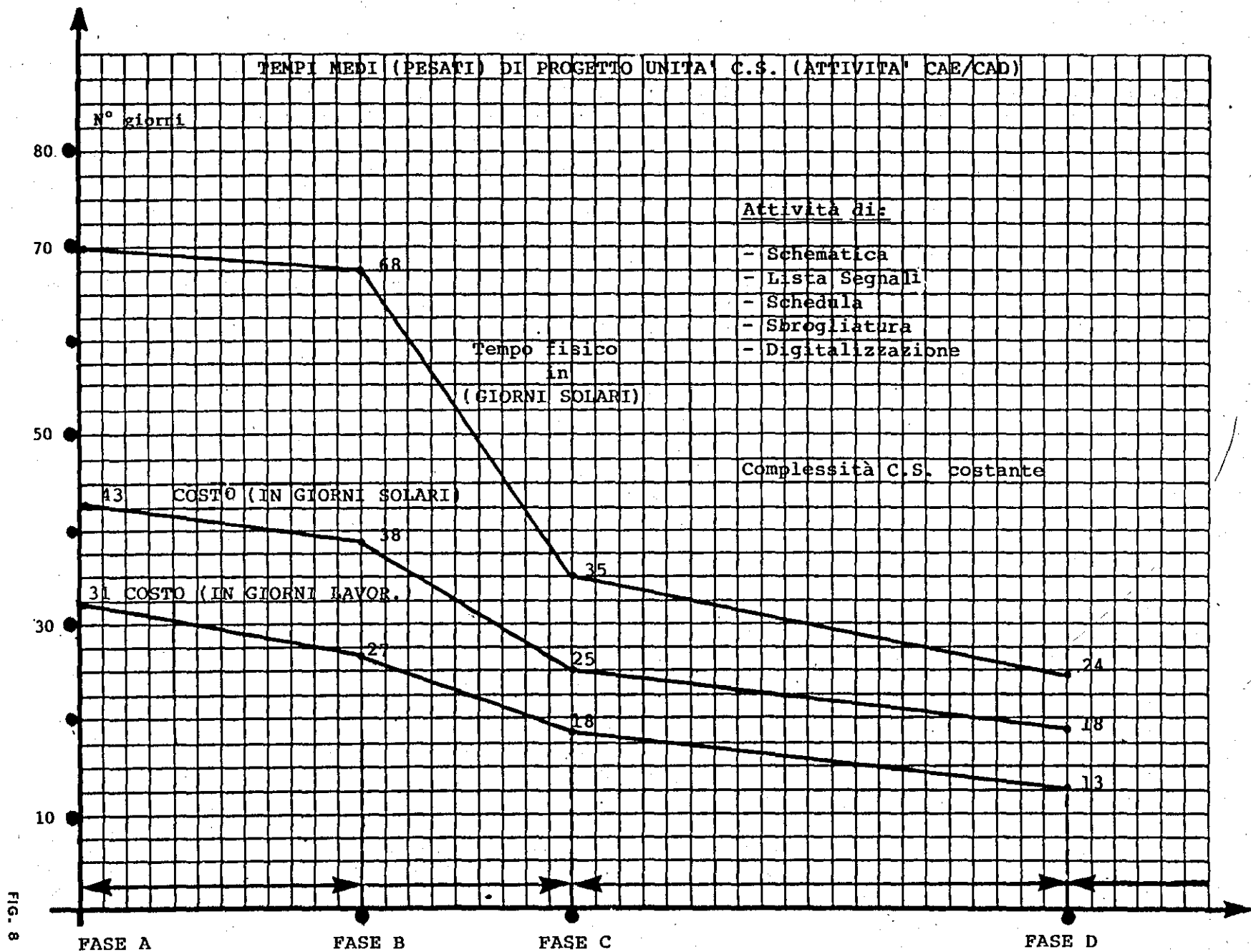


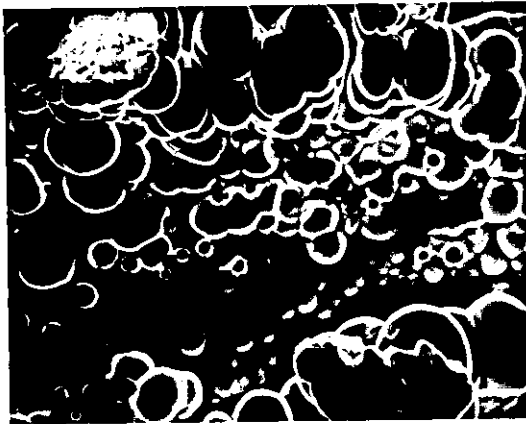
FIG. 8



a) x1,000, 0° tilt



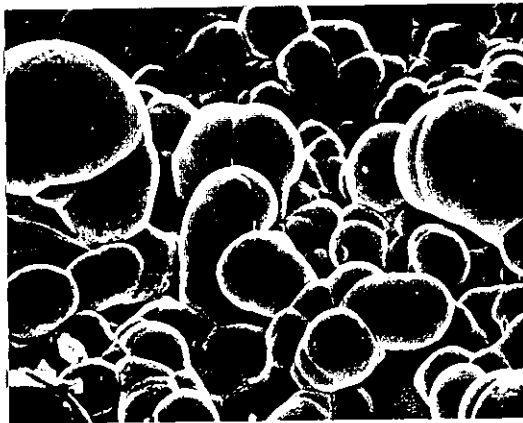
b) x200, 0° tilt



c) x100, 0° tilt



d) x30,000, 0° tilt



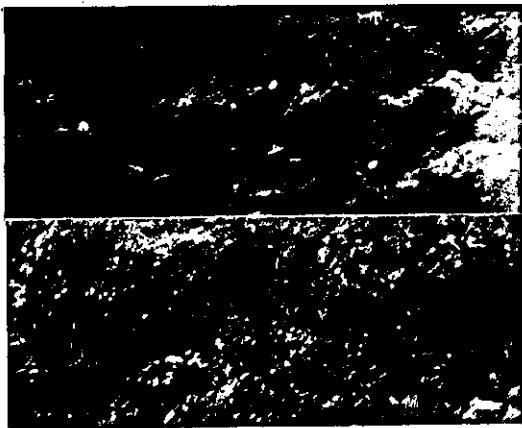
e) x200, 45° tilt



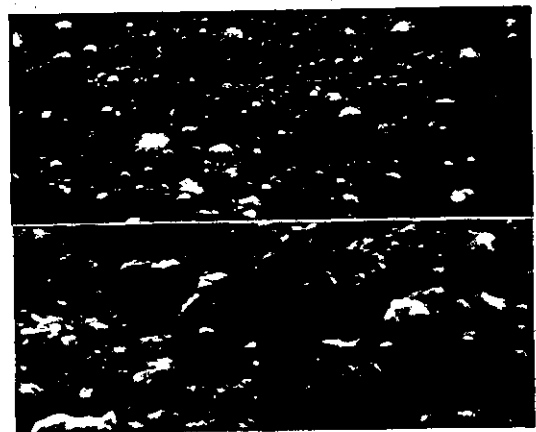
f) x500, 45° tilt

Fig.4.76 SEM micrographs of surfaces of foils of nickel deposited at $Re\ 6,000 \pm 400$ ($60^\circ C$, $L/de \sim 11.7$), leading edge sections.

- a) $0.53\ A\ cm^{-2}$
- b) $0.64\ A\ cm^{-2}$
- c) $0.78\ A\ cm^{-2}$
- d) $0.78\ A\ cm^{-2}$, nodule structure
- e) $0.89\ A\ cm^{-2}$
- f) $1.00\ A\ cm^{-2}$



a) Top: x2,000
bottom: x10,000
35° tilt



b) Top: x2,000
bottom: x10,000
0° tilt



c) x2,000 20° tilt

Fig.4.77 SEM micrographs of surfaces of foils of nickel deposited at $Re\ 6,600 \pm 400$ ($60^\circ C$, $L/de \sim 11.7$), sections adjacent to leading edge

- a) $0.53\ A\ cm^{-2}$
- b) $0.64\ A\ cm^{-2}$
- c) $0.78\ A\ cm^{-2}$

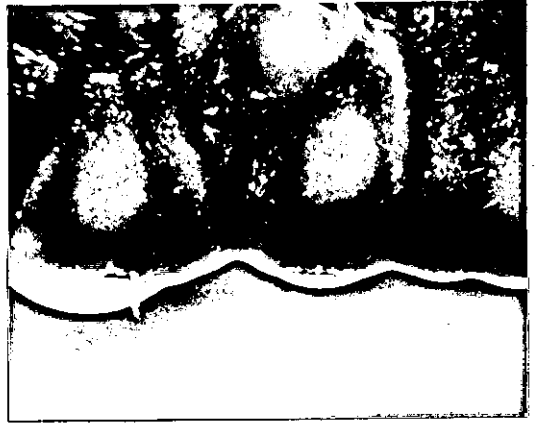
edge. At current densities $<0.53 \text{ A cm}^{-2}$, this area was relatively featureless. The trailing edge ridge became more bulbous at 0.53 and 0.64 A cm^{-2} (cf. Fig. 4.78 a and b). At 0.78 A cm^{-2} a nodular powder structure was deposited (Fig. 4.78c). Simultaneous deposition of powder nodules and hydroxide occurred at 0.89 and 1.0 A cm^{-2} (Fig. 4.78 e and f). This type of deposit was $<20\%$ of the foil surface area even at 1.0 A cm^{-2} .

Close to the trailing edge, the deposit was very fine grained (Fig. 4.79) and visibly brighter. Some larger features were present (Fig. 4.79a). The grains were less well defined at high current densities. At 0.78 A cm^{-2} , small perforations in the foil were found (Fig. 4.79c).

At $\text{Re } 6,750 \pm 200$, the maximum current density for a good deposit was 0.7 A cm^{-2} .



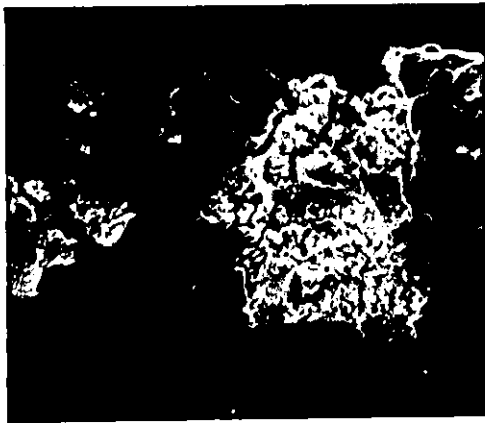
a) x200, 0° tilt



b) x200, 0° tilt



c) x200, 0° tilt



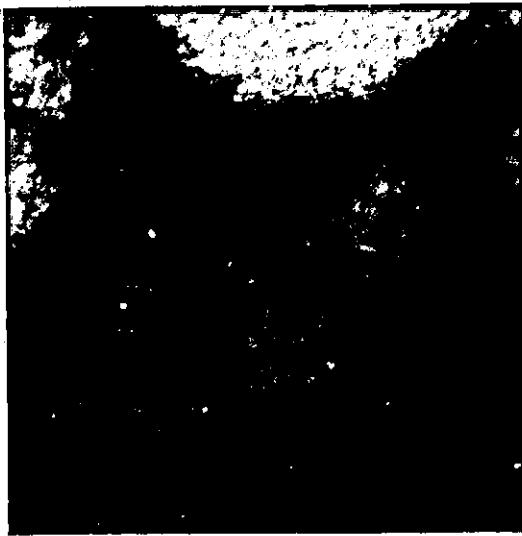
d) x100, 0° tilt



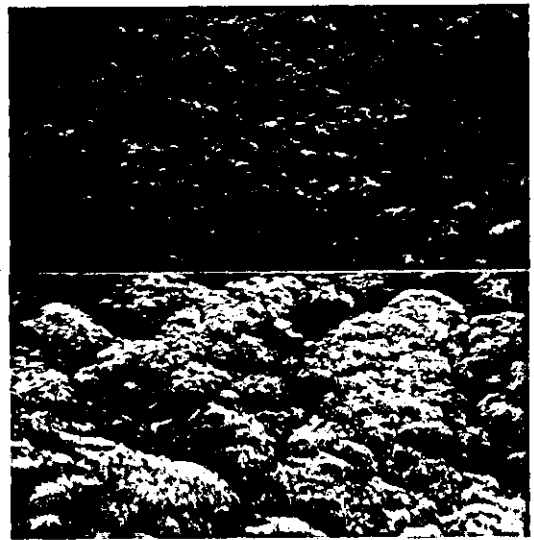
e) x1,000, 0° tilt

Fig.4.78 SEM micrographs of surfaces of foils of nickel deposited at $Re\ 6,600 \pm 400$ ($60^\circ C$, $L/de \sim 11.7$), trailing edge sections.

- a) $0.53\ A\ cm^{-2}$
- b) $0.64\ A\ cm^{-2}$
- c) $0.78\ A\ cm^{-2}$
- d) $0.89\ A\ cm^{-2}$
- e) $1.00\ A\ cm^{-2}$



a) x2,000, 0° tilt



b) Top: x2,000
bottom: x10,000
0° tilt



c) x2,000, 0° tilt

Fig.4.79 SEM micrographs of surfaces of foils of nickel deposited at $Re\ 6,600 \pm 400$ ($60^\circ C$, $L/de \sim 11.7$)

- a) $0.53\ A\ cm^{-2}$
- b) $0.64\ A\ cm^{-2}$
- c) $0.76\ A\ cm^{-2}$

(iv) Nickel foils deposited at high flow rates, Re 12,400 ± 500

Nickel foils 19-24 m thick were deposited at Re 12,400 ± 500 over the current density range 0.60 to 0.89 A cm⁻². The details of the deposition conditions are given in Table 4.29. Schematic representations of the visual appearance of the electroforms are shown in Fig.4.80.

The foils deposited at current densities <0.78 A cm⁻² were of good visual appearance. Visible porosity tended to increase with increasing current density. The current efficiency was ~100%. At higher current densities, hydroxide and powdery deposits were found in some areas of the electroform (Fig.4.80c and d). The current efficiency remained close to 100%.

Foil surfaces were examined in detail in the SEM, after removal from the substrate.

Main deposit

The main deposit sections were all fine grained (Fig.4.81a,b and d). The grain size of the deposits were in the range 1 to 4 μm, the proportion of smaller grains increasing at higher current densities. The grains appeared smoother and grain boundaries poorly defined at high current densities (Fig.4.81d). Foils electroformed at 0.75 A cm⁻² were particularly porous with many pits and small holes in them (Fig.4.81c). At 0.89 A cm⁻², a large proportion of the main deposit was fine grained (4.81d), although in some areas a green-brown hydroxide was deposited over a very fine-grained underlying nickel deposit (Fig.4.81e).

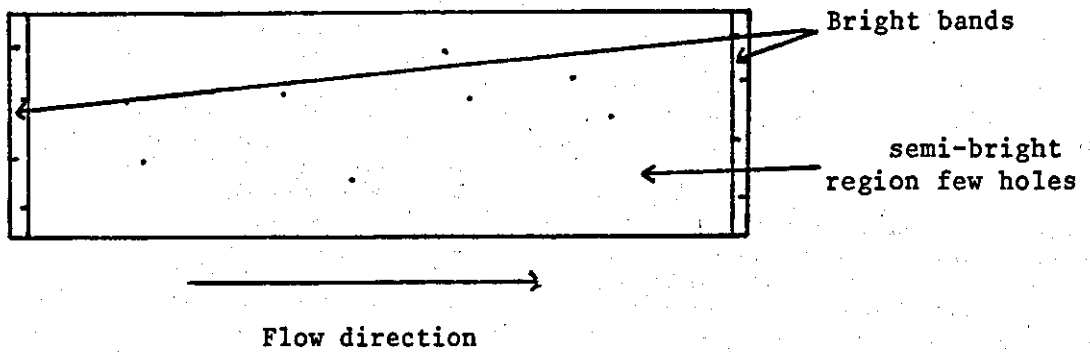
Edge effects

At 0.6 A cm⁻², the leading edge was a smooth bulbous ridge (Fig.4.82a). Adjacent areas were very fine grained with micro-cavities (Fig.4.82b). An increased leading edge roughness was observed at 0.75 A cm⁻² (Fig.4.82c). Close to the edge, the foil surface appeared very fine grained (Fig.4.82d).

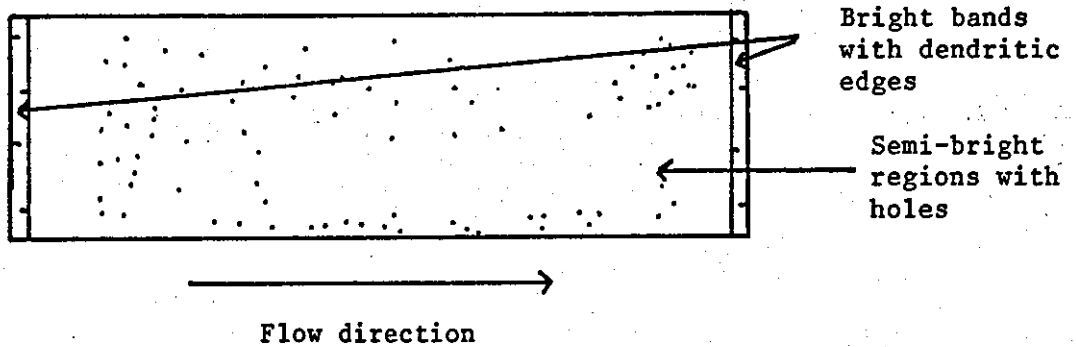
Flow Rate U cms ⁻¹ .	Reynolds Number Re	Average Current Density i A cm ⁻²	Time t s	Average Deposit Thickness μm	Weight Deposited g	Current Efficiency %
166.7	11,883	0.60	90	19	0.4879	101
166.7	11,883	0.75	94	24	0.6370	99
166.7	11,883	0.79	90	24	0.6489	100
180.9	12,900	0.89	76	23	0.6049	98

Table 4.29 Nickel foils deposited at Re 12,400 ± 500
(60°C, L/de ~11.7)

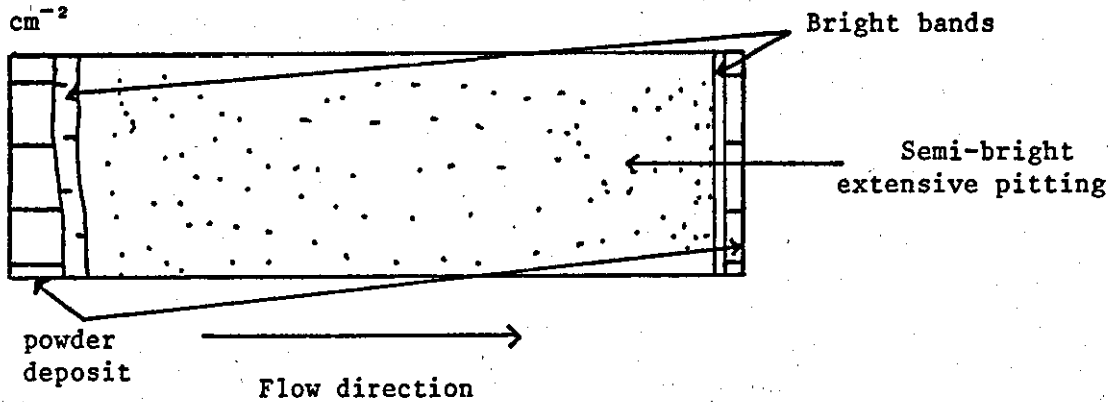
a) 0.60 A cm^{-2}



b) 0.75 A cm^{-2}



c) 0.79 A cm^{-2}



d) 0.89 A cm^{-2}

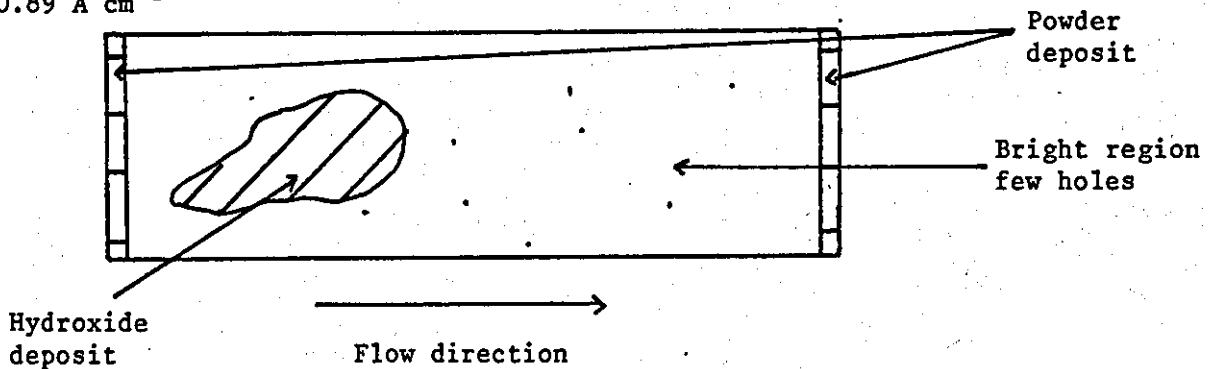
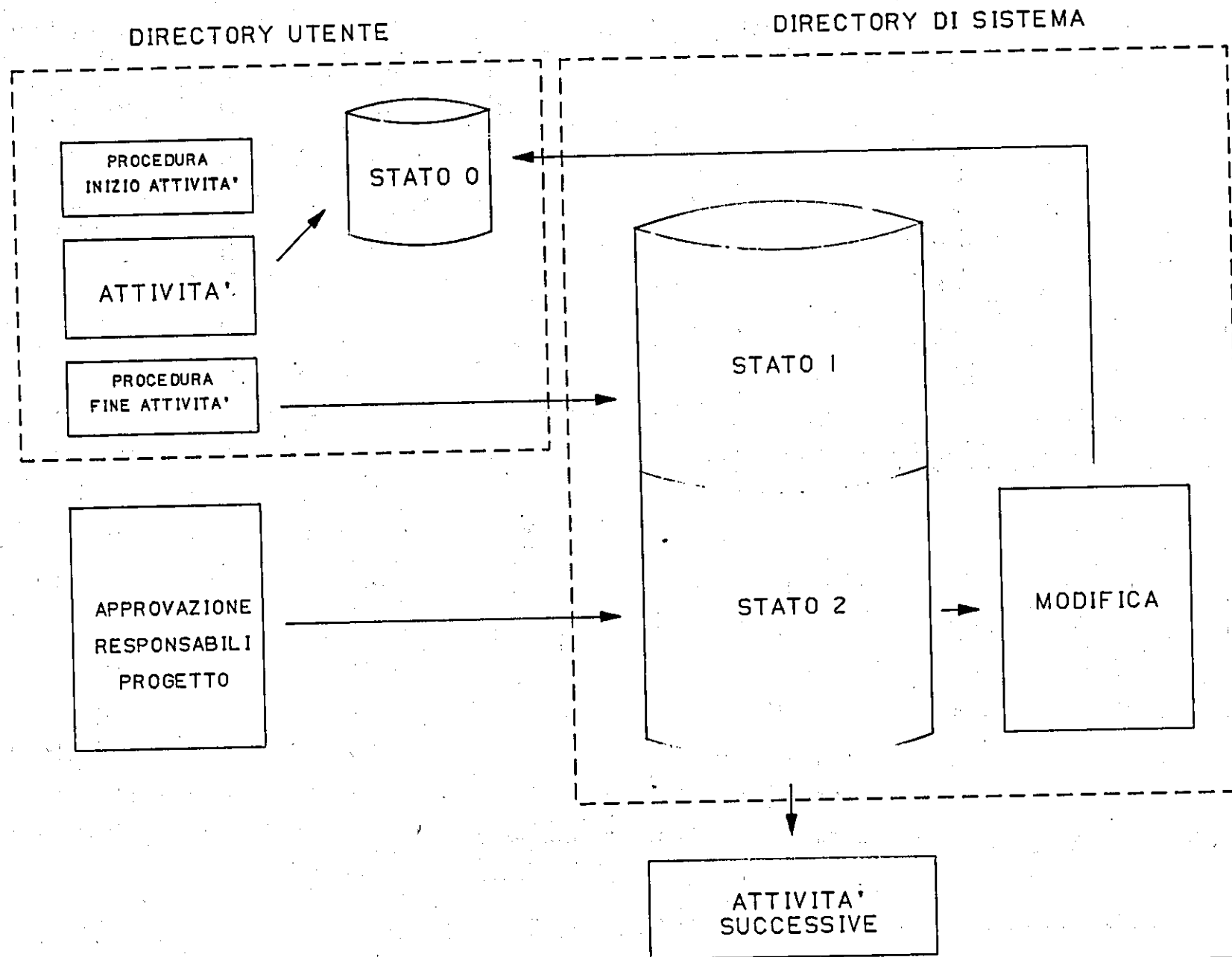
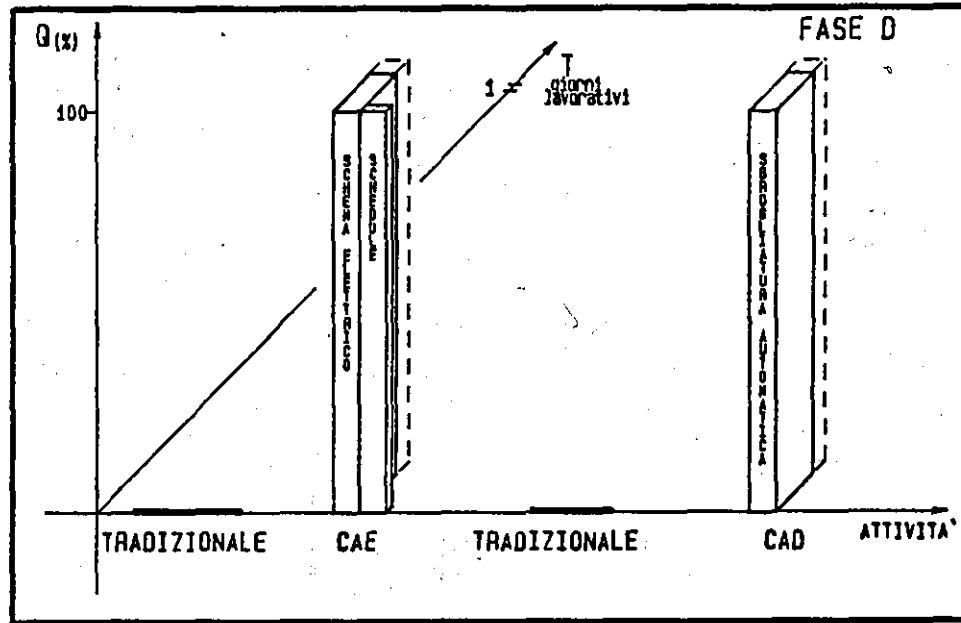
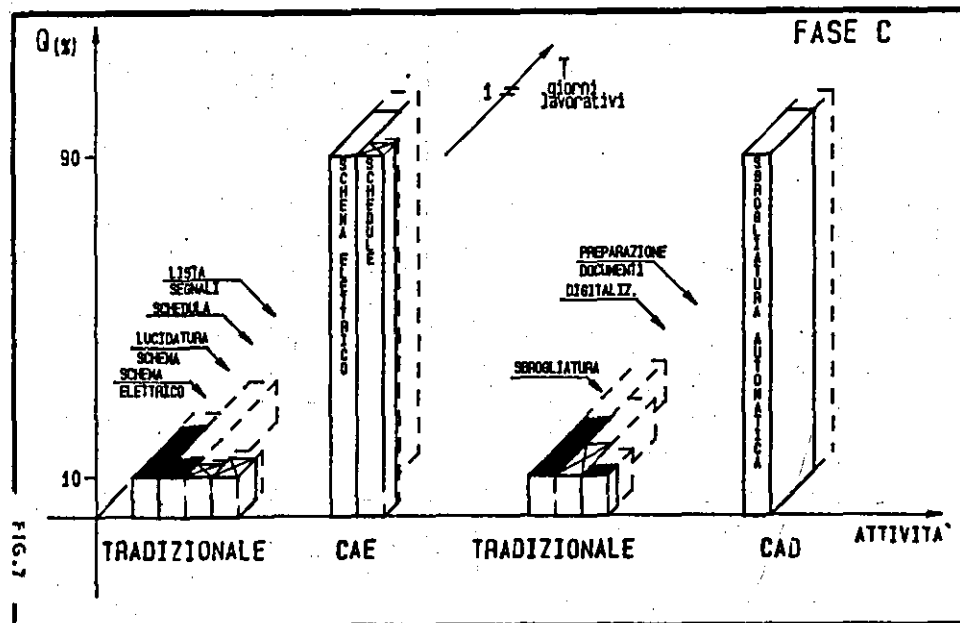
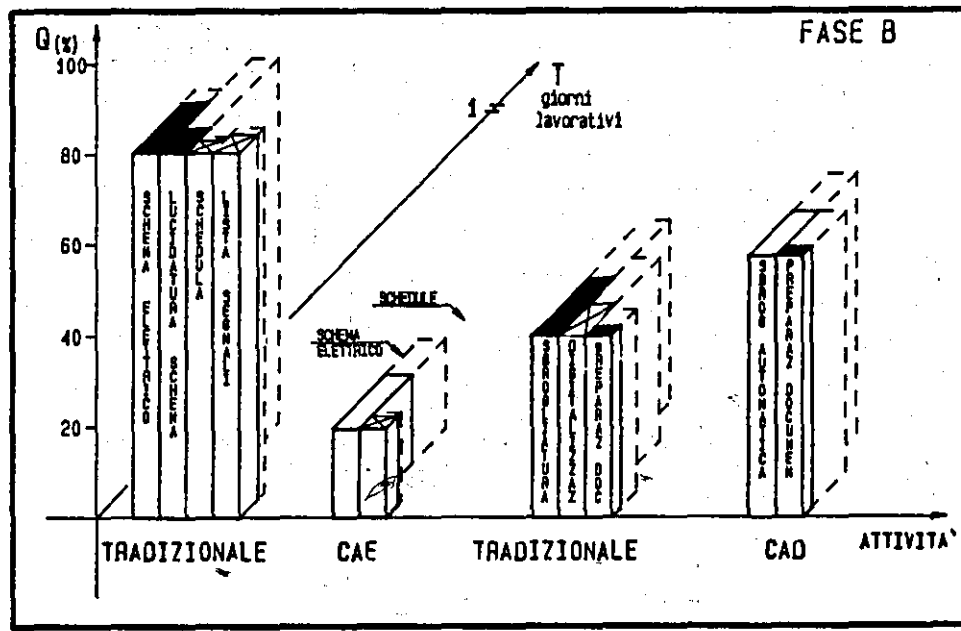
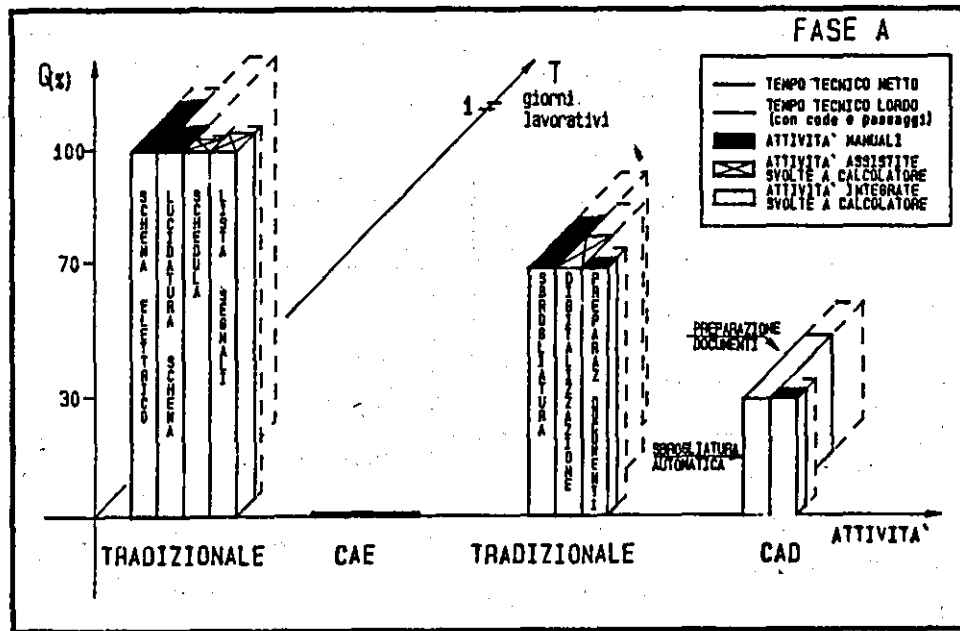


Fig. 4.80 Schematic representation of the visual appearance of nickel foils electrodeposited at $\text{Re } 12,400 \pm 500$. (60°C , $L/d_e \sim 11.7$)





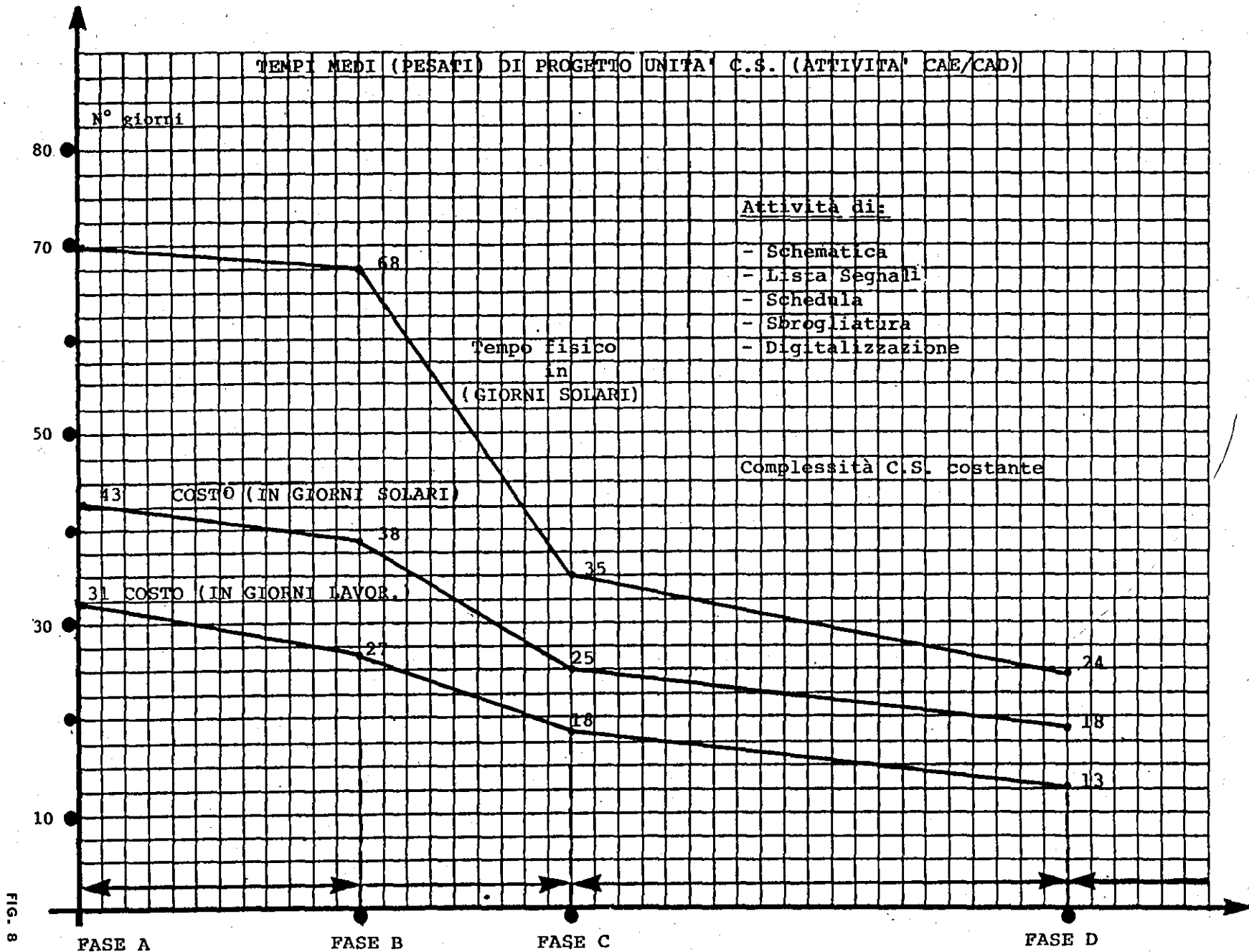
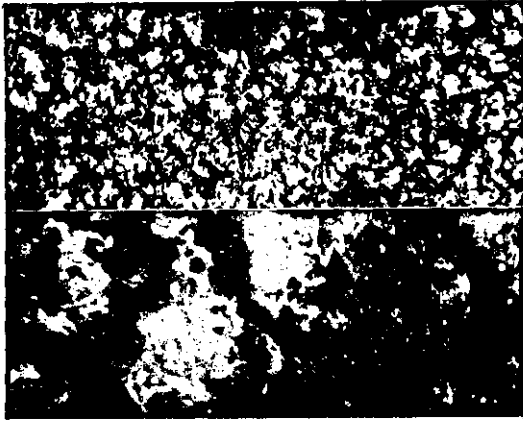
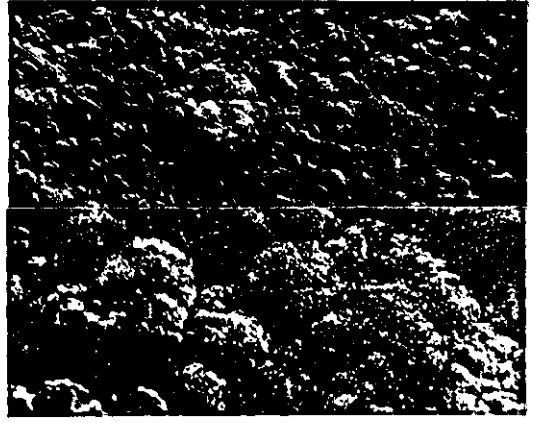


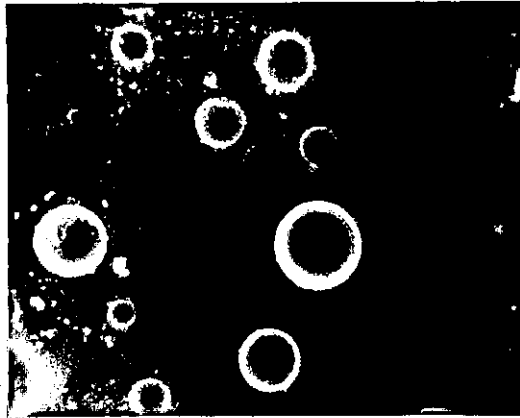
FIG. 8



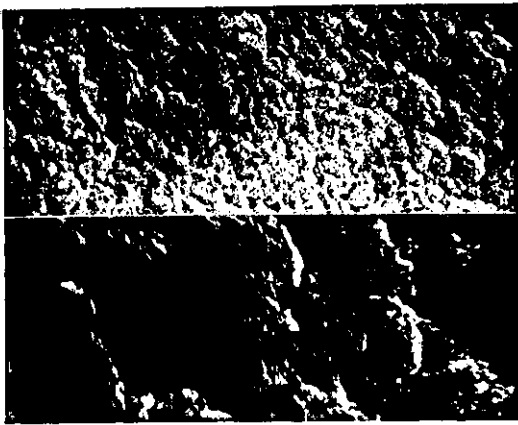
a) Top: x2,000
bottom: x10,000
0° tilt



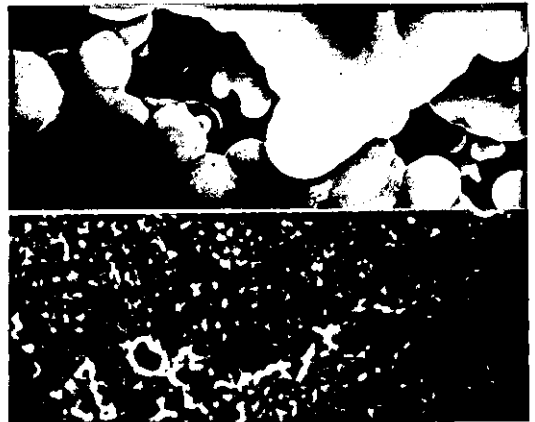
b) Top: x2,000
bottom: x10,000
0° tilt



c) x200, 0° tilt



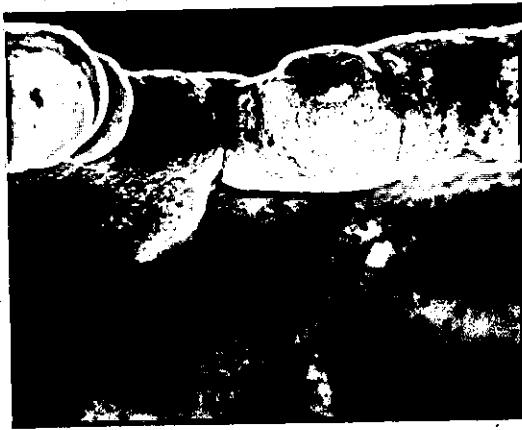
d) Top: x2,000
bottom: x10,000
20° tilt



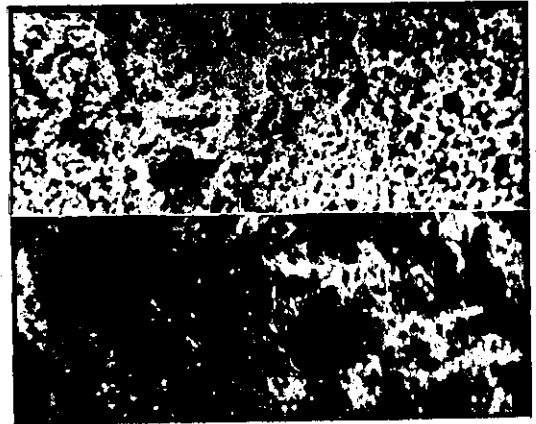
e) Top: x1,000
bottom: x20,000
0° tilt

Fig.4.81 SEM micrographs of surfaces of foils of nickel deposited at $Re\ 12,400 \pm 500$ ($60^\circ C$, $L/de \sim 11.7$) main deposit sections.

- a) $0.60\ A\ cm^{-2}$
- b) $0.75\ A\ cm^{-2}$
- c) $0.75\ A\ cm^{-2}$, pitted and perforated area
- d) $0.89\ A\ cm^{-2}$
- e) $0.89\ A\ cm^{-2}$, hydroxide area (top)
underlying deposit (bottom)



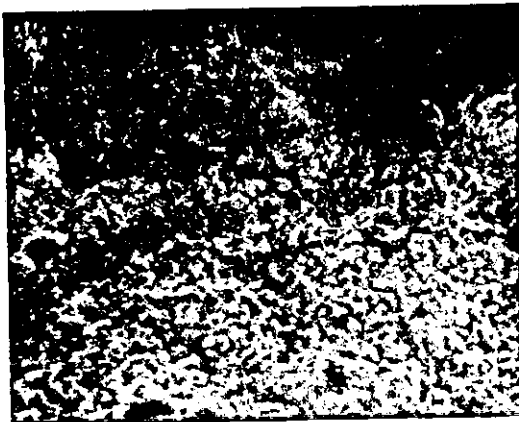
a) x500, 0° tilt



b) Top: x2,000
bottom: x10,000
0° tilt



c) x100, 0° tilt



d) x10,000, 20° tilt



e) x100, 0° tilt

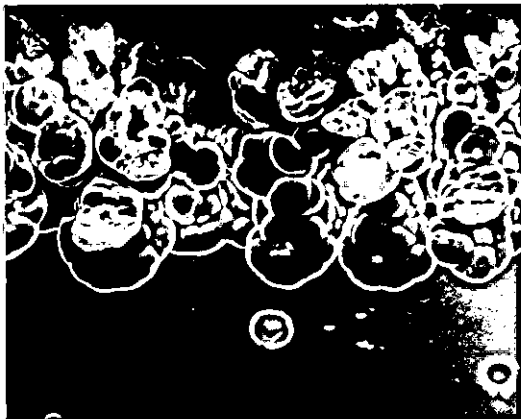
Fig.4.82 SEM micrographs of surfaces of foils of nickel deposited at $Re\ 12,400 \pm 500$ ($60^\circ C$, $L/de \sim 11.7$), leading edge sections.

- a) $0.60\ A\ cm^{-2}$
- b) $0.60\ A\ cm^{-2}$, $\sim 0.004\ cm$ from leading edge
- c) $0.75\ A\ cm^{-2}$
- d) $0.75\ A\ cm^{-2}$, $\sim 0.07\ cm$ from leading edge
- e) $0.89\ A\ cm^{-2}$

At 0.89 A cm^{-2} , a nodular powder growth had developed at the leading edge (Fig.4.82e).

Similar features were noted at the trailing edge of the foils. At 0.6 A cm^{-2} , the edge was smooth and fine grained. At 0.75 A cm^{-2} , the foil edge was more nodular, with pitting and holes in bright bands adjacent to the trailing edge (Fig.4.83a). A nodular powder deposit was formed at the highest current density (0.89 A cm^{-2}) (Fig.4.83b). Close to the powder region the deposit was fine grained with micro-cavities at the grain boundaries (Fig.4.83c).

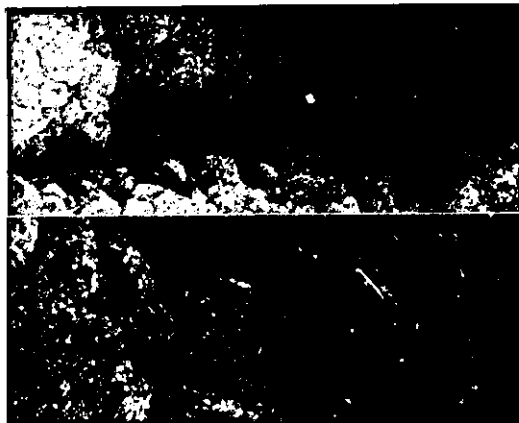
At a flow rate corresponding to the $12,400 \pm 500$, the maximum current density for a 100% sound deposit was $\sim 0.8 \text{ A cm}^{-2}$.



a) x100, 0° tilt



b) x200, 0° tilt



c) Top: x2,000
bottom: x10,000
0° tilt

Fig.4.83 SEM micrographs of surfaces of foils of nickel deposited at $Re\ 17,400 \pm 500$, ($60^\circ C$, $L/de \sim 11.7$), trailing edge sections.

a) $0.75\ A\ cm^{-2}$

b) $0.89\ A\ cm^{-2}$

c) $0.89\ A\ cm^{-2}$, $\sim 0.06\ cm$ from trailing edge

Summary of major features

Deposition of nickel at 60°C on 'long' electrodes (L/de 11.7) produced several interesting results, summarised as follows:

- a) Nickel was electroformed over 100% of the foil area at relatively high current densities (up to 0.8 A cm^{-2}) on electrodes 11.7 equivalent diameters in length.
- b) The cathode current efficiency was close to 100% under all deposition conditions.
- c) Fine grained, sound deposits were produced in the main central region of the cathode under most conditions. Significant changes in deposit morphology i.e. powder deposits, were mainly confined to the leading and trailing edge region.
- d) All foils were generally lustrous. Bright deposits were produced at current densities $>0.8 \text{ A cm}^{-2}$ on main sections of the foils.
- e) Significant increases in deposit microhardness were noted near the entry and exit regions. In these areas the deposit was very fine grained and visually brighter. The main deposit region x/L 0.1 to x/L 0.9 was of more uniform microhardness. The microhardness of this area tended to increase with increasing current density.
- f) Maximum deposition rates were lower than those obtained for shorter electrodes. This observation would be in agreement with mass transfer theory.
- g) On 'long' electrodes the deposits tended to have greater visible porosity than on 'short' electrodes. This observation may be related to downstream accumulation of evolved gas.

In Fig.4.84, the nature of the deposit, i.e. sound (fine grained) or unsound (powdery) is plotted from the data obtained from the experimental study, as described previously (p.171). The approximate

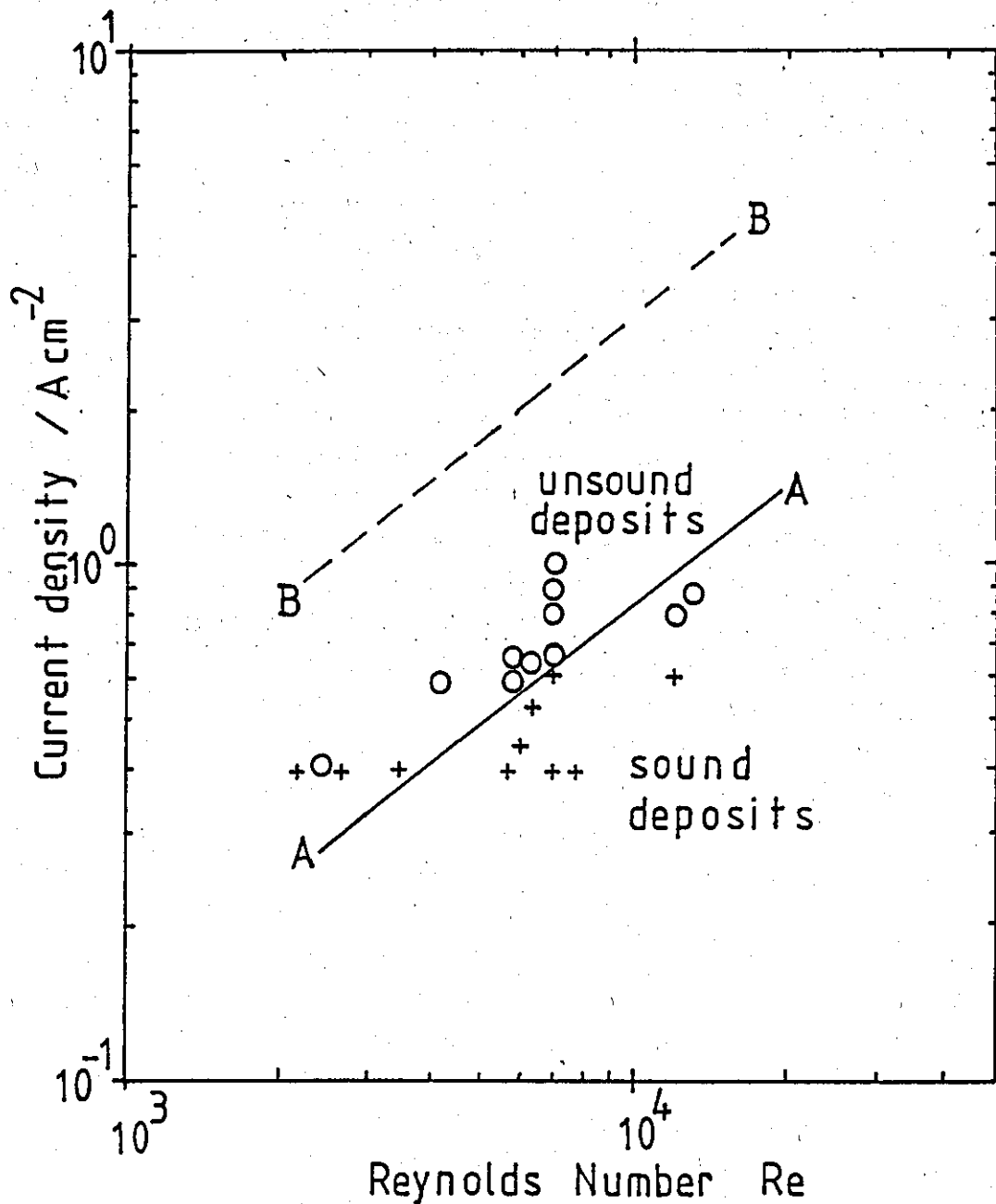


Fig.4.84 The relationship between the flow rate (Reynolds Number) and the maximum current density (i_{max}) for a sound deposit

$T \sim 60^{\circ}\text{C}$, $L/d_e \sim 11.7$

o - powdery and/or hydroxide deposit

+ - coherent nickel electroform

mass transfer limited current densities were calculated from the design equation for the cell (p.128). This is shown (for turbulent flow) as the broken line B-B of slope 0.8 in Fig.4.84. The solid line A-A in Fig.4.84 of slope 0.8 is in approximate agreement with the division between sound and unsound deposits obtained under turbulent flow conditions. At low flow rates, the deposition rate would appear to be higher than expected. The experimentally determined relationship indicates that the maximum current densities for sound deposits are less than the mass transfer limited current densities.

(c) Direct comparison of foils produced at constant flow rate
Re $6,400 \pm 250$) and current density (0.67 A cm^{-2}) as a
function of electrode length (L/d_e ratios 2.3, 2.9, 3.5,
4.7 and 11.7).

In this section of the investigation, deposition was carried out at a current density of 0.67 A cm^{-2} and a flow rate corresponding to $\text{Re } 6,400 \pm 250$ on to electrodes of different lengths. The changes in current efficiency, visual appearance and deposit structure were noted as the cathode length was increased.

In each experiment electrolysis was carried out for a specified period of time to produce a deposit 18 to $26 \mu\text{m}$ thick for subsequent visual and microscope examination, after removal of the foil from the substrate. The deposition conditions are summarised in Table 4.30 and the visual appearance of the electroforms are presented in Fig.4.85.

The central main deposit region of all foils were lustrous and showed no evidence of powder type deposits. Significant changes in the deposit structure appeared to be confined to the foil edges. Most foils were deposited at current efficiencies approaching 100%. Variations in current efficiency were more apparent with short cathode lengths, where the leading and trailing edge regions represent a greater proportion of the total electrode area.

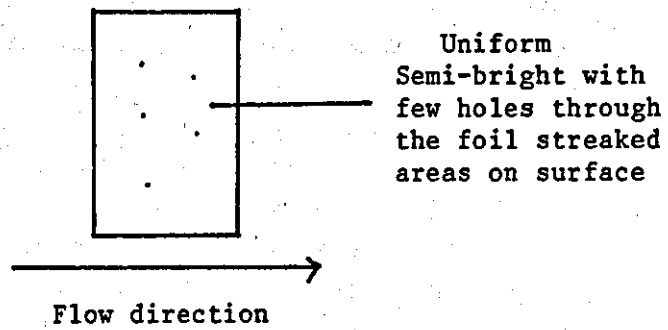
The number of pits and perforations through the foil tended to increase with increasing electrode length. During deposition gas evolving near the leading edge of the electrode accumulated and coalesced further downstream. The rate and location of gas evolution may also be related to cathode length.

Foils produced with the shortest cathode length (2.3 d_e) were of smooth uniform appearance (Fig.4.85a) with 'streaking' on the foil surface. With cathode lengths of 2.92 and 3.5 d_e , bands of brighter nickel were deposited at the leading edges of the foils (Fig.4.85c). The foil edges were more nodular and powdery with longer electrode lengths (Fig.4.85d and e).

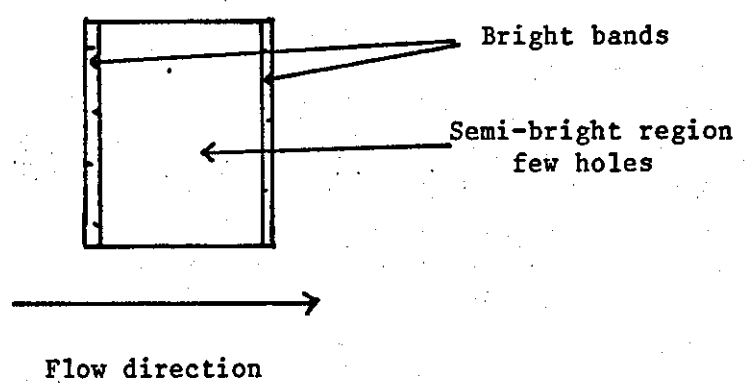
L/de	Current Density i/A cm ⁻²	Deposition Time s	Weight Deposited g	Current Efficiency %	Deposit Thickness μm
2.3	0.69	92	0.1028	89	19
2.3	0.70	93	0.1140	96	21
2.92	0.68	97	0.1416	94	22
2.92	0.70	103	0.1553	95	23
3.5	0.68	104	0.1832	94	23
3.5	0.70	104	0.1730	87	22
4.7	0.69	105	0.1789	68	18
4.7	0.64	112	0.2439	93	23
11.7	0.64	116	0.6897	102	26
11.7	0.65	118	0.7041	101	26

Table 4.30 Nickel foils deposited at 0.67 ± 0.02 A cm⁻² and Re $6,400 \pm 250$ (Cell 2, 60°C, de 0.857cm).

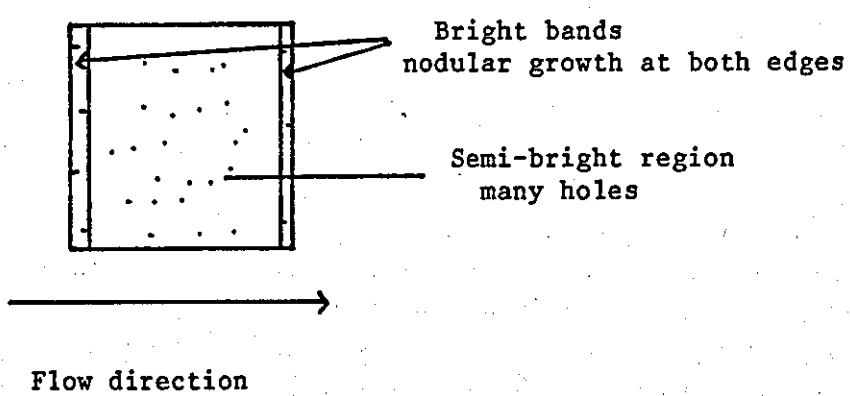
a) $L/d_e \sim 2.3$



b) $L/d_e \sim 2.92$



c) $L/d_e \sim 3.5$



d) $L/d_e \sim 4.7$

Hydroxide deposit
Powder deposit

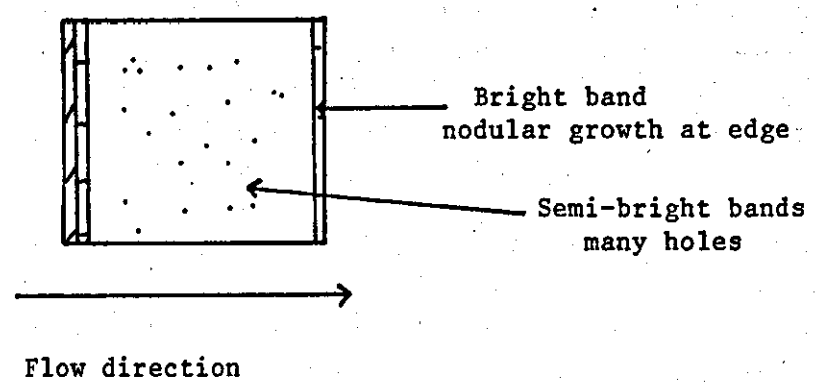


Fig.4.85 Schematic representation of the visual appearance of nickel foils deposited at 0.64 cm^{-2} and $Re \ 6,400 \pm 250$. (60°C).

e) $L/d_e \sim 11.7$

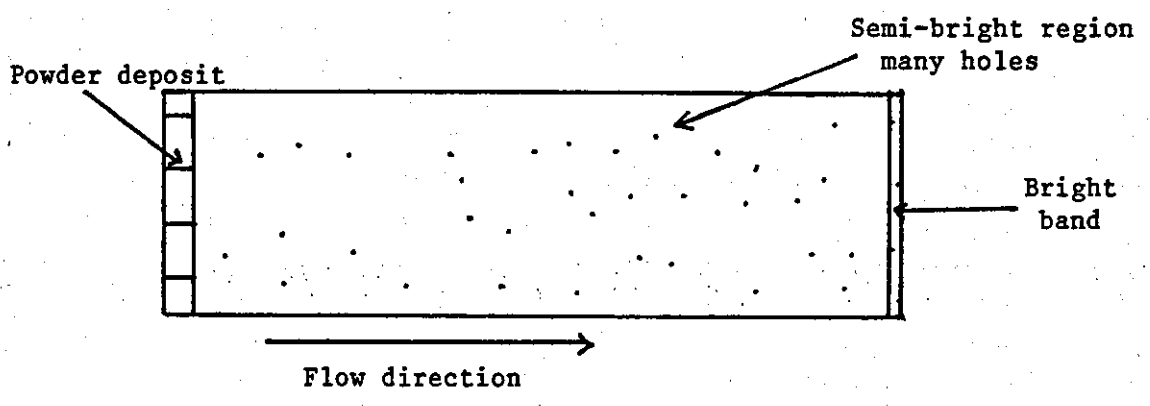


Fig. 4.85 continued

More detailed information on the structure of the deposits was obtained by SEM examination of the stripped foils.

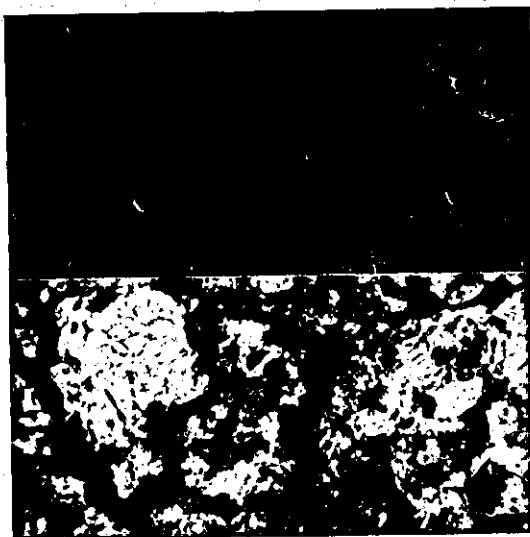
Main deposit

The micrographs of the main deposit sections are shown in Figs.4.86 and 4.87 for each cathode length. All the deposits were of relatively uniform fine grain structure over >90% of the foil surface. The grain size was between 2 and 5 μ m. The distribution of grain sizes appeared to be more uniform at longer electrode lengths (cf Fig.4.86 and Fig.4.87). On shorter cathodes (2.3 and 2.92 de), surface streaks (Fig.4.86a) and larger features (Fig.4.86b) were observed. Some micro-porosity was found at the grain boundaries (Fig.4.86d).

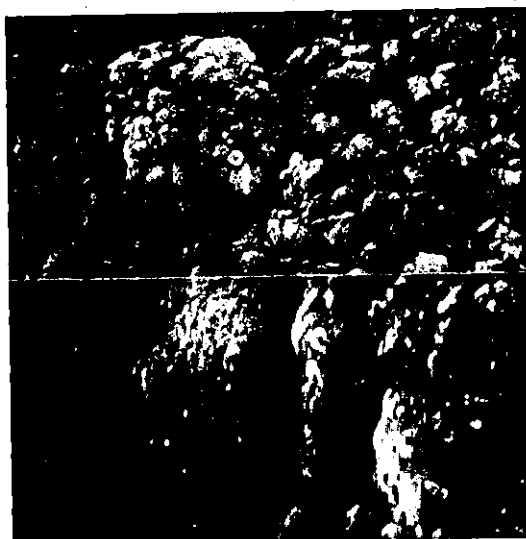
Edge effects

At the shortest cathode length (2.3 de) the leading edge was smooth and free of large features. At high magnification the deposit was very fine grained (1-2 μ m) (Fig.4.88a). Small micro-pits were present in this area. With an increased cathode length of 2.92 de, the leading edge of the deposit was fine grained and ridges were also observed (Fig.4.88b). At 3.5 de, the foil edge was clearly defined and as a bulbous ridge, 50 μ m in width (Fig.4.88c). Immediately downstream of the leading edge ridge, a coarse grain structure was observed. A nodular powder deposit was formed at the leading edge region of cathodes 4.7 de in length (Fig.4.88d). The nodules were 20 to 100 μ m in diameter. In this area of the deposit partial exfoliation of the foil surface had occurred. Downstream of the powder deposit the morphology was generally fine grained, with some larger features (Fig. 4.88e). The current efficiency was low (68%).

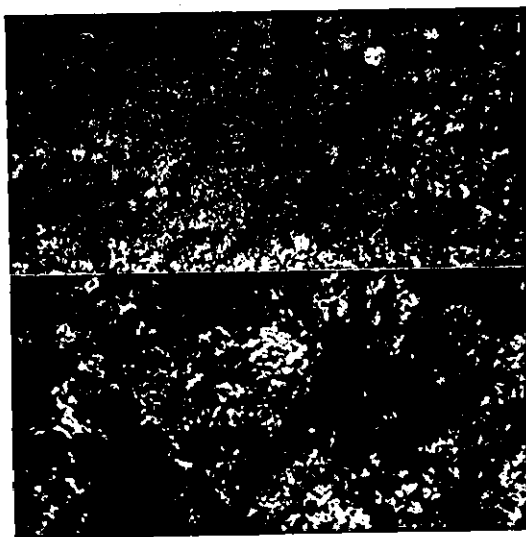
On increasing the cathode length to 11.7 equivalent diameters, powder nodules 20 to 100 μ m in diameter were deposited (Fig.4.89a). Pitting and porosity were found in this area (Fig.4.89b). Downstream of the powder region, a bulbous ridge was formed, dividing this area from the fine grained main deposit.



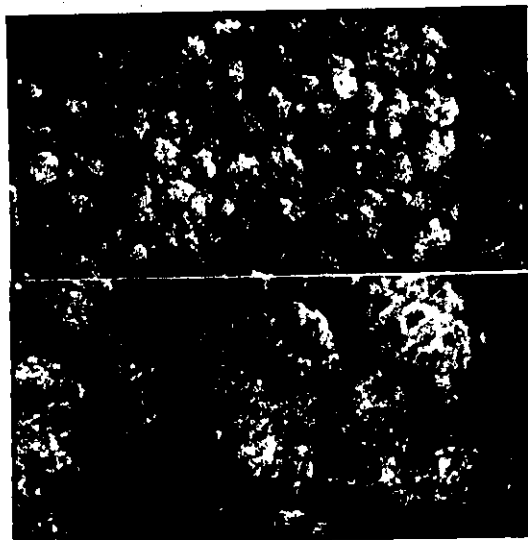
a)



b)



c)



d)

Fig. 4.86 SEM micrographs of surfaces of foils of nickel deposited at $0.67 \pm 0.03 \text{ A cm}^{-2}$, $\text{Re } 6,400 \pm 250$, (60°C), main deposit sections. (Top: 2,000x; bottom: 10,000x, 0° tilt)

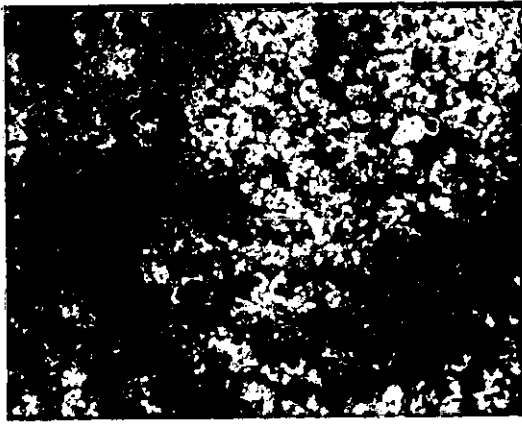
- a) $L/de \sim 2.3$, streaked area
- b) $L/de \sim 2.9$
- c) $L/de \sim 3.5$
- d) $L/de \sim 4.7$



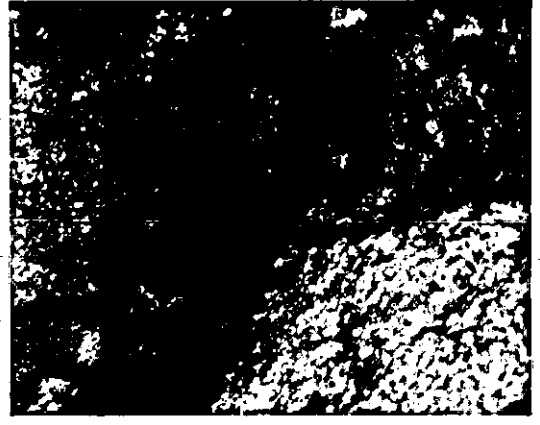
Fig. 4.87 SEM micrograph of the surface of nickel foil deposited at $0.67 \pm 0.03 \text{ A cm}^{-2}$, $\text{Re } 6,400 \pm 250$, main deposit section.

$L/d_e \sim 11.7$, 60°C

(x2,000, 45° tilt)



a) x2,000



b) x2,000



c) x200



d) x50



e) x2,000

Fig.4.88 SEM micrographs of surfaces of foils of nickel deposited at $0.67 \pm 0.03 \text{ A cm}^{-2}$; $\text{Re } 6,400 \pm 250$, (60°C), leading edge sections (0° tilt).

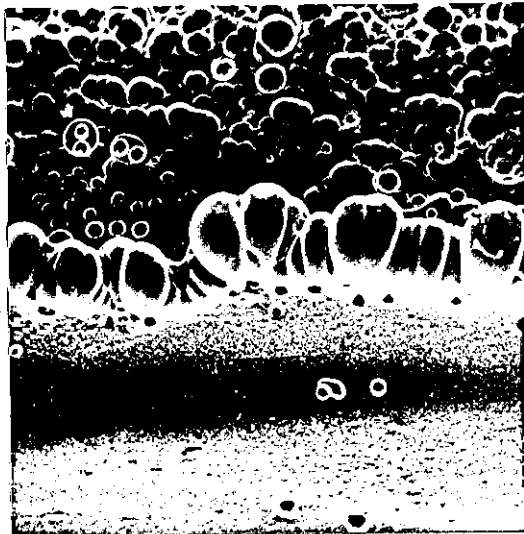
a) $L/d_e \sim 2.3$

b) $L/d_e \sim 2.9$

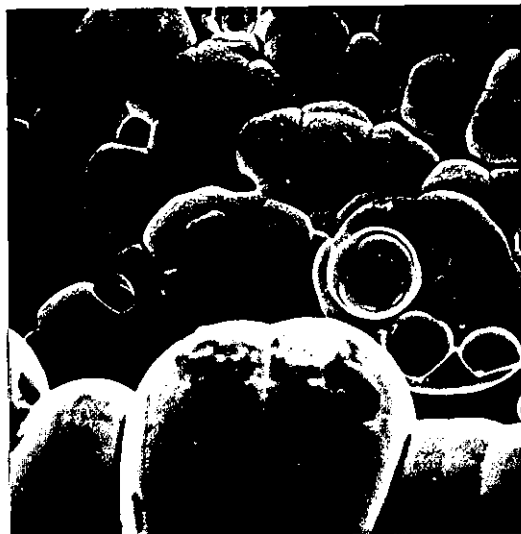
c) $L/d_e \sim 3.5$

d) $L/d_e \sim 4.7$, powdery edge region

e) $L/d_e \sim 4.7$, downstream of powder region



a) x50, 45° tilt



b) x2,000, 45° tilt

Fig.4.89 SEM micrographs of the surfaces of foils of nickel deposited at $0.67 \pm 0.03 \text{ A cm}^{-2}$, $\text{Re } 6,400 \pm 250$, (60°C , $L/d_e \sim 11.7$), leading edge sections.

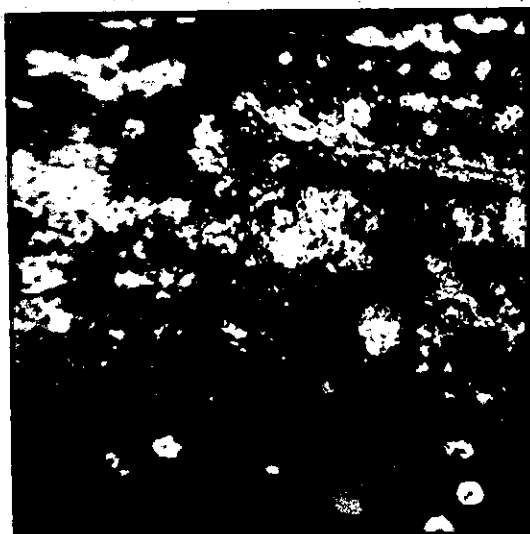
The trailing edges of all the electroforms were relatively smooth, developing increased ridging as the cathode length increased (Fig.4.90). Some roughening of the foil surface was also observed in this area (Fig.4.90b).

As the trailing edge was approached, the grain size tended to increase. Near the exit edge of the 11.7 de electrode ($\sim 3000\mu\text{m}$ from the edge) the grains were small ($1-5\mu\text{m}$ in dia.), (Fig.4.91c). At a distance of $\sim 300\mu\text{m}$ from the trailing edge, the grains were larger (5 to $10\mu\text{m}$) (Fig.4.91b). At the trailing edge, prominent bulbous features were found (Fig.4.91a).

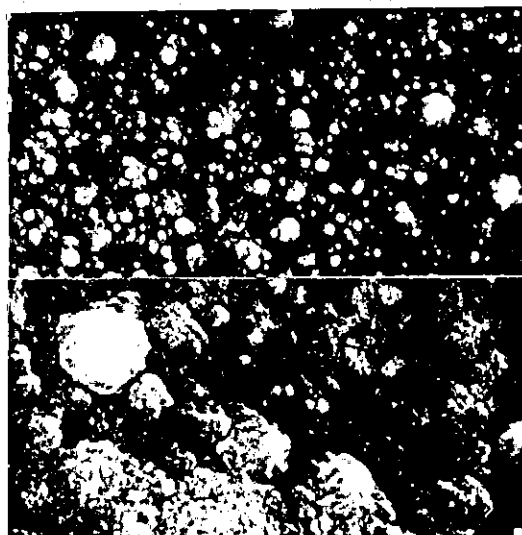
At a current density of $0.67 \pm 0.03 \text{ A cm}^{-2}$, and a flow rate of $\text{Re } 6,400 \pm 250$, changes in deposit structure at the leading and trailing edges were found for cathode lengths $>4.7 \text{ de}$.

Summary of major features

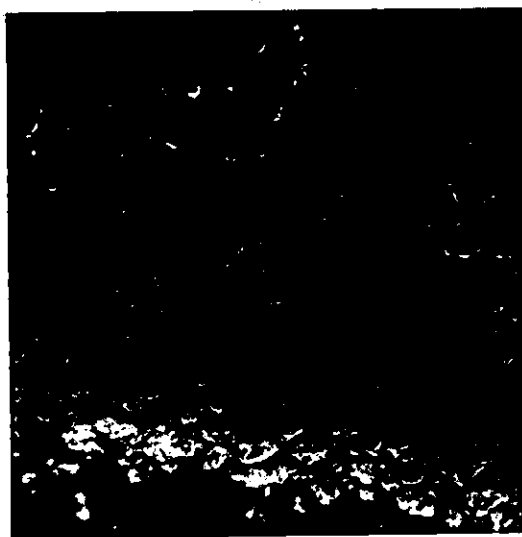
- a) The main central region of all the deposits was found to be sound and fine grained. For the experimental conditions used, the cathode length related effects were confined to the leading edge of the electroform. As the cathode length was increased, at constant current density and flow rate, the leading edge became rougher and powdery. Higher current densities were obtained on shorter cathodes.
- b) The current efficiency for most electroforms was $\sim 95\%$. Decreases in current efficiency became more noticeable on shorter cathodes, where the edge region is proportionately greater in area.
- c) The number and density of pits and foil perforations increased with increasing cathode length. Hydrogen gas bubbles evolving near the leading edge of the foil accumulated and coalesced downstream. In addition the total volume of hydrogen evolved (and hence the number of bubbles) will also be greater on longer electrodes.
- d) The formation of hydroxide layers at the inlet or exit regions of the cathode may form a resistive layer. Hence the current density on the areas of sound deposit will increase and the effective length of the cathode decrease resulting in complex inter-related effects.



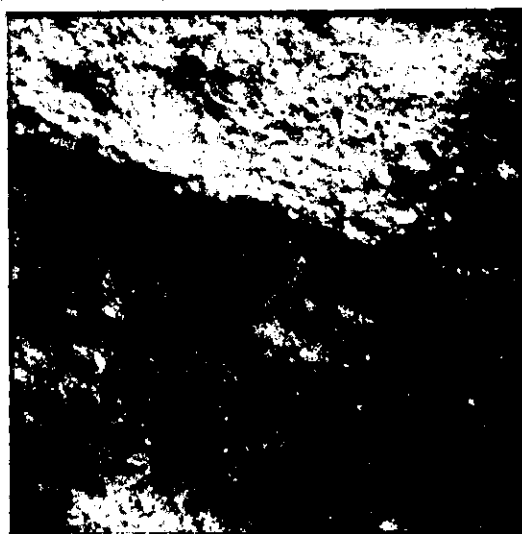
a) x200, 0° tilt



b) Top: x2,000
bottom: x10,000
0° tilt



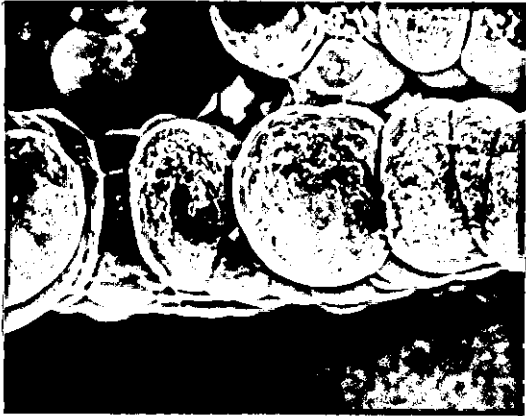
c) x2,000, 0° tilt



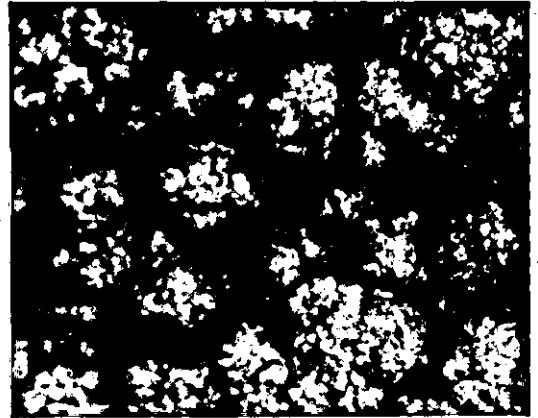
d) x10,000, 0° tilt

Fig.4.90 SEM micrographs of surfaces of nickel foils deposited at $0.67 \pm 0.03 \text{ A cm}^{-2}$, $\text{Re } 6,400 \pm 250$, trailing edge sections (60°C).

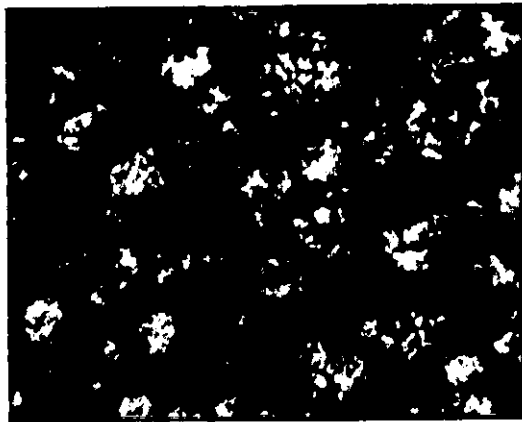
- a) $L/d_e \sim 2.3$
- b) $L/d_e \sim 2.9$, behind leading edge ridge
- c) $L/d_e \sim 3.5$
- d) $L/d_e \sim 4.7$, behind trailing edge ridge



a) x200, 0° tilt



b) x2,000, 0° tilt



c) 2,000, 0° tilt

Fig.4.91 SEM micrographs of surfaces of foils of nickel deposited at $0.67 \pm 0.03 \text{ A cm}^{-2}$, $\text{Re } 6,400 \pm 250$, (60°C , $L/d_e \sim 11.7$) - trailing edge sections

- a) trailing edge
- b) $300 \mu\text{m}$ from trailing edge
- c) $3,000 \mu\text{m}$ from trailing edge

4.3.2 The effects of temperature on the relationships between foil structures, flow rates and current densities using a long electrode system.

The maximum recommended operating temperature for the sulphamate electrolyte under normal plating conditions is 70°C and it was desirable to investigate the system under flowing electrolyte conditions at this temperature since mass transport effects had not been studied. The effects on foil structures were also unknown. Some increase in maximum deposition rates might well be expected. The major programme of work was carried out at 70°C. This study included deposition under conditions of laminar flow (Re 1318 - 2004) and turbulent flow (Re 3312 - 13,203). A restricted investigation was also carried out at 50°C and 65°C (Re 6575 ± 75) to give an overview of temperature effects.

- (a) The electroforming of nickel foils at 70°C using a long electrode system $L/d_e \sim 11.7$
- (i) Deposition under conditions of laminar flow (Re 1,318 - 2,000) at 70°C.

At very low Reynolds numbers (laminar flow) large hydrogen gas bubbles adhered to the cathode surfaces and obstructed the smooth flow of electrolyte. Within the Reynolds number range Re: 1,000 - 2,000, some bubbles did accumulate on the electrode and were swept slowly downstream. Fast deposition of reasonably fine grained deposits was carried out under these conditions. Nickel foils (26µm thick), were electroformed in this flow regime at current densities of 0.95 and 1.01 A cm⁻². The current efficiency was close to 100%.

Both foils were of relatively uniform lustrous appearance over the electrode length (Fig.4.92). Narrow bands of brighter material were deposited at the leading edge of the electroforms. The deposits were more uniform (with no prominent edge effects), and of decreased microhardness value (289 ± 9 kg mm⁻²), although less bright, than foils produced at 60°C.

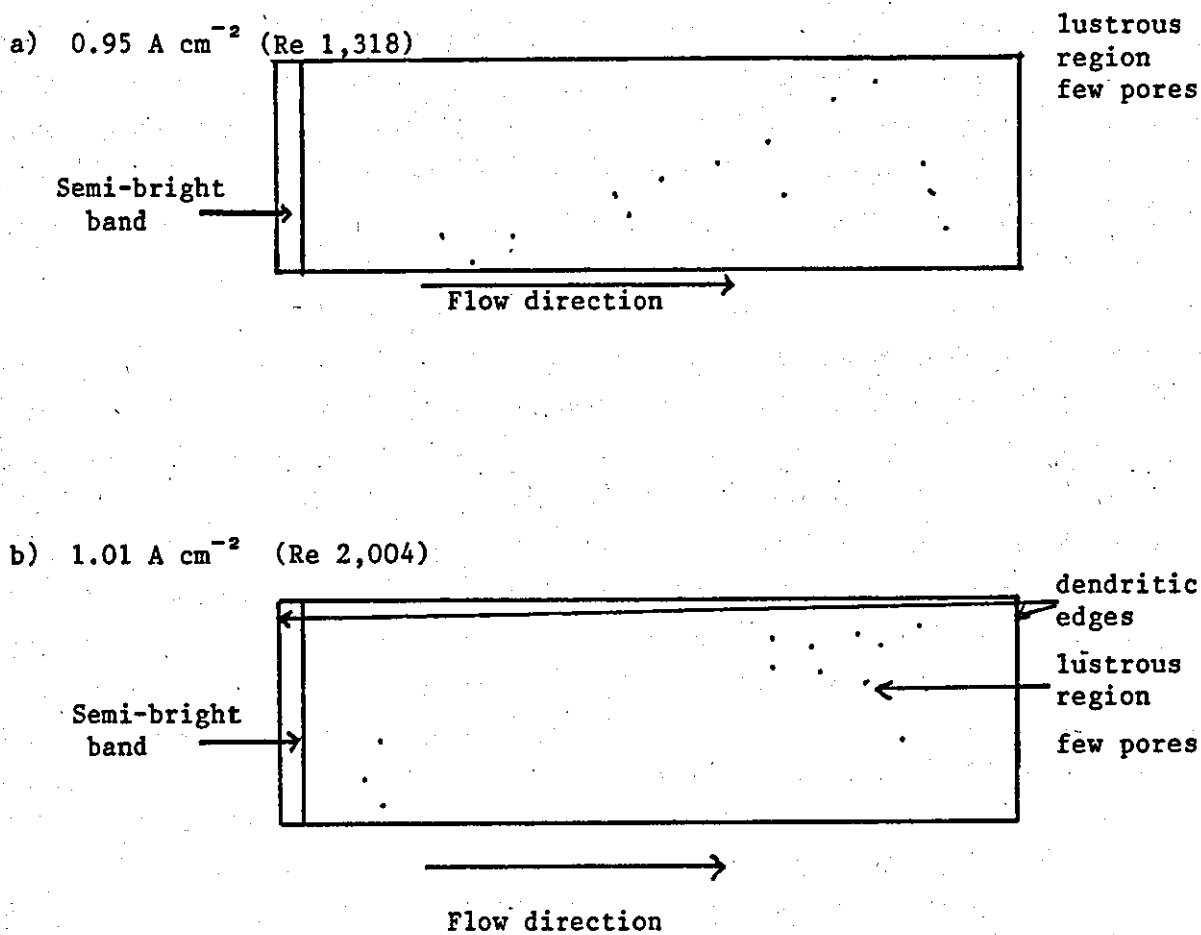


Fig.4.92 Schematic representation of the visual appearance of nickel foils deposited in laminar flow (Re 1,318 - 2,004) (70°C , $L/d_e \sim 11.7$)

The low visible porosity was an interesting feature considering the large numbers of gas bubbles on the electrode surface at low flow rates. The porosity was considerably less than observed for comparable 60°C foils.

Electroforms were examined in detail in the SEM, after removal from the substrate and typical foil structures are shown in Figs.4.93 and 4.94.

Main deposit

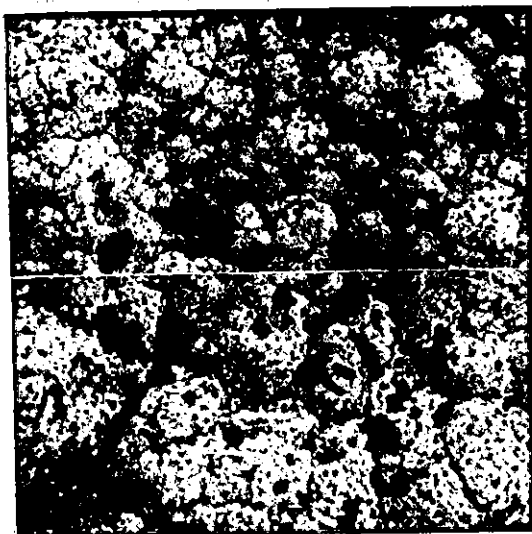
Within the main deposit region, two areas of interest were found. About 80% of the surface was of the typical fine grain morphology (Fig.4.93a), similar to structures observed at 60°C. The grains were relatively uniform and 3-5 μm in diameter. However towards the outlet end of the foil, the deposit was of a comparatively coarse structure. Here the features were much larger (7-20 μm), with well defined boundaries and fine inter-granular fissures in some areas (Fig.4.93 b,c and d). About 10% of the electroform was of the above morphology.

Edge effects

The leading edge of the foil exhibited coarse and nodular features (Fig.4.94a) and these were about 300 μm in width. Immediately downstream, the finer scale morphological features were interspersed with some larger features. This structure corresponded with the semi-bright band observed visually.

At the trailing edge, a coarser structure was observed (Fig.4.94 b and c). The nodular features were similar to those observed in the powder-type deposits at 60°C (cf Fig.4.94c and Fig.4.69c).

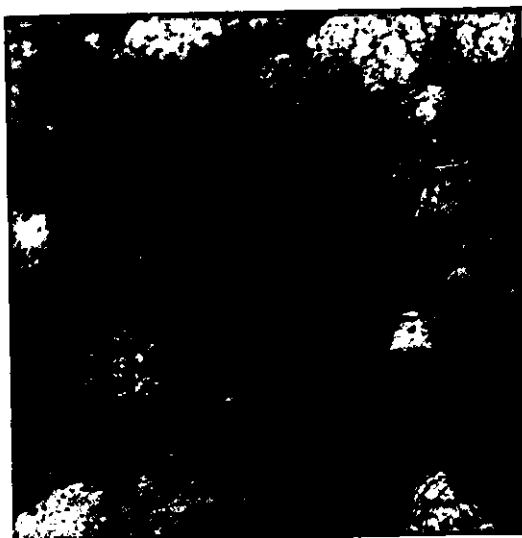
In laminar flow good deposits were obtained at very high current densities at 70°C. With a reasonable flow rate (corresponding to $Re \sim 1,500$), nickel foil was deposited at $\sim 1.0 \text{ A cm}^{-2}$, a current density much higher than was achieved at 60°C ($< 0.5 \text{ A cm}^{-2}$).



a) Top: x2,000;
bottom: x10,000
0° tilt



b) Top: x2,000;
bottom: x10,000
0° tilt



c) x1,000, 0° tilt



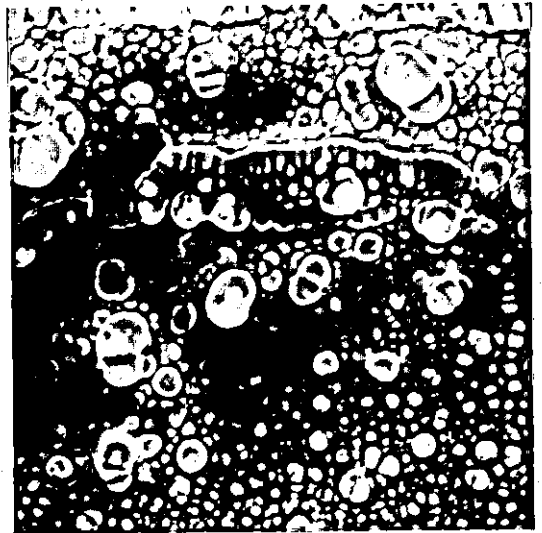
d) x2,000, 0° tilt

Fig.4.93 SEM micrographs of surfaces of foils of nickel deposited in laminar flow, main deposit sections
Re 1,318, 0.95 A cm^{-2} (70°C , $L/d_e \sim 11.7$)

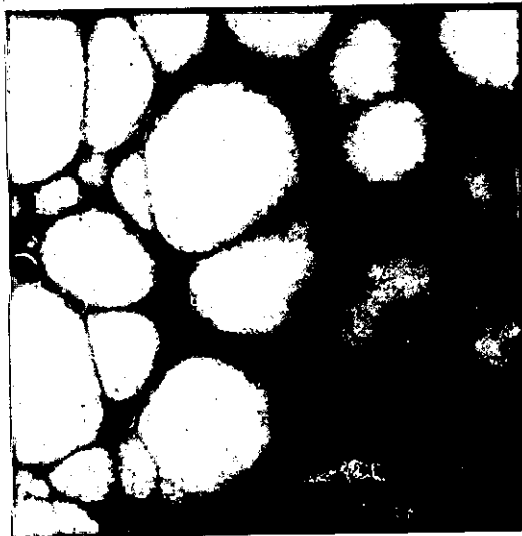
- a) Typical uniform fine grain structure
- b) ~9cm from leading edge, grain boundary cracks
- c) ~9cm from leading edge, coarse structure
- d) as above, cavity at boundary.



a) x200, 0° tilt



b) x100, 0° tilt



c) x1,000, 0° tilt

Fig.4.94 SEM micrographs of the surfaces of foils of nickel deposited at the leading and trailing edge of the electrode, $Re\ 1,318$, $0.95\ A\ cm^{-2}$ ($60^{\circ}C$, $L/d_e \sim 11.7$)

- a) leading edge section
- b) trailing edge section
- c) trailing edge section, nodule structure

(ii) Deposition under conditions of turbulent flow at 70°C

In turbulent flow ($Re > 2,200$), gas bubble adhesion was minimised and deposition was carried out over a range of experimental conditions. A series of electrolyses was carried out at flow rates of 40.0 to 166.7 cm s^{-1} with corresponding Reynolds numbers of Re 3,312 to 13,803. In each experiment, electrolysis was carried out for a specified period of time to give deposits $26 \pm 3 \mu\text{m}$ thick.

Nickel was electroformed, over a range of current densities, in the following flow regimes:

- low flow rates (Re 3,330 \pm 30);
- intermediate flow rates, Re 4,800 \pm 100 and
 Re 7,450 \pm 300; and
- high flow rates (Re 13,803).

The foils were examined visually and microscopically both before and after removal of the deposit from the electrode surface.

Nickel electroforms deposited in the flow range Re 3,300 \pm 30

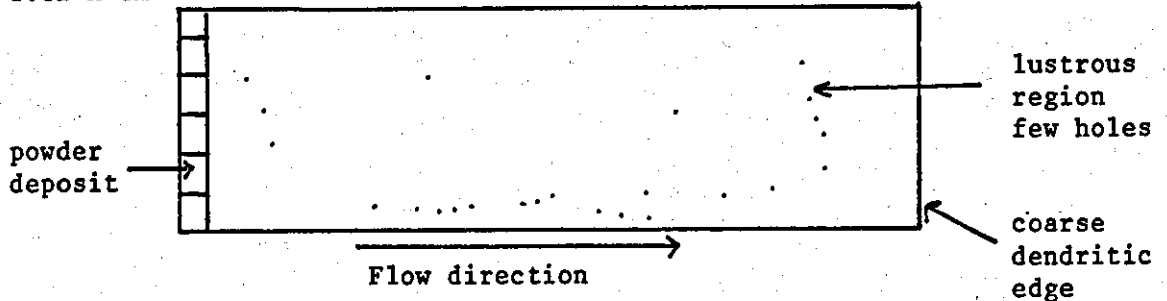
Two nickel foils, $25 \pm 1 \mu\text{m}$ thick were electroformed at current densities of 1.12 and 1.30 A cm^{-2} . The visual appearance of the foils are shown schematically in Fig.4.95. The high current efficiency (98%) reflected the good appearance of deposits over 95% of the foil surfaces.

Main deposit

The main deposit regions of both foils were lustrous and of good visual appearance. Visible porosity was generally low increasing slightly at the higher current density. Detailed SEM examination of foil morphology was carried out along the length of the deposit.

Downstream of the inlet edge, the foil morphology was comparatively fine grained at 1.12 and 1.3 A cm^{-2} . At the lower current density grain sizes were in the range 2-4 μm , with some surface reliefs (Fig.4.96a).

a) 1.12 A cm^{-2}



b) 1.30 A cm^{-2}

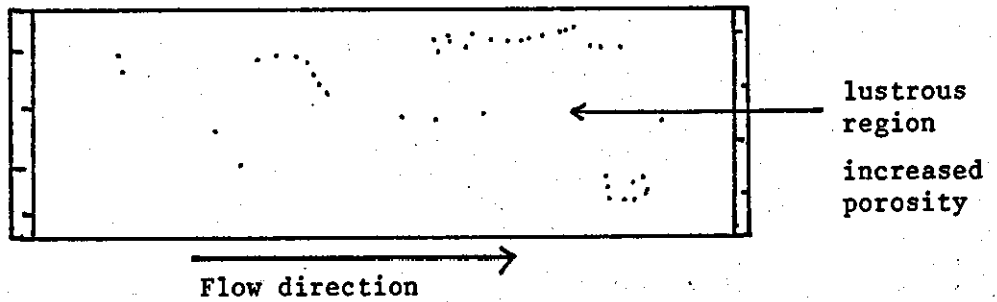
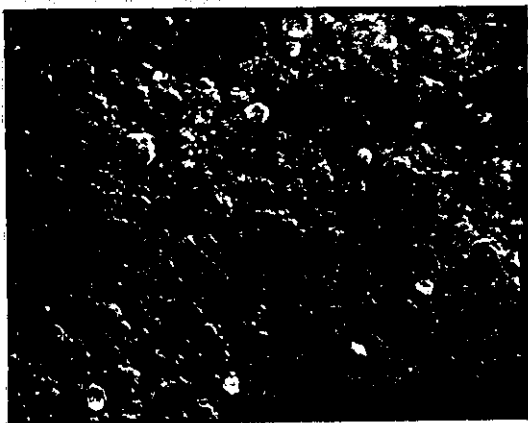
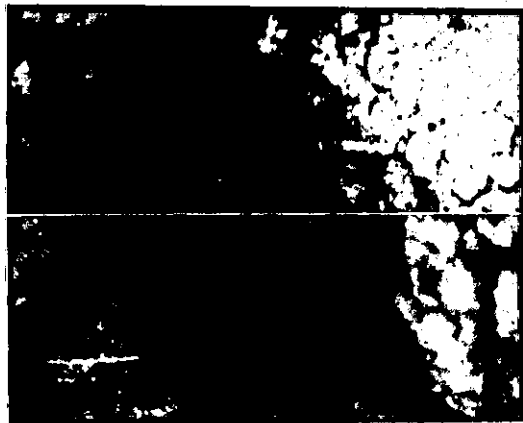


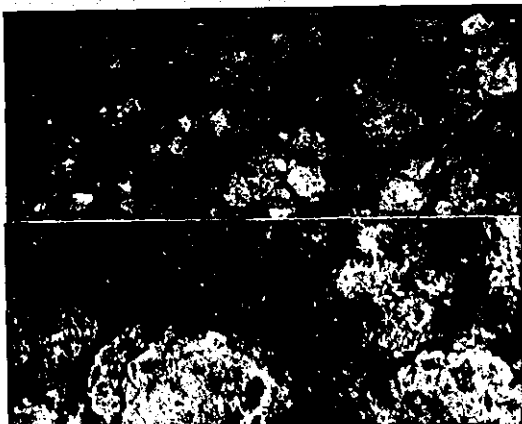
Fig.4.95 Schematic representation of the visual appearance of nickel foils deposited at $\text{Re } 3,330 \pm 30$. (70°C , $L/d_e \sim 11.7$).



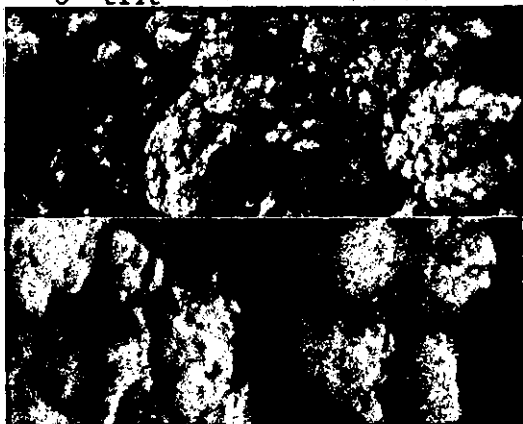
a) x2,000, 0° tilt



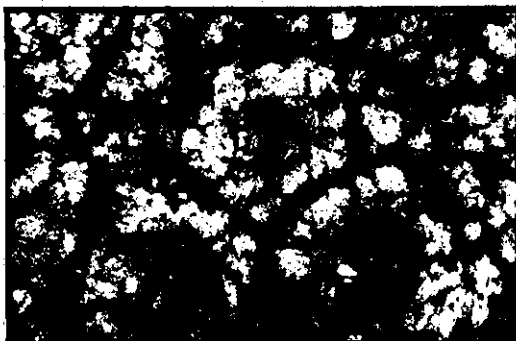
d) Top: x2,000
bottom: x10,000
0° tilt



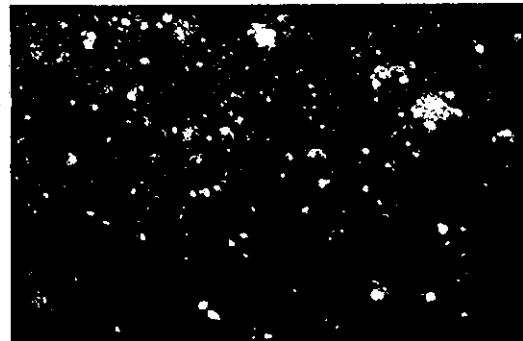
b) x2,000, 20° tilt



e) Top: x2,000
bottom: x10,000
0° tilt



c) Top: x2,000
bottom: x10,000
30° tilt



f) x2,000, 0° tilt

Fig. 4.96 SEM micrographs of surfaces of foils of nickel deposited at $Re\ 3,330 \pm 30$, ($70^\circ C$, $L/de \sim 11.7$)

- a) $1.12\ A\ cm^{-2}$, near leading edge
- b) $1.12\ A\ cm^{-2}$, central area
- c) $1.12\ A\ cm^{-2}$, near trailing edge
- d) $1.30\ A\ cm^{-2}$, near leading edge
- e) $1.30\ A\ cm^{-2}$, central area
- f) $1.30\ A\ cm^{-2}$, near trailing edge

At 1.3 A cm^{-2} , the structure appeared to be coarser, with features of $5\text{-}10\mu\text{m}$ in diameter (Fig.4.96d). Some larger features ($10\text{-}20\mu\text{m}$ diameter) were apparent, and these had a distinct sub-structure. This morphology type corresponded to the bright bands observed close to both leading and trailing edges.

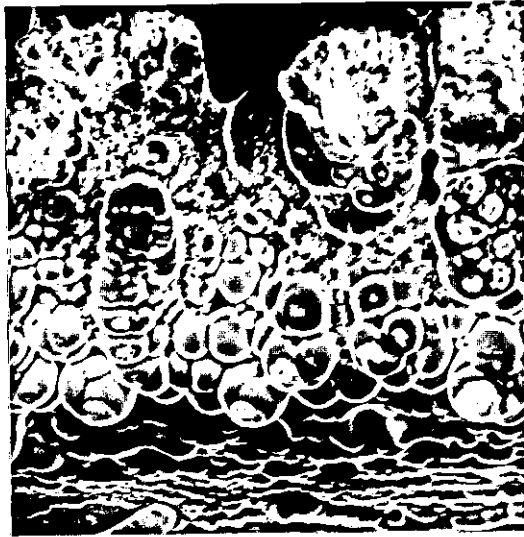
The central sections of both foils were of similar appearance with grain sizes of $2\text{-}5\mu\text{m}$ and well defined grain boundaries (cf Fig. 4.96b and e). The proportion of smaller grains was greater at 1.3 A cm^{-2} .

Towards the trailing edge of the electroform deposited at 1.12 A cm^{-2} , the structure became more nodular and coarse (Fig.4.96c). Conversely, at 1.3 A cm^{-2} , the size of the observed features increased in this area to $5\text{-}10\mu\text{m}$, but the deposit had a smooth appearance.

Edge effects

At 1.12 A cm^{-2} , a narrow band ($1\text{-}2 \text{ mm}$) of a dark grey powdery type material was deposited at the leading edge of the foil. Detailed SEM examination of this area (Fig.4.97a) showed a coarse nodular structure with many unusual 'cauliflower' features. At 1.3 A cm^{-2} , the leading edge of the foil appeared to be rough but without the band of powdery material. SEM examination (Fig.4.97b) confirmed the presence of the 'cauliflower' features similar to the previous observations. However, the nodular structure was absent. The trailing edges of both foils were of similar relatively featureless visual appearance. Detailed examination identified a coarse surface structure in this area of the foils (cf Fig.4.98a and b). Some larger more bulbous features were present at the higher current density.

It would appear that, at 70°C , high current density areas near the leading and trailing edges have a coarse nodular structure and other centres of roughness. However, good main deposit structures may be obtained even at very high current densities. At $\text{Re } 3,300 \pm 50$, the maximum deposition rate was about 1.12 A cm^{-2} .



a) x100, 0° tilt



b) x200, 0° tilt

Fig.4.97 SEM micrographs of surfaces of foils of nickel deposited at $Re\ 3,300 \pm 30$, leading edge sections ($70^\circ C$, $L/de \sim 11.7$).

a) $1.12\ A\ cm^{-2}$

b) $1.30\ A\ cm^{-2}$



a) x200, 0° tilt



b) x200, 0° tilt

Fig.4.98 SEM micrographs of surfaces of foils of nickel deposited at $Re\ 3,300 \pm 30$, trailing edge sections ($70^{\circ}C$, $L/de \sim 11.7$).

- a) $1.12\ A\ cm^{-2}$
- b) $1.30\ A\ cm^{-2}$

Nickel electroforms deposited in the flow range $Re\ 4,800 \pm 100$

A series of nickel foils 25-29 μm thick was electroformed over the current density range 0.86 to 1.12 A cm^{-2} and details are given in Table 4.31. At all current densities the current efficiency was about 95%. The main deposit areas of all foils were lustrous and of good visual appearance as illustrated schematically in Fig.4.99. At the lower current densities, (0.86 - 0.91 A cm^{-2}), the electroforms exhibited many small perforations (Fig.4.99a and b), and a heavily pitted narrow band of brighter deposit at the leading edge. However, foil porosity tended to decrease on increasing the deposition rate.

A gradual coarsening of the deposit at the inlet and outlet edges of the electroform was observed at higher current densities. At 1.12 A cm^{-2} the leading edge section appeared to be powdery.

Detailed examinations of the structures of foil surfaces were carried out in the SEM after removal of the deposit from the substrate.

Main deposit area

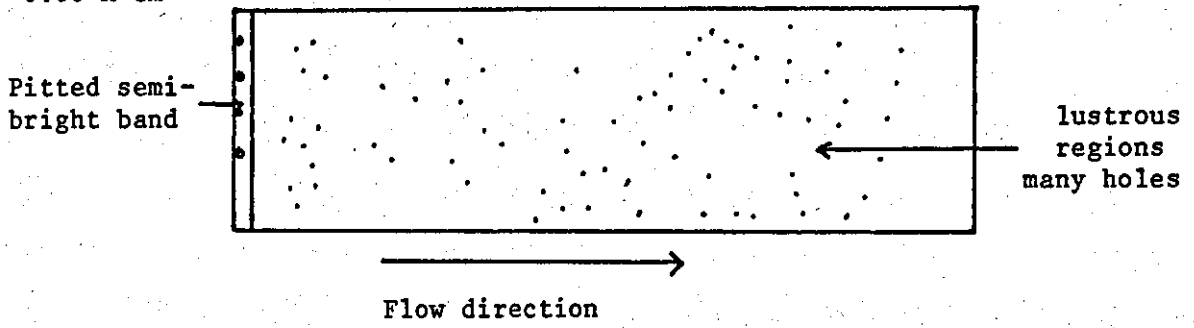
The main deposit sections of all foils exhibited the fine grained structures typical of good deposits (Fig.4.100). At current densities $\sim 1.01\ \text{A cm}^{-2}$, the irregular grains were 2-5 μm in diameter with deep grain boundaries. Some sub-structure was discernible (cf Fig.4.100a and b).

At the high current density (1.12 A cm^{-2}), and over most of the surface, the foil morphology appeared smoother with less sub-grain structure (cf Fig.4.100b and c). Some grain refinement (1-3 μm) was evident. However, towards the trailing edge of the deposit, the foil surface appeared rougher, with surface reliefs similar to powder type features (Fig.4.100a).

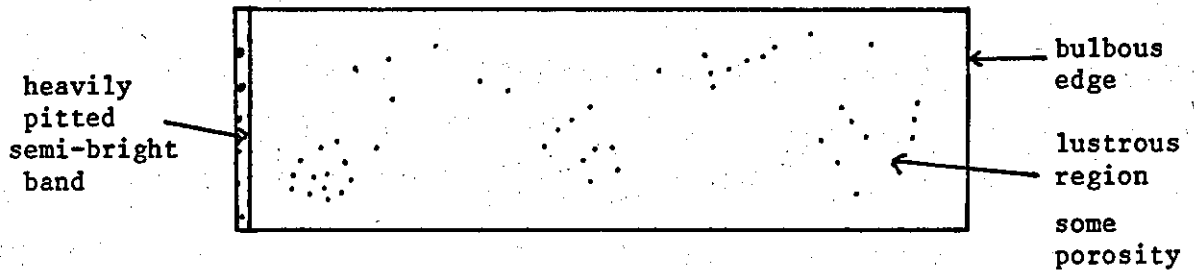
Flow Rate U cm s ⁻¹ .	Reynolds Number Re	Average Current Density i A cm ⁻²	Time t s	Average Deposit Thick- ness d μm	Weight Deposited g	Current Efficiency %
57.7	4,778	0.86	88	26	0.6612	96
57.7	4,778	0.90	81	25	0.6395	96
57.7	4,778	0.91	81	25	0.6408	95
57.7	4,778	1.01	83	29	0.7286	95
56.8	4,703	1.11	68	25	0.6643	96
58.7	4,861	1.12	68	26	0.6526	94

Table 4.31 Nickel foils deposited at Re 4,800 ± 100
(70°C, L/d_e ~ 11.7)

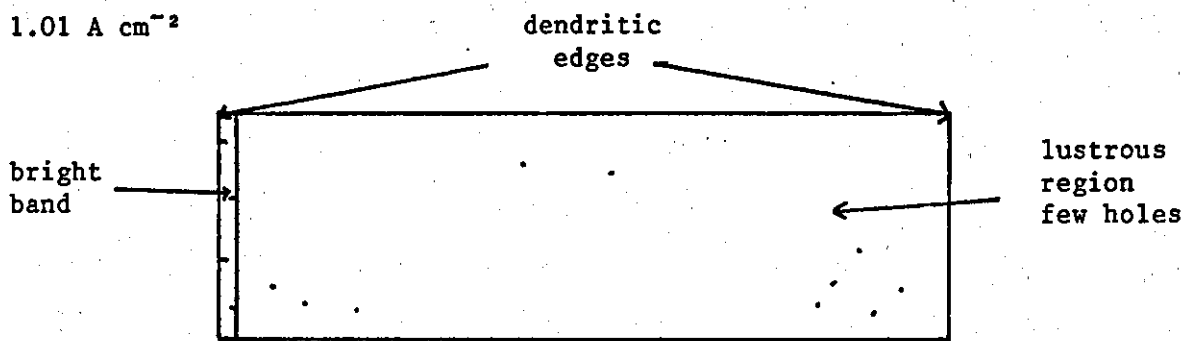
a) 0.86 A cm^{-2}



b) $0.90/0.91 \text{ A cm}^{-2}$



c) 1.01 A cm^{-2}



d) $1.11/1.12 \text{ A cm}^{-2}$

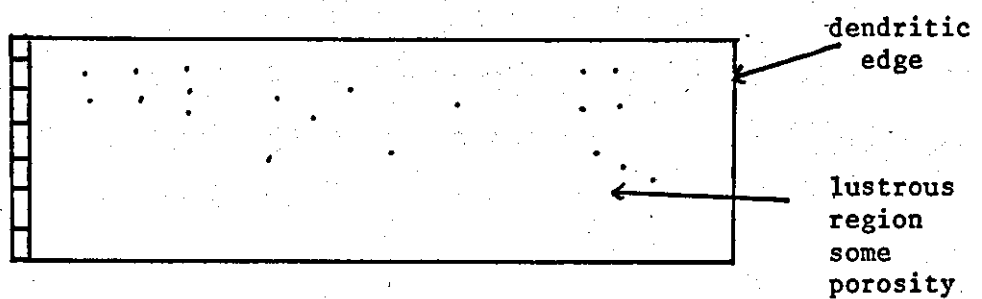
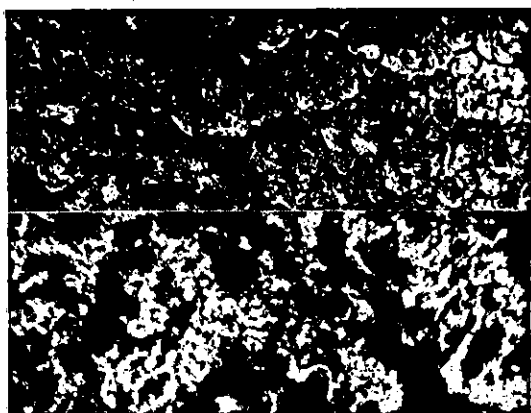
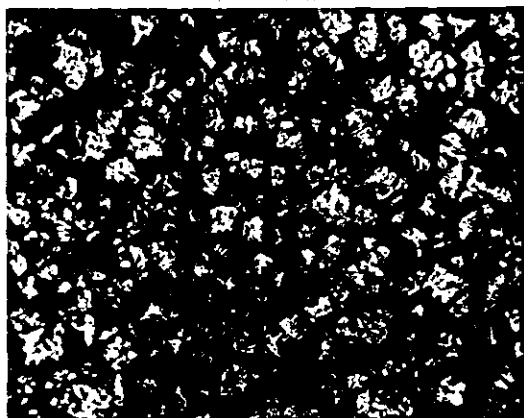


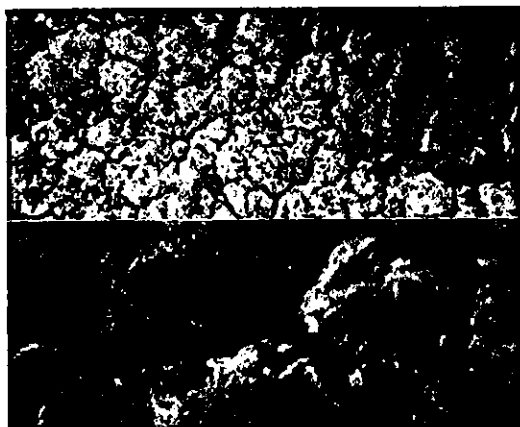
Fig.4.99 Schematic representation of the visual appearance of nickel foils deposited at $\text{Re } 4,800 \pm 100$. (70°C , $L/d_e \sim 11.7$).



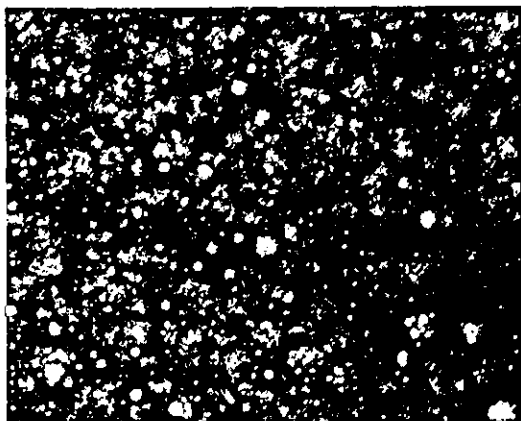
a) Top: x2,000
bottom: x10,000
0° tilt



b) x2,000, 0° tilt



c) Top: x2,000
bottom: x10,000
0° tilt



d) x2,000, 0° tilt

Fig.4.100 SEM micrographs of the surfaces of foils of nickel deposited at the $4,800 \pm 100$ (70°C , $L/de \sim 11.7$) main deposit sections.

- a) 0.91 A cm^{-2}
- b) 1.01 A cm^{-2}
- c) 1.12 A cm^{-2}
- d) 1.12 A cm^{-2} , rough area near the trailing edge

Edge effects

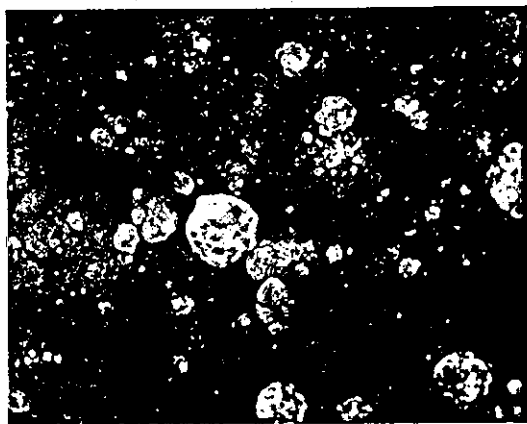
The leading edge growth features were more dendritic in character than previously observed particularly at higher current densities. At 0.91 A cm^{-2} , downstream of the bulbous ridge, the foil surface was heavily pitted (Fig.4.101a) coinciding with the bright band observed visually (cf Fig.4.99b). In this region, the deposit structure was comparatively rough (Fig.4.101b). The leading edge of deposits prepared at $1.01 - 1.12 \text{ A cm}^{-2}$ were of similar nodular appearance (cf Fig.4.101c and e). At the highest current density, the powdery type deposit was more extensive. Immediately downstream of the edge, the structure was very fine grained, although some larger features up to $20 \mu\text{m}$ in diameter were evident (Fig.4.101d and f).

Trailing edge sections were less dendritic, with some nodular type growth (Fig.4.102a). Adjacent pitted areas were associated with bright band formations (Fig.4.102c). In this region the very fine grain structure was superimposed on some larger features (Fig.4.102b and d). At the highest current density (1.12 A cm^{-2}), the edge was of the bulbous ridge structure (Fig.4.102e). An interesting coarsening of the deposit was apparent near the trailing edge (Fig.4.102f). The rough, slightly nodular morphology may be the precursor to the formation of a powder type structure.

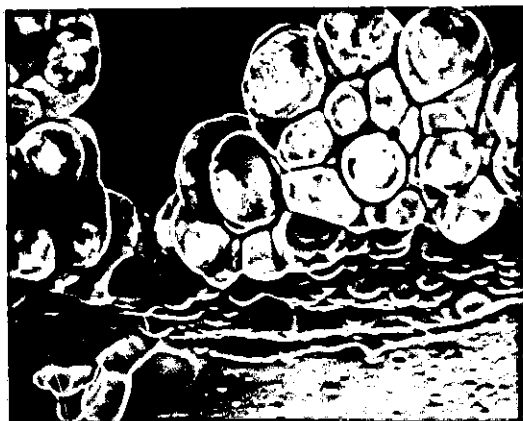
At $\text{Re } 4,800 \pm 100$ the maximum current density for satisfactory foil formation was about 1.12 A cm^{-2} .



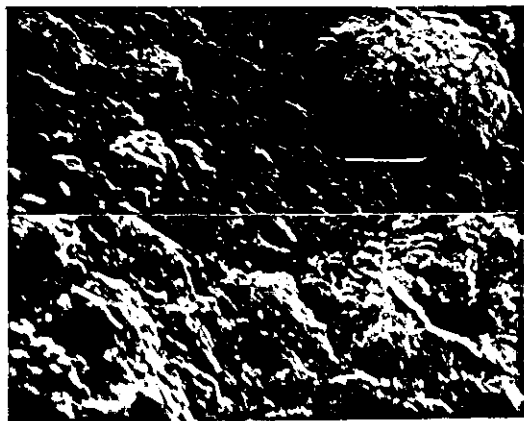
a) x100, 0° tilt



b) x2,000, 0° tilt



c) x100, 0° tilt



d) Top: x2,000
bottom: x10,000



e) x200, 0° tilt



f) x2,000, 0° tilt

Fig.4.101 SEM micrographs of surfaces of foils of nickel deposited at $Re\ 4,800 \pm 100$ ($70^\circ C$, $L/de \sim 11.7$) leading edge sections.

a) $0.91\ A\ cm^{-2}$

b) $0.91\ A\ cm^{-2}$, $\sim 0.05\ cm$ from leading edge

c) $1.01\ A\ cm^{-2}$

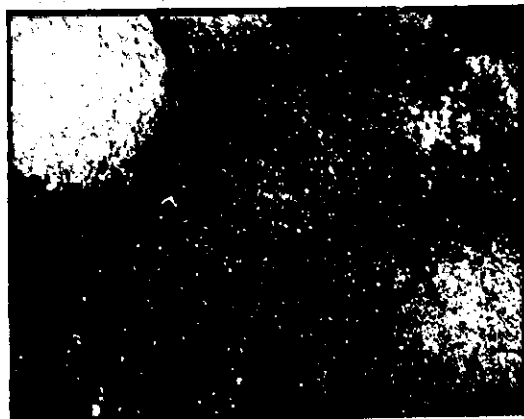
d) $1.01\ A\ cm^{-2}$, $\sim 0.05\ cm$ from leading edge

e) $1.12\ A\ cm^{-2}$

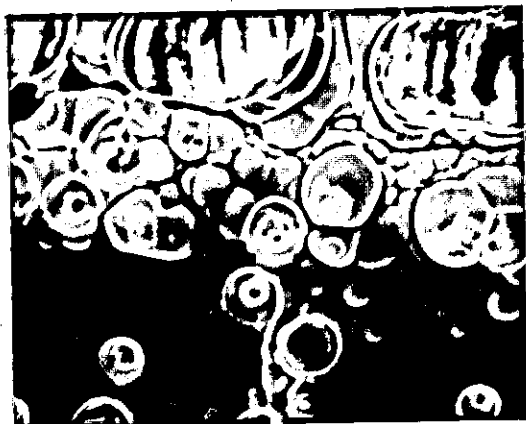
f) $1.12\ A\ cm^{-2}$, $\sim 0.1\ cm$ from leading edge



a) x200, 0° tilt



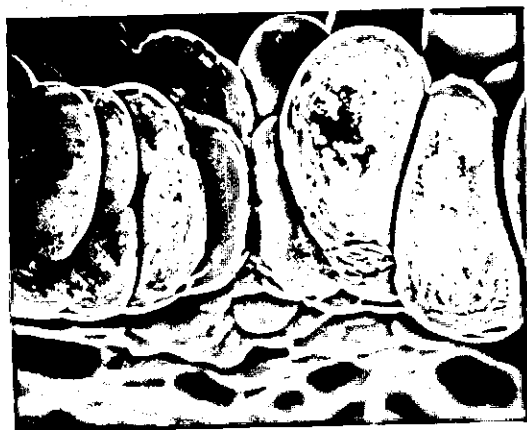
b) x2,000, 0° tilt



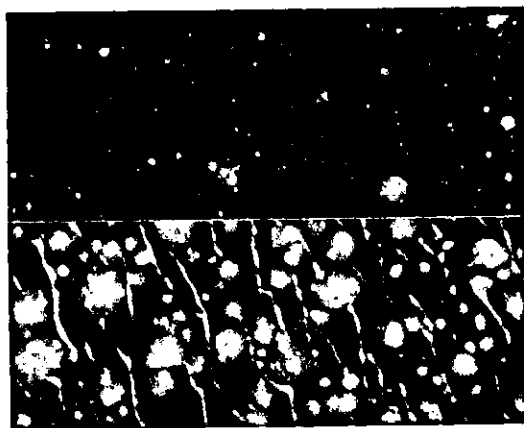
c) x100, 0° tilt



d) x2,000, 0° tilt



e) x200, 0° tilt



f) Top: x2,000
bottom: x10,000
0° tilt

Fig.4.102 SEM micrographs of surfaces of foils of nickel deposited at $Re\ 4,800 \pm 100$ ($70^\circ C$, $L/de \sim 11.7$), trailing edge sections.

- a) $0.91\ A\ cm^{-2}$
- b) $0.91\ A\ cm^{-2}$, 0.05 cm from trailing edge
- c) $1.01\ A\ cm^{-2}$
- d) $1.01\ A\ cm^{-2}$, 0.05 cm from trailing edge
- e) $1.12\ A\ cm^{-2}$
- f) $1.12\ A\ cm^{-2}$ 0.05 cm from trailing edge

Nickel foils deposited in the flow range Re 7,450 ± 300

A series of nickel foils 24-27 μ m thick was deposited over the current density range 0.8 to 1.4 A cm⁻². The details of the deposition conditions are given in Table 4.32 and schematic representations of the visual appearance of the electroforms are shown in Fig.4.103. At current densities <1.15 A cm⁻², the current efficiency was high (96-97%) and sound lustrous deposits were obtained greater than 95% of the foil surface. Main deposit porosity was generally low, although increasing at higher current densities (>1.15 A cm⁻²).

At the foil entry and exit edges, narrow pitted bands of brighter deposit were visible at 0.80 and 0.91 A cm⁻². At 1.15 A cm⁻², the leading edge appeared to be powdery. The deposit produced at 1.4 A cm⁻² was semi-bright in appearance. Green hydroxide was present at the leading edge (Fig.4.103c). The electroforms were examined in detail in the SEM.

Main deposit

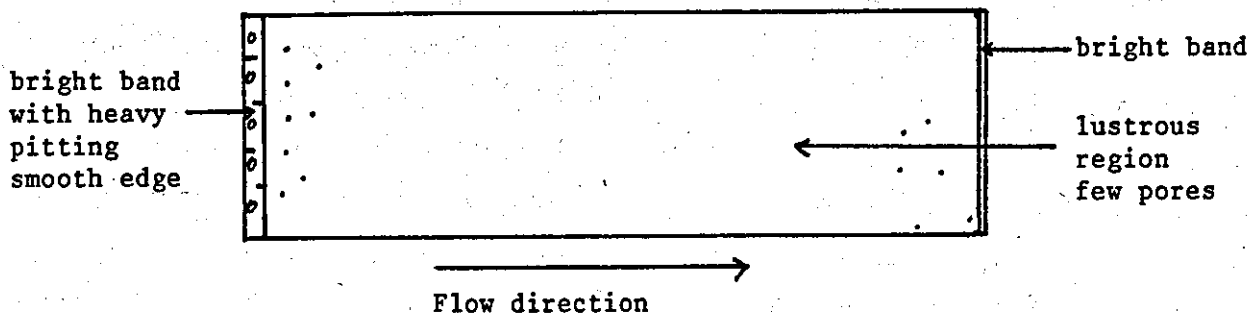
Typical surface structure for the main deposit region at current densities of 0.8, 0.91 and 1.15 A cm⁻², are shown in Fig.4.104. All deposits were fine grained with well defined grain boundaries. At 0.8 A cm⁻², the irregular grains were 1-6 μ m in diameter (Fig.4.104a). Ion beam etched cross-sections of the foil indicated that the foil had a columnar structure (Fig.4.105), typical of high speed deposits.

At higher current densities, grain sizes tended to be more uniform, with some grain refinement (Fig.4.104b and c). The average microhardness of the main deposit area was 265 ± 4 kg mm⁻² at 0.8 A cm⁻², 277 ± 6 kg mm⁻² at 0.91 A cm⁻² and 290 ± 9 kg mm⁻² at 1.15 A cm⁻². The slight increase in microhardness value may be associated with increased grain refinement. The electroforms tended to be of a lower microhardness value than those deposited at 60°C (c.f. p.195).

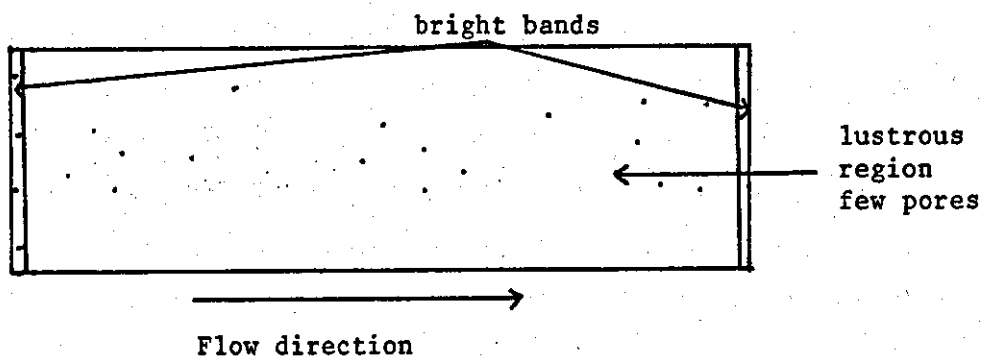
Flow Rate U cm s ⁻¹ .	Reynolds Number Re	Average Current Density i A cm ⁻²	Time t s	Average Deposit Thick- ness d μm	Weight Deposited g	Current Efficiency %
93.6	7,750	0.80	94	26	0.6760	96
86.8	7,187	0.91	81	25	0.6510	97
90.1	7,451	1.15	68	27	0.6870	96
86.8	7,187	1.40	50	24	-	-

Table 4.32 Nickel foils deposited at Re 7,450 ± 300
(70°C, L/d_e ~11.7)

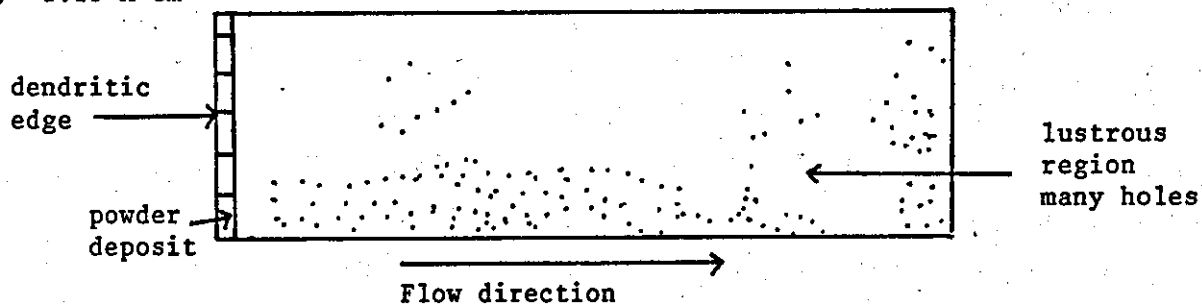
a) 0.80 A cm^{-2}



b) 0.91 A cm^{-2}



c) 1.15 A cm^{-2}



d) 1.40 A cm^{-2}

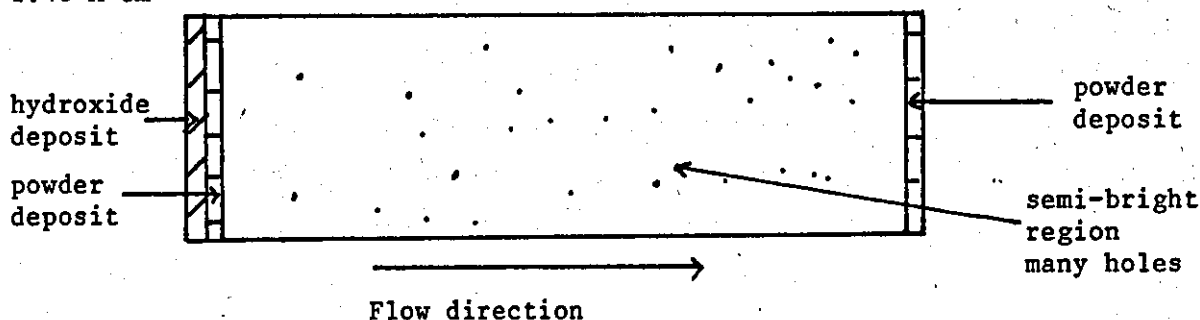
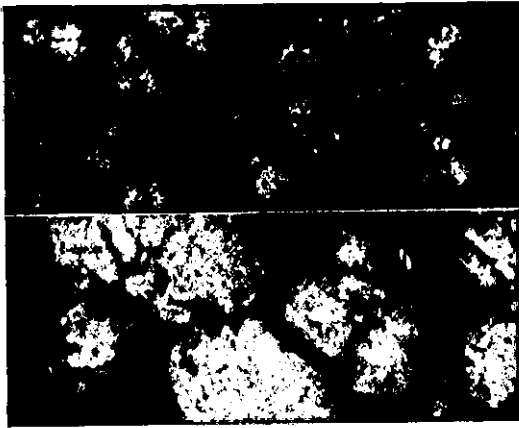
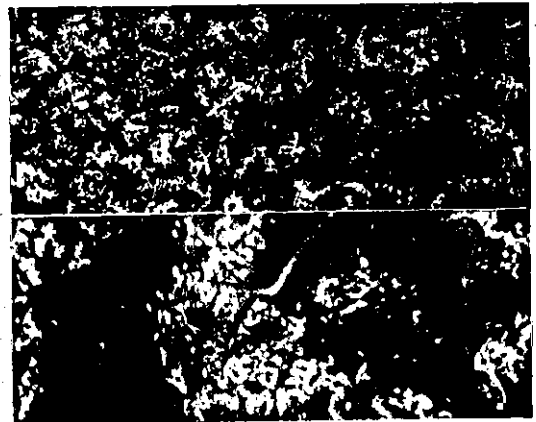


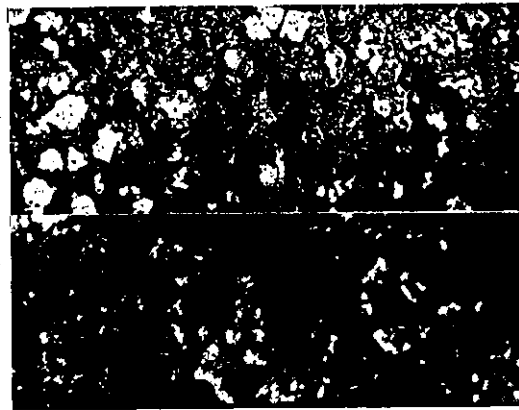
Fig.4.103 Schematic representation of the visual appearance of nickel foils deposited at $\text{Re } 7,450 \pm 300$ (70°C , $L/d_e \sim 11.7$).



a) Top: x2,000;
bottom: x10,000
0° tilt



b) Top: x2,000;
bottom: x10,000
0° tilt



c) Top: x2,000;
bottom: x10,000
0° tilt

Fig.4.104

SEM micrographs of surfaces of foils of nickel deposited at $Re\ 7,450 \pm 300$, ($70^{\circ}C$, $L/d_e \sim 11.7$), main deposit sections.

- a) $0.80\ A\ cm^{-2}$
- b) $0.91\ A\ cm^{-2}$
- c) $1.15\ A\ cm^{-2}$

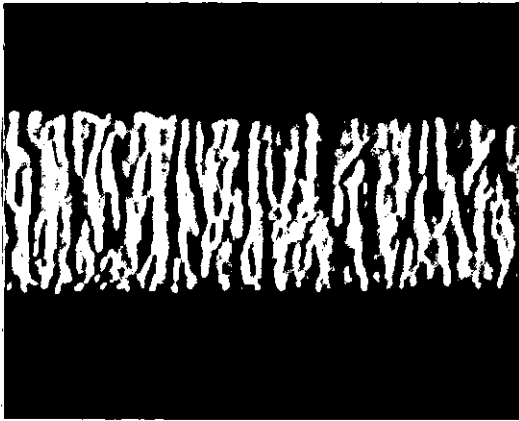


Fig.4.105 Optical micrograph of etched cross section of nickel foil deposited at 0.8 A cm^{-2} ,
Re $7,450 \pm 300$
(70°C , $L/d_e \sim 11.7$) (x 1,000)

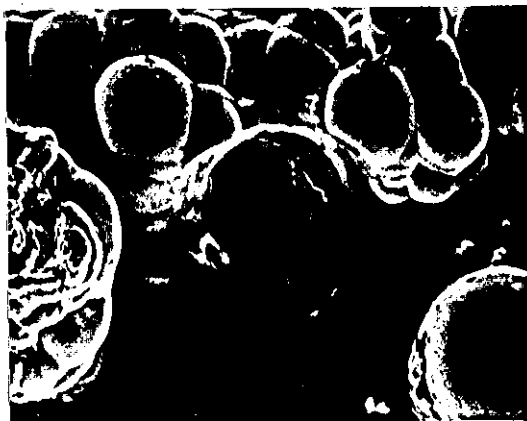
Edge effects

The appearance of the leading edge section was similar at 0.8 and 0.91 A cm⁻². Both edge sections were bulbous and without the more dendritic features observed previously (cf Fig.4.106a and b with Fig. 4.101c). Adjacent to the leading edge the deposit was heavily pitted. However, the morphology was very fine grained although with many larger features up to 20 μm in diameter (Fig.4.106c).

At 1.15 A cm⁻², a nodular powder formation was deposited at the leading edge (Fig.4.106d). Several 'cauliflower' type features were evident. 0.1 mm from the leading edge, the morphology was again very fine grained (1-3 μm), with many larger surface reliefs (Fig.4.106e).

The trailing edge sections of all three foils were of very similar appearance (Fig.4.107a,b and d). The bulbous ridge tended to increase in width at higher current densities. A fine grained deposit, with some larger features, was found near the trailing edge (Fig.4.107 c and e).

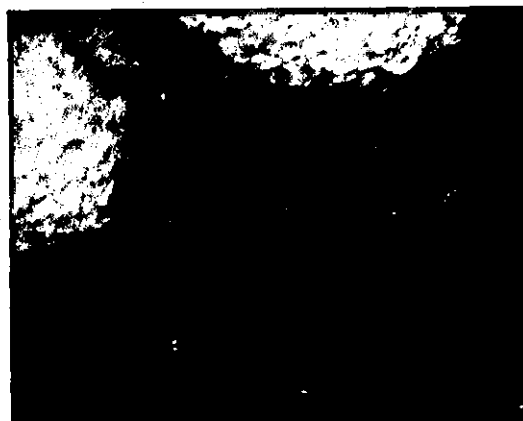
The maximum current density for formation of satisfactory foils at Re 7,450 ± 300 was about 1.15 A cm⁻².



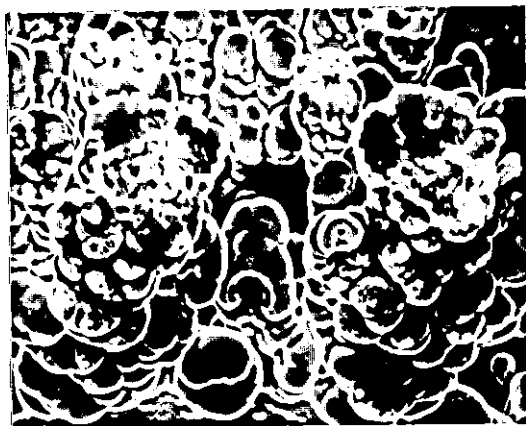
a) x200, 0° tilt



b) x200, 0° tilt



c) x2,000, 0° tilt



d) x100, 0° tilt



e) x2,000, 0° tilt

Fig. 4.106

SEM micrographs of surfaces of foils of nickel deposited at $Re\ 7,450 \pm 300$ ($70^\circ C, L/de \sim 11.7$), leading edge sections.

a) $0.80\ A\ cm^{-2}$

b) $0.91\ A\ cm^{-2}$

c) $0.91\ A\ cm^{-2}$, $\sim 0.025\ cm$ from leading edge

d) $1.15\ A\ cm^{-2}$

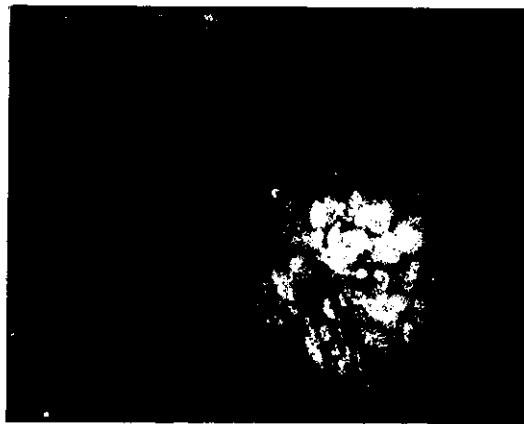
e) $1.15\ A\ cm^{-2}$, $\sim 0.07\ cm$ from leading edge



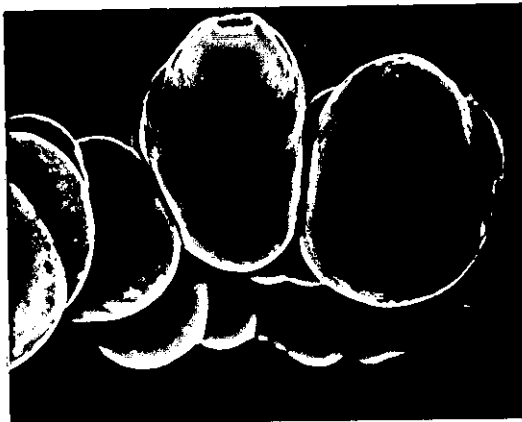
a) x200, 0° tilt



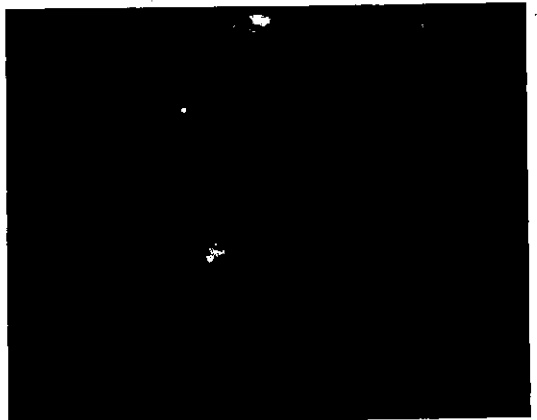
b) x200, 0° tilt



c) x2,000, 0° tilt



d) x200, 0° tilt



e) x2,000, 0° tilt

Fig.4.107 SEM micrographs of surfaces of foils of nickel deposited at $Re\ 7,450 \pm 300$ ($70^\circ C$, $L/de \sim 11.7$), trailing edge sections.

- a) $0.80\ A\ cm^{-2}$
- b) $0.91\ A\ cm^{-2}$
- c) $0.91\ A\ cm^{-2}$, $\sim 0.02\ cm$ from trailing edge
- d) $1.15\ A\ cm^{-2}$
- e) $1.15\ A\ cm^{-2}$, $\sim 0.025\ cm$ from trailing edge

Nickel foils deposited at Re 13,803

At the highest flow rate two foils were deposited at current densities above and below the minimum current density. The schematic representation of the two electroforms deposited at 1.18 and 1.51 A cm⁻² are shown in Fig.4.108.

Main deposit

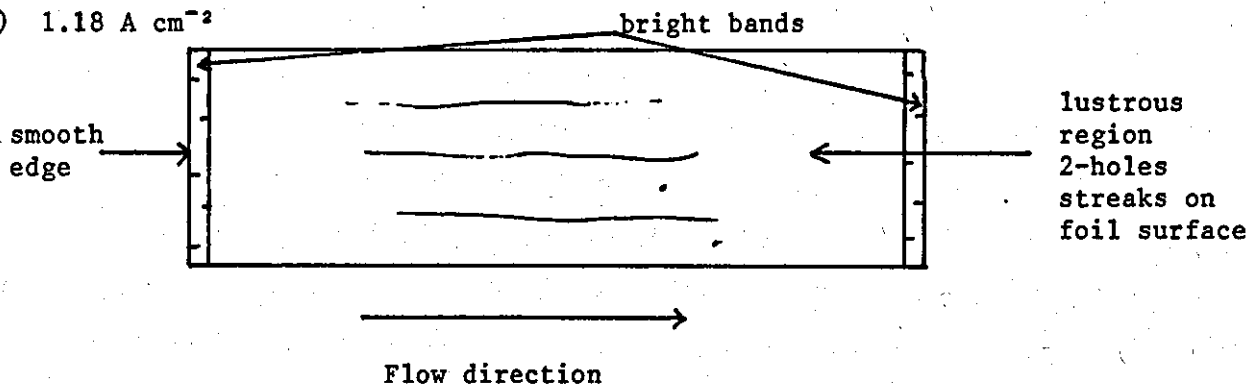
At 1.18 A cm⁻², the deposit was lustrous and sound over the entire electrode length, with semi-bright bands at leading and trailing edges. The current efficiency was 99%. Two or three small holes in the foil were visible. A streaking effect, parallel with the flow direction was evident in the main deposit area (Fig.4.108a). This phenomenon may be the result of gas bubbles moving along the electrode surface. When examined in the SEM, a well defined grain structure was evident (Fig.4.109a and b). The grain size was between 2 and 5 μm. A few grains had a 'truncated' appearance and may be associated with the gas 'streaking' effect.

At 1.51 A cm⁻², green hydroxide deposit and powder type deposits were observed at the inlet and outlet edges of the foil (Fig.4.108b). The current efficiency remained high (95%). The main deposit area was ~95% of the total surface area and of semi-bright appearance. Many small holes through the foil were observed. Surface streaking was also visible. On more detailed examination in the SEM, the structure appeared more coarse (Fig.4.109c and d), than that found at the lower current density. Larger features (6 μm) were present in a matrix of smaller grains (1-3 μm).

Edge effects

At 1.18 A cm⁻² the leading edge was a ridge of interlocking bulbous forms (Fig.4.110a). Adjacent areas were rough but fine grained (Fig.4.110b). Streaking effects were observed. At 1.51 A cm⁻², the maximum current density was exceeded, and hydroxide was deposited at the leading edge. Further downstream a nodular powder deposit was formed (Fig.4.110c).

a) 1.18 A cm^{-2}



b) 1.51 A cm^{-2}

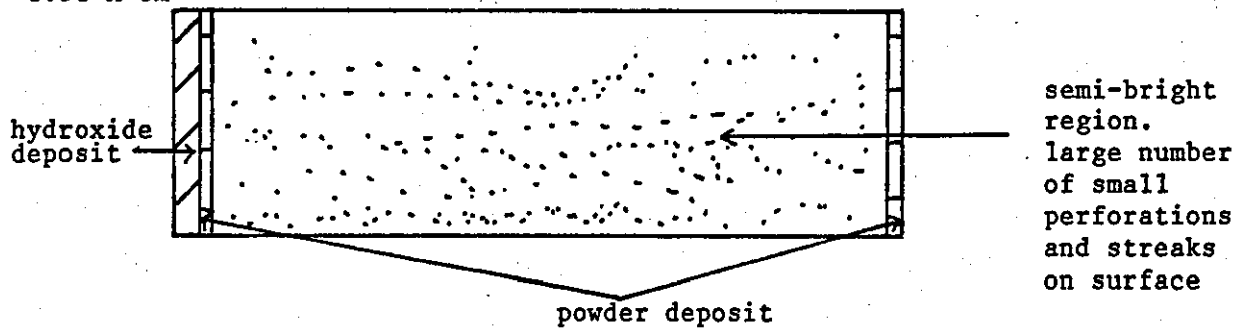
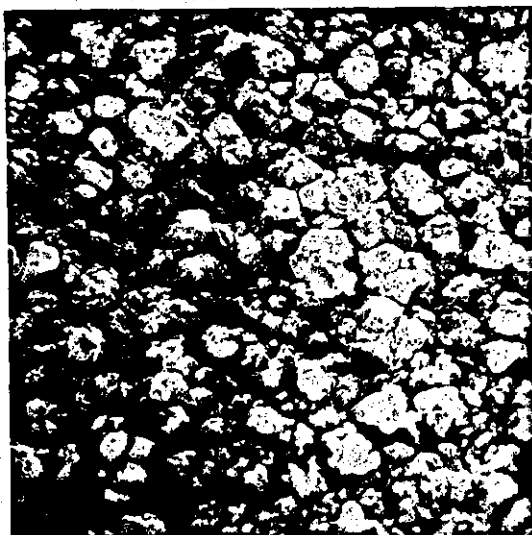


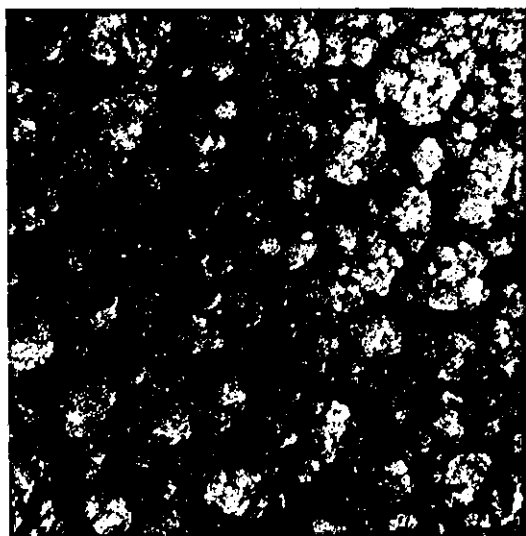
Fig.4.108 Schematic representation of the visual appearance of nickel foils deposited at $\text{Re } 1,803$ (70°C , $L/d_e \sim 11.7$).



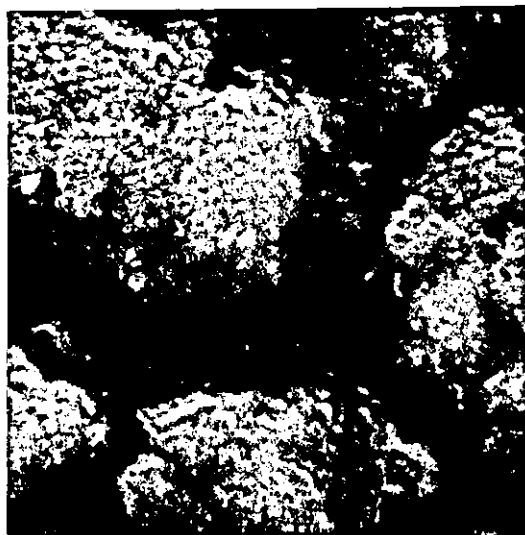
a) x2,000, 0° tilt



b) x10,000, 0° tilt



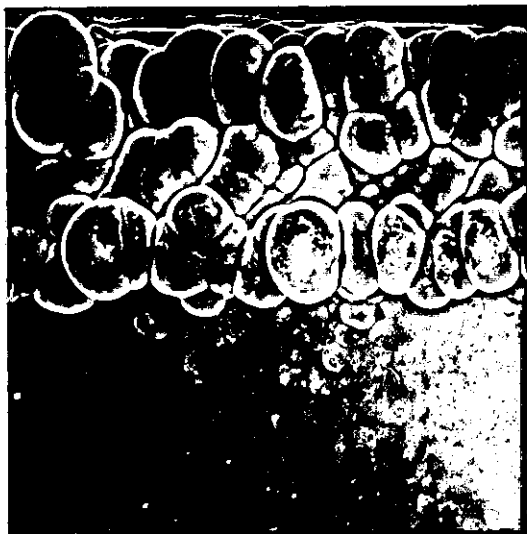
c) x2,000, 0° tilt



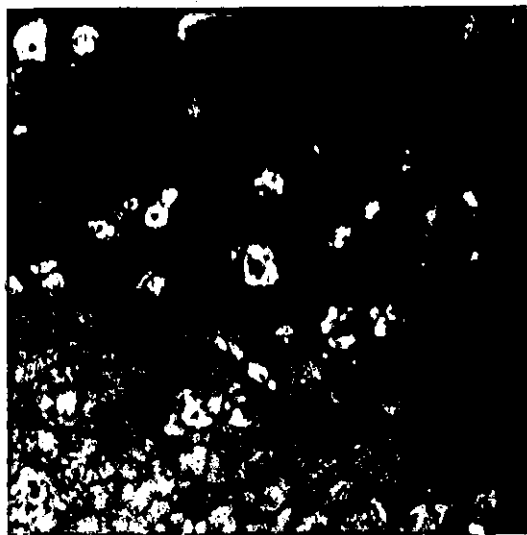
d) x10,000, 0° tilt

Fig.4.109 SEM micrographs of surfaces of foils of nickel deposited at Re 13,803 (70°C, $L/de \sim 11.7$), main deposit section.

- a) 1.18 A cm⁻²
- b) 1.18 A cm⁻²
- c) 1.51 A cm⁻²
- d) 1.51 A cm⁻²



a) x200, 0° tilt



b) x2,000, 0° tilt



c) x100, 0° tilt

Fig. 4.110 SEM micrographs of surfaces of foils of nickel deposited at Re 13,803 (70°C, $L/de \sim 11.7$), leading edge sections.

a) 1.18 A cm⁻²

b) 1.18 A cm⁻², ~0.02 cm from leading edge

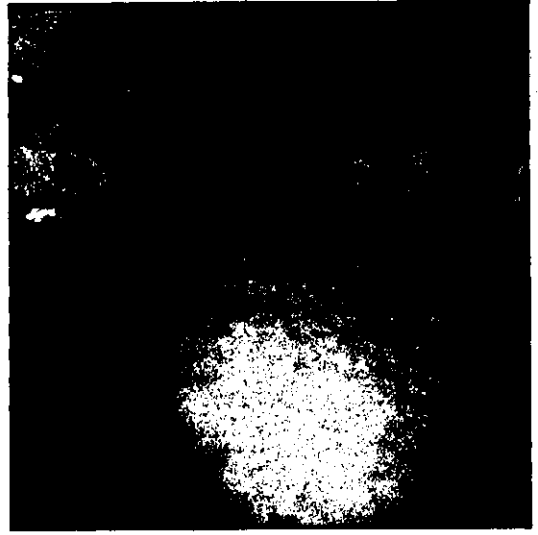
c) 1.51 A cm⁻²

At the trailing edge, the structure was more dendritic. At 1.18 A cm^{-2} , the bulbous formations were growing outwards (Fig.4.111a). Similarly, at 1.51 A cm^{-2} the powder nodules were more dendritic (Fig.4.111c). Immediately adjacent to the trailing edge the foil surface was very fine grained with some larger ($20\mu\text{m}$) surface reliefs.

The maximum current density for satisfactory deposits was estimated to be about 1.3 A cm^{-2} under these conditions.



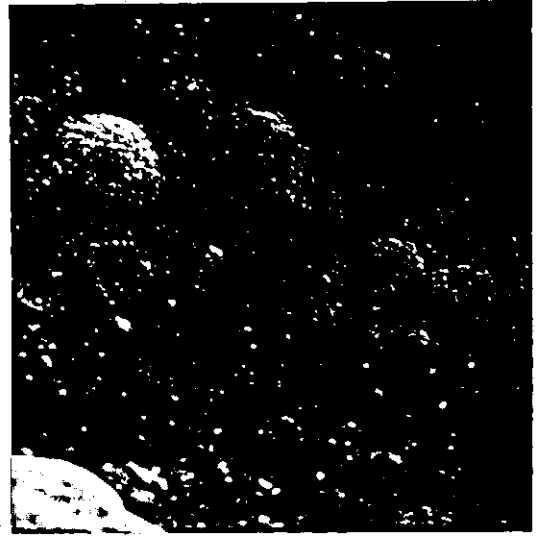
a) x200, 0° tilt



b) x2,000, 0° tilt



c) x100, 0° tilt



d) x1,000, 0° tilt

Fig. 4.111 SEM micrographs of surfaces of foils of nickel deposited at Re 13,803 (70°C, $L/d_e \sim 11.7$), trailing edge sections.

a) 1.18 A cm^{-2}

b) 1.18 A cm^{-2} , $\sim 0.03 \text{ cm}$ from trailing edge

c) 1.51 A cm^{-2}

d) 1.51 A cm^{-2} , $\sim 0.08 \text{ cm}$ from trailing edge

Summary of major features

Several significant results were obtained by operating the system at 70°C. These may be summarised as follows:

- a) A 10°C rise in electrolyte temperature resulted in considerable increases in deposition rate. Good deposits were produced at current densities in excess of 1 A cm⁻² under all flow conditions.
- b) The cathode current efficiency for nickel deposition was ~95% under all deposition conditions.
- c) Adhesion of gas bubbles to the cathode was less marked at 70°C. This enabled reasonable deposits, of very low porosity, to be produced even in laminar flow conditions.
- d) Under all flow conditions deposits were fine grained in the main central area of the deposit. Grain sizes were generally larger than found under equivalent conditions at 60°C.
- e) All foils were relatively lustrous. Bright deposits were only produced at very high current densities (>1.4 A cm⁻²) in turbulent flow.
- f) The microhardness of deposits increased with decreasing grain size. The deposits were less hard than foils electroformed at 60°C.
- g) Major changes in the foil structure were again found in the entry and exit regions.
- h) Large increases in the electrolyte velocity resulted in comparatively small increases in the maximum current density for satisfactory deposits. The relationship between deposition rate and Reynolds number was less clearly defined at 70°C.

At 70°C good (fine grained) deposits, of low porosity were obtained at very high current densities. However, the maximum

current density for a sound deposit, was not always well defined. In Fig.4.112 the nature of the deposit i.e. sound (uniform fine grained) or unsound (powdery and nodular) is plotted from the data obtained in the experimental study as described previously (p.171). The approximate theoretical mass transfer-limited current densities were calculated from the design equation for the cell (p.128) and the limiting current densities are shown as B-B (of slope 0.8) in Fig.4.112. As can be seen, the experimentally determined data indicates that the maximum current densities for sound deposits are less than the mass transfer limited current densities, although the two converge at lower turbulent flow rates.

In laminar flow, the theoretical line C-C in Fig.4.112 has a slope of 0.33 and the experimental points indicate that sound nickel deposits were obtained at higher current densities than might have been expected. These effects may be associated with the influence of gas evolution on the mass transfer processes. In addition, at 70°C and very high current densities, localised heating effects at the interface may increase the deposition range. This may help to obscure the maximum current density.

(b) The electroforming of nickel foils at 50° and 65°C using a long electrode system ($L/d_e = 11.7$) under constant flow conditions ($Re = 6575 \pm 75$)

Nickel electroforms 25 μ m thick were prepared at 50° and 65°C for comparison with the more comprehensive 60° and 70°C study. An intermediate Reynolds number ($Re \sim 6,600$) was used for all electrolyses.

50°C deposits

At 50°C three deposits were produced at current densities of 0.3, 0.4 and 0.8 A cm⁻² as shown in Table 4.33. The schematic representations of the deposit appearance is shown in Fig.4.113. At 0.3 and 0.4 A cm⁻², a sound and uniform semi-bright deposit was produced over >95% of the foil surface.

Main deposit

SEM examination of the stripped foils showed fine grain structures of both current densities (Fig.4.114a and b). Grain sizes were about 2-5 μ m. At 0.4 A cm⁻², the main deposit morphology was smoother with cavities at the grain boundaries. At the high current density (0.8 A cm⁻²) nickel metal was not deposited. The deposit was a thick film of black-brown and green hydroxide (Fig.4.113c). SEM examination of the deposit showed the black-brown areas to be relatively featureless (Fig.4.115a and b), whereas, the green areas were thick platelets (Fig.4.115c and d).

Edge effects

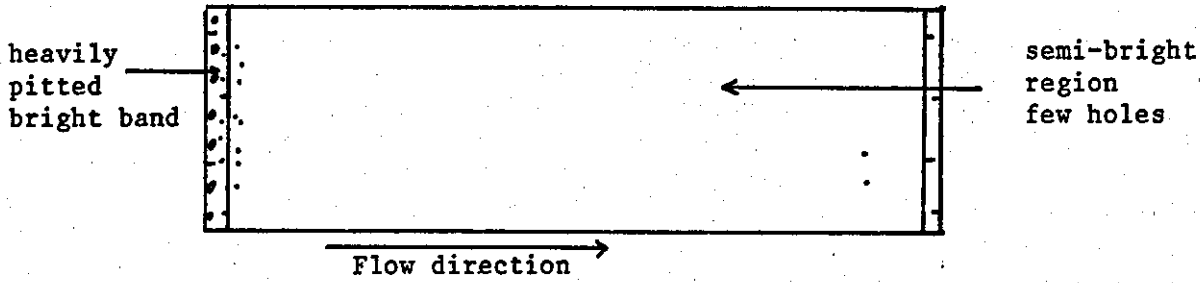
Near the trailing edge of the electroform deposited at 0.4 A cm⁻², the structure was very fine grained (1-2 μ m) with cavities of similar dimensions (Fig.4.114c). Visual examination revealed many small perforations in the foil. The outlet edges of both foils were smooth with narrow bands of brighter material (Fig.4.113a and b).

At 0.3 A cm⁻² the leading edge of the deposit was relatively featureless, although heavily pitted (Fig.4.116a). The narrow band of bright nickel observed in this area had an unresolvable grain structure

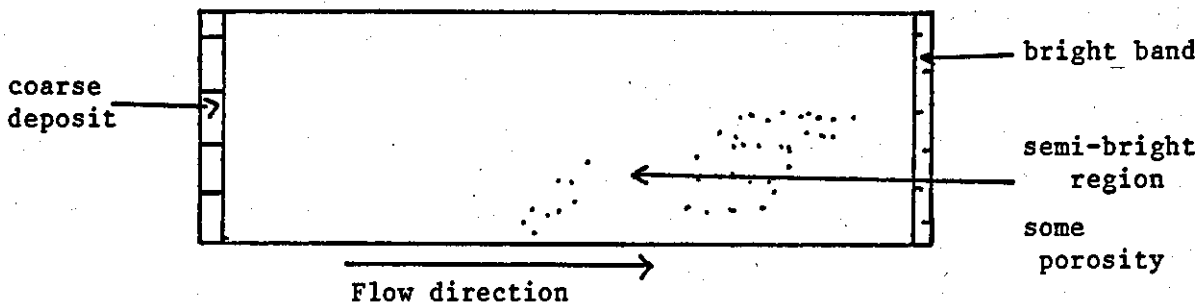
Flow Rate	Reynolds Number	Average Current Density	Time	Average Deposit Thickness	Weight Deposited	Current Efficiency
U cm s^{-1}	Re	i A cm^{-2}	t s	d μm	g	%
114.5	6,577	0.3	244	25	0.6613	99
114.5	6,577	0.4	183	25	0.6547	98
115.7	6,655	0.8	92	-	-	-

Table 4.33 Nickel foils deposited at 50°C and
 Re 6,575 \pm 75 ($L/d_e \sim 11.7$)

a) 0.3 A cm^{-2}



b) 0.4 A cm^{-2}



c) 0.8 A cm^{-2}

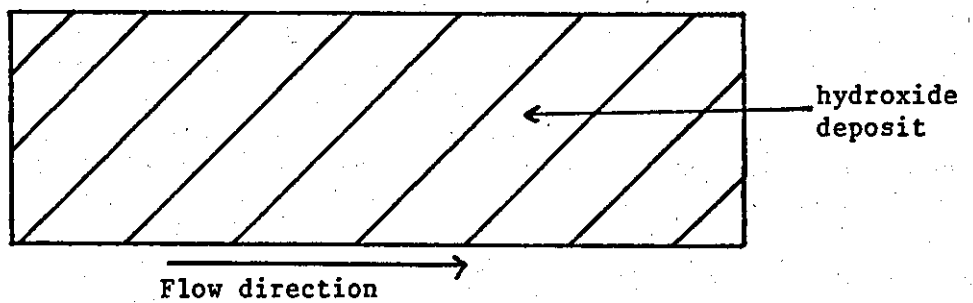
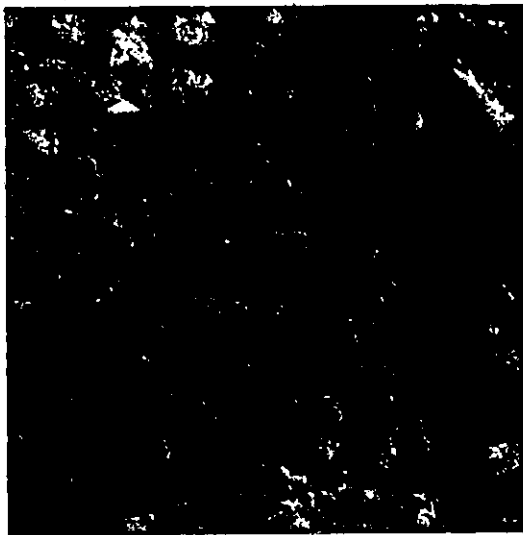
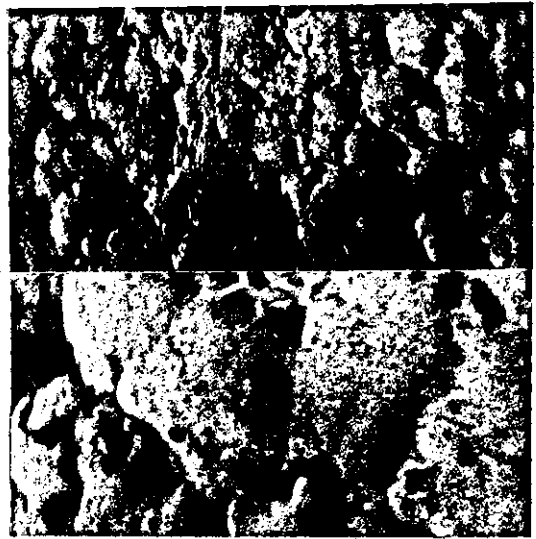


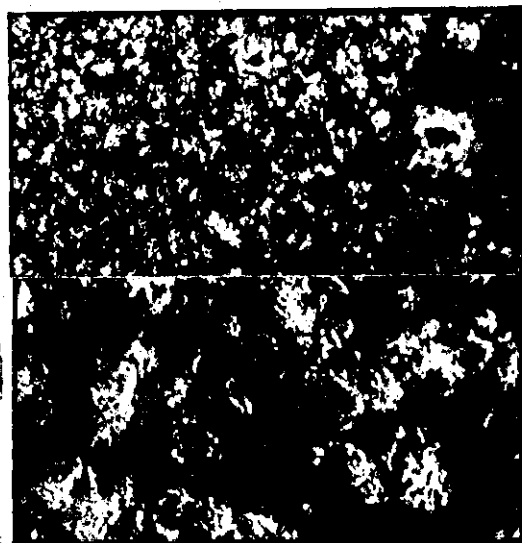
Fig.4.113 Schematic representation of the visual appearance of nickel foils deposited at 50°C and $\text{Re } 6,575 \pm 75$ ($L/d_e \sim 11.7$).



a) 35° tilt



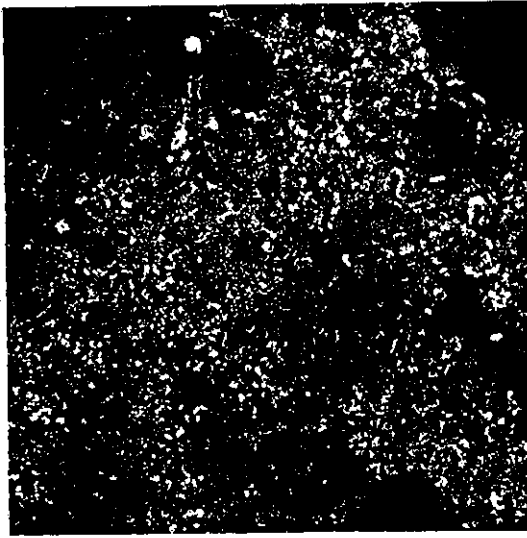
b) 30° tilt



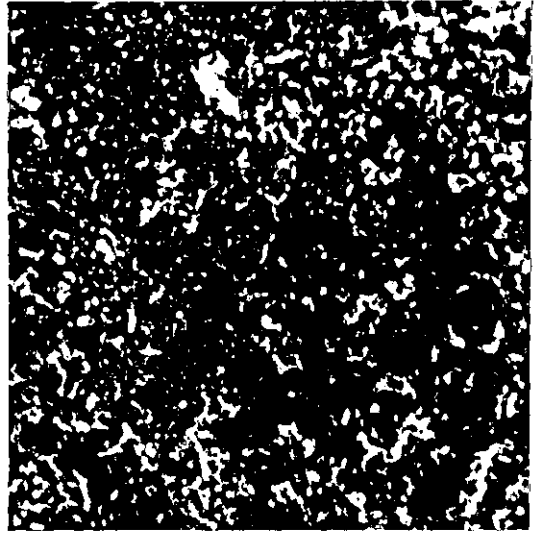
c) 0° tilt

Fig. 4.114 SEM micrographs of the surfaces of nickel foils deposited at 50°C and Re 6,575 ± 75. (70°C, $L/de \sim 11.7$).

- a) 0.3 A cm⁻², main deposit area, (2,000x)
- b) 0.4 A cm⁻², main deposit area, (top: 2,000x; bottom: 10,000x)
- c) 0.4 A cm⁻², main deposit area, near trailing edge (top: 2,000x; bottom: 10,000x).



a) 30° tilt



b) 30° tilt



c) 30° tilt



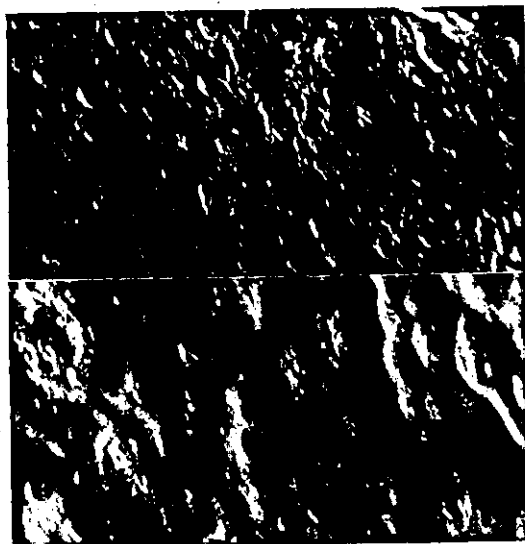
d) 30° tilt

Fig.4.115 SEM micrographs of hydroxide deposited at 50°C,
0.8 A cm⁻² and Re 6,575 ± 75 (L/de ~11.7)

- a) Brown-black area (2,000x)
- b) Brown-black area (10,000x)
- c) Green area (2,000x)
- d) Green area (10,000x)



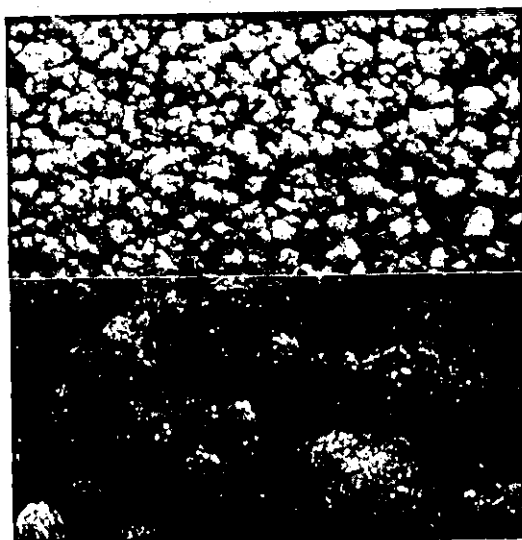
a) 35° tilt



b) 35° tilt



c) 30° tilt



d) 0° tilt

Fig.4.116 SEM micrographs of surfaces of nickel foils deposited at 50°C and $Re\ 6,575 \pm 75$ ($L/de \sim 11.7$)

a) $0.3\ A\ cm^{-2}$, leading edge section (100x)

b) $0.3\ A\ cm^{-2}$, $\sim 0.02\ cm$ from leading edge (top: 2,000x; bottom: 10,000x)

c) $0.4\ A\ cm^{-2}$, leading edge section (100x)

d) $0.4\ A\ cm^{-2}$, $\sim 0.05\ cm$ from leading edge (top: 2,000x; bottom: 10,000x)

(Fig. 4.116b). At 0.4 A cm^{-2} the leading edge appeared powdery. The deposit structure was very coarse with bulbous cylindrical growth (Fig.4.116b). Adjacent areas were fine grained ($1\text{-}2\mu\text{m}$ diameter (Fig.4.116d).

65°C deposit

At this temperature deposition was studied at 0.81 A cm^{-2} only. The deposit was sound over $\sim 95\%$ of the electrode surface. The current efficiency was high (95%). The foil characteristics are shown schematically in Fig.4.117. The main deposit area was very porous with many lines of holes parallel to the flow direction. The foil was examined in detail in the SEM.

Main deposit

The deposit structure was fine grained over most of the foil (Fig.4.118). Close to the leading edge there was some evidence of grain refinement, with a preponderance of smaller grains (cf Fig.4.118a and b with c). This area was visually brighter. The central region appeared to be slightly smoother (Fig.4.118c). A similar structure was observed near the trailing edge (Fig.4.118d and e).

Edge effects

At the leading edge, the deposit was powdery, heavily pitted with exfoliation of the foil (Fig.4.119a). The powder type deposit was large grained with some nodular growth (Fig.4.119b). The trailing edge was comparatively smooth with a few large features and extensive pitting (Fig.4.120).

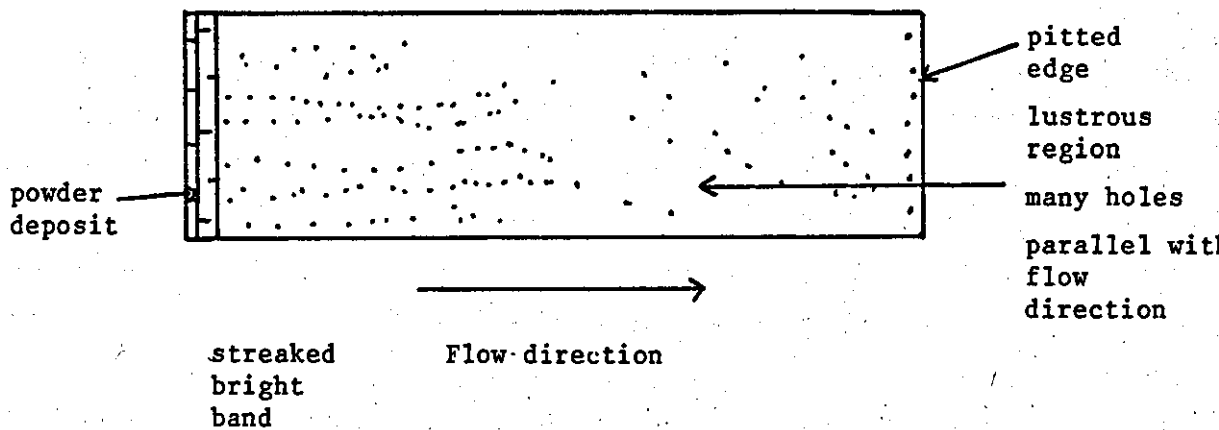
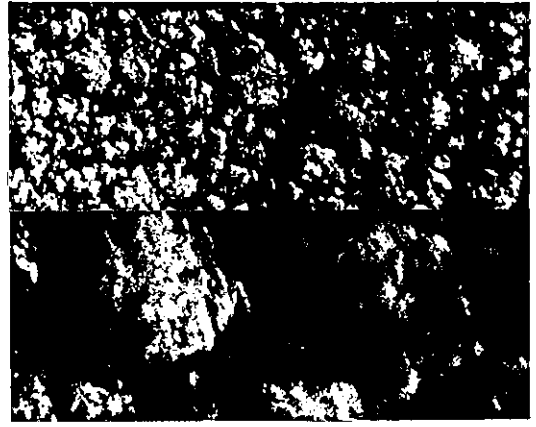


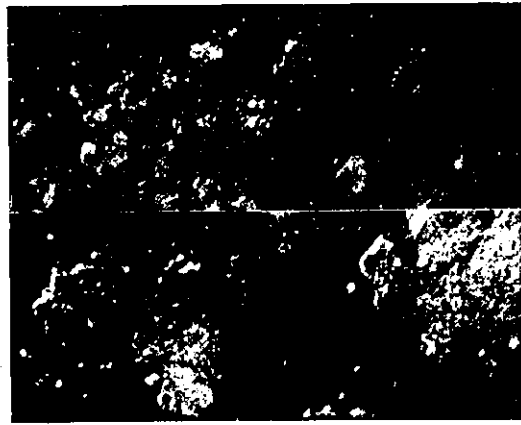
Fig. 4.117 Schematic representation of the visual appearance of nickel foil deposited at 65°C, 0.8 A cm⁻² and Re 6,575 ± 75 (L/de ~11.7).



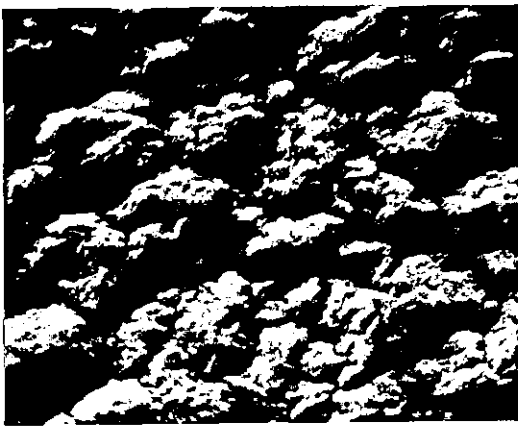
a) 0° tilt



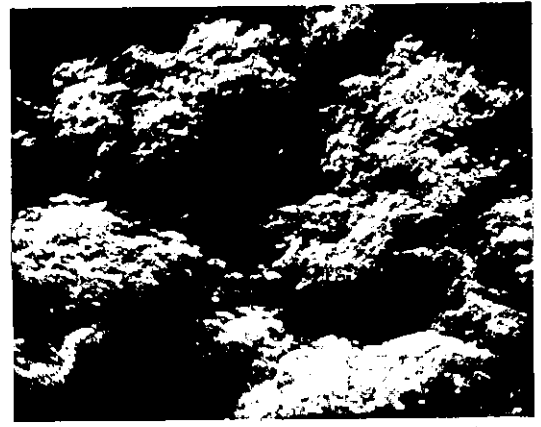
b) 0° tilt



c) 0° tilt



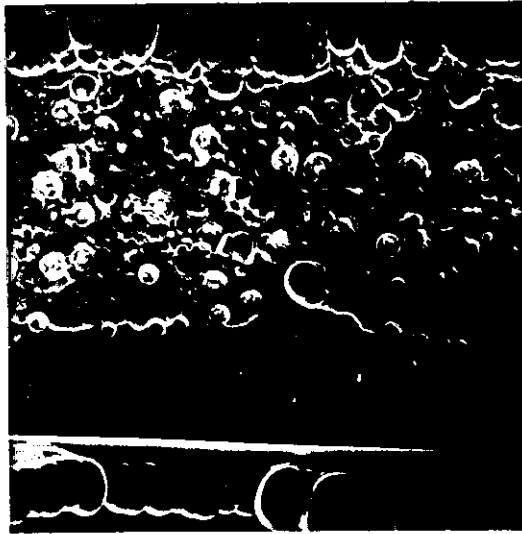
d) 0° tilt



e) 0° tilt

Fig. 4.118 SEM micrographs of surfaces of nickel foil deposited at 65°C, 0.8 A cm⁻² and Re 6,575 ± 75 (L/d_e ~ 11.7)

- a) 0.15 cm from leading edge (top: 2,000x; bottom: 10,000x)
- b) 0.5 cm from leading edge (top: 2,000x; bottom: 5,000x)
- c) Main deposit central area (top: 2,000x; bottom: 10,000x)
- d) 9.97 cm from the leading edge (2,000x)
- e) 9.97 cm from the leading edge (10,000x)



Flow direction

a) 0° tilt



b) 0° tilt

Fig.4.119 SEM micrographs of surfaces of nickel foil deposited at 65°C, 0.81A cm⁻² and Re 6,575 ± 75.

- a) leading edge section (50x)
- b) powder deposit (1,000x)

Flow direction



Fig. 4.120 SEM micrograph of the trailing edge surface of nickel foil deposited at 65°C , 0.81 A cm^{-2} and $\text{Re } 6,575 \pm 75$. ($\times 900$, 0° tilt) ($L/d_e \sim 11.7$)

Summary of major features

At 50°C good relatively uniform fine grained deposits were produced over >95% of the foil area. Grain size tended to decrease with increasing current density, particularly close to the leading edge. The maximum current density was $\sim 0.4 \text{ A cm}^{-2}$. Excessively high current densities resulted in hydroxide deposition.

At 65°C similar fine grained deposits were prepared at the maximum deposition rate of $\sim 0.8 \text{ A cm}^{-2}$.

(c) Summary of temperature effects

- i) Sound fine grained deposits could be produced at comparatively rapid deposition rates and high current efficiencies over the temperature range 50 - 70°C.
- ii) The maximum deposition rate increased with increasing temperature. At a Reynolds number of $Re\ 6,600 \pm 300$, the maximum current densities were as follows:

- i) 50°C - $\sim 0.4\ A\ cm^{-2}$
- ii) 60°C - $\sim 0.6\ A\ cm^{-2}$
- iii) 65°C - $\sim 0.8\ A\ cm^{-2}$
- iv) 70°C - $\sim 1.15\ A\ cm^{-2}$

At temperature $>60^\circ C$, the current density for sound deposits increased considerably.

- iii1) At a constant current density, the grain size of sound nickel deposits increased with increasing temperature (cf Fig.4.75d and 4.104b). An associated decrease in microhardness and deposit brightness with increasing temperature was also noted.
- iv) Deposits were less porous at higher temperatures.

4.4 Current distribution studies and polarisation measurements using the Mark 2 Parallel Plate Cell

Throughout the foil deposition studies in the previous sections there was evidence of non-uniform current distribution at the foil surfaces. Current distribution has been investigated using a segmented cathode and variable anode-cathode geometry. Details of the segmented electrode, current measuring instrumentation and calibration, experimental procedures and sample calculations have been given in Chapter 3. The main studies have been carried out with the long ($L/d_e = 11.7$) segmented electrode at 60° and 70°C, and some additional studies using a short electrode ($L/d_e = 2.92$) and variable anode geometry have been carried out for comparison purposes. The current distribution studies are presented in Section 4.4.1.

Although polarisation studies are difficult experimentally in flowing electrolyte systems and a non-ambient temperature it was believed that it would be useful to have some background information concerning both the anodic and cathodic reactions. Information concerning the anodic processes is important in relation to development of the process and anode design. There is also considerable doubt concerning the deposition reaction mechanism. It was hoped that measurements of cathodic polarisation curves would perhaps provide information which would explain the almost invariable cathode current efficiency at all current densities. The polarisation studies are presented in Section 4.4.2.

4.4.1 Current distribution effects in the electroforming of nickel foils

(a) Studies using long segmented cathodes ($L/d_e = 11.7$) at 60° and 70°C

(i) Current distribution studies at 60°C

The cathodic current distribution was determined using the 10cm segmented cathode at anode lengths of 25, 10, 9, 8 and 7 cm. The relationship between the average current density and current distribution was examined for each anode length and a flow rate of $Re\ 6,425 \pm 525$.

Additional experiments on the effect of flow rate on the distribution of current were also carried out. The results were correlated with data from experiments on electroformed foils. Details of the experimental method are given in Section 3.5.

25cm anode and 10cm cathode

This geometry was the normal operating condition for foil preparation studies in Cell 2. The current distribution was measured longitudinally, using the segmented cathode at average current densities of 0.33, 0.66 and 1.00 A cm⁻² (Fig.4.121).

At current densities ≤ 0.66 A cm⁻² (i.e. less than the maximum current density for a good deposit), the current distributions were similar. High current densities ($\sim 1.5 i_{av}$) were observed at the leading and trailing edge of the cathode, and the current distribution was relatively symmetrical. This type of distribution is similar to a primary current distribution. The high current density areas would appear to correspond with the localised areas of deposit brightness, increased microhardness and small grain size observed previously (Section 4.3.1).

The coating in the central region was deposited at a current density of $\sim 0.9 i_{av}$. This plateau was $\sim 70\%$ of the total electrode length.

The high edge current densities ($\sim 1.5 i_{av}$) were also observed at an average current density of 1.00 A cm⁻² (Fig.4.121). However, at this current density, hydroxide deposits were found at the leading edge of the cathode. Poor deposits were formed on the three leading edge segments. The resulting resistive layer of hydroxide and increased hydrogen gas evolution tended to decrease the local current density in this region of the cathode ($\frac{x}{L} \sim 0.1$ to 0.4). Hence the local current densities on the remaining segments were increased, resulting in a distortion of the current distribution.

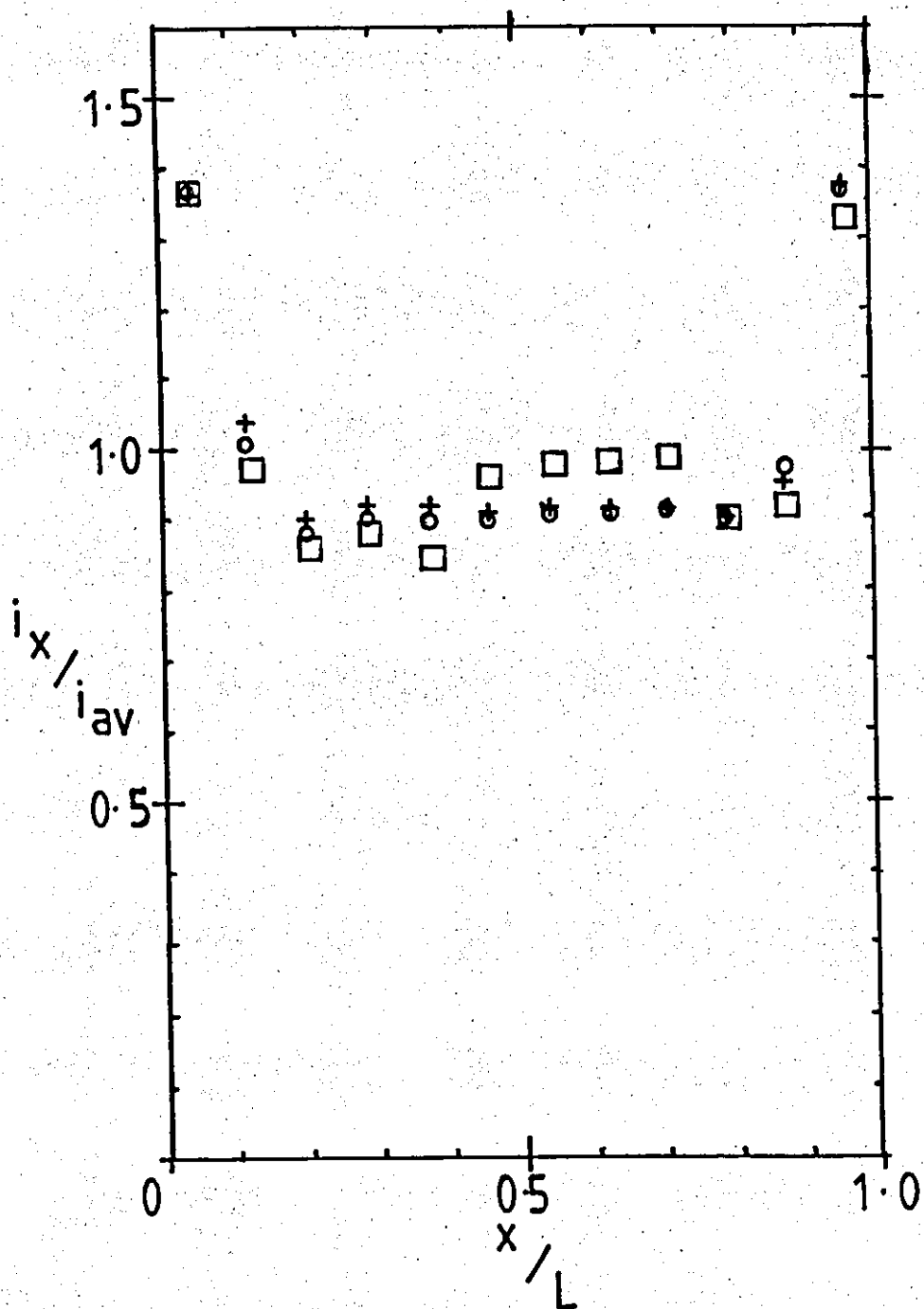


Fig. 4.121 Longitudinal current distribution (nickel deposition) along a segmented cathode 11.7 equivalent diameters in length at 60°C and $Re\ 6,425 \pm 525$.
Anode length = 25cm.

- + - $i_{av} = 0.33\ A\ cm^{-2}$
- o - $i_{av} = 0.66\ A\ cm^{-2}$
- - $i_{av} = 1.01\ A\ cm^{-2}$

10cm anode and 10cm cathode

An anode to cathode ratio of unity was equivalent to the normal foil preparation condition for Cell I. The current distribution was measured longitudinally at current densities of 0.33 and 0.66 A cm⁻² (Fig.4.122). The deposits were sound at both current densities. The overall form of the distributions was similar to those produced with a 25cm anode. However, the current density at the leading and trailing edges ($\sim 1.15 i_{av}$) was less than observed previously. The coating in the main central area ($\sim 80\%$ of the total area) was deposited at $\sim 0.95 i_{av}$.

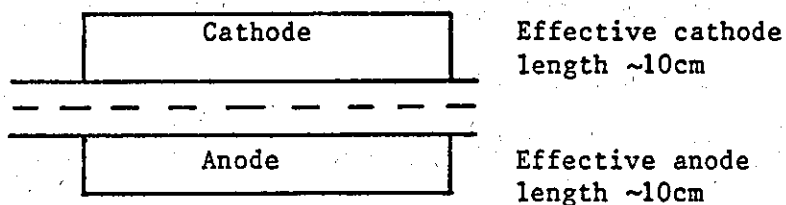
Visual observation of nickel foils electroformed at 0.74, 0.83 and 1.03 A cm⁻² (Table 4.34) showed changes in deposit appearance in the high current density areas. The main deposit was uniform at all current densities. At 0.74 A cm⁻² the leading and trailing edge bands were bright and at 1.03 A cm⁻² nickel hydroxide was deposited in these areas. The maximum current density for a good deposit was ~ 0.8 A cm⁻². This value was slightly greater than observed for a 25cm anode (~ 0.65 A cm⁻²).

An additional investigation of the effect of flow rate on local current densities was also carried out at an average current density of 0.33 A cm⁻². The coating in the main central region was deposited at a uniform current density over the Reynolds number range Re 2,000 - 10,000. The visual appearance of electroformed foils indicated that they were uniform in this area. At the leading edge segment a small increase in current density from 1.06 to 1.1 i_{av} was observed. A decrease in current density would have been expected if the process was under simple mass transfer control. At the trailing edge, the local current density increased from 1.23 to 1.35 i_{av} (Fig.4.123). The increases in current density in the inlet and outlet regions may be associated with interference due to gas flow patterns.

9cm anode/10cm cathode

A series of experiments were carried out in turbulent flow and a brief confirmatory study in laminar flow.

Electrode Geometry



	Average cathode current density $i_c/A_{cm^{-2}}$	Time t secs	Average deposit thickness μm	Average anode current density $i_a/A_{cm^{-2}}$	Visual appearance of electroform
Re 6,425 \pm 525	0.74	105	27	0.74	
	0.83	95	27	0.83	
	1.03	73	26	1.03	

Table 4.34 Nickel foils deposited on cathodes 11.7 de in length at 60°C. Anode length 10cm.

key to diagrams

- sound deposit
- bright deposit
- powder deposit
- hydroxide deposit

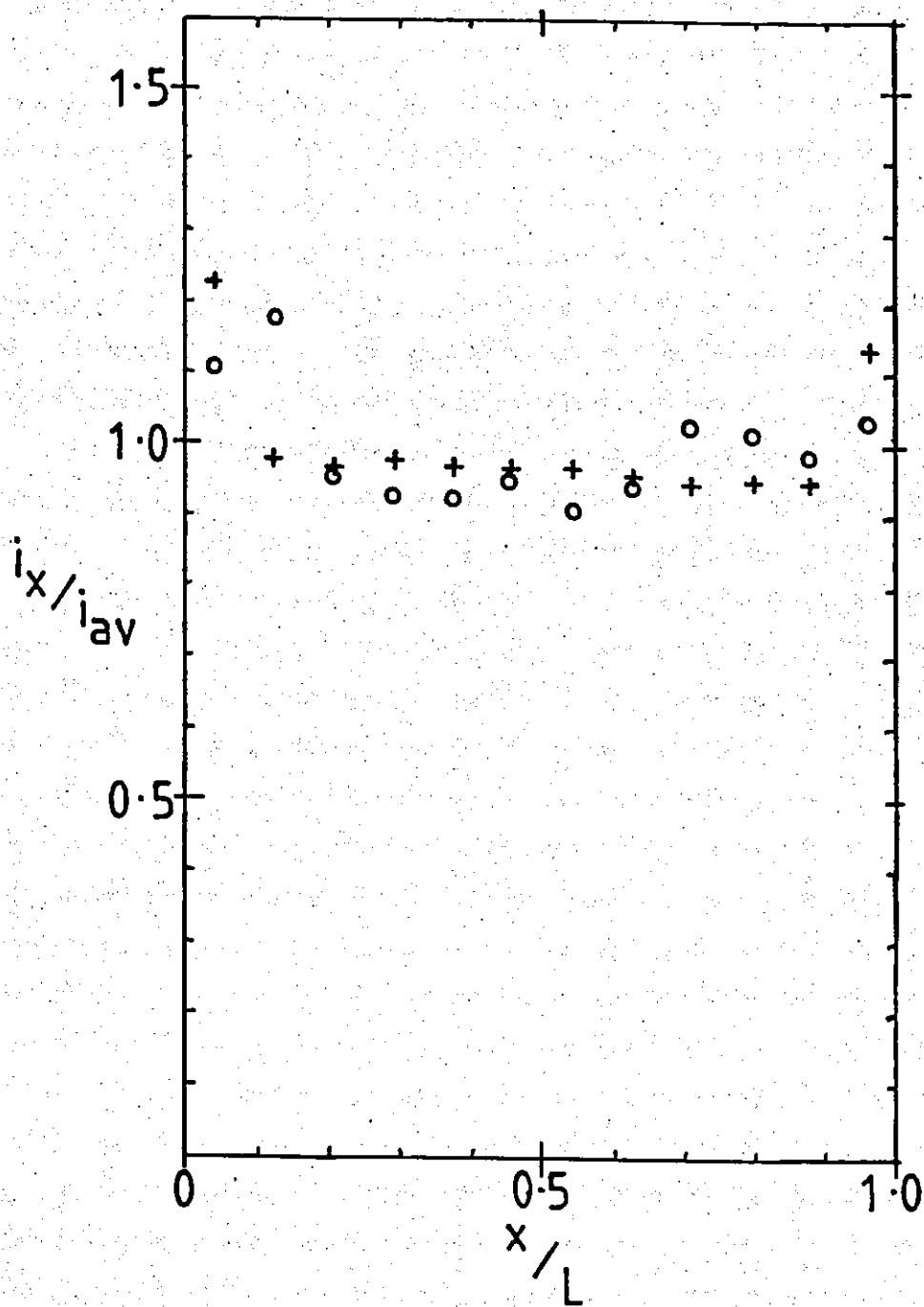


Fig. 4.122 Longitudinal current distribution (nickel deposition) along a segmented cathode 11.7 equivalent diameters in length at 60°C and $Re\ 6,425 \pm 525$.
Anode length = 10cm.

+ - $i_{av} = 0.33 \text{ A cm}^{-2}$

o - $i_{av} = 0.65 \text{ A cm}^{-2}$

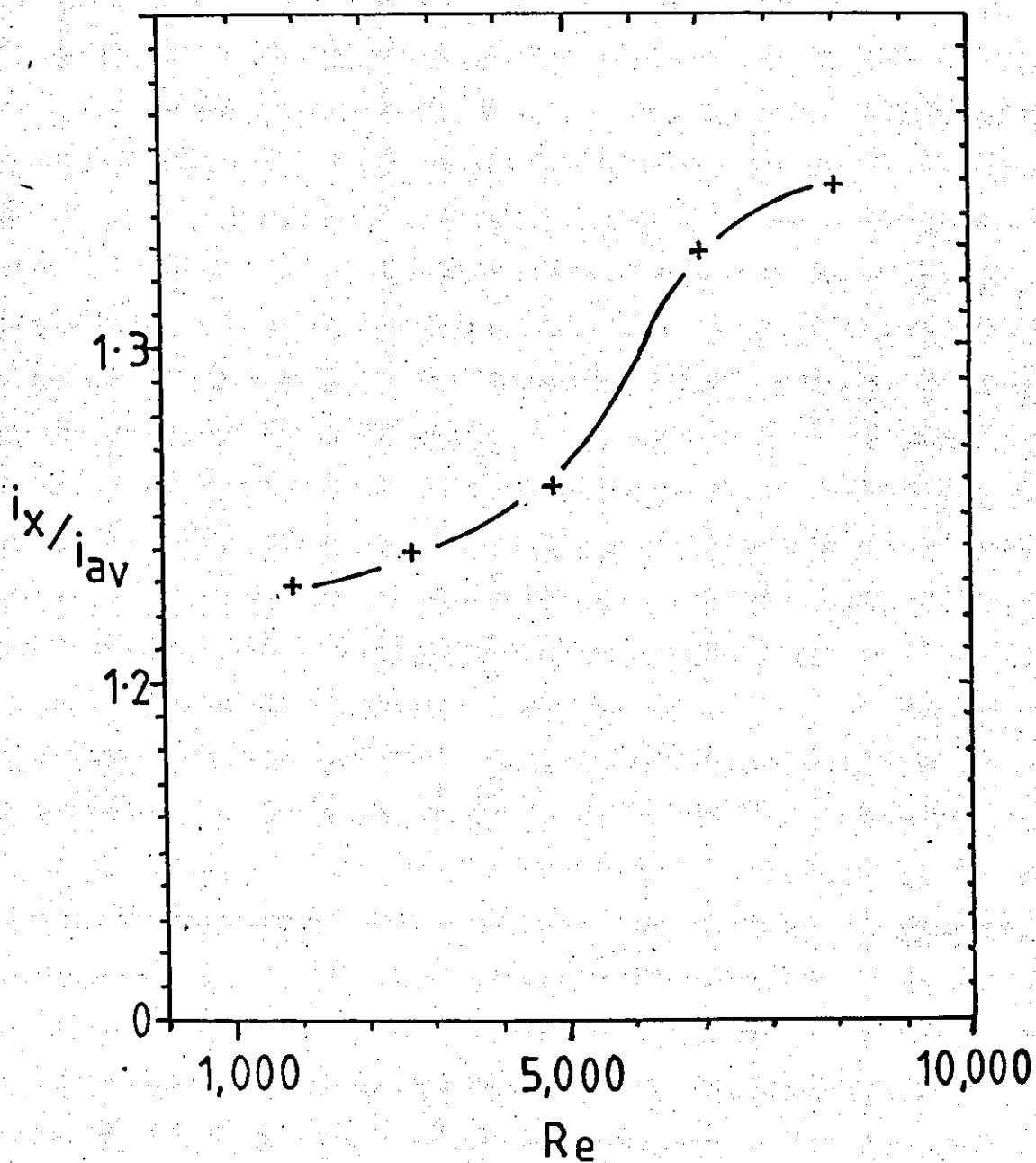


Fig.4.123 Effect of flow rate on the local current density (nickel deposition) at the trailing edge segment at an average current density of 0.33 A cm^{-2} . Anode length = 10cm.

Turbulent flow

The current distribution was measured over the current density range 0.33 to 1.27 A cm^{-2} at $\text{Re } 6,425 \pm 525$. At current densities $< 1.19 \text{ A cm}^{-2}$, electroforms of good visual appearance were deposited. The relatively uniform current distribution, observed using this electrode geometry is shown in Fig.4.124. The local current density was $1.02 \pm 0.04 i_{av}$ on all electrode segments.

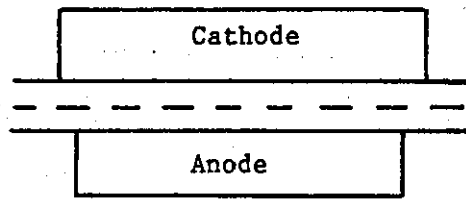
S.E.M. examination of a nickel foil electroformed at 1.0 A cm^{-2} and a current efficiency of 97% (Table 4.35) confirmed deposit uniformity and hence the uniformity of current distribution. The main deposit area was of a fine structure with grains $< 3 \mu\text{m}$ in diameter (Fig.4.125), although less well-defined nearer the leading edge. The average microhardness was $334 \pm 39 \text{ kg mm}^{-2}$. Some slight ridging and pitting was observed close to the leading edge (Fig.4.126a). The trailing edge features were similar.

At current densities $> 1.19 \text{ A cm}^{-2}$, hydroxide was deposited in the leading edge region (Table 4.35). The formation of a resistive layer of hydroxide distorted the current distribution resulting in a marked decrease in current density ($< 0.05 i_{av}$) in these areas (Fig. 4.127). An increased current density (up to $\sim 1.4 i_{av}$) was observed in the central area of the cathode. The higher local current densities may result in greater hydroxide formation. However, a shorter effective cathode length, as a result of hydroxide deposits, may enable higher deposition rates to be maintained.

An additional study of the effect of flow rate on the current density distribution obtained with the 9cm anode configuration was carried out at a current density of 0.9 A cm^{-2} (Fig.4.128). Good coherent deposits were electroformed over the flow rate range $\text{Re } 1,901 - 9,902$.

At low flow rates ($\text{Re } 1,901$), the current density was highest ($\sim 1.15 i_{av}$) at $x/L < 0.46$ and decreased to $\sim 0.82 i_{av}$ at the trailing edge segment. Small gas bubbles accumulated near the trailing edge at low Reynolds numbers.

Electrode Geometry



Effective Cathode length ~10cm

Effective anode length ~9cm

	Average cathode current density i_c/Acm^{-2}	Time t secs	Average deposit thickness μm	Average anode current density i_a/Acm^{-2}	Visual appearance of electroform
Re 6,425 \pm 525	1.00	74	25	1.11	
	1.33	55	25	1.51	
	1.55	48	25	1.72	
Re 11,900 \pm 1,000	1.01	74	26	1.12	
	1.01	74	26	1.12	
	1.33	57	26	1.51	

Table 4.35 Nickel foils deposited on cathodes 11.7 de in length at 60°C. Anode length 9 cm.

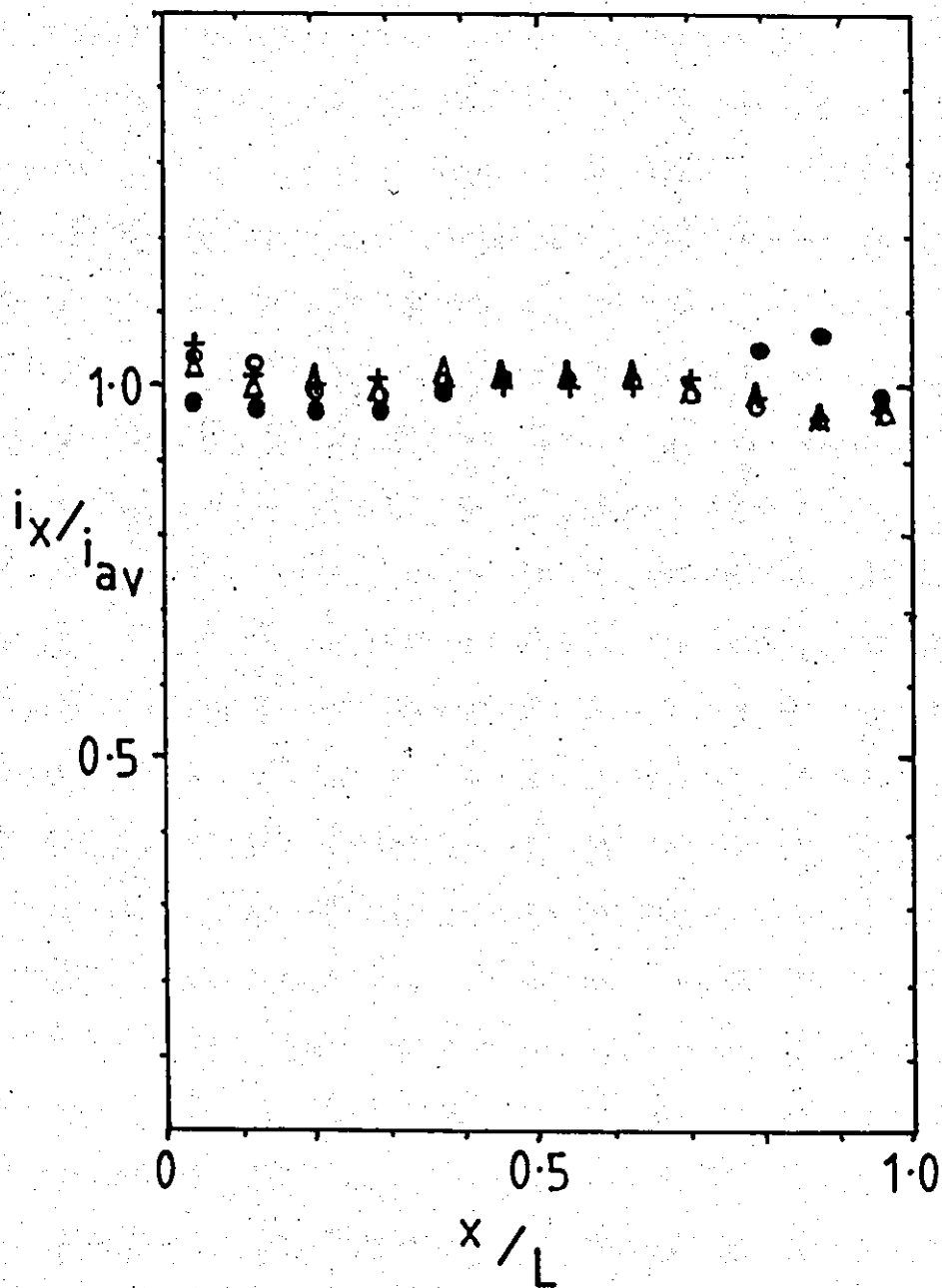


Fig.4.124 Longitudinal current distribution (nickel deposition) along a segmented cathode 11.7 equivalent diameters in length at 60°C and $Re\ 6,425 \pm 525$.
Anode length = 9cm.

- + - $i_{av} = 0.33\ A\ cm^{-2}$
- O - $i_{av} = 0.66\ A\ cm^{-2}$
- Δ - $i_{av} = 0.98\ A\ cm^{-2}$
- - $i_{av} = 1.19\ A\ cm^{-2}$



Fig. 4.125. SEM micrographs of surface of nickel foil deposited at 1.01 A cm^{-2} , $\text{Re } 6,425 \pm 525$, cathode length 10 cm and anode length 9 cms (60°C). Main deposit section (top 2,000x, bottom 10,000x, 30° tilt).



a) 0° tilt



b) 50° tilt

Fig. 4.126

SEM micrographs of surfaces of foils of nickel deposited at 1.01 A cm^{-2} , cathode length 10 cm and anode length 9 cm (60°C).

a) $\text{Re } 6,425 \pm 525$, leading edge section (200x)

b) $\text{Re } 11,900 \pm 1,000$, trailing edge section (200x; 50° tilt).

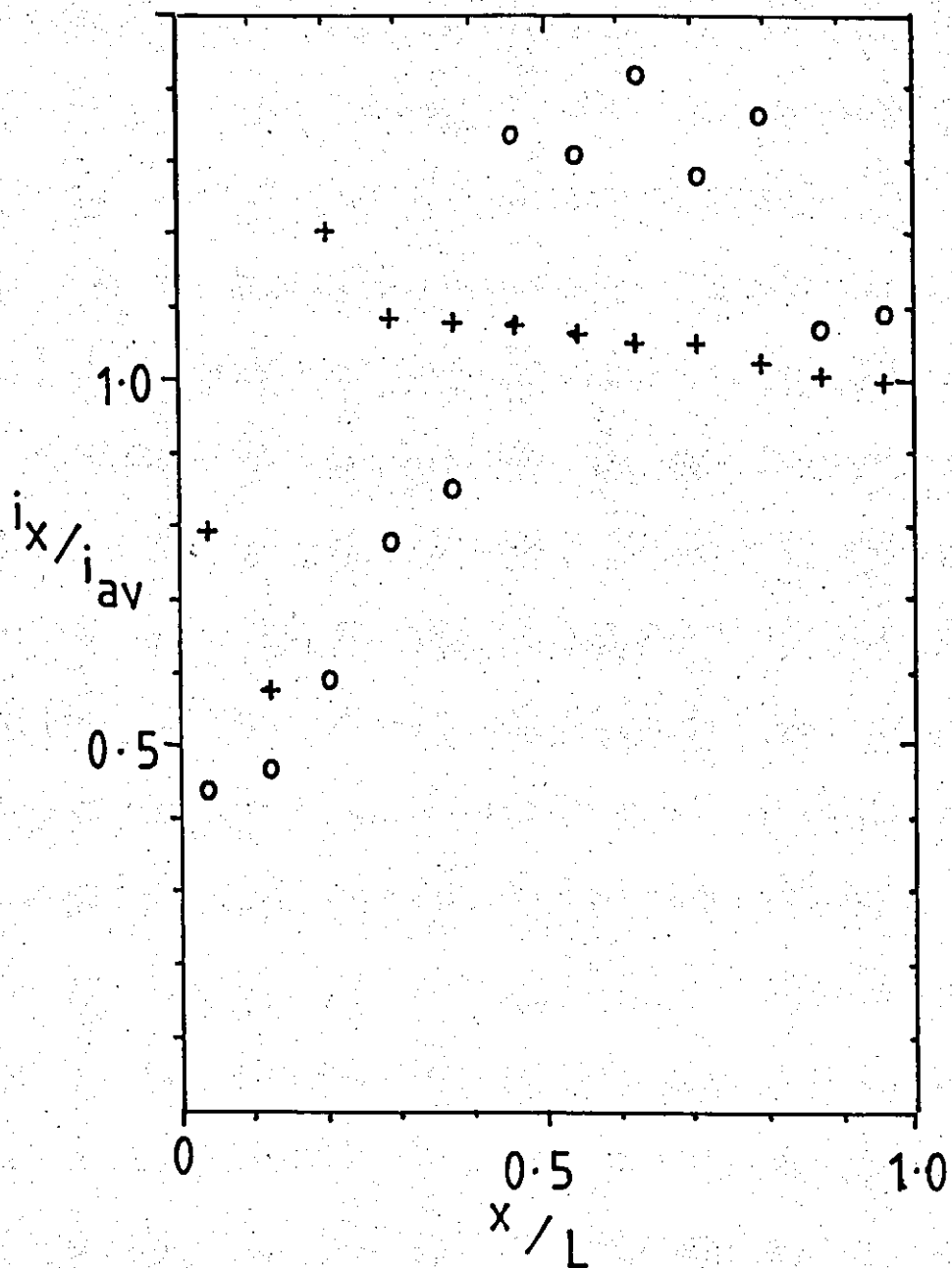


Fig.4.127 Longitudinal current distribution (nickel deposition) along a segmented cathode 11.7 equivalent diameters in length at 60°C and $Re\ 6,425 \pm 525$. Anode length = 9cm. Average current density = $1.26\ A\ cm^{-2}$.

$$+ - i_{av} = 1.26\ A\ cm^{-2}$$

$$o - i_{av} = 1.27\ A\ cm^{-2}$$

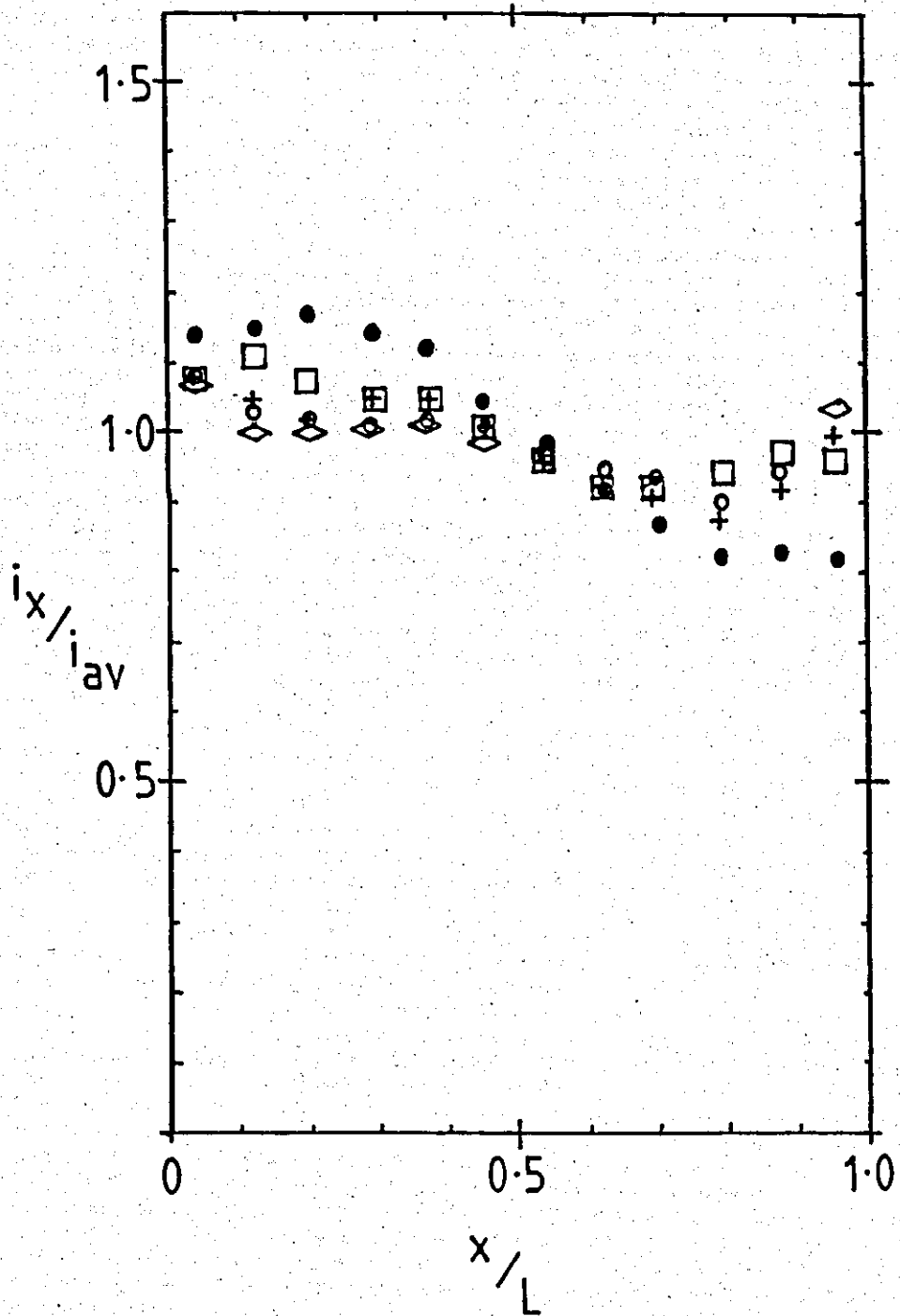


Fig.4.128 Effect of flow rate on the current distribution (nickel deposition) along a segmented cathode 11.7 equivalent diameters in length at 60°C and an average current density of 0.9 A cm⁻². Anode length = 9cm.

- - Re 1,901
- - Re 3,763
- + - Re 5,783
- - Re 7,921
- ◇ - Re 9,902

Over the Reynolds number range Re 3,763 - 9,902 a more uniform current distribution was obtained. The current density was $1.02 \pm 0.06 i_{av}$ on all segments. Fewer gas bubbles were observed on the cathode at high Reynolds numbers.

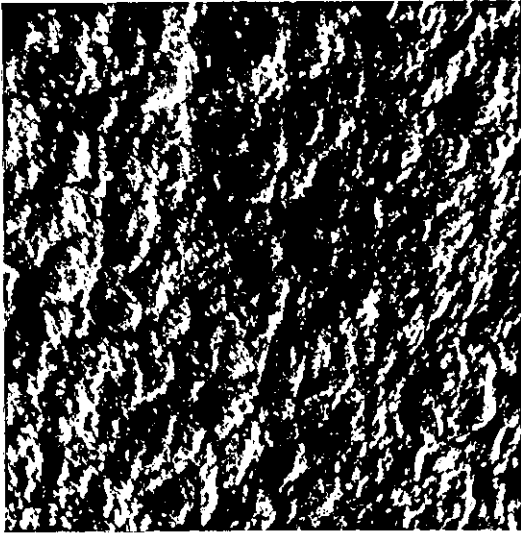
Nickel foils electroformed at $1 A cm^{-2}$ and Re $11,900 \pm 1,000$ (Table 4.35), were of a more uniform fine grain structure than those observed at lower flow rates (cf Fig.4.125 and 4.129). These areas had microhardnesses of $347 \pm 30 kg mm^{-2}$. The high Reynolds number resulted in reduced pitting particularly in the leading and trailing edge regions (cf Fig.4.126a and b).

A sound nickel foil was also electroformed at the high current density of $1.33 A cm^{-2}$ (Table 4.35). Extensive pitting of the main deposit area (Fig.4.130a) was observed (in the absence of a wetting agent). The grain structure was unresolvable, although there was evidence of micro-porosity and some larger features (Fig.4.130b). Further reductions in pitting were obtained by addition of a wetting agent (0.038% Fluowet SP) to the electrolyte. Sound and coherent deposits were electroformed at $1 A cm^{-2}$, and 99% current efficiency without significant changes in deposit structure (cf Figs.4.129 and 4.131). In this case pitting was not evident at the leading and trailing edge of the cathode.

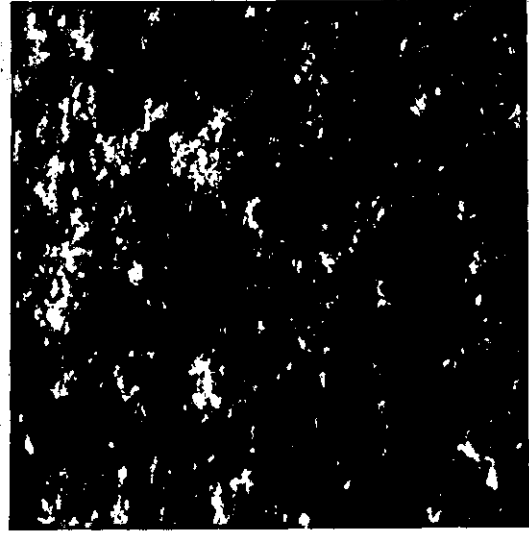
Laminar flow

It was of interest to briefly investigate the effect of very low flow rates on the current density profile. Current distributions were determined at 0.33 and $0.64 A cm^{-2}$ at a flow rate corresponding to Re 670 (Fig.4.132). Deposits of good visual appearance were produced at both current densities.

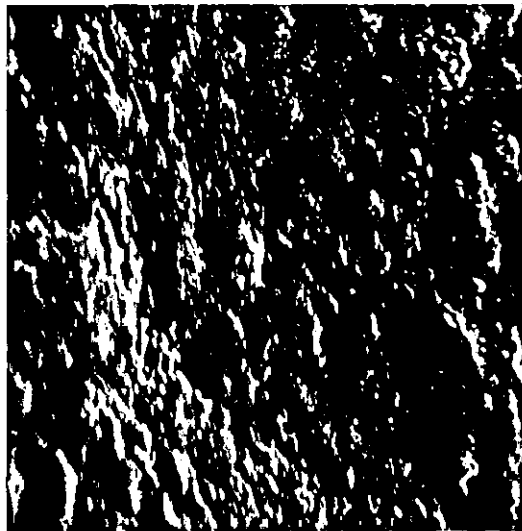
During the deposition period, the current density at each cathode segment oscillated between 0.8 and $1.2 i_{av}$. In general current densities were greater near the leading edge. Large volumes



a) 40° tilt



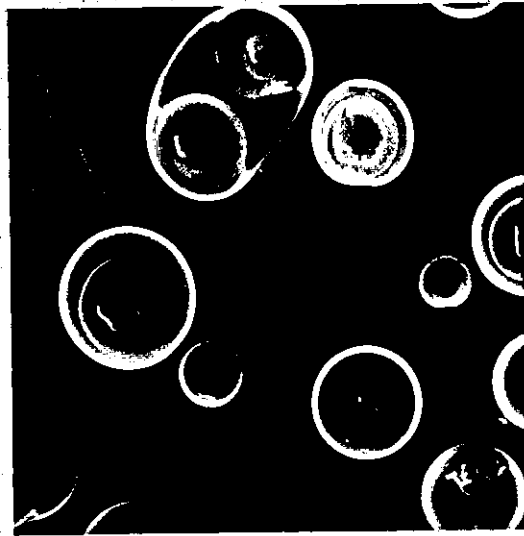
b) 30° tilt



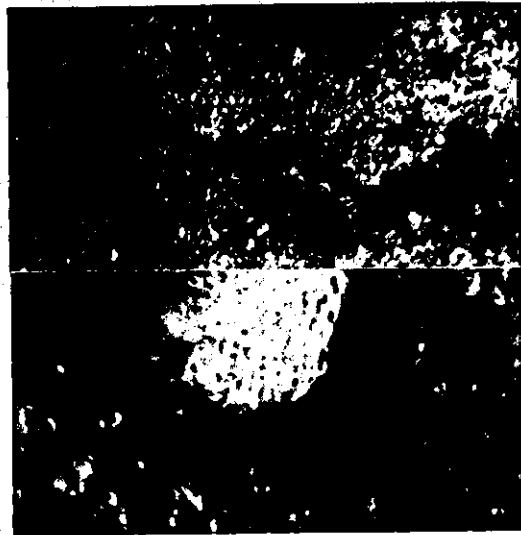
c) 50° tilt

Fig.4.129 SEM micrographs of surfaces of foils of nickel deposited at 1.01 A cm^{-2} , $\text{Re } 11,900 \pm 1,000$, cathode length 10 cm and anode length 9 cm (60°C). Main deposit sections (10,000x).

- a) ~0.5 cm from leading edge
- b) ~5 cm from leading edge
- c) ~9.5 cm from leading edge



a) 30° tilt



b) 0° tilt

Fig.4.130

SEM micrographs of surfaces of foils of nickel deposited at 1.33 A cm^{-2} , $Re 11,900 \pm 1,000$, cathode length 10 cm and anode length 9 cm (60°C). Main deposit sections

a) pitted area (200x)

b) ~5 cm from leading edge (top 2,000x, bottom 10,000x).

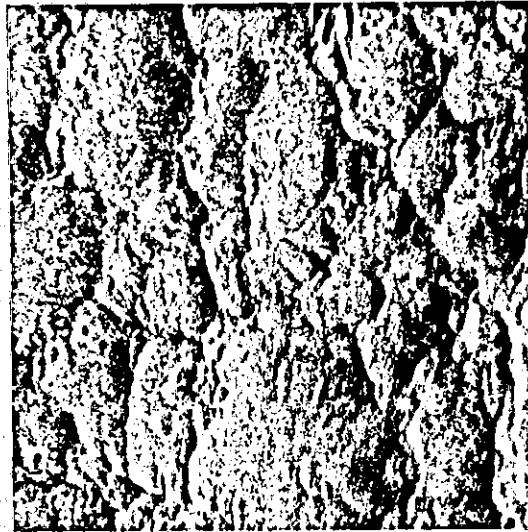


Fig.131 SEM micrograph of surface of nickel foil deposited at 1.01 A cm^{-2} , $Re 11,900 \pm 1,000$ cathode length 10 cm and anode length 9 cm (60°C). Electrolyte contained $\sim 0.038 \text{ wt } \%$ 'Fluowet SP'. Main deposit section (30° tilt, $10,000\times$).

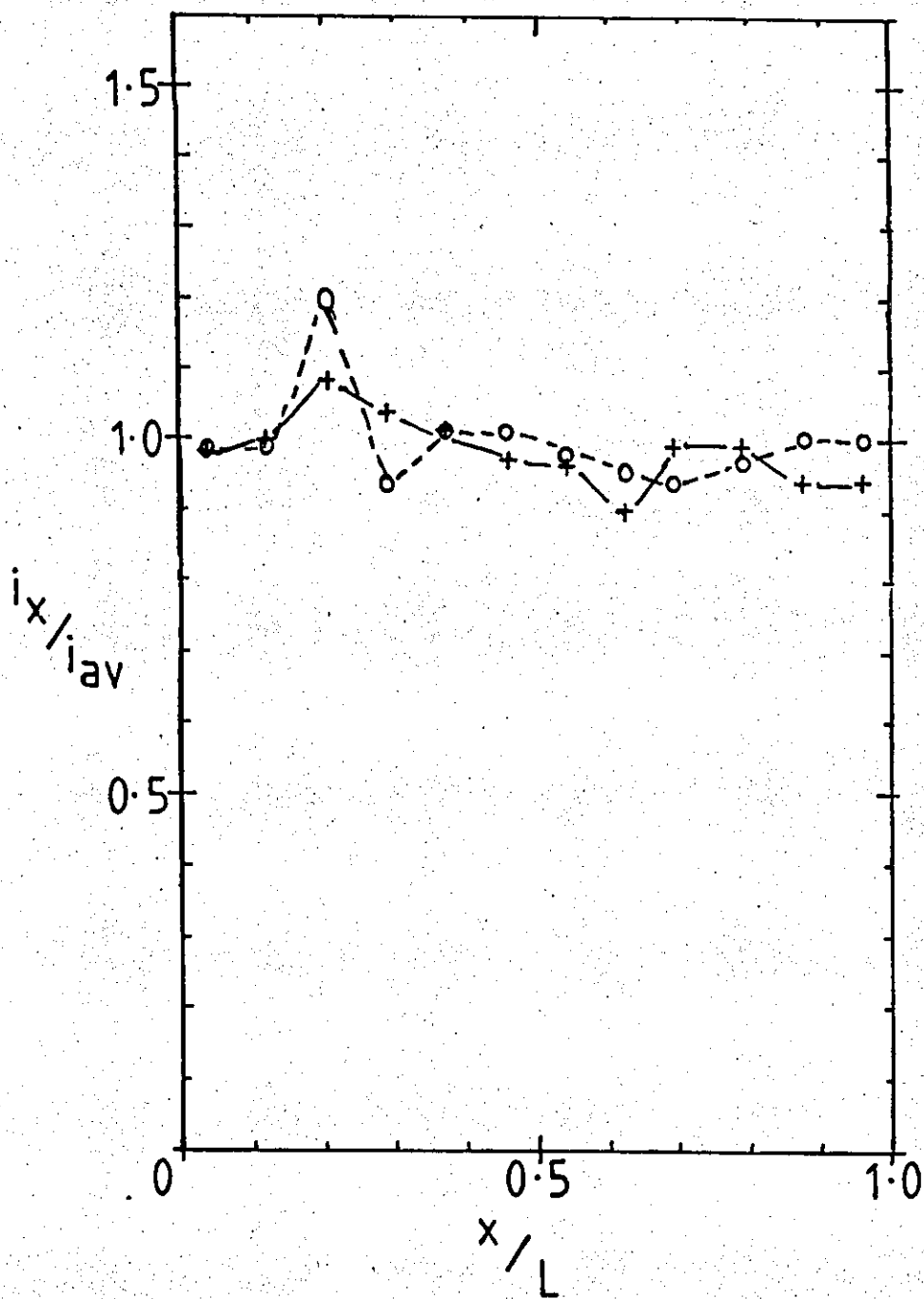


Fig. 4.132 Longitudinal current distribution (nickel deposition) along a segmented cathode, 11.7 equivalent diameters in length at 60°C and very low flow rates (Re 670). Anode length = 9cm.

+ - $i_{av} = 0.31 \text{ A cm}^{-2}$

o - $i_{av} = 0.64 \text{ A cm}^{-2}$

of gas were observed to evolve from the leading edge segments and bubbles adhered to the electrode further downstream. The bubbles grew in size until detached by the flowing electrolyte.

8cm anode and 7cm anodes with 10cm cathodes

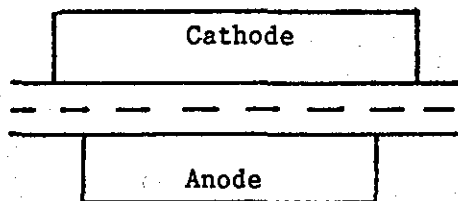
The current distribution was measured using 7 and 8cm anodes at average current densities of 0.33 and 0.65 A cm⁻². (Fig.4.133 and 4.134). Deposits of good visual appearance were produced at both deposition rates. The current distribution was unaffected by flow rates within the turbulent flow regime.

The highest current densities ($\sim 1.14 \pm 0.05 i_{av}$) were observed in the central main deposit area ($x/L \sim 0.3$ to 0.7). The lowest edge current densities ($\sim 0.7 i_{av}$) were observed with 7cm anodes.

Electroforms of good visual appearance were produced at current densities up to ~ 1.5 A cm⁻² (Tables 4.36 and 4.37). The central main deposit was brighter than the edge regions. At higher current densities nickel hydroxide was deposited in some areas of the cathode. Localised gas flow patterns may effect the current distribution at high current densities.

S.E.M. examination of poor deposits showed the hydroxide material (Fig.4.135a) on the surface. The underlying material was very fine ($\sim 0.1\mu\text{m}$), and was most probably a mixture of fine metal and hydroxide powders (Fig.4.135b).

Electrode geometry



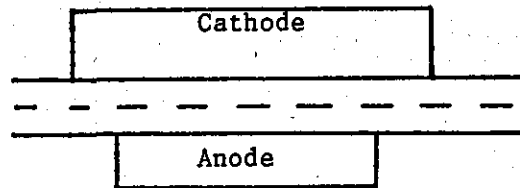
Effective cathode length ~10cm

Effective anode length ~8cm

	Average cathode current density i_c/Acm^{-2}	Time t secs	Average deposit thickness μm	Average anode current density i_a/Acm^{-2}	Visual appearance of electroform
Re $6,425 \pm 525$	1.54	50	26	2.00	

Table 4.36 Nickel foils deposited on cathodes 11.7 de in length at 60°C. Anode length 8 cm.

Electrode Geometry



Effective cathode length ~10cm

Effective anode length ~7cm

	Average cathode current density i_c/Acm^{-2}	Time t secs	Average deposit thickness μm	Average anode current density i_a/Acm^{-2}	Visual appearance of electroform
Table D ₁ Re 4,050 ± 200	1.03	73	26	1.48	
Table D ₂ Re 6,425 ± 525	0.86	86	25	1.22	
	1.01	73	25	1.44	
	1.01	75	26	1.44	
	1.52	48	25	2.17	
	1.73	42	25	2.48	
	1.75	45	27	2.50	
	~2.00	45	~31	2.86	
Table D ₃ Re 11,900 ± 1,000	~2.00	37	~25	2.86	

Table 4.37 Nickel foils deposited on cathodes 11.7 de in length at 60°C. Anode length 7 cm.

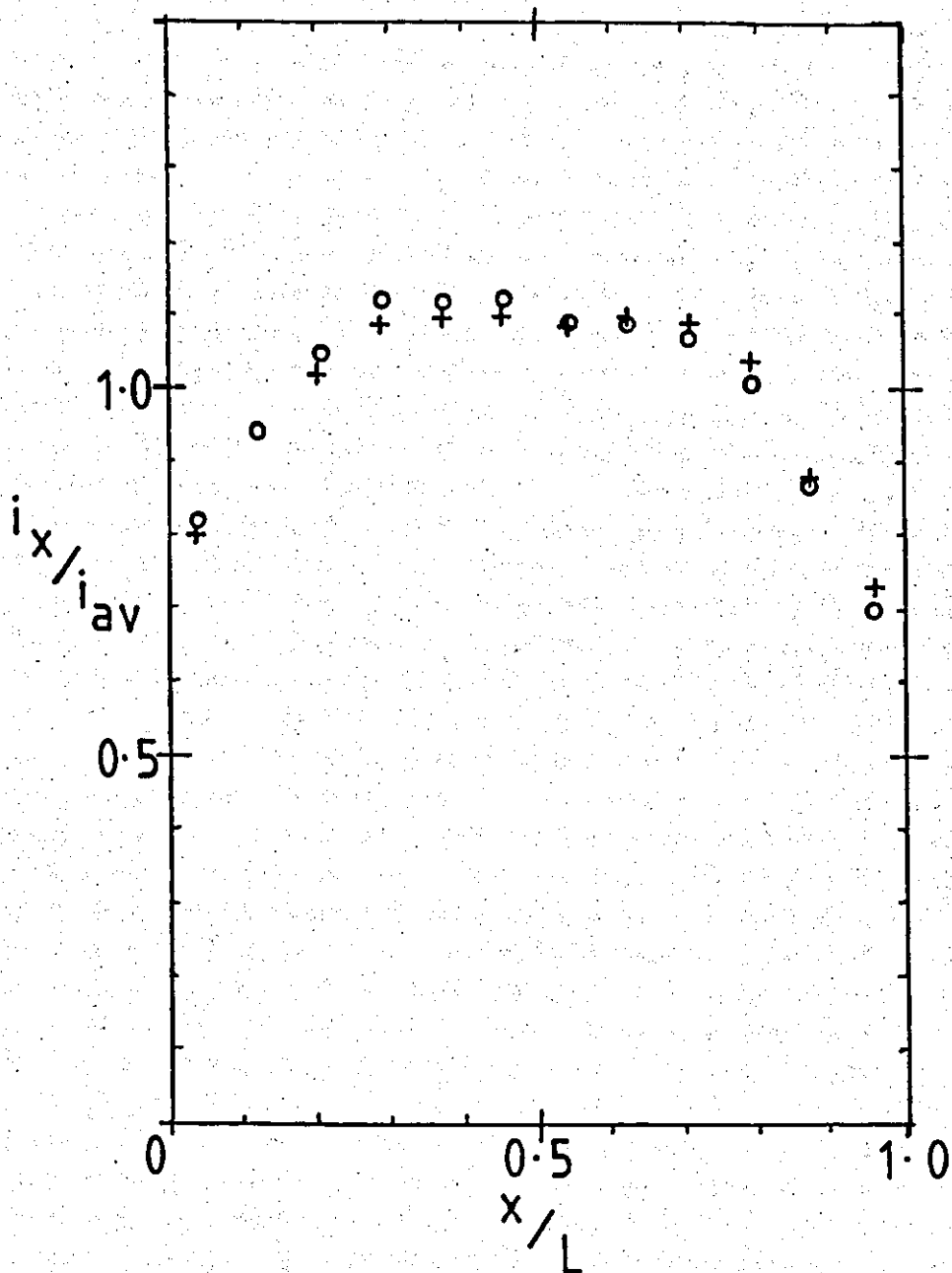


Fig.4.133 Longitudinal current distribution (nickel deposition) along a segmented cathode, 11.7 equivalent diameters in length, at 60°C and $Re\ 6,425 \pm 525$.
Anode length = 8cm.

+ - $i_{av} = 0.33\ A\ cm^{-2}$

o - $i_{av} = 0.65\ A\ cm^{-2}$

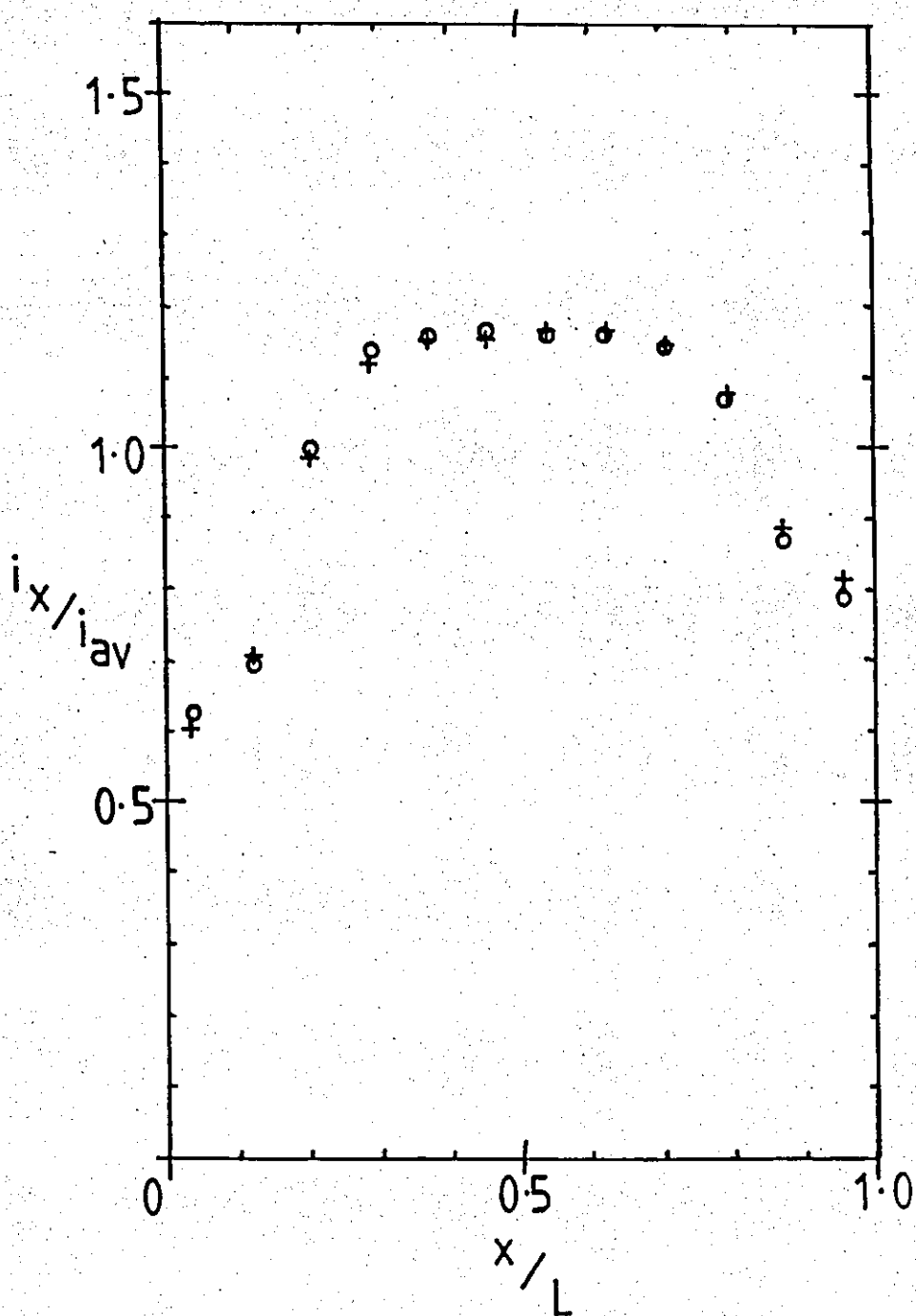


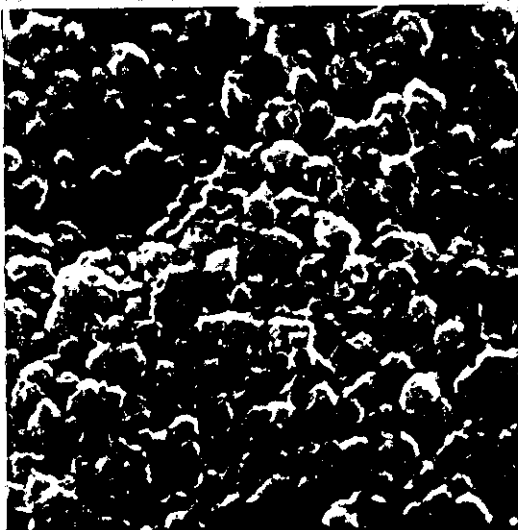
Fig. 4.134 Longitudinal current distribution (nickel deposition) along a segmented cathode, 11.7 equivalent diameters in length, at 60°C and $Re\ 6,425 \pm 525$.
Anode length = 7cm.

+ - $i_{av} = 0.32\ A\ cm^{-2}$

o - $i_{av} = 0.64\ A\ cm^{-2}$



a)



b)

Fig.4.135 SEM micrographs of surfaces of foils of nickel deposited at 1.75 A cm^{-2} , $\text{Re } 6,425 \pm 525$, cathode length 10 cm and anode length 7 cm (60°C). Main deposit sections (30° tilt).

a) green area (2,000x)

b) black-brown area (50,000x).

Summary of current distributions at 60°C

Turbulent flow

With an anode length greater or equal to the cathode length (10cm) very high current densities were observed at the leading and trailing edges of the cathode. However, the current density distribution was uniform in the main deposit region. This area represented >70% of the total cathode area.

With an anode length less than the cathode length, the high current density area was found in the main deposit region and low current densities at the electrode edges. The area of uniform current distribution was reduced to <40% of the cathode area. The maximum average current density for a good coherent deposit was observed to increase with decreasing anode length.

Optimum anode length

With a 9cm anode the current distribution was reasonably uniform over the cathode length. This offered the possibility of producing foils of uniform structure at very high current densities.

In turbulent flow, few significant effects on the current distribution were observed. However, the current density tended to decrease towards the rear of the cathode, at low flow rates, possibly due to gas bubble effects.

Using a 9cm anode, the addition of a wetting agent (0.038% Fluowet SP) to the electrolyte resulted in good high current density deposits of decreased porosity without significant changes in surface structure.

Laminar flow

In laminar flow, the velocity of the electrolyte was insufficient to remove evolved gas from the cathode surface. Hence large gas bubbles grew on the electrode surface, before being detached. This

resulted in current oscillations at individual cathode segments.

It should be noted that the typical mass transfer controlled current distribution was not observed for any experimental conditions.

(ii) Current distribution studies at 70°C

The broad trends in the results obtained at 60°C were confirmed by a more limited investigation at 70°C. The cathodic current distribution was determined using the 10cm segmented cathode, with corresponding anode lengths of 9cm, 8cm and 7cm. The relationship between the average current density and current distribution was examined for each anode length and a flow rate Re of 9.450 ± 250 . Additional experiments on flow rate effects were also carried out using 9cm anodes. The results were correlated with data from experiments on electroformed nickel foils.

9cm anode / 10cm cathode

The current distribution was measured over the current density range 0.31 to 2.07 $A\ cm^{-2}$. At all current densities, electroforms of good visual appearance were deposited at high current efficiency. The distribution was relatively uniform at all current densities (Fig.4.136 and 4.137). Minor distortions in the current distributions were the result of slight differences in the alignment of the anode and the effect of gas evolution. The very high edge current densities (observed at 60°C, Figs.4.121) were not observed at 70°C. At 70°C the precipitation of hydroxide was not observed and current densities were limited to $\sim 2\ A\ cm^{-2}$ by the available power supply.

When the flow rate was increased to $Re\ 16,250$ the maximum current density increased to 2.22 $A\ cm^{-2}$ and the cell voltage exceeded 30V. The current distribution was uniform ($i_x = 1.00 \pm 0.05\ i_{av}$) over the cathode length (Fig.4.138).

A detailed study of the effect of flow rate on the current distribution was carried out at an average current density of $1.12 \pm 0.03\ A\ cm^{-2}$ over the flow rate range $Re\ 1,500$ to $Re\ 12,550$ (Fig.4.139).

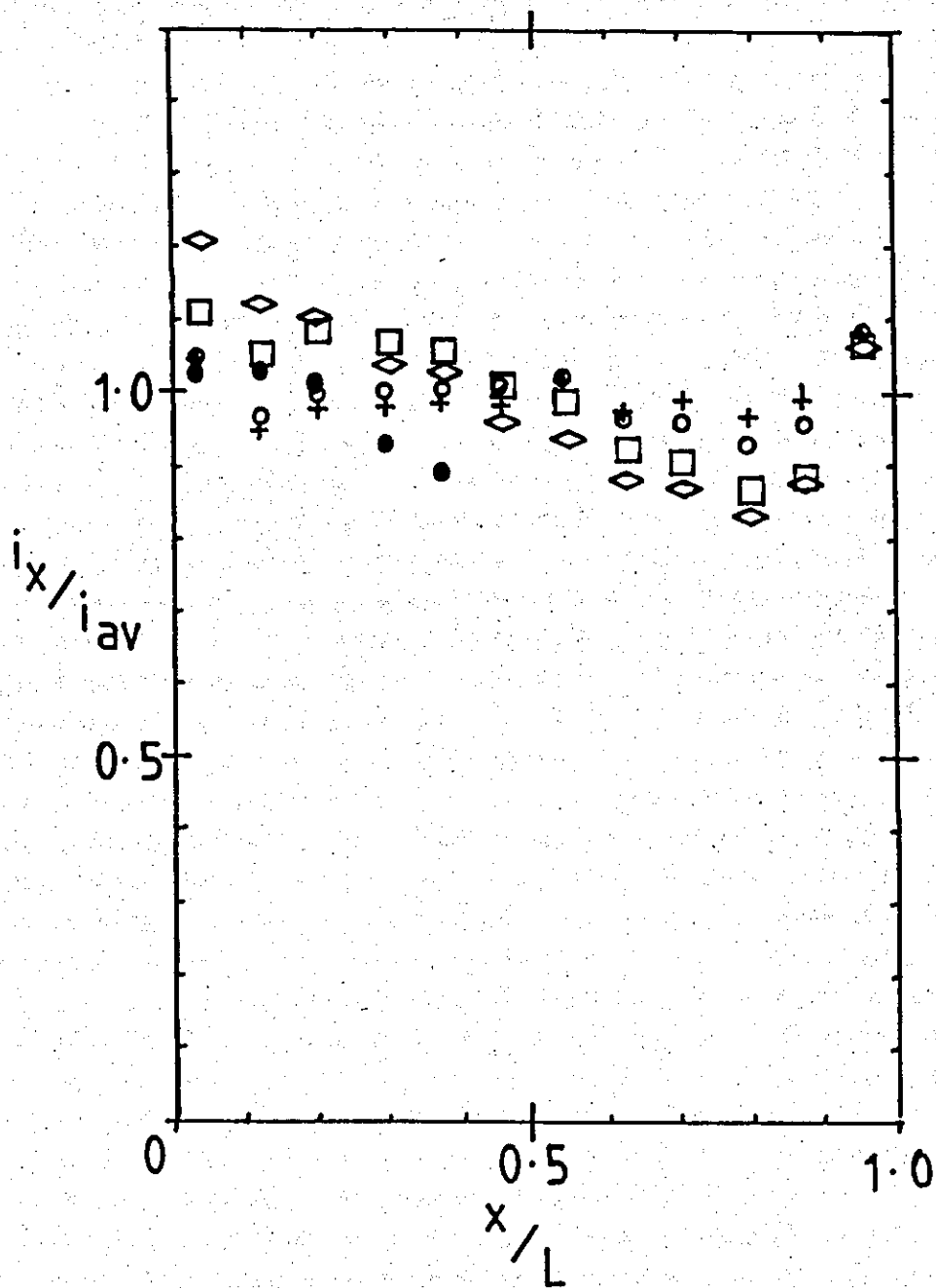


Fig.4.136 Longitudinal current distribution (nickel deposition) on a segmented cathode, 11.7 equivalent diameters in length, at 70°C and an average current density of $1.12 \pm 0.03 \text{ A cm}^{-2}$. Anode length = 9cm.

- + - Re 1,500
- o - Re 2,200
- - Re 4,280
- ◇ - Re 6,700
- - Re 12,550

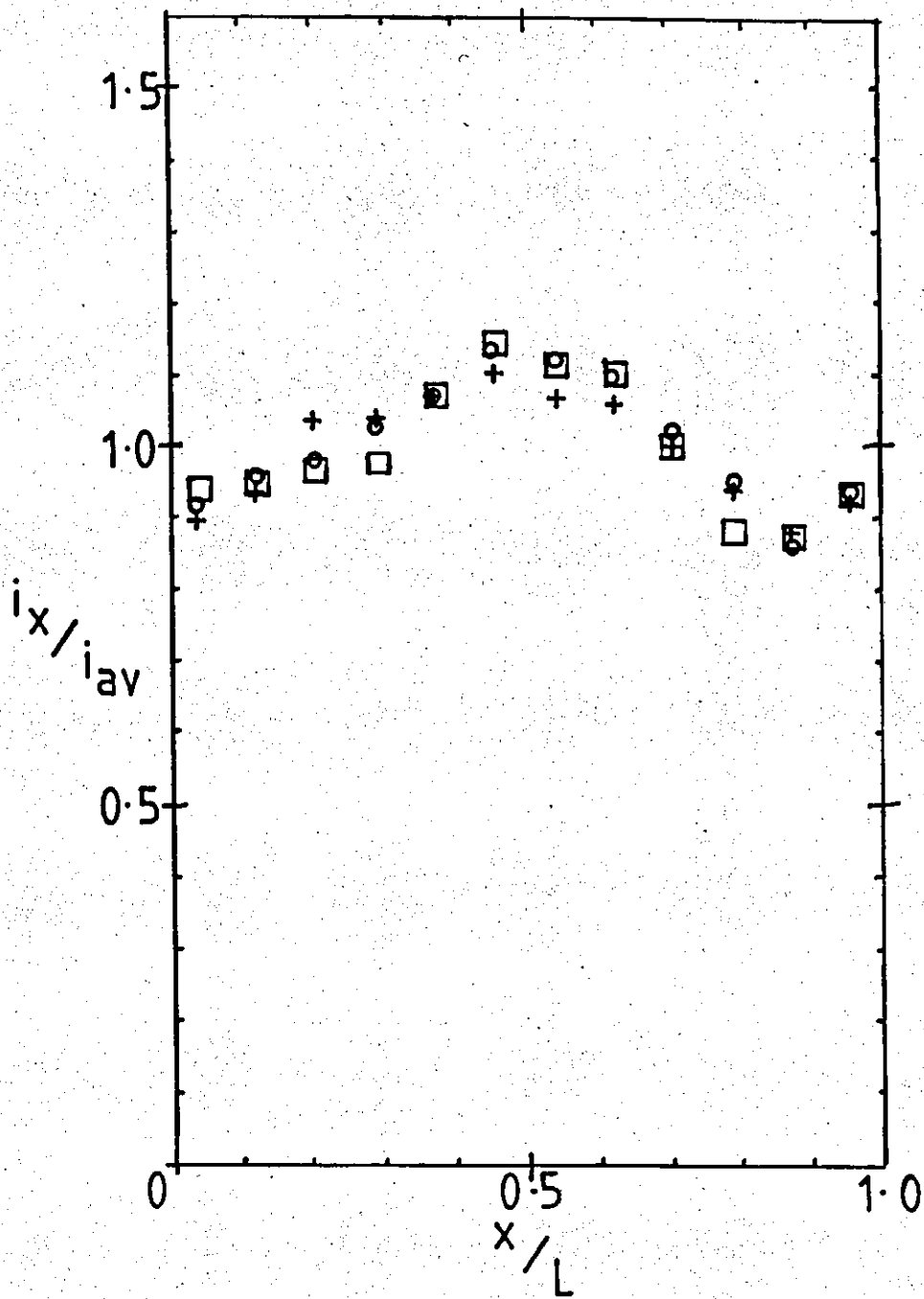


Fig.4.137 Longitudinal current distribution (nickel deposition) along a segmented cathode, 11.7 equivalent diameters in length, at 70°C and $Re\ 9,450 \pm 250$.
Anode length = 9 cm.

+ - $i_{av} = 1.15\ A\ cm^{-2}$

O - $i_{av} = 1.68\ A\ cm^{-2}$

□ - $i_{av} = 2.00\ A\ cm^{-2}$

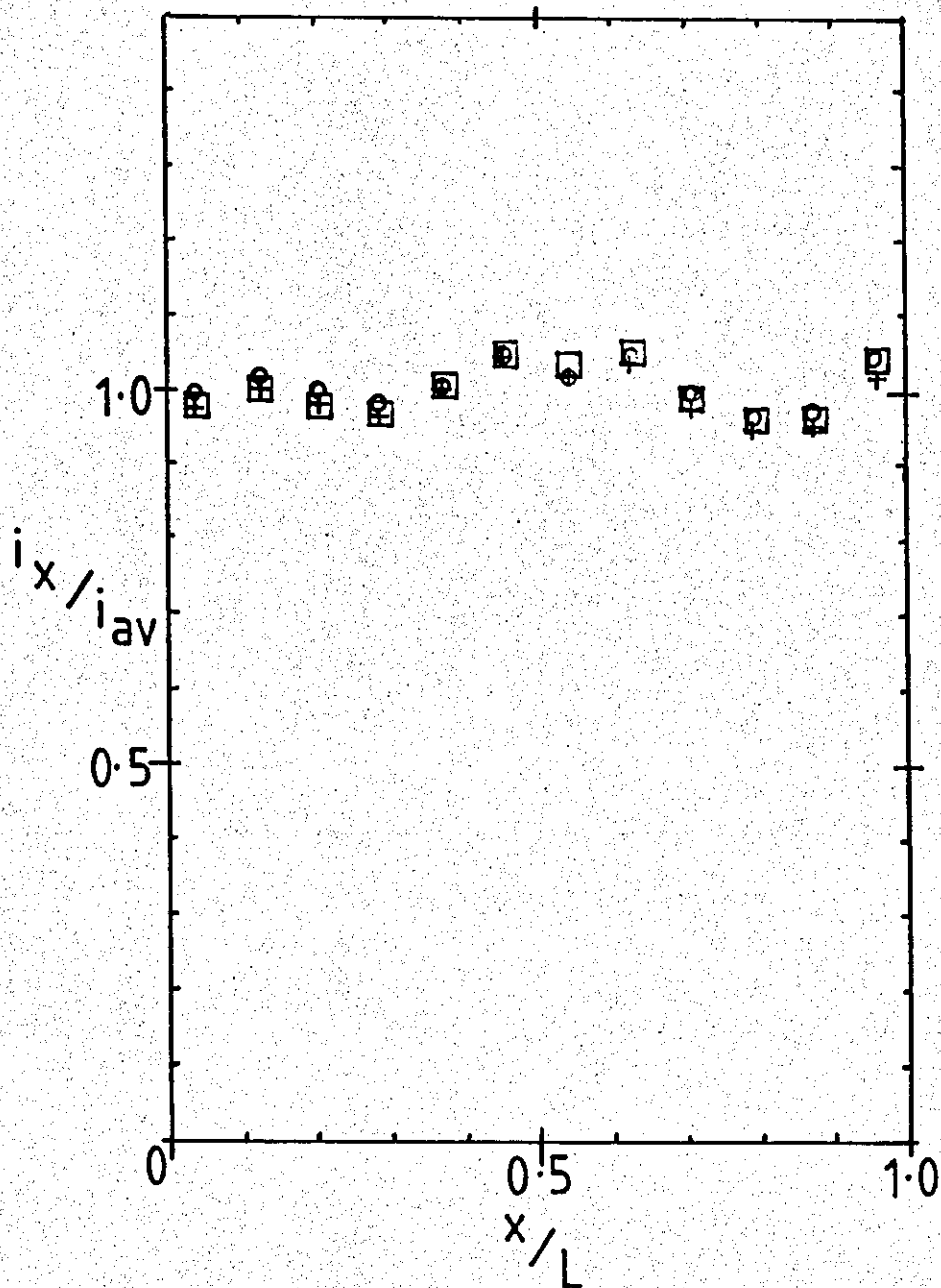


Fig.4.138 Longitudinal current distribution (nickel deposition) along a segmented cathode, 11.7 equivalent diameters in length, at 70°C and Re 16,250.

Anode length = 9cm.

+ - $i_{av} = 2.20 \text{ A cm}^{-2}$

o - $i_{av} = 2.22 \text{ A cm}^{-2}$

□ - $i_{av} = 2.22 \text{ A cm}^{-2}$

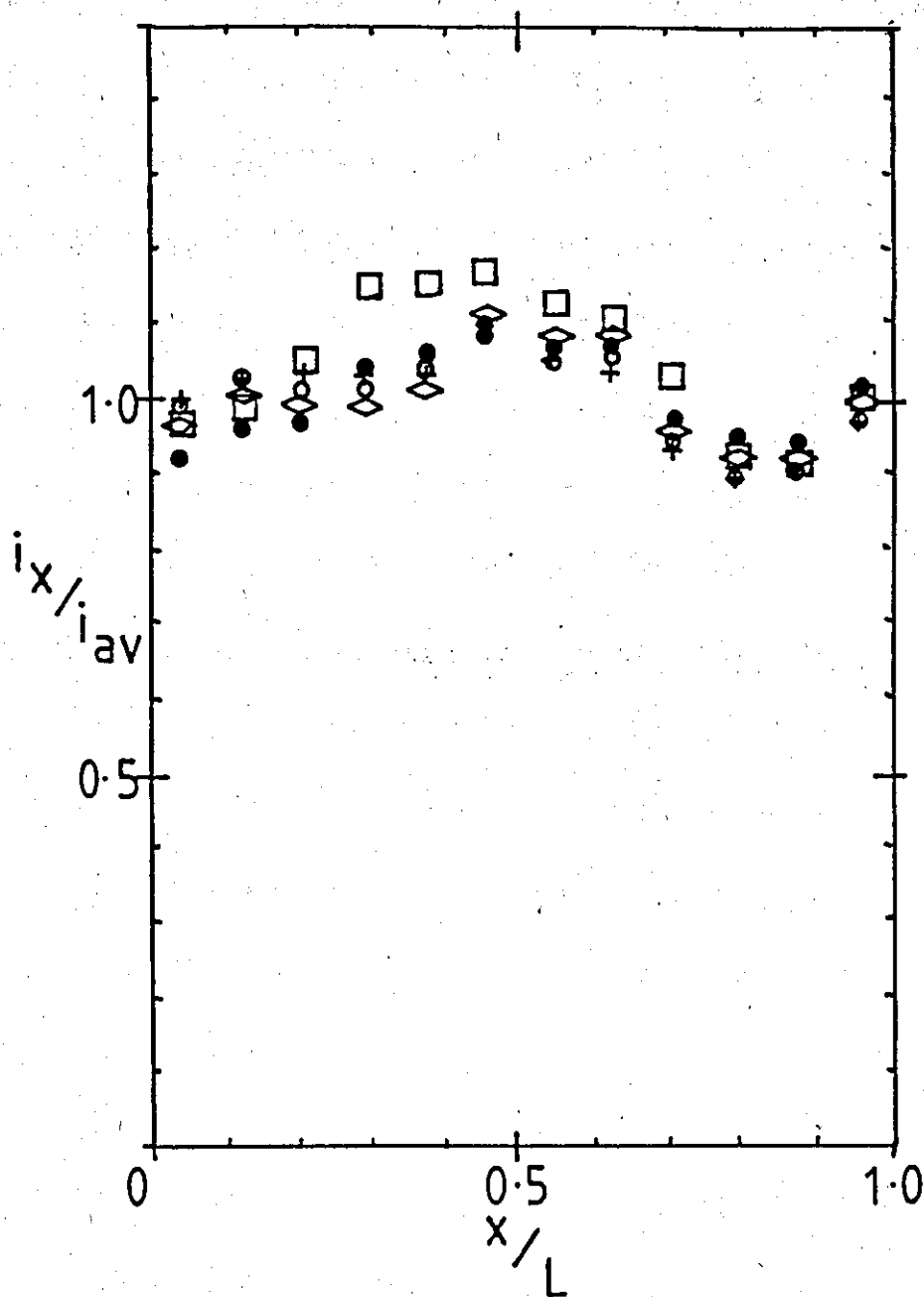


Fig. 4.139 Effect of flow rate on the current distribution on a segmented cathode 11.7 equivalent diameters in length, at an average current density of $1.12 \pm 0.03 \text{ A cm}^{-2}$. Anode length = 9 cm. 70°C

- + - Re 1,500
- o - Re 2,200
- - Re 4,280
- ◇ - Re 6,700
- - Re 12,550

All the deposits were sound and coherent. The current distribution was relatively uniform at all flow rates ($i_x = 1.0 \pm 0.1 i_{av}$). In general the local current density decreased at the leading edge and increased at the trailing edge as the electrolyte velocity increased.

Nickel foils were electroformed at 1 A cm^{-2} and flow rates of $Re\ 4,050 \pm 250$ and $Re\ 13,200 \pm 700$ (Table 4.38). Both foils were sound and deposited at high current efficiency (98%), Visually brighter regions were observed close to the leading edge.

The main deposit areas were of similar fine grain structure at both flow rates (Fig.4.140). Some sub-grain structure was observed at $Re\ 13,200 \pm 700$ (Fig.4.140). The microhardness of the foils was $264 \pm 25 \text{ kg mm}^{-2}$. Deposit porosity was less than at 60°C .

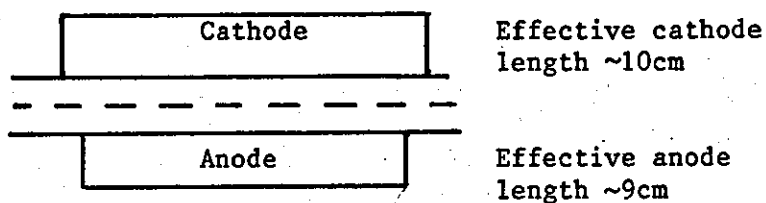
At the lower flow rate ($Re\ 4,050 \pm 250$) leading and trailing edge sections showed a bulbous structure (e.g. Fig.4.141a). Close to the edge the deposit was fine grained. At the high flow rate ($Re\ 13,200 \pm 700$) the bulbous ridge was not observed and only fine structures were observed (Fig.4.140b).

8cm anodes and 7cm anodes with 10cm cathodes

The current distribution was measured using 7 and 8cm anodes over an average current density range of 0.31 to 0.93 A cm^{-2} . (Fig. 4.142 and 4.143). Deposits of good visual appearance were produced at all current densities. The highest local current densities ($1.11 \pm 0.06 i_{av}$) were observed in the central main deposit area ($x/L\ 0.3 - 0.7$). The lowest edge current densities ($<0.7 i_{av}$) were observed with 7cm anodes. In these areas slight changes in local current densities were observed. The overall pattern here at 70°C was similar to that observed at 60°C (cf.Figs. 4.133 and 4.134).

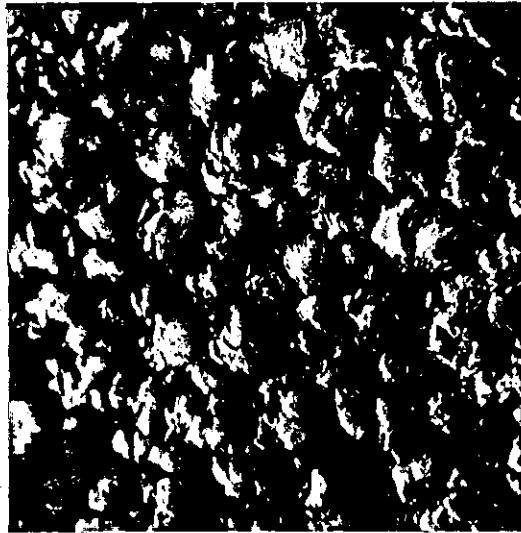
Examination of electroformed nickel foils showed that the brighter regions were in the central main deposit area (Table 4.39).

Electrode Geometry

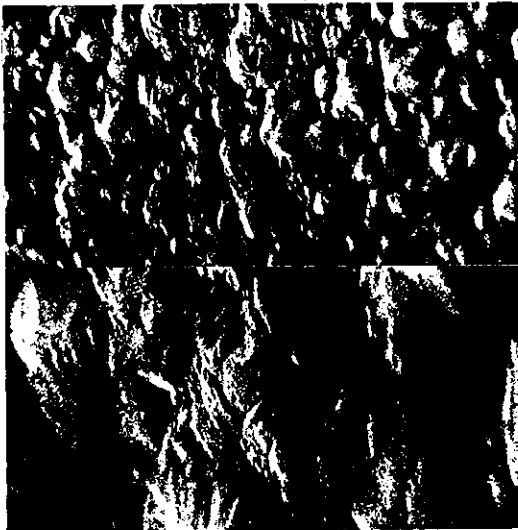


	Average cathode current density i_c/Acm^{-2}	Time t secs	Average deposit thickness μm	Average anode current density i_a/Acm^{-2}	Visual appearance of electroform
Re 4,050 \pm 250	1.01	74	26	1.12	
Re 13,200 \pm 700	1.01	74	26	1.12	

Table 4.38 Nickel foils deposited on cathodes 11.7 de in length at 70°C. Anode length 9cm.



a) 25° tilt



b) 30 ° tilt



c) 30° tilt

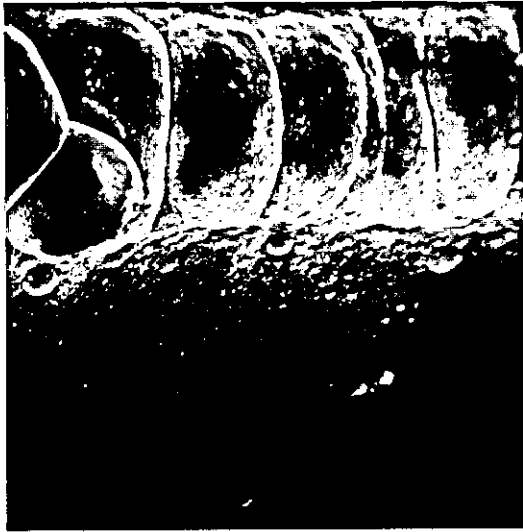
Fig.4.140

SEM micrographs of surfaces of foils of nickel deposited at 1.01 A cm^{-2} , cathode length 10 cm and anode length 9 cm (70°C). Main deposit sections.

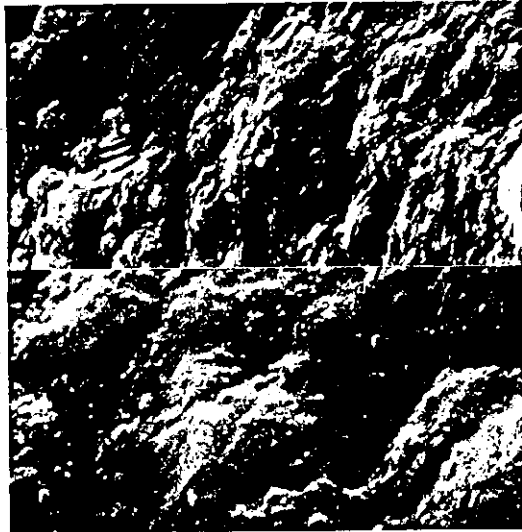
a) Re $4,050 \pm 250$, ~ 9.6 cm from leading edge (2,000x)

b) Re $13,200 \pm 700$, ~ 5 cm from leading edge (top 2,000x, bottom 10,000x)

c) Re $13,200 \pm 700$, ~ 5 cm from leading edge (50,000x)



a)



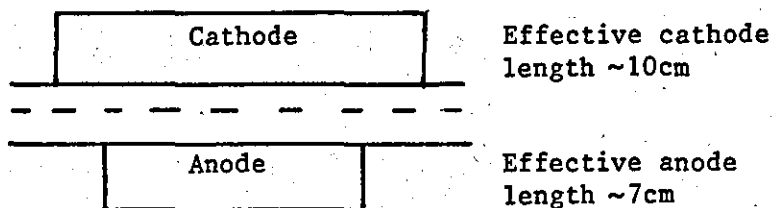
b)

Fig.4.141 SEM micrographs of surfaces of foils of nickel deposited at 1.01 A cm^{-2} , cathode length 10 cm and anode length 9 cm (70°C). Leading edge sections (30° tilt).

a) $\text{Re } 4,050 \pm 250$, leading edge (200x)

b) $\text{Re } 13,200 \pm 700$, leading edge (top 2,000x, bottom 10,000x)

Electrode Geometry




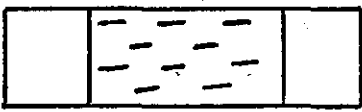
	Average cathode current density i_c / Acm^{-2}	Time t secs	Average deposit thickness μm	Average anode current density i_a / Acm^{-2}	Visual appearance of electroform
$\text{Re } 4,050 \pm 250$	1.53	50	26	2.19	
$\text{Re } 13,200 \pm 700$	1.97	42	28	2.81	 Flow direction

Table 4.39 Nickel foils deposited on cathodes 11.7 de in length at 70°C. Anode length 7cm.

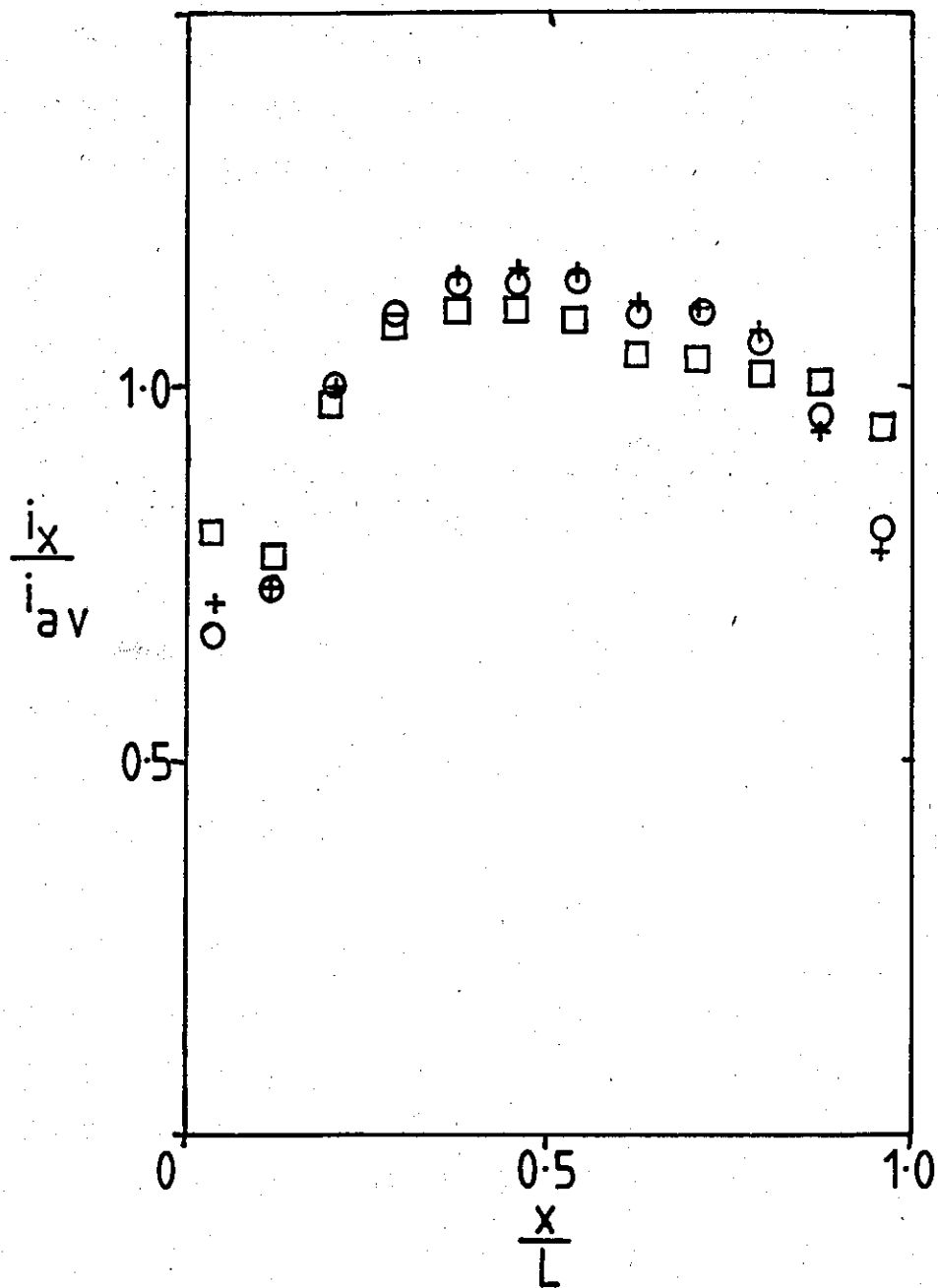


Fig.4.143 Longitudinal current distribution (nickel deposition) along a segmented cathode, 11.7 equivalent diameters in length at 70°C and $Re\ 9,450 \pm 250$.
Anode length = 8cm.

+ - $i_{av} = 0.31$ A cm $^{-2}$
 O - $i_{av} = 0.62$ A cm $^{-2}$
 □ - $i_{av} = 0.94$ A cm $^{-2}$

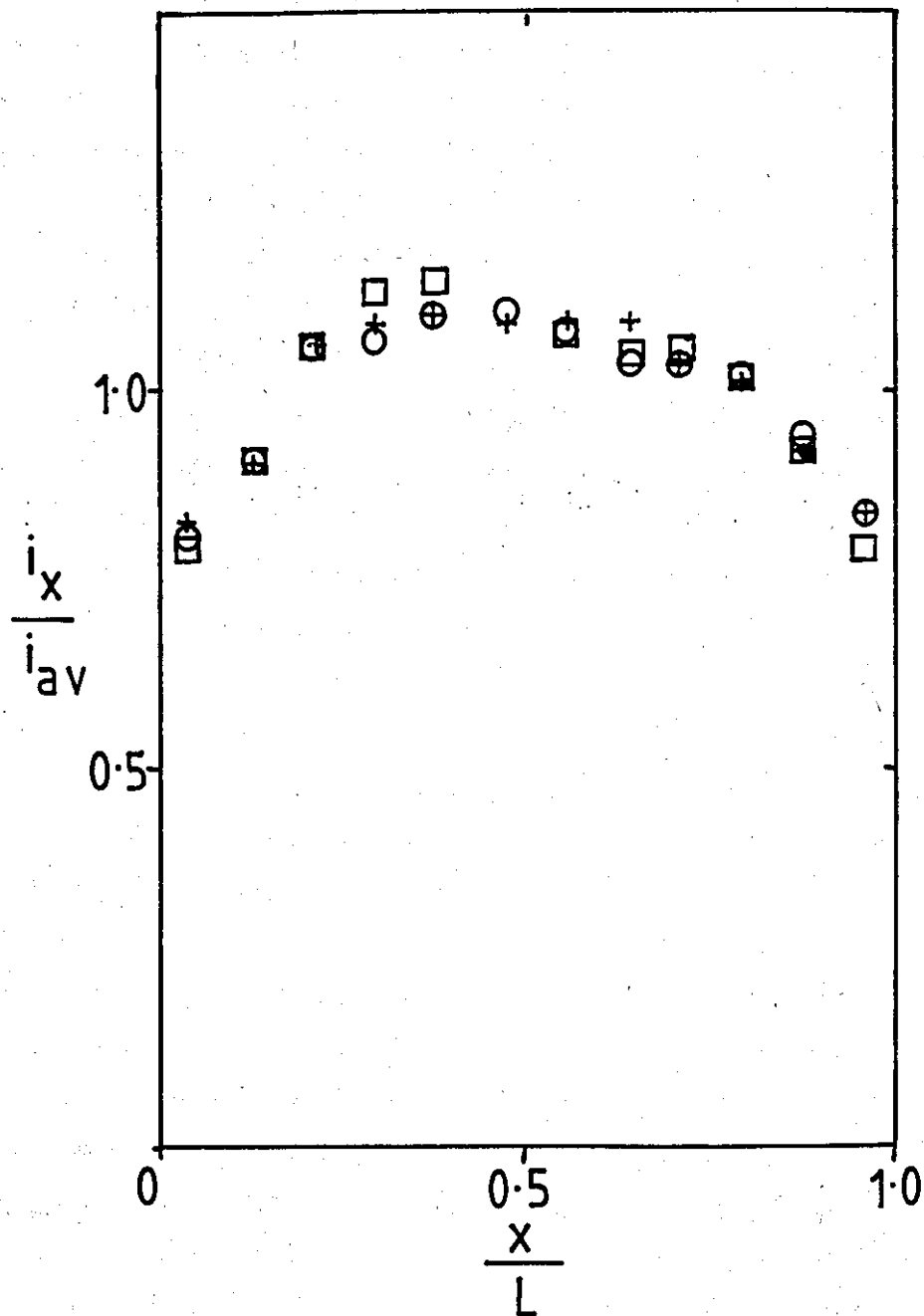


Fig.4.142 Longitudinal current distribution (nickel deposition) along a segmented cathode, 11.7 equivalent diameters in length at 70°C and $Re\ 9,450 \pm 250$.
Anode length = 7cm.

- + - $i_{av} = 0.31 \text{ A cm}^{-2}$
- O - $i_{av} = 0.63 \text{ A cm}^{-2}$
- - $i_{av} = 0.94 \text{ A cm}^{-2}$

The current densities (1.53 and 1.97 A cm^{-2}) were the maximum attainable with the available power supply at each flow rate ($\text{Re } 4,050 \pm 250$ and $13,200 \pm 700$ respectively). At 1.53 A cm^{-2} , the main deposit region was fine grained with well defined grain boundaries (Fig.4.144). Near the leading and trailing edges, the structure was less well defined and there was pitting in the leading edge area. Some larger features $10\text{-}15\mu\text{m}$ in diameter were also observed.

At 1.97 A cm^{-2} , the deposit appeared 'streaked' in lines parallel with the flow direction. At high magnification no distinct grain structure was observed although microporosity was present.

The leading edge of the foil deposited at 1.97 A cm^{-2} was bulbous (similar to that shown in Fig.4.141a). Many "mounds" and parallel ridges were observed close to the leading and trailing edges (e.g. Fig.4.145).

Summary of current distribution effects at 70°C , $L/d_e = 11.7$

The results were in agreement with the previous findings at 60°C (p.226). A reasonably uniform cathodic current distribution was observed when using a 9cm anode. With this optimised geometry and high flow rates ($>\text{Re } 13,000$), good sound deposits may be obtained at current densities in excess of 2 A cm^{-2} . At lower flow rates ($\text{Re } 4,050 \pm 250$) good deposits may be electroformed at a current density of 2 A cm^{-2} . At all flow rates, the maximum current density was limited by the cell voltage requirement exceeding 30V .

(b) Studies using short electrodes ($L/d_e = 2.92$) at 70°C

It was of interest to carry out a limited experimental study of the effect of anode length on current distribution at short cathodes ($2.92 d_e$) to provide broad confirmation of the long electrode work. As the measurement of local current densities was difficult, due to the short electrode length, the programme was confined to electroforming studies at very high current densities in the range

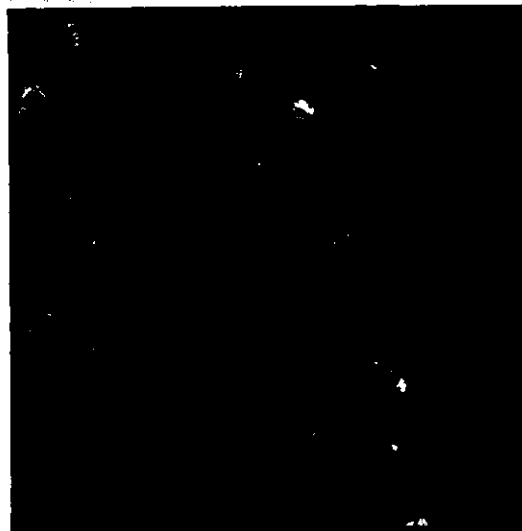


Fig.4.144 SEM micrograph of surface of nickel foil deposited at 1.53 A cm^{-2} , $\text{Re } 4,050 \pm 250$, cathode length 10 cm and anode length 7 cm (70°C). Main deposit section ~ 5 cm from leading edge ($2,000\times, 0^\circ$ tilt).

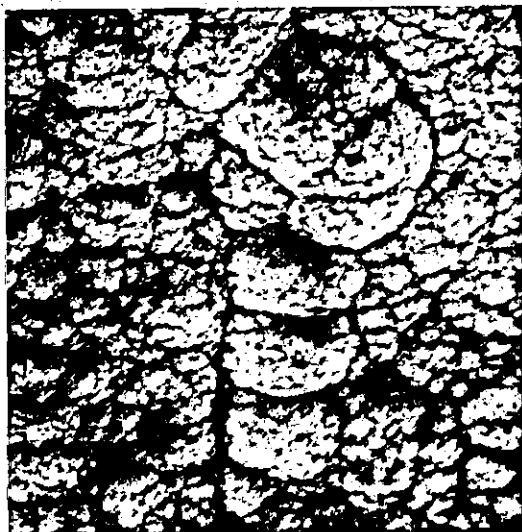


Fig.4.145 SEM micrograph of surface of nickel foil deposited at 1.97 A cm^{-2} , $\text{Re } 13,200 \pm 700$, cathode length 10 cm and anode length 7 cm (70°C), ~ 0.04 cm from leading edge (0° tilt, 1,000x).

1.89 to 2.48 A cm⁻². Nickel foils were deposited using anode lengths of 25, 1.85, 1.3, 1.0 and 0.85 cm and the distribution of sound deposit noted in each case.

The foils were electroformed from the concentrated nickel sulphamate solution at 70°C and a high flow rate, corresponding to Re 12,950 ± 1,000 to effect very fast deposition rates.

The prepared Nickel 200 substrates were 2.92 in length. The cathode occupied the full width of the square channel 3cm in width and equivalent diameter 0.857 cm. The electrolytic nickel anode was positioned directly opposite the cathode.

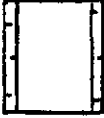





In each experiment, electrolysis was continued for a specified period of time sufficient to deposit foils 26 to 47µm thick for subsequent visual and microscope examination after removal from the cathode surface.

Deposition using 25cm anodes

This anode length corresponds to the normal geometry of cell used for electroforming studies at 60°C (p.185). The experimental conditions and the foil appearance are summarised in Table 4.40.

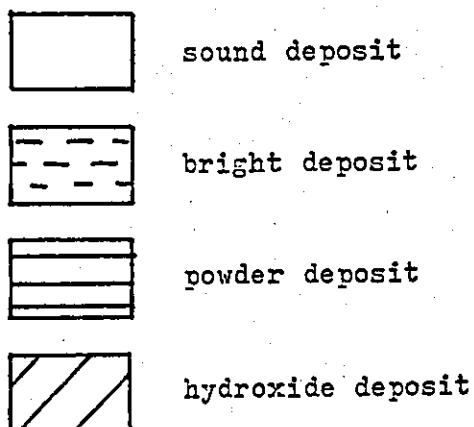
The attempt at electroforming nickel at a current density of 2.48 A cm⁻² resulted in the deposition of green-black hydroxide deposits on the cathode surface. During electrolysis, the cell voltage was about 30V and large volumes of gas were evolved. However, a nickel foil was electroformed at 1.2 A cm⁻², to give a deposit of 21µm thick. The foil was sound and coherent and deposited at high current efficiency (~95%). The main deposit was uniform and semi-bright in appearance. A narrow band (1mm) of bright nickel was observed at the leading and trailing edges. There was little visible porosity. The maximum current density for a good deposit under these conditions was about 1.4 A cm².

Further experiments were designed to examine the effect of the anode length on the edge effects and the maximum current density.

Anode length cm	Average cathode current density $A\ cm^{-2}$	Time t secs	Average deposit thickness μm	Average anode current density $A\ cm^{-2}$	Visual appearance of electroforms
25	1.2	50	21	0.52	
25	2.48	29	-	1.0	
1.85	2.48	29	25	3.4	
1.3	2.48	31	26	4.8	
1.0	2.31	60	47	5.8	
0.85	1.89	65	42	5.6	

Flow direction
→

Table 4.40 Nickel foils deposited on cathodes 2.92 equivalent diameters (2.5cm) in length at 70°C and $Re\ 12,950 \pm 1,000$.



Deposition using anodes 1.85 and 1.3 cm in length

The foils were electroformed at a current density of 2.48 A cm^{-2} to give deposits $28 \pm 3 \mu\text{m}$ thick.

Using anodes 1.85cm in length, 80% of the foil area was sound and coherent. The structure of the main deposit section was very fine and individual grains were unresolvable (Fig.4.146c). Some larger features and small micro-cavities were observed. A band of green-black hydroxide, $\sim 0.5\text{cm}$ in width was deposited at the leading edge. Towards the trailing edge, the foil was visibly brighter.

Sound and bright central main deposit areas were also observed for electroforms deposited using 1.3cm anodes. This region of the deposit showed no visible porosity. Hydroxide was deposited at the leading and trailing edges of the foil.

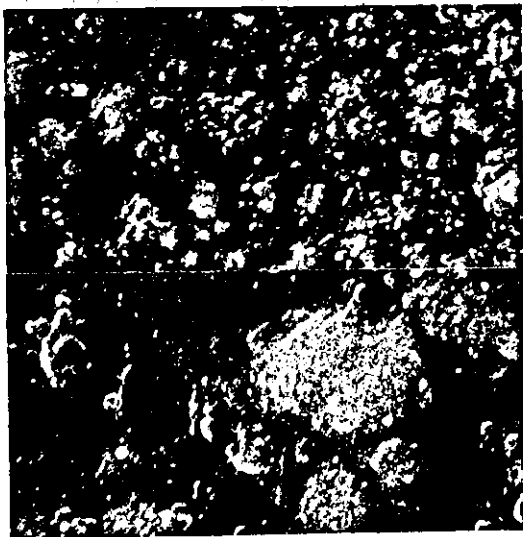
During deposition, the cell voltage was 30V. The anodic current density exceeded 4.5 A cm^{-2} and a large volume fraction of gas was evolved within the inter-electrode gap. Therefore the high electrolyte resistance in this region resulted in high cell voltages.

Deposition using anodes 1.0 and 0.85cm in length

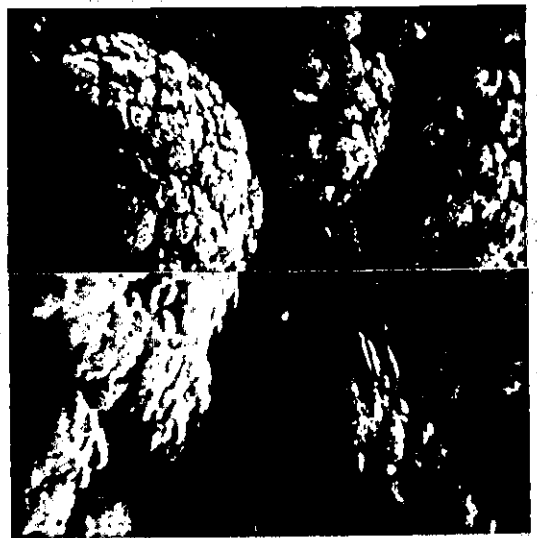
Foils were electroformed at 2.31 and 1.89 A cm^{-2} using respectively 1.0 and 0.85cm anode lengths to give deposits $44 \pm 2 \mu\text{m}$ thick. The current efficiency was close to 100%.

Using 1cm anodes, more than 95% of the foil area was sound and coherent. The main deposit area was bright and pore free. The structure was fine grained ($< 2 \mu\text{m}$), although many larger features were apparent (Fig.4.146b). The leading edge showed indications of a powder type deposit but the trailing edge was semi-bright in appearance.

The anodic current density was $> 5.7 \text{ A cm}^{-2}$ and hence the electrolyte resistance was high. The cell voltage ($> 30\text{V}$) exceeded the maximum output of the power supply. A maximum deposition current density of $\sim 2.3 \text{ A cm}^{-2}$ was found using 1cm anodes.



a) 0° tilt



b) 30° tilt



c) 30° tilt

Fig.4.146 SEM micrographs of surfaces of foils of nickel deposited at $Re\ 12,950 \pm 1,000$ on cathodes 2.5 cm ($70^\circ C$, $L/de \sim 2.92$) in length. Main deposit sections.

- a) $1.89\ A\ cm^{-2}$, anode length $\sim 0.85\ cm$
- b) $2.31\ A\ cm^{-2}$, anode length $\sim 1\ cm$
- c) $2.48\ A\ cm^{-2}$, anode length $\sim 1.85\ cm$
(top 2,000x, bottom 10,000x).

The main deposit section of foil deposited at 1.89 A cm^{-2} using 0.85cm anodes was bright with no visible porosity. S.E.M. examination showed the foil surface to be fine grained with some micro-porosity at the grain boundaries (Fig.4.146a). A few larger mound type features were also observed. The average microhardness of this area was 324 kg mm^{-2} .

Narrow bands (2mm) of semi-bright nickel were observed at leading and trailing edges. Optical microscopy of this area indicated many ridge type features and other surface reliefs parallel with the flow direction (Fig.4.147).

The maximum cathodic current density obtained with a 0.85cm anode was 1.89 A cm^{-2} . At this current density the corresponding anodic current density was $>5.7 \text{ A cm}^{-2}$ and the cell voltage exceeded 30V. Further increases in current density were not possible using the existing power supply with a maximum output of 30V.

Summary of current distribution at 70°C , L/de 2.92

- a) With a cathode 2.92 equivalent diameter (2.5cm) in length, a reduction in anode length, from 25cm to $<2\text{cm}$, resulted in an increase in the maximum current density for a sound deposit. Edge effects were less pronounced. Good nickel deposits may be electroformed at current densities of $\sim 2 \text{ A cm}^{-2}$ with an anode $<1\text{cm}$ in length and a flow rate of Re $12,950 \pm 1,000$.
- b) At high cathodic current densities and very short anodes, the anodic current density was very high and large volumes of anodic gas may be rapidly evolved on an electrode of very small area. The large volume fraction of gas within the inter-electrode gap may result in an increased electrolyte resistance and hence high cell voltages if the gas cannot be removed from this region at a sufficiently fast rate.

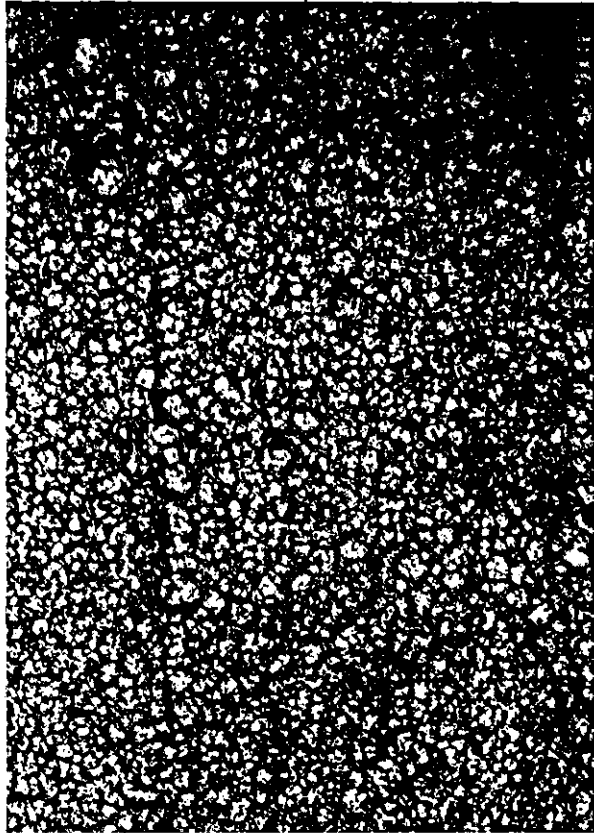


Fig.4.147 Optical micrograph of the surface of a foil of nickel deposited at $Re\ 12,950 \pm 1,000$ and $1.89\ A\ cm^{-2}$ on cathodes 2.5 cm ($70^{\circ}C$, $L/de\ \sim 2.92$) in length with an anode length of 0.85 cm. Leading edge section (200x).

- c) The maximum deposition rate (for anodes <1cm in length) was limited by the 30V maximum output voltage of the power supply. A cell voltage of 30V was achieved when the anodic current density was $>4.5 \text{ A cm}^{-2}$ at $\text{Re } 12,950 \pm 1,000$.

4.4.2 Polarisation measurements in the electroforming of nickel foils

(a) Anodic polarisation measurements

The polarisation curves for the anodic behaviour of nickel anodes were determined in Cell 2 using 9cm long anodes and 10cm long cathodes and the Luggin capillary arrangements previously described (Section 3.5.2) with a 3.8m calomel reference electrode. At low current densities ($<0.06 \text{ A cm}^{-2}$) a potentiodynamic technique was used whereas at high current densities ($0.006 - 1.1 \text{ A cm}^{-2}$) the cell was operated galvanostatically. Polarisation curves were determined under the following conditions:

- (i) The low current density polarisation curves were determined at 60°C for Reynolds numbers in the range $\text{Re } 3800 - 12,210$ in a solution containing no chloride ions.
- (ii) Polarisation curves were determined at 60°C at $\text{Re } 5825 \pm 75$ in solutions containing 5.5 g l^{-1} nickel chloride (as $\text{NiCl} \cdot 6\text{H}_2\text{O}$) for both low and high current density ranges.
- (iii) For comparison purposes the low current density polarisation curves were determined at 70°C at $\text{Re } 5825 \pm 75$ in solutions containing no chloride ions.

(i) Anodic polarisation in the absence of chloride ions at 60°C

The low current density ($i < 0.06 \text{ A cm}^{-2}$) polarisation curves for the Reynolds number range $\text{Re } 5,700$ to $\text{Re } 12,210$ are shown on semi-logarithmic co-ordinates in Fig.4.148. The anode potential was referred to the Standard Hydrogen Electrode (SHE) and the current density to the apparent electrode area. The rest potentials of the electrolytic nickel anode were found to be in the range 0.036 to 0.13V (SHE).

At potentials $E_a < 0.15\text{V}$ (SHE), the potential/log. (current density) relationship was linear in form. In this region active dissolution of nickel was occurring (A-B, Fig.4.148).

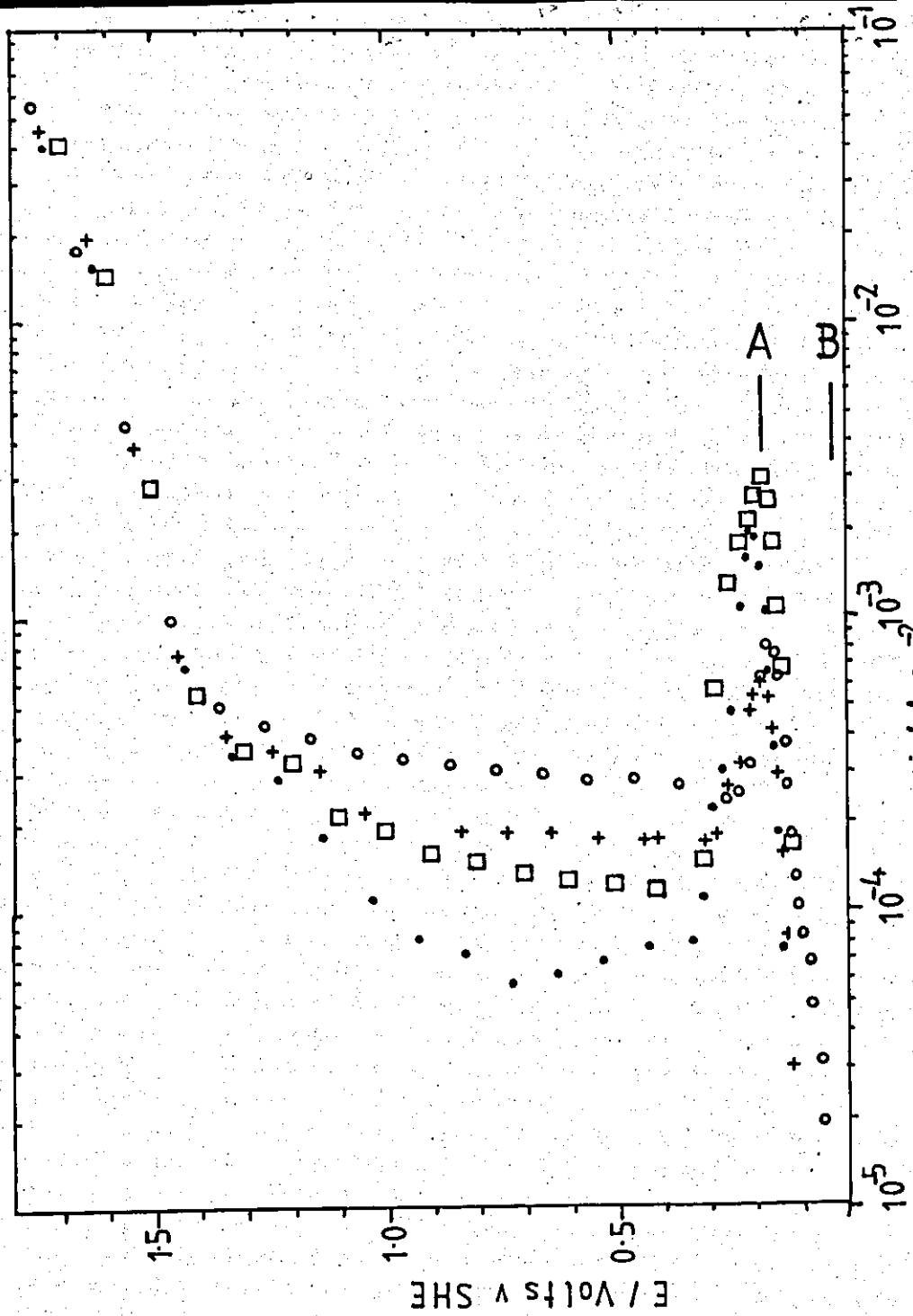


Fig.4.148 Anodic polarisation of electrolytic nickel at 60°C ($E < + 1.761$ V SHE).

electrolyte composition : $600 \text{ g l}^{-1} \text{ Ni (NH}_2\text{SO}_3)_2$
 $40 \text{ g l}^{-1} \text{ H}_3\text{BO}_3$

- + - Re 5,750
- o - Re 5,750
- - Re 7,950
- - Re 12,210

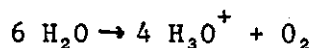
A peak in the current density was observed at potentials between 0.15 and 0.21V (SHE). The maximum current density for active dissolution was designated i_{crit} . The values of i_{crit} were in the range 2.8×10^{-4} A cm^{-2} to 3.05×10^{-3} A cm^{-2} and tended to increase with increasing flow rate. Further increases in potential resulted in the onset of passivity and a decrease in the current density.

It is interesting to note that the range of current densities over which active nickel dissolution predominates are very low as compared to the normal operating current densities during foil formation (Sec.4.3) (0.05 to >2 A cm^{-2}).

The complete passivation of the anode was marked by an inflection at potentials of $\sim 0.3 \pm 0.02$ V (SHE) (Flade potential, E_f). The passivation current density was between 3×10^{-5} and 3×10^{-4} A cm^{-2} . There was no clear relationship between the passivation current density and Reynolds number.

It would appear that, in the absence of chloride, the anode would be in the passive state during foil formation and the main anodic process would be oxygen evolution.

At potentials $E_a > 1.0$ V (SHE) the current density began to increase. The increase in current density was particularly marked at $E_a > 1.4$ V (SHE) and oxygen was evolved on the anode surface by the overall reaction



The simultaneous production of hydrogen ions resulted in a decrease in the pH of the electrolyte.

On the completion of the potential scan a brown film was observed on the anode surface.

(ii) Anodic polarisation in solutions containing chloride at 60°C

The low current density polarisation curve ($i < 0.06 \text{ A cm}^{-2}$) determined at $Re \ 5,825 \pm 75$ in solution containing 5.5 g l^{-1} nickel chloride is shown in Fig.4.149.

At potentials $E_a > 0.08 \text{ V (SHE)}$, the potential/log (current density) relationship was linear in form (A-B). This region represented the active dissolution of nickel and reached a current density maximum at 0.12 V (SHE) . This current density maximum was similar to that observed in the absence of chloride (cf Fig.4.148). The value of $i_{crit}(a)$ was $2.7 \times 10^{-3} \text{ A cm}^{-2}$, i.e. slightly higher than that observed previously in the absence of chloride. At higher potentials, the anode current density decreased and then increased within the potential range (0.1 - 0.4V).

A second current density maximum was observed at $E_a \approx 0.49 \text{ V (SHE)}$, with a critical current density ($i_{crit}(b)$) of $3.0 \times 10^{-3} \text{ A cm}^{-2}$.

The anode was passivated at a potential $E_f(b) = 0.61 \text{ V (SHE)}$. The passivation current density was comparable to that observed in the absence of chloride ($10^{-4} - 10^{-5} \text{ A cm}^{-2}$).

The current density increased again at potentials $E_a > 0.95 \text{ V (SHE)}$. Oxygen was evolved on the anode surface at potentials $> 1.25 \text{ V (SHE)}$. (cf $> 1.4 \text{ V (SHE)}$ in the absence of chloride).

It would appear that, with the low levels of chloride used no significant improvement in the active dissolution of nickel was observed. The second active dissolution peak may be associated with a nickel-chloride complex.

At high current densities ($> 10^{-3} \text{ A cm}^{-2}$), the predominant reaction was oxygen evolution. (Fig.4.150). This represents the normal cell operating conditions. The high rate of gas evolution results in a significant volume fraction of gas in the region close to the anode surface (particularly at low flow rates) At the highest current densities, an extra series resistance may be included in the potential

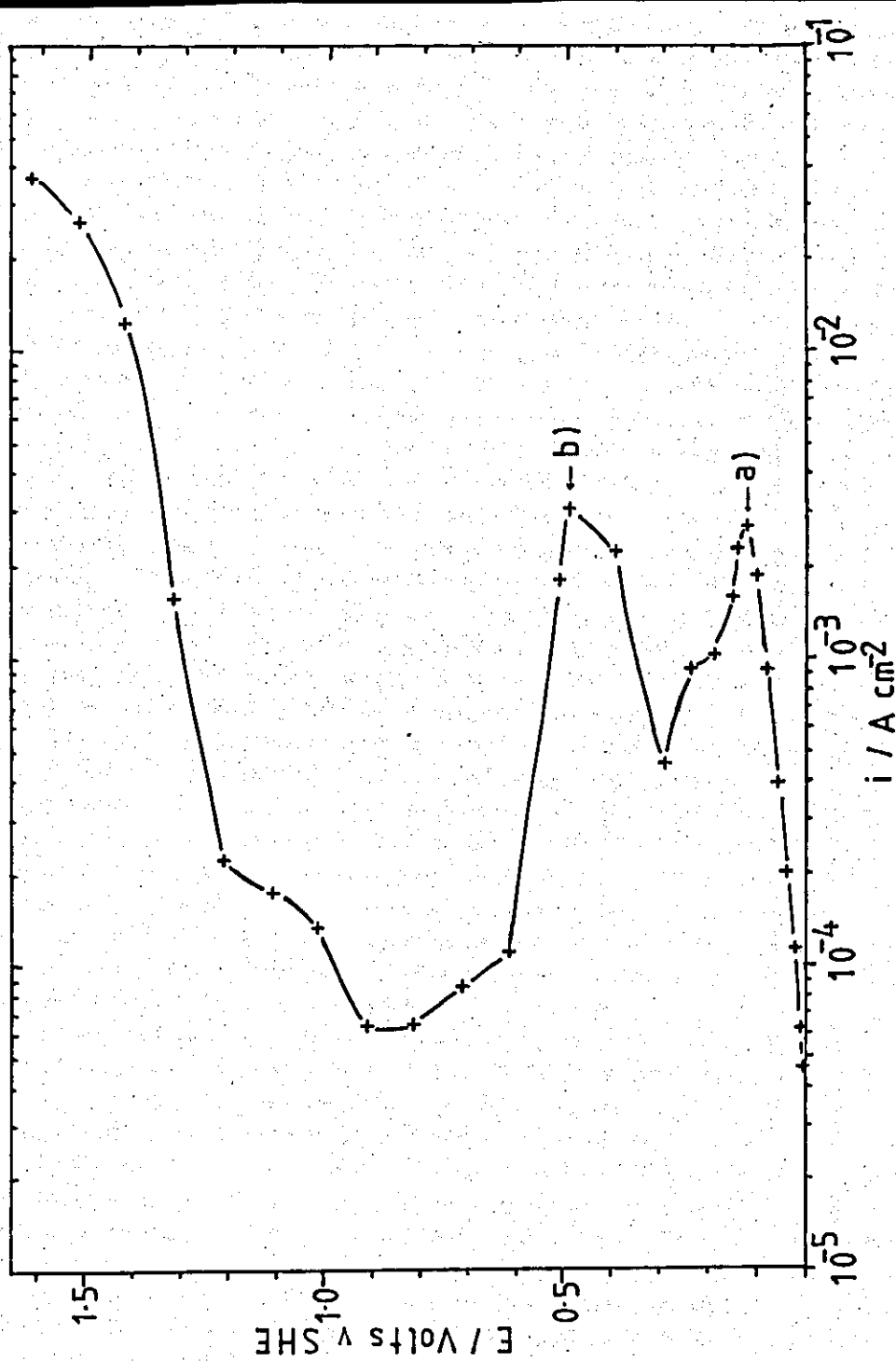


Fig.4.149 Anodic polarisation of electrolytic nickel at 60°C and $Re\ 5,875 \pm 75$ ($E < + 1.761$ SHE).
 electrolyte composition: 600 g l⁻¹ Ni(NH₂SO₃)₂
 40 g l⁻¹ H₃BO₃
 5.5 g l⁻¹ NiCl₂ · 6H₂O

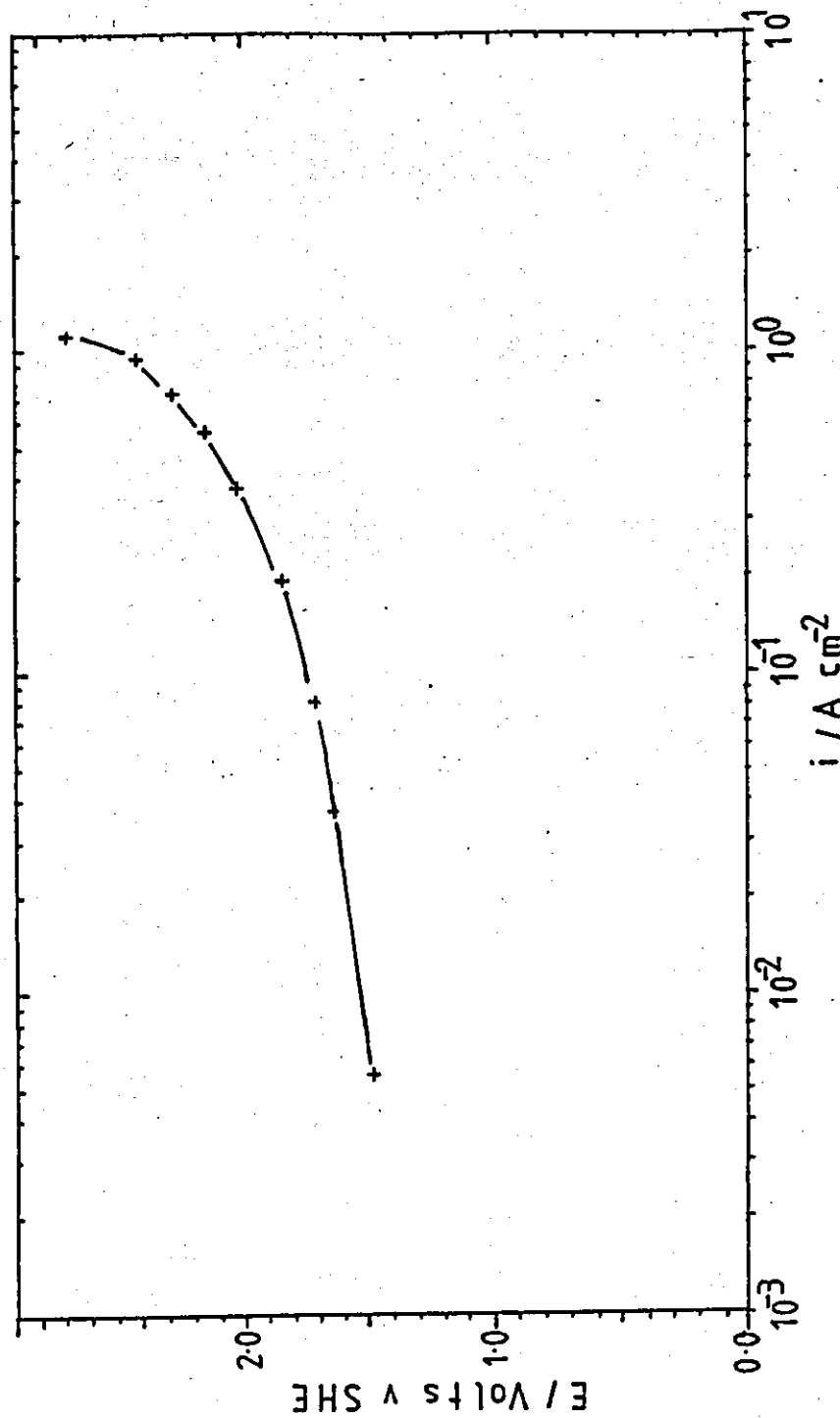


Fig.4.150 Anodic polarisation of electrolytic nickel at 60°C and $Re\ 5,825 \pm 75$ ($E > + 1.474$ V SHE)
 electrolyte composition : 600 g l^{-1} $\text{Ni}(\text{NH}_2\text{SO}_3)_2$
 40 g l^{-1} H_3BO_3
 5.5 g l^{-1} $\text{NiCl}_2 \cdot 6\text{H}_2\text{O}$

measurements. Film formation was not observed on anodes operated at very high current densities.

(iii) Anodic polarisation in the absence of chloride ions at 70°C

The low current density ($i < 0.06 \text{ A cm}^{-2}$) polarisation curve determined at $Re \ 5,825 \pm 75$ is shown on semi-logarithmic coordinates in Fig.4.151. The features of the curve are similar to those observed at 60°C (cf. Fig.4.148). The linear region of active dissolution, at potentials 0.15V (SHE) (A-A) reaches a maximum current density (i_{crit}) at $\sim 1.5 \times 10^{-3} \text{ A cm}^{-2}$. This value is slightly greater than that observed at 60°C ($\sim 7 \times 10^{-4} \text{ A cm}^{-2}$, p.258). Passivation of the anode was complete at a potential (E_f) of $\sim 0.3\text{V}$ (SHE). Similar values were found at 60°C. Oxygen was evolved on the passive nickel surface at $E > 1.4\text{V}$ (SHE). Anode corrosion was not improved significantly by cell operation at 70°C.

Summary of anodic polarisation studies

- a) At 60°C in the absence of chloride, the region of active dissolution was characterised by a single current density maximum (Fig.4.148). This current density (i_{crit}) was $< 10^{-2} \text{ A cm}^{-2}$ for all flow conditions. However, the value of i_{crit} did tend to increase with increasing Reynolds number.
- b) At 70°C a slight increase in the value of i_{crit} was observed.
- c) The onset of passivity occurred at $0.3 \pm 0.02\text{V}$ (SHE) (E_f) at both 60° and 70°C (cf Fig.4.148 and 4.151).
- d) Oxygen was evolved on the passivated nickel surface at potentials $> 1.4\text{V}$ (SHE) at both 60° and 70°C (cf Fig.4.148 and 4.151).
- e) In the presence of chloride, two current density maxima were observed in the active dissolution region (Fig.4.149). The current density for active dissolution was $< 10^{-2} \text{ A cm}^{-2}$. The addition of chloride to the electrolyte did not result in significant improvements in anode corrosion for normal cell operation.

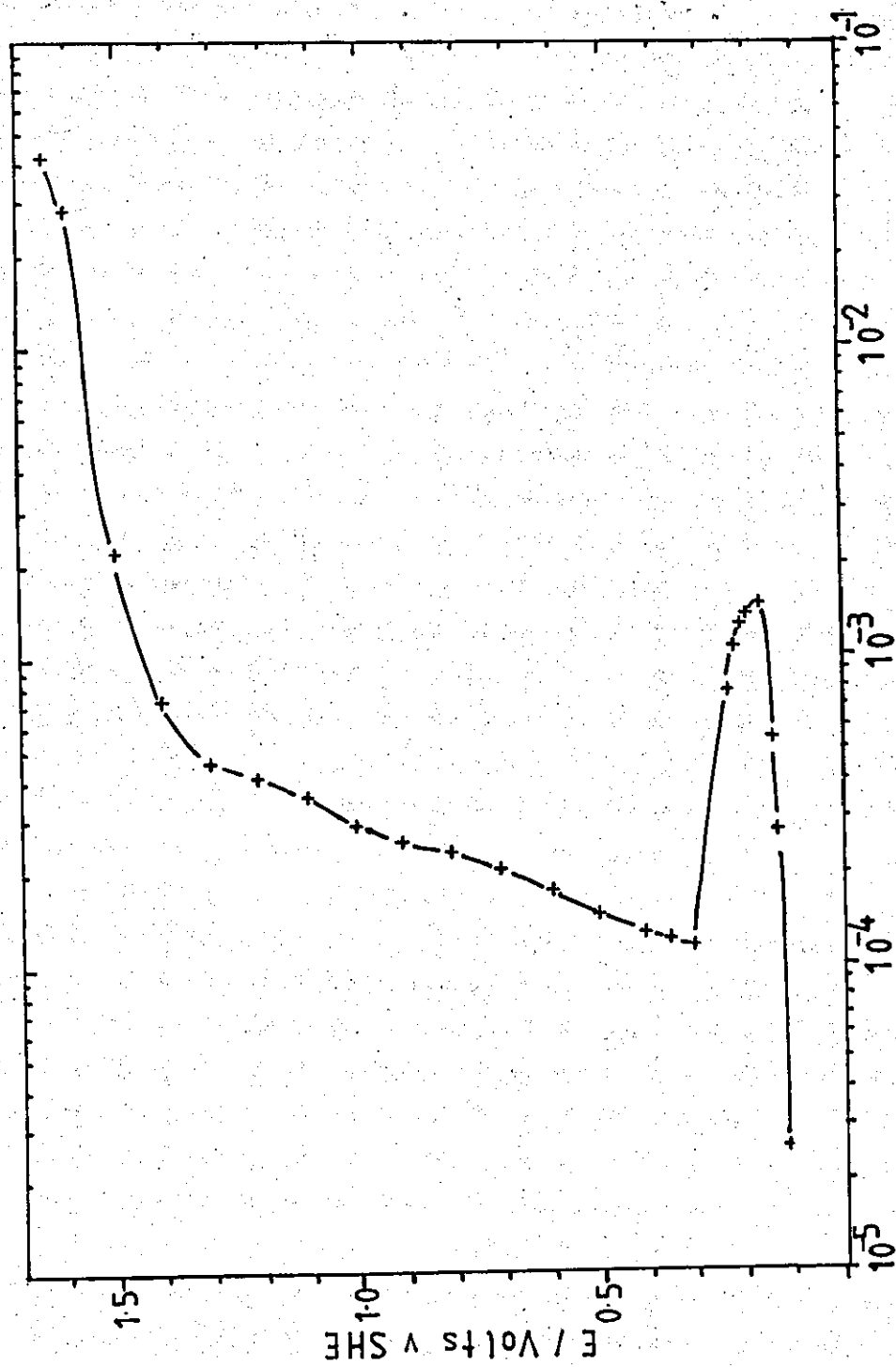


Fig.4.151 Anodic polarisation of electrolytic nickel at 70°C
 and $Re\ 5,825 \pm 75$ ($E < + 1.761$ V SHE)
 electrolyte composition : $600\ g\ l^{-1}\ Ni(NH_2SO_3)_2$
 $40\ g\ l^{-1}\ H_3BO_3$

f) Oxygen was evolved at potentials $>1.3V$ (SHE) in the presence of chloride.

The values of i_{crit} and E_f for solutions without chloride ions operated at $60^\circ C$ are summarised in Table 4.41 for the Reynolds number range Re 3,800 to Re 12,210. The peak current density increased with increasing flow rate. In Fig.4.152, i_{crit} is shown as a function of Reynolds number (on log coordinates). The slope of this line was ~ 2 , indicating a proportionality of the following form

$$i_{crit} \propto Re^2$$

It is apparent that even at the highest cell flow velocities, the anode would remain passivated at current densities $>10^{-2} A cm^{-2}$. The predominant reaction would therefore be oxygen evolution. Evolution of large volumes of oxygen, close to the anode surface may result in a significant increase in apparent electrolyte resistance.

Prolonged use of the anode, under these conditions resulted in heavily pitted anodes. The average anode dissolution efficiency was estimated to be $<25\%$.

(b) Cathodic Polarisation

The cathodic polarisation relationships for the electrolysis of the concentrated nickel sulphamate electrolyte were determined in Cell 2. The cathodes were 10cm long and pre-plated with nickel. Anodes 9cm long were used. The Luggin capillary arrangements described previously (Section 3.5.2) with a 3.8 M calomel reference electrode were again used. At low current densities ($<0.06 A cm^{-2}$) the potentiodynamic technique was used and at higher current densities ($0.06 - 2.0 A cm^{-2}$) the cell was operated galvanostatically. Polarisation curves were determined under the following conditions:

- i) The high current density polarisation relationships were determined at $50^\circ C$ for Reynolds numbers in the range Re 3,010 - 8,750 in solutions containing no chloride ions.

Reynolds No. Re	i_{crit} A cm ⁻²	E_f Volts
3,800	0.00028	~ 0.305
3,800	0.00034	~ 0.285
3,800	0.00046	~ 0.30
5,750	0.00060	~ 0.310
5,750	0.00080	~ 0.310
7,930	0.00194	~ 0.320
12,210	0.00305	~ 0.315

Table 4.41 Values of critical current density (i_{crit}) and passivation potential (E_f) during the anodic passivation of electrolytic nickel in 600 g l⁻¹ nickel sulphamate electrolyte at 60°C, as a function of Reynolds Number.

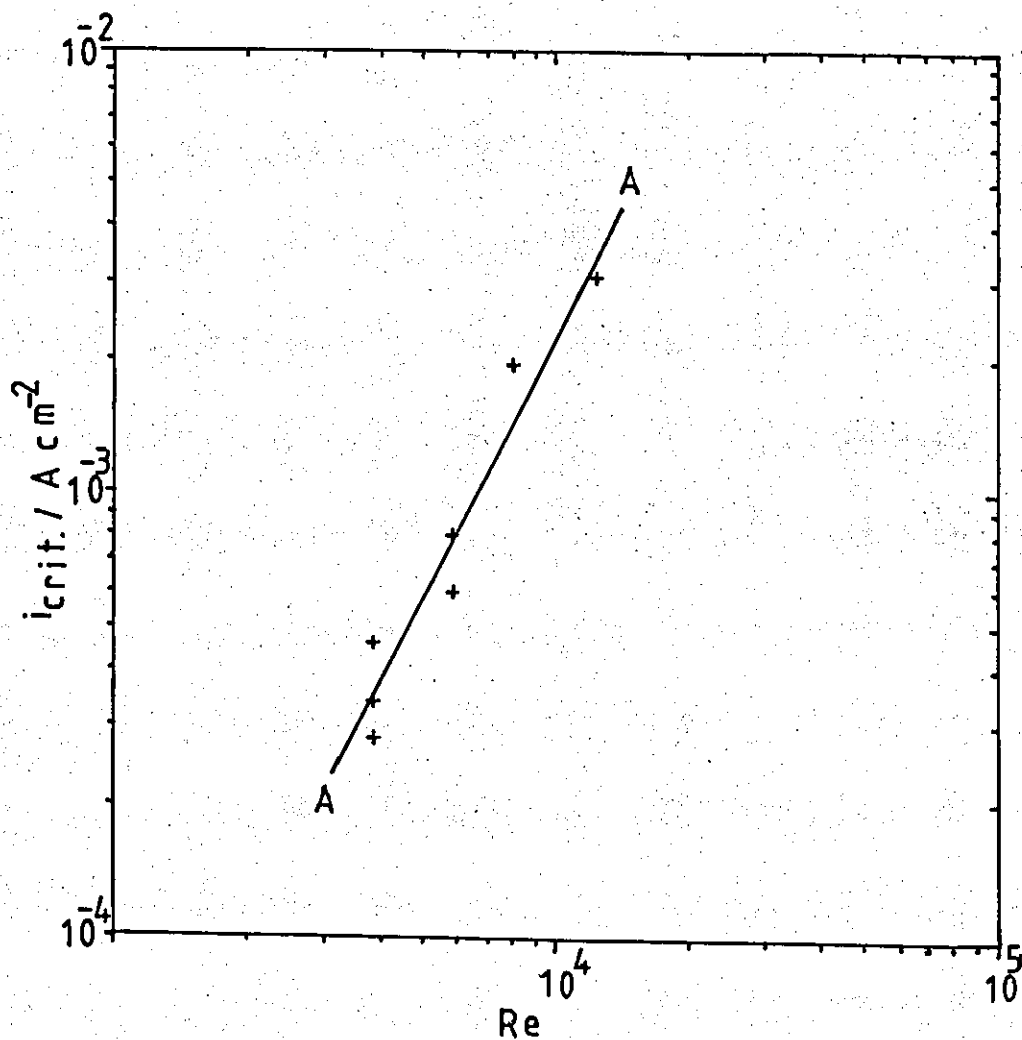


Fig.4.152 Correlation of the critical current density (i_{crit}) for the passivation of electrolytic nickel with Reynolds number at 60°C.

electrolyte composition : 600 g ℓ^{-1} $Ni(NH_2SO_3)_2$
 40 g ℓ^{-1} H_3BO_3

A - A : $i \propto Re^2$

ii) Comparative studies of cathodic polarisation at 60° and 70°C were also made for Reynolds numbers in the range Re 560 - 11,850. Polarisation measurements were carried out at both low and high current densities in solutions containing no chloride ions.

iii) Additional experiments were also carried out at 60°C to investigate other factors including the effects of chloride ions and a wetting agent on cathodic polarisation.

i) Cathodic polarisation at 50°C in the absence of chloride

The high current density ($i > 0.006 \text{ A cm}^{-2}$) polarisation curves for the Reynolds number range Re 3,010 - 8,750 are shown on semi-logarithmic coordinates in Fig.4.153. The cathode potential was referred to the Standard Hydrogen Electrode. The rest potentials of the pre-plated cathode was $0.08 \pm 0.02\text{V (SHE)}$.

The three polarisation curves were similar at current densities $< 0.34 \text{ A cm}^{-2}$ ($E > -0.98\text{V (SHE)}$). At higher current densities the polarisation curves began to separate and for a constant potential the current density increased with increasing Reynolds number. Hydroxide precipitation was observed to occur on the electrode surfaces at high current densities and as significant proportions of the electrode surfaces became covered with hydroxide, the voltage rapidly increased. Hydroxide precipitation occurred at high current densities at higher Reynolds numbers. Over the Reynolds number range Re 3,010 - 8,750, the current density for the onset of hydroxide precipitation increased from $\sim 0.6 \text{ A cm}^{-2}$ to $\sim 0.8 \text{ A cm}^{-2}$.

At these relatively high current densities, the curves showed appreciable curvature and showed pseudo-limiting current densities.

ii) Cathodic polarisation at 60° and 70°C in the absence of chloride

The low current density ($i < 0.06 \text{ A cm}^{-2}$) polarisation curves for a Reynolds number of $6,300 \pm 400$ and temperatures of 60° and 70°C are

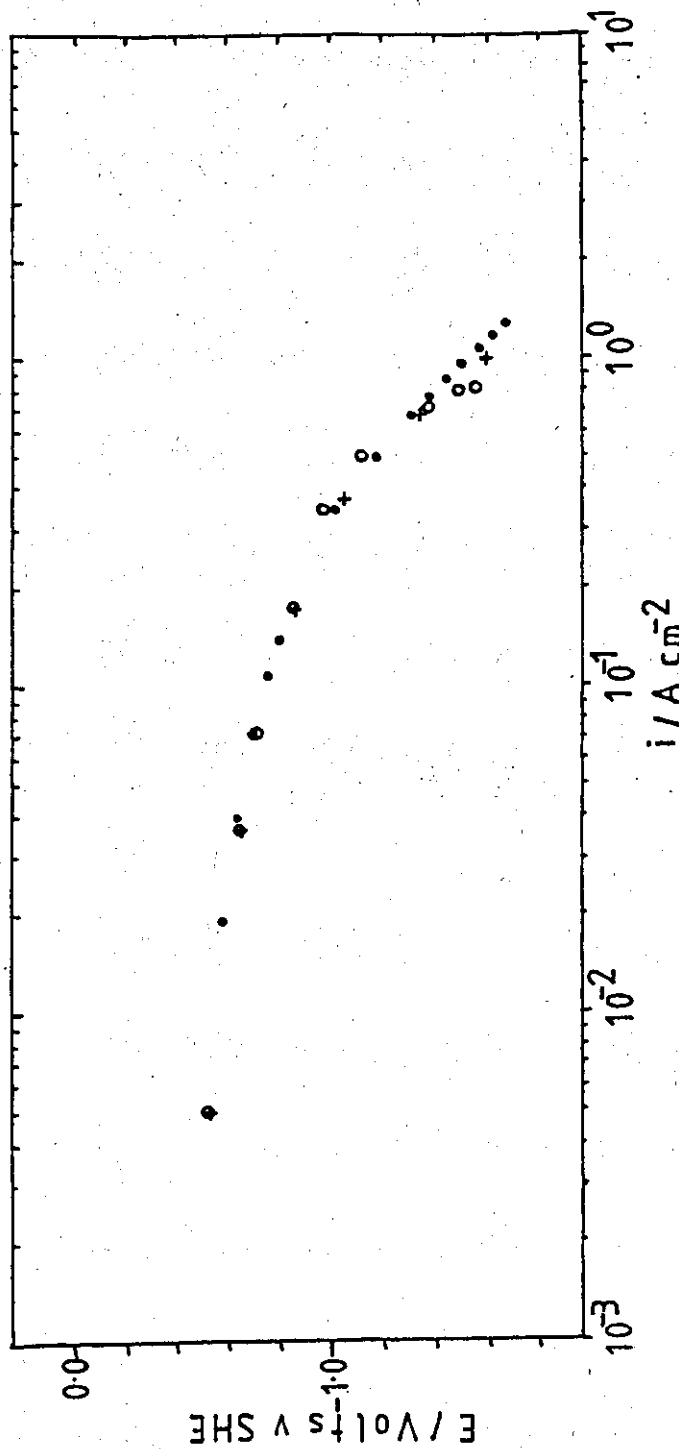


Fig.4.153 Cathodic polarisation during the electrolysis of concentrated nickel sulphamate electrolyte, in the absence of chloride, at 50°C ($E < -0.6$ V SHE).

- a) 0 0 0 - Re 3,010
- b) + + + - Re 6,320
- c) ● ● ● - Re 8,750

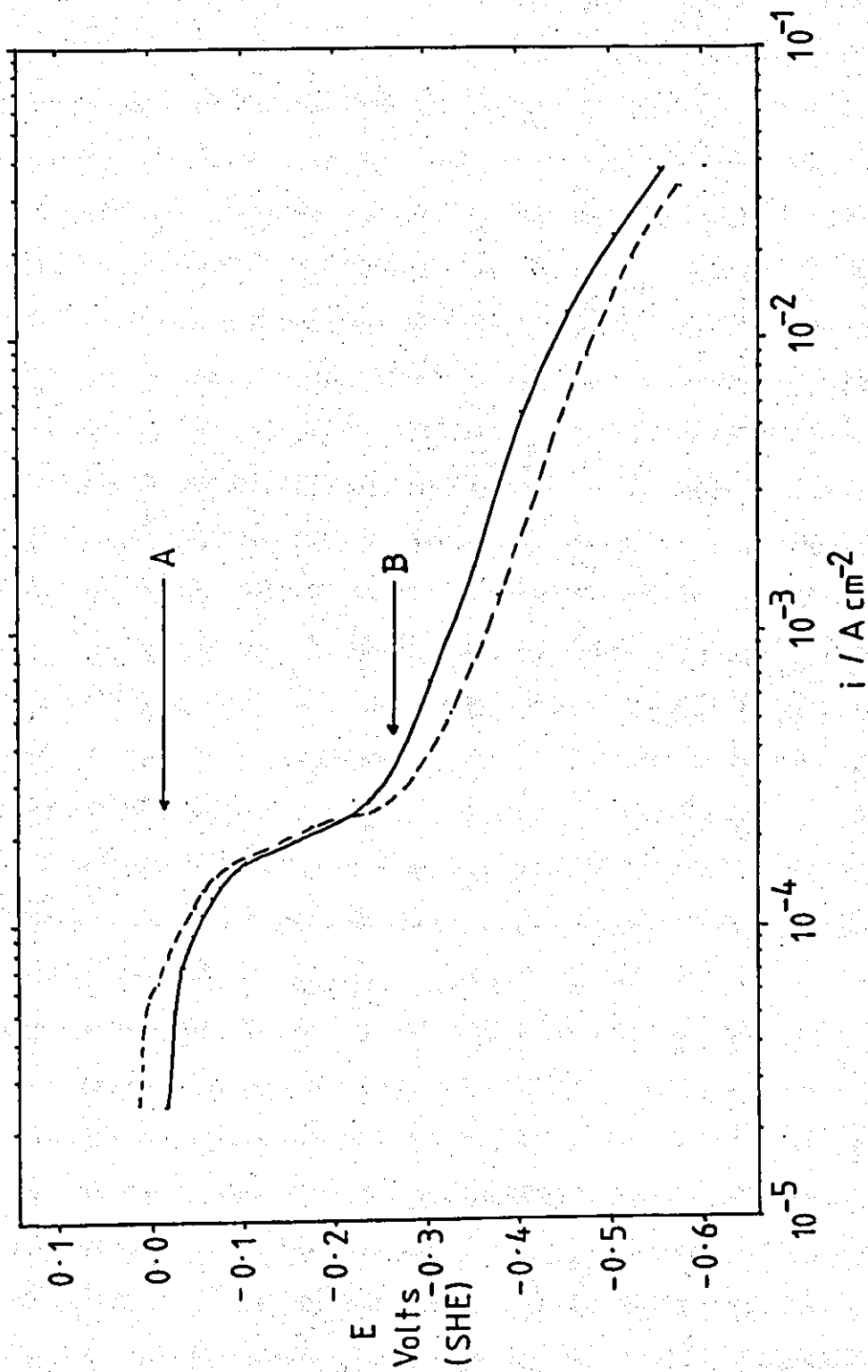


Fig.4.154 Cathodic polarisation during the electrolysis of concentrated nickel sulphamate electrolyte, in the absence of chloride, at $Re\ 6,300 \pm 400$ ($E > -0.6$ V SHE)

- a) - - - - 60°C
 b) ——— - 70°C

shown in Fig.4.154. The rest potentials of the pre-plated cathodes were $0.045 \pm 0.045\text{V}$ (SHE) at 60° and $0.00 \pm 0.02\text{V}$ (SHE) at 70°C .

The prominent feature of the curves are the regions (A-B) observed between $E \approx -0.05$ and -0.25V (SHE). The current density plateaux are of similar magnitude ($2 \times 10^{-4} \text{ A cm}^{-2}$) at both temperatures. It has been established that the plateaux are associated with the reduction of dissolved oxygen (p.241). The dissolved oxygen was partially removed by passing nitrogen through the electrolyte reservoir (Fig.4.155). The current density plateau was reduced to $\sim 2 \times 10^{-5} \text{ A cm}^{-2}$. At potentials more negative than -0.2V (SHE), the two curves were corrected for the effect of the oxygen reduction current. The corrected curves are shown in Fig.4.155. Linear behaviour was shown over approximately three decades of current density. A 10°C increase in temperature resulted in a doubling of the current density at a given potential.

The high current density polarisation curves at 60° and 70°C and $Re\ 7,820 \pm 80$ are shown on linear coordinates in Fig.4.156. A polarisation curve obtained at 50°C is also shown for comparison. At 50° and 60°C small inflections (A and B) were often observed, and these corresponded to the onset of hydroxide precipitation. (The inflection is not obvious in the 60°C example). At 70°C , a significant step (x-y) in the polarisation curve was observed. This feature may be associated with a localised high temperature effect and changes in gas flow patterns close to the cathode surface at high current densities and was observed only at 70°C .

Effect of flow rate

The high current density ($i > 0.006 \text{ A cm}^{-2}$) polarisation curves at 60°C for the Reynolds number range $Re\ 560$ to $10,940$ are shown on semi-logarithmic coordinates in Fig.4.157. The features of the curves are similar to those observed at 50°C (p.239). At high current densities ($> 0.5 \text{ A cm}^{-2}$) the three curves began to separate until limited by significant hydroxide precipitation. In the laminar flow regime, large gas bubbles were formed on the cathode surface. Over this range of Reynolds numbers, the current density for the onset of hydroxide precipitations increased from $\sim 0.9 \text{ A cm}^{-2}$ to $\sim 1.4 \text{ A cm}^{-2}$.

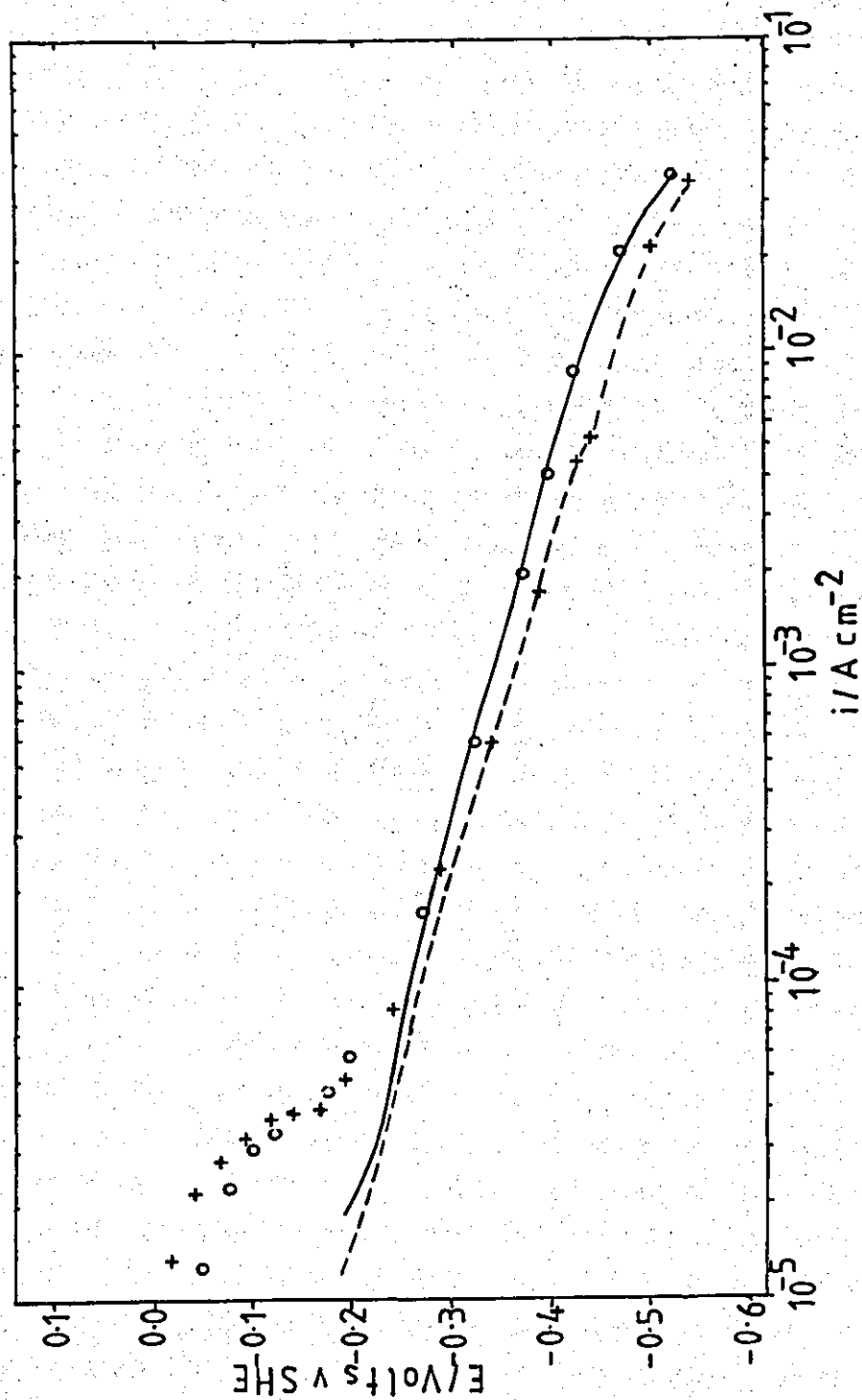


Fig.4.155 Cathodic polarisation during the electrolysis of concentrated nickel sulphamate electrolyte (in the absence of chloride) at $Re\ 6,300 \pm 400$, corrected for dissolved oxygen reduction ($E > -0.6\ V\ SHE$)

- a) + + +, 60°C - - - - corrected curve
 b) o o o, 70°C ——— corrected curve

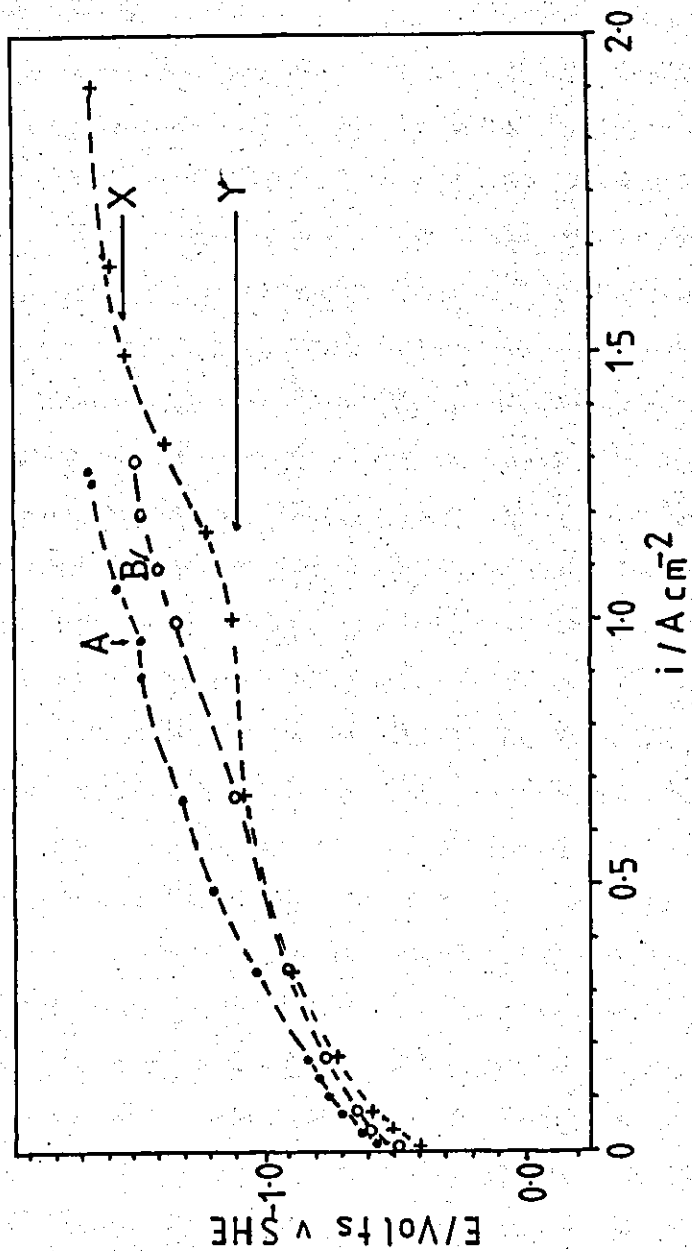


Fig.4.156 Cathodic polarisation during the electrolysis of concentrated nickel sulphamate electrolyte, in the absence of chloride, at $Re\ 7,830 \pm 80$

- a) ● ● ● , 50°C
- b) ○ ○ ○ , 60°C
- c) + + + , 70°C

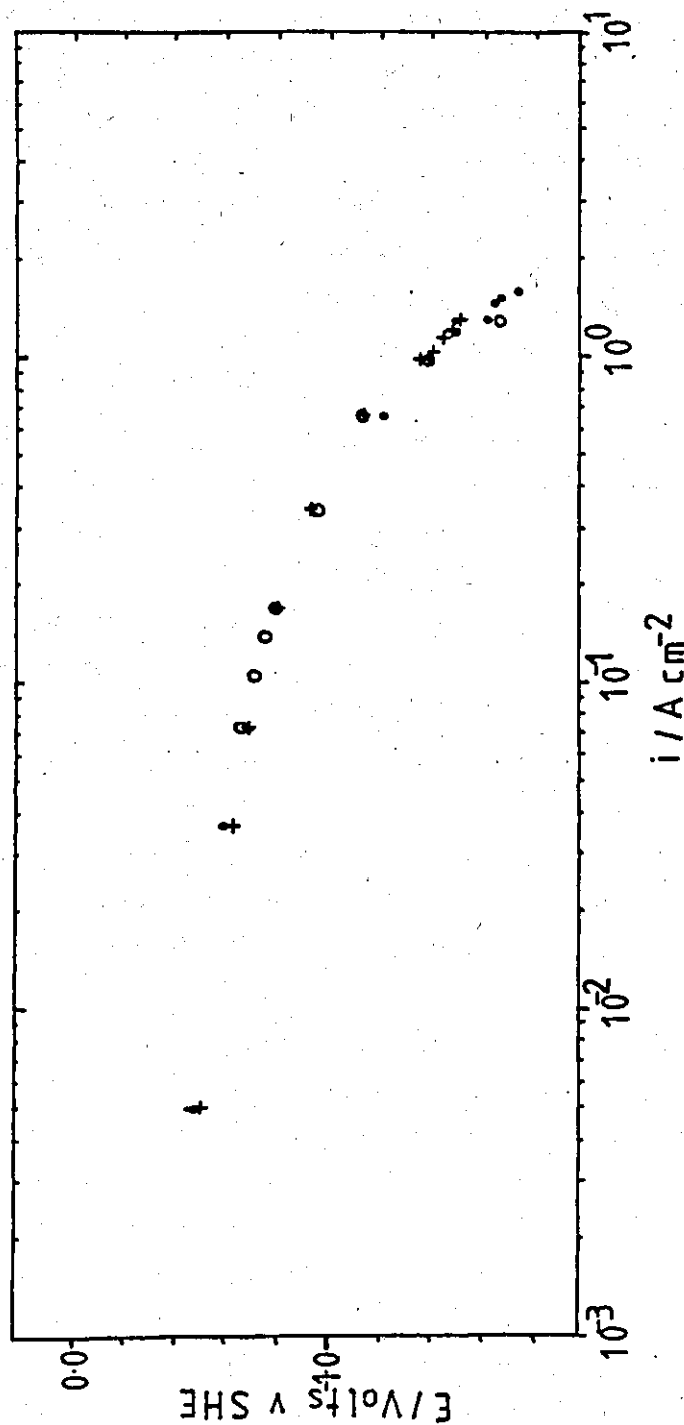


Fig.4.157 Cathodic polarisation during the electrolysis of concentrated nickel sulphamate electrolyte, in the absence of chloride, at 60°C ($E < -0.6$ V SHE).

- | | | |
|----|-------|-----------|
| a) | ○ ○ ○ | Re 560 |
| b) | + + + | Re 5,850 |
| c) | ● ● ● | Re 10,940 |

A similar series of polarisation curves was obtained at 70°C over the Reynolds number range Re 4,300 to 11,850 (Fig.4.158). At 70°C, hydroxide precipitation was not observed and measurements were limited to those recorded by the available power supply. At Re 4,300 the maximum current density was 1.1 A cm^{-2} . The current density obtainable was greater at higher flow rates. The maximum current density was $\sim 2 \text{ A cm}^{-2}$, with no evidence of hydroxide formation. This value was almost double that found at 60°C. The regions A-B are again associated with the increasing resistance of gas films on the electrode surface.

iii) Additional diagnostic experiments at 60°C

a) Effect of flow rate on cathode potential at constant current density

Further experiments were carried out to study the effect of flow rate on concentration overpotential. An increase in Reynolds number would be expected to shift the cathode potential to less negative values if concentration overpotential was present.

The cathode potential was monitored using the Luggin capillary and 3.8 M calomel electrode arrangement described previously for a series of Reynolds numbers at constant current densities of 0.17, 0.33 and 0.66 A cm^{-2} .

At 0.17 A cm^{-2} (Fig.4.159) the observed cathode potential was at a minimum value (-1.3V (SHE)) at very low flow rates ($\sim Re$ 100). At low Reynolds numbers, the large gas bubbles formed on the electrode surface may distort the current distribution and give an increased series resistance adjacent to the electrode. The potential tended to move to more positive values at higher Reynolds numbers and was about constant at $Re > 2,000$.

At a higher current density (0.33 A cm^{-2}), large changes in cathode potential were not observed. The potential tended to move to more positive values by about 10mV over the Reynolds number range Re 3,000 - 15,000. However, at 0.66 A cm^{-2} , the potential moved to more negative values by $\sim 80\text{mV}$ over a similar range of flow rates (Fig.4.160). This

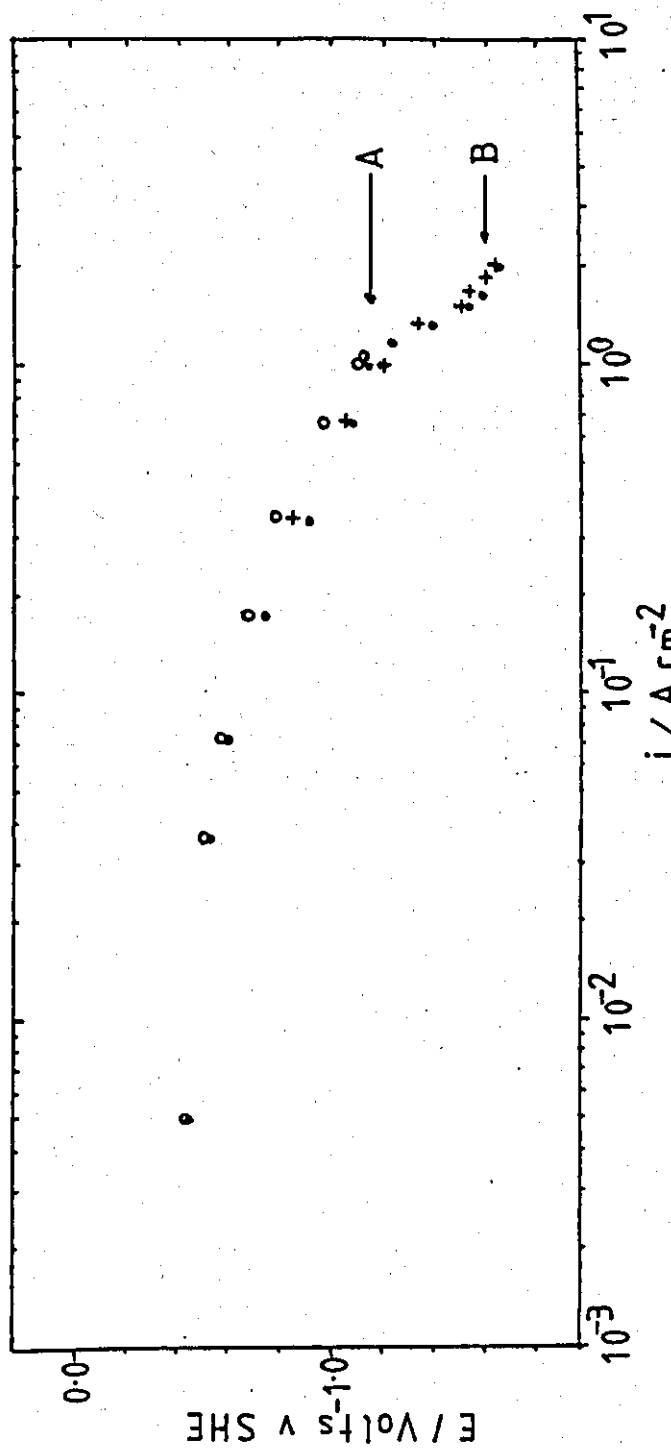


Fig.4.158 Cathodic polarisation during the electrolysis of concentrated nickel sulphamate electrolyte, in the absence of chloride, at $70^{\circ}C$ ($E > -0.6$ V SHE).

- a) ○ ○ ○ , Re 4,300
- b) ● ● ● , Re 7,910
- c) + + + , Re 11,850

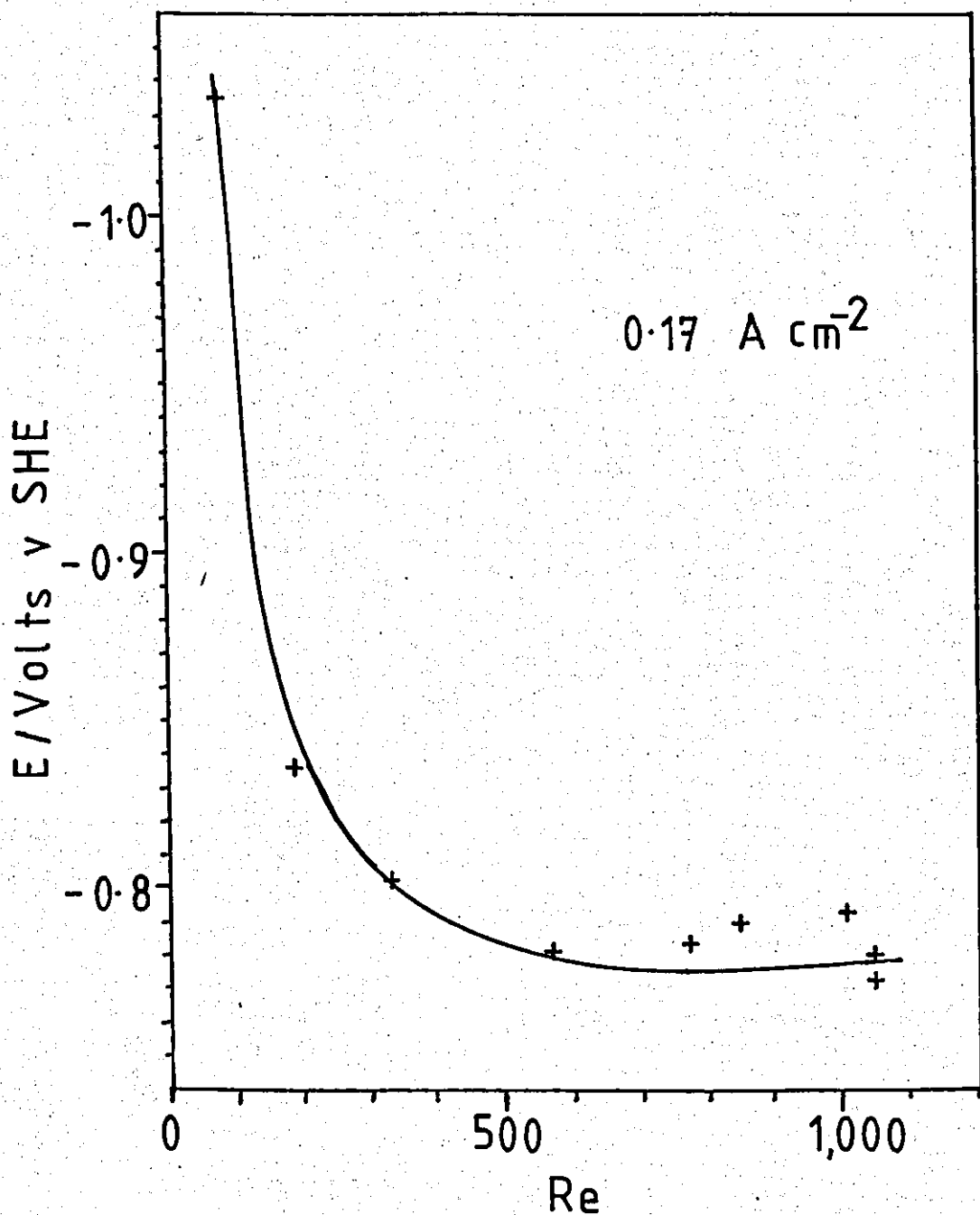


Fig.4.159 Effect of Reynolds number on the cathode potential during the electrolysis of concentrated nickel sulphamate electrolyte (in the absence of chloride), at a constant current density of 0.17 A cm^{-2} (60°C).

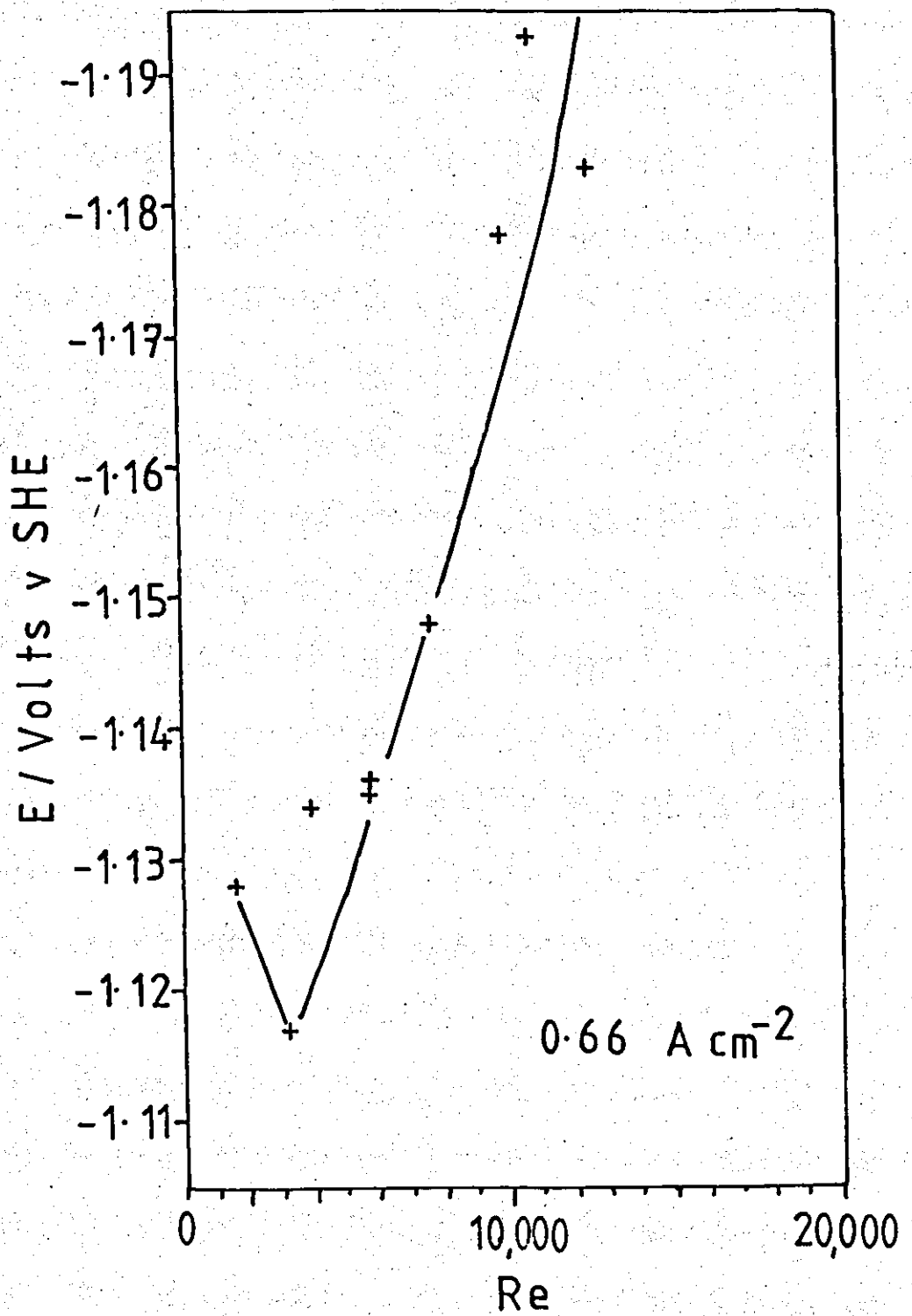


Fig.4.160 Effect of Reynolds number on the cathode potential during the electrolysis of nickel sulphamate electrolyte, (in the absence of chloride), at a constant current density of 0.66 A cm⁻² (60°C).

effect may be associated with the compression of the gas layer close to the cathode surface at high flow rates, resulting in an increase in the electrolyte resistance in this region.

b) Effect of chloride ions and a wetting agent on cathodic polarisation

A comparative study of cathodic polarisation at high current densities ($>0.06 \text{ A cm}^{-2}$) was carried out at Re 5,850 in electrolytes containing 5.5 g l^{-1} nickel chloride ($\text{NiCl}_2 \cdot 6\text{H}_2\text{O}$) and chloride plus a wetting agent (0.052 g l^{-1} Fluowet SP). The surfactant was added to reduce the surface tension of the electrolyte, improve the flow of gas bubbles over the electrode surface and reduce the porosity of the deposits. The polarisation curves are shown in Fig.4.161, together with that obtained in the nickel sulphamate electrolyte without additions.

The addition of chloride to the electrolyte resulted in a shift to lower current densities for a given potential. Conversely, the addition of the wetting agent resulted in a shift to higher current densities for a given potential. Neither chloride ions nor Fluowet SP had any effect on the maximum current density of $\sim 1 \text{ A cm}^{-2}$.

c) Additional low current density experiments on reduction of dissolved oxygen at 60° and 70°C

The current density plateau previously observed in cathodic polarisation curves at low current densities (Section 4.42b) was associated with the reduction of dissolved oxygen. This was confirmed by operating the cell at a constant cathode potential of $E \approx -0.11\text{V}$ (SHE), corresponding to the potential of the current density plateau. The current density was measured as a function of time (t) (Table 4.42 and Fig.4.162).

In the absence of nitrogen bubbling, the current density decreased slightly to 0.17 mA cm^{-2} as the reactant was depleted by reduction (A-B). Nitrogen was then bubbled through the electrolyte reservoir at a cylinder head pressure of 2 p.s.i. The current density decreased to $0.11 \times 10^{-3} \text{ A cm}^{-2}$ in $\sim 480 \text{ s}$ (B-C). When the nitrogen pressure was increased to 4 p.s.i.

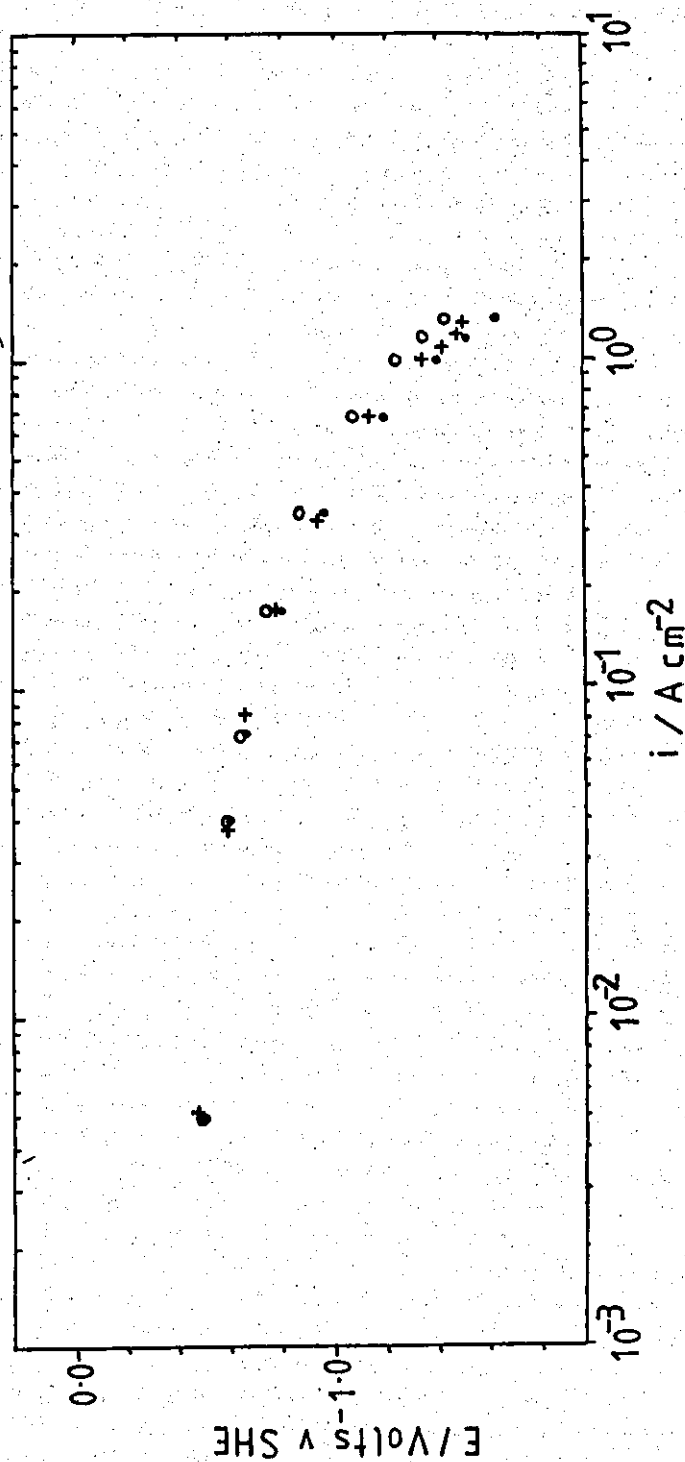


Fig.4.161 Cathodic polarisation during the electrolysis of concentrated nickel sulphamate electrolyte at 60°C.

	electrolyte composition
a) + + + ,	600 g l ⁻¹ Ni(NH ₂ SO ₃) ₂ 40 g l ⁻¹ H ₃ BO ₃
b) • • • ,	600 g l ⁻¹ Ni(NH ₂ SO ₃) ₂ 40 g l ⁻¹ H ₃ BO ₃ 5.5 g l ⁻¹ NiCl ₂ · 6H ₂ O
c) o o o ,	600 g l ⁻¹ Ni(NH ₂ SO ₃) ₂ 40 g l ⁻¹ H ₃ BO ₃ 5.5 g l ⁻¹ NiCl ₂ · 6H ₂ O 0.052 g l ⁻¹ 'Fluowet SP'

Nitrogen Pressure lb in ²	Time t/s	Current I/Amps x 10 ⁻³	Current Density i/A cm ⁻² x 10 ⁻³
0 p.s.i.	60	5.30	0.177
	120	5.27	0.176
	170	5.23	0.174
	230	5.20	0.173
	290	5.18	0.173
	350	5.13	0.171
	410	5.12	0.171
	450	5.11	0.170
	750	5.07	0.169
	1,050	5.03	0.168
2 p.s.i.	1,350	5.02	0.167
	1,500	4.20	0.140
	1,650	3.73	0.124
	1,830	3.23	0.108
	1,950	2.47	0.0823
4 p.s.i.	2,100	1.96	0.0653
	2,250	1.62	0.0540
	2,550	1.27	0.0423
	2,850	1.08	0.0360
	3,150	0.96	0.0320
	3,450	0.93	0.0310
	3,750	0.90	0.0300
	3,930	0.85	0.0283

Table 4.42 Effect of nitrogen bubbling on the electrolysis of concentrated nickel sulphamate electrolyte at 60°C, Re 6,300 ± 400 and a constant cathode potential of -0.106V (SHE).

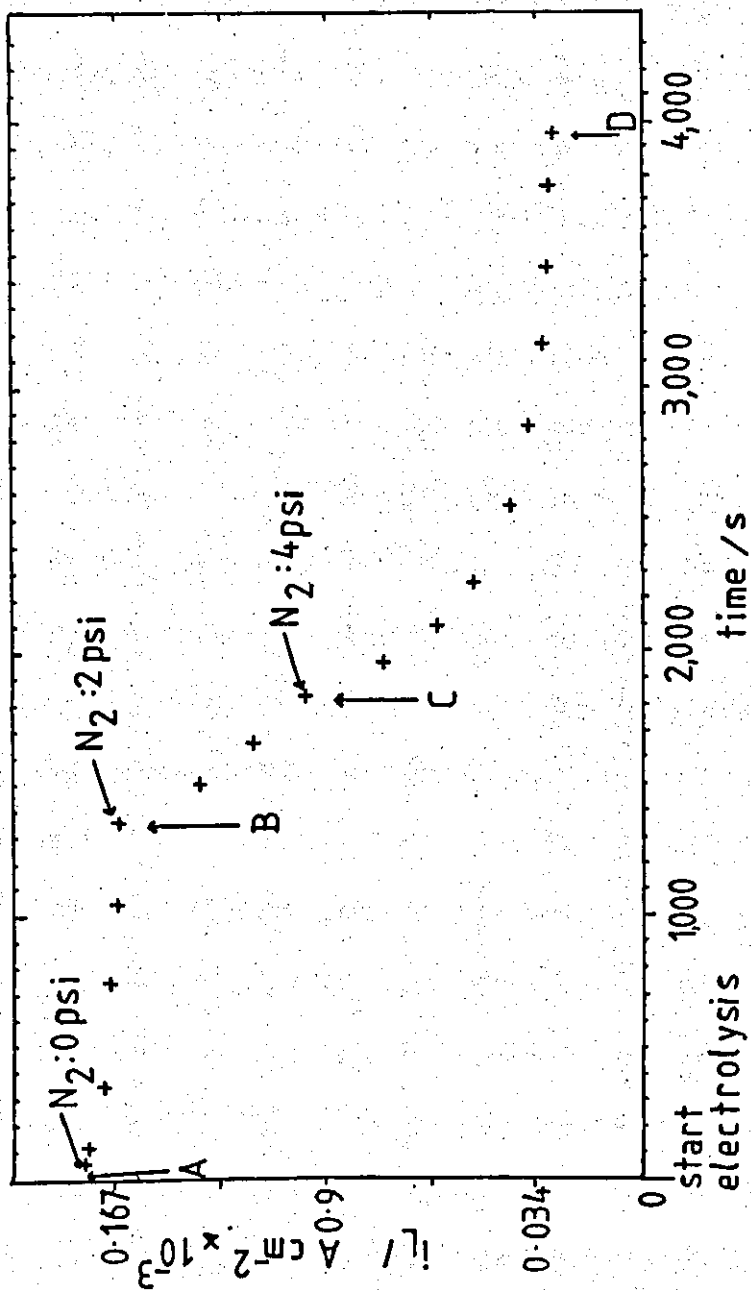


Fig.4.162 Electrolysis of concentrated nickel sulphamate electrolyte at 60°C, Re $6,300 \pm 400$ and a constant cathodic potential of $-0.106 V_{SHE}$. Dissolved oxygen concentration reduced by bubbling nitrogen through the electrolyte at pressures of 2 p.s.i. and 4 p.s.i.

the current density decreased to $0.03 \times 10^{-3} \text{ A cm}^{-2}$ in 1,200 s before becoming approximately constant (C-D). The limiting current density was due to oxygen reduction and was reduced to a low value by nitrogen bubbling.

Nitrogen was passed through the electrolyte reservoir for ~1.5 h prior to recording the polarisation curves of Fig.4.163, at nitrogen pressures of 2 and 4 p.s.i. At both pressures, a significant inflection (A-A) due to the mass transfer controlled reductions of oxygen was evident.

Summary of cathodic polarisation studies

- a) At all the temperatures studied, the polarisation curves showed no definite evidence of a limiting current density due to the mass transfer controlled reduction of nickel ions, although inflections in the curves were often observed at current densities $>0.8 \text{ A cm}^{-2}$. These phenomena appear to be associated with the initiation of hydroxide precipitation or gas bubble effects at the electrode-electrolyte interface.
- b) At 70°C current densities up to 2 A cm^{-2} were readily achieved without precipitation of hydroxide. At such high current densities localised heating of the electrolyte adjacent to the cathode may occur. The potential measurements were limited by the cell voltage exceeding the output of the power supply (30V).
- c) At 50° and 60°C , the potential measurements were limited by the precipitation of hydroxide deposits and a sharp increase in the cathode potential was observed.
- d) For a given potential, the deposition rate increased with increasing temperature and flow rate. There is some evidence that the flow rate, particularly in laminar flow, may effect the adhesion and distribution of gas bubbles close to the cathode.

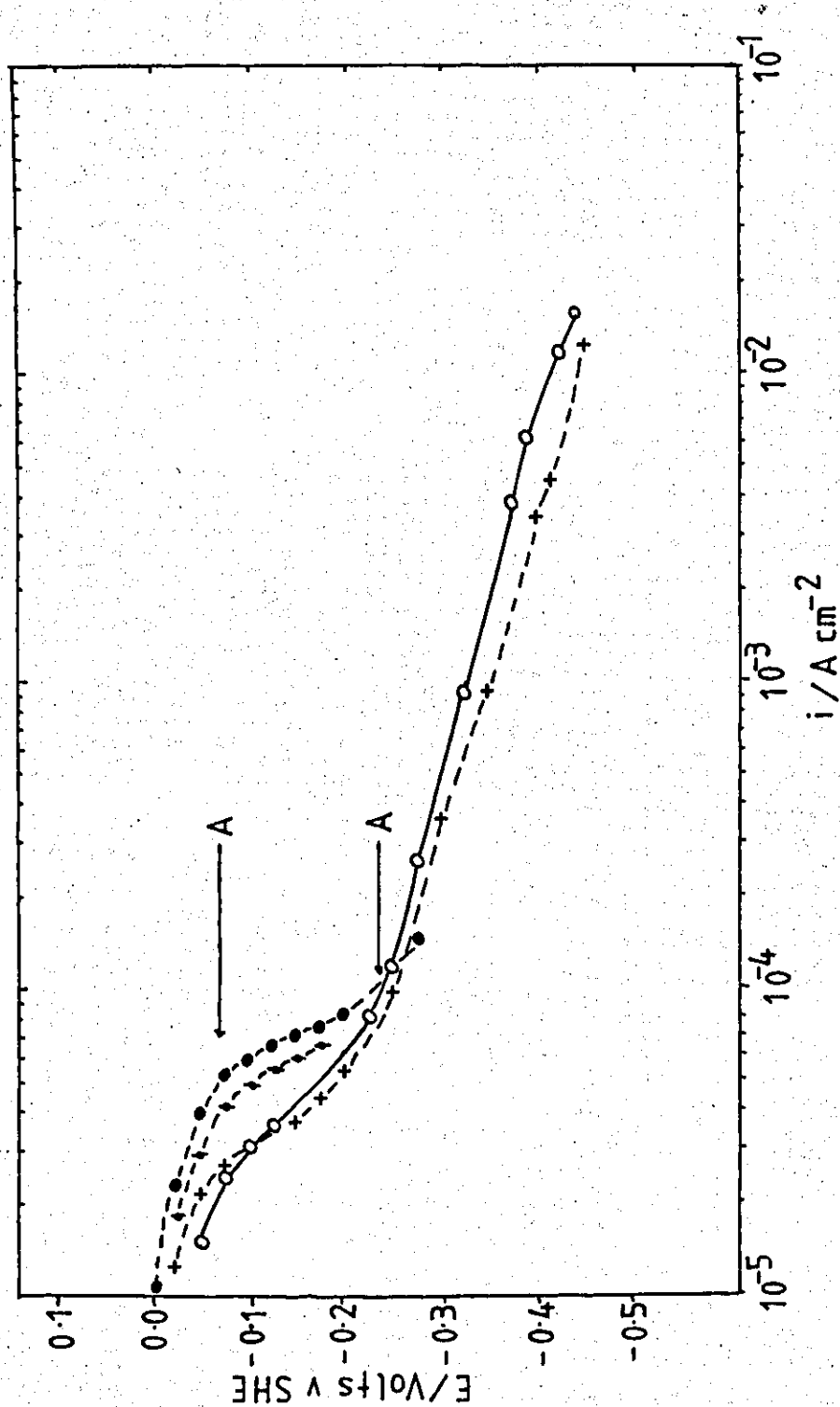


Fig.4.163 Cathodic polarisation during the electrolysis of concentrated nickel sulphamate electrolyte at $Re\ 6,300 \pm 400$, with nitrogen bubbling.

- a) ● ● ● , 60°C, nitrogen pressure 2 p.s.i.
- b) + + + , 60°C, nitrogen pressure 4 p.s.i.
- c) ○ ○ ○ , 70°C, nitrogen pressure 4 p.s.i.

Overall Summary of Section 4.4

The significant results of the polarisation measurements and current distribution studies were as follows:

- a) There was no clear evidence of a limiting current density plateau for the reduction of nickel ions. It was therefore difficult to separate the nickel deposition and hydrogen evolution reactions. The relationship between the flow rate and the cathode polarisation was not clear.
- b) Oxygen evolution would be the principal anode reaction for most deposition conditions.
- c) The cathodic current distribution was non-uniform using an anode length of 25cm and a cathode length of 10cm. A uniform current distribution was observed using 9cm anodes. Similar results were found at both 60° and 70°C. A mass transport controlled current distribution was not observed for any experimental conditions. However, there was some evidence for interference effects from gas evolution, particularly at low flow rates.

A significant increase in the maximum current density was obtained when operating the cell with a uniform current distribution. Current densities in excess of 2 A cm⁻² (at 70°C) could be achieved under these conditions.

From this investigation it would appear that there is some evidence for a complex deposition mechanism leading to less predictable experimental results. It is also evident that the hydrogen evolution reaction may take up to 5% of the total current density. Hence a significant volume of gas may be evolved close to the cathode surface. Therefore it was of considerable interest to study the effect of gas evolution on mass transfer during nickel electroforming. Since limiting current densities were unobtainable using the nickel system, a 'tracer' method was required as will be seen in the following section.

4.5 Mass transport studies in nickel sulphamate solutions

Since mass transport relations could not be determined from limiting current density measurements it was necessary to determine data for nickel by using a silver tracer method. Using this method data were determined for mass transport to short electrodes (L/d_e 2.92) and long electrodes (L/d_e 11.7). The results of these investigations are presented in Section 4.5.1. As will be seen these measurements indicated that the ratio of mass transfer to the cathode under turbulent flow conditions were about an order of magnitude greater than expected theoretically. A model for predicting the mass transfer correlations for parallel plate cells with enhanced mass transport due to simultaneous gas evolution has been developed in order to offer a possible explanation of the experimental results obtained in Section 4.5.1. The details of the model are presented in Section 4.5.2.

4.5.1 Silver tracer studies of mass transport in nickel sulphamate solutions at 60°C

The mass transfer correlations for the cell have been determined from the transport controlled deposition of copper. This is a simple, single reaction system. However experimental studies have indicated that the deposition of nickel at high current densities is accompanied by the evolution of significant quantities of hydrogen. The presence of gas bubbles, close to the cathode surface may affect mass transfer rates. It was therefore necessary to ensure that mass transfer relationships related (as far as possible), to practical operating conditions of the cell and plating solution.

The conventional technique for the measurement of mass transfer coefficients in electrochemical cells, is to relate the experimentally measured limiting current density (i_L) as determined from polarisation curves, to the mass transfer coefficient (k_L) using the equation

$$k_L = \frac{i_L}{zF c_b} \quad \dots \dots (2.15)$$

However, for the nickel deposition system studied, a limiting current density was not observed (Section 4.42b). This necessitated the use of an alternative technique to obtain comparative mass transfer data. Ettel (344) developed a method for determining the relative rates of mass transfer in air agitated electrowinning cells. This method was also applicable to parallel plate cells.

The method involves the simultaneous reduction of a second ion, present in the plating solution at very low concentration (a few p.p.m.). The minor constituent was co-deposited under mass transport control and mass transfer data may be determined from the composition of the resulting alloy and the metal concentration in the electrolyte.

Theoretical background

The mass transfer coefficient for silver ions $k_L^{Ag^+}$ is given by the expression

$$k_L^{Ag^+} = \frac{i_L}{zF c_{Ag^+}} \dots \dots (3.2)$$

where $i_L^{Ag^+}$ - limiting current for silver ions

and

c_{Ag^+} - bulk solution concentration of silver ions

For simple mass transfer to plane parallel electrodes in channel flow, the mass transfer coefficient is proportional to the cell and flow parameters, e.g.

$$k_L^{Ag^+} = x d e^a U^b v^c D_{Ag^+}^d L^e$$

where the exponents a, b, c, d and e are constants for a given cell geometry and flow regime and x is the constant of proportionality.

The mass transfer coefficient for nickel ions, $k_L^{Ni^{2+}}$ is given by a similar expression

i.e.
$$k_L^{Ni^{2+}} = x d e^a U^b v^c D_{Ni^{2+}}^d L^e$$

When the two species are co-deposited under mass transfer conditions, the ratio of the two coefficients $k_L^{Ag^+}$ and $k_L^{Ni^{2+}}$ is given by

$$\frac{k_L^{Ag^+}}{k_L^{Ni^{2+}}} = \left[\frac{D_{Ag^+}}{D_{Ni^{2+}}} \right]^d \quad \dots \dots (4.5a)$$

where D_{Ag^+} , $D_{Ni^{2+}}$ are the diffusion coefficients of the two ions.

All other parameters are equal under conditions of simultaneous codeposition.

Dimensional analysis of the design equations (e.g. Equation 2.67b) indicated that the value of the exponent d , was 0.66 for all cell geometries and flow conditions. Hence equation (4.5a) may be written as:

$$\frac{k_L^{Ag^+}}{k_L^{Ni^{2+}}} = \left[\frac{D_{Ag^+}}{D_{Ni^{2+}}} \right]^{0.66} \quad \dots \dots (4.5b)$$

or

$$k_L^{Ni^{2+}} = k_L^{Ag^+} \left[\frac{D_{Ag^+}}{D_{Ni^{2+}}} \right]^{0.66} \quad \dots \dots (4.5c)$$

Consequently, the correlation between mass transfer coefficient and flow rate was identical for both reduced species. In addition, the value of $k_L^{Ni^{2+}}$ may be estimated if the two diffusion coefficients are known.

For this investigation, 6 to 15 g cm⁻³ of silver (as Ag NO₃) was added to the plating solution (chloride ions were omitted from the solution to prevent the precipitation of Ag Cl). The rates of mass transfer to electrodes of two lengths were studied. The cathodes were 2.92 equivalent diameters and 11.7 equivalent diameters in length - designated 'short' and 'long' electrodes respectively. The anode was 25cm in length and the electrolyte temperature was 60°C.

In both cases nickel-silver alloys were electroformed on stainless steel or Nickel 200 substrates over a range of flow rates (Re 1343 - 7414) at a constant current density of 0.4 A cm^{-2} . At this current density the current efficiency was 95% at all flow rates. Electrolysis was continued for a specified time of 165 s to deposit foils $\sim 23 \mu\text{m}$ thick, containing $<0.7\%$ silver.

Some additional experiments were also carried out using cathodes 2.92 de in length at Re 7413 and 0.7 A cm^{-2} to assess the effect of a higher deposition rate on the mass transfer coefficient for silver.

a) Mass transfer to 'short' electrodes ($L/d_e \sim 2.92$)

Nickel-silver alloy electroforms were deposited at 0.4 A cm^{-2} over the range of Reynolds numbers Re 1,343 to Re 7,414. At lower laminar flow rates (Re $<1,343$), bubbles of hydrogen were observed on the cathode surface and meaningful measurements were impossible. At each flow rate, the electrolyte and the deposit were analysed for silver (see Section 3.5.3). The primary analytical results are shown in Table 4.43. In Table 4.44 the calculated values of the bulk concentration of silver ions in the plating solution ($c_b^{\text{Ag}^+}$), the weight of silver deposited (G) the limiting current density ($i_L^{\text{Ag}^+}$) and the mass transfer coefficient ($k_L^{\text{Ag}^+}$) are given for each flow rate (see Section 3.53 for details).

The mass transfer relationships between $k_L^{\text{Ag}^+}$ and Re are shown in Fig.4.164 (log. coordinates). In laminar flow (Re $<2,000$), the mass transfer coefficient decreased with increasing flow rate, as shown by the solid line A-A. A minimum $k_L^{\text{Ag}^+}$ value of about $2 \times 10^{-2} \text{ cm s}^{-1}$ was observed at Re $\sim 1,900$.

Theoretical values of $k_L^{\text{Ag}^+}$ were calculated from the design equation for Cell 2 in laminar flow

$$\text{Sh}_{\text{Av}}^{\text{Ag}^+} = 1.85 \left\{ \text{Re} \frac{d_e}{L} \text{Sc} \right\}^{0.33} \dots \dots (2.49)$$

Ag ⁺ ion concentration in diluted plating solution					Ag ⁺ ion concentration in diluted solution from dissolution of electrodeposit					
Reynolds number Re	Dilution factor a	Absorbance x 10 ⁻²			Concentration of Ag ⁺ x μg cm ⁻³	Dilution factor b	Absorbance x 10 ⁻²			Concentration of Ag ⁺ y μg cm ⁻³
		x+0	x+1	x+2			y+0	y+1	y+2	
1,343	25/2	16	33	49	0.979	50x ^{25/5}	39	56	70	2.537
1,447	25/2	16	34	49	0.995	250x ^{25/5}	9	31.5	51	0.450
1,576	25/2	12	32.5	53	0.585	50x ^{25/5}	20	42	60	1.027
1,808	25/2	19.5	51	70.5	0.810	50x ^{50/5}	22	43	63	1.081
2,377	25/2	15	39	61	0.667	50x ^{50/5}	19	44	67	0.805
2,971	25/2	19	36	54	1.076	50x ^{25/5}	33	52	68	1.907
3,100	25/2	13	30	45	0.831	100x ^{25/5}	9	27	42.5	0.559
3,358	25/2	10	30	46	0.586	50x ^{25/5}	22	41	58	1.238
4,417	25/2	13	34	54	0.642	50x ^{25/5}	27.5	50.5	70.5	1.299
4,443	25/1	9	39	67	0.321	50x ^{25/5}	56	82	107	2.202
5,244	25/2	18	34	51.5	1.058	50x ^{25/5}	43	59	75	2.688
5,502	25/2	15	39	60	0.686	50x ^{25/5}	44	69	93	1.802
5,502	25/2	16	41	66	0.640	50x ^{25/3}	39	63	84	1.752
6,587	25/2	11	33	54.5	0.510	50x ^{25/5}	21	43.5	63	1.020
6,897	25/2	12	39.5	63.5	0.486	50x ^{25/5}	20	39	56.5	1.108
7,233	25/2	16	34	49	0.979	50x ^{25/5}	51.5	66.5	79.5	3.694
7,414	50/2	9.5	33.5	56	0.419	50x ^{50/5}	15	24	32.5	1.723
7,414	25/1	9	27	47.5	0.444	50x ^{25/5}	15.5	21	29	2.198

Table 4.43

Analysis of nickel sulphamate solutions and nickel electroforms for silver content (L/de ~2.92, 60°C).

Reynolds number Re	Bulk Soln. concentration of Ag ⁺ $c_b^{Ag^+}$ mole cm ⁻³	Wt. of silver present in deposit G g	Limiting current density for reduction of Ag ⁺ $i_L^{Ag^+}$ A cm ⁻²	Mass transfer coefficient $k_L^{Ag^+}$ cm s ⁻¹
1,343	1.13 x 10 ⁻⁷	6.34 x 10 ⁻⁴	4.59 x 10 ⁻⁴	4.20 x 10 ⁻²
1,447	1.15 x 10 ⁻⁷	5.63 x 10 ⁻⁴	4.07 x 10 ⁻⁴	3.67 x 10 ⁻²
1,576	6.78 x 10 ⁻⁸	2.57 x 10 ⁻⁴	1.86 x 10 ⁻⁴	2.84 x 10 ⁻²
1,808	9.39 x 10 ⁻⁸	2.70 x 10 ⁻⁴	1.95 x 10 ⁻⁴	2.15 x 10 ⁻²
2,377	7.73 x 10 ⁻⁸	2.01 x 10 ⁻⁴	1.45 x 10 ⁻⁴	1.95 x 10 ⁻²
2,971	1.25 x 10 ⁻⁷	4.77 x 10 ⁻⁴	3.45 x 10 ⁻⁴	2.86 x 10 ⁻²
3,100	9.63 x 10 ⁻⁸	2.80 x 10 ⁻⁴	2.02 x 10 ⁻⁴	2.18 x 10 ⁻²
3,358	6.79 x 10 ⁻⁸	3.10 x 10 ⁻⁴	2.24 x 10 ⁻⁴	3.42 x 10 ⁻²
4,417	7.44 x 10 ⁻⁸	3.25 x 10 ⁻⁴	2.35 x 10 ⁻⁴	3.27 x 10 ⁻²
4,443	7.44 x 10 ⁻⁸	5.51 x 10 ⁻⁴	3.98 x 10 ⁻⁴	5.54 x 10 ⁻²
5,244	1.23 x 10 ⁻⁸	6.72 x 10 ⁻⁴	4.86 x 10 ⁻⁴	4.09 x 10 ⁻²
5,502	7.95 x 10 ⁻⁸	4.51 x 10 ⁻⁴	3.26 x 10 ⁻⁴	4.25 x 10 ⁻²
5,502	7.42 x 10 ⁻⁷	4.38 x 10 ⁻⁴	3.16 x 10 ⁻⁴	4.42 x 10 ⁻²
6,587	5.91 x 10 ⁻⁸	2.55 x 10 ⁻⁴	1.84 x 10 ⁻⁴	3.23 x 10 ⁻²
6,897	5.63 x 10 ⁻⁸	2.77 x 10 ⁻⁴	2.00 x 10 ⁻⁴	3.68 x 10 ⁻²
7,233	1.13 x 10 ⁻⁷	9.24 x 10 ⁻⁴	6.68 x 10 ⁻⁴	6.12 x 10 ⁻²
7,414	9.71 x 10 ⁻⁸	8.62 x 10 ⁻⁴	6.22 x 10 ⁻⁴	6.65 x 10 ⁻²
7,414	1.03 x 10 ⁻⁷	5.50 x 10 ⁻⁴	3.97 x 10 ⁻⁴	4.00 x 10 ⁻²

$$L/d_e = 2.92$$

Temperature : 60°C; Total Current Density : 0.4 A cm⁻²
 Thickness of Deposit : ~23µm; Electrode Area : 7.5 cm²
 Deposition Time : ~165.1 s

Table 4.44 Summary of electrolysis conditions and derived data for deposition of experiments with added silver tracer.

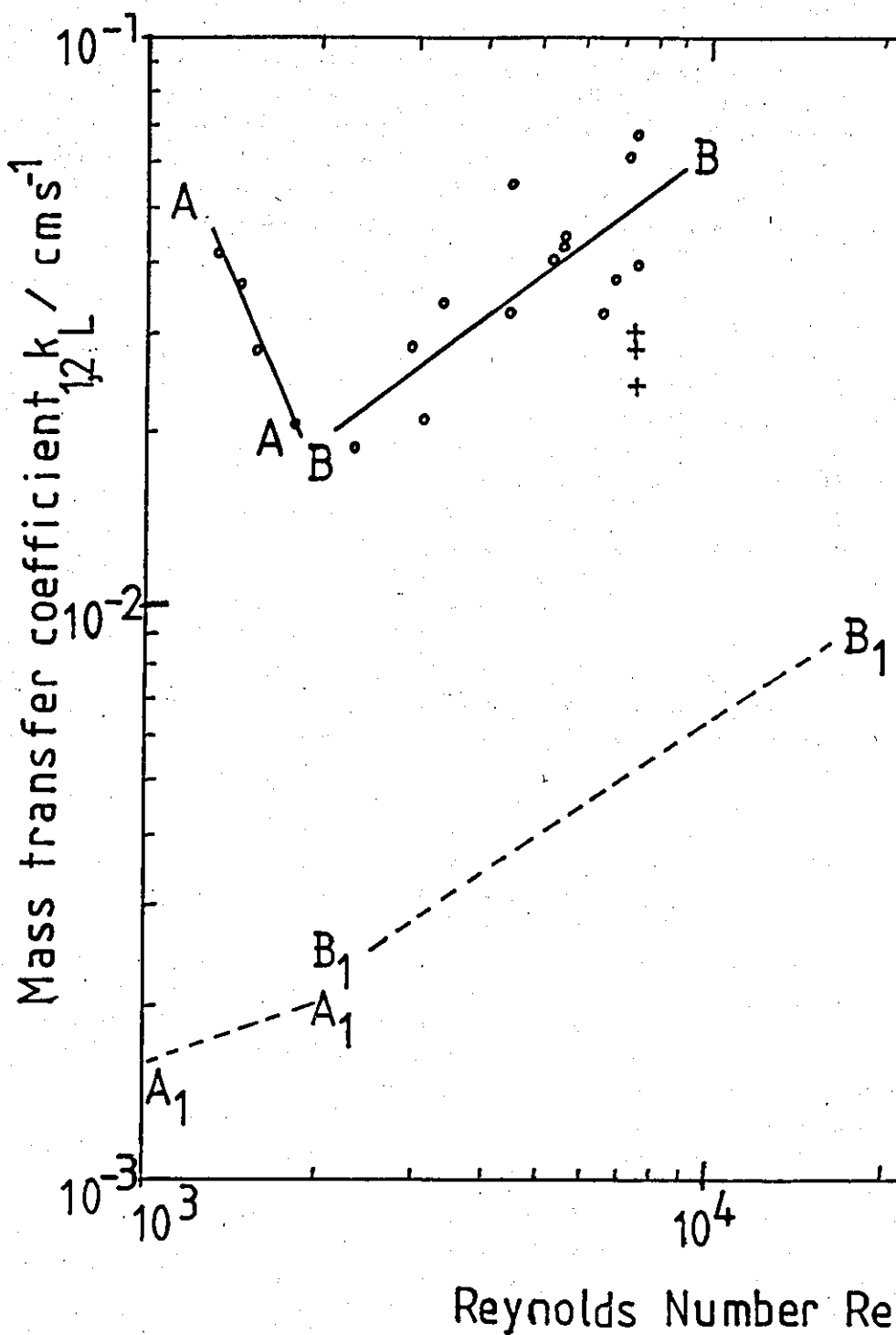


Fig.4.164 Rate of mass transfer of Ag^+ to cathodes 2.92 de in length, as a function of Reynolds number, during the electroforming of nickel at 60°C .

○ deposition current density = 0.4 A cm^{-2}

+ deposition current density = 0.7 A cm^{-2}

— line of best fit of data

- - - - Theoretical correlation (in the absence of gas evolution).

A₁ - A₁ , Equation 2.46

B₁ - B₁ , Equation 2.67

Detailed calculations of this type are described in Appendix 2b. The solution of Equation (2.49), in terms of $k_L^{Ag^+}$ is shown in Fig.4.164 by the broken line A₁ - A₁. As may be seen, in contrast to the experimental findings, the mass transfer rate increases with flow rate with a slope of 0.33. In addition, the experimental values of $k_L^{Ag^+}$ are at least one order of magnitude greater than predicted.

In turbulent flow (Re >2,000), the mass transfer coefficient increased with increasing flow rate. Linear regression analyses of the data resulted in a slope of 0.72 (r² ~0.76). The solid line B-B in Fig.4.164 represents the line of best fit of the data.

In turbulent flow, the values of $k_L^{Ag^+}$ were calculated from the relevant design equation (Appendix 2b).

$$Sh_{Av}^{Ag^+} = 0.145 Re^{0.667} Sc^{0.33} \dots \dots (2.67)$$

The solution of equation (2.67) is shown in Fig.4.164 by the broken line B₁ - B₁ of slope 0.67. It is evident that slopes of lines B-B and B₁ - B₁ are similar. However, the experimental results indicate an increase in $k_L^{Ag^+}$ of about one order of magnitude. The enhanced rate of mass transfer and other phenomena may be associated with the hydrogen gas evolution observed at the cathode affecting the transport mechanism.

The experimental mass transfer data for electroforms deposited at 0.7 A cm⁻² and Re 7,413 are summarised in Tables 4.45 and 4.46 and are also shown in Fig.4.164. The mean value of $k_L^{Ag^+}$ was ~2.8 x 10⁻² ± 0.3 x 10⁻² cm s⁻¹. At this flow rate the mass transfer coefficient would appear to be slightly less than observed at 0.4 A cm⁻². This effect may be due to differences in the distribution and size of the gas bubbles at higher current densities.

Mass transfer to 'long' electrodes (L/de ~11.7)

Nickel silver alloy electroforms were deposited at 0.4 A cm⁻² over the range of Reynolds numbers Re 2,067 to Re 7,388. In laminar flow (Re < 2,000), bubbles of hydrogen accumulated on the downstream end

Ag ⁺ ion concentration in diluted plating solution					Ag ⁺ ion concentration in diluted solution from dissolution of electrodeposit					
Reynolds Number	Dilution factor	Absorbance x 10 ⁻²			Concentration of Ag ⁺ x μg cm ⁻³	Dilution	Absorbance x 10 ⁻²			Concentration of Ag ⁺ y μg cm ⁻³
		x+0	x+1	x+2			y+0	y+1	y+2	
7,413	50/5	20.5	40	55.5	1.200	50 x 25/5	19.5	40	58.5	1.015
7,413	50/5	28.5	49.5	70.5	1.357	50 x 25/5	22	42	58	1.250
7,413	50/5	28.5	47	68	1.419	50 x 25/5	25	45.5	71	1.043

Table 4.45 Analysis of nickel sulphamate solutions and nickel electroforms for silver content

(L/de ~ 2.92, 60°C)

Reynolds Number	Bulk Soln. Concentration of Ag ⁺ c _b ^{Ag⁺} moles cm ⁻³	Wt. of silver present in deposit G g	Limiting current density for reduction of Ag ⁺ i _L ^{Ag⁺} A cm ⁻²	Mass Transfer Coefficient k _L ^{Ag⁺} cm s ⁻¹
7,413	1.11 x 10 ⁻⁷	2.53 x 10 ⁻⁴	3.04 x 10 ⁻⁴	2.83 x 10 ⁻²
7,413	1.26 x 10 ⁻⁷	3.12 x 10 ⁻⁴	3.79 x 10 ⁻⁴	3.08 x 10 ⁻²
7,413	1.32 x 10 ⁻⁷	2.60 x 10 ⁻⁴	3.12 x 10 ⁻⁴	2.45 x 10 ⁻²

Temperature : 60°C; Total Current Density : 0.70 A cm⁻²;
Thickness of Deposit : ~23μm; Electrode Area : 7.5 cm⁻²;
Deposition Time ~97 s

Table 4.46 Summary of electrolysis conditions and derived data in deposition experiments with added silver tracer

of the cathode and consequently the measurements were limited to flow rates greater than $Re\ 2,000$. At each flow rate, the electrolyte and the electroform were analysed for silver. The results are summarised in Tables 4.47 and 4.48.

The mass transfer relationships between $k_L^{Ag^+}$ and Re are shown in Fig.4.165 (log. coordinates). In turbulent flow, between $Re\ 2,583$ and $7,388$, the mass transfer coefficient increased with increasing flow rate. Linear regression of the data resulted in a slope of 0.75 ($r^2 \sim 0.92$). This is shown by the solid line A-A in Fig.4.165. At low flow velocities in the laminar - turbulent transition zone ($Re\ 2,067$) a marked decrease in the mass transfer coefficient was observed and this coincided with gas bubble adhesion.

For the 'long' electrode system, mass transfer coefficients were calculated from the following design equation (Appendix 2b):

$$Sh_{av}^{Ag^+} = 0.023 Re^{0.8} Sc^{0.33} \dots (2.66)$$

This solution of Equation 2.66 is shown in Fig.4.165 by the broken line $A_1 - A_1$ of slope 0.8 .

The experimental mass transfer coefficients were observed to be at least one order of magnitude greater than predicted by Equation 2.66. However, the slope of the experimental relationship is in good agreement with theory. The increased mass transfer rate is again probably due to microconvective mass transfer resulting from the concomitant hydrogen evolution.

Summary of Section 4.5.1

The following observations resulted from the mass transfer technique during foil deposition at constant current density.

- a) The rate of mass transfer of Ag^+ to both long (11.7) and short (2.92 de) cathodes in turbulent flow was at least one order of magnitude greater than predicted from the design equations.

Ag ⁺ ion concentration in diluted plating solution						Ag ⁺ ion concentration in diluted solution from dissolution of electrodeposit				
Reynolds number Re	Dilution factor a	Absorbance x 10 ⁻²			Concentration of Ag ⁺ \bar{x} μg cm ⁻³	Dilution factor b	Absorbance x 10 ⁻²			Concentration of Ag ⁺ y μg cm ⁻³
		x+0	x+1	x+2			y+0	y+1	y+2	
2,067	25/2	18.5	38	56.5	0.982	250x ^{25/5}	5.5	27	48	0.263
2,583	25/2	14.5	31	44.5	0.993	50x ^{25/5}	7	23	40	0.414
3,358	25/2	17	35.5	54	0.919	250x ^{25/5}	21	41	58.5	1.139
5,502	25/2	18	38	56.5	0.947	250x ^{25/5}	30	48.5	67.5	1.595
6,716	25/2	18.5	38.5	56.5	0.989	250x ^{25/5}	28.5	47.5	67	1.476
7,388	25/2	13.5	28.5	43.0	0.921	250x ^{25/5}	32	47.5	62.5	2.104

Table 4.47 Analysis of nickel sulphamate solutions and nickel electroforms for silver content

(L/de ~ 11.7, 60°C)

Reynolds number Re	Bulk soln. concentration of Ag^+ $c_b^{\text{Ag}^+}$ moles cm^{-3}	Wt. of silver G g	Limiting current density for reduction of Ag^+ $i_L^{\text{Ag}^+}$ A cm^{-2}	Mass transfer coefficient $k_L^{\text{Ag}^+}$ cm s^{-1}
2,067	1.14×10^{-7}	3.29×10^{-4}	5.94×10^{-5}	5.46×10^{-3}
2,583	1.15×10^{-7}	1.04×10^{-3}	1.88×10^{-4}	1.69×10^{-2}
3,358	1.07×10^{-7}	1.43×10^{-3}	2.58×10^{-4}	2.50×10^{-2}
5,502	1.10×10^{-7}	1.99×10^{-3}	3.59×10^{-4}	3.39×10^{-2}
6,716	1.15×10^{-7}	1.85×10^{-3}	3.34×10^{-4}	3.01×10^{-2}
7,388	1.07×10^{-7}	2.63×10^{-3}	4.75×10^{-4}	4.60×10^{-2}

$$L/d_e = \sim 11.7$$

Temperature : 60°C ; Total Current Density : 0.40 cm^{-2}
 Thickness of Deposit : $\sim 23 \mu\text{m}$; Electrode Area : 30 cm^{-2}
 Deposition Time : 165.1 s

Table 4.48 Summary of electrolysis conditions and derived data in deposition experiments with added silver tracer

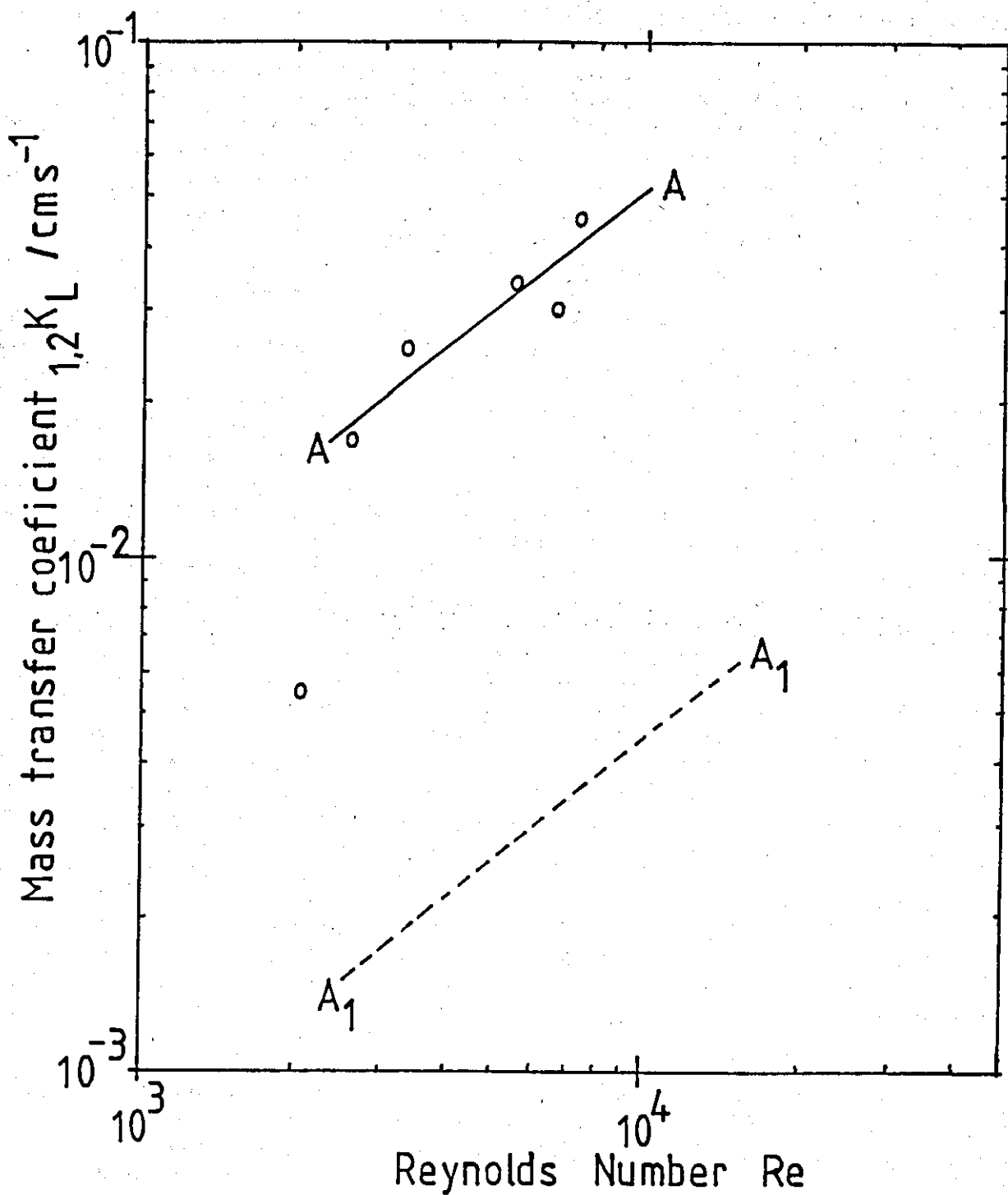


Fig.4.165 Rate of mass transfer of Ag^+ to cathodes 11.7 de in length as a function of Reynolds number, during the electroforming of nickel at 60°C and 0.4 A cm^{-2} .

A ——— A line of best fit of data
 - - - theoretical correlation (in the absence of gas evolution)

$A_1 - A_1$, Equation 2.46

$B_1 - B_1$, Equation 2.66

- b) Using short electrodes in turbulent flow, $k_L^{Ag^+}$ was found to be proportional to $[Re]^{0.72}$, which is in reasonable agreement with the design equation (Equation 2.67, $k_L^{Ag^+} \propto R^{0.66}$).
- c) Using long electrodes in turbulent flow, $k_L^{Ag^+}$ was found to be proportional to $Re^{0.75}$, which is in reasonable agreement with the design equation (Equation 2.66, $k_L^{Ag^+} \propto Re^{0.8}$).

The corresponding mass transfer coefficient for nickel ions ($k_L^{Ni^{2+}}$) is related to $k_L^{Ag^+}$ by

$$k_L^{Ni^{2+}} = k_L^{Ag^+} \left[\frac{D_{Ag^+}}{D_{Ni^{2+}}} \right]^{0.66} \dots \dots (4.5c)$$

as described previously (p.247). It is therefore evident that the mass transfer rate for nickel deposition is directly proportional to $k_L^{Ag^+}$. Hence the mass transfer correlations will be the same.

The visual observations of gas bubbles close to the cathode surface has suggested an association between the additional agitation of the electrolyte caused by bubble movement at the electrode - electrolyte interface and the enhanced rates of mass transfer. The possible effects of this microconvection will be examined in more detail in the following section.

4.5.2 A model for predicting the mass transfer correlation for parallel plate cells with enhanced mass transfer due to concomitant gas evolution

It is well established that gases evolving at an electrode do result in appreciable disturbances of the boundary layer (see Section 2.3c). Stephan and Vogt (211) have produced a model for correlating mass transfer data at gas evolving electrodes (p.67).

For mass transfer by gas bubbles alone the data were correlated by:

$$Sh_g = 0.93 Re_g^{0.5} Sc^{0.487} \dots \dots (2.85)$$

where:

$$Sh_g = \frac{k_L d}{D}$$

$$Re_g = \frac{V_g d}{\nu A_g}$$

d is the average diameter of gas bubbles (cm);

V_g is the volumetric rate of gas evolution (cm^3s^{-1});

and A_g is the area of gas evolving electrode (cm^2).

The case of mass transfer at gas evolving electrodes with superposition of hydrodynamic flow has been less fully investigated.

Vogt (217) has proposed the following equation for the superposition of macro-convective (hydrodynamic flow) and micro-convective (gas evolution), mass transfer (p.70).

$${}_{1,2} k_L = k_L^{\text{TOTAL}} = \left[1 + \left(\frac{{}_2 k_L}{{}_1 k_L} \right)^2 \right]^{0.5} \dots \dots (2.83)$$

where:

k_L^{TOTAL} = overall effective mass transfer coefficient cm s^{-1}

${}_1 k_L$ = mass transfer coefficient for macro-convections cm s^{-1}

${}_2 k_L$ = mass transfer coefficient for micro-convection cm s^{-1}

The micro-convective mass transfer coefficient k_L^2 may be calculated from Equation (2.85). The macro-convective mass transfer coefficient ${}_1 k_L^1$ was determined by solution of the design equations for 'long' and 'short' electrodes (Equations (2.49), 2.66) and (2.67).

Calculation of volumetric rate of hydrogen evolution

The approximate rate of hydrogen gas evolution per unit area, $\frac{V_g}{A_g}$, may be found by assuming a current efficiency of ~5% for the hydrogen evolution reaction. Therefore, for a total current density

of 0.40 A cm^{-2} , the hydrogen current density will be, $i \sim 0.02 \text{ A cm}^{-2}$. The operating temperature of the solution was 333.2 K (60°C) and the cell pressure $P \sim 1.5 \times 10^6 \text{ dynes cm}^{-2}$. The molar volume, V_g , of hydrogen is given by:

$$V_g = \frac{RT}{P}$$

$$V_g = \frac{8.314 \times 10^7 \times 333.3}{1.5 \times 10^6}$$

$$V_g = \underline{1.82 \times 10^4 \text{ cm}^3 \text{ mol}^{-1}}$$

The volumetric rate of hydrogen evolution per unit area, $\frac{Q_g}{A}$ is obtained from:

$$\frac{Q_g}{A} = V_g \frac{I/A}{zF} = V_g \frac{i}{zF}$$

and for production of H_2 , $z = 2$, hence:

$$\begin{aligned} \frac{Q_g}{A} &= 1.82 \times 10^4 \times \frac{0.02}{2 \times 9,6500} \\ &= \underline{1.9 \times 10^{-3} \text{ cm}^3 \text{ s}^{-1}} \end{aligned}$$

Calculation of gas bubble Reynolds numbers, Re_g

To evaluate Re_g requires an estimate of the average gas bubble diameter (d). Stephan and Vogt (211) have stated a gas break off diameter for hydrogen bubbles of $\sim 60 \mu\text{m}$ in acidic solutions. However, this value applied to nearly stagnant solutions. In a flowing electrolyte, gas bubble diameters are probably considerably less than $60 \mu\text{m}$.

There is evidence to suggest that large numbers of bubbles $< 2 \mu\text{m}$ in diameter may be formed in flowing nickel sulphamate solutions (Section 4.1 and 4.2 and Appendix 4b).

Gas Reynolds numbers were calculated for a range of bubble diameters from $60\mu\text{m}$ down to $0.1\mu\text{m}$, as shown below:

$$\text{Re}_g = \frac{V_g d}{\nu_{Ag}}$$

$$d \sim 60\mu\text{m} \equiv 60 \times 10^{-4} \text{ cm}$$

$$\nu \sim 1.202 \times 10^{-2} \text{ cm s}^{-1}$$

$$\frac{V_g}{A_g} \sim 1.9 \times 10^{-3} \text{ cm s}^{-1}$$

$$\text{Re}_g^{60\mu\text{m}} \approx \frac{1.9 \times 10^{-3} \times 60 \times 10^{-4}}{1.202 \times 10^{-2}}$$

$$\text{Re}_g^{60\mu\text{m}} \approx \underline{\underline{9.5 \times 10^{-4}}}$$

The gas Reynolds numbers are summarised in Table 4.49.

Calculation of microconvective mass transfer coefficients $k_L^{Ag^+}$ and $\frac{\text{Sh}_{Ag^+}}{g}$

The microconvective mass transfer correlations of Stephan and Vogt,

$$\text{Sh}_g = 0.93 \text{Re}_g^{0.5} \text{Sc}^{0.487} \dots \dots (2.85)$$

was used to predict mass transfer coefficients for the transport controlled reduction of silver ions in a nickel sulphamate electrolyte. The value of the diffusion coefficient (D_{Ag^+}) was taken to be $\sim 1.0 \times 10^{-5} \text{ cm}^2 \text{ s}^{-1}$ (344).

Then

$$\text{Sc} = \frac{\nu}{D_{Ag^+}}$$

$$\nu \sim 1.202 \times 10^{-2} \text{ cm}^2 \text{ s}^{-1}, D_{Ag^+} \sim 1.0 \times 10^{-5} \text{ cm}^2 \text{ s}^{-1}$$

$$\text{Sc} \approx \frac{1.202 \times 10^{-2}}{1.0 \times 10^{-5}}$$

$$\text{Sc} \sim \underline{\underline{1202}}$$

Gas bubble diameter $d_{\mu\text{m}}$	Reynolds number $\text{Re}_g \times 10^{-4}$	Sherwood number $\text{Sh}_g^{\text{Ag}^+}$	Mass Transfer coefficient $k_L^{\text{Ag}^+}$ cm s^{-1}
60	9.5	0.84	1.41×10^{-3}
2	0.32	0.154	7.70×10^{-3}
1	0.16	0.109	10.9×10^{-3}
0.5	0.079	0.077	15.4×10^{-3}
0.2	0.032	0.049	24.4×10^{-3}
0.1	0.016	0.034	34.4×10^{-3}

$$\frac{V_g}{A_g} \sim 1.9 \times 10^{-3} \text{ cm s}^{-1}$$

$$D \sim 1 \times 10^{-5} \text{ cm}^2 \text{ s}^{-1}$$

$$\text{Sc} \sim 1202$$

$$\text{Sh} = 0.93 \text{Re}_g^{0.5} \text{Sc}^{0.477}$$

Table 4.49 Dimensionless variables and theoretical mass transport coefficients for the microconvective (gas only) transport of silver tracer in nickel sulphamate solutions.

For 60 μm bubbles, $Re_g^{60\mu\text{m}} \sim 9.3 \times 10^{-4}$

and hence

$$60\mu\text{m} Sh_g^{Ag^+} = 0.93 \times (9.3 \times 10^{-4})^{0.5} \times (1202)^{0.487}$$

$$60\mu\text{m} Sh_g^{Ag^+} \approx \underline{0.84}$$

Now as,

$$60\mu\text{m} Sh_g^{Ag^+} = \frac{k_L^{Ag^+} d}{D_{Ag^+}}$$

then

$$60\mu\text{m} {}^2k_L^{Ag^+} \approx \frac{0.84 \times 1.0 \times 10^{-5}}{60 \times 10^{-4}}$$

$$60\mu\text{m} {}^2k_L^{Ag^+} \approx \underline{1.41 \times 10^{-3} \text{ cm s}^{-1}}$$

Calculated values of $Re_g^{Ag^+}$, $Sh_g^{Ag^+}$ and ${}^2k_L^{Ag^+}$ are shown in Table 4.49 for bubble diameters of 60, 2, 1, 0.5, 0.2 and 0.1 μm . As may be seen, the higher rates of mass transfer will be favoured by a small bubble size.

a) Mass transfer correlation for 'long' electrodes ($L/de \sim 11.7$), at 60°C.

Calculation of macroconvective mass transfer coefficients

Mass transfer coefficients for the reduction of silver ions in nickel sulphamate electrolyte, were calculated from Equation (2.49) for laminar flow,

$$Sh_{de}^{Ag^+} = 1.85 \left\{ Re_{de} \frac{de}{L} Sc \right\}^{0.333} \dots (2.49)$$

and Equation (2.66)

$$Sh_{de}^{Ag^+} = 0.023 Re_{de}^{0.8} Sc^{0.333} \dots (2.66)$$

for turbulent flow.

The values of the macroconvective mass transfer coefficients $Sh_{de}^{Ag^+}$ and ${}_1k_L^{Ag^+}$ were calculated (as shown in Appendix 2b) and are given in Table 4.50 for Reynolds numbers of 1,000, 2,000, 4,000, 8,000 and 16,000.

Calculation of the combined macro- and micro-convective mass transfer coefficient ${}_{1,2}k_L^{Ag^+}$

The combined mass transfer coefficient, ${}_{1,2}k_L^{Ag^+}$ for both macro and micro convection was calculated from the Vogt equation:

$${}_{1,2}k_L = {}_1k_L \left[1 + \left(\frac{{}_2k_L}{{}_1k_L} \right)^2 \right]^{0.5} \dots \dots (2.88)$$

Macroconvective mass transfer coefficients ${}_1k_L^{Ag^+}$ were calculated and are shown in Table 4.50, for a series of Reynolds numbers. The estimated microconvective mass transfer coefficients ${}_2k_L^{Ag^+}$ calculated previously, were taken from values given in Table 4.49, for a series of average bubble diameters and a gas evolution rate of $1.9 \times 10^{-3} \text{ cm s}^{-1}$.

For example:

$$Re \approx 1,000, \quad {}_1k_L^{Ag^+} \sim 1.01 \times 10^{-3} \text{ cm s}^{-1} \dots \dots (\text{Table 4.45})$$

and

$$d \approx 60\mu\text{m}, \quad {}_2k_L^{Ag^+} \sim 1.41 \times 10^{-3} \dots \dots (\text{Table 4.44})$$

The combined mass transfer coefficient, ${}_{1,2}k_L^{Ag^+}$ is then given by

$${}_{1,2}k_L^{Ag^+} \approx 1.41 \times 10^{-3} \left[1 + \frac{1.01 \times 10^{-3}}{1.41 \times 10^{-3}}^2 \right]^{0.5}$$

$${}_{1,2}k_L^{Ag^+} \approx \underline{\underline{1.73 \times 10^{-3} \text{ cm s}^{-1}}}$$

Hence, the combined mass transfer coefficient ${}_{1,2}k_L^{Ag^+}$ for the reduction of silver on electrodes 11.7 equivalent diameters in length with a linear flow equivalent to Re 1,000 and concomitant gas evolution at a rate of $1.9 \times 10^{-3} \text{ cm s}^{-1}$ with gas bubbles 60 μm in diameter was calculated to be $1.73 \times 10^{-3} \text{ cm s}^{-1}$.

Reynolds number Re_{de}	Sherwood number $Sh_{de}^{Ag^+}$	Mass Transfer coefficient $k_L^{Ag^+}$ $cm\ s^{-1}$
1,000	86.7	1.01×10^{-3}
2,000	109	1.28×10^{-3}
4,000	286	2.17×10^{-3}
8,000	324	3.78×10^{-3}
16,000	565	6.59×10^{-3}

$$L/de \sim 11.7$$

$$D_{Ag^+} \sim 1 \times 10^{-5} \text{ cm}^2 \text{ s}^{-1}$$

$$Sc \sim 1202$$

Laminar Flow

$$Sh = 1.85 \left\{ Re \frac{de}{L} Sc \right\}^{0.333}$$

Turbulent Flow

$$Sh = 0.023 Re^{0.8} Sc^{0.333}$$

Table 4.50 Dimensionless variables and theoretical mass transfer coefficients for the macro-convective (flow only) transport of silver tracer in nickel sulphamate solution. 'Long' electrodes.

The results for other values of Re_{de} and gas bubble diameter are shown in Table 4.51. As may be seen with a small bubble size, microconvective (gas assisted) mass transfer will dominate.

Interpretation

The results obtained for combined effect mass transfer to electrodes 11.7 equivalent diameters in length are displayed graphically on logarithmic co-ordinates as combined mass transfer coefficient versus solution flow Reynolds number for each bubble diameter (Fig.4.166). The line A-A represents the mass transfer correlation in the absence of gas evolution as given by the solution of the appropriate design equations (p.128). The general effect of gas evolution is to increase mass transfer coefficients.

When the bubble size is $\sim 60\mu\text{m}$ (line B-B) in diameter, significant increases in the value of $k_{L,2}^{Ag^+}$ occur at low Reynolds numbers. As the flow becomes turbulent, the contribution of micro-convective mass transfer to the combined mass transfer coefficient decreases. The effect of micro-convection is negligible at $Re,6,000$ and mass transfer due to solution flow dominates.

A bubble size of $\sim 2\mu\text{m}$ results in enhanced mass transfer at Reynolds numbers from 1,000 to 16,000 (line C-C). The mass transfer correlation is dominated by mass transfer enhancement due to gas bubbles over the Reynolds number range $Re \sim 1,000$ to $Re \sim 5,000$. Mass transfer coefficients are practically constant over this range. At $Re > 5,000$ the mass transfer due to turbulent flow becomes more apparent and overall mass transfer rates increase. At very high Reynolds numbers ($Re \gg 16,000$), macro-convective mass transfer will again predominate.

Mass transfer enhancement due to bubbles $\sim 0.1\mu\text{m}$ in diameter will dominate over solution flow over the Reynolds number range $Re 1,000$ to $Re 16,000$ (line D-D). The combined mass transfer coefficient will be independent of solution Reynolds number.

Reynolds number Re_{de}	Combined mass transfer Coefficient $\frac{{}_1,{}_2k_L}{d_e} \text{ cm s}^{-1}$ Gas bubble diameter		
	60 μm	2 μm	0.1 μm
1,000	1.73×10^{-3}	7.77×10^{-3}	34.2×10^{-3}
2,000	1.90×10^{-3}	7.81×10^{-3}	34.5×10^{-3}
4,000	2.59×10^{-3}	8.00×10^{-3}	34.5×10^{-3}
8,000	4.03×10^{-3}	8.58×10^{-3}	34.7×10^{-3}
16,000	6.74×10^{-3}	10.1×10^{-3}	35.1×10^{-3}

$$L/d_e \sim 11.7$$

$$D \sim 1 \times 10^{-5} \text{ cm}^2 \text{ s}^{-1}$$

$$Sc \sim 1,202$$

$${}_1,{}_2k_L = {}_1k_L \left[1 + \left(\frac{{}_2k_L}{{}_1k_L} \right)^2 \right]^{0.5}$$

${}_1k_L$ - macro-convection

${}_2k_L$ - micro-convection

Table 4.51 Summary of the theoretical combined mass transfer coefficients for the transport of silver in nickel sulphamate solutions. 'Long' electrodes.

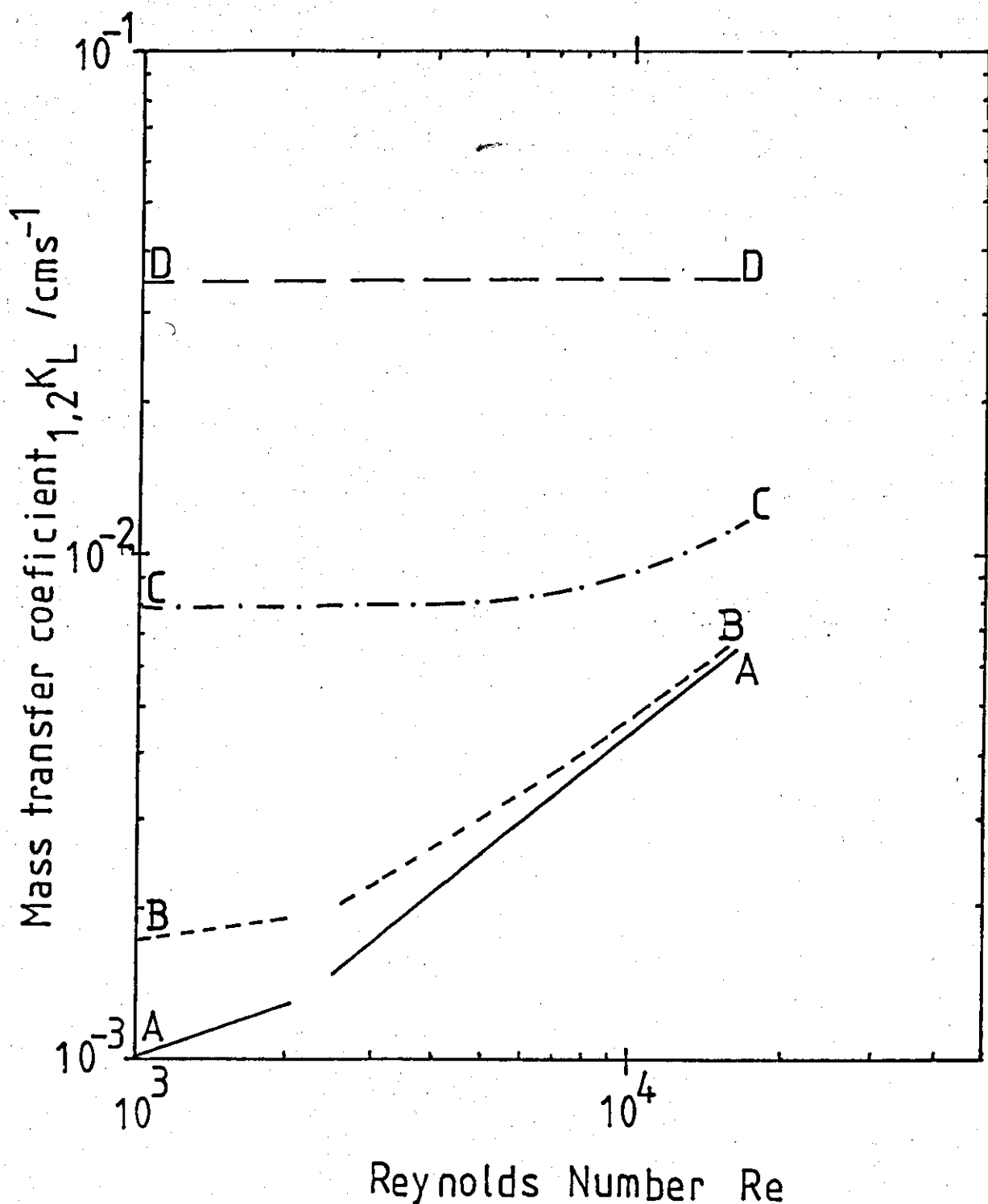


Fig.4.166 Theoretical correlation of the rate of mass transfer of Ag^+ to cathodes 11.7 de in length as a function of Reynolds number, with gas assisted mass transfer.

A — A - mass transfer in the absence of gas evolution (Equations 2.46 and 2.66)

gas assisted mass transfer rates calculated from Equations 2.46, 2.66, 2.85 and 2.88 for the following bubble diameters

B - - - B , 60 μm bubbles
 C - · - C , 2 μm bubbles
 D — — D , 1 μm bubbles

A bubble size of ~0.1µm results in very high rates of mass transfer, of the same order of magnitude as the experimental values (cf Fig.4.165).

b) Mass transfer correlation for 'short' electrodes ($L/d_e \sim 2.92$) at 60°C

Calculation of macro convective mass transfer coefficients

Mass transfer coefficients for the reduction of silver ions in nickel sulphamate electrolyte were calculated from Equation (2.49) for laminar flow

$$Sh_{de}^{Ag^+} = 1.85 \left\{ Re_{de} \frac{de}{L} Sc \right\}^{0.333} \dots \dots (2.49)$$

and from Equation (2.67)

$$Sh_{de}^{Ag^+} = 0.145 Re^{0.567} Sc^{0.333} \frac{de}{L}^{0.25} \dots \dots (2.67)$$

for turbulent flow.

The values of the macroconvective mass transfer coefficients, $Sh_{de}^{Ag^+}$, $k_L^{Ag^+}$ were calculated (as described in Appendix 2b) and are given in Table 4.47 for Reynolds numbers (Re_{de}) of 1,000, 2,000, 4,000, 8,000 and 16,000.

Calculation of combined macro- and micro-convective mass transfer coefficients

The combined mass transfer coefficient $k_{L,2}^{Ag^+}$ for both micro- and macro- convection was calculated from the Vogt equation

$$k_{L,2}^{Ag^+} = k_{L,1}^{Ag^+} \left[1 + \left(\frac{k_{L,2}^{Ag^+}}{k_{L,1}^{Ag^+}} \right)^2 \right]^{0.5} \dots \dots (2.88)$$

The estimated microconvective mass transfer coefficients $k_{L,1}^{Ag^+}$ were calculated previously (Table 4.49) for a series of average bubble diameters and a gas evolution rate of $1.9 \times 10^{-3} \text{ cm s}^{-1}$. The calculated values of $k_{L,2}^{Ag^+}$ are given in Table 4.52 for each bubble diameter. The method of calculation of the combined mass transfer coefficient, $k_{L,2}^{Ag^+}$ using Equation (2.88) was shown on page 256.

Reynolds number Re_{de}	Sherwood number $Sh_{de}^{Ag^+}$	Mass Transfer coefficient $k_L^{Ag^+}$ $cm\ s^{-1}$
1,000	137.6	1.61×10^{-3}
2,000	173.4	2.02×10^{-3}
4,000	297.2	3.47×10^{-3}
8,000	471.8	5.51×10^{-3}
16,000	748.9	8.74×10^{-3}

$$L/de \sim 2.92$$

$$D \sim 1 \times 10^{-5} \text{ cm}^2 \text{ s}^{-1}$$

$$Sc \sim 1,202$$

Laminar Flow

$$Sh = 1.85 \left\{ Re \frac{de}{L} Sc \right\}^{0.333}$$

Turbulent Flow

$$Sh = 0.145 Re^{0.667} Sc^{0.333} \frac{de}{L}^{0.25}$$

Table 4.52 Dimensionless variables and theoretical mass transfer coefficients for the macro-convective (flow only) transport of silver tracer in nickel sulphamate solutions. 'Short' electrodes.

The values of $_{1,2}k_L^{Ag^+}$ were estimated for Reynolds numbers of 1,000, 2,000, 4,000, 8000 and 16,000 and bubble diameters of 60, 2 and 0.1 μ m. The data are shown in Table 4.53.

Interpretation

The calculated values of the combined mass transfer coefficient $_{1,2}k_L^{Ag^+}$, of Table 4.53 is displayed graphically on logarithmic coordinates as a function of solution Reynolds number, for each average bubble diameter (Fig.4.167).

The line A-A of Fig.4.167 represents the mass transfer correlation in the absence of gas evolution as determined by solution of the appropriate design equation. The overall effect of gas evolution will be to increase the mass transfer coefficients. However, the increased rate of 'flow only' mass transfer to electrodes 2.92 equivalent diameters long will result in a smaller micro-convective contribution to the combined mass transfer coefficient when compared to combined mass transfer to electrodes 11.7 equivalent diameters in length.

An average bubble size of $\sim 60\mu$ m (line B-B) will result in appreciable increases in mass transfer rate in laminar flow. In turbulent flow, the increase in mass transfer coefficient is relatively insignificant.

As the bubble size is reduced the influence of microconvection progressively dominates. With an average bubble diameter of $\sim 2\mu$ m (line C-C) mass transfer coefficients will tend to be independent of flow rate, particularly in laminar flow. Macro-convective mass transfer begins to be significant at about Re, 3,000. At Re, 16,000 the combined mass transfer coefficient approaches the 'flow only' mass transfer coefficient.

However, a further decrease in bubble size to an average bubble diameter of $\sim 0.2\mu$ m (line D-D) will result in the predominance of micro-convection over macro-convection. The combined mass transfer coefficient is almost independent of Reynolds number up to Re, 16,000. At very high Reynolds numbers the macroconvective contribution will again become significant.

Reynolds number	Combined mass transfer Coefficient _{1,2} k _L ^{Ag⁺} cm s ⁻¹ Gas bubble diameter		
	60 μm	2 μm	0.1 μm
1,000	2.14 x 10 ⁻³	7.87 x 10 ⁻³	34.5 x 10 ⁻³
2,000	2.46 x 10 ⁻³	7.96 x 10 ⁻³	34.5 x 10 ⁻³
4,000	3.75 x 10 ⁻³	8.45 x 10 ⁻³	34.6 x 10 ⁻³
8,000	5.69 x 10 ⁻³	9.47 x 10 ⁻³	34.9 x 10 ⁻³
16,000	8.85 x 10 ⁻³	11.7 x 10 ⁻³	35.5 x 10 ⁻³

$$L/d_e \sim 2.92$$

$$D \sim 1 \times 10^{-5} \text{ cm}^2 \text{ s}^{-1}$$

$$Sc \sim 1,202$$

$${}_{1,2} k = {}_1 k_L \left[1 + \left(\frac{{}_2 k_L}{{}_1 k_L} \right)^2 \right]^{0.5}$$

${}_1 k_L$ - macro-convection

${}_2 k_L$ - micro-convection

Table 4.53 Summary of the theoretical combined mass transfer coefficients for the transport of silver in nickel sulphamate solutions. 'Short' electrodes.

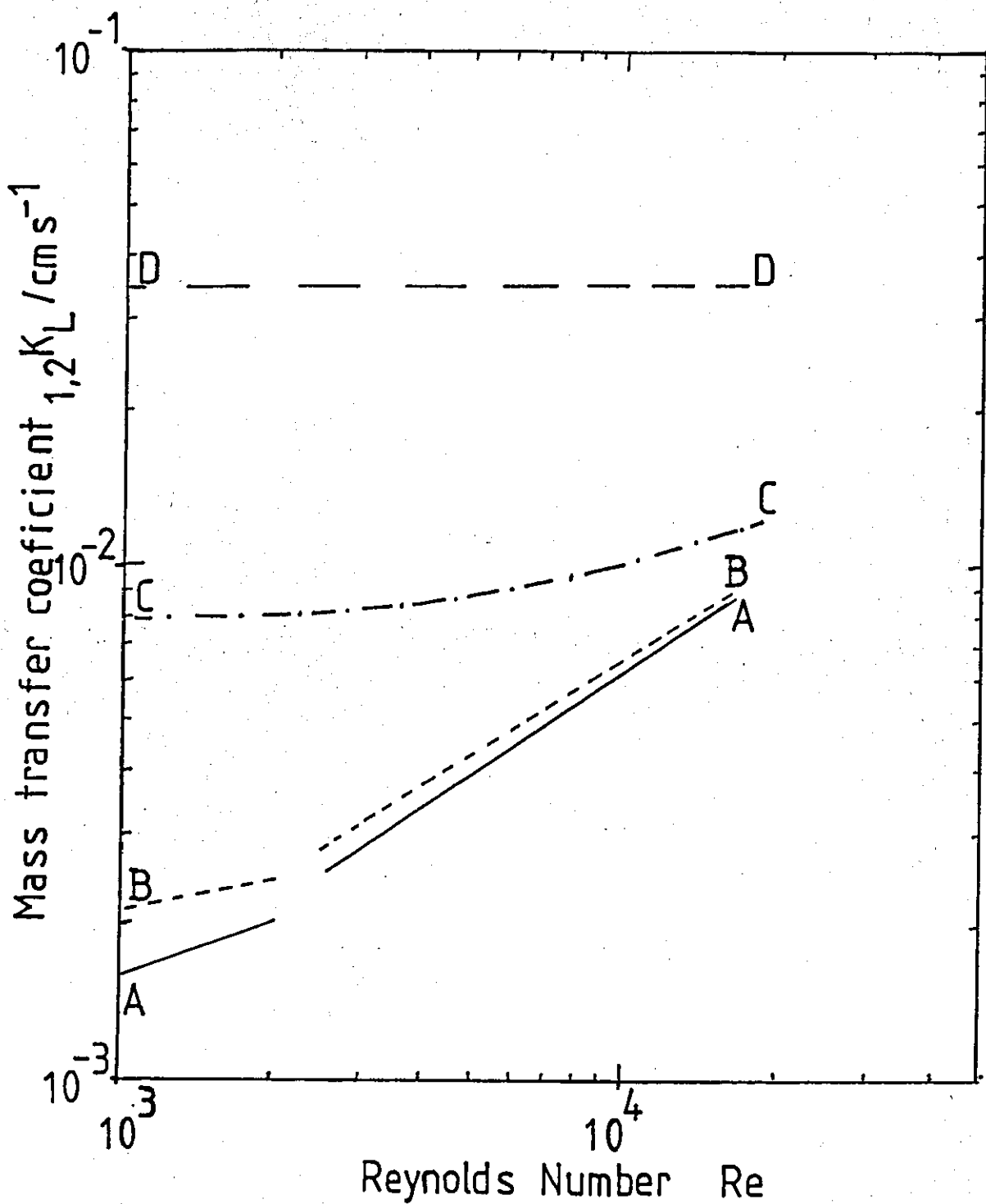


Fig.4.167 Theoretical correlation of the rate of mass transfer of Ag^+ to cathodes 2.92 de in length as a function of Reynolds number, with gas assisted mass transfer,

A — A - mass transfer in the absence of gas evolution (Equations 2.46 and 2.67)

gas assisted mass transfer rates calculated from Equations 2.46, 2.67, 2.85 and 2.88 for the following bubble diameters

- B - - - B , 60 μm bubbles
- C - . - C , 2 μm bubbles
- D - - - D , 1 μm bubbles

With a gas bubble diameter of about $0.1\mu\text{m}$, the rates of mass transfer are comparable with the experimental results (Section 4.5.1).

In practice it is probable that gas bubbles with a wide range of bubble diameters may be produced. The average bubble diameter is probably a function of the flow rate and the rate of gas evolution (see Section 2.3c). At high Reynolds numbers the bubble size will be smaller than at lower Reynolds numbers. Hence the experimental mass transfer correlation may be complex, as the contribution of micro-convection to the overall rate changes with the flow conditions and the deposition rate.

Overall summary of mass transport studies in nickel sulphamate solution

The experimental study using the silver tracer method, has indicated that in turbulent flow the rate of mass transport in nickel sulphamate solutions may be an order of magnitude greater than expected from a simple theoretical transport analysis. This applies to both long and short cathode geometries. Additional anomalies were observed in laminar flow, where gas bubble adhesion was evident.

The concomitant hydrogen gas evolution at the cathode may also tend to increase transport rates and may provide an explanation of the experimental results.

The model for the combined effects of solution flow and gas evolution has indicated that for small gas bubbles ($\sim 0.1\mu\text{m}$), the rates of mass transfer are comparable to that observed experimentally.

An overview of the results

The preliminary studies in Cell 1 have shown that sound nickel foils may be deposited at high current densities. At the maximum current density (i_{\max}), nickel hydroxide and powder was deposited. However, it was noted that anode gases contact the cathode, particularly at low flow rates and may influence the cathodic processes.

The Cell 2 design incorporated a dividing diaphragm to separate the anode from the cathode. This unusual cell design was characterised using the mass transfer controlled deposition of copper from a dilute acid copper sulphate electrolyte.

Detailed electroforming studies in Cell 2 have shown that sound and coherent nickel foils may be deposited, at high current efficiency (>95%) at current densities up to $\sim 1.3 \text{ A cm}^{-2}$. Hydrogen bubbles were observed streaming along the cathode length.

The maximum current density (i_{\max}) was observed to increase, with increasing flow rate and temperature, and decreasing cathode length. However the absolute value of i_{\max} was found to be significantly less than the value of i_L , as calculated from the design equations.

Current distribution studies have shown that under the normal operating conditions (i.e. anode length greater or equal to the cathode length) high current densities were observed at the leading and trailing edges. A mass transfer controlled current distribution was not observed. The maximum current density was significantly increased to $>2 \text{ A cm}^{-2}$ by operating the cell with a uniform current distribution to produce deposits of a more uniform structure.

An investigation of the anodic polarisation behaviour has shown that oxygen evolution was the principal anode reaction. The low concentration of chloride used in the present work was ineffective in promoting anode corrosion.

There was no clear evidence of a cathodic limiting current density. Inflections observed during cathodic polarisation studies may be

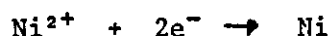
associated with the reduction of oxygen or effects related to the evolution of hydrogen.

Finally it has been shown, using the silver tracer technique, that mass transfer rates during nickel deposition were greater than expected from the design equations. A model of mass transfer, in a flowing system (macroconvection) with superimposed hydrogen evolution (microconvection), has indicated that mass transfer rates are enhanced by gas evolution.

It is clear that the experimental results are not consistent with a 'simple' mass transfer model, involving the transport of aqueous nickel ions. This inconsistency is examined further in the following Chapter.

5. DISCUSSION

An initial survey of the literature had provided no direct evidence of mechanistic complexity in the nickel sulphamate system. An overall process of the form



was therefore assumed. Hence at the outset of the present work a rather simplistic approach was adopted in devising the experimental programme. Hence it was reasonable to assume that the expected characteristics of a mass transfer controlled reaction would be observed.

However as has been seen, the nickel sulphamate system proved to be more complex than at first envisaged, providing little or no evidence of a simple mass transfer controlled (m.t.c.) process. For this reason the discussion of the results is presented in direct comparison with the relatively simple m.t.c. process of copper deposition from dilute acid copper sulphate electrolyte.

The discussion is presented in four sections. The mass transport and current distribution aspects of the electro-deposition are examined in Sections 5.1 and 5.2 respectively. In both sections the case of copper and nickel deposition are discussed separately.

The polarisation behaviour of the nickel system and the evidence relating to the structure and properties of the nickel electroforms are discussed in Sections 5.3 and 5.4 respectively.

The final section (Section 5.5) consists of some general and practical implications of the present work with regard to the fast electrodeposition of nickel and includes an overall summary of the discussion.

5.1 Mass Transport Studies

(a) Mass transport studies in the $\text{CuSO}_4 - \text{H}_2\text{SO}_4$ system

It was of interest to study the deposition of copper, to establish the mass transfer characteristics of Cell 2 independently from the Ni-based system. This also provided some direct comparison with the nickel deposition system.

The cathodic deposition of copper from a dilute acid copper sulphate system has been widely used in previous studies of the mass transport characteristics of a range of electrochemical cell designs (e.g. 25-29). The system offers several advantages for mass transport studies, of which the occurrence of a well-defined limiting current density is of major importance. Values of the necessary physical properties of the electrolyte (density, viscosity and diffusion coefficient) are readily available from the literature. The system is also cheap, chemically stable and simple to analyse (by A.A.S.)

Dilute copper solutions (usually $< 0.1 \text{ M Cu}$) are preferred for the following reasons:

- (i) Changes in the diffusion coefficient close to the electrode/electrolyte interface due to a decreased copper concentration within the mass transfer boundary layer are minimised.
- (ii) The effect of free convection at low Reynolds Numbers ($\text{Re} < 500$) resulting from significant changes in the copper concentration and hence the electrolyte density within the mass transfer boundary layer are minimised.
- (iii) Convenient values of the limiting current densities are produced to enable the use of cathodes of a reasonable size. This avoids the need for high current output instrumentation.
- (iv) Well defined limiting current densities are obtained in less concentrated solutions. At much higher copper concentrations

mass transfer rates are high and deposits may become rough and powdery. The resulting increase in the effective surface area and the cathode and hence the current requirements, may obscure the limiting current.

The acid component of the electrolyte (1.5M H₂SO₄) acts as a supporting electrolyte and minimises the migration of copper ions in the electric field. The acid also ensures that the solution has a high electrical conductivity.

For the present study, the system 0.014M CuSO₄ - 1.5M H₂SO₄ was selected, since the temperature dependence of the diffusion coefficient, viscosity and density of this system were well known (342). The anode reaction was copper dissolution, which proceeds at 100% efficiency under the conditions used (in contrast to the nickel system).

Cathodic polarisation behaviour

Before discussing the effects of the various experimental variables on the deposition rate, it is of interest, for later comparison with the nickel sulphamate system, to briefly examine the mechanism and cathodic polarisation behaviour of the copper deposition system.

The deposition of copper from dilute sulphate solutions represents a relatively simple process (involving aquo-cations). Although the overall reduction process may be written as



it has been shown (6) that the reaction proceeds in two steps:



The simple electron charge transfer step (5.1a) is rate determining at potentials not too near the reversible potential. At lower potentials the reaction may become mass transfer controlled. In general, the separation between the potential at which the reaction becomes mass

transfer limited and the discharge potential of hydrogen (the secondary reaction) is sufficient to result in a clearly defined limiting current.

The above features were clearly observed in the experimental cathodic polarisation curves, particularly in laminar flow (e.g. Fig.4.30). The charge transfer step is rate determining at overpotentials $>-50\text{mV}$ and the deposition process becomes mass transfer controlled at lower over potentials. The limiting current plateau was generally observed over the potential range -100 to -600 mV (vs.Cu reference).

However, at higher temperatures, turbulent flow rates (e.g. Fig.4.43) and short cathode lengths (e.g. Fig.4.53), where mass transfer rates are greatest, the limiting current plateau may be distorted. This effect was probably due to the observed increase in the roughness of the deposit at high rates of mass transfer resulting in an effective increase in the surface area of the cathode and hence higher currents.

However, it should be noted that even at the highest temperatures ($\sim 60^\circ\text{C}$) and Reynolds number ($\text{Re} \sim 30,000$) and the shortest cathodes ($L/d_e \sim 0.5$), a limiting current density was clearly observed.

As has been seen (Section 2.1a and 2.3a), the deposition rate is directly related to the limiting current density and hence to the mass transfer coefficient. It was evident that, for the present investigation, the results may be discussed in terms of the three principal factors affecting the deposition rate i.e. temperature, cathode length and flow rate.

The above variables were combined in a series of dimensionless mass transfer correlations, which describe the mass transfer performance of the cell over specific ranges of experimental conditions.

i) The effect of temperature (at constant flow rate and cathode length)

The theoretical aspects of the effect of temperature on the deposition rate were described previously in Section 2.1b. In general, a higher temperature favours a faster rate of mass transfer and hence

higher limiting current densities. This was confirmed by the experimental results, in both laminar (Fig.4.39) and turbulent (Fig.4.49) flow.

As has been seen (Section 2.1b), an increase in the temperature of the electrolyte affects both the value of the diffusion coefficient (D) and the kinematic viscosity (ν) and both terms appear in the design equations for the cell. For example, in turbulent flow (long electrode system, p.128), the design equation is:

$$Sh_{av} = 0.023 Re^{0.8} Sc^{0.33} \dots\dots(2.65)$$

or in expanded form

$$\frac{k_L de}{D} = 0.023 \left(\frac{U de}{\nu} \right)^{0.8} \left(\frac{\nu}{D} \right)^{0.33} \dots\dots(2.65a)$$

Therefore in terms of the mass transfer coefficient, k_L

$$k_L = 0.023 U^{0.8} d_e^{-0.2} \nu^{-0.47} D^{0.67} \dots\dots(2.65b)$$

The relative change $\frac{k_L}{k_L}$ in the rate of mass transport over the temperature change T_1 to T_2 is given, for a constant flow rate u and equivalent diameter, de by

$$\frac{k_L}{k_L} = \left[\frac{\nu_1}{\nu_2} \right]^{-0.47} \left[\frac{D_1}{D_2} \right]^{0.67} \dots\dots(5.1a)$$

where the subscripts 1 and 2 refer to the value of ν and D at temperatures T_1 and T_2 respectively.

Similarly at constant Reynolds number $\left(\frac{U de}{\nu} \right)$

$$\frac{k_L}{k_L} = \left[\frac{\nu_1}{\nu_2} \right]^{0.33} \left[\frac{D_1}{D_2} \right]^{0.67} \dots\dots(5.1b)$$

The relative change in the mass transfer coefficient $\frac{k_L}{k_L}$ for the copper deposition system used in the present work over the temperature range 50° to 60°C, may be calculated as follows:

When $T_1 = 50^\circ\text{C}$, $v_1 = 0.63 \times 10^{-2} \text{ cm}^2 \text{ s}^{-1}$, $D = 9.8 \times 10^{-6} \text{ cm}^2 \text{ s}^{-1}$
 and $T_2 = 60^\circ\text{C}$, $v_2 = 0.49 \times 10^{-2} \text{ cm}^2 \text{ s}^{-1}$, $D_2 = 12 \times 10^{-6} \text{ cm}^2 \text{ s}^{-1}$
 (Data from Table 4.12)

then, at constant u and d_e (from Equn. 5.1a)

$$\frac{50^\circ k_L}{60^\circ k_L} = \left[\frac{0.63 \times 10^{-2}}{0.49 \times 10^{-2}} \right]^{-0.47} \left[\frac{9.8 \times 10^{-6}}{12 \times 10^{-6}} \right]^{-0.67}$$

$$= \underline{0.78}$$

The experimental mass transport studies confirmed the theoretical calculation. For example (from Fig.4.49), when $u = 100 \text{ cm s}^{-1}$,
 $i_L = 2.15 \times 10^{-2} \text{ A cm}^{-2}$ at 50°C and $i_L = 2.75 \times 10^{-2}$ at 60°C ,

then

$$\frac{50^\circ i_L}{60^\circ i_L} = \frac{50^\circ k_L}{60^\circ k_L} = \frac{2.15 \times 10^{-2}}{2.75 \times 10^{-2}} = \underline{0.78}$$

Therefore, at a constant flow rate, an increase in temperature from 50° to 60°C resulted in a 22% increase in the mass transfer coefficient (and the deposition rate), as expected from the design equation.

ii) The effect of cathode length (at constant flow rate and temperature)

An analysis of mass transport in parallel plate electrochemical cells (Section 2.3b) has demonstrated that the effect of the cathode length on the average rate of mass transfer (as defined by the average limiting current density) is dependent upon whether the flow regime is laminar or turbulent.

In laminar flow, where mass transport entrance lengths are expected to be significant for cathodes of reasonable length (i.e. $L/d_e \ll \infty$), the average limiting current density is predicted to be a function of

cathode length. As expected the experimental results (e.g. Fig.4.41) tended to confirm the theoretical prediction, that the average limiting current density decreases with increasing cathode length.

However, in turbulent flow, the mass transfer boundary layer develops more rapidly and mass transport entrance lengths are shorter. According to Pickett (150), the mass transfer boundary layer should be fully developed over a cathode length of $L/de < 7.5$. Consequently, the average limiting current density is expected to be substantially unaffected by further increases in cathode length. The experimental results (e.g. Fig.4.55) are consistent with this view.

A quantitative estimate of the effect of the cathode length on the average limiting current density may be deduced from the design equation for Cell 2 in turbulent flow, with short electrodes (p.128). A relationship of the form, $Sh_{av} \propto \frac{(de)}{L}^{0.25}$ would be expected (all other parameters being constant). Since $Sh_{av} \propto_{av} i_L$ then

$$\frac{i_{L1}}{i_{L2}} = \left[\frac{de/L_1}{de/L_2} \right]^{0.25}$$

or

$$\frac{i_{L1}}{i_{L2}} = \left[\frac{L_2/de}{L_1/de} \right]^{0.25} \dots \dots \dots (5.2)$$

for cathodes of length L_1 and L_2 respectively.

For example, (using data from Table 4.15) when $L_1/de = 7.1$ and $L_2/de = 3.0$, the relative change in the limiting current density

$\frac{7.1 i_L}{3.0 i_L}$ predicted was (from Equation (5.2))

$$\frac{7.1 i_L}{3.0 i_L} = \left[\frac{3.0}{7.1} \right]^{0.25} \sim 0.8$$

and from the experimental results, the relative change in the limiting

current density was

$$\frac{7.1 i_L}{3.0 i_L} = \frac{10.6 \times 10^{-3}}{14.1 \times 10^{-3}} \sim 0.8$$

As may be seen in the case of copper deposition, reasonable agreement was found between the value of $\frac{7.1 i_L}{3.0 i_L}$, predicted from

Equation (5.2) and that determined experimentally.

iii) The effect of the flow rate (at constant temperature and electrode length)

As has been seen (Section 4.2.1), the experimental work has clearly demonstrated an increase in the limiting current density ($i_{av L}$) with increasing flow rate (U) in laminar (Fig.4.39), and turbulent flow for both 'long' cathodes (e.g. Fig.4.49) and 'short' cathodes (e.g. Fig.4.54). This observation is a fundamental aspect of mass transport in aqueous solutions (e.g. Sections 2.1b and 2.3). In laminar flow, a single relationship between $i_{av L}$ and U is to be expected. However, in turbulent flow, it has been shown (Section 2.3b) that the form of the relationship between $i_{av L}$ and U is dependent on the electrode length. The proportionalities observed experimentally and those expected from the design equations may be summarised as follows:

	<u>Experimental</u>	<u>Design equation</u>
Laminar flow (Re < 2,400)	$i_L \propto U^{0.3}$	$i_L \propto U^{0.33}$ (from Equn. (2.49))
Turbulent flow - 'long' electrode system (L/d _e = 11.4)	$i_L \propto U^{0.8}$	$i_L \propto U^{0.8}$ (from Equn. (2.65))
Turbulent flow - 'short' electrode system (L/d _e ≤ 9.4)	$i_L \propto U^{0.6}$	$i_L \propto U^{0.67}$ (from Equn. (2.67))

As may be seen, the experimental relationships were in reasonably good agreement with those predicted from the design equations. In the case of the 'short' electrode system in turbulent flow, the experimentally determined relationship was found to be applicable for cathode lengths $L/d_e \leq 9.4$. According to Pickett (150) the design equation (Eqn.(2.67)) for this electrode system is suitable for electrode lengths, $L/d_e \leq 7.5$. However, the design equation for 'short' electrodes may also be applied with minimal error, to slightly longer electrodes (e.g. $L/d_e \leq 9.4$), since a narrow range of intermediate electrode lengths between 'short' and 'long' electrodes would be expected.

iv) The mass transfer correlations

As has been seen (Section 4.2.1), the experimental results were correlated by three dimensionless mass transfer correlations. The experimentally derived relationships and the comparable design equations may be summarised as follows:

	<u>Experimental correlation</u>	<u>Design correlation</u>
Laminar flow ($Re < 2,400$)	$Sh = 2.8 [Re Sc \frac{de}{L}]^{0.33}$ (Eqn.(4.1))	$Sh = 1.85 [Re Sc \frac{de}{L}]^{0.33}$ (Eqn.(2.49))
Turbulent flow 'long electrode system' ($L/d_e = 11.4$)	$Sh = 0.023 Re^{0.87} Sc^{0.32}$ (Eqn.(4.2))	$Sh = 0.023 Re^{0.8} Sc^{0.33}$ (Eqn.(2.65))
Turbulent flow 'short' electrode system ($L/d_e \leq 9.4$)	$Sh = 0.181 Re^{0.72} \frac{de^{0.42}}{L}$ $Sc^{0.33}$ (Eqn.(4.3))	$Sh = 0.145 Re^{0.67} \frac{de^{0.25}}{L}$ $Sc^{0.33}$ (Eqn.(2.67))

The experimental correlations, for all flow conditions and cathode lengths, were in reasonable agreement with the correlations used for cell design purposes. However, it would appear that the mass transfer rates are slightly greater than expected theoretically. As has been stated elsewhere (p.181), the increased rate of mass transport may be associated with the comparatively unusual split cell design, possibly resulting in

the use of an inappropriate value of the equivalent diameter of the cell (d_e) and an unequal division of flow between the upper and lower cell compartments.

It is also evident, that, for parallel plate cells of small dimensions, an improved prediction of mass transfer rates in laminar flow would be obtained using Equations (2.53) (cf Equation (4.1))

$$Sh_{av} = 2.54 \left\{ Re Sc \frac{d_e}{L} \right\}^{0.3} \dots (2.53)$$

as opposed to Equation (2.49) (see also p.51-54).

However, it should be noted that, the relationships used in designing the cells were only expected to give a good approximation to actual cell performance. In addition, a greater mass transport rate can only be beneficial for fast rate electrodeposition studies. The results of the mass transport studies in the copper system are compared with the nickel system in the following section.

5.1(b) Mass transfer aspects of the electroforming of nickel foils in the sulphamate system

As has been seen (Section 4.42b) there is no clear evidence of a limiting current density in the nickel sulphamate system (see also Section 5.3b). Hence the conventional method of measuring mass transfer coefficients, as used in the copper deposition studies, was not available.

Alternatively mass transfer data could be obtained from measurements of current efficiency (as a function of current density). Assuming a simple m.t.c. reaction, a gradual decrease in current efficiency may be expected as the H.E.R. becomes the predominant reaction (e.g. ref.213). However, as has been seen, (e.g. Section 4.3) the current efficiency was maintained at $\geq 95\%$ for the deposition of a sound and coherent nickel deposit. It was only when significant quantities of nickel hydroxide were deposited that a marked decrease in the current efficiency was detected (see also Section 5.3b).

Similarly, it may be expected that a graduated deterioration in the morphology and properties of the deposit may be observed as the reaction becomes mass transfer controlled, resulting in a gradual roughening of the deposit and the appearance of powder deposits as the current density approaches i_L . Such features were commonly observed during the electrodeposition of copper (e.g.p.176) and are associated with spherical diffusion, of the reacting ion, to the electrode (p.90).

However, in the case of nickel deposition it was useful to define a maximum current density (i_{max}) up to which the deposit remained sound and coherent (p.171). At i_{max} the deposit morphology deteriorated over a very narrow range of current densities (typically $\ll 0.05 \text{ A cm}^{-2}$), showing evidence of both hydroxide and powder deposits simultaneously (e.g. Fig.4.78e and f).

It is important to note that the measured values of i_{max} were considerably lower than the value of i , calculated from the design equations.

Since i_{max} was the factor which was readily determined and may also be related to mass transfer effects in the nickel sulphamate system, the variation of i_{max} with the various experimental parameters was examined, as described in Sections 4.1 and 4.3.

In this Section the effect of flow rate (Reynolds number), electrode length and temperature, on the maximum current density for a sound deposit, will be discussed, in comparison with the copper system. Finally, the implications of gas evolution, for mass transport processes in the nickel sulphamate system and the absolute values of i_{max} , will be considered.

The effect of flow rate (at a constant temperature and flow rate

The results obtained in laminar flow at 60°C were inconclusive and irreproducible. Since large bubbles of hydrogen were observed adhering to the cathode (e.g. p.156 and p.190), it would appear that it is under conditions of insufficient agitation, that gas evolution may have

a deleterious effect on the deposition rate and the nature of the deposit (see also Sections 5.2b and 5.4).

However, in turbulent flow (at 60°C), the results indicated an increase in i_{\max} with increasing flow rate (e.g. Figs. 4.64 and 4.84). The experimental relationship between i_{\max} and the Reynolds number, although somewhat approximate, may be summarised as follows:

	<u>Experimental</u>	<u>Design Equation</u>
Cell 1, $L/d_e \sim 3.3$	$i_{\max} \propto Re^{0.6}$	$i_L \propto Re^{0.67}$ (from Equn.2.67)
Cell 2, $L/d_e \sim 2.9$	$i_{\max} \propto Re^{0.6}$	$i_L \propto Re^{0.67}$ (from Equn.2.67)
Cell 2, $L/d_e \sim 11.7$	$i_{\max} \propto Re^{0.8}$	$i_L \propto Re^{0.8}$ (from Equn.2.65)

The proportionalities expected from the design equations are also shown for comparison purposes. As may be seen, the experimental results are in reasonable agreement with those expected from the design equation, (although the latter are based on the limiting current density), and therefore compare well with the results obtained from the copper system (Section 5.1a). This would clearly suggest that a mass transfer controlled process of some type was taking place. However, there is no clear evidence to support the view that i_{\max} is equivalent to i_L , or even related to i_L .

Unexpectedly, the results obtained at 70°C were in contrast with those obtained at the lower temperature. Although the deposition rates tended to be considerably higher than those observed at 60°C, there was no clear relationship between the flow rate and i_{\max} . In addition, no significant differences in the value of i_{\max} , or the nature of the deposit, were observed between foils electroformed in laminar or turbulent flow.

This may be compared with the copper system, where a constant relationship between flow rate and i_L was observed over the temperature

range 28° to 60°C (e.g. Fig.4.49).

This would suggest that mass transport phenomena are more complex in the nickel system, particularly at 70°C. This subject is discussed further on page 276 and in Section 5.3b.

The effect of cathode length (at constant flow rate and temperature)

It was clearly evident that higher values of i_{max} were possible using L/d_e ratios of up to about 5 (cf. Figs.4.64 for short electrodes and 4.84 for long electrodes. The results also indicated that the relationships between flow rate and i_{max} are a function of cathode length (see previous page).

These findings are in broad agreement with mass transfer theory (Section 2.3b) and hence the experimental results of the copper system, where length effects were found to be significant for $L/d_e < 7$ (see p.269).

A semi-quantitative view of the effect of cathode length (L/d_e) on i_{max} may be determined, in a similar manner to that described previously for the copper system (p.269), using the following equation:

$$\frac{i_L}{i_L} = \left[\frac{L/d_e}{L_1/d_e} \right]^{0.25} \dots \dots (5.2)$$

and when $L/d_e = 2.9$ and $L_1/d_e = 4.7$, the proportional increase in the limiting current density (i_L) is given by:

$$\frac{i_L}{i_L} = \left[\frac{2.92}{4.7} \right]^{0.25} \approx \underline{0.9}$$

However, the corresponding increase in the maximum current density (i_{max}) for the same decrease in cathode length was (Table 4.30)

$$\frac{4.7 i_{max}}{2.92 i_{max}} \approx \frac{0.7}{1.0} \approx \underline{0.7}$$

As can be seen there is some evidence of a mass transfer effect resulting from changes in cathode length. However, the increase in i_{\max} is not as great as would be expected. If we were to assume that i_{\max} is equivalent to or directly related to i_L this may infer additional complexity such as current distribution effects, in the deposition process (see also Section 5.2).

The effect of temperature

It was evident from the results that i_{\max} significantly increased with increasing temperature (e.g. p.219). As has been seen from the copper system (Section 5.1a), this would be expected for a m.t.c. reaction, operating at the limiting current density.

However, discrepancies between practice and theory are again evident when the results are examined semi-quantitatively. The relative change (at const.Re) in i_L (or k_L) was calculated from the equation (see Section 5.1a).

$$\frac{i_L}{2i_L} = \left[\frac{v_1}{v_2} \right]^{0.33} \left[\frac{D_1}{D_2} \right]^{0.67} \dots \dots (5.1b)$$

using data from Table A1 (Appendix 2e).

The theoretical change in $\frac{i_L}{60i_L}$ over the temperature range 50°

to 60°C was

$$\begin{aligned} \frac{50^\circ i_L}{60^\circ i_L} &= \left[\frac{1.492 \times 10^{-2}}{1.202 \times 10^{-2}} \right]^{0.33} \left[\frac{0.54 \times 10^{-5}}{0.64 \times 10^{-5}} \right]^{0.67} \\ &= \underline{0.96} \end{aligned}$$

and similarly over the temperature range 60° to 70°C

$$\begin{aligned} \frac{60^\circ i_L}{50^\circ i_L} &= \left[\frac{1.202 \times 10^{-2}}{1.035 \times 10^{-2}} \right]^{0.33} \left[\frac{0.64 \times 10^{-5}}{0.83 \times 10^{-5}} \right]^{0.67} \\ &= \underline{0.88} \end{aligned}$$

In practice, the following changes in maximum current densities were recorded (at $Re\ 6,600 \pm 300$, p.219)

$$\frac{50^\circ i_{\max}}{60^\circ i_{\max}} = \frac{0.4}{0.6} \quad \sim \underline{0.66}$$

and

$$\frac{60^\circ i_{\max}}{70^\circ i_{\max}} = \frac{0.6}{1.15} \quad \sim \underline{0.52}$$

It is therefore evident that a $10^\circ C$ increase in temperature resulted in a 30 to 50% increase in i_{\max} , in contrast to the 4 to 12% predicted from mass transfer theory.

This would suggest that temperature has a more significant effect on the diffusion coefficient than assumed (see Appendix 2e) or that i_{\max} has a complex relationship with i_L . Additional factors such as IR heating effects at the electrolyte/electrode interface and the temperature coefficients of the complex solution equilibria that may be involved in the nickel deposition process may also be of some importance (see also Sections 5.2b, 5.3, and 5.4).

The implications of gas evolution for mass transport in the nickel sulphamate system

The deposition of copper from the dilute acid copper system was not accompanied by the evolution of hydrogen until the limiting current density was exceeded (p.173). In contrast, nickel deposition was always accompanied by hydrogen evolution which, as has been seen, may significantly alter the nature of the deposit, the distribution of current in the cell, and the rate of mass transfer.

The results of silver tracer experiments have demonstrated that the mass transfer rates (at least for silver ions) in the nickel sulphamate system tend to be about an order of magnitude greater than expected from a simple mass transfer theory (e.g. Figs.4.164 and 4.165). The most

likely explanation for the increased mass transfer rates is a superimposed microconvective mass transfer resulting from the concomitant hydrogen evolution accompanying nickel deposition (p.251). As has been seen from the literature (Section 2.3c) many theoretical and experimental studies have confirmed that such gas related effects are to be expected. In this respect the nickel system differs significantly from the copper system.

Mass transfer rates of the same order of magnitude, as determined experimentally, have been calculated using the gas model (Section 4.52). However, comparable mass transfer rates are only likely when the diameter of the gas bubbles is $< 0.1 \mu\text{m}$, and when the overall (combined) rate of mass transfer is dominated by microconvection. It should also be noted that the development of the model assumed a constant volume of evolved gas and a constant gas bubble diameter (see also p.260).

In general it would appear from a semi-empirical analysis that as the total current density (and the cathodic overpotential) increases, the volume of gas will increase and the bubble diameter decrease. Similarly, as the flow rate increases the average bubble diameter will tend to decrease. Hence the mass transfer rate may increase with increasing deposition current density and flow rate. It should be noted (Fig.4.164) that variability in mass transfer rates has been observed experimentally, particularly at low flow rates.

The absolute value of i_{max} and the relationship to i_L

As has been seen, i_{max} was less than i_L , based on a 'flow only' model of the transport of $\text{Ni}_{\text{aq}}^{2+}$ ions.

Now West (5) has calculated that the nickel system is unlikely to be mass transfer controlled at $i/i_L < 0.8$ (see also Section 5.2). (This is in contrast to the copper system where concentration polarisation may be observed at $i/i_L < 0.4$). Since, (even for a 'simple' mass transfer model), $i_{\text{max}}/i_L < 0.3$, this would suggest that i_{max} and i_L are not directly comparable.

It is clear that the co-deposition of hydrogen gas does not, in itself, explain the difference between i_{\max} and i_L . As has been seen (Section 2.4b) several other species (apart from Ni_{aq}^{2+}) may be involved in the deposition process and may also be subject to the effects of combined mass transfer. Some of the processes will be examined further in the following sections.

5.2 Current Distribution Studies

a) Current distribution studies in the copper sulphate system

Although theoretical and empirical solutions of current distribution are available for some simple electrode geometries, the problems of current distribution for complex electrode geometries are less well understood. However, empirical relationships for metal (and hence current) distribution are common in commercial electroplating.

Segmented cathodes have been used in previous current distribution studies (e.g. 28). The method represents a simple, yet effective, means of measuring local current densities particularly at sub-limiting current densities.

Current distribution is a topic of some complexity. However, for simplicity, this part of the present work is discussed in terms of: (i) current distribution in the absence of significant electrode polarisation; (ii) current distribution at sub-limiting current densities; and (iii) current distribution at the limiting current density.

i) Current distribution in the absence of significant electrode polarisation

For a more complete understanding of current distribution in parallel plate cells, it is necessary to briefly examine some theoretical aspects of the subject relevant to the discussion of the results.

In the absence of electrode polarisation, a primary current distribution will dominate the electrode behaviour. Primary current distributions are determined by geometric considerations alone and the solution potential in the cell obeys a general relationship known as Laplace's equation:

$$\nabla^2 \phi = 0$$

Although Laplace's equation is difficult to solve, Newman (355) has given the solution for the simple case of current distribution between equal parallel plates opposite each other in a channel as:

$$\frac{i_x}{i_{av}} = \frac{\epsilon \cosh \epsilon / K (\text{Tanh}^2 \epsilon_1)}{\sqrt{\sinh \epsilon - \sinh^2(2x \epsilon / L)}} \dots (5.3)$$

where: $\epsilon = \pi L / 2S$
 $L =$ electrode length
 $S =$ distance between the electrodes
 $X =$ distance from the centre of the electrode
and K is the complete integral of the 1st kind
 $= \int_0^{\pi/2} (1 - m \sin^2 \theta)^{-1/2} s \theta$
and $m = \frac{1}{\text{Tanh} \epsilon}$

Equation (5.3) was solved for the Cell 2 geometry and a series of cathode lengths (2 to 6.8 cm), to produce the theoretical current distributions shown in Fig.(5.1). (However, the integral K was solved by repeated numerical integration and the value of K becomes increasingly more unreliable for cathode lengths > 5 cm). As may be seen the primary current distribution tends to become more uniform as the cathode length increases. (The current distribution is uniform when $L \rightarrow \infty$).

In the absence of significant electrode polarisation, the current densities at the leading and trailing edges of the cathode tend towards infinity. However, in practical electrode-electrolyte systems infinite current densities are not observed and the overall current distribution will be modified by the secondary current distribution (e.g. Fig.5.2).

ii) Current distribution at sub-limiting current densities

With slow electrode kinetics, polarisation of the electrode will attempt to readjust the potential distribution in the solution, so as to reduce the infinite current densities at the electrode edges. The problem may be regarded as the result of imposing an additional resistance, the charge transfer resistance, at the electrode-electrolyte interface.

As may be seen from the experimental results (Fig.4.59), the deposition of copper at sub-limiting current densities ($0.5 i_L$) produced

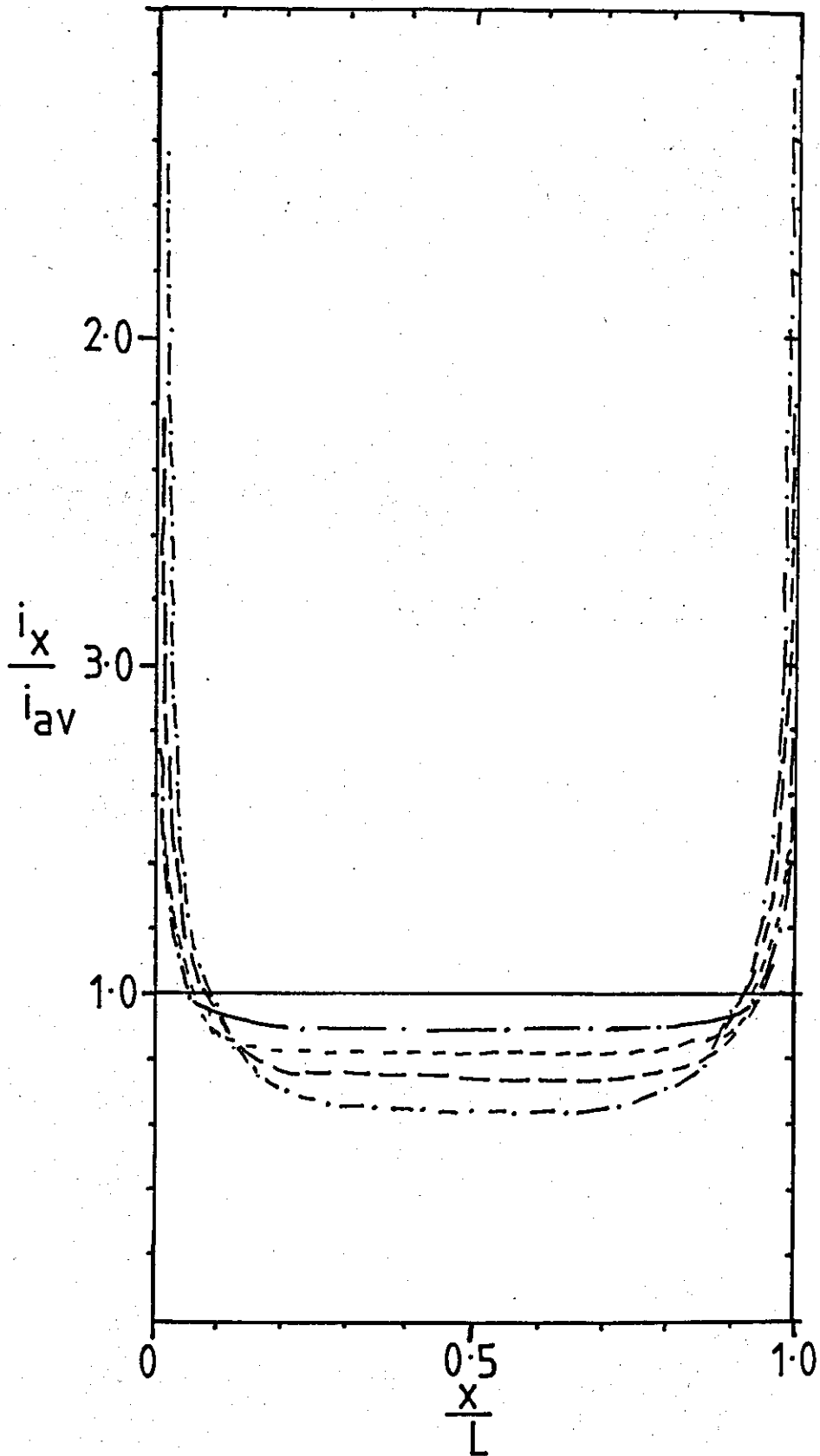


Fig. 5.1 Theoretical primary current distribution for Cell 2.

Anode length = cathode length (L)

- 2 cm cathode
- - - - - 3 cm cathode
- · · · · 5 cm cathode
- · - · - 6.8 cm cathode
- L + ∞

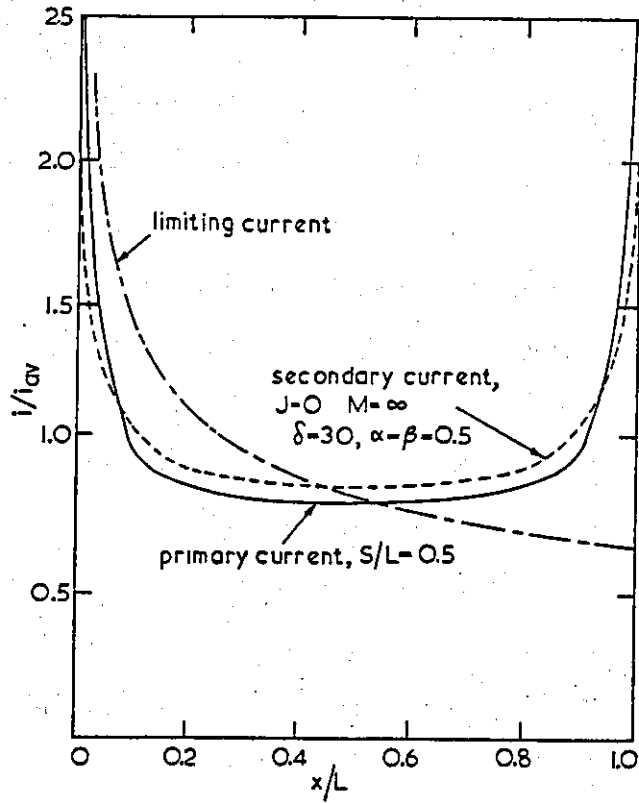


Fig.5.2 Primary/secondary current distribution (after Newman (355))

—— secondary current distribution
 - - - primary current distribution

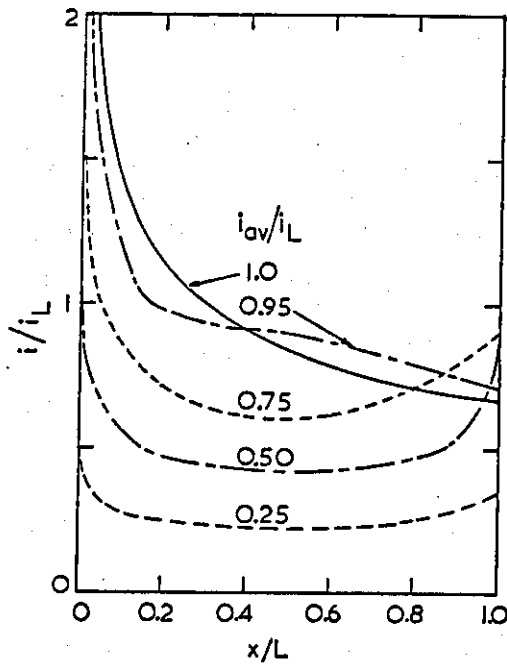


Fig.5.3 Current distributions at or near the limiting current density (after Newman (356,357))

a more symmetrical, modified primary - secondary current distribution, consistent with theoretical predictions.

However, it should be noted that at current densities which are a significant fraction of i_L , the problem is complex due to the combined effect of all the contributing factors. Newman (356,357), has provided a solution of the problem of complex current distributions in parallel plate cells operating over a range of conditions, by applications of Laplaces equation with complicated and/or non-linear boundary conditions. His results have indicated that distortions of the current distribution at significant fractions of i_L are possible (Fig.5.3).

It would appear that, for a fast reaction (such as copper deposition), mass transport effects may influence the current distribution at current densities $< 0.5 i_L$. (It is of interest to note that the results of calculations by West (5) have suggested that for the copper system, concentration overpotential is comparable with the activation overpotential at $i/i_L \approx 0.4$). Hence at $0.5 i_L$ mass transport effects may be contributing to the observed current distribution.

iii) Current distribution at the limiting current density

The primary-secondary current distribution is only valid when the electrolyte has a uniform composition. It is an implicit assumption of the Laplace equation, that the concentration of metal ions in the solution is constant throughout the cell, whereas for a mass transport controlled reaction (one occurring at or very near the limiting current density), the concentration approaches zero at the electrode-electrolyte interface and Laplaces equation is invalid. At the limiting current density, the distribution of current is determined solely by mass transfer considerations (e.g. Fig.5.3).

The experimental results have indicated that, for both laminar and turbulent flow (Figs.4.57 to 4.59), the current density is highest at the leading edge of the cathode where fresh solution reaches the electrode and decreases downstream as the solution becomes depleted. These findings are consistent with the theoretical predictions:

In laminar flow, the mass transfer coefficient and hence the local current density (i_x) is expected to be a function of the distance along the electrode (e.g. Equation (2.48)). The experimental results (e.g. Fig.4.57) have provided some qualitative confirmation of this. Here, the mass transfer boundary layer continues to develop along the entire length of the cathode, as metal ions in solution are progressively depleted, resulting in a higher partial limiting current density at the leading edge and a progressive decrease in the local value of $i_x/i_{L,av}$ along the electrode.

In contrast, mass transfer entrance lengths are fully developed over a much shorter distance in turbulent flow. For electrode lengths $> 8de$, the average current density is unaffected by the electrode length (at constant Re). This was assumed in the use of the Chilton-Colburn equation

$$Sh_{av} = 0.023 Re^{0.8} Sc^{1/3} \dots \dots (2.45)$$

as a design equation (Section 2.3b).

The form of the current distribution may be compared with earlier results for the effect of electrode length on the average rate of mass transfer (cf. Figs.4.58 with 4.41 and 4.55). However, whereas the former show the local mass transfer rate (as a local limiting current density) at a point (x) along the length of the cathode, $11.4 de$ in length, the latter show the average mass transfer rate over an electrode of length, L . The use of the segmented electrode for the measurement of current distribution studies enables even a low order length dependency of the mass transfer coefficient to be detected.

The experimental results have shown that the mass transfer boundary layer developed rapidly in turbulent flow (Fig.4.58) and occupies $<25\%$ of the cathode length. The distribution of current was relatively constant over most of the cathode length and hence a low order-length dependency of the average mass transfer coefficient would be observed. As expected, the distribution of current was also relatively unaffected by the flow rate.

The results of the current distribution studies in the copper system may be compared with those relating to current distribution in the nickel system, as described in the following section.

5.2b Current distribution studies in the nickel sulphamate system

The distribution of nickel will be discussed in three parts. The case of anode and cathode of equal length (~10cm) will be examined first, since this was directly comparable with the experimental conditions used for the copper deposition (p.172). In this case the current distribution was non-uniform. The deposition of nickel with uniform current distribution will be discussed in the second part. This investigation proved useful for diagnostic purposes. In addition, the deposition of nickel at high current densities was optimised using this configuration.

Finally, non-uniform current distribution (since this was the configuration used for most of the electroforming studies) will be briefly discussed.

i) Current distribution using anode and cathode of equal length (10cm)

It was hoped that this part of the investigation would provide some evidence of mass transport control and assist in interpretation of the observed changes in the morphology along the length of electrodeposited foils.

However, with an anode and cathode of equal length, high current densities were localised at both the leading and trailing edges of the cathode and the current distribution resembled that of the primary/secondary current distribution (cf.Figs.4.122 and 5.1). The distribution was maintained up to the maximum current density for a good deposit (i_{\max}). This may be contrasted with the m.t.c. current distribution observed previously for copper deposition at the limiting current density (e.g. Fig. 4.58).

In the case of nickel deposition, the observed slight increase in the local current density at the trailing edge segments with increasing flow rate (at constant current density) (e.g. Fig.4.123), although expected for a m.t.c. reaction, was probably associated with changes in the gas flow pattern and masking of the electrode with gas bubbles. It is clear that, under these conditions, there is no evidence of a mass transport controlled current distribution in the nickel sulphamate system.

ii) Uniform current distribution

Some of the features observed with a non-uniform current distribution may be attributable to the deposition process being dominated by the primary current distribution. Hence a secondary reaction (such as hydrogen evolution and hydroxide precipitation) may occur on one part of the electrode (e.g. the leading and trailing edges) before the limiting current density is attained on another part of the same electrode (151). A more uniform current distribution may enable the primary/secondary and m.t.c. current distributions to be separated.

As has been seen (e.g. Fig.4.124), a reasonably uniform current distribution was achieved with the optimum anode length of 9 cm (10cm cathode) at both 60° and 70°C. Using this electrode geometry, the problem of high edge current densities, resulting in hydroxide precipitation, at the leading and trailing edges was diminished. Hence, with a uniform current distribution the maximum current density for a good deposit was increased to ~1.3 A cm⁻² at 60°C and in excess of 2 A cm⁻² at 70°C (at the highest Reynolds number), (cf. Section 4.4.1). The resulting electroforms were of a more uniform structure.

Current distribution and the effect of hydroxide precipitation

At 60°C, there was no evidence of a mass transfer controlled current distribution even at current densities $> i_{\max}$ (e.g. Fig.4.127). However, the precipitation of hydroxide at leading edge electrode segments at i_{\max} , resulted in a redistribution of current, due to the resistive nature of the precipitate and the corresponding reduction in current efficiency. It

was also evident that hydroxide precipitation in localised areas results in a decrease in the effective area of the cathode. Hence the deposition current density on unaffected areas will tend to increase. However, since shorter cathodes can sustain higher current densities (see Section 4.3.1c), this may prevent additional hydroxide precipitation. (It is of interest to note that although primary current distribution theory predicts greater edge current densities at shorter cathodes (e.g. Fig.5.1), experimentally, higher values of i_{\max} are observed at short cathodes. This is evidence of a mass transfer effect).

In contrast to the results at 60°C, hydroxide precipitation was not observed at 70°C even at the very high current densities used ($>2 \text{ A cm}^{-2}$) (p.227). At high deposition rates and/or low flow rates the current density was limited by the voltage output (30V) of the current source. However, the maximum current density was about twice that observed at 60°C (cf. Section 5.1b).

As has been seen calculations have indicated that the copper deposition reaction may come under mass transport control at about $0.4 i_L$. However, comparable calculations for a 'slow' reaction, such as nickel deposition, have suggested that mass transport control may only be significant at current densities $> 0.8 i_L$ (ref.5). Since there is no evidence of a mass transport controlled current distribution, even at current densities at which nickel hydroxide may be deposited, this would suggest that at this point the reduction of nickel ions is not mass transport controlled and $i_{\max} \ll 0.8 i_L$.

The effect of evolved gases on the current distribution

At low flow rates ($Re \sim 2,000$ and a constant average current density) the local current density tended to increase at the leading edge and decrease at the trailing edge segments (e.g. Fig.4.128). (A similar effect was also noted on increasing the average current density at constant flow rate, e.g. Fig.4.139). Although this observation may be considered to be consistent with an m.t.c. current distribution, it may be more readily interpreted in terms of a 'build-up' of evolved gas (from both the anode and cathode) towards the trailing edge of the electrodes. This effect would

would result in an increased electrolyte resistance in the trailing edge region and a subsequent redistribution of current.

The evidence for gas interference with the current distribution was particularly significant at very low laminar flow rates (Re 670), where time-dependent current oscillations were observed on individual cathode segments (e.g. Fig.4.132). The oscillations coincided with the growth and detachment of large bubbles of hydrogen on the cathode surface. Such behaviour could, under some conditions, result in the maximum current density being exceeded on some areas of the electrode resulting in the precipitation of hydroxide

iii) Additional comments relating to non-uniform current distributions

Non-uniform current distributions were observed when using 10cm cathodes and anodes greater or less than 9cm in length. Mass transfer controlled current distributions were not observed.

When the local current density exceeds i_{max} , nickel hydroxide may be deposited in the high current density areas, resulting in a distortion of the current distribution (e.g. Fig.4.121). These areas also correspond to areas of increased deposit brightness, and microhardness and of significant structural changes (see Section 5.4).

It was of interest to note that the maximum current density tended to increase with decreasing anode length, since for a reaction under mass transport control, the cathodic current distribution is independent of the size and position of the anode.

Non-uniform current distributions were unsuitable for high speed electroforming applications, resulting in deposits of non-uniform structure and properties.

The absence of a m.t.c. current distribution, even at current densities in excess of i_{max} , is clear evidence that the precipitation of hydroxide at i_{max} is not associated with the mass transport controlled reduction of Ni_{aq}^{2+} ions.

Electroforms of uniform structure and properties were deposited, at significantly increased values of i_{max} , with a uniform current distribution (e.g. a 10cm cathode and a 9cm anode). However, gas bubble adhesion may result in a distortion of the current distribution.

5.3 Polarisation studies in nickel sulphamate electrolytes

The Luggin capillary technique for the measurement of electrode potentials is commonly used in aqueous electro-chemistry. Although the Luggin capillary has been used previously in flowing electrolytes (e.g. 23), detailed experimental descriptions were not available.

The present investigation is unusual in combining a gas evolving system, operating at moderately high temperatures (50 to 70°C) and at a relatively high operating pressures (>1 atm). The experimental method was designed to prevent contamination of the electrolyte and to operate at high pressures in the presence of gas evolution.

Both anodic and cathodic polarisation studies were carried out using a 9 cm anode to ensure a uniform cathodic current distribution (see previous section). The polarisation studies are discussed in two parts. In part a) the anodic aspects are examined and in part b) the cathodic aspects are considered.

a) Anodic polarisation studies

The anodic polarisation behaviour of electrolytic nickel anodes in a flowing nickel sulphamate electrolyte does not appear to have been studied previously. Hence a short study of the polarisation behaviour of the nickel anode in the flow cell was thought necessary to assist in interpretation of the results and further process development.

i) Anodic polarisation in the absence of chloride ions

No information regarding the behaviour of nickel anodes in chloride free nickel sulphamate solutions appears to be available. However, the observed single active dissolution peak at potentials <0.21 V (e.g. Fig. 4.148) is in accordance with the known behaviour of nickel in acid solutions (ref.246). The dissolution probably proceeds via a NiOH^+ intermediate (p.85).

The experimental values of i_{crit} ($<10^{-3}$ A cm^{-2} , Table 4.41) did not differ greatly from those observed previously in other low chloride nickel plating electrolytes (e.g. 278), but were found to be a function of flow

rate (at 60°C). The Flade potential was $0.3 \pm 0.01V$, and showed no clear relationship with the flow rate.

At potentials $>0.3V$, the anode passivated with dissolution occurring through a passive layer, probably associated with the formation of a semi-conducting film of NiO (ref.274,275).

The post-passivation behaviour was characterised by copious oxygen evolution at potentials $>1.4V$.

An increase in temperature from 60 to 70°C had little significant effect on the polarisation behaviour (cf.Figs.4.149 and 4.151).

Effect of flow rate on i_{crit}

As has been seen the value of i_{crit} (at 60°C) was found to be a function of flow rate (Fig.4.152), i.e. $i_{crit} \propto Re^2$. A relationship of some form may be expected from a consideration of the mechanism of the anodic passivation of nickel (see p.86).

The process is thought to occur by an accumulation of $NiOH^+$ ions close to the electrode surface, resulting in precipitation of $Ni(OH)_2$, at a sufficiently high current density. Hence the concentration of $NiOH^+$ at the interface will be governed by mass transport considerations. However, the solution of the mass transport equations are expected to be complex, particularly in the case of a potentiodynamic experiment, since passivation is a time dependent phenomenon.

ii) Anodic polarisation in the presence of chloride

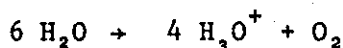
In the presence of chloride ions, multiple active dissolution peaks within the potential range 0.1 to 0.5V are a common feature of polarisation curves (277). Two peaks were observed over this potential range in the present work. The first peak ($E_F \sim 0.3V$) probably corresponds to active dissolution via a $NiOH^+$ intermediate (cf. polarisation in the absence of chloride). The second peak ($E_F \sim 0.61V$) may possibly arise from the formation of a nickel-chloro complex.

The value of i_{crit} for both peaks ($<10^{-2}$ A cm^{-2}) did not differ greatly from that observed in the absence of chloride.

At potentials $>0.61V$, the anode was passivated. However, chloride is an aggressive anion which may cause partial breakdown of the passive film resulting in pitting of the anode. In addition, a complexing anion such as chloride, may stabilise higher oxidation states of nickel in solution resulting in dissolution of the passive layer at higher potentials. The decrease in the potential (by $\sim 0.2V$) for the transpassive condition observed previously (277,278) and in the present work (cf. Figs. 4.148 and 4.149) may be as a result of the complexation of nickel in a higher oxidation state.

At potentials $>1.2V$, oxygen was evolved, since the activity of chloride ions was comparatively low.

It would therefore appear that, for the purposes of the current study, neither chloride ions, increased flow rates nor temperature significantly improved the rate of anode dissolution which was generally $<10^{-2}$ A cm^{-2} . Hence the principle anodic reaction, for the fast deposition studies, was oxygen evolution as represented by Fig.4.150. Oxygen was evolved by the overall reaction



The normal cell operation resulted in a gradual decrease in the pH (and nickel ion concentration) of the electrolyte which was compensated for by additions of nickel hydroxide to the solution.

At high current densities, the anode was mechanically depassivated by the evolving gas, hence no passive film or anode sludge was observed on the electrode. Heavy pitting corrosion of the anode was evident after continual usage. Although the anode dissolution efficiency was estimated to be $\sim 25\%$, it is likely that uneven and incomplete corrosion may have resulted in the production of undissolved nickel particles and other insoluble products.

An increase in the anode area (in Cell 2) was found to be ineffective in promoting efficient anode corrosion, since current distribution effects resulted in anode dissolution occurring opposite the cathode.

The use of S-nickel anodes was avoided to eliminate the possibility of contamination of the electrolyte. In addition S-nickel anode material was not available in a suitable form.

Although in an undivided cell (e.g. Cell 1), anode gases may effect mass transfer at the cathode, this problem was successfully overcome by the cell diaphragm used in Cell 2. Hence the principal effect of anodic gas evolution was an increased electrolyte resistance due to gas voidage. However, gas related effects could be 'designed out' of the system by, for example, constructing a dual flow system, utilising a high concentration chloride solution as the anolyte.

b) Cathodic polarisation studies in nickel sulphamate electrolytes

At the outset of the present work it was hoped that the cathodic polarisation associated with the nickel deposition and hydrogen evolution reactions could, at some point, be separated and a limiting current density for the reduction of nickel ions observed. This type of polarisation behaviour was typical of the dilute acid copper sulphate system discussed elsewhere (Section 5.1a).

However, in contrast to the copper system, the nickel sulphamate bath used in the current investigation has a very high concentration of nickel ions and the absence of a supporting electrolyte. Hence the limiting current densities (i_L) would be expected to be very high, with a significant contribution from the migration current (p.42).

However, as has been seen (Chapter 4.42b) the results provided no clear evidence of a limiting current density over the range of experimental conditions used.

At 50° and 60°C the reaction was limited by the precipitation of nickel hydroxide, whereas at 70°C the cell voltage exceeded the voltage

output of the instrumentation used. It is of interest to note that at 70°C sound nickel electrodeposits could be obtained at very high current densities, in excess of 2 A cm^{-2} , with no evidence of a limiting current density or hydroxide precipitation. This represented almost a two-fold increase in the maximum current density observed at 60°C (for similar flow conditions) (see also Section 5.2b)

The relationship between i_{max} and i_L

It has often been assumed that the precipitation of nickel hydroxide occurs when the reduction of nickel ions becomes mass transfer controlled (i.e. at or near i_L) and the rate of hydrogen evolution increases resulting in an increase in the pH of the electrolyte close to the electrode. However, as has been seen from a more detailed examination of the literature (Chapter 2.4), the processes which may occur at or close to the electrode are more complex than might be expected. Since the current densities at which nickel hydroxide was deposited experimentally were considerably lower ($\ll 0.5 i_L$) than the calculated values of the limiting current density (e.g. Fig.4.84), it would appear unlikely that the precipitation of hydroxide was associated with the limiting current density for the reduction of nickel ions.

Tafel slopes and the temperature coefficient of the overpotential

Although the present investigation was not intended to produce detailed electrochemical or mechanistic information, it was of interest to note that the experimental Tafel slopes of $\sim 0.106 \text{ V dec}^{-1}$ (at 60°C) and $\sim 0.081 \text{ V dec}^{-1}$ (at 70°C) (calculated over the current density range $\sim 10^{-4}$ to $\sim 10^{-2} \text{ A cm}^{-2}$ from Fig.4.155) were in reasonable agreement with the results of Piontelli and Serravalle (Table 2.7) obtained in a $1 \text{ m Ni(SO}_3\text{NH}_2)_2 - 0.5 \text{ m H}_3\text{BO}_3$ electrolyte at 50° - 65°C. Tafel slopes within the range 60 to 100mV dec^{-1} are common for the nickel deposition reaction from most common electrolytes, although the slope tends towards the lower value at higher temperatures (Section 2.4bi).

Over the temperature range 60° to 70°C there was no marked decrease in the overpotential. The experimental value of 2 to 3 mV°C (at current

densities $< 10^{-1} \text{ A cm}^{-2}$) was in agreement with previous studies (248, see also p.78). There was therefore little evidence that the significantly greater current densities and the absence of hydroxide precipitation (at current densities up to $\sim 2 \text{ A cm}^{-2}$) observed at 70°C were related to fundamental changes in the polarisation behaviour of the nickel system.

Concentration polarisation

There was also no clear evidence of concentration polarisation. It would be expected that, for a mass transport controlled cathodic reaction, the electrode potential would increase (positive shift) with increasing flow rate. Although such a result was observed at very low flow rates ($\text{Re} < 500$ e.g. Fig.4.159) it was apparent that this effect was probably associated with gas bubbles adhering to the cathode surface. Hence, at low flow rates the effective area of the cathode was reduced and, in addition, the ohmic contribution to the overpotential was increased. An increase in the flow rate tended to remove adhering bubbles from the cathode surface and resulted in an increase in the potential.

In contrast to the low flow rate behaviour, at higher flow rates, within the turbulent flow range, the cathode potential decreased (negative shift), by a few millivolts, with increasing flow rate (e.g. Fig. 4.160). This effect may be associated with the compression of the gas layer close to the electrode surface at high flow rates and a consequent increase in the ohmic contribution to the overpotential. It should be noted that this effect may be more significant at higher current densities since more gas may be evolved.

The nickel deposition reaction has often been considered to be under mass transport control, even at comparatively low current densities, within the conventional plating range ($< 0.1 \text{ A cm}^{-2}$). However, the reaction is unlikely to exhibit significant concentration polarisation at current densities $< 0.8 i_L$. (see also p.278). Furthermore, since the maximum current densities obtained in the present investigation were generally well below ($< 0.5 i_L$) the theoretical values of i_L , it is unlikely that true concentration polarisation would be observed for the experimental conditions used.

The role of NiOH⁺

As has been seen (p.79) nickel deposition may take place through a complex, probably NiOH⁺, in the absence of other complexing anions although this hypothesis has been subject to criticism (349). Since the sulphamate ion is not generally considered to be a complexing anion, it would appear feasible that this is the reactive species (as opposed to the simple Ni²⁺_{aq} ion) and the supply of NiOH⁺ to the electrode is the rate determining step.

The NiOH⁺ ions are in equilibrium with other solution species (p.83) and at pH4, the bulk concentration of this ion would be about 2×10^{-5} M (from Equation 2.9a).

However, the pH at the cathode surface may be greater than that corresponding to the bulk hydrogen ion concentration (i.e. \gg pH4). The concentration of NiOH⁺ will be at a maximum of $\sim 2 \times 10^{-3}$ m at pH 6.6. At a higher pH, nickel hydroxide may be precipitated. Calculations suggest that a limiting current density of $< 0.01 \text{ A cm}^{-2}$ would be expected, with no contribution from ionic migration (since Ni²⁺_{aq} ions would act as a supporting electrolyte).

Since i_L was not observed and i_{max} was $\gg 0.01 \text{ A cm}^{-2}$, it is clear that the rate of production of NiOH⁺ is not rate controlling at $i \leq i_{\text{max}}$. (see also Section 5.2b).

Although a complex deposition mechanism involving NiOH⁺ and hydrogen evolution (such as Reactions (2.5) and (2.6)) may not be completely discounted, nickel hydroxide deposition (at i_{max}) is more likely to be associated with the boundary layer pH exceeding 6.6. The factors affecting the boundary layer pH will now be re-examined.

The co-deposition of hydrogen and pH changes at the electrode/electrolyte interface

As has been seen (p.82 - 85), the two possible mechanisms by which hydrogen may be deposited and which would result in an increase in the pH of the electrolyte at the interface are as follows:



and



Reaction (2.7a) has often been considered to be the principle process by which hydrogen is evolved in nickel electroplating. However, the literature suggests that this is not the case and the reduction of H_3O^+ ions becomes mass transport controlled before nickel hydroxide is precipitated.

On closer inspection of the polarisation curves for nickel deposition (e.g. Fig.4.155), a slight inflection was observed at $\sim -0.4\text{V}$ ($4 \times 10^{-3} \text{ A cm}^{-2}$). This feature may be associated with the reduction of H_3O^+ (reaction 2.7a).

The cathodic evolution of hydrogen on nickel has been studied previously (e.g. 359), but generally only at very low pH. To facilitate the further interpretation of the present work, some additional bench scale cathodic polarisation measurements were made, in the absence of nickel ions, at pH4 (60° and 70°C) and the resulting polarisation curves are shown in Fig.5.4. The inflection in the curve (A-B) over the potential range ~ -0.3 to 0.8V , is probably associated with the mass transport controlled reduction of H_3O^+ (Reaction 2.7a). (The reversible electrode potential of this reaction is -0.26V at 60°C). At higher potentials hydrogen is evolved by reaction (2.11). (The reversible electrode potential of this reaction is $\sim -0.83\text{V}$ at 60°C). The inflection noted previously in the nickel polarisation curves probably resulted from reaction (2.7a) becoming mass transport controlled. However, it would seem probable that nickel was already deposited at this stage, since it is known that the current efficiency generally exceeds 90% at $\sim 0.01 \text{ A cm}^{-2}$ (e.g. Fig.5.5 (225)). Therefore any additional increase in pH probably results from the reduction of water at $E > -0.83\text{V}$, and the subsequent production of OH^- ions. The pH profile will be modified by the buffer reactions (involving H_3BO_3 , NiOH^+ and other metal ion complexes) and mass transport processes occurring within the boundary layer. It is primarily the mass transport of OH^- away from the cathode and H_3O^+ towards the cathode which controls the pH at the interface and the value of i_{max} .

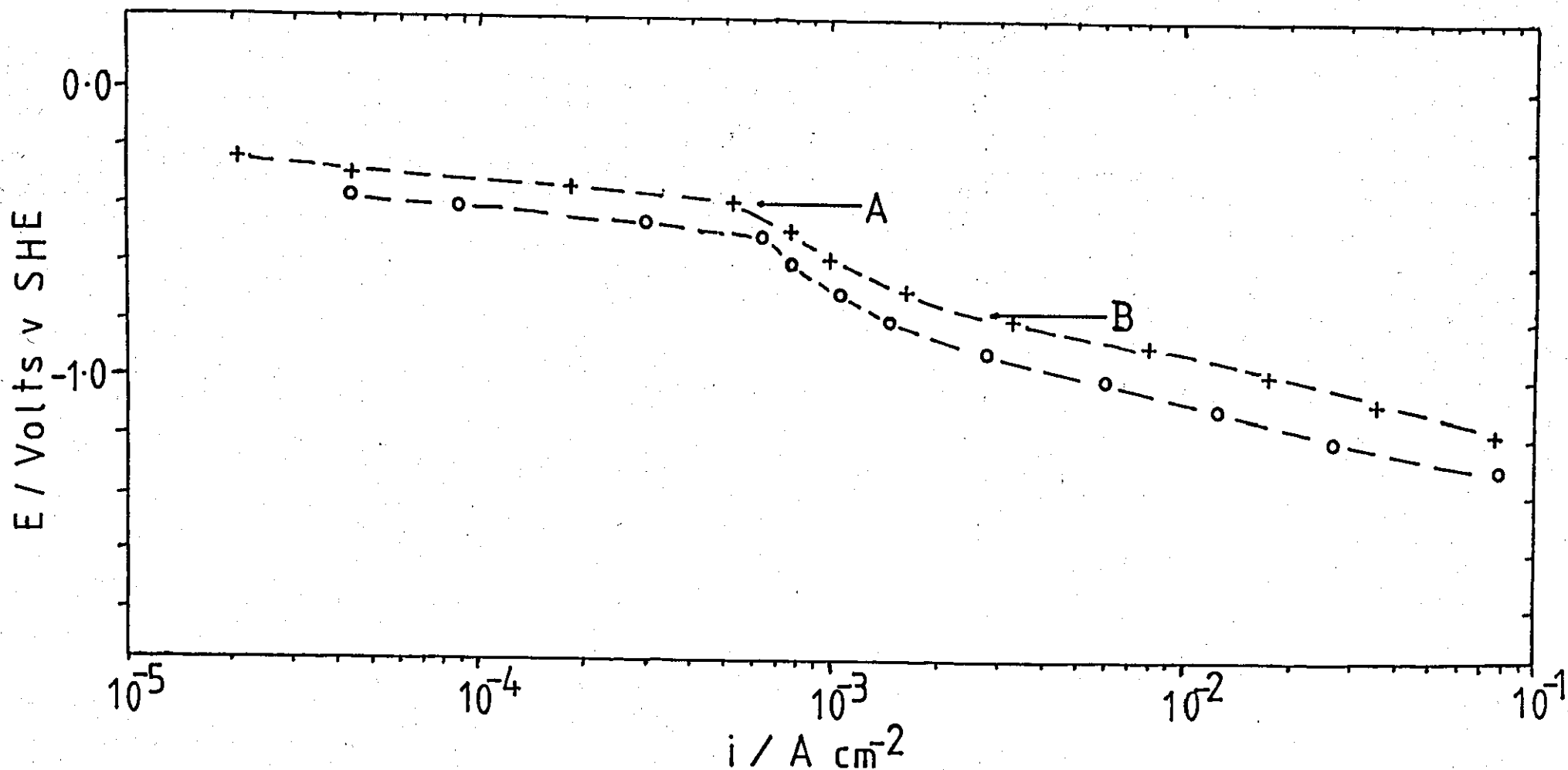


Fig.5.4 Cathodic polarisation behaviour during the electrolysis of a solution containing 40g l^{-1} H_3BO_3 and 100g l^{-1} Na_2SO_4 . Nickel cathode.

o - o 60°C

+ - + 70°C

pH 4.93, $\text{N}_2 = 250 \text{ cm}^3 \text{ min}^{-1}$, electrode area = 1.15 cm^2

The current efficiency for nickel deposition

The increase in the current efficiency for nickel deposition with increasing current density ($i < \sim 0.1 \text{ A cm}^{-2}$), noted in previous investigations of the nickel sulphamate solution (e.g. Fig.5.5), may also be attributed to the reduction of H_3O^+ ions becoming mass transfer controlled. Hence at low current densities, the hydrogen evolution reaction (HER) (2.7a) represents a significant fraction of the total current. The results of the present work would suggest that this reaction would represent $< 0.1\%$ of the total plating current at a current density of 1 A cm^{-2} . However, in solutions containing dissolved air (as is common in commercial electroplating), the current efficiency for nickel deposition may also be reduced slightly by the mass transport controlled reduction of oxygen (e.g. Fig.4.162). The contribution of this reaction to the overall current density may be of a similar magnitude to the HER (as given by reaction (2.7a)) i.e. $\sim 10^{-3} \text{ A cm}^{-2}$. Hence, the current efficiency for nickel deposition should be $> 99\%$ at current densities $> 0.1 \text{ A cm}^{-2}$.

Further reductions in current efficiency at higher current densities can only be due to the reduction of water. At this point ($E < -0.83\text{V}$) a significant increase in the pH of the electrolyte close to the electrode and subsequent hydroxide precipitation may become possible.

Inflections due to gas related effects and hydroxide deposition

As has been seen (e.g. Fig.4.156) inflections were observed on the polarisation curves at current densities $> 0.5 \text{ A cm}^{-2}$. At 50° and 60°C it was clear that these features were generally associated with the precipitation of $\text{Ni}(\text{OH})_2$ at the leading edge region of the cathode. This resulted in a decrease in the effective area of the working electrode and hence an increase in the current density in this region. However, changes in the quantity of evolved hydrogen and/or the gas flow pattern may also contribute to an apparent increase in cathode polarisation.

The inflections observed at 70°C may also be attributed to similar gas effects. It is possible that the potential at which these features were observed coincides with the reduction of water (i.e. $\sim 0.83\text{V}$).

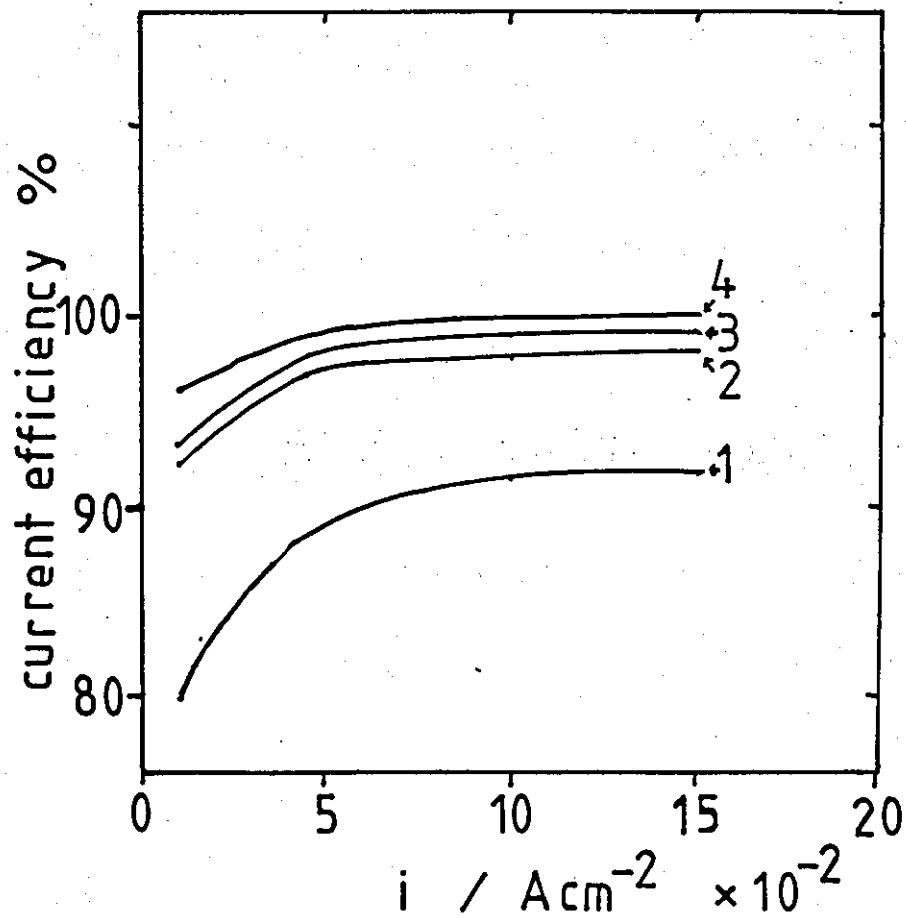


Fig. 5.5. The current efficiency of nickel deposition from 'conventional' nickel sulphamate solutions (from Lainer (225)).

- 1 pH 1
- 2 pH 2
- 3 pH 3
- 4 pH 4

The 'pseudo limiting current densities', that were particularly noticeable on semi-logarithmic plate (e.g. Fig.4.157), may be attributed to an increase in the ohmic overpotential at high current densities. This may be associated with the greater volume of gas that may be evolved in this region.

It was of interest to note that neither the addition of chloride ions nor a wetting agent significantly affected the high current density polarisation behaviour, although the addition of a wetting agent slightly increased (positive shift) the cathode potential. This is to be expected due to the decreased surface coverage of the cathode with gas bubbles, and hence a reduction of the ohmic contribution to the overpotential.

It is evident that gas evolution may significantly affect cathode polarisation by 'blanketing' of the cathode at low flow rates and by an increased contribution to the ohmic overpotential at higher flow rates.

At cathode potentials $> -0.4V$ ($i < 10^{-3} A cm^{-2}$), the predominant reaction is probably the reduction of H_3O^+ ions and, in the presence of air, the reduction of dissolved oxygen. Hence the current efficiency for nickel deposition would be expected to be low. At cathode potentials $\ll -0.4V$ ($i > 10^{-1} A cm^{-2}$) the nickel deposition reaction predominates, as the former reactions become mass transport controlled, and the current efficiency would be expected to approach 100%. However, at potentials $< -0.83V$ the reduction of water is possible, resulting in additional hydrogen evolution and the generation of OH^- ions. If the increase in the pH at the interface is not moderated by buffer reaction and mass transport processes, then nickel hydroxide will be precipitated. It is these processes which control the value of i_{max} .

5.4 The nature of the nickel deposit

Structure and microhardness of deposits

There was no clear evidence of structural effects directly related to the Reynolds number or the cell and electrode geometry. However, a change in these parameters will effect the maximum current density for a good deposit. Hence the general observations regarding both deposit micro-structure and micro-hardness may be discussed in terms of the deposition rate and temperature. The trends described are common to the main deposit sections of all good deposits in the absence of addition agents.

a) The effect of deposition rate (at constant temperature)

The results provided some evidence of two trends:

- i) The grain size tends to decrease with increasing current density; and
- ii) As the grain size decreases the macrohardness value increases.

For example, at 60°C the grain size decreased from up to 10µm to less than 2µm, over the current density range 0.2 to 1 A cm⁻² (cf. Figs.4.21a and 4.25b). This was accompanied by an increase in the proportion of the smaller grains at the faster deposition rates. The corresponding increase in microhardness was 260 to 340 kg mm⁻² (cf. Fig.2.29).

The grain refinement is consistent with the expected trend, since at more negative potentials (higher current densities), the number of available nucleation sites increases and more grains nucleate and grow.

Impurity incorporation (e.g. Ni(OH)₂) may also result in a small grain size. It is also to be expected that a small grain size may result in harder deposits, although hardness may also be related to the incorporation of impurities and other factors. In previous studies (239,322) of nickel deposits, an increased deposit hardness and a decreased grain size have been observed when the solution pH was greater than pH5. This has been associated with the incorporation of Ni(OH)₂

into the deposit (see pages 88-89 and 94-95). At very high current densities, the pH at the electrode/electrolyte interface may exceed this value and have a similar effect.

While grain refinement with increasing current density has been observed in nickel deposited from other electrolytes, previous studies (239,320,321) of sulphamate nickel deposits, over a narrower range of current densities ($<0.6 \text{ A cm}^{-2}$), were inconclusive with regard to this relationship.

Kendrick (1) has reported the microhardness values of about 225 kg mm^{-2} over the current density range 0.2 to 0.4 A cm^{-2} for sulphamate nickel deposits (Fig.2.29). Hardness values of up to 360 kg mm^{-2} have been found for fast rate deposits from other electrolytes (67). The results of the present study were in reasonable agreement with previous investigations.

b) The effect of temperature (at constant current density)

Once again two trends were evident from the results:

- i) The grain size increased with increasing temperature; and
- ii) The microhardness increased with decreasing grain size.

These effects were more noticeable over the temperature range 60° to 70°C . A typical change in grain size over this temperature range at 1 A cm^{-2} , was from $<5\mu\text{m}$ to $<3\mu\text{m}$ (cf. Figs. 4.129 and 4.140).

The corresponding change in the microhardness value of the deposit was from $\sim 335 \text{ kg mm}^{-2}$ to $\sim 275 \text{ kg mm}^{-2}$. A decrease in microhardness would be expected to accompany an increase in grain size (cf. current density effects).

An increase in temperature will result in an increase in the cathode polarisation (positive shift). Hence fewer nucleation sites are available and grain size will increase. However, the temperature increase will also effect solution reactions and the stability of solution species.

c) Special features

Certain other features were evident from the deposition studies. These features may be divided into:

- (i) structural features of the main deposit sections;
- (ii) brightness of the main deposit sections; and
- (iii) entry and exit effects.

(i) Structural features

Three other types of special macro-features were noted. These were: (a) mound type features; (b) ridge type features; and (c) powder and hydroxide deposits.

(a) Mound type features were observed for all experimental conditions. The size and distribution of mounds tended to increase with increasing current density or decreasing temperature. Such features were also observed at very high current densities where a well-defined grain structure was not apparent (eg. Figs.4.131 and 4.138).

This type of growth would suggest preferential growth at certain sites. This may be due to energetically favourable sites for nucleation or alternatively a localised mass transfer and current distribution phenomenon. Similar features have been observed previously by other workers (89,326).

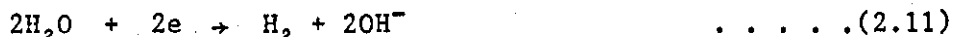
(b) Ridge type features were observed at very high current densities ($>1 \text{ A cm}^{-2}$) and at very low (laminar) flow rates (e.g. Figs. 4.3 and 4.14). The ridges were parallel to the flow direction. These features probably resulted from a localised current distribution effect due to the streaming of hydrogen gas along the cathode surface.

(c) Powder and hydroxide deposits were observed at deposition rates in excess of the maximum current density for a sound deposit (i_{max}). At the maximum current density, areas of the deposit particularly near the leading edge developed a nodular powdery appearance. At higher current densities large areas of the cathode were coated in some cases with a

green-black hydroxide deposit. Hydroxide deposition has often been thought to be associated with an increase in the pH of the electrolyte close to the electrode surface (p.82), the change in pH resulting from the reduction of hydroxonium ions and the evolution of hydrogen.



However, as has been seen in the case of the electrolysis of nickel solutions, the above reaction is probably complete prior to the deposition of nickel. It has been shown that the increased pH may be associated with the reduction of water



The rate of production of OH^- ions will depend on the current efficiency and the overall current density.

The current efficiency for deposition of all sound nickel deposits was greater than 95%. Therefore, only at very high current densities and/or with insufficient agitation will the pH increase and nickel hydroxide precipitate at the electrode-electrolyte interface.

The powder deposits and 'dendritic' type structures could be considered to be indicative of an m.t.c. reaction (p.90), however, in the absence of other evidence of mass transfer control, the structures are more likely to be associated with local growth inhibition by H_2 , NiOH^+ and $\text{Ni}(\text{OH})_2$. For example, such structures may be formed by the incorporation of hydroxide particles, followed by overgrowth of nickel.

Deposit porosity was observed in all sound electroforms. The size and number of pin-holes through the foil decreased with increasing flow rate, current density and temperature. However, it should be noted that most electroforms were deposited in the absence of a wetting agent and there is some evidence to suggest that pore-free deposits may be obtained by lowering the surface tension of the electrolyte, without significantly changing the deposit structure or the maximum current density.

ii) Deposit brightness

Most electroforms were semi-bright in appearance. However, the deposit brightness was observed to increase with increasing current density and decreasing temperature. It is of interest to note that bright deposits are unusual in the absence of addition agents. The increasing deposit brightness was often accompanied by a grain refinement of the deposit. However, it is not to be construed as suggesting that the two observations are directly linked. The increase in brightness was probably associated with a decrease in the micro-roughness of the deposit, since larger macro-features were often observed on the deposit surface.

iii) Deposit exit and entry effects

The deposit structure at the leading and trailing edges of the cathode were often different from that of the main deposit region, particularly with a non-uniform current distribution.

The mound and ridge type features discussed previously were often observed, near the leading and trailing edges at current densities $< 1 \text{ A cm}^{-2}$. In addition the edge structures may be bulbous in appearance. At the maximum current density for a good deposit, powder and hydroxide type deposits were usually initially observed in this region. Bands of brighter metal were also a common feature of the entry and exit area. The longitudinal microhardness profiles have indicated that the foil is harder at the edges where microhardness values of up to $\sim 400 \text{ kg mm}^{-2}$ have been measured.

The evidence suggests that the current density at both leading and trailing edges was greater than the main deposit region. This is indicative of the primary/secondary type current distribution which should be observed at the lower current densities. However, near the maximum current density a mass transfer (or tertiary) current distribution would be expected if the reaction is a simple mass transfer controlled process. These observations are consistent with the current distribution studies discussed previously (section 5.2b).

5.5 General and practical implications for the fast-rate electrodeposition of nickel from sulphamate solutions

The results of the present work (Chapter 4) have demonstrated that sound and coherent nickel foils may be electroformed from sulphamate solutions at very high current densities ($\sim 1.3 \text{ A cm}^{-2}$ at 60°C (Fig.4.130b), and $>2 \text{ A cm}^{-2}$ at 70°C (Fig.4.14b), and high current efficiencies ($>95\%$). These rates are comparable with those attained in most other studies of the fast-rate electrodeposition of nickel, from non-chloride solutions (e.g. Table 2.1, 2.2 and 2.3), (although Eisner claimed a maximum current density of $\sim 5.4 \text{ A cm}^{-2}$ for the deposition of nickel from sulphamate solutions in the vibratory tub electroplating facility (Table 2.2)). The results of Wesley et al (67) would suggest that the maximum deposition rates may be faster in All-Chloride electrolytes. This is probably due to the stabilisation of nickel species by complexation with chloride ions.

However, studies of the electrodeposition of nickel from sulphamate solutions, using a rotating cylinder electrode (358) have indicated that deposition at higher current densities is possible. Nickel foils were deposited, at high current efficiency at current densities $>2.2 \text{ A cm}^{-2}$ at 60°C (Fig.5.6) and $>2.4 \text{ A cm}^{-2}$ at 70°C (Fig.5.7) (see also p.27). It is of interest to note that current efficiencies $>100\%$ were observed at 60°C . This may be attributed to the incorporation of Ni(OH)_2 into the deposit (cf. p.88-89). It is thought that the higher rate of mass transfer, the uniform current distribution and the increased efficiency of removal of gas bubbles from the cathode surface may all contribute to the faster deposition rate. This would suggest that, in a flowing system a higher Reynolds number may also result in further improvements in the maximum current density.

The nickel foils electroformed in the present work, at high current densities, tended to be harder and brighter than conventional deposits obtained in the absence of addition agents. This may also be related to Ni(OH)_2 incorporation.

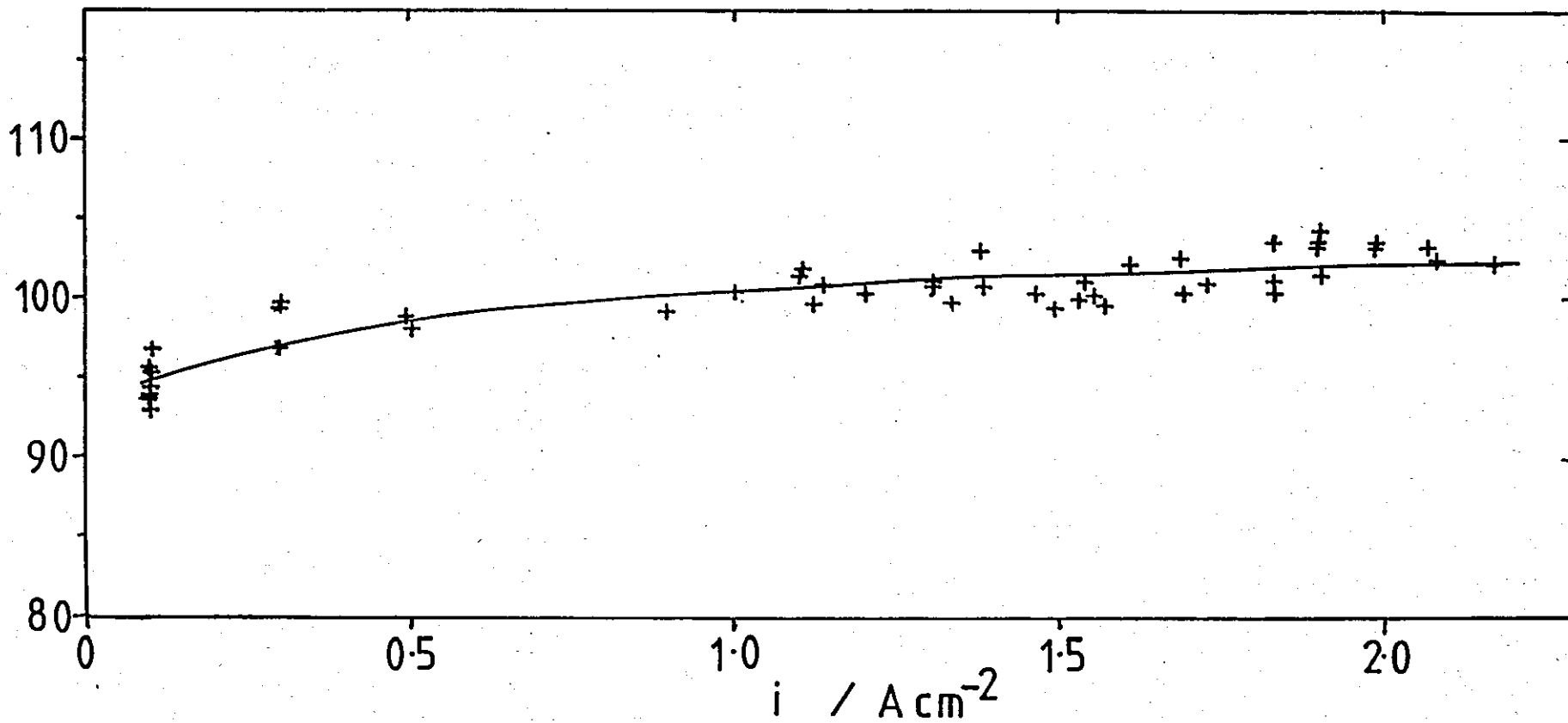


Fig. 5.6 Current efficiency of nickel deposition from 'Concentrated' nickel sulphamate solutions at a rotating cylinder electrode at 60°C (358).

2R = 1 cm, 2,200 r.p.m., Re 19,900.

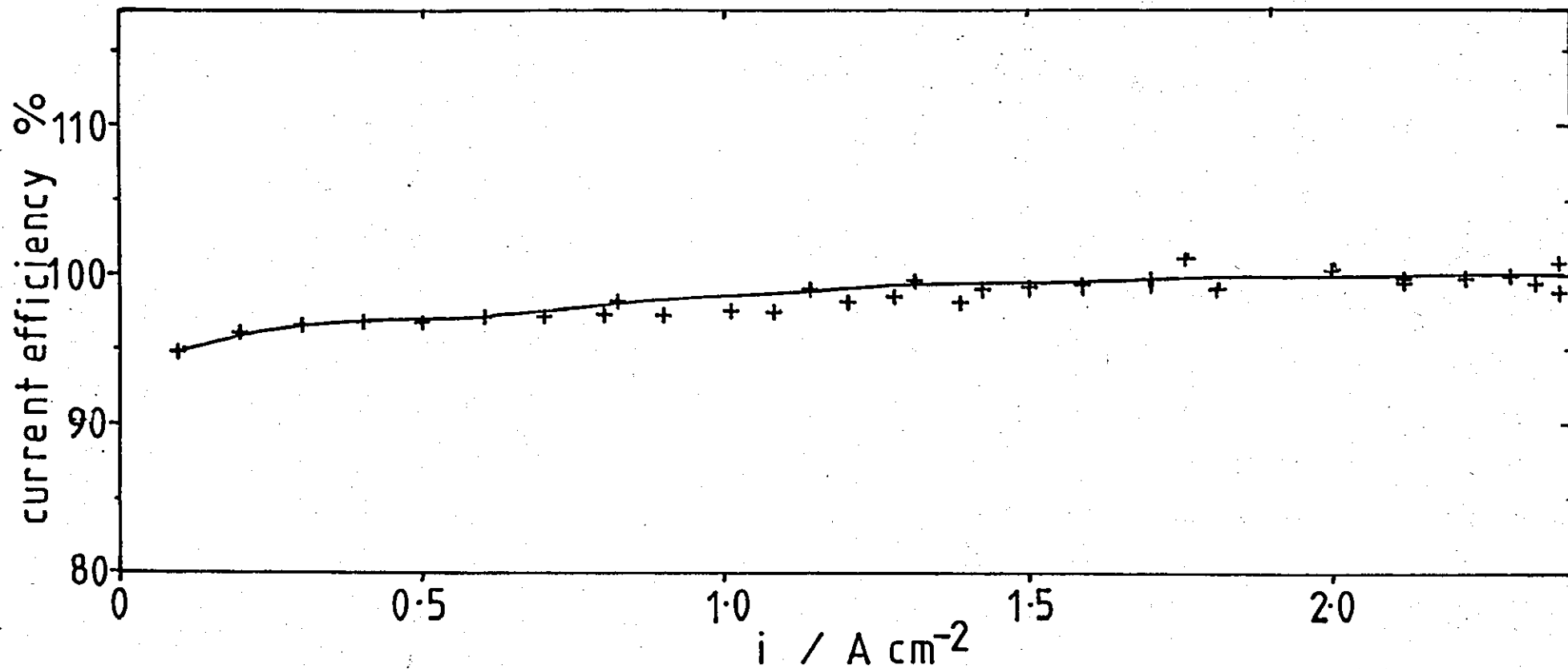


Fig.5.7 Current efficiency of nickel deposition from 'Concentrated' nickel sulphamate solutions at a rotating cylinder electrode at 70°C (358).
2R = 1 cm, 2,200 r.p.m., Re 19,700.

Although many deposits were pitted and porous it was clear that low porosity is favoured by higher temperatures, deposition rates and flow rates and shorter cathode lengths. The high flow rates are essential to ensure the removal of gas bubbles from the cathode surface and in preventing a distortion of the current distribution. However, the addition of surfactants to the electrolyte will probably reduce porosity to an acceptable level.

Since the electroforming studies at 70°C were restricted by the limitations of the voltage output of the available power supply (30V) (see Fig.5.8), a reduction in cell voltage is necessary to extend this investigation.

Calculations, based on the cell geometry and the conductivity of the electrolyte (Table 3.3), have suggested that the resistance of the solution and the polarisation of the electrodes account for less than 25V. (The resistance of the diaphragm was taken as ~4x the resistance of an equivalent thickness of the electrolyte (0.15cm) (ref.150). The remaining 5V potential difference resulting from the additional resistance of a gas filled electrolyte. A significant reduction in cell voltage may be obtained by a reduction in the inter-electrode gap and by the use of a more rapid flow rate to remove the evolved gases. Improved anode corrosion would also be advantageous in reducing the volume of evolved oxygen.

As has been seen, it is at 70°C that the most significant improvements in the maximum current density are observed. However, the limits of i_{\max} have yet to be determined at this temperature.

In electroforming practice, the maximum deposition rate for a good deposit may be doubled by increasing the electrolyte temperature from 60° to 70°C. With suitable conditions nickel foils may be electroformed at up to 50x the conventional deposition rates. As is apparent, to attain such rapid deposition rates and maintain a sound and uniform structure, close control of the current distribution is essential. A uniform current distribution is preferable. It is clear that high current density operation requires high flow rates and high rates of mass transfer.

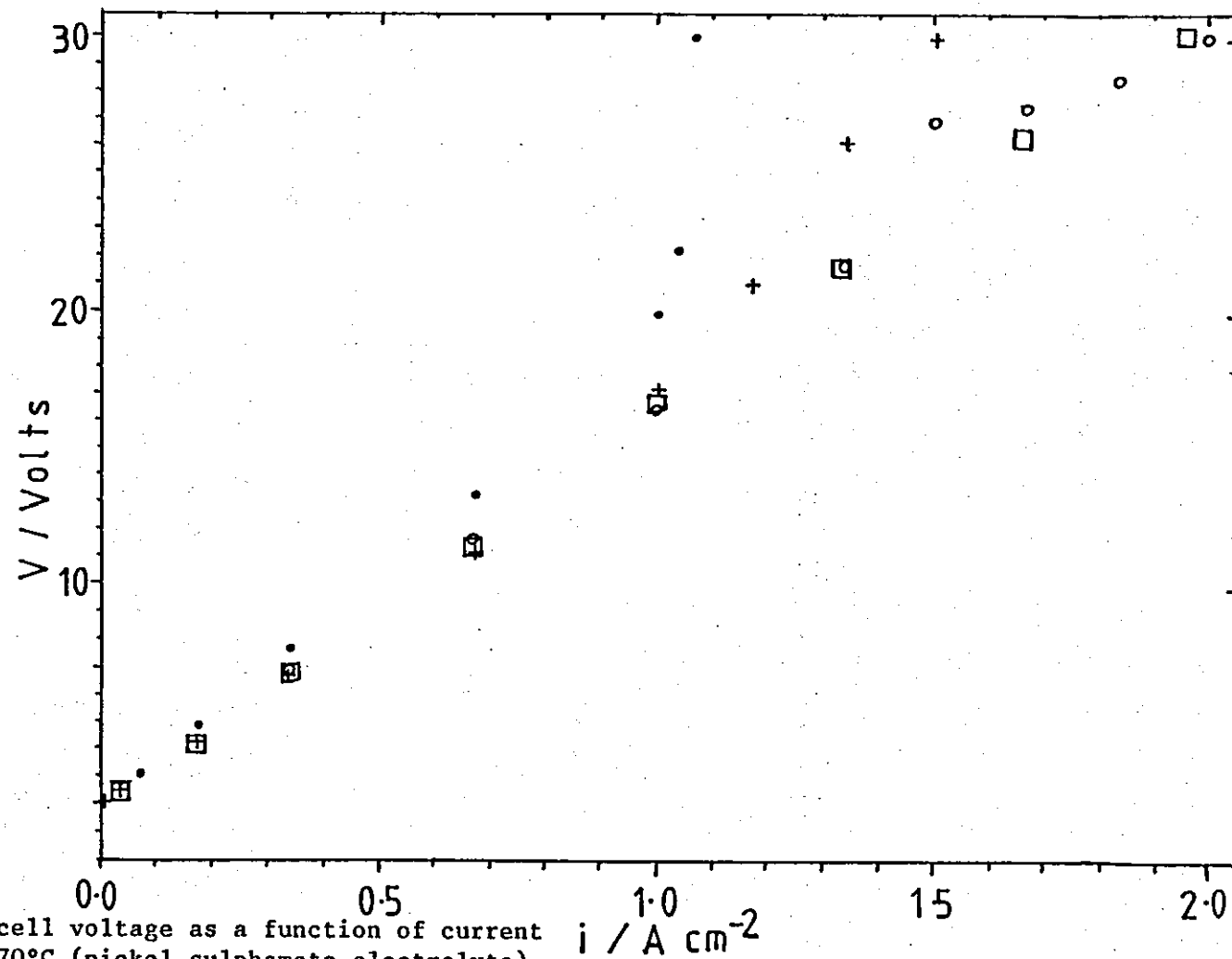


Fig.5.8

The Cell 2 cell voltage as a function of current density at 70°C (nickel sulphamate electrolyte).

- - ● - ● Re 4,300
- + - + - + Re 7,910
- - ○ - ○ Re 11,850
- - □ - □ Re 16,200

Overall summary of the discussion

A 'divided' cell configuration has been found necessary to eliminate anode gases effecting mass transport processes at the cathode. The cell performance was characterised by the study of the mass transport controlled deposition of copper and as expected, was consistent with the original cell specification.

It has been shown that mass transport, current distribution and cathodic polarisation processes, in the nickel sulphamate system, differ considerably from the 'simple' copper system.

The mass transport processes in the nickel system are enhanced by the concomitant hydrogen evolution. Furthermore, no specific evidence of the mass transport of 'simple' aqueous nickel ions has been observed.

The absence of a clear separation of the nickel reduction reaction and the hydrogen evolution reaction provides some evidence of mechanistic complexity, possibly involving a NiOH^+ species. It is clear that the deposition process is limited by the precipitation of hydroxide and consequently a rapid decrease in current efficiency.

Finally, it has been shown that the evidence indicates that the reduction of nickel ions is not mass transport controlled at current densities less than i_{max} . The maximum current density is determined by the changes of pH within the boundary layer. The pH profile across the boundary layer will be complicated by buffer reactions and the mass transport processes. Nickel hydroxide will be precipitated when the rate of accumulation of OH^- ions is greater than the rate of removal of OH^- ions and the pH at the interface exceeds 6.6.

It is unlikely that nickel hydroxide will be precipitated at cathode potentials $> E_{\text{rev.}}^{\text{H}_2\text{O}}$, even in non-agitated solutions, since micro-convection and free convection will continually supply H_3O^+ ions and $\text{Ni}_{\text{aq}}^{2+}$ ions to the interface. This potential will be attained before concentration polarisation arises in the nickel system.

However, under suitable conditions, the increase in the pH is moderated to produce sound and coherent electroforms at current densities in excess of 2 A cm^{-2} .

6. CONCLUSIONS AND SUGGESTIONS FOR FURTHER WORK

The major conclusions of the present work are as follows:

1. The unusual split cell - single flow circuit design was characterised using a 'simple' copper deposition system and found to be consistent with the original design specification.
2. At current densities greater than 0.01 A cm^{-2} the electrolytic nickel anode was passivated. The primary anode reaction was oxygen evolution. The low concentration of chloride ions ($\sim 5 \text{ g l}^{-1} \text{ NiCl}_2 \cdot 6\text{H}_2\text{O}$), commonly used in concentrated nickel sulphamate solutions, is ineffective in promoting anode corrosion.
3. i_{max} was defined as the maximum current density for a sound and coherent nickel electroform. At current densities $> i_{\text{max}}$, powder and hydroxide is deposited.
4. Sound, fine grained nickel deposits were electroformed, without addition agents, at very high current densities (up to i_{max}) and at $>95\%$ current efficiency.
5. The maximum current density attained, at $Re \sim 14,000$ with a uniform current distribution, is $\sim 1.3 \text{ A cm}^{-2}$ at 60°C and $> 2 \text{ A cm}^{-2}$ at 70°C .
6. A significant decrease in current efficiency ($<95\%$) was not observed for current densities $< i_{\text{max}}$.
7. The grain size of the electrodeposit tends to decrease with increasing current density.
8. The brightness and hardness of the nickel foils tends to increase with decreasing grain size. The deposits tend to be brighter and harder than conventional deposits.
9. A uniform current distribution is necessary to electroform foils of uniform structure at high current densities and avoid entry/exit effects.

10. A uniform current distribution is achieved using a 10cm cathode and a 9cm anode.
11. At 60°C the value of i_{\max} tended to increase with increasing flow rate. The following proportionalities are observed in turbulent flow:

$$\begin{array}{ll} L/d_e < 4.5 & i_{\max} \propto Re^{\frac{2}{3}} \\ L/d_e \sim 11.7 & i_{\max} \propto Re^{0.8} \end{array}$$

At 70°C the relationship between i_{\max} and Re is not clear.

12. In laminar flow large gas bubbles tend to accumulate on the cathode surface, resulting in poor deposit quality and irreproducible values of i_{\max} .
13. High electrolyte velocities are necessary to remove hydrogen bubbles from the cathode, reduce deposit porosity and ensure a uniform deposit structure. Deposit porosity may be eliminated by the addition of wetting agents.
14. The absolute values of i_{\max} are less than the values of i_L calculated from the design equations. The value of i_{\max} is not equivalent to i_L and may indicate mechanistic complexity in the reaction.
15. At constant Re and temperature, the value of i_{\max} tends to increase with decreasing cathode length for $L/d_e < 4.5$. However, the relationship between L/d_e and i_{\max} is not that expected for a mass transfer controlled relationship.
16. At constant Re and L/d_e , the value of i_{\max} increases significantly with increasing temperature (>40% increase between 60° and 70°C). The increase in i_{\max} is considerably greater than that calculated for a simple mass transfer process.
17. A mass transfer controlled current distribution is not observed. The experimental current distribution is similar to the primary/secondary current distribution.

18. A limiting current density for nickel deposition is not observed and there is no clear evidence of concentration polarisation at current densities $< i_{\max}$. The difficulty in separating the nickel and hydrogen deposition reactions may also be indicative of mechanistic complexity.
19. The concomitant evolution of hydrogen gas enhances mass transfer rates at the cathode. The 'gas model' suggests that microconvective (gas only) mass transfer may dominate the transport processes when the average bubble size is $< 1.0 \mu\text{m}$.
20. There is no clear evidence of the mass transport control of aqueous Ni^{2+} ions at current densities $\leq i_{\max}$.
21. Nickel hydroxide is precipitated at the cathode as a result of the pH at the electrode/electrolyte interface exceeding 6.6.
22. The increased pH results from the reduction of water by the reaction



23. The rate of accumulation of OH^- ions will be determined by the overall current density and by the mass transport processes controlling the rate of removal of OH^- ions. The pH will also be modified by the solution buffers such as H_3BO_3 , NiOH^+ and other metal-ion complexes.

Suggestions for further work

It is clear from the present work that a further investigation of nickel electroforming at 70°C , would be of considerable interest. A reduction in cell voltage and/or an uprated power supply would be required to extend this work.

A redesigned cell, with a narrower inter-electrode gap and a maximum Reynolds number in the range Re 50,000 - 100,000 would be advantageous in reducing the cell voltage. Furthermore, an increased flow rate would assist in removing gas bubbles and increase the rate of mass transfer. This would require some modification to the flow circuit. The inclusion of a dual flow system (separate anolyte and catholyte) may permit improved anode corrosion. In future developments a rotating drum, for continuous foil production, could be incorporated.

Additional studies could include the following:

- i) an examination of the internal stress and other properties of nickel foils deposited at high current densities using X ray and other methods; and
- ii) a detailed study of the effect of agitation on the incorporation and behaviour of addition agents.

It would appear that some clarification of the mechanistic complexity in the nickel system is required (particularly at high current densities). This could include:

- i) a detailed T.E.M. study of hydroxide incorporation in nickel electroforms;
- ii) the use of electrochemical techniques and impedance measurements to separate the nickel deposition and hydrogen evolution reactions; and
- iii) the use of laser techniques (e.g. laser anemometry) and spectroscopy to examine the structure and composition of the boundary layer.

These investigations could be complemented by the mathematical modelling of the pH changes within the boundary layer.

Finally, the electrodeposition of metals in a parallel plate cell may also be applicable to other systems such as alloy and composite plating, where the effects of agitation have not been fully investigated.

References

1. R.J.Kendrick, Proceedings 6th International Conference on Electrodeposition and Metal Finishing, Trans I.M.F., 42, 235-241, (1964).
2. J.O'M. Bockris and A.K.N.Reddy, 'Modern Electro-chemistry', Plenum Press, N.Y., (1970).
3. E.Raub and K.Müller, 'Fundamentals of Metal Deposition', Elsevier Publishing Company, (1967).
4. J.A. von Fraunhofer, 'Basic Metal Finishing', Elek Science, London, (1976).
5. J.M.West, 'Electrodeposition and Corrosion Processes', Van Nostrand Reinhold, London, (1971).
6. J.O'M. Bockris and G.A.Razumney, 'Fundamental Aspects of Electrocrystallization', Plenum Press, (1967).
7. Bockris and Mathews, Proc.Roy.Soc. London, Ser. A292, 479 (1966).
8. Conway and Bockris, Proc.Roy.Soc. London, Ser.A248, 394, (1958), Electrochim Acta, 3, 340, (1961).
9. Seiter and Fischer, Z.Electrochem 63, 249, (1959).
10. J.Sato, Electrochem.Soc., 106, 206, (1959).
11. J.Newman, in Adv. Electrochem.Eng. 5, 87, (1967).
12. J.R.Selman, C.W. Tobias, in Adv.Chem.Eng., 10, 216, (1978).
13. J.Newman, Ind.Eng.Chem. 60, 12, (1968).
14. J.B.Mohler, Metal Finishing J. 29-33, (1974).
15. A.T.Tvarusko, Plating, 139-145, (1974).
16. W.H.Safranek, Plating Surf.Fin., 67, 28-30, (1980).
17. A.Kiemidzu, Mech.Eng., 25, 122-123, (1977).
18. D.Jahn, Interfinish 8 , Basle, Switzerland, Paper A20, (1972).
19. J.B.Mohler, Metal Finishing, 81, 41, (1983).
20. A.C.Hart, Trans.I.M.F., 55, 65-69, (1977).
21. D.R.Gabe, Metal Finishing J., Pt.1 340-345, (1970),
Pt.2 370-376, (1970).

22. W.J.Blaedal, C.L.Olson, L.R.Sharma, *Anal.Chem.*, 35, 2,100, (1963).
23. D.J.Pickett, K.L.Ong, *Electrochim.Acta*, 19, 875, (1974).
24. D.W.Lightfoot, E.N.Hubbard, *Ind.Eng.Chem.Fund.*, 5, 370, (1966).
25. A.T.Kuhn, B.Marquis, *J.App.Electrochem.*, 2, 275, (1972).
26. G.Wranglen, O.Nilsson, *Electrochim.Acta*, 7, 121, (1962).
27. D.J.Pickett, B.R.Stanmore, *J.App.Electrochem.*, 2, 151, (1972).
28. C.W.Tobias, R.G.Hickman, *Z.Phys.Chem.*, 229, 145, (1965).
29. T.K.Ross, A.A.Wragg, *Electrochim.Acta.*, 10, 1093, (1965),
Ibid. 12, 1,431, (1967).
Ibid. 13, 2,192, (1968).
30. D.R.Gabe, F.C.Walsh, *J.App.Electrochem.*, 13, 3-22, (1983).
31. D.R.Gabe, *J.App.Electrochem.*, 4, 91, (1974).
32. C.Deslouis, I.Epelboin, *Electrochim.Acta*, 22, 921, (1977).
33. R.V.Bular, A.Bartin, V.Melea, *Electrochim.Acta*, 23, 641, (1978).
34. R.V.Bular, A.Bartin, *Electrochim.Acta*, 24, 173, (1979).
35. N.Ibl, in *Adv. in Electrochemistry and Electrochemical Eng.*
2, 49, (1962).
36. M.Fleischman, F.Goodridge, J.P.Bockhurst, *Brit.Pat.*1194181, (1970).
37. Various authors, 'Novel Electrode Systems for Dilute Metal Bearing Liquors', *Chemistry and Industry*, 447, (1978).
38. A.Bettley, A.Tyson, S.A.Cotgreave, N.A.Hampson, *Surface Tech.*,
12, 15, (1981).
39. J.Ghoroghchian, R.E.W.Jansson, D.Jones, *J.App.Electrochem.*,
437, (1977).
40. S.Mahanta, T.Z.Fahidy, *J.App.Electrochem.*, 7, 437, (1977).
41. A.R.Despić, M.N.Konjović, M.Mitrović, *J.App.Electrochem.*, 7, 545,
(1977).
42. G.H.Sedahmed, A.Abdel Khalik, A.M.Abdallah, M.M.Farahat,
J.App.Electrochem., 9, 563, (1979).
43. D.N.Bennion, J.Newman, *J.App.Electrochem.*, 2, 113, (1973).
44. M.S.Spencer, P.J.H.Carnell, W.J.Skinner, *Ind.Eng.Chem.Process.*
Des. and Dev. 8, 191, (1969).

45. A.Storck, P.M.Robertson, N.Ibl, *Electrochim.Acta*, 24, 323, (1977).
46. P.Naderbaum, T.Z.Fahidy, *J.App.Electrochem.*, 5, 249, (1975).
47. A.T.Kuhn, R.W.Houghton, *J.App.Electrochem.*, 4, 69, (1974).
48. A.K.P.Chu, M.Fleischmann, G.J.Hills, *J.App.Electrochem.*, 4, 323, (1974).
49. D.Hutin, F.Coeuret, *J.App.Electrochem.*, 7, 463, (1977).
50. A.T.S.Walker, A.A.Wragg, *Electrochim.Acta*, 25, 323, (1980).
51. D.J.Gabe, D.R.Robinson, *Trans.I.M.F.*, 48, 35, (1970).
52. D.J.Gabe, F.C.Walsh, *Surf.Tech.*, 12, 25, (1981).
53. N.Ibl, Ph.Jovet, F.Stahel, *Electrochim.Acta*, 17, 733, (1972).
54. J.Bannard, *J.App.Electrochem.*, 7, 267, (1977).
55. M.Datta, D.Landholt, *J.Electrochem.Soc.*, 124, 483, (1977).
56. M.Datta, D.Landholt, *J.App.Electrochem.*, 7, 247, (1977).
57. D.Landholt, R.H.Muller, C.W.Tobias, *J.Electrochem.Soc.*, 116, 1,384, (1969).
58. D.Landholt, M.Datta, *Electrochim.Acta*, 25, 1,255, (1980).
59. D.Landholt, M.Datta, *J.Electrochem.Soc.*, 122, 1,466, (1975).
60. E.D.Farmer, A.H.Webb, *J.App.Electrochem.*, 2, 123, (1972).
61. G.P.Rothwell, T.P.Hoar, *Electrochim.Acta*, 10, 403, (1965).
62. O.D.Macdonald, B.C.Syrett, S.S.Wing, *Corrosion*, 34, 289, (1978).
63. J.Postlethwaite, E.Fiadzigbe, S.Aruliah, *Corrosion*, 34, 85, (1978).
64. G.Bianchi, G.Fiori, P.Longhi, F.Mazza, *Corrosion*, 34, 396, (1978).
65. A.M.Max, M.L.Whitehurst, *Tech.Proc.Amer.Electroplat.Soc.*, 40, 181, (1959).
66. R.A.Dimon, *Proc.Amer.Electroplat.Soc.* 35, 169, (1948).
67. W.A.Wesley, W.W.Sellers, E.J.Roehl, *Proc.Amer.Electroplating Soc.* 36, 79, (1949).
68. H.Angerer, N.Ibl, *J.App.Electrochem.*, 9, 219, (1979).
69. M.A.La Boda, A.H.Holden, J.P.Hoare, *J.Electrochem.Soc.*, 127, 1,709, (1980).

70. J.P.Hoare, M.A.La Boda, A.H.Holden, *Plating Surf.Fin.*, 69, 101, (1982).
71. W.H.Safranek, C.H.Layer, *Trans.I.M.F.*, 53 121, (1975).
72. W.H.Safranek, C.H.Layer, *Metal Ceramics Inform.Cent.Rep.*, M.C.I.C. - 74-17, 103, (1974).
73. J.G.Zimmerman, *Trans.Amer.Electrochem.Soc.*, 3, 245, (1903).
74. C.W.Bennett, H.C.Kenny, R.P.Dugliss, *Trans.Amer.Electrochem.Soc.*, 25, 335, (1914).
75. C.W.Bennett, C.C.Rose, L.G.Tinkler, *Trans.Amer.Electrochem.Soc.*, 28, 339, (1915).
76. K.C.Narasimham, H.V.K.Udupa, *Met.Fin.J.*, 11-17, 32-34, (1972)..
77. W.J.Albery, M.L.Hitchman, 'Ring Disc Electrodes' O.U.P. (1971).
78. V.G.Levich, 'Physiochemical Hydrodynamics', Prentice Hall, N.Y., (1962).
79. J.Newman in 'Electroanalytical Chemistry', 6, 187-352, Marcel Dekker, N.Y., (1972).
80. J.Newman, *Electrochim Acta*, 22, 903, (1977).
81. M.R.H.Hill, G.T.Rogers, K.J.Taylor, *J.Electroanal.Chem.*, 96, 87, (1979).
82. V.Velinov, E.Beltowska, A.Riesenkampf, *Surface coatings and Tech.*, 29, 77, (1986).
83. D.R.Turner, G.R.Johnson, *J.Electrochem.Soc.*, 109, 798, (1962).
84. V.Marathe, J.Newman, *J.Electrochem.Soc.*, 116, 1,704, (1969).
85. M.Eisenberg, L.W.Tobias, C.R.Wilkes, *J.Electrochem.Soc.*, 101, 306, (1954).
86. D.A.Swalheim, *Trans.Electrochem.Soc.*, 86, 395, (1944).
87. L.R.Beard, D.R.Gabe, S.H.Melbourne, *Trans.I.M.F.*, 44, 1, (1966).
88. A.K.Graham, H.L.Pinkerton, *Proc.Amer.Electroplaters Soc.*, 50, 135, (1963).
89. R.E.Bailey, *Proc.Symposium on the Electrodeposition of Metals for Selected Applications*, 21-36, (1972).
90. K.Suzuki, M.Tada, K.Nakjima, *Proc.JSLE-ASLE Int. Lubrication Conf.*, 597-604, (1976).
91. D.E.Reichard, *Products Fin.(Cincinnati)*, 38, 48, (1974).

92. S.Suzuki, K.Yoda, H.Suzuki, I.Yaguchi, H.Karasawa,
U.S.Patent 4,080, 268, (1978).
93. A.Storck, F.Coeuret, Chem.Eng.J., 20, 149, (1980).
94. A.T.S.Walker, A.A.Wragg, Electrochim Acta, 25, 323, (1980).
95. D.Hutin, A.Storck, J.App.Electrochem., 9, 361 (1979).
96. F.Goodridge, Electrochim.Acta, 22, 929, (1977).
97. D.Hutin, A.Storck, F.Coeuret, J.App.Electrochem., 9, 361, (1979).
98. D.Hutin, F.Coeuret, J.App.Electrochem., 7, 463, (1977).
99. T.K.Sherwood, R.L.Pigford, C.R.Wilke, 'Mass Transfer', p.153,
McGraw-Hill, (1975).
100. N.Ibl, J.Venczel, Metalloberflache, 24, 365, (1970).
101. S.Eisener, Trans.I.M.F., 51, 13, (1973).
102. G.C.Pini, P.L.Deanna, Electrochim.Acta, 22, 1423, (1977).
103. L.L.Lopez-Cacicedo, Trans.I.M.F., 53, 74, (1975).
104. P.LeGoff, F.Vergnes, F.Coeuret, J.Bordet, Ind.Eng.Chem., 61,
12, (1969).
105. F.Vergnes, Corrosion (Rueil-Malmaison), 17, 131, (1969).
106. B.A.Shenoi, K.S.Indira, R.Subramanian, Met.Fin.J.,
Pt.1 July 1970, p.40
Pt.2 Aug.1970, p.57.
Pt.3 Sept.1970, p.56.
107. R.Walker, J.F.Clements, Met.Fin.J., Apr.1970, p.100.
108. S.G.Kockergin, G.Y.Vyaseleva, 'Electrodeposition of metals in
Ultrasonic Fields', Consultants Bureau, New York, (1966).
109. L.Dominikov, Met.Fin.J., July 1966, p.68.
110. A.I.Sobolev, Machinery (Lond.), 94, 85, (1961).
111. T.G.Kosav, Plating, 52, 540, (1962).
112. R.Walker, Trans.I.M.F., 53, 40, (1975).
113. R.Walker, Proc. 12th Seminar on Electrodeposition, Kordi Kudar,
India, (1972), p.385.
114. R.Walker, C.T.Walker, Proc.Ultrasonics International, (1975), p.28.

115. R.Walker, C.T.Walker, Nature Physical Science, 244, 141, (1973).
116. R.Walker, C.T.Walker, Ultrasonics, March 1979, p.79.
117. M.P.Drake, Trans.I.M.F., 58, 67, (1980).
118. S.Eisener, N.F.Wisdom, Plating, 58, 993, (1971).
119. S.Eisener, N.F.Wisdom, Plating, 58, 1,099, (1971).
120. S.Eisener, N.F.Wisdom, Plating, 58, 1,183, (1971).
121. M.Kawasaki, S.Mizumoto, J.Met.Fin.Soc., Japan, 21, 119, (1970).
122. Nippon Steel, Japan, Metall., 35, 914, (1981).
123. Electroplating Engineers of Japan, DOS 2620995 (75).
124. H.Do Duc, J.App.Electrochem., 10, 385, (1980).
125. R.J.U.Gutfield, C.C.Puippe, Oberfläche-Surf., 22, 294, (1981).
126. A.Tvarusko, Plating, 60, 354, (1973).
127. J.H.Conolly, R.Rimback, Trans.Electrochem.Soc., 84, 293, (1943).
128. A.E.Carlson, Proc.Amer.Electroplating Soc., 42, 43, (1955).
129. E.J.Smith, Plating, 60, 311, (1973).
130. T.Inagaki, Plating Surf:Fin., 67, 51, (1980).
131. Trefietaux (France), UK Pat.Appl., 2,000, 522, (1977).
132. Sankuesto KK, Jap.Pat., 53, 119, 227 (1977).
133. H.Benninghoff, A.Augustini, Drahtwelt, 66, 348, (1980).
134. A.Krepler, 4th Symp.on Electroplating, 323, (1973).
135. R.Mills, C.J.Thwaites, Sheet Metal Industries, 31, 733, (1954).
136. R.S.R.Goria, J.Electrochem.Soc., 125, 865, (1978).
137. A.Tvarusko, J.Electrochem.Soc., 120, 87, (1973).
138. L.W.Oholm, Chem.Abs. 31, 2,904, (1937).
139. Product Finishing, June 1984, p.29.
140. P.K.Subramonyan, W.M.King, Plating Surf.Fin., 69, 49, (1982).
141. M.Jacob, D.Maestri, Interfinish 8, Basle, Switzerland, (1972),
Paper A18.

142. Agence Nationale de Valorisation de la Recherche (ANVAC), Fr. Pat. 2, 140, 310, (1971).
143. D.T.Chin, Plating Surf.Fin., 64, 57, (1977).
144. J.P.Hoare, M.A. La Boda, A.H.Holden, Plating Surf.Fin., 69, 64, (1982).
145. M.A.La Boda, Surf.Tech., 11, 91, (1980).
146. M.A.La Boda, U.S.Pat., 4, 111, 761, (1978).
147. G.H.Poll, Product Finishing, 66, No.11, (1964).
148. R.D.Naybour, J.Electrochem.Soc., 116, 520, (1969).
149. J.M.Coulson, J.F.Richardson, 'Chemical Engineering', Pergamon, Vol.1 (1977), Vol.6 (1983).
150. D.J.Pickett, 'Electrochemical Reactor Design', Elsevier Scientific, (1977).
151. J.S.Newman, 'Electrochemical Systems', Prentice-Hall, (1973).
152. W.M.Rohsenow, H.Choi, 'Heat, Mass and Momentum Transfer', Prentice-Hall, (1961).
153. R.B.Bird, W.E.Stewart, E.N.Lightfoot, 'Transport Phenomena', John Wiley and Sons, (1960).
154. B.S.Massey, 'Mechanics of fluids,' Van Nostrand Reinhold (1984).
H.R.Valentine, 'Applied Hydrodynamics,' Butterworths, (1969).
A.J.Reynolds, 'Turbulent Flows in Engineering,' John Wiley and Sons (1974).
155. W.Nernst, E.S.Merriam, Z.Phys.Chem, 53, 235, (1905).
156. V.G.Levich, 'Physiochemical Hydrodynamics', Prentice-Hall, (1963).
157. H.Blasius, Forsch Ver deut Ing, 131, 1, (1913).
158. L.Prandtl, Z Ver deut Ing, 77, 105, (1933).
159. J.Nikuradse, Forsch Ver dent Ing, 356, (1932), 361 (1933).
160. E.R.Corino, R.S.Brookey, J.Fluid Mech.37, 1, (1969).
161. H.Schlichting, 'Boundary Layer Theory' McGraw-Hill, (1968).
162. M.A.Lévêque, Ann.Mines, Ser.12, 13, 201, 305, 331, (1928).
163. K.L.Ong, Hydrodynamic and Mass Transfer entrance effects on the performance of parallel plate electrochemical flow cells, Ph.D thesis, Univ.of Manchester, (1972).

164. L.Rousor, J.Hatomsky, V.Cezner, B.Stverak, J.Electrochem. Soc., 118, 881, (1971).
165. D.J.Pickett, B.R.Stanmore, J.Appl.Electrochem., 2, 151, (1972).
166. D.J.Pickett, K.L.Ong, Electrochim.Acta, 19, 875, (1974).
167. L.S.Lin, R.W.Moulton, G.L.Putnam, Ind.Eng.Chem., 45, 636, (1953).
168. R.G.Deissler, NACA TN 3145, Washington, D.C., (1954).
169. R.G.Deissler, NACA Report 1210, Washington, D.C., (1955).
170. T.H.Chilton, A.P.Colburn, Ind.Eng.Chem., 26, 1183, (1934).
171. F.W.Dittus, L.M.K.Boelter, Univ.of California, Publ.Eng.2, 443, (1930).
172. E.R.G.Eckert, R.M.Drake, 'Heat and Mass Transfer,' McGraw-Hill, (1959).
173. N.Ibl, Chemie.Eng.Techn. 43, 202, (1971).
174. International Critical Tables, 3, 272, (1929).
175. H.Vogt, Electrochim.Acta, 25, 527, (1980).
176. J.P.Glas, J.W.Weswater, Int.J.Heat and Mass Transfer, 7, 1, 427, (1964).
177. M.S.E.Abdo, T.Z.Fahidy, J.Electroanal Chem., 123, 163, (1981).
178. T.Z.Fahidy, M.S.E.Abdo, Electrochim.Acta, 27, 1521, (1982).
179. L.E.Scriven, Chem.Eng.Sci, 10, 1, (1959).
180. B.Kabonov, A.Frumkin, Z.Physik.Chem. A165, 433, (1933).
A166, 316, (1933).
181. W.Fritz, Physik.Z., 36, 379, (1935).
182. Stanizewski, Techn.Rep.No.16, M.I.T. (1970).
183. D.Landholt, R.Acosta, R.H.Muller, C.W.Tobias, J.Electrochem.Soc., 117, 839, (1970).
184. A.Coehn, Z.Electrochem., 29, 306, (1923).
185. R.Mazza, P.Pedefferri, R.Piontelli, A.Tongnoni, Electrochim. Metallorium, 2, 385, 257, (1967).
186. C.W.M.P.Sillen, Commission for European Communities Rept., Eur.6085, 337, (1978).
187. A.T.Kuhn, M.Stevenson, Electrochim.Acta, 27, 329, (1982).

188. L.J.J.Janssen, J.G.Hoogland, *Electrochim.Acta*, 27, 329, (1982).
189. I.Řoušar, J.Kacin, E.Lippert, F.Smirous, V.Cezner, *Electrochim. Acta*, 20, 295, (1975).
190. R.P.Loomba, Ph.D. thesis, UMIST, (1973).
191. F.H.H.Valentin, 'Absorption in gas liquid dispersions,' E.F.N.Spon Ltd. (London), (1967).
192. L.S.Tong, 'Boiling Heat Transfer and Two Phase Flow,' p.138, John Wiley and Sons, (1965).
193. C.I.Elsner, S.L.Machiano, *J.App.Electrochem.*, 12, 735, (1982).
194. J.Venczel, Dissertation, ETH, Zürich, No.3019, (1961).
195. L.J.J.Janssen, J.G.Hoogland, *Electrochim.Acta*, 15, 1,013, (1970).
196. L.J.J.Janssen, *Electrochim.Acta*, 23, 81, (1978).
197. L.J.J.Janssen, E.Barendrecht, *Electrochim.Acta*, 24, 693, (1979).
198. B.Roald, W.Beck, *J.Electrochem.Soc.*, 98, 277, (1951).
199. M.Green, P.H.Robinson, *J.Electrochem.Soc.*, 106, 253, (1959).
200. M.G.Fouad, G.H.Sedahmed, *Electrochim.Acta*, 18, 55, (1973).
201. M.G.Fouad, G.H.Sedahmed, H.A.El-Abd, *Electrochim.Acta*, 18, 279, (1973).
202. G.H.Sedahmed, *J.App.Electrochem.*, 9, 37, (1979).
203. M.G.Fouad, G.H.Sedahmed, *Electrochim.Acta*, 20, 615, (1975).
204. S.Mohanta, T.Z.Fahidy, *J.App.Electrochem.*, 7, 235, (1977).
205. G.H.Sedahmed, *J.App.Electrochem.*, 10, 351, (1980).
206. G.H.Sedahmed, I.A.S.Mansour, A.A.Zatout, N.A.Abdel-Hay, *J.App.Electrochem.*, 10, 543, (1980).
207. T.R.Beck, *J.Electrochem.Soc.*, 116, 1,038, (1969).
208. L.J.J.Janssen, J.G.Hoogland, *Electrochim.Acta*, 18, 543, (1973).
209. N.Ibl, *Chemie.Ing.Tech.*, 35, 353, (1963).
210. I.Řoušar, V.Cezner, *Electrochim.Acta*, 20, 289, (1975).
211. K.Stephan, H.Vogt, *Electrochim.Acta*, 24, 11, (1979).
212. K.Stephan, *Chemie.Ing.Tech.*, 35, 775, (1963).

213. H.Vogt, Surf.Tech. 17, 301, (1982).
214. G.H.Sedahmed, Y.A.El-Towed, O.A.Hassan, Surf.Tech. 14, 109, (1981).
215. M.D.Birkett, A.Kuhn, Electrochim.Acta, 22, 1,427, (1977).
216. F.Z.Fahidy, J.App.Electrochem., 9, 101, (1979).
217. H.Vogt, Electrochim.Acta, 23, 203, (1978).
218. W.M.Rohsenow, 'Developments in Heat Transfer', M.I.T.Press, Cambridge, Mass., (1964).
219. S.S.Kutateladze, Int.J.Heat and Mass Trans., 4, 31, (1961).
220. J.K.Dennis, T.E.Such, 'Nickel and Chromium Plating', Newnes-Butterworths, (1972).
221. R.Brugger, 'Nickel Plating', Draper, (1970).
222. A.K.Graham, 'The Electroplating Engineering Handbook', Reinhold, (1955).
223. F.A.Lowenheim, 'Modern Electroplating', Wiley, (1974).
224. The Canning Handbook, Canning, (1982).
225. V.I.Lainer, 'Modern Electroplating', I.P.S.T.Cat.No.5512, (1970).
226. P.Spiro, 'Electroforming,' Robert Draper Ltd., (1971).
227. O.P.Watts, Trans.Am.Electrochem.Soc. 59, 379, (1931).
228. J.W.Carey, W.A.Carey, Trans.Electrochem.Soc., 75, 209, (1939).
229. E.J.Roehl, A.J.Wesley, Trans.Electrochem.Soc., 82, 37, (1942).
230. L.Cambi, R.Piontelli, Rend.Inst.Lombardo Sci., 72, 128, (1938).
231. R.A.F.Hammond, Metal Fin.J., Pt.I, June 1970, p.169.
Pt.II, July 1970, p.205.
Pt.III, Aug.1970, p.234.
Pt.IV, Sept.1970, p.276.
Pt.V, Sept.1970, p.279.
232. R.C.Barrett, Plating, 41, 1,027, (1954).
233. M.B.Diggin, Metal Progress, 66, 132, (1954).
234. M.B.Diggin, Trans. I.M.F., 31, 243, (1954).

235. L.B.Bicelli, G.Serraville, *Metal Ital.*, 52, 703, (1960).
236. L.P.Bicelli, G.Serraville, *Metal Ital.*, 55, 165, (1963).
237. T.L.Rama Char, *Electroplating*, 11, 343, (1958).
238. S.Sathyanarayana, T.L.Rama Char, 16A, 78, (1957).
239. D.A.Fanner, R.A.F.Hammond, *Trans.I.M.F.*, 36, 32, (1959).
240. F.Foerster, F.Krueger, *Z.Electrochem.*, 33, 418, (1927).
241. R.C.V.Piatti, A.J.Arvia, J.J.Podesta, *Electrochim.Acta*, 14, 541, (1969).
242. A.T.Vagramyan, L.A.Uvarov, *Zv. Akad.Nauk SSSR*, 9, 1,520, (1962).
243. A.T.Vagramyan, L.A.Uvarov, *Dokl.Akad.Nauk SSR*, 146, 635, (1962).
244. A.T.Vagramyan, M.A.Zhamagortsyan, L.A.Uvarov, A.A.Yavich, *Zashch.Metal*, 5, 74, (1969).
245. A.T.Vagramyan, M.A.Zhamagortsyan, L.A.Uvarov, A.A.Yavich, *Elektrokhimiya*, 6, 733, (1970), *Ibid* 6, 755, (1970).
246. *Encyclopedia of the Electrochemistry of the Elements*, Ed.A.J.Bard, Vol.III, p.212-399, Marcel-Dekker (N.Y.), (1975).
247. O.O.Schaus, R.J.Gale, W.H.Gauvin, *Plating*, Aug, 801, (1971).
248. R.Piontelli, G.Serrovile, *Trans.I.M.F.*, 34, 293, (1957).
249. M.L.Kronenberg, J.L.Banter, E.Yeager, F.Hovorka, *J.Electrochem. Soc.*, 110, 1,007, (1963).
250. J.Yeager, J.P.Cels, E.Yeager, F.Hovorka, *J.Electrochem.Soc.*, 106, 328, (1959).
251. K.E.Heusler, L.Gaiser, *Electrochim.Acta*, 13, 59, (1968).
252. J.Matulis, R.Slízys, *Electrochim.Acta*, 9, 1,117, (1964).
253. I.Epelboin, R.Wiart, *J.Electrochem.Soc.*, 118, 1,577, (1971).
254. I.Epelboin, M.Jousselin, R.Wiart, *J.Electroanal.Chem.*, 119, 61, (1981).
255. F.Ovari, A.L.Rotinyan, *Elektrokhimiya*, 6, 755, (1970).
256. F.Ovari, A.L.Rotinyan, *Elektrokhimiya*, 6, 516, (1970).
257. K.Higashi, H.Fukushima, *J.Jap.Inst.Metals*, 40, 765, (1975).

258. W.A.Wesley, *J.Electrochem.Soc.*, 103, 296, (1956).
259. G.A.DiBari, J.V.Petrocelli, *J.Electrochem.Soc.*, 112, 99, (1965).
260. R.Parsons, *Handbook of Electrochemical Constants*, Butterworths, (1959).
261. O.O.Schaus, R.J.Gale, W.H.Gauvin, *Plating*, Sept.,901, (1971).
262. D.J.MacNaughton, G.E.Gardam, R.A.F.Hammond, *Trans.Faraday Soc.*, 29, 729, (1933).
263. S.Glasstone, 'Introduction to Electrochemistry,' Von Nostrand, (N.Y.), (1942).
264. R.K.Dorsch, *J.Electroanal.Chem.*, 21, 495, (1969).
265. R.P.Slizhis, *Proc.10th Lithuanian Conf.of Electrochemists*, (1968).
266. A.L.Rotinyan, T.M.Ovchinnika, M.V.Simonova, V.V.S.Y.Soeva, *7th Phys.Chem.*, 38, 1,614, (1964).
267. J.J.Lurge, *Handbook of Analytical Chemistry*, p.191, Gaskhimizdat, Moscow, (1962).
268. B.V.Tilak, A.S.Gendron, M.A.Mosoiu, *J.App.Electrochem.*, 7, 495, (1977).
269. L.B.Harris, *J.Electrochem.Soc.*, 120, 1,034, (1973).
270. K.A.Burkov, L.S.Lilic, L.G.Sillen, *Acta Chem.Scand.*, 19, 14, (1965).
271. R.Näsäven, *Acta Chem.Scand.*, 3, 179, (1949).
272. N.Sato, G.Okamoto, *J.Electrochem.Soc.*, 111, 897, (1964).
273. J.O'M. Bockris, A.K.N.Reddy, B.Rad, *J.Electrochem.Soc.*, 113, 1,133, (1966).
274. U.Ebersbach, K.Schwabe, K.Ritter, *Electrochim Acta*, 12, 927, (1967).
275. U.Ebersbach, K.Schwabe, P.Koenig, *Electrochim.Acta*, 14, 773, (1969).
276. G.Truempler, R.Keller, *Helv.Chim.Acta*, 44, 1,691, (1961).
277. T.S.DeGromoboy, L.L.Shrier, *Electrochim.Acta*, 11, 895, (1966).
278. B.B.Knapp, F.X.Carlin, *INCO Electroforming Seminar*, New York, (1964).
279. J.Krupski, H.G.Feller, *Z.Metalkde*, 65, 401, (1974).

280. B.MacDougall, M.Cohen, *J.Electrochem.Soc.*, 122, 283, (1975).
281. W.Sellers, F.X.Carlin, *Plating*, 52, 215, (1965).
282. A.N.Chatterjee, S.K.Ray, *Electroplating Met.Fin.*, Aug., 244, (1967).
283. G.Prassler, *Neue Hutte*, 19, 392, (1974).
284. W.A.Wesley, *Trans.I.M.F.*, 33, 452, (1950).
285. S.A.Watson, *Met.Fin.J.*, 18, 18, (1972).
286. S.A.Watson, *Met.Fin.J.*, 18, 36, (1972).
287. N.Pangarov, *Electrochim.Acta*, 7, 139, (1962).
288. N.Pangarov, *Electrochim.Acta*, 9, 721, (1964).
289. N.Pangarov, *J.Electroanal.Chem.*, 9, 70, (1965).
290. A.K.N.Reddy, S.R.Rajogopalan, *J.Electroanal.Chem.*, 6, 141, 153, 159, (1963).
291. H.Wilman, *Trans.I.M.F.*, 32, 281, (1955).
292. H.Fischer, *Electrodep.Surf.Treat*, 1, 239, (1973).
293. H.Fischer, *Electrodep.Surf.Treat.*, 1, 319, (1973).
294. J.Amblard, M.Froment, *Faraday Symp.of the Chem.Soc.*, No.12, (1977).
295. J.Amblard, M.Froment, N.Spyrellis, *Surf.Tech.*, 5, 205, (1977).
296. J.Amblard, I.Epelboin, M.Froment, G.Maurin, *J.App.Electrochem.*, 9, 233, (1979).
297. V.Landa, M.Černak, J.Vitek, *Surf.Tech.*, 8, 313, (1979).
298. A.Brenner, V.Zentner, C.W.Jennings, *Plating*, 39, 865, (1952).
299. J.K.Dennis, J.J.Fuggle, *Electroplating Met.Fin.*, 20, 376, (1967), *Ibid.* 21, 16, (1968).
300. J.A.Crossley, P.A.Brook, J.W.Cuthbertson, *Electrochim.Acta*, 11, 1,153, (1966).
301. A.G.Ives, J.W.Edington, G.P.Rothwell, *Electrochim.Acta.*, 15, 1,797, (1970).
302. S.Nakahara, *J.Electrochem.Soc.*, 125, 1,049, (1978).
303. B.C.Banerjee, P.C.Walker, *J.Electrochem.Soc.*, 109, 436, (1962).

304. S.Nakahara, E.C.Felder, *J.Electrochem.Soc.*, 129, 45, (1982).
305. J.P.G.Farr, A.J.S.McNeil, *Faraday Symp.Chem.Soc.*, No.12, (1977).
306. T.P.Hoar, D.J.Arrowsmith, *Trans.I.M.F.*, 36, 1, (1958/59).
307. S.R.Rashikov, N.Pangarov, *Electrochim.Acta*, 14, 17, (1969).
308. V.Velinova, S.Vitkova, N.Pangarov, *Surf.Tech.*, 6, 19, (1977).
309. S.Tajima, M.Ogata, *Electrochim.Acta*, 13, 1,845, (1968).
310. S.Tajima, M.Ogata, *Electrochim.Acta*, 15, 1,559, (1970).
311. J.W.Diggle, *Electrochim.Acta*, 15, 1,559, (1970).
312. B.B.Knapp, *Plating*, Dec., 1,187, (1971).
313. A.C.Hart, W.R.Wearmouth, A.C.Warner, *Trans.I.M.F.*, 54, 56, (1976).
314. R.J.Kendrick, *Trans.I.M.F.*, 42, 235, (1974).
315. O.J.Klingenmaier, *Plating*, 52, 1,138, (1965).
316. R.J.Kendrick, S.A.Watson, *Proc.Symp.on Sulphamic Acid and its Electrometallurgical Applications*, Milan, p.197, (1966).
317. J.L.Marti, *Plating*, 53, 61, (1966).
318. A.F.Greene, *Plating*, 55, 594, (1968).
319. H.I.McCutchen, *U.S.Patent*, 3,374, 154, (1968).
320. R.J.Kendrick, S.A.Watson, *Electrochim.Metallorium*, 1, 320, (1966).
321. G.M.C.Lee, W.J.D.Jones, *Trans.I.M.F.*, 55, 70, (1977).
322. J.L.Marti, G.P.Lanza, *Proc.Symp.on Sulphamic Acid and its Electrometallurgical Applications*, (1966), p.215.
323. S.K.Verma, H.Wilman, *J.Phys.D: Appl.Phys.*, 4, 1,167, (1971).
324. S.K.Verma, H.Wilman, *J.Phys.D : Appl.Phys.*, 4, 2,051, (1971).
325. B.Rivolta, L.P.Bicelli, G.Razzini, *J.Phys.D: Appl.Phys.*, 8, 2,025, (1975).
326. M.Saleem, B.A.Brook, J.W.Cuthbertson, *Electrochim.Acta*, 12, 553, (1967).
327. K.C.Belt, J.A.Crossley, R.J.Kendrick, *Proc.7th Int.Met.Fin. Conf.*, Hanover, (1968), p.222.

328. W.R.Wearmouth, K.C.Belt, *Trans.I.M.F.*, 52, 114, (1974).
329. A.J.Dill, *Plating*, Nov., 1,001, (1974).
330. J.M.Notley, *Trans.I.M.F.*, 52, 78, (1974).
331. M.Ponnuthurai, S.Chakrapani, *Finishing Industries*, 2, 20, (1978).
332. J.W.Dini, H.R.Johnson, *J.Mat.Sci.*, 10, 1,253, (1975),
Ibid, 11, 1,778, (1976).
333. J.R.Weber, *Plating Surf.Fin.*, Aug., 780, (1975).
334. W.Kleinekathöfer, Ch.J.Raub, E.Raub, *Metalloberfloche*,
36, 411, (1982).
335. I.Jenei, B.Lengyel, *Zs. Labor*, 4th Symp.on Electroplating,
(1973), p.341.
336. R.Krishnasway, *Met.Fin.J.*, June, 34 (1975).
337. *Products Finishing (Cincinnati)*, 47, 86, (1982).
338. J.W.Dini, H.R.Johnson, *Surf.Tech.*, 4, 217, (1976).
339. H.Benninghof, *Metalloberfloche*, 36, 561, (1982).
340. Z.V.Semenova, G.A.Sadakov, E.Kh.Burygina, Yu.M.Polukarov,
Elektrokhimiya, 13, 1,547, (1977).
341. G.L.J.Bailey, S.A.Watson, L.Winkler, *Electroplating and Metal
Finishing*, 22ii, 21, (1969).
342. D.J.Robinson, Ph.D.Thesis, Univ.Sheffield, (1970).
343. P.Cavallotti, D.Colombo, *General Discussion of the 12th Faraday
Symposium of the Chemical Society*, (1977), p.197.
344. V.A.Ettel, B.V.Tilak, A.S.Gendron, *J.Electrochem.Soc.*, 121,
867, (1974).
345. 'Handbook of Chemistry and Physics', Chemical Rubber Publishing
Co., (1981).
346. A.I.Vogel, 'Textbook of Quantative Inorganic Analysis',
Longman, (1978).
347. *Electropolishing, 'Anodizing and Electrolytic Pickling of Metals',
N.P.Fedot'ev, S.Ya. Grilikhes, Robert Draper*, (1959).
348. *IL151 Users Manual*, Instrument Laboratories.
G.F.Kirkbright, M.Sargent, 'Atomic Absorption and
Fluorescence Spectroscopy', Academic, (1974).

349. M.F.Fleischmann, A.Saraby-Reintjes, *Electrochem.Acta*, 29, 157, 169, (1984).
A.Saraby-Reintjes, *Electrochim.Acta*, 30, 387, 403, (1985).
350. S.Bretznader, 'Predictions of transport and other physical properties of fluids', Pergamon, (1971).
351. B.Mazza, A.Alberti-Oggioni, *Ric.Sci.Rend.Sez.A.(Milan)*, 8, 1,394, (1965).
352. Perry's Chemical Engineers Handbook, McGraw-Hill (1984).
D.H.Bacon, R.C.Stephens, *Fluid Mechanics for technicians* 3/4, Butterworth, (1982).
353. J.M.Hornut, G.Valentin, A.Storck, *J.App.Electrochem.*, 15, 237, (1985).
F.Lapique, A.Storck, *J.App.Electrochem.*, 15, 925, (1985).
354. E.H.Enberg, *Met.Fin.*, 66, 8, (1968).
355. W.R.Parrish, J.Newman, *J.Electrochem.Soc.*, 117, 43, (1970).
356. W.R.Parrish, J.Newman, *J.Electrochem.Soc.*, 116, 169, (1969).
357. J.O'M.Bockris, A.M.Azzam, *Trans.Farad.Soc.*, 48, 145, (1952).
Idem., Nature, 165, 403, (1950).
J.O'M.Bockris, E.C.Potter, *J.Chem.Phys.*, 20, 614, (1952).
358. C.Gould, unpublished work.

APPENDICES

- Appendix 1. Notation
- Appendix 2. Additional factors relating to cell and flow circuit design
- (a) The effect of B and S on the Reynolds number
 - (b) Calculations of maximum mass transfer coefficients and limiting current densities at 60°C.
 - (c) Pressure losses in flow circuits
 - (d) The characteristics of centrifugal pumps
 - (e) Rotameter selection and calibration
 - (f) Diffusion coefficients in concentrated nickel electrolytes
- Appendix 3. Calculation of microhardness values and optimum indenter load.
- Appendix 4. Additional measurements relating to the electroforming of nickel in Cell 2.
- a) Comparison of momentum and mass transfer in the nickel sulphamate system
 - b) Estimation of the range of pore diameters in nickel foils.

Appendix 1Notation

The notation commonly used in this thesis is as follows:

A	electrode area, cm^2 .	
Ag	area of a gas evolving electrode, cm^2 .	
Am	area of masked electrode, cm^2 .	
As	area of a segment (of a segmented cathode), cm^2 .	
a	Tafel constant ($\eta = a + b \log_{10} i$), V.	
a	adhesion diameter (of a gas bubble), cm.	
B	duct breadth.	
b	Tafel constant ($\eta = a + b \log_{10} i$), V decade ⁻¹ .	
C	concentration at time t.	} Equation (2.99).
Co	original concentration of reactant	
c	concentration (units as specified).	
c_p	skin friction factor.	
c_s	concentration of reactant at electrode surface.	
c_b	concentration of reactant in bulk solution.	
D	diffusion coefficient, $\text{cm}^2 \text{s}^{-1}$	
d	thickness of electrodeposit, μm .	
d	diameter of a pipe.	
d	average diameter, or equivalent breakoff diameter of a gas bubble.	

de	equivalent diameter of a rectangular duct	$= \frac{4BS}{2(B+S)}$	cm.
d _{cr}	critical length of a hydrodynamic system.		
E	electrode potential, V or mV.		
E _c	cathodic potential.		
E _a	anodic potential.		
E _r	reversible electrode potential.		
E _o	standard reversible potential.		
E _{chem}	chemical equivalent.		
E _{electro}	...	electrochemical equivalent	$= \frac{E_{chem}}{F}$, C ⁻¹
E _F	Flade potential.		
F	Faraday constant = 96,494.5 ± 1.5 C.		
F	total friction loss in a flowing system.		
F	force acting on a gas bubble.		
f	Fanning friction factor (=2φ).		
G	Gibbs free energy.		
g	acceleration due to gravity = 981 cm s ⁻² .		
H	height of a gas bubble.		
h _f	head loss due to friction, cm. of fluid.		
I	total current, Amps.		
I _L	total current corrected for 'leakage' current through masked area of cathode.		
I _{xcorr}	total current at distance x from leading edge of cathode.		

i	current density, $A\text{ cm}^{-2}$.
i_{\max}	maximum current density for a sound and coherent electrodeposit, $A\text{ cm}^{-2}$.
i_L	limiting current density.
i_0	exchange current density.
i_{crit}	critical current density for passivation.
i_{pass}	passivation current density.
i_{av}	average current density.
i_x	current density at distance x from leading edge of cathode (local current density).
i_L^{corr}	current density corrected for 'leakage' current through masked area of cathode.
J	mass flux
J_s	mass flux at the wall.
J_D	diffusional component of mass flux.
J_m	migrational component of mass flux.
J_{conv}	convective component of mass flux.
k	mass transfer coefficient, cm s^{-1} .
k_L	mass transfer coefficient, determined at the limiting current density.
k_{av}	average mass transfer coefficient.
k_x	local mass transfer coefficient, at distance x from leading edge of cathode.
k_L^1	macroconvective (flow) mass transfer coefficient.
k_L^2	microconvective (gas) mass transfer coefficient

$k_L^{\text{TOTAL}} = 1,2k_L$	combined (micro-and macro-convective) mass transfer coefficient
L electrode length, cm.
L distance along electrode from cell entrance (Equations (2.68) and (2.69)).
L_e hydrodynamic entrance length, cm.
L pipe length, cm.
N molecular flux.
P pressure (units as specified).
P_L solution pressure.
P_s gas pressure
p component of total pressure
Q volumetric flow rate (units as specified).
Q charge passed (=It), C.
Qg volumetric rate of gas evolution, $\text{cm}^3 \text{s}^{-1}$
R Gas Constant = $8.314 \text{ J } ^\circ\text{C}^{-1} \text{ mol}^{-1}$.
R radius of curvature of a gas bubble.
$R(=-R_0)$... shear stress at pipe wall ($y=0$), dyne cm^{-2}
R_y shear stress at distance y from pipe wall ($=-\eta \frac{du_x}{dy}$)
r radius of a pipe, cm.
r mean bubble radius.
r_h hydraulic radius ($= \frac{de}{4}$), cm.
S duct height, cm.

s	distance from centre line of a pipe, cm.
T	temperature, °C or k.
t	time, s.
$U=U_{av}$	mean flow velocity, cm s^{-1}
U_{cr}	critical velocity of a hydrodynamic system.
U_g^t	terminal velocity of bubble rise.
$u_{x,y \text{ or } z}$...	component of flow velocity.
u_s	velocity at distance s from centre line (of a pipe) or free-stream velocity (flat plate theory).
$u_{C.L.}$	centre-line velocity (of a pipe).
V	volume, cm^3
V	velocity of a rising gas bubble, cm s^{-1}
V_g	molar volume of evolved gas, $\text{cm}^3 \text{mol}^{-1}$
x	distance from leading edge of an electrode or flat plate, cm.
x_{cr}	laminar-turbulent transition distance for flow over a flat plate.
x_0	distance from cell entrance (Equations (2.70) to (2.73)).
y	distance from pipe wall
z	static head, cm of fluid.
z	charge number of ion
z	drag coefficient (Equation (2.84)).

x, y, z	Cartesian coordinates
α	transfer coefficient (of Tafel equation)
γ	surface tension, dyne cm^{-2}
δ	thickness of the diffusion layer or hydrodynamic boundary layer.
δ_N	Nernst diffusion layer
δ_t	thickness of turbulent boundary layer
δ_b	thickness of laminar sub-layer.
ϵ	eddy kinematic viscosity
ϵ_D	eddy diffusivity
η	overpotential, V or mV.
η	dynamic viscosity, $\text{g cm}^{-1} \text{s}^{-1}$
η^a	activation overpotential
η^c	concentration overpotential
η^o	ohmic overpotential
Θ	fractional surface area covered by gas bubbles.
Θ	wetting angle, $^\circ$
Λ	equivalent conductivity, $\text{cm}^3 \text{equiv.}^{-1}$
ν	kinematic viscosity, $\text{cm}^2 \text{s}^{-1}$
ρ	fluid density, g cm^{-3}
σ	specific conductivity, $\text{ohms}^{-1} \text{cm}^{-1}$
φ	friction factor ($= R/pU^2$)

- ϕ potential difference, v.
- χ correction factor for parallel plate cell of finite width (Equation (2.51)).
- Ψ total energy per unit mass of fluid moving with velocity, U (Equation (2.16)).
- Ψ aspect ratio ($=\frac{S}{13}$).

Dimensionless numbers

- Re Reynolds Number - dimensionless flow rate ($=\frac{U_{cr}d_{cr}}{v} = \frac{Ude}{v}$)
- Re_g gas Reynolds Number ($=\frac{Q_g d}{Av}$)
- Sh Sherwood Number - dimensionless mass transfer coefficient
($=\frac{k_L de}{D}$)
- Sh_{av} average Sherwood Number for electrode.
- Sh_x local Sherwood Number at distance x from leading edge of electrode.
- Sh_L Sherwood Number based on the distance, L, from cell entrance, i.e.:
 $Sh_L = \frac{k_L L}{D}$ (Equation (2.68)).
- Sh_g microconvective (gas) Sherwood Number ($=\frac{k_L^1 d}{D}$)
- Sc Schmidt Number ($=\frac{v}{p}$)
- j-factor... dimensionless mass transfer coefficient. ($=Sh Sc^{-\frac{1}{3}} Re^{-1}$)
- de/L or L/de... dimensionless electrode length.
- x/L dimensionless distance along electrode.
- Le/de dimensionless hydrodynamic entrance length.

i_x/i_{av} ... dimensionless local current density

f, φ friction factor ($\varphi = \frac{f}{2} = \frac{R}{\rho u^2}$)

Ψ aspect ratio ($= \frac{S}{B}$).

Appendix 2 Additional factors relating to cell and flow circuit design.a) Effect of B and S on the Reynolds number

The cell geometry was examined with the objective of achieving Reynolds numbers of about Re 14,000. To comply with the boundary conditions for mass transfer to short electrodes in turbulent flow (i.e. $L/d_e \leq 7.5$) the equivalent diameter must have a minimum value of about 0.7cm for an electrode length of 5cm. (see p.112).

For an electrolyte of kinematic viscosity $1 \times 10^{-2} \text{ cm}^2 \text{ s}^{-1}$, the maximum flow velocity (U_{max}) required for $d_e = 0.7$ is

$$U_{\text{max}} = \frac{Re \nu}{d_e} = \frac{14,000 \times 10^{-2}}{0.7} \\ \sim 200 \text{ cm s}^{-1}$$

and the cross sectional area of the cell (BS) necessary to give a flow velocity of 200 cm s^{-1} for a volumetric flow rate of 20 l min^{-1} (p.112) is given by

$$BS = \frac{1000 Q}{U \cdot 60} = \frac{1000 \times 20}{200 \times 60} \\ \sim 1.7 \text{ cm}^2$$

Therefore to achieve Re 14,000 with $d_e 0.7$ would require a duct of very small dimensions. Larger values of B and S would be more convenient and also increase the equivalent diameter of the cell.

b) Calculation of maximum mass transfer coefficients and limiting current densities at 60°C.Cell 1

Using values of the physical properties of the electrolyte summarised in Table A1, the values of Re, Sh, K_L and i_L for a maximum volumetric flow rate of 20 l min^{-1} were calculated as follows:

$$\text{The maximum flow velocity } U_{\text{max}} = \frac{Q \cdot 1000}{60 BS} \\ = \frac{20 \times 1000}{60 \times 3 \times 1} \sim 111 \text{ cm s}^{-1}$$

$$\text{Therefore } Re_{\text{max}} = \frac{U_{\text{max}} d_e}{\nu} = \frac{111 \times 1.5}{1.202 \times 10^{-2}} \sim 13,866$$

Since the turbulent flow, range commences at about Re 2,500, this gave a useful range of operation as far as Reynolds numbers were concerned.

Information relating to the diffusion coefficients of nickel sulphamate electrolytes was not readily available from the literature. It was therefore necessary to estimate values of the diffusion coefficient for use in further calculations. The factors affecting and the methods of estimating the diffusion coefficients are described in Appendix 2f. The estimated values of D are also shown in Table A1.

$$\text{Since } Sc = \frac{v}{D} = \frac{1.202 \times 10^{-2}}{0.64 \times 10^{-5}} \sim 1,878$$

$$\text{and } \frac{d_e}{L} = \frac{1.5}{5} \sim 0.3$$

It follows therefore that

$$Sh_{av} = 0.145 Re^{\frac{2}{3}} Sc^{\frac{1}{3}} \frac{d_e}{L}^{\frac{1}{4}} \dots \dots \dots (2.67)$$

$$= 0.145 \times (13,866)^{\frac{2}{3}} \times (1,878)^{\frac{1}{3}} \times (0.3)^{\frac{1}{4}}$$

$$\sim 764$$

Also since

$$Sh_{av} = \frac{k_L d_e}{D} \quad \text{and} \quad k_L = \frac{Sh_{av} D}{d_e} = \frac{i_L^0}{zFc_b}$$

$$\therefore k_L = \frac{764 \times 6.64 \times 10^{-5}}{1.5} \sim 3.3 \times 10^{-3} \text{ cm s}^{-1}$$

$$\text{and } i_L^0 = k_L zF c_b$$

$$\therefore i_L^0 = 3.3 \times 10^{-3} \times 2 \times 96,000 \times 1.89 \times 10^{-3} = \underline{\underline{1.19 \text{ A cm}^{-2}}}$$

This represents the contribution to the limiting current density from diffusion and convection. However, in a concentrated nickel sulphamate electrolyte containing a low concentration of supporting electrolyte, the migration current will contribute significantly to the overall limiting current density (p.17). The migration current contribution

(i_L/i_{L0}) may be estimated from the equation of Storck et al (35.3)

$$i_L/i_{L0} = 1 - \frac{z_a}{z_1 + 2r z_2} \left\{ 1 + 2r - (2r)^{-z_1/z_2 - z_1} \left[-\frac{z_2}{z_1}^{-z_1/z_2 - z_1} + \frac{z_2}{z_1}^{-z_2/(z_2 - z_1)} \right] \right\} \quad \dots(A1)$$

where

$$r = \frac{C_{H^+}}{C_{(SO_3NH_2)^-}}$$

$$= \frac{1 \times 10^{-4}}{3.76} = \underline{2.6 \times 10^{-5}}$$

and

$$z_a = \text{Charge number of } Ni^{2+} \text{ ion} = +2$$

$$z_1 = \text{Charge number of } (SO_3NH_2)^- \text{ ion} = -1$$

$$z_2 = \text{Charge number of } H^+ \text{ ion} = +1$$

then

$$\frac{i_L}{i_{L0}} = 1 - \frac{2}{(-1) + (2 \times 2.6 \times 10^{-5} \times 1)} \left[\frac{1 + (2 \times 2.6 \times 10^{-5}) - (2 \times 2.6 \times 10^{-5})^{-(-1)/[1 - (-1)]}}{\left(-\frac{1}{(-1)}^{-(-1)/(1 - [-1])} + \frac{-1}{(-1)}^{-(-1)/1 - (-1)} \right)} \right]$$

$$\frac{i_L}{i_{L0}} = \underline{2.98} \approx 3$$

The maximum possible limiting current density (i_L) is given by:

$$i_L = i_{L0} \times 3$$

and

$$i_L = 1.19 \times 3$$

$$\approx \underline{3.6 \text{ A cm}^{-2}}$$

Similar calculations may be carried for the laminar flow regime using the equation:

$$Sh_{av} = 1.85 \left[Re Sc \frac{d_e}{L} \right]^{\frac{1}{3}} \dots \dots (2.49)$$

The selected design would give a satisfactory initial operating range and allow some correlation between mass transfer data and deposit growth morphology.

Cell 2

The mass transfer analysis was similar to that used for Cell 1 (p.2-1). The physical properties of the electrolyte were obtained from Table . For a maximum flow rate of 3.5 lmin⁻¹, the flow velocity (U_{max}) is,

$$U_{max} = \frac{Q1000}{60BS} = \frac{35 \times 1,000}{60 \times 1 \times 3} \sim 194 \text{ cm s}^{-1}$$

Therefore $Re_{max} = \frac{U_{max} d_e}{\nu} = \frac{194 \times 0.857}{1.202 \times 10^{-2}} \sim 13,832$

and $Sc (= \frac{\nu}{D}) \sim 1,878$

The values of Sh, k_L and i_L were obtained as follows:

Turbulent flow - $\frac{L}{d_e} \sim 2.92$

The relevant design equation is

$$Sh_{av} = 0.145 Re^{\frac{2}{3}} Sc^{\frac{1}{3}} \left(\frac{d_e}{L} \right)^{\frac{1}{4}} \dots \dots (2.67)$$

and substitution of the relevant numerical values gives

$$Sh_{av} = 0.145 (13,832)^{\frac{2}{3}} (1,878)^{\frac{1}{3}} (0.34)^{\frac{1}{4}} \sim 789$$

also

$$k_L = \frac{Sh_{av} D}{d_e} = \frac{789 \times 0.64 \times 10^{-5}}{0.857} \sim 5.9 \times 10^{-3} \text{ cm s}^{-1}$$

and

$$i_{L0} = k_L z F c_b = 5.9 \times 10^{-3} \times 2 \times 96,500 \times 1.89 \times 10^{-3}$$

$$i_{L0} \sim \underline{2.15 \text{ A cm}^{-2}}$$

and the contribution from the migration current was previously calculated from Equation (A1)

$$i_L / i_{L0} = 3$$

then

$$i_L = 3 \times 2.15$$

$$\approx \underline{6.5 \text{ A cm}^{-2}}$$

Turbulent flow - $L/d_e \sim 11.7$

The relevant design equation is:

$$Sh_{av} = 0.023 Re^{0.8} Sc^{0.33} \dots \dots (2.65)$$

and substitution of the appropriate numerical values gives

$$Sh_{av} = 0.023 (13,832)^{0.8} (1,878)^{0.33}$$

$$\sim 583$$

and

$$k_L = \frac{583 \times 0.64 \times 10^{-5}}{0.857} \sim 4.4 \times 10^{-3} \text{ cm s}^{-1}$$

therefore

$$i_{L0} = 4.4 \times 10^{-3} \times 2 \times 96,500 \times 1.89 \times 10^{-3}$$

$$= 1.59 \text{ A cm}^{-2}$$

and

$$i_L = 1.59 \times 3$$

$$\approx \underline{4.8 \text{ A cm}^{-2}}$$

Similar calculations were carried out for the laminar flow regime using the equation

$$Sh_{av} = 1.85 \left[Re Sc \frac{d_e}{L} \right]^{0.33} \dots \dots (2.49)$$

	50°C	60°C	70°C
Dynamic viscosity η , g cm ⁻¹ s ⁻¹	2.042x10 ⁻²	1.640x10 ⁻²	1.403x10 ⁻²
Density ρ , g cm ⁻³	1.369	1.364	1.356
Kinematic viscosity $\nu = \frac{\eta}{\rho}$, cm ² s ⁻¹	1.492x10 ⁻²	1.202x10 ⁻²	1.035x10 ⁻²
Diffusion coefficient D, cm ² s ⁻¹ (estimated)	0.54x10 ⁻⁵	0.64x10 ⁻⁵	0.83x10 ⁻⁵
Schmidt No. $Sc = \frac{\nu}{D}$	2,753	1,878	1,247
Bulk concentration of nickel ions c_b , mol cm ⁻³	~ 1.89		

Table A1 Physical property data for the concentrated nickel sulphamate electrolyte at 50, 60 and 70°C (see also Section 3.1).

It was evident that higher current densities, for a given Reynolds number, were possible using the 'short' electrodes. According to this analysis, a different Reynolds number dependency would be expected for 'long' and 'short' electrodes and the mass transfer rate would be independent of electrode length for 'long' electrodes. Significantly greater rates of mass transfer were possible with the Cell 2 geometry compared to Cell 1.

c) Calculation of the pressure loss in the flow circuit

The line pressure-drop was determined using the modified version of the Bernoulli equations (p.42)

$$\frac{\Delta U^2}{2} + \frac{1}{\rho} (P_2 - P_1) + g \Delta z + \frac{F}{\rho} = 0 \dots (2.18)$$

or in terms of head of fluid

$$\frac{1}{\rho g} (P_2 - P_1) = \frac{\Delta U^2}{2g} + \Delta z + \frac{F}{g}$$

and the total head of fluid (differential pressure) was given by

ΔP discharge - ΔP suction. This method of calculation assumes the flow to be turbulent.

The line losses were calculated for the flow circuit of Fig.3.22 and for a maximum flow rate (Q) of 35 dm³ min⁻¹. The total loss of head (suction) was calculated as follows:

Size of pipe = 4 cm

Line length = 30 cm.

$$\begin{aligned} \text{Maximum velocity } u &= \frac{1000 Q}{60 \pi \left(\frac{d}{2}\right)^2} = \frac{1000 \times 35}{60 \pi \left(\frac{4}{2}\right)^2} \\ &= 46 \text{ cm s}^{-1} \end{aligned}$$

$$\begin{aligned} \text{Maximum Reynolds number } Re &= \frac{ud}{\nu} \dots (2.12) \\ &= \frac{46 \times 4}{1.202 \times 10^{-4}} \\ &= 15,307 \end{aligned}$$

Assuming the pipes are 'smooth', the friction factor may be calculated from the Blasius equation, $\phi = \frac{f}{2} = 0.0396 \text{ Re}^{-0.25}$ (2.24)

$$\text{and } f = 0.079 \text{ Re}^{-0.25}$$

$$\therefore f = 0.079 \times 15,307^{-0.25} = 0.0071$$

and the line loss may be obtained from

$$h_f = 4f \frac{L}{d} \frac{U^2}{2g} \quad \dots \dots (2.26)$$

or the number of velocity heads ($= \frac{U^2}{2g}$) lost = $4f \frac{L}{d}$

$$= 4 \times 0.0071 \times \frac{30}{4}$$

$$= \underline{0.23} \text{ velocity heads}$$

An additional frictional loss will occur across fittings such as bends, valves, etc. Typical pressure losses are given in the literature (352) for various common fittings. The pressure losses are conventionally stated in terms of the number (K) of velocity heads lost as fluid flows through the fitting, viz:

$$K = \frac{\Delta h_f}{\frac{U^2}{2g}}$$

where Δh_f is the additional frictional loss for a centre line length of straight pipe.

Hence for the 4 cm pipe (suction side)

$$1 \times \text{diaphragm valve} = K = 2.3$$

$$2 \times \text{unions} = 2 \times K = 2 \times 0.04 = 0.08$$

$$\therefore \text{total additional loss} = \underline{2.38} \text{ velocity heads.}$$

A further loss of head occurs on entry of the fluid from the reservoir into the pipe (a contraction). A typical head loss for a contraction is about $h_c = 0.5 \frac{U^2}{2g}$ (352) or half a velocity head.

(It should be noted that a loss of head will also occur when the section of a pipe is suddenly enlarged. In this case the head loss (h_e) may be found from

$$h_e = 1 - \frac{A_1}{A_2} \frac{U^2}{2g}$$

where A_1 and A_2 are the areas of the pipe upstream and downstream of the

enlargement respectively. At the exit of a pipe into the reservoir, A_2 is infinite so the loss is $u^2/2g$, i.e. all the kinetic energy at exit is wasted).

Therefore the total head loss for the 4 cm line (suction) is:

$$\text{line loss} = 0.23$$

$$\text{additional loss} = 2.38$$

$$\text{entry loss} = \underline{0.5}$$

$$\text{of fluid} = 3.11 \frac{u^2}{2g}$$

$$= 3.11 \times \frac{46^2}{2 \times 981}$$

$$= \underline{3.35 \text{ cm of fluid.}}$$

A similar set of calculations were carried out for the 2 cm pipe on the suction side, to give a total head loss of 4.15 velocity heads = 78.2 cm of fluid.

The static head (suction), z_1 is the height of the surface of the electrolyte in the reservoir above the pump = 186 cm of fluid.

The overall suction head is given by $z_1 - 78.2 - 3.35 = 104.6$ cm of fluid.

A similar set of calculations were carried out for the discharge side and these are shown on the Pump and Line Calculation Sheet (Table A2). Additional head losses for the filter and Rotameter were included. The static head (discharge), z_2 , was taken as the height of the surface of the electrolyte in the reservoir above the pump and the total discharge head was given by the sum of all the contributions to the total head (i.e. $z_2 + \text{line loss} + \text{additional loss} + \text{equipment}$). (The differential head = discharge head - suction head, and the differential pressure = differential head $\times \rho \times g$).

As may be seen from Table A2, the maximum differential pressure was calculated to be 7.6 kPa (~11 psi).

In practice the differential head may be two or three times greater than this figure due to the complexity of the system. Therefore in

Fluid		600g l ⁻¹ Nickel sulphamate soln.			DISCHARGE					CALCULATION				
Temperature °C	60	Line size cm		Item	Head loss for max. flow	Units	Line size cm		Item	Head loss for max. flow	Units			
ρ Density g cm ⁻³	1.364			Velocity	186	cm s ⁻¹			velocity	194	cm s ⁻¹			
ν Kinematic viscosity cm ² s ⁻¹	1.202 x 10 ⁻²			Re	30,948	-			Re	13,832	-			
Maximum volumetric flow rate cm ³ s ⁻¹	583 (35 l min ⁻¹)			f	0.006	-			f	0.0073	-			
				L	143	cm			L	110.5	cm			
				4f L/d	3.70	velocity heads			4f L/d	3.76	velocity heads			
SUCTION CALCULATION														
Line size cm		Item	Head loss for max. flow	Units										
4 cm (round glass pipe)	u	Velocity	46	cm s ⁻¹	2 cm (round polyprop. pipe)	u	Velocity	186	cm s ⁻¹	0.837 cm (rectangular section parallel plate cell, d _h)	u	velocity	194	cm s ⁻¹
	Re		13,307	-		Re		30,948	-		Re		13,832	-
	f		0.0071	-		f		0.006	-		f		0.0073	-
	L	line length	30	cm		L	line length	143	cm		L	line length	110.5	cm
	4f L/d	line loss	0.23	velocity heads		4f L/d	line loss	3.70	velocity heads		4f L/d	line loss	3.76	velocity heads
		fittings					fittings					fittings		
	K	a) diaphragm valve	2.3	" "		K	a) 4 x unions	0.16			K	a) 2 x square bends	2.6	
	K	b) 2 x unions	0.08	" "		K	b) 1 x 90° sq. bend	1.3				additional loss expansion	2.6	velocity heads
		additional loss	2.38	velocity heads			additional loss	1.46	velocity heads			(10) sub-total	7.14	velocity heads
		entrance loss	0.5	" "			contraction expansion	0.5				(11) total head	137	cm
	(1) sub total	3.11	velocity heads		(6) sub total	3.79	velocity heads		(10) x u ² /2g	(11) total head	137	cm		
	(2) total head	3.35	cm		(7) total head	66.8	cm							
2 cm (round polyprop. pipe)	u	velocity	186	cm s ⁻¹	2.5 cm (round glass pipe)	u	velocity	119	cm s ⁻¹	4 cm	u	velocity	46	cm s ⁻¹
	Re		30,948	-		Re		24,750	-		Re		13,307	-
	f		0.006	-		f		0.0063	-		f		0.0071	-
	L	line length	140	cm		L	line length	350	cm		L	line length	112	cm
	4f L/d	line loss	1.67	velocity heads		4f L/d	line loss	3.53	velocity heads		4f L/d	line loss	0.80	velocity heads
		fittings					fittings					fittings		
	K	a) 4 x union	0.16	" "		K	a) 18 x unions	0.72			K	a) 2 x 90° bend	1.5	
	K	b) 1 x 90° sq. bend	1.3	" "		K	b) Tee piece	0.4			K	b) 4 x unions	0.16	
		additional loss	1.46	" "			c) diaphragm valve	2.3				additional loss	1.66	velocity heads
		contraction	0.5	" "			d) 90° bend	0.75				(12) sub-total	2.46	velocity heads
	expansion	0.52	" "		e) 90° square bend	1.3			(13) total head	2.7	cm			
	(3) sub total	4.15	velocity heads		additional loss expansion	0.56	velocity heads		equipment (14) a) Filter (15) b) Rotameter	200	cm			
	(4) total head	78.2	cm		contraction	0.5			(7)+(9)+(11)+(13)+(14)+(15)	Dynamic loss	-488	cm		
	static head	186	cm		exit loss	1			z ₂	static head	186	cm		
	z ₁ - (2) - (4)	(5) suction head head	-105.6	cm		(8) sub total	11.06	velocity heads	z ₂ + (16)	discharge head	-674	cm		
						(9) total head	79.8	cm	(5)	suction pressure	-105			
										differential head	-569	cm		
										differential pressure	7.6 x 10 ³	dyne cm ⁻²		
											7.6	kPa		
											11	p.s.i.		

Table A2. Pump and Line Calculation Sheet for Cell 2.

selecting a pump a maximum head of 15 metres (Appendix 2C) was allowed for. For this purpose a small, single stage, centrifugal pump was suitable.

d) Characteristics and selection of the centrifugal pumps

The operating characteristics of a pump are normally shown by the performance curve (e.g. Fig.A1, constructed from manufacturers' data). The curve shows the head developed by the pump versus the flow capacity (with water as the fluid). Each pump will have an individual performance curve. However, the efficiency of the pump will be maximised over only a narrow range of operating conditions.

The virtual (theoretical) head h , developed by a centrifugal pump is (352)

$$h = \frac{r^2 \omega^2}{g} - \frac{Q \omega}{2 \pi b g \tan \beta} \quad \dots \dots (A2)$$

where

- r - radius of rotation at outlet of pump
- ω - angular velocity of the impeller
- Q - Volumetric flow rate of the liquid
- b - width of impeller
- β - angle between the tangential direction and the blade of the impeller at the tip.

The head developed by the pump is therefore independent of the density of the fluid and hence the pressure will be directly proportional to the density (since $P = h\rho g$). The maximum pressure is developed when the whole of the excess kinetic energy of the fluid is converted to pressure energy, i.e. when $Q \rightarrow 0$.

The actual head is always less than the virtual head due to turbulence and friction losses in the pump (particularly with high viscosity fluids).

The performance curves for the PV-31 pump and the ITT, 21510-200 1" pump (used for operating Cell 1 and Cell 2 respectively) are shown in

Fig.A1. The head developed by the PV-31 pump decreased as the throughput increases. This implies that the tips of the blades of the impeller are inclined backwards, since (from Equation A2) when β is less than 90° and $\tan \beta$ is positive. (If β was greater than 90° , $\tan \beta$ would be negative and the head would increase as the delivery increased). The head developed by the 21510-200 pump is strongly dependent on throughput, (probably as a result of a flexible impeller) and the head increases rapidly with decreasing delivery. This pump was therefore a self-priming type.

The estimated flow circuit head loss (the system curve) may be approximated by the line C-C in Fig.A1 (based on a maximum flow rate of 35 l min^{-1} and a maximum head loss of $2 \times 7.6 \approx 15.2 \text{ dm}^3 \text{ min}^{-1}$ of water (see Appendix 2C) shown by point X).

The maximum flow rate would be about 25 l min^{-1} using the PV 31 pump and about 40 l min^{-1} for the 21510-200 pump. However, the head developed and the pumping efficiency may decrease as a result of the increased viscosity of the nickel sulphamate electrolyte, but both pumps should be capable of attaining the specified delivery rate.

e) Rotameter selection and Calibration

The manufacturers' specifications for Rotameter tubes are supplied in terms of the maximum measurable volumetric flow rate of water through the tube at combined temperatures. A comparison between the liquid of interest and that of the calibration fluid, which is normally water, may be made using the following expression, (from the manufacturers' literature)

$$\frac{F_1}{F_2} = \sqrt{\frac{(\rho - \rho_1)\rho_2}{(\rho - \rho_2)\rho_1}}$$

where F_1 , F_2 are the volumetric flow rates and ρ_1 , ρ_2 , the densities of fluids 1 and 2 respectively. ρ is the mean density of the Rotameter float. The density correction is applicable in turbulent flow.

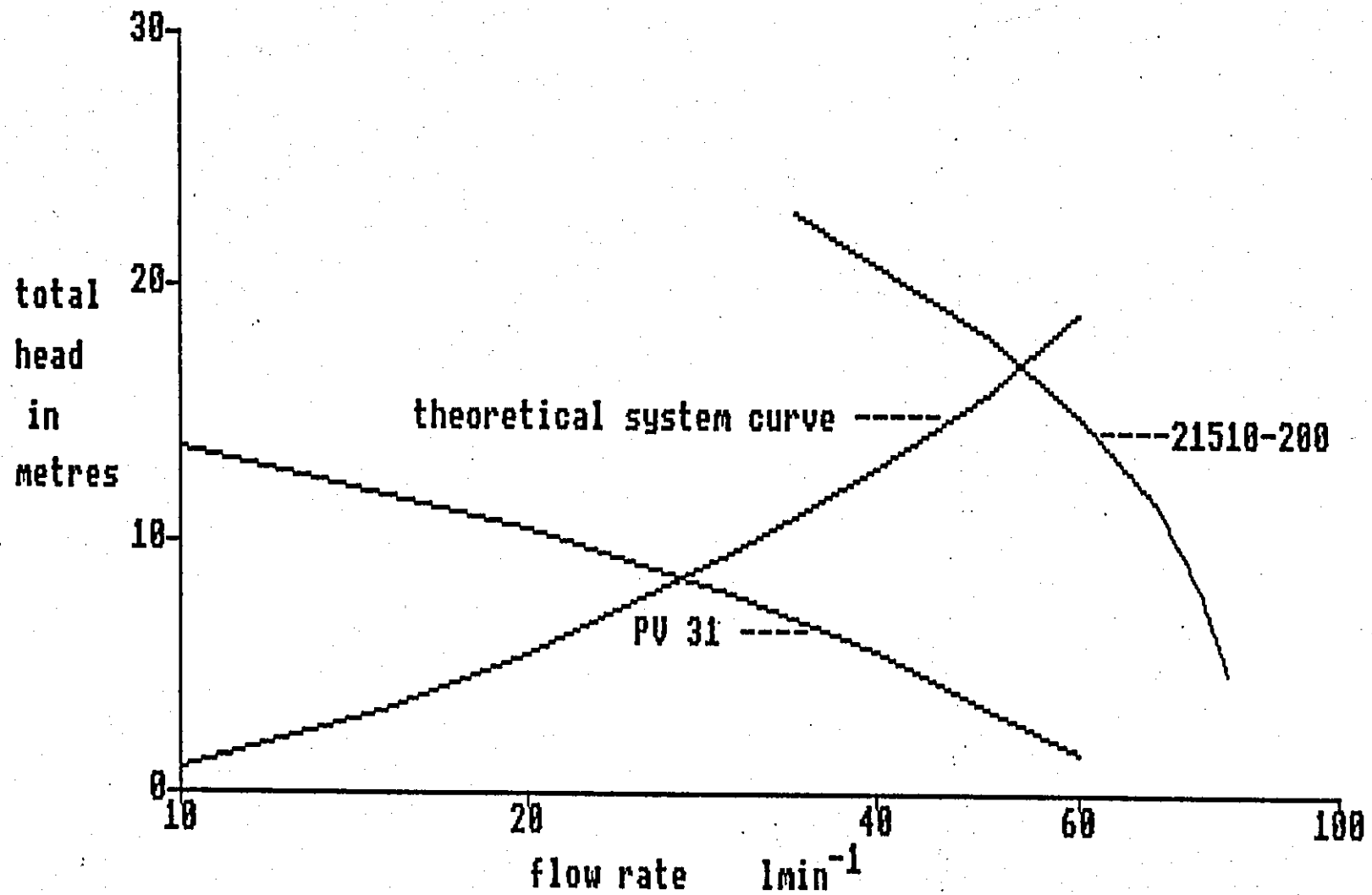


Fig.A1. Performance curves for the centrifugal pumps PV31 and 21510-200.

Therefore, when the density of the electrolyte $\rho_1 = 1.364 \text{ g cm}^{-3}$, the density of water $\rho_2 = 1.0 \text{ g cm}^{-3}$ and the density of the Koranite float $\rho = 2.53 \text{ g cm}^{-3}$, the correction factor was,

$$\frac{F_1}{F_2} = \sqrt{\frac{(2.53 - 1.364)1.0}{(2.53 - 1.0)1.364}}$$

$$= 0.75$$

For example, in Cell 2 a maximum measurable flow rate of $35 \text{ dm}^3 \text{ min}^{-1}$ was required. The manufacturers specifications for a type 102 Rotameter tube, size 47 gives a maximum volumetric flow rate of water of $47 \text{ dm}^3 \text{ min}^{-1}$.

The equivalent flow rate of the nickel sulphamate electrolyte at 60°C was calculated by application of the density factor. The maximum measurable flow rate of nickel sulphamate solution F , was

$$F = 0.75 F_2$$

$$= 0.75 \times 47$$

$$= 35 \text{ dm}^3 \text{ min}^{-1}$$

Hence the size 47 tube was suitable for this application. Two other Rotameters (35X and 18X) were selected in a similar manner.

Calibration of the Rotameters

Three Rotameters were employed, covering three ranges of flow rate. The Rotameters were denoted by the manufacturers codings, 18X, 35X and 47. All Rotameters were volumetrically calibrated with nickel sulphamate and copper sulphate solutions as follows.

The downpipe to the electrolyte reservoir of the flow system was replaced with a QVF hose connector (Type KHF 1), to which was fitted a length of 0.875 in o.d., terylene reinforced pvc tubing. The temperature of the electrolyte was raised to the required value by re-circulating it through the cell and by-pass via the reservoir.

The float height of the Rotameter to be calibrated was adjusted by valves No.1 and 2 (Fig.3.22). When the equilibrium temperature had been reached, the electrolyte was pumped into a previously calibrated, 25 l polythene aspirator. For very low flow rates a 1 l measuring cylinder was substituted for the aspirator. The time taken to deliver a given volume was measured using a stop watch.

Calculation

The volumetric flow rate was calculated from

$$\text{Volumetric flow rate} = \frac{\text{Volume discharged}}{\text{delivery time}} \quad \text{cm}^3 \text{ s}^{-1}$$

Then from a knowledge of the cross sectional area of the cell, the linear flow velocity (U), through the cell was found from

$$U = \frac{\text{Volumetric flow rate}}{\text{Cross sectional area}} \quad \text{cm s}^{-1}$$

For both cells the cross sectional area was 3 cm². (Section 3.2).

The Reynolds numbers (Re) were then calculated from:

$$Re = \frac{U d_e}{\nu_{T^{\circ}c}} \quad \dots \dots (2.12)$$

where $\nu_{T^{\circ}c}$ = kinematic viscosity of electrolyte at T and d_e = equivalent diameter of the cell. For Cell 1, $d_e = 1.5$ cm (Section 3.2) and for Cell 2, $d_e = 0.857$ cm (Section 3.3).

Rotameter calibration curves for nickel electrolytes are given in terms of the Reynolds number for Cells 1 and 2 (Figs.A2 to A6).

For convenience the calibration curves for copper solutions are given as the flow velocity through the cell (Figs. A7 to A9).

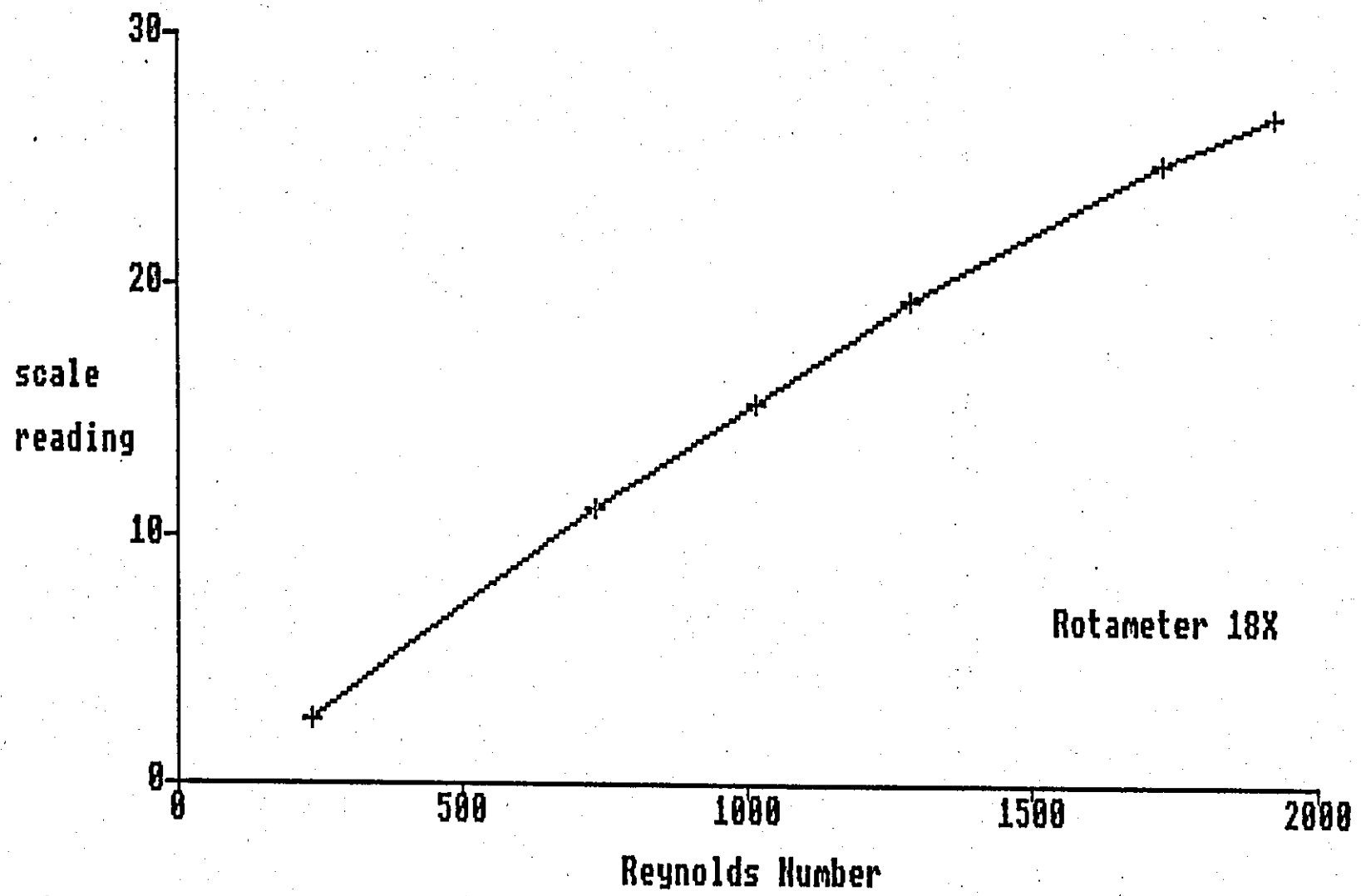


Fig.A2. Calibration of Rotameter 18X with $600 \text{ g}\ell^{-1}$ nickel sulphamate electrolyte at 60°C (Cell 1, $d_e \sim 1.5 \text{ cm}$).

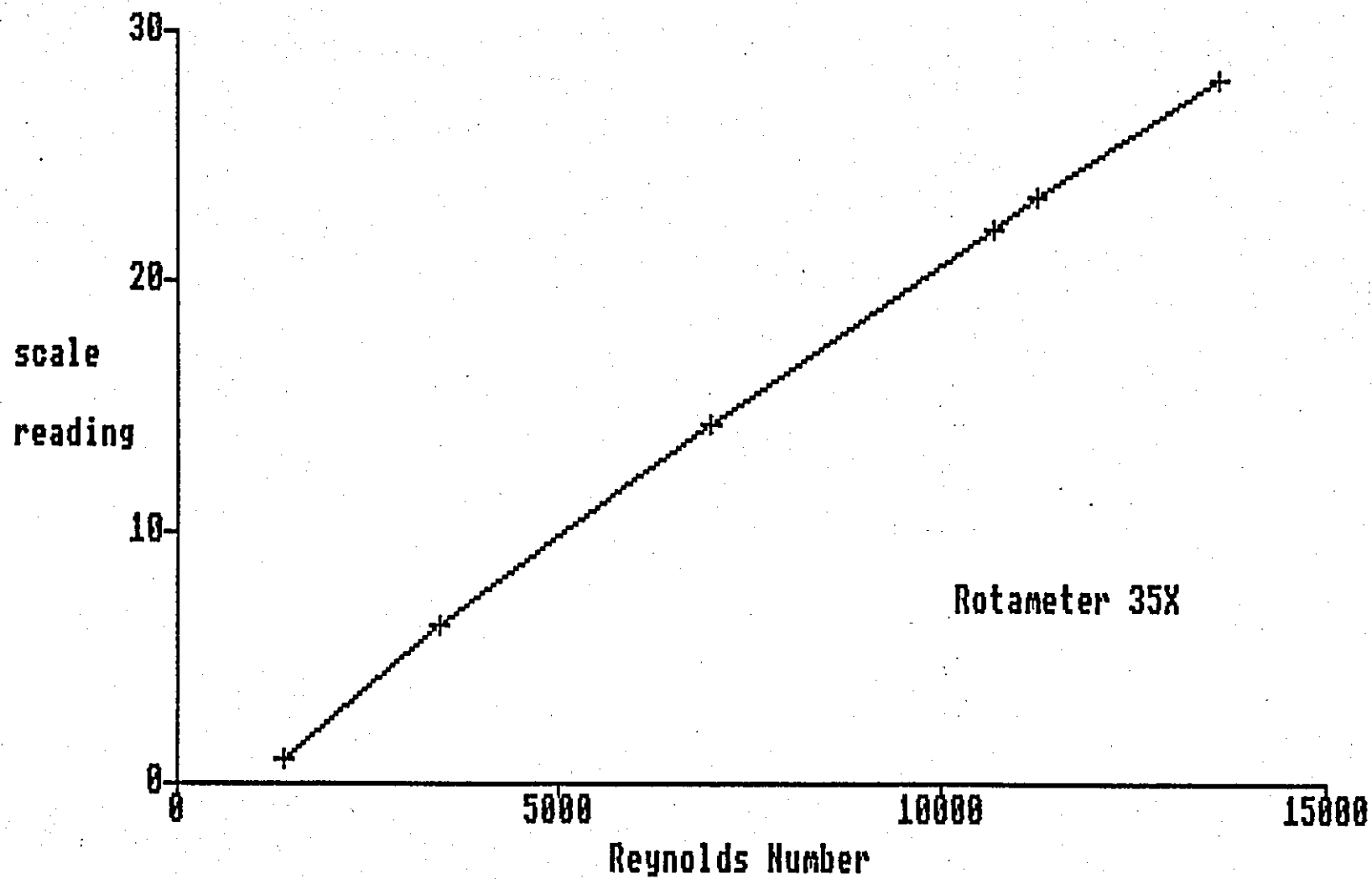


Fig.A4. Calibration of Rotameter 35X with 600 g l^{-1} nickel sulphamate electrolyte at 60°C (Cell 1, de 1.5 cm).

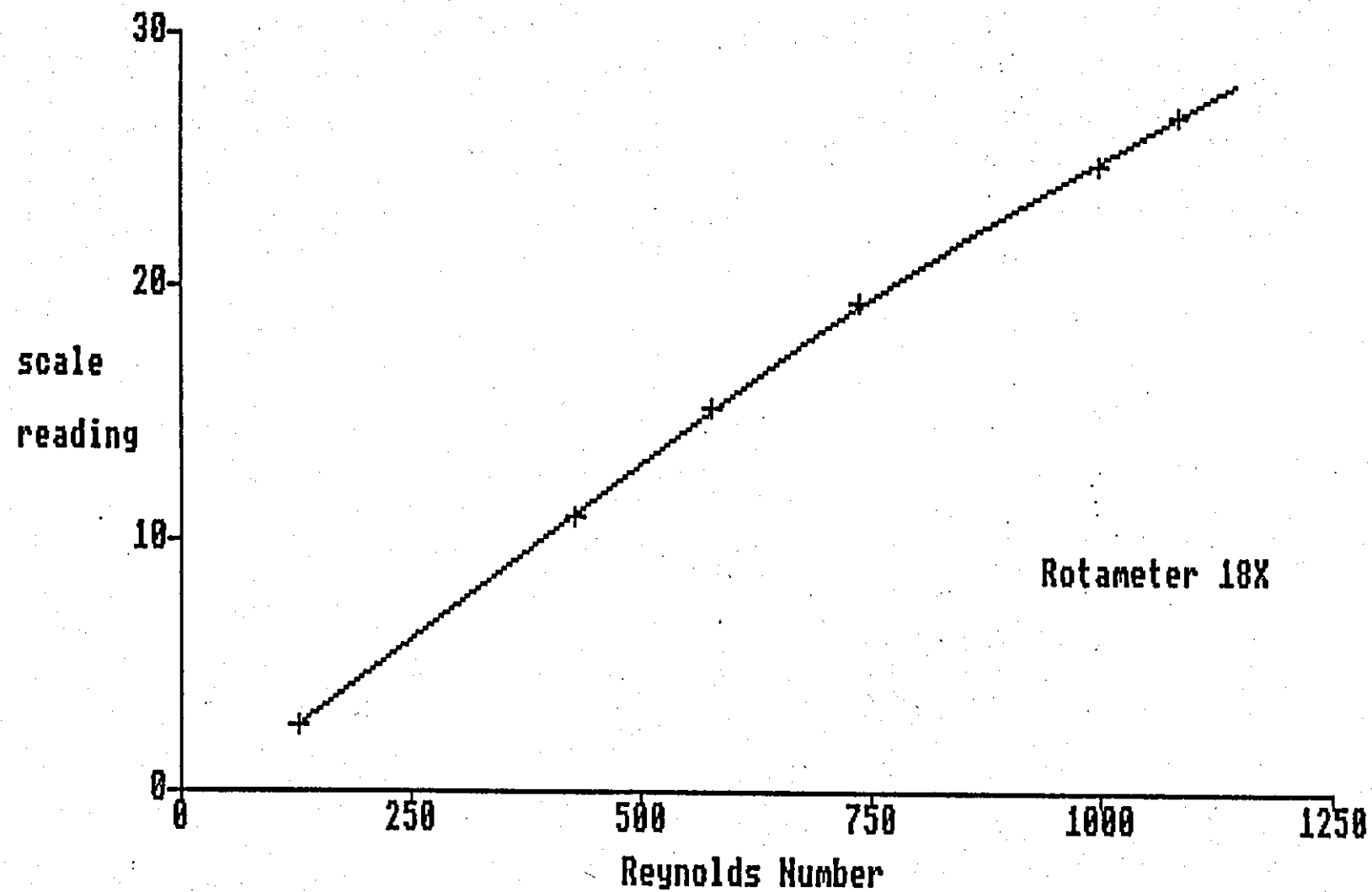


Fig.A3. Calibration of Rotameter 18X with 600 g l^{-1} nickel sulphamate electrolyte at 60°C (Cell 2, $d_e \sim 0.857 \text{ cm}$).

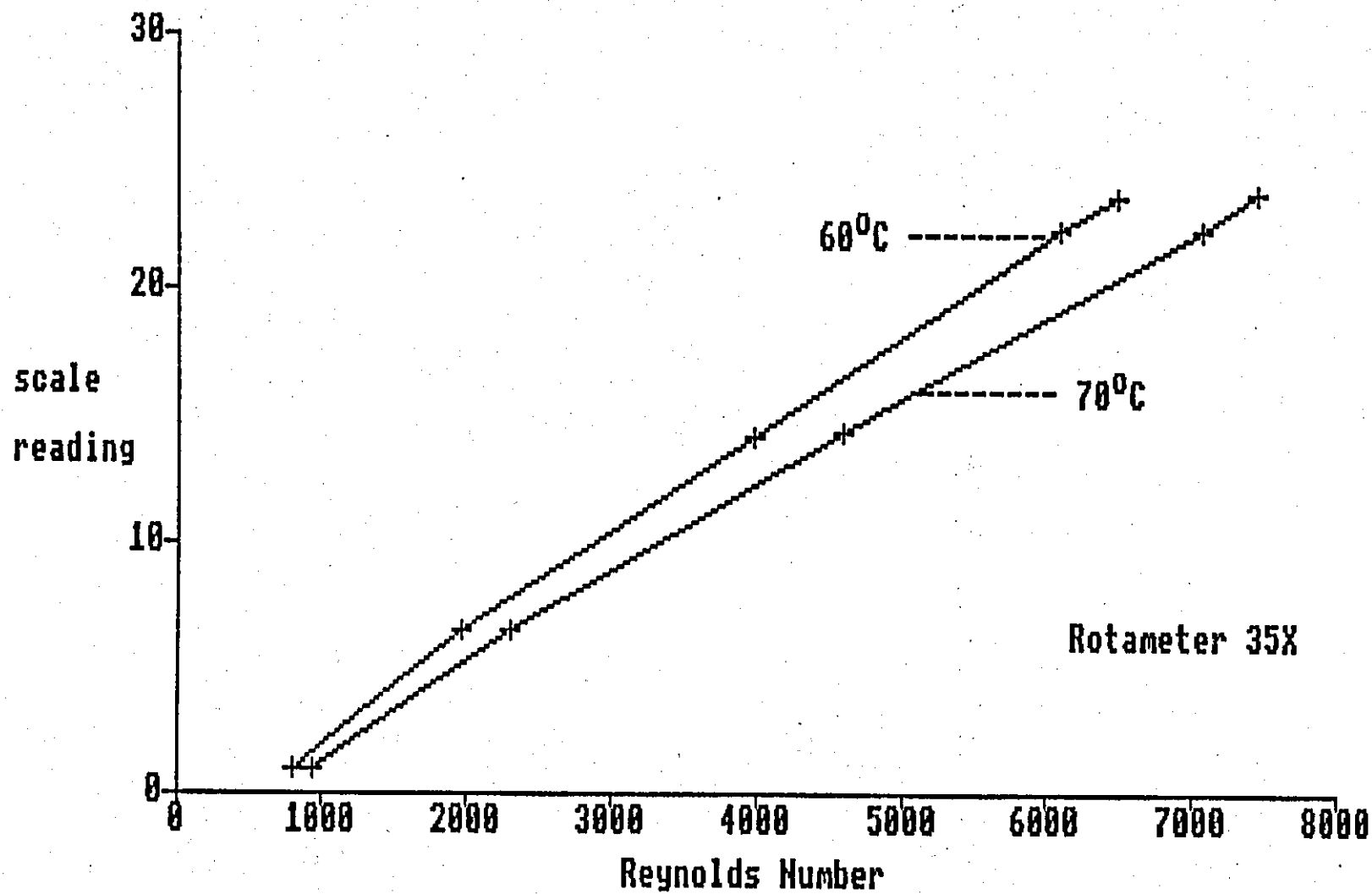


Fig.A5. Calibration of Rotameter 35X with 600 g l^{-1} nickel sulphamate electrolyte (Cell 2, $d_e \sim 0.857 \text{ cm}$).

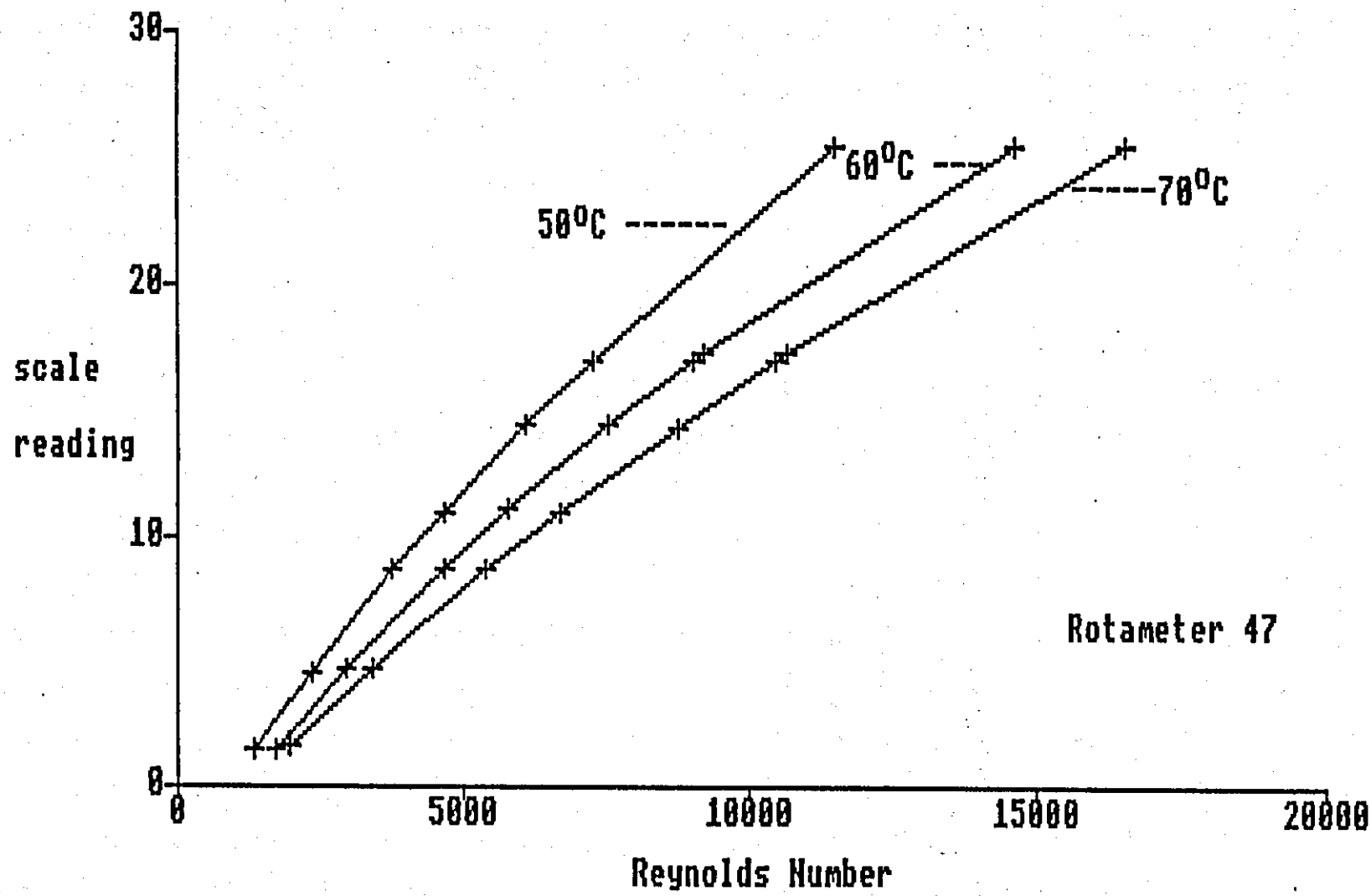


Fig.A6. Calibration of Rotameter 47 with 600 g l^{-1} nickel sulphamate electrolyte (Cell 2, $d_e \sim 0.857 \text{ cm}$).

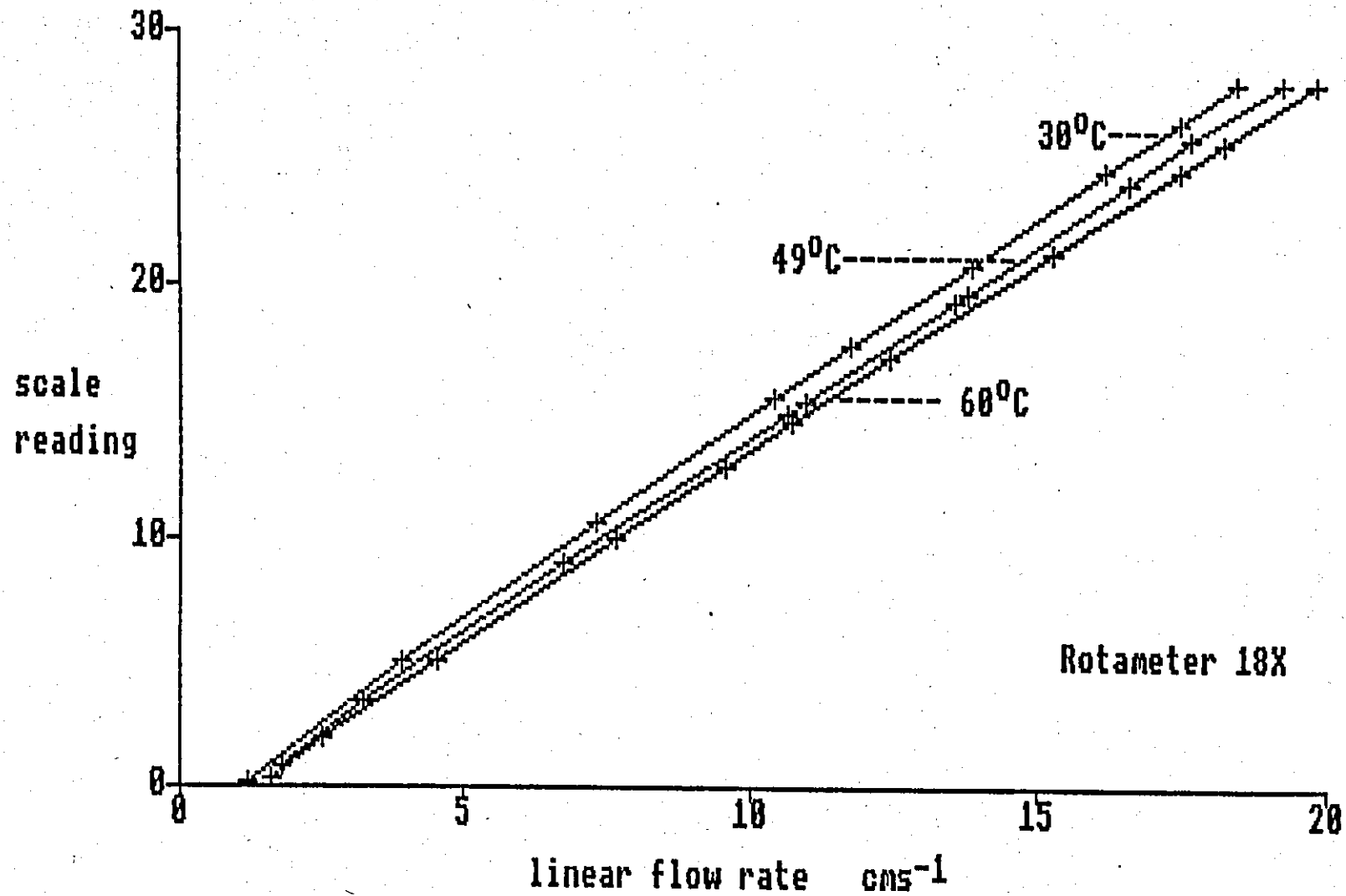


Fig.A7. Calibration of Rotameter 18X with 0.014M copper sulphamate electrolyte (Cell 2, $d_e \sim 0.857$ cm).

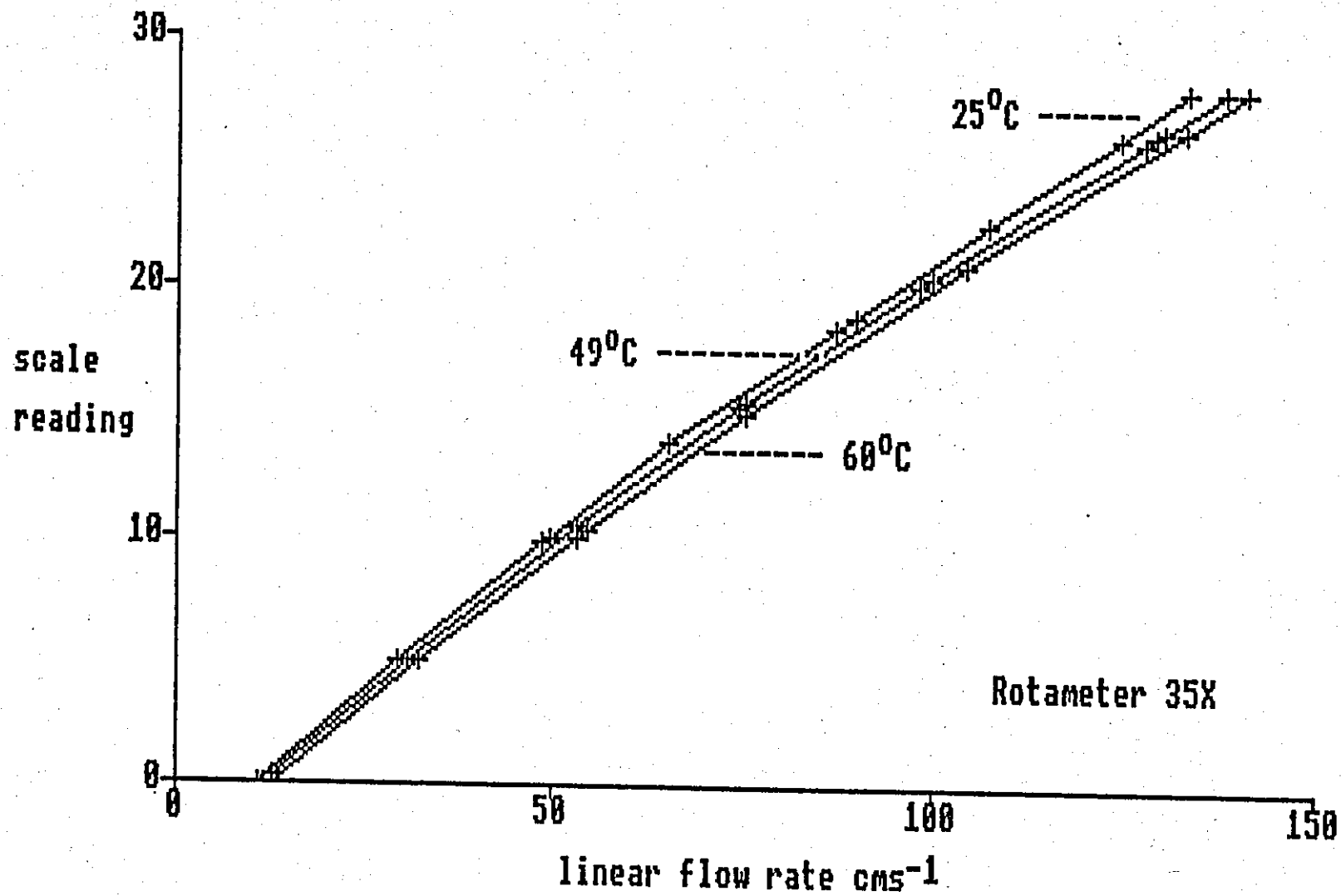


Fig.A8. Calibration of Rotameter 35X with 0.014M copper sulphate electrolyte (Cell 2, $d \sim 0.857$ cm).

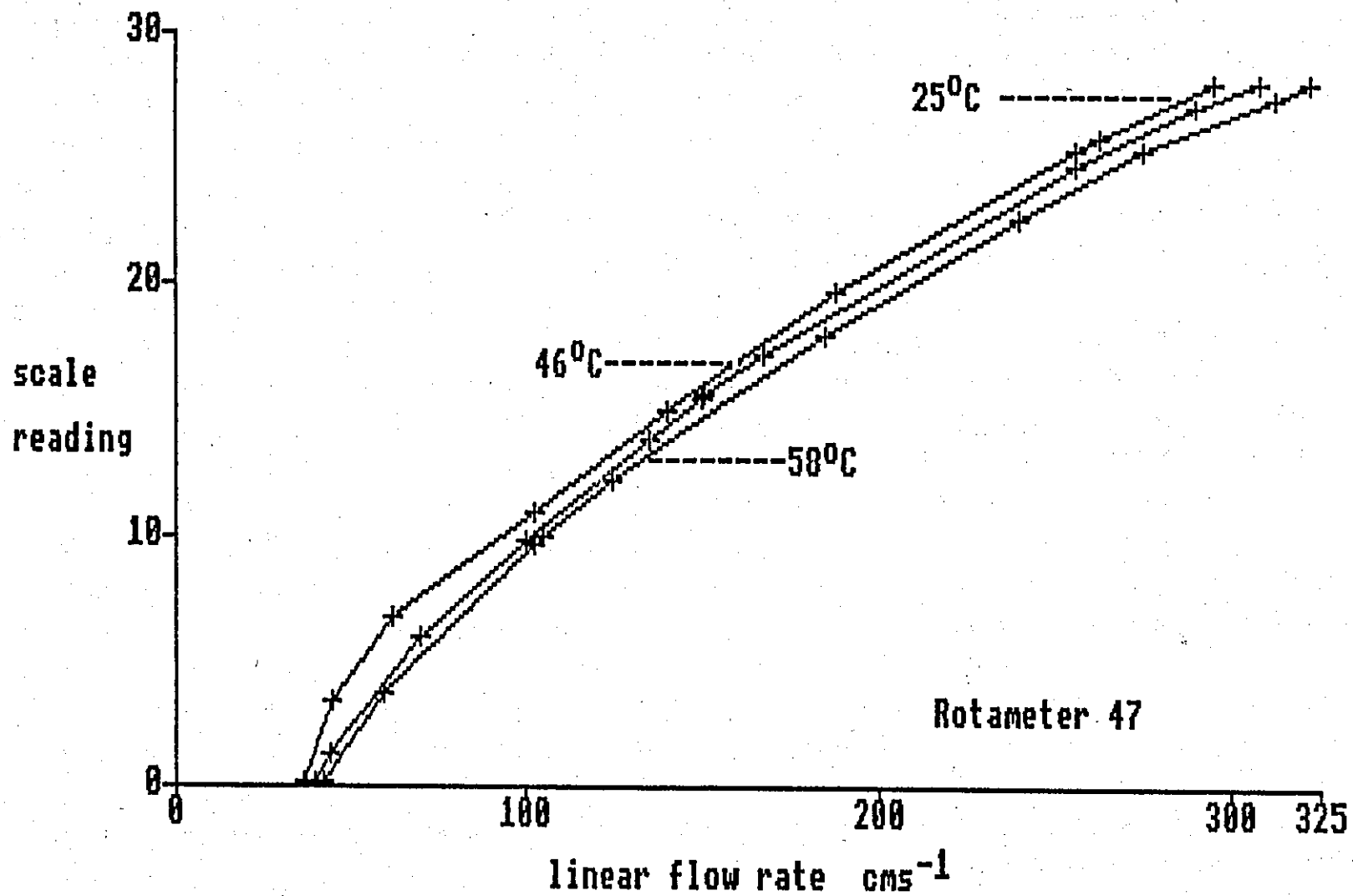


Fig.A9. Calibration of rotameter 47 with 0.014M copper sulphate electrolyte (Cell 2, $d \sim 0.857 \text{ cm}$).

f) Calculation of the diffusion coefficients of concentrated nickel sulphamate electrolytes

The available information regarding the diffusion coefficients of concentrated nickel salts, was sparse, although many values may be obtained for the independent ions at infinite dilution (e.g. ref.149). Ohlm (167) has determined the diffusion coefficients for three nickel salts, NiCl₂ and NiSO₄ and Ni(NO₃)₂ at 20°C over a range of concentrations. A temperature increase to ~60°C would be expected to at least double these values. As described earlier (p.33), Wesley, Sellers and Roehl (67) extrapolated Ohlms data to 70°C. However, the validity of their calculations is doubtful since the calculations appear to be in error (p.33).

It was of interest to examine the factors which effect the value of the diffusion coefficients and to calculate some appropriate values for use in theoretical mass transport calculations.

The diffusion coefficient, $D_{\infty Ni^{2+}}^{25^{\circ}C}$ for nickel ions (Ni²⁺) at infinite dilution has been given as $0.72 \times 10^{-5} \text{ cm}^2\text{s}^{-1}$ at 25°C (149). An analogous value for the diffusion coefficient of sulphamate ions (SO₃NH₂⁻) was not evident in the literature. However, most common anions have values around $1.5 \times 10^{-5} \text{ cm}^2\text{s}^{-1}$ (for example :

$$D_{\infty Cl^{-}}^{25^{\circ}C} = 2.032 \times 10^{-5} \text{ cm}^2\text{s}^{-1} \text{ and } D_{\infty SO_4^{2-}}^{25^{\circ}C} = 1.065 \times 10^{-5} \text{ cm}^2\text{s}^{-1} (149).$$

The diffusion coefficient $D_{\infty NH_2SO_3^{-}}^{25^{\circ}C}$ for sulphamate ions at infinite dilution was taken to be $1.5 \times 10^{-5} \text{ cm}^2\text{s}^{-1}$.

An approximate value of the average value for the overall diffusion coefficient $D_{\infty Ni(NH_2SO_3)_2}^{25^{\circ}C}$ was calculated from the following equation (149):

$$D_{av} = \frac{D^{-} D^{+} (|z^{+}| + |z^{-}|)}{[(D^{+} |z^{+}|) + (D^{-} |z^{-}|)]} \dots \dots (A3)$$

Substituting the above values for the diffusion coefficients of the individual ions and appropriate values of the charge number into Equation (A3) gives

$$D_{\infty \text{Ni}(\text{NH}_2\text{SO}_3)_2}^{25^\circ\text{C}} = \frac{0.72 \times 10^{-5} \times 1.5 \times 10^{-5} \times (2 + 1)}{(0.72 \times 10^{-5} \times 2) + (1.5 \times 10^{-5} \times 1)}$$

$$\sim 1 \times 10^{-5} \text{ cm}^2\text{s}^{-1}$$

However, the value of the calculated diffusion coefficient relates to a concentration approaching zero and a temperature of 25°C. A large increase in the concentration of nickel sulphamate would result in significant increases in the electrolyte viscosity η . The relationship between the dynamic viscosity, η , the absolute temperature T and the diffusion coefficient D , is demonstrated by the Stokes-Einstein equation (2):

$$D = \frac{kT}{6 \pi r \eta}$$

where k - Boltzmann constant and r , the effective radius of the diffusing ion. The formation of ion pairs in concentrated solutions may dramatically effect the value of r .

An approximate guide to the influence of electrolyte temperature and the dynamic viscosity may be obtained from the empirical equation (350):

$$\frac{D_1 \eta_1}{T_1} = \frac{D_2 \eta_2}{T_2}$$

or

$$D_2 = \frac{T_2 D_1 \eta_1}{T_1 \eta_2} \quad (\text{cf. Equn. 2.13})$$

At infinite dilution, the electrolyte viscosity would approach that of water, $\eta^{25^\circ\text{C}} \sim 1 \times 10^{-2}$ poise (345) at 298.2 K (25°C). The viscosity of the nickel sulphamate solution was $\eta_{\text{H}_2\text{O}}^{60^\circ\text{C}} \sim 1.64 \times 10^{-2}$ poise $\text{Ni}(\text{NH}_2\text{SO}_3)_2$

(Table A1) at 333.2 K (60°C), and using the estimated value of

$$D_{\infty \text{Ni}(\text{NH}_2\text{SO}_3)_2}^{25^\circ\text{C}}$$

$$D_{\infty}^{60^{\circ}\text{C}} \text{Ni}(\text{NH}_2\text{SO}_3)_2 = \frac{333.2 \times 1 \times 10^{-5} \times 1 \times 10^{-2}}{298.2 \times 1.64 \times 10^{-2}}$$

$$= \underline{0.68 \times 10^{-5}} \text{ cm}^2\text{s}^{-1}$$

The diffusion coefficient is related to the mean activity coefficient f_{\pm} of the diffusing ions by (ref 2)

$$D_c = D_{\infty} (1 \div \frac{1}{2} \log f_{\pm})$$

and the activity coefficient is given by the Debye-Huckel limiting law

$$\log f_{\pm} = -A (z^+ z^-) I^{\frac{1}{2}}$$

where A is a constant dependent upon the temperature and dielectric properties of the solvent. The ionic strength, I is given by

$$I = \frac{1}{2} \sum C_j z_j^2$$

C_j is the concentration of species j.

It should be noted that application of the Debye-Huckel limiting law is not strictly applicable in concentrated solutions, since it assumes point charges and takes no account of ion-pair formation or hydration. When these are considered, the calculations become very complex. However, for a first approximation the Debye-Huckel law is adequate.

The concentration of the anion and cation and their respective charges are

$$\text{Ni}^{2+}, C \sim 1.89 \times 10^{-3} \text{ mol cm}^{-3}, z^+ = 2$$

$$\text{and } \text{NH}_2\text{SO}_3^-, C \sim 3.76 \times 10^{-3} \text{ mol cm}^{-3}, z^- = 1$$

Then

$$I = \frac{1}{2} [(1.89 \times 10^{-3} \times 2^2) + (3.76 \times 10^{-3} \times 1^2)]$$

$$\sim 6 \times 10^{-3} \text{ mol cm}^{-3}$$

The constant A, for water at 60°C, is given as 0.5494 (ref.2).

$$\therefore \log f_{\pm} = -0.5494 (2 \times 1) (6 \times 10^{-3})^{\frac{1}{2}}$$

$$= \underline{-0.085}$$

and

$$f_{\pm} = \underline{0.82}$$

$$\begin{aligned}
 \text{also } D_{1.89M \text{ Ni(NH}_2\text{SO}_3)_2}^{60^\circ\text{C}} &= D_{\infty \text{ Ni(NH}_2\text{SO}_3)_2}^{60^\circ\text{C}} \left(1 + \frac{1}{2} \log f_{\pm}\right) \\
 D_{1.89M \text{ Ni(NH}_2\text{SO}_3)_2}^{60^\circ\text{C}} &= 0.68 \times 10^{-5} \left(1 + \frac{-0.083}{2}\right) \\
 &= \underline{\underline{0.64 \times 10^{-5} \text{ cm}^2\text{s}^{-1}}}
 \end{aligned}$$

Values of the diffusion coefficient at 50° and 70°C were calculated by a similar method. The estimated values of the diffusion coefficient are shown in Table A3. The results of these calculations are, of necessity, somewhat approximate and probably on the low side. However, the relationships between diffusion coefficients at each temperature are probably of the right order of magnitude. Therefore, the estimated values of the diffusion coefficient were used in all further calculations. The Schmidt number, Sc , of the electrolyte was calculated from:

$$Sc = \frac{\nu}{D}$$

The estimated values of D and the experimental values of the kinematic viscosity, ν (Section 3.1) were substituted into the above equation and are also shown in Table (A3) for temperatures of 50, 60 and 70°C.

Temperature		Constant A	Activity Coefficient f_{\pm}	Dynamic Viscosity η /poise	Diffusion Coefficient $D/\text{cm}^2\text{s}^{-1}$	Kinematic Viscosity $\nu/\text{cm}^2\text{s}^{-1}$	Schmidt No. Sc
$^{\circ}\text{C}$	K						
50	323.2	0.5373	0.83	2.042×10^{-2}	0.54×10^{-5}	1.492×10^{-2}	2,763
60	333.2	0.5494	0.82	1.640×10^{-2}	0.65×10^{-5}	1.202×10^{-2}	1,878
70	343.2	0.5625	0.82	1.403×10^{-2}	0.83×10^{-5}	1.035×10^{-2}	1,247

Table A3 Physical property data for concentrated nickel sulphamate solutions at 50, 60 and 70°C (see also Section 3.1)

Appendix 3The calculation of microhardness values and the optimum load on the indenter

Vickers microhardness values were determined by means of the microhardness attachment of the Reichert optical microscope (model MeF2).

The hardness of a material is defined as a force per unit area:

$$H = \frac{P}{m} \text{ kg mm}^{-2}$$

where

P = the force acting on the indenter

m = surface area of the pyramid shaped indentation

The indenter was a diamond in the form of a square pyramid of apex angle (α) 136° . The surface area m , excluding the base area, of a square pyramid of apex angle (α) and base diagonal (d) is given by:

$$m = \frac{d^2}{2 \cdot \sin \alpha/2} \text{ mm}^2$$

For the pyramid of the Vickers diamond with an apex angle of 136° , the surface area of the indentation is given by

$$\begin{aligned} m &= \frac{d^2}{2 \cdot \sin 136/2} \\ &= \frac{d^2}{2 \times 0.9272} \\ &= \frac{d^2}{1.8544} \end{aligned}$$

and hence the Vickers microhardness (mHv) is given by

$$\text{mHv} = 1.8544 \frac{P}{d^2} \text{ kg mm}^{-2} \text{ (V.P.N.)}$$

However, for effective measurement of the microhardness of thin foils, the depth of penetration of the indenter should not exceed 10%

of the total foil thickness (354). Greater penetration depths may lead to erroneous results owing to the substrate material influencing the measurement. Conversely at very low indentation loads the microhardness becomes load dependent and subject to errors due to vibration or impact loading.

The optimum load necessary to achieve reproducible results, within the penetration depth limitation, was calculated as follows.

With reference to Fig.A10, the penetration depth is given by the expression

$$y = \frac{x}{\tan 68}$$

When the average thickness of the foil is 25 μ m a maximum penetration depth of 2.5 μ m (2.5×10^{-3} mm) is permissible then.

$$\begin{aligned} x &= 2.5 \times 10^{-3} \times \tan 68 \\ &= 6.19 \times 10^{-3} \text{ mm} \end{aligned}$$

The value of d may be evaluated from

$$\begin{aligned} \left(\frac{d}{2}\right)^2 &= 2x^2 \\ \text{or } d &= 2\sqrt{2x^2} \\ d &= 2\sqrt{2(6.19 \times 10^{-3})^2} \\ &= 17.5 \times 10^{-3} \text{ mm} \end{aligned}$$

The minimum microhardness value for nickel electrodeposited from sulphamate solution is about 250 kg mm $^{-2}$ (1). The maximum indentation load may be calculated from Equation (A4)

$$\text{mHv} = 1.8544 \frac{P}{d^2} \dots \dots \dots (A4)$$

rearranging $P = \text{mHv } d^2 / 1.8544$

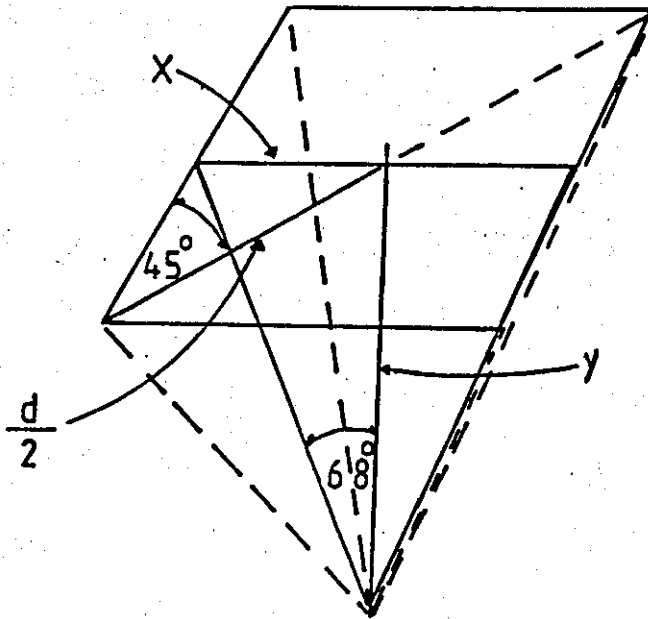


Fig.A10. Schematic diagram of an indentation produced by the diamond pyramid indenter.

The maximum value of d for a 25 μm foil is 17.5×10^{-3} mm

$$\begin{aligned} \therefore P &= \frac{250 \times (17.5 \times 10^{-3})^2}{1.8544} \\ &= 4.13 \times 10^{-2} \text{ kg} \quad \underline{41.3\text{g}} \end{aligned}$$

To ensure that the penetration depth of the indenter did not exceed the 10% of total foil thickness requirement, an indentation load of 40g was employed for all microhardness measurements.

Appendix 4Additional measurements relating to the electroforming of nickel in Cell 2.a) Comparison of momentum and mass transfer measurements in Cell 2

It can be shown that the mechanism of mass and momentum transfer have a similar mechanism (the Reynolds Analogy) and hence, may be correlated with flow rate by similar equations (ref.148).

The measurement of pressure loss across a known length provides a simple method of determining the rate of momentum transfer, (or shear stress) as a friction factor, for a range of flow rates. Nickel sulphamate electrolyte was used as the fluid.

The results of these measurements are then compared with a mass transfer correlation derived from the results of mass transfer measurements in the copper system (Section 4.2.1).

Correlation of dimensionless shear stress (friction factor) measurements with flow rate in Cell 2

The pressure difference along a 50cm length (x) of Cell 2 was measured for a series of electrolyte flow rates (1.33 to 207 cm s^{-1}), using a mercury or methanol manometer. The pressure difference (ΔP) and shear stress (R_0) was calculated from the measurements of manometer height difference (Δh). The results were correlated in terms of the friction factor (ϕ) (p.45) for the two flow regimes corresponding to:

a) Laminar flow (Re 95 to Re 2,139) at 60°C ,

and

b) Turbulent flow (Re 3,050 to Re 17,112) at 60 and 70°C .

Example calculations

From the difference in height (Δh) between the liquid level in each arm of the j-tube manometer the frictional pressure difference (ΔP_f) was calculated from the equation:

$$\Delta P_f = \Delta h \rho_L g$$

where g = acceleration due to gravity
 $\approx 981 \text{ cm s}^{-1}$

and ρ_L = density of manometer liquid
 $\approx 13.6 \text{ g cm}^{-3}$ for mercury
 or $\approx 0.792 \text{ g cm}^{-3}$ for methanol

$\Delta h \approx 1.0 \text{ mm}$ at a flow rate $U \approx 1.333 \text{ cm s}^{-1}$

$$\therefore \Delta P_f = 0.1 \times 0.792 \times 981$$

$$\approx \underline{77.7} \text{ dynes cm}^{-2}$$

The shear stress R_0 was then given by:

$$-R_0 = -\Delta P_f \frac{d_e}{4x}$$

x = distance along which the ΔP_f was measured
 $\approx 50 \text{ cm}$

d_e = equivalent diameter of cell $\approx 0.857 \text{ cm}$

$$\therefore -R_0 = 77.7 \frac{0.857}{4 \times 50}$$

$$\approx \underline{0.333} \text{ dyne cm}^{-2}$$

The Reynolds number (Re) was calculated from the equation:

$$Re = \frac{U d_e}{\nu}$$

The kinematic viscosity of the electrolyte was

$\nu = 1.202 \times 10^{-2} \text{ cm}^2 \text{ s}^{-1}$ at 60°C
 and $\nu = 1.035 \times 10^{-2} \text{ cm}^2 \text{ s}^{-1}$ at 70°C

when $U \approx 1.333 \text{ cms}^{-1}$ at 60°C ,

$$\text{Re} = \frac{1.333 \times 0.857}{1.202 \times 10^{-2}}$$

$$\approx \underline{95.1}$$

The shear stress may be expressed as a dimensionless number, the friction factor, ϕ .

$$\phi = \frac{f}{2} = \frac{R_0}{\rho U^2}$$

where ρ = density of the electrolyte

$$\approx 1.364 \text{ g cm}^{-3} \text{ at } 60^\circ\text{C}$$

and $\approx 1.356 \text{ g cm}^{-3} \text{ at } 70^\circ\text{C}$

$$\text{Hence, } \phi = \frac{77.7}{1.333 \times 1.364}$$

$$\approx \underline{13.7 \times 10^{-2}}$$

i) Laminar Flow

The experimental and calculated data for laminar flow (Re 95 to 2,139) are shown in Table A4. The friction factor (ϕ) was plotted versus the electrolyte Reynolds number on logarithmic coordinates (Fig.A11). The relationship was linear in the laminar flow region (Re <2,200). Linear regression showed that the data may be correlated by the equation:

$$\phi = \frac{f}{2} = \frac{8.58}{\text{Re}^{0.9}} \quad \dots \dots \text{(A5)}$$

with a correlation coefficient (r^2) of 0.99. The solution of the above equation is shown in Fig.A11, by the solid line A-A, of slope 0.9.

The theoretical analysis of laminar flow in pipes (Section 2.3a) has shown that in laminar flow ϕ and Re are related by the following equation (p.45):

$$\phi = \frac{f}{2} = \frac{8}{\text{Re}}$$

Flow Rate vU cm s^{-1}	Reynolds Number Re	Pressure Difference Δh mm CH_3OH	Pressure Difference ΔP_f Dyne cm^{-2}	Shear Stress $-R_0$ Dyne cm^{-2}	Friction Factor $\phi \equiv f/2$ $\times 10^{-2}$
1.333	95.1	1.0	77.70	0.333	13.7
1.889	134.7	1.5	116.5	0.499	10.3
3.333	237.6	2.5	194.2	0.832	5.49
5.556	396.1	4.5	349.6	1.498	3.56
8.056	574.3	7.0	543.9	2.331	2.63
10.83	772.4	9.5	738.1	3.163	1.977
13.61	970.0	13.0	1,010	4.328	1.713
15.28	1,089	15.5	1,204	5.160	1.620
16.67	1,188	16.0	1,243	5.327	1.405
21.67	1,545	23.5	1,826	7.824	1.222
30.00	2,139	40.5	3,147	13.48	1.098

Table A4. Measurement of dimensionless shear stress (friction factor) in laminar flow at 60°C. (manometer fluid - methanol $\rho_{\text{CH}_3\text{OH}} = 0.792 \text{g cm}^{-3}$).

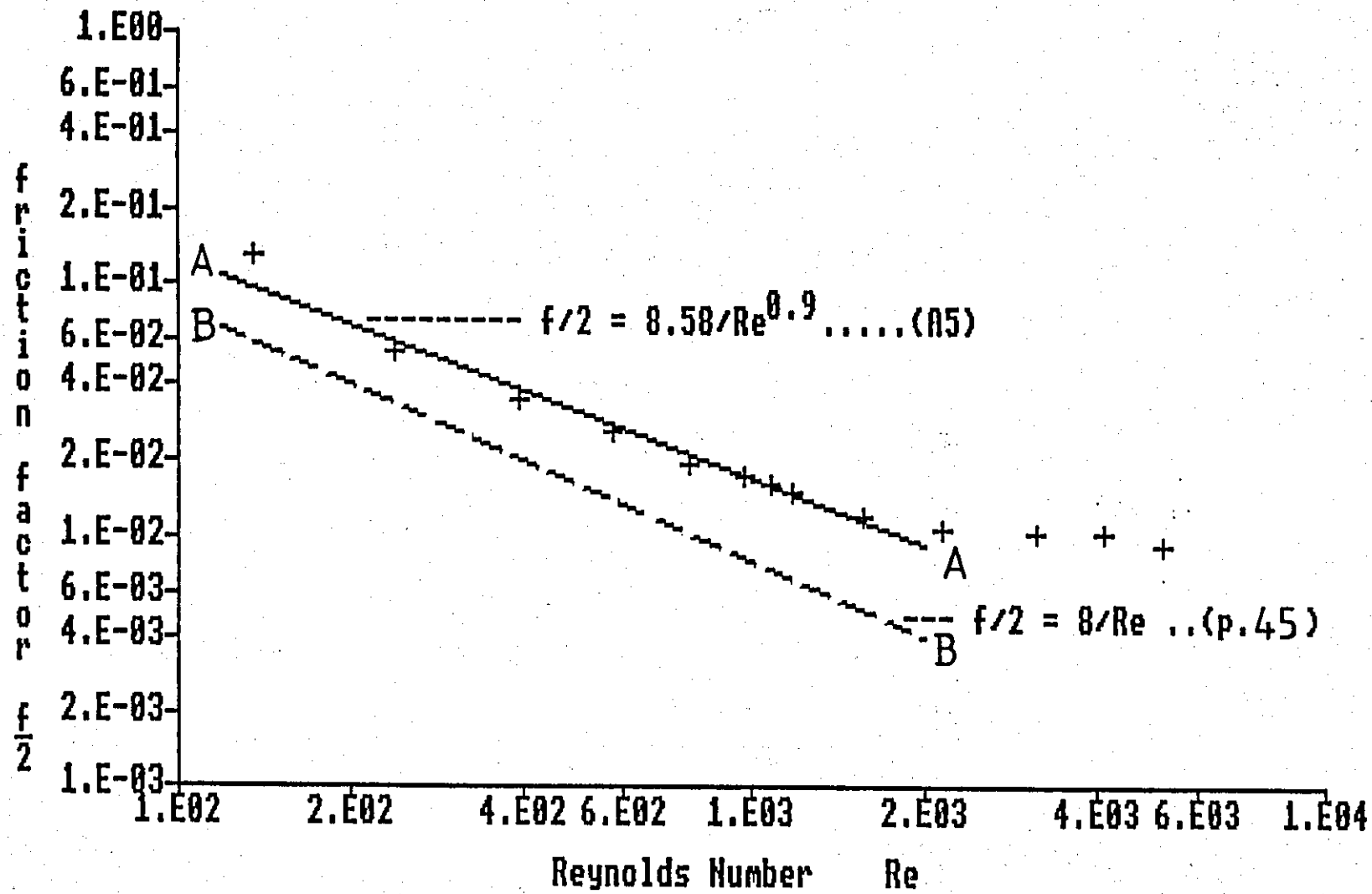


Fig.A11. Correlation of friction factor data in laminar flow at 60°C (600g l⁻¹ nickel sulphamate solution)

The solution of this equation is shown in Fig.A4 by the broken line B-B. The experimental value of the friction factor was greater, and hence the shear stress greater, than predicted for simple pipe flow.

ii) Turbulent Flow

At higher flow rates ($Re > 2,500$) the flow undergoes transition to turbulent flow, accompanied by a change of shape of the experimental data. The experimental and calculated data for turbulent flow (Re 3,050 to 17,112) are summarised in Table A5 (60°C) and A6 (70°C). The data was plotted, as for laminar flow, in Fig.A12. As may be seen similar values of the friction factor were observed at both 60 and 70°C, hence the data was correlated by a single equation:

$$\phi = \frac{f}{2} = 0.055 Re^{-0.19} \quad \dots \dots (A6)$$

with a correlation coefficient r^2 of 0.85. The solution of Equation (A6) is shown by the solid line A-A in Fig.A12.

An empirical relationship for friction factor correlation in turbulent flow is given by the equation (Chapter 2.3a):

$$\phi = \frac{f}{2} = 0.0396 Re^{-\frac{1}{4}} \quad \dots \dots (2.29)$$

The solution of the Equation (2.29) is also shown in Fig.A12 by the broken line B-B of slope -0.2. The experimental data exhibits a higher friction factor than predicted from the Equation (2.29) (cf Laminar flow).

Summary

Friction factors were calculated from pressure drops along Cell 2 and correlated with flow rate in a) laminar flow and b) turbulent flow.

i) In laminar flow at 60°C, the dimensionless shear stress (friction factor, $f/2$) was correlated with flow rate by the equation:

$$\frac{f}{2} = \frac{8.58}{Re^{0.9}} \quad \dots \dots (A5)$$

Flow Rate U cm s ⁻¹	Reynolds Number Re	Pressure Difference Δh mm Hg	Pressure Difference ΔP_f Dyne cm ⁻²	Shear Stress $-R_0$ Dyne cm ⁻²	Friction Factor $\phi \equiv f/2$ $\times 10^{-2}$
42.8	3,050	5.0	6,671	28.6	1.145
57.8	4,119	9.0	12,007	51.5	1.130
75.6	5,387	15.0	20,012	85.8	1.101
91.7	6,536	20.0	26,683	114.3	0.997
111.1	7,922	29.0	38,691	165.8	0.985
131.1	9,348	39.0	52,032	223.0	0.951
150.0	10,695	48.0	64,040	274.4	0.894
170.0	12,121	60.0	80,050	343.0	0.870
190.0	13,547	76.0	101,396	434.5	0.882
206.7	14,735	90.0	120,074	514.5	0.883

Table A5. Measurement of dimensionless shear stress (friction factor) in Turbulent flow at 60°C (manometer fluid - mercury, $\rho_{Hg} = 1.364 \text{ g cm}^{-3}$).

Flow Rate U cm s ⁻¹	Reynolds Number Re	Pressure Difference Δh mm Hg	Pressure Difference ΔP_f Dyne cm ⁻²	Shear Stress $-R_0$ Dyne cm ⁻²	Friction Factor $\phi \equiv \frac{f}{2}$ $\times 10^{-2}$
27.2	2,254	2.5	3,335	14.3	1.425
43.9	3,634	6.0	8,005	34.3	1.313
58.3	4,830	9.5	12,675	54.3	1.178
74.4	6,164	15.0	20,012	85.8	1.143
91.7	7,590	21.5	28,684	122.9	1.078
111.1	9,200	31.0	41,359	177.2	1.059
131.1	10,856	40.5	54,034	231.5	0.993
150.0	12,420	52.5	70,043	300.1	0.984
170.0	14,076	67.0	89,389	383.0	0.977
190.0	15,732	79.0	105,399	451.6	0.923
206.7	17,112	92.0	122,743	526.0	0.908

Table A6. Measurement of dimensionless shear stress (friction factor) in turbulent flow at 70°C (manometer fluid - mercury, $\rho_{\text{Hg}} = 1.364 \text{ g cm}^{-3}$).

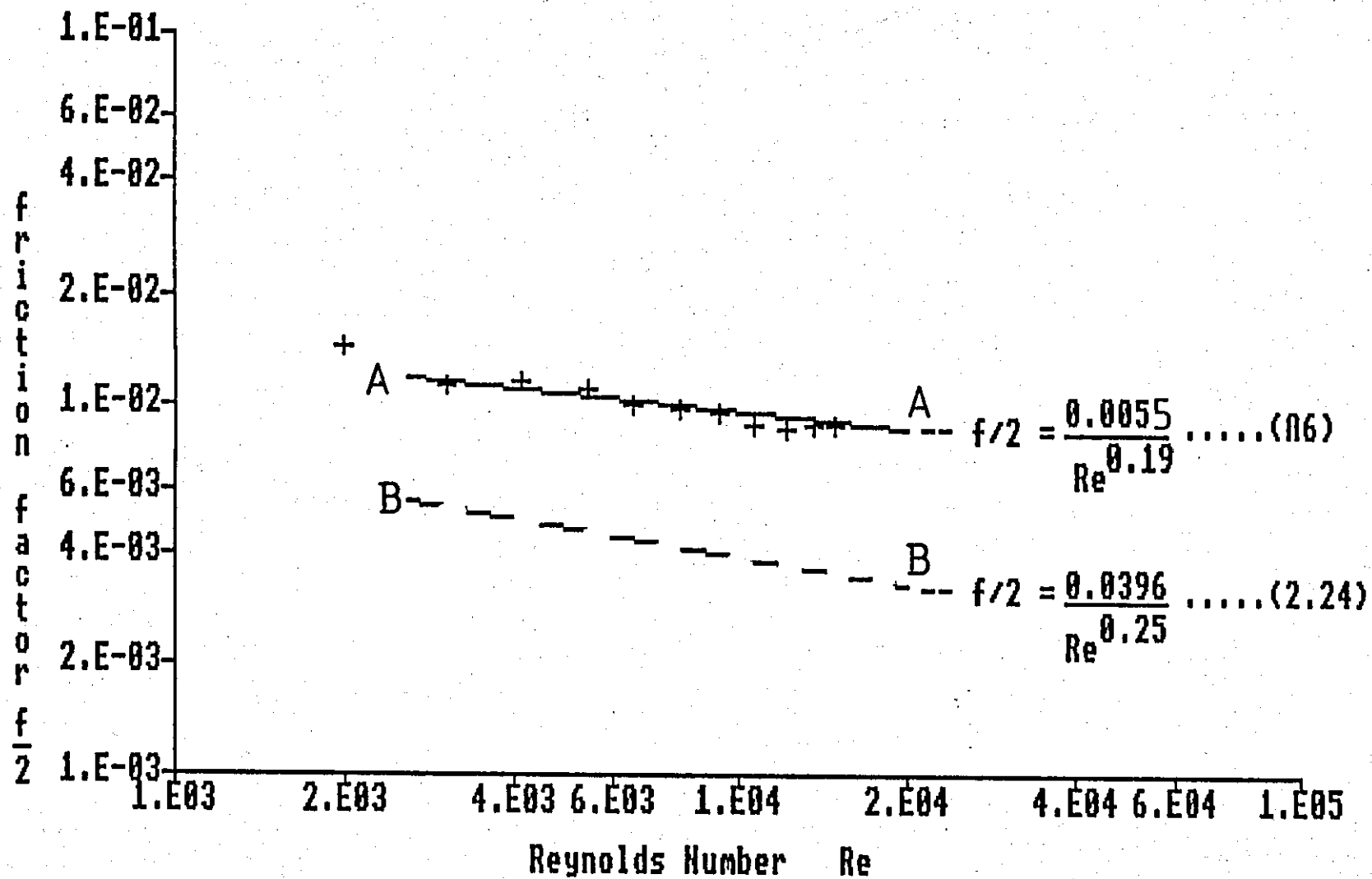


Fig.A12. Correlation of friction factor data in turbulent flow at 60° and 70°C (600g l^{-1} nickel sulphamate solution)

Experimental values of shear stress were slightly greater than predicted from theory.

ii) In turbulent flow, the dimensionless shear stress was correlated with flow rate by the equation:

$$f/2 = \frac{0.055}{Re^{0.19}} \dots\dots(A6)$$

At both 60 and 70°C the correlation between shear stress and flow rate was very similar. However, experiment values of $f/2$ were greater than predicted theoretically (Equation 2.29).

In both laminar and turbulent flow the exponents of the Reynolds number were in reasonable agreement with the theoretical values, but the friction factors and hence the shear stress (and the rate of shear) were greater than expected (see Equation (2.19)). Since the mechanism of the transfer of momentum and mass are similar then high shear rates (or transfer of momentum) may be associated with higher rates of mass transfer. In the following section a comparison is made between the rate of mass transfer of copper ions and the rate of momentum transfer in nickel sulphamate solution.

Comparison of the friction factor correlation with the mass transfer correlation for copper deposition on long electrodes in turbulent flow

The rate of mass transfer to long electrodes may be redefined in terms of the j-factor

$$j = Sh Sc^{-0.333} Re^{-11}$$

Then re-arranging Equation (2.65) it may be shown that:

$$j = 0.023 Re^{-0.2} \dots\dots(A7)$$

This is a corrected form of the Reynolds Analogy and assumes that:

$$j \equiv \phi \equiv \frac{f}{2}$$

The experimental mass transfer data for copper deposition in turbulent flow was recalculated in terms of the j-factor (Table 4.13). In Fig. A13, the j-factors are plotted versus Re on logarithmic co-ordinates.

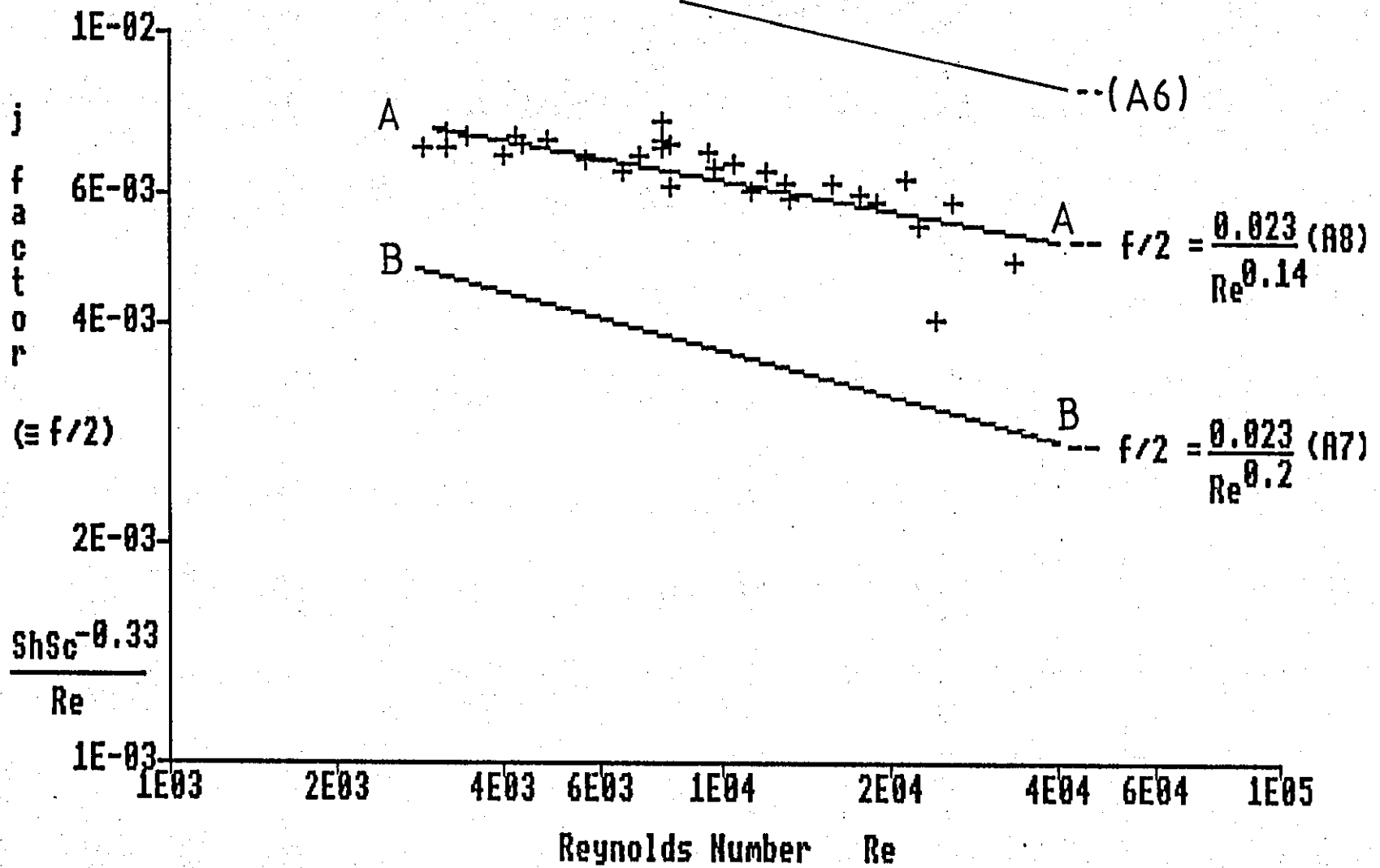


Fig.A13. Correlation of mass transfer data for copper deposition in turbulent flow, recalculated in terms of the j-factor.

Linear regression analysis has shown that the data may be described by the expression:

$$j = 0.023 \text{ Re}^{-0.142} \dots \dots (A8)$$

with a correlation coefficient (r^2) of 0.769. The solution to this equation is shown by the solid line A-A in Fig.A13. The solution to Equation (A7) is also shown, as the broken line B-B. (The experimental value of the constant (0.023) is in very good agreement with the value expected by flat plate theory (Equation 2.28). However, the value of the j-factor was found to be greater than expected. The solution of the experimental friction factor correlation (Equation A6) is also shown for comparison in Fig.A13. Therefore, both friction factor correlation using nickel sulphamate electrolyte and the mass transfer correlation for copper deposition, predict a greater value of $f/2$, and also mass transfer rates, in turbulent flow, than expected from the design equation. (The discrepancy between the results of each method is probably associated with the different 'lengths' over which the measurements were made, i.e. 50cm for friction factor and 10cm for mass transfer coefficients).

b) Estimation of the range of pore diameters

The diameter of pores in nickel foils are probably related to the size of gas bubbles. The average diameters of surface pores and pits was estimated using a quantitative microscope technique. The nickel foil sample examined, was deposited at 60°C, a current density of 0.70 A cm⁻² and a flow rate equivalent to Re~6,600. The electrode was 3.5 equivalent diameter in length. The deposit was 22µm thick.

The nickel foil was removed from the electrode and mounted on a steel backing plate. When examined using the Quantimet microscope the pits and pores appeared black on a grey background. The number of pits/pores and the fractional pore area per point was measured for 81 separate points. Each point represented an area of 0.008mm².

Example calculation

Experimental values of number of pores per point and the fractional pore area per point are given in Table A7. The average area per pore was then calculated from:

$$\text{Fractional average area per pore } A = \frac{\text{fractional pore area per point}}{\text{total number of pores per point}}$$

The average diameter, d, of a pore (assumed to be circular) was calculated from the equation:

$$d = 2\sqrt{\frac{0.008A}{\pi}} \times 10^{-3} \mu\text{m}$$

$$\text{Total number of pores per point} = 6$$

$$\text{Fractional area of pores per point} = 0.0013$$

$$\text{Average area per pore } A = \frac{0.0013}{6}$$

and

$$d = 2\sqrt{\frac{0.008 \times 0.000217}{\pi}} \times 10^{-3}$$

$$d = \underline{1.5\mu\text{m}}$$

No. of pores per point	Fractional area of pores per point	Fractional area of pores A= Total no. of pores	Average diameter of pores d μm
6	0.0013	0.000217	1.5
6	0.0054	0.0009	3.0
11	0.0019	0.000173	1.33
13	0.0030	0.000231	1.53
7	0.0004	0.000057	0.76
10	0.0012	0.00012	1.1
4	0.0005	0.000125	1.1
13	0.0011	0.000085	0.93
3	0.0003	0.0001	1.0
30	0.0175	0.000583	2.4
12	0.0031	0.000258	0.16
7	0.0013	0.000186	1.38
11	0.0020	0.000182	1.4
33	0.0098	0.000297	1.7
19	0.0142	0.000747	2.7
12	0.0022	0.000183	1.37
20	0.0038	0.00019	1.4
4	0.0005	0.000125	1.1
6	0.0039	0.00065	2.0
2	0.0003	0.00015	1.2
8	0.0009	0.000113	1.1
3	0.0002	0.000067	0.83
5	0.0045	0.0009	3
11	0.0093	0.000845	2.9
11	0.0045	0.000409	2.0
40	0.0466	0.001165	3.4
25	0.0585	0.00234	4.8
11	0.0177	0.001609	4.0
10	0.0037	0.00037	1.9

Table A7. The average diameter of pores in nickel foil deposited at 0.7 A cm^{-2} and $\text{Re } 6,750 \pm 100$ (60°C , Cell 2).

/continued

Table A7. continued

No. of pores per point	Fractional area of pores per point	Fractional area of pores A = Total no. of pores	Average diameter of pores d μm
7	0.0038	0.000543	2.4
21	0.0431	0.002052	4.6
17	0.0086	0.000506	2.3
21	0.0374	0.001781	4.3
3	0.0013	0.000433	2.1
27	0.1418	0.00525	7.3
7	0.0010	0.000143	1.2
20	0.0095	0.000475	2.2
56	0.0237	0.000423	2.1
7	0.0054	0.000771	2.8
25	0.0042	0.000168	1.3
13	0.0063	0.000485	2.2
8	0.0212	0.00265	5.2
7	0.0423	0.00604	7.8
10	0.0095	0.00095	3.1
8	0.0035	0.000438	2.1
11	0.0094	0.000855	3.0
31	0.0523	0.001687	4.1
23	0.0031	0.000135	1.2
14	0.0063	0.00045	2.1
20	0.0153	0.000765	2.8
12	0.0066	0.00055	2.4
7	0.0069	0.000986	3.2
18	0.0344	0.001911	4.4
18	0.0857	0.004761	7.0
17	0.0030	0.000176	1.3
10	0.0037	0.00037	1.9
11	0.0042	0.000382	2.0
9	0.0092	0.001022	3.2

/continued

Table A7 continued

No. of pores per point	Fractional area of pores per point	Fractional area of pores A= Total no. of pores	Average diameter of pores d μm
12	0.0268	0.002233	4.8
16	0.0103	0.000644	2.6
27	0.0319	0.001181	3.5
14	0.0039	0.000279	1.7
44	0.2598	0.005905	7.8
19	0.0718	0.003779	6.2
13	0.0019	0.000146	1.2
15	0.0141	0.00094	3.1
16	0.0122	0.000763	2.8
4	0.0029	0.000725	2.7
5	0.0006	0.000120	1.1
6	0.0045	0.00075	2.8
31	0.0164	0.000529	2.3
24	0.0044	0.000183	1.4
10	0.0014	0.00014	1.2
17	0.0416	0.002447	5.0
15	0.0034	0.000227	1.5
12	0.0452	0.003767	6.2
4	0.0009	0.000225	1.5
7	0.0061	0.000359	1.9
10	0.0051	0.00051	2.3
28	0.0461	0.001646	4.1
18	0.0053	0.000294	1.7

The pore distribution

The range of pore diameters was estimated to be from 0.5 to 8 μ m. The total number of pores found in a test area of 0.648 mm² was 1,104. The number of pores per unit area was 1,704 mm⁻².

The calculated average pore diameter was divided into 16 ranges of width 0.5 μ m. The relative frequency of occurrence within each range was then determined. The results are displayed in the form of a histogram in Fig.A14. The graph indicates that pores of diameter 1 to 1.5 μ m occur most frequently (26%). Few pores are found with diameters > 5 μ m, although bubbles of this size are known to exist. It should be noted that pores with sub-micron diameters may be difficult to detect under the microscope.

If it is assumed that the pore diameter is equivalent to the size of the gas bubbles, then a large number of bubbles are formed of a diameter likely to result in significant mass transport enhancement.

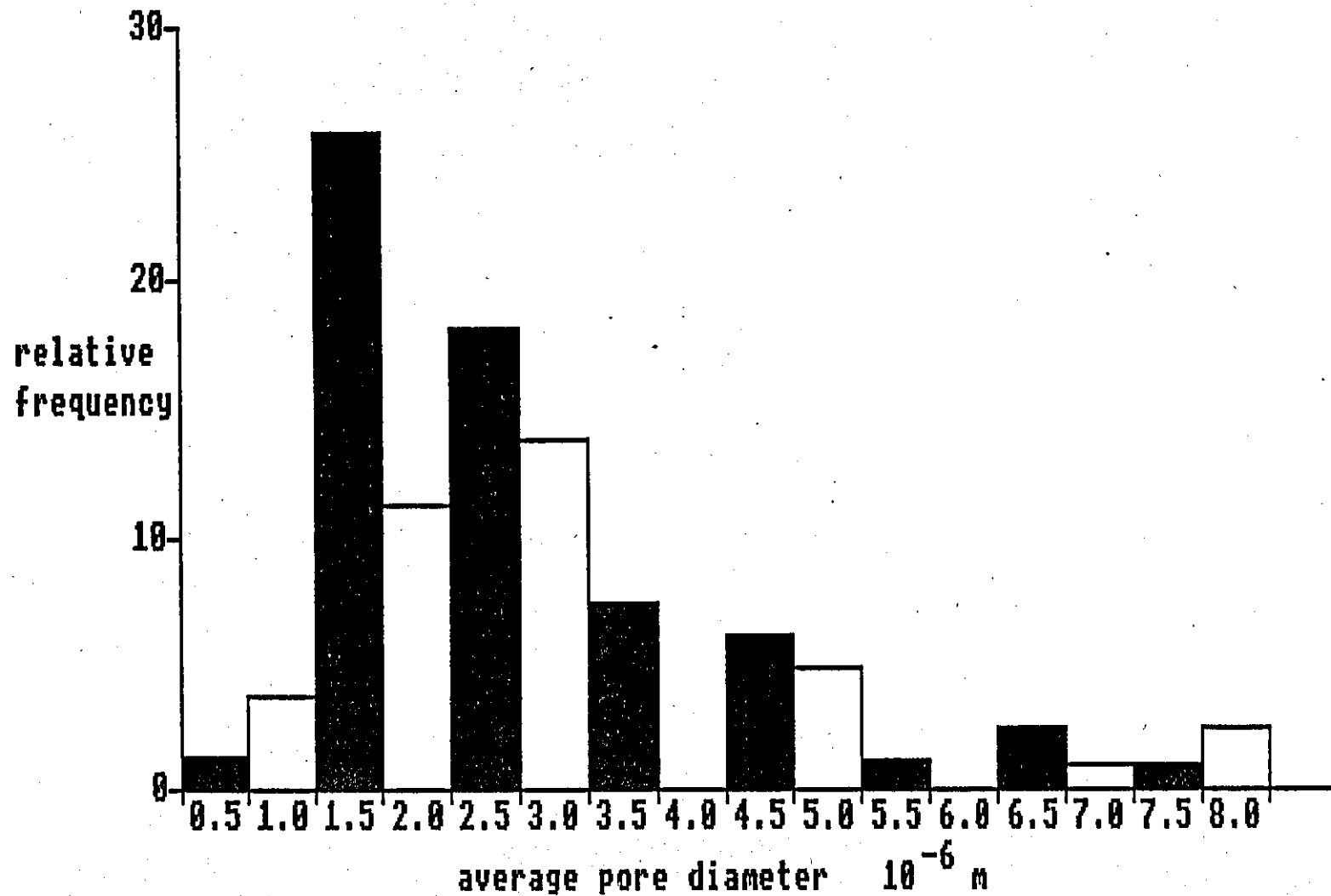


Fig.A14. The relative frequency of occurrence of pores of a given diameter in nickel foil electroformed at 0.7 A cm^{-2} and $\text{Re } 6,750 \pm 100$ (60°C , Cell 2).

